

CP 204

PREDICTION OF AERODYNAMIC LOADING

FDP

AD A 038763

AGARD-CP-204

AGARD-CP-204

# AGARD

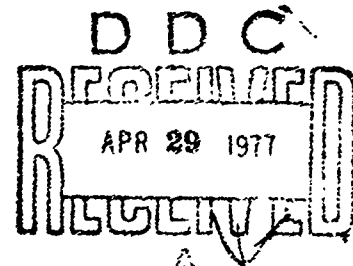
ADVISORY GROUP FOR AEROSPACE RESEARCH & DEVELOPMENT

7 RUE ANCELLE 92200, NEUILLY SUR SEINE FRANCE

AGARD CONFERENCE PROCEEDINGS No. 204

on

## Prediction of Aerodynamic Loading



NORTH ATLANTIC TREATY ORGANIZATION



DISTRIBUTION AND AVAILABILITY  
ON BACK COVER

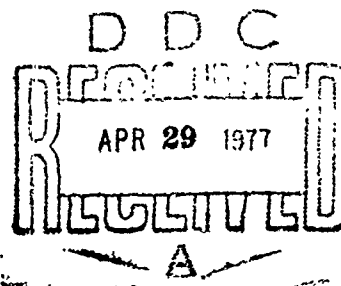
UTION STATEMENT A  
oved for public release;  
Distribution Unlimited

AD No.   
DDC FILE COPY

NORTH ATLANTIC TREATY ORGANIZATION  
ADVISORY GROUP FOR AEROSPACE RESEARCH AND DEVELOPMENT  
(ORGANISATION DU TRAITE DE L'ATLANTIQUE NORD)

9 AGARD Conference Proceedings No. 204

6 PREDICTION OF AERODYNAMIC LOADING



DISTRIBUTION STATEMENT A  
Approved for public release;  
Distribution Unlimited

Papers and Discussions from the Fluid Dynamics Panel Symposium held at  
the NASA Ames Research Center, Moffett Field, California, USA,  
27-29 September, 1976.

400 043

Free

## THE MISSION OF AGARD

The mission of AGARD is to bring together the leading personalities of the NATO nations in the fields of science and technology relating to aerospace for the following purposes:

- Exchanging of scientific and technical information;
- Continuously stimulating advances in the aerospace sciences relevant to strengthening the common defence posture;
- Improving the co-operation among member nations in aerospace research and development;
- Providing scientific and technical advice and assistance to the North Atlantic Military Committee in the field of aerospace research and development;
- Rendering scientific and technical assistance, as requested, to other NATO bodies and to member nations in connection with research and development problems in the aerospace field;
- Providing assistance to member nations for the purpose of increasing their scientific and technical potential;
- Recommending effective ways for the member nations to use their research and development capabilities for the common benefit of the NATO community.

The highest authority within AGARD is the National Delegates Board consisting of officially appointed senior representatives from each member nation. The mission of AGARD is carried out through the Panels which are composed of experts appointed by the National Delegates, the Consultant and Exchange Program and the Aerospace Applications Studies Program. The results of AGARD work are reported to the member nations and the NATO Authorities through the AGARD series of publications of which this is one.

Participation in AGARD activities is by invitation only and is normally limited to citizens of the NATO nations

The content of this publication has been reproduced directly from material supplied by AGARD or the authors.

NTS	White Symbols	<input checked="" type="checkbox"/>
CC	Black Symbols	<input type="checkbox"/>
DATE	1977	<input type="checkbox"/>
JUSTIFICATION		
BY		
DISTRIBUTION/AVAILABILITY CODES		
Dist.	AVAIL. AND A. SYMBOL	
A		

Published February 1977

Copyright © AGARD 1977  
All Rights Reserved

ISBN 92-835-1238-4



Printed by Technical Editing and Reproduction Ltd  
Harford House, 7-9 Charlotte St, London, W1P 1HD

## AGARD FLUID DYNAMICS PANEL

CHAIRMAN: Mr J.P.Hartzuiker  
NLR, Anthony Fokkerweg 2  
Amsterdam 1017, Netherlands

DEPUTY CHAIRMAN: Mr J.Lloyd Jones  
NASA Ames Research Center, Moffett Field  
California 94035, United States

## PROGRAM COMMITTEE MEMBERS

Mr C.L.Bore (Chairman)  
Head of Research  
Hawker Siddeley Aviation Ltd  
Richmond Road, Kingston-Upon-Thames  
Surrey KT2 5QS, UK

Mr P.P.Antonatos  
Chief, Flight Mechanics Division  
Air Force Flight Dynamics Laboratory  
Wright-Patterson Air Force Base  
Ohio 45433, USA

Prof. Dr J.Barche  
DFVLR, Göttingen  
Bunsenstrass 10  
34 Göttingen, Germany

M. l'Ing. de l'Armement A.Coursimault  
Section "Etudes Générales"  
Service Technique de l'Aéronautique  
4 Avenue de la Porte d'Issy  
75996 Paris Armées, France

Dr Ing. U.Sacerdote  
Direttore del Settore Spazio  
Aeritalia - Corse Marche 41  
10146 Torino, Italy

Dr B.M.Spee  
NLR, Anthony Fokkerweg 2  
Amsterdam 1017, Netherlands

FMP. Dipl. Ing. H.Max  
Leiter des Bereichs "Berechnung &  
Versuch", Dornier GmbH  
7990 Friedrichshafen/Bodensee  
Postfach 317, Germany

SMP: Mr N.F.Harpur  
Chief Technician  
BAC Ltd, Filton Division, PO Box 77  
Bristol BS99 7AR, UK

## PANEL EXECUTIVE

Mr Michael C.Fischer

## FOREWORD

This Symposium was primarily concerned with the fluid dynamic aspects of predicting aerodynamic loads on aircraft and their external stores, and in particular those loads that represent difficult design and operating problems. Emphasis was on theoretical and semi-empirical methods for determining the level and distribution of the expected loading, and on assessing and evaluating the accuracy of the predicted values through comparison with available experimental data from windtunnels or from flight tests.

Four sessions were conducted. Experimental and Semi-Empirical; External Stores and Vortex Interactions; Calculation; Quasi-Steady Loads; and Transient or Fluctuating Loads. Following the last session, a Round Table Discussion was conducted, led by session Chairmen, in which all participants were invited to comment. This is reported here.

The Fluid Dynamics Panel expresses its appreciation to the United States National Delegates to AGARD, who were the hosts for this Meeting, and are grateful for the provision of the facilities required to ensure a successful Meeting.



## CONTENTS

### AGARD FLUID DYNAMICS PANEL OFFICERS, PROGRAM COMMITTEE AND FOREWORD

Page

iii

Reference

#### SESSION I – EXPERIMENTAL AND SEMI-EMPIRICAL

##### EXAMPLES OF LOAD-PREDICTION DIFFICULTIES

by C.L.Boer

1

##### SECTIONAL LOADS TECHNIQUE

by H.P.Franz and B.F.wald

2

##### PREDICTION OF AERODYNAMIC LOADINGS ON THE LEADING-EDGE SLATS OF THE FOKKER F.28 AIRLINER

by P. de Boer

3

##### PREDICTION OF AERODYNAMIC EFFECTS OF SPOILERS ON WINGS

by G.V.Parkinson and P.Tam Doo

4

#### SESSION II – EXTERNAL STORES AND VORTEX INTERACTIONS

##### A TECHNIQUE FOR PREDICTING EXTERNAL STORE AERODYNAMIC LOADS

by A.R.Rudnicki, Jr, E.C.Waggoner, Jr and R.D.Gallagher

5

##### PREDICTION OF EXTERNAL-STORES AND TIP-TANK LOADS ON WING-FUSELAGE CONFIGURATIONS

by S.R.Ahmed

6

##### COMPARISON OF PREDICTED AERODYNAMIC LOADING WITH FLIGHT TEST RESULTS

by J.Kloos

7

##### PREDICTION OF AERODYNAMIC LOADS ON CLOSE-COUPLED CANARD CONFIGURATIONS

by R.W.Hale and D.E.Ordway

This paper not included in this report.

~~8~~

##### WING-VORTEX LIFT AT HIGH ANGLES OF ATTACK

by R.P.White, I.

9

##### VORTEX/JET/WING INTERACTION BY VISCOUS NUMERICAL ANALYSIS

by R.M.Scruggs, J.F.Nash and C.J.Dixon

10

#### SESSION III – CALCULATIONS, QUASI-STEADY LOADS

##### COMPARISONS OF THEORETICAL AND EXPERIMENTAL PRESSURE DISTRIBUTIONS ON AN ARROW-WING CONFIGURATION AT SUBSONIC, TRANSONIC AND SUPERSONIC SPEEDS

by M.E.Manro, P.J.Bobbitt and J.T.Rogers

11

##### THREE DIMENSIONAL SUPERSONIC FLOW ABOUT SLICED BODIES

by G.Colasurdo and M.Pandolfi

12

##### A METHOD FOR ESTIMATING THE LOADING DISTRIBUTION ON LONG SLENDER BODIES OF REVOLUTION AT HIGH ANGLES OF ATTACK IN INCOMPRESSIBLE FLOW

by E.Atraghji

13

##### ASSESSMENT OF EXISTING ANALYTIC METHODS FOR PREDICTION OF HIGH ANGLE-OF-ATTACK LOADS ON DELTA WINGS AT SUPERSONIC SPEEDS

by E.J.Landrum and J.C.Townsend

14

**ON THE CALCULATION OF THE PRESSURE DISTRIBUTION OF WING-BODY  
COMBINATIONS IN THE NON-LINEAR ANGLE OF ATTACK RANGE**

by G.Gregor'ou

15

**PREDICTION METHOD FOR STEADY AERODYNAMIC LOADING ON  
AIRFOILS WITH SEPARATED TRANSONIC FLOW**

by P.G.Thiede

16

**PRESSURE DISTRIBUTIONS FOR A SWEEP WING BODY CONFIGURATION  
OBTAINED FROM COUPLING TRANSONIC POTENTIAL FLOW CALCULATIONS  
AND BOUNDARY LAYER CALCULATIONS**

by S.G.Hedman

17

**AERODYNAMIC LOADS NEAR CRANKS, APEXES AND TIPS OF THIN LIFTING  
WINGS IN INCOMPRESSIBLE FLOW**

by R.T.Medan

18

**VORTEX LATTICE APPROACH FOR COMPUTING OVERALL FORCES ON  
V/STOL CONFIGURATIONS**

by C.W.Lucchi and W.Schmidt

19

**SESSION IV - TRANSIENT OR FLUCTUATING LOADS**

**AIRCRAFT MANEUVERS AND DYNAMIC PHENOMENA RESULTING IN  
RAPID CHANGES OF LOAD DISTRIBUTIONS OR/AND FLUCTUATING SEPARATION**

by D.B.Benepe, Sr.

20

**THE THEORETICAL PREDICTION OF STEADY AND UNSTEADY AERODYNAMIC  
LOADING ON ARBITRARY BODIES IN SUPERSONIC FLOW**

by D.L.Woodcock

21

**THE PREDICTION OF BUFFET ONSET AND LIGHT BUFFET BY MEANS OF  
COMPUTATIONAL METHODS**

by G.Redeker and H.-J.Proksch

22

**PRELIMINARY EVALUATION OF A TECHNIQUE FOR PREDICTING BUFFET  
LOADS IN FLIGHT FROM WIND-TUNNEL MEASUREMENTS ON MODELS OF  
CONVENTIONAL CONSTRUCTION**

by G.F.Butler and G.R.Spavins

23

**QUASI-STEADY AND TRANSIENT DYNAMIC STALL CHARACTERISTICS**

by L.E.Ericsson and J.P.Reding

24

**THEORY OF WING SPAN LOADING INSTABILITIES NEAR STALL**

by E.S.Levinsky

25

**DYNAMIC LOADING ON AN AIRFOIL DUE TO A GROWING SEPARATED  
REGION**

by J.D.Lang and M.S.Francis

26

**PRESSIONS SUR UNE CARENE DE PRISE D'AIR A LEVRE MINCE FONCTIONNANT  
EN SUBSONIQUE A DEBIT REDUIT**

par G.Laruelle et P.Levart

27

**ROUND TABLE DISCUSSION**

RTD

## EXAMPLES OF LOAD-PREDICTION DIFFICULTIES

C. L. Bore

Hawker Siddeley Aviation Ltd., Kingston, Surrey, England.

## SUMMARY

This paper discusses some aspects of load-prediction techniques which still need improvement, in an attempt to counter-balance the success stories that are usually the main subject of symposia.

## INTRODUCTION

It is human nature to be proud of one's positive achievements, and this pride has often spurred people to accomplishments far beyond their nominal duties. We will hear of some such feats in this symposium, in relation to load prediction. So it happens that we become accustomed to hear parades of triumphs, which may leave some of us wondering if there is any scope left to devise one more triumph (even a little one?) before the field is completely worked out. Perhaps this paper may bring some solace in this respect!

However, although vanity is a tremendous incentive to worthy achievements (and consequently it is a substantial virtue) the engineers in charge of industrial enterprises should not regard glamorous challenges as the "raison d'être" of industry. Some glamorous challenges may not be worthwhile, and some worthwhile challenges may not be glamorous. So it can be useful, occasionally, to consider afresh the "aim of the game" and list the more prominent difficulties hindering economical achievement of the aims, so that we may devise ways round or through those difficulties. That is the main aim of this paper. With typical modesty, I will claim no responsibility for the troubles discussed.

## LOAD PREDICTION

Reasons

There are basic (by three reasons for predicting the loads on aircraft.

1. Performance :

To design so that the aircraft will carry its required payload over the specified range in given time. Few loads in this category cause much trouble, and in any case drag and lift are topics best dealt with in their own right.

2. Flying Qualities :

To ensure that the manoeuvrability shall be satisfactory at all relevant conditions. In this category the loads arising from undemanding manoeuvres (such as wing rocking, nose alices and other departures) are difficult to predict, and fin loads can be particularly troublesome.

3. Structural Integrity

To ensure that the structure of the airframe will stay intact until the scheduled servicing. In this category trouble arises from problems of predicting the distribution of pressure, and the magnitude and frequency of repeated or fluctuating loads.

Underlying all these technical objectives is the fundamental economic aim of producing an adequate aircraft at the least cost. Because modifications rapidly rocket in expense as the manufacturing programme proceeds, it generally follows that the best stage to predict loads is the earliest.

## DIFFICULT CASES

A. Flying Qualities

Most of the problems in this category arise from either post-buffet manoeuvres, local boundary-layer separations, from transient manoeuvres, or from the difficulties of predicting fin loads.

## 1. Post-buffet manoeuvres

Buffeting is usually associated with fluctuating separation of the wing boundary layer, over a substantial area. The pressure fluctuates and consequently fluctuating forces are experienced, superimposed on the time-average load, and thereby posing fatigue problems. If the forces are not symmetrical, then wing rocking motions or yawing motions may develop, which can generate unsymmetrical tailplane loads and fin loads which, in some cases, are not predictable even with knowledge of the motion and the quasi-steady aerodynamic coefficients.

It seems likely that the unsteady boundary-layer separations generate unsteady wake flow fields which substantially affect the tail (as well as the wing). It is known that in some cases (e.g. refs. 1, 2, 3) the conditions under which rocking occurred, and the magnitude of the motion in flight, correlated with the fluctuating rolling moments measured (at constant Mach number and incidence) on a wind-tunnel model of normal stiffness (see figs. 1, 2). Thus it is clear that such rolling moments are not a consequence of the motion of the aircraft, but must be regarded as fluctuating forces that cause the motion. Such cases have been experienced in what would otherwise be the light-buffet to medium-buffet band.

rolling moment

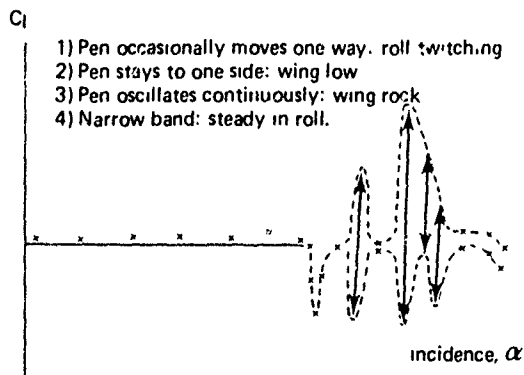


Fig. 1. Interpretation of on-line unsteady rolling moment charts.

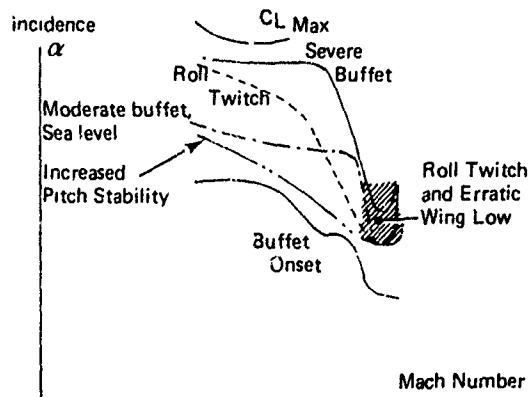


Fig. 2. Flight control boundaries as indicated by wind tunnel tests -- confirmed in flight.

On the other hand, when the wing flow is largely separated at high incidence, it is possible for coupled rolling and yawing motions (Dutch roll) to build up, which are explainable in terms of the stability coefficients. More research is needed on the former type of undemanding manoeuvre.

In some places on the wing, the pressure fluctuations due to flow separation can cause major fluctuations in the loads on such components as flaps and ailerons with their actuator rods, and even outer wing panels and rear spar reaction lugs. The flap loads are less easily predicted in less familiar circumstances, such as intermediate positions (on civil aircraft) or when lowered  $10^\circ$  or  $15^\circ$  for high-speed manoeuvring (on fighters). The fatigue damage is usually associated with large numbers of moderate loads (which may occur typically at frequencies from 10 to 50 Hertz).

## 2. Manoeuvres not readily predicted in number or magnitude

The number and magnitude of loads can be specified plausibly by estimating the proportions of various types of sortie expected - but the differences of fatigue load spectrum thus predicted can be quite substantial (fig. 3). Even if the spectrum of sorties and manoeuvres is predicted correctly, some of the uncertainties discussed previously still remain: fluctuating loads during buffet, fluctuating centre of pressure and so on.

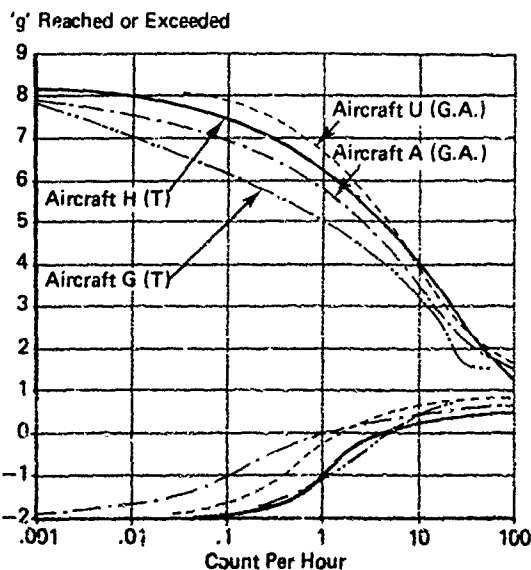


Fig. 3. Normal force spectra for two ground-attack aircraft and two trainers.

However, there are further problems, even for specified manoeuvres. In rapid pull-ups, for example, the transient tailplane load is not well-defined, and in rapid pull-ups into buffet, it is suspected that the maximum time-average load may exceed the value given by the downward-curving lift-curve (which corresponds, of course, with the established time-average load).

Fin loads can be very uncertain for various reasons. Since my firm first started developing and fitting fatigue-life gauges (4, 5) it has been shown that different aircraft of given type on the same squadron can suffer very different fatigue loading. On the famous "Red Arrows" formation team of Gnats, for example, it was found that the aircraft "in the box" of the formation suffered much more fatigue loading of the fin (fig. 4). In another case, it was found that fatigue failure of a fin was

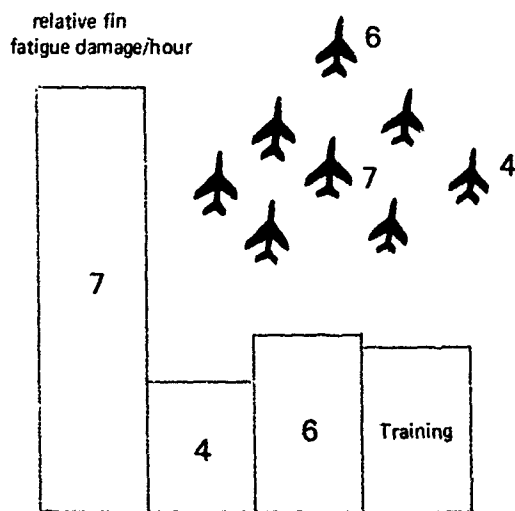


Fig. 4. Relative fatigue damage to fin according to formation duty

accurately explained by the heavy-footed rudder control of a particular pilot ! But it is one matter to explain a failure after it has happened, and quite a different matter to predict the whole spectrum of loads at the drawing-board stage ! Nevertheless, systematic measuring of loads in flight should be part of a programme to achieve a better capability of prediction.

The difficulties of predicting fin loads do not end there, for if the model fuselage is distorted to accommodate a sting mounting, the flow over the rear fuselage can be so distorted that the measured fin effectiveness bears little resemblance to flight values, and rudders are rarely tested in the tunnel. Furthermore, boundary layer separations arising from the fuselage or fuselage-mounted air intakes may not be representative, and any jet-efflux effects may not be represented properly on the wind-tunnel model. Moreover, it was remarked earlier that in some undemanding wing-rock manoeuvres, even full knowledge of the motion of the aircraft and the quasi-steady derivatives did not afford an adequate link between calculation and flight test.

## B. Structural Integrity

### 1. Store Loads

We will hear later on about some fine and painstaking work on how to predict the loads on external stores, but in the U.K. at present the feeling is that any large store of unusual shape needs special high-speed wind-tunnel tests. Remarkably large differences of load have occurred for given stores carried on apparently rather similar aircraft (fig. 5). How much of these differences are due to fundamental differences and how much due to details and tunnel techniques is open to speculation.

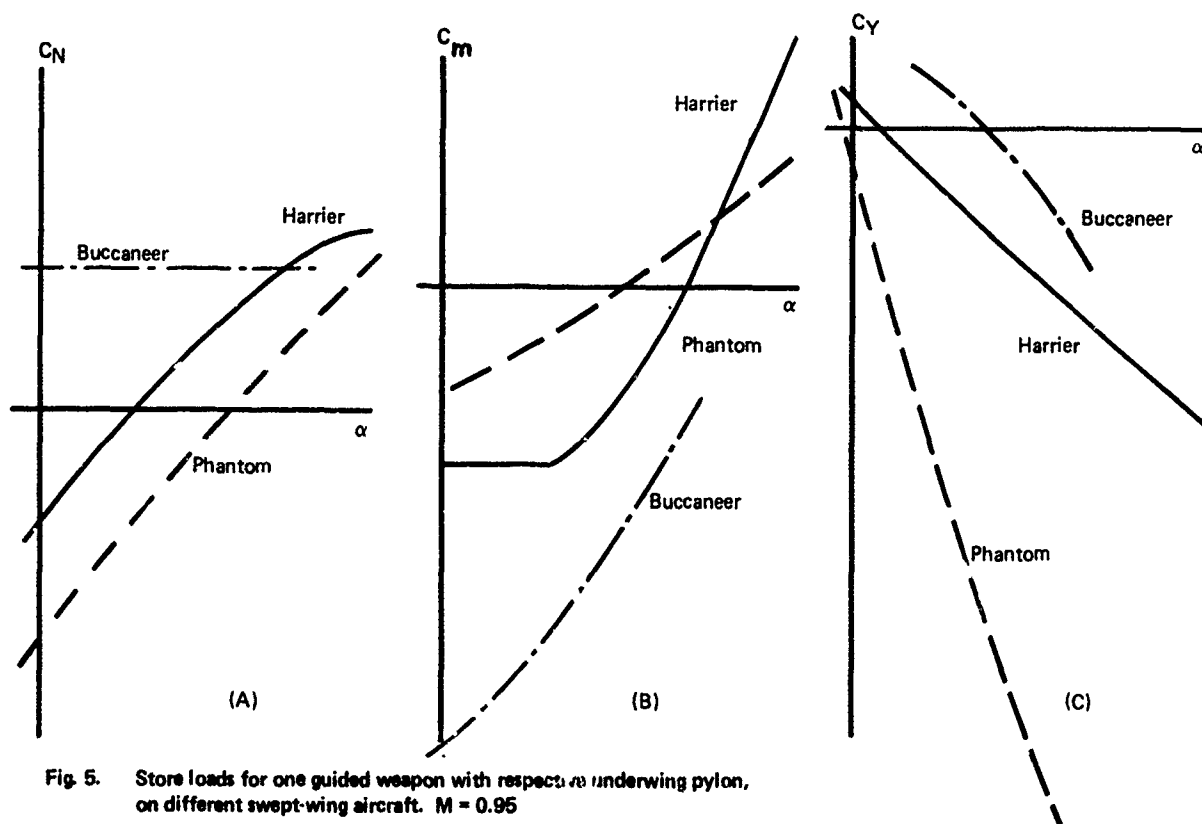


Fig. 5. Store loads for one guided weapon with respect to underwing pylon, on different swept-wing aircraft.  $M = 0.95$

Similarly, in arrays of closely-spaced stores, the loads arising on stores at different positions can be substantially affected by interferences (fig. 6).

Sometimes the supercritical flow that develops at the back of large stores under wings has induced strong shock-waves and boundary-layer separations on the lower surface of the wing, that have caused skin cracking on the ailerons. The concave undersurfaces now contemplated for wings with substantial rear loading may re-awaken this problem.

In one case, the nose of a twin-store carrier bent in high-speed flight, partly because it deflected under load and thus became even more heavily loaded.

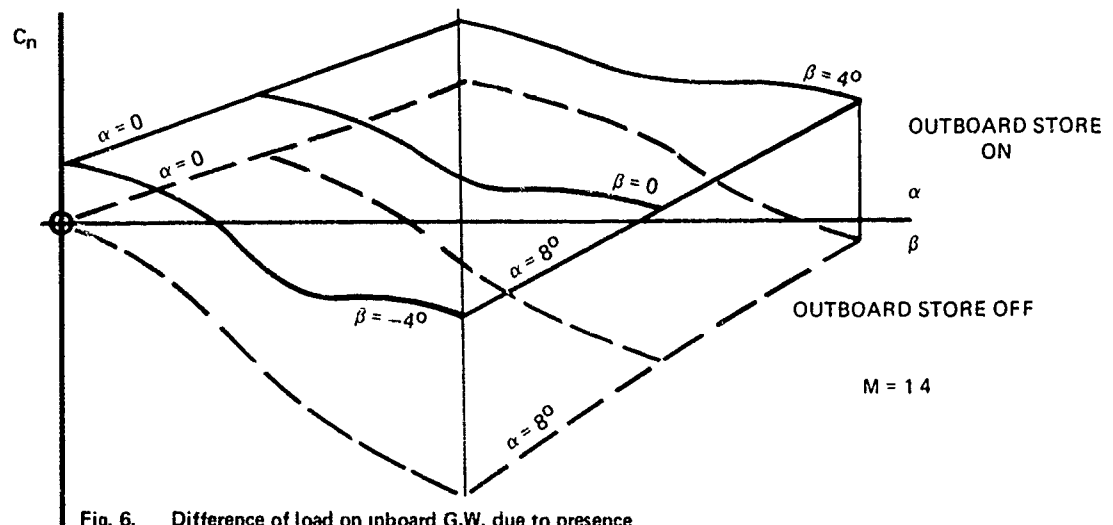


Fig. 6. Difference of load on inboard G.W. due to presence or absence of G.W. on outer pylon. (unpublished RAE report).

## 2. Proximity of Jets

Jet effluxes passing close to tailplanes can cause both stability changes and large unsteady forces, and similarly fins on stores can be affected. If the efflux passes very close to fuselage or other skin panels it is possible to get cracking of the skins under the intense pressure fluctuations.

## 3. Panel or Bay Venting

In a number of circumstances, the effective structural pressure loading depends on the level of pressure that pertains to the "back" of the panel skin. Often, that pressure arises as an intermediate pressure consequent upon all the various leakage flows into and out of the bay concerned, and clearly this may be transient with a substantial time constant. It is possible to provide a vent deliberately placed to minimise the loading, but the problem of transient conditions remains. Next, a major problem involving bay volume venting and internal flow aerodynamics will be described.

## 4. Air Intake Surge Loading (Concorde Example).

Engine surge causes strong pressure waves to travel up the air intake ducts, which act to slam any auxiliary intake doors forcefully, and which can impose major transient loads on the main structure of the duct and on such components as variable - angle inlet ramps. Indeed, in the case of Concorde it was the surge loadings which dictated the design of the auxiliary inlets as single thick vanes with dampers, rather than the more efficient multiple-vane design.

The case described (ref. 6) preoccupied the Concorde aerodynamics/structures departments over the decade 1963-73, and involved highly instrumented flight testing of prototype and preproduction aircraft and the flying engine testbed, in addition to full scale ground tests and various small scale model tests. No pre-existing methods were able to predict the severity of the transient loads eventually measured in flight.

The air intake structure for Concorde (fig. 7) had to be defined well in advance of reliable engine surge data for the correct engine, and at that stage it was necessary to rely on a little data produced by overfueling an earlier Olympus engine, on the Vulcan flying test-bed. The scarcity of data and inadequate understanding at that time led to a significant underestimate of the surge pressure pulse, which was remedied when full scale engine tests in the NGTE Cell 4 and flight test data became available.

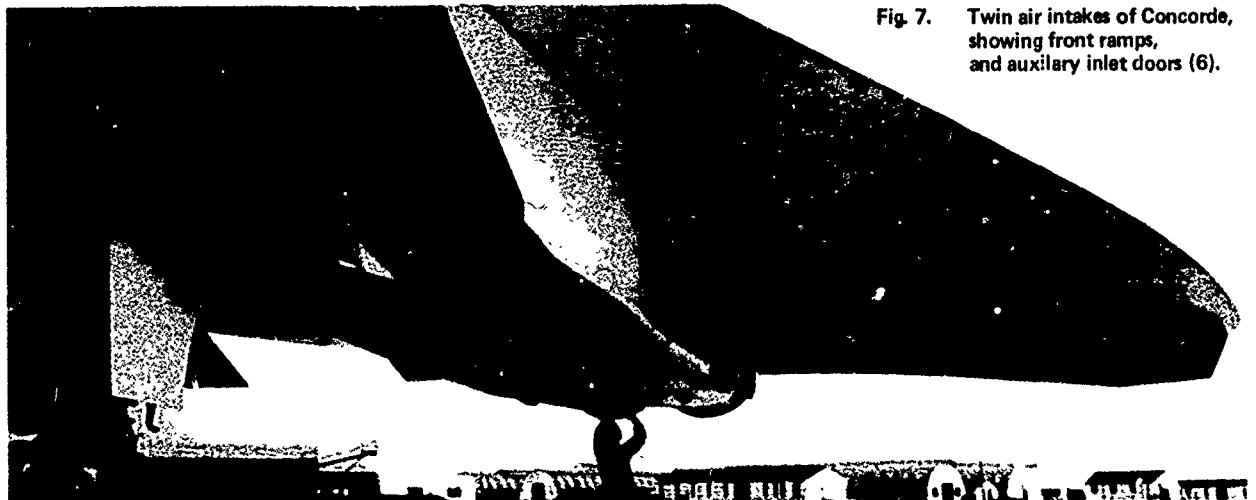


Fig. 7. Twin air intakes of Concorde, showing front ramps, and auxiliary inlet doors (6).

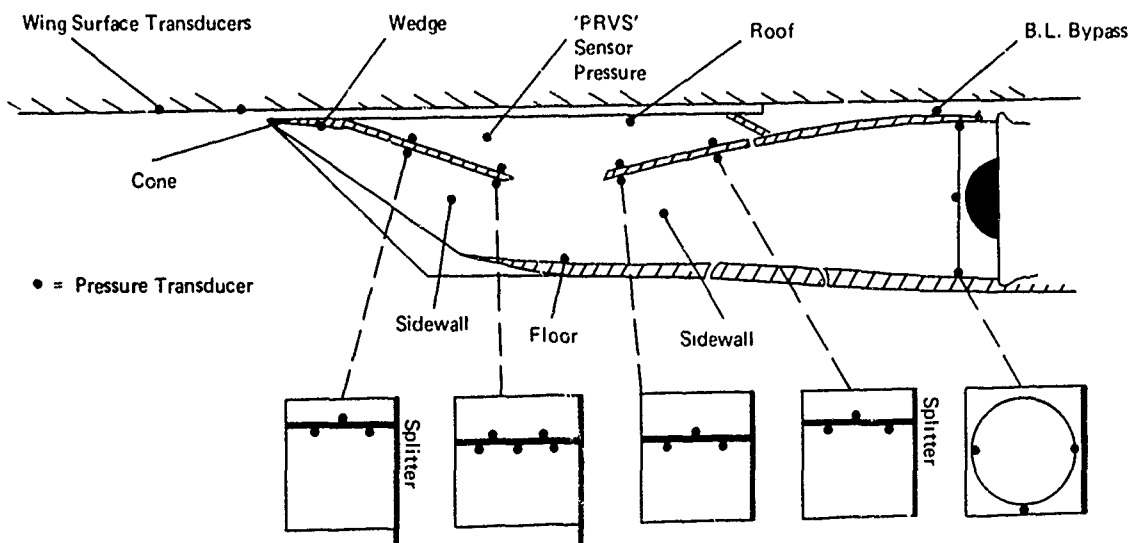


Fig. 8. Instrumentation in Concorde intakes, for surge loading investigation.

An empirical relationship was eventually derived for the flight engines which may be useful for other straight jets but which, it is felt, may not be appropriate for bypass engines (fig. 9). Perhaps some pooling of information from various sources would contribute to a wider solution of the basic problem.

The first attempt to understand the propagation of the surge pulse used a one-tenth scale model with a cyclic valve. This valve matched the engine surge pulse in terms of waveform and frequency, but it was incapable of producing more than 100% flow stoppage - whereas a surging engine produces substantial reversal of the flow. Consequently the results from these tests needed interpretation to full-scale, and the predictions were sometimes optimistic. About two years later, the results of full-scale engine tests, in Cell 4b, became available (only a year before prototype flying) and even these did not reveal the whole story that was subsequently found by prototype flight testing.

During flight 122 of the prototype, the No. 4 engine lost its forward intake ramp as a result of a high-power interactive surge at Mach 2.0. The immediate cause of this surge was understood: it was associated with a transient overspeeding of the No. 3 engine when reheat was cancelled, causing this engine to surge - and the aerodynamic interaction in turn caused No. 4 engine to surge.

Careful examination of the damage and the flight recordings of pressure, strain and ramp position revealed the precise sequence of failure. There was nothing new about the initial surge: the new and hitherto unsuspected factor was the possibility that interaction effects could lead to differential pressures on the front ramps significantly higher than had been measured on tests of isolated intakes. The consequence of that experience was an intensive series of flight tests during which surges were deliberately induced at high Mach number and power, while the intake loads were measured in great detail (fig. 8). In retrospect, it is possible to isolate the interactive effect for Concorde, but it remains unclear how such effects could be predicted at an early stage for other aircraft.

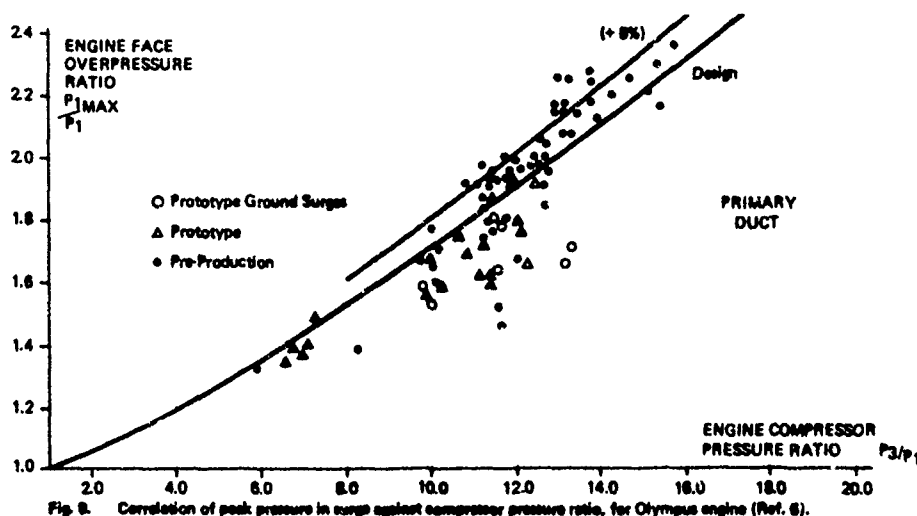


Fig. 9. Correlation of peak pressure in surge against compressor pressure ratio, for Olympus engine (Ref. 6).

Simple theoretical solutions were used as part of the design process, but they were found to be unreliable in predicting the peak pressure loadings in at least three key areas: the pressure acting in the ramp void, which largely determines the link loads; the transient loads imposed on the ramps, and the loads tending to slam the auxiliary inlet doors during low-speed surges. With current knowledge it is believed possible to obtain useful solutions using time-dependent finite-volume methods, and such methods are under development at Filton.

## CONCLUDING REMARKS

This interactive engine surge example of a load-prediction difficulty serves to illustrate how a novel design feature may cause major new load-prediction problems, and entail a great deal of expense if the methods available at the drawing-board stage prove to be inadequate.

Of the problems discussed earlier, many involve transient loadings and many repetitions of loading. Loads due to pressure fluctuations under separated boundary-layer conditions are difficult, and so are the loads arising from uncommanded manoeuvres. Other cases which are difficult to predict include those where the control actions of pilots dominate the fatigue load spectrum, and various aspects of fin loads.

It is hoped that these discussions will help to reassure aerodynamic researchers that there is still work to be done in this field, despite all the triumphs we shall hear about in the next few days.

I wish to thank my colleagues in the U.K. aircraft industry for their helpful suggestions, notably T. W. Frown (of B.A.C. Filton) for the Concorde surge problem, - and also S. F. Stapleton, E. J. Dalley, A. Peacock, and J. W. H. Thomas (of three different H.S.A. design teams), and Mike Salisbury of B.A.C. Weybridge.

## REFERENCES

1. C. L. Bore                    The Hawker Siddeley Harrier : Chapter 6; Aerodynamic Design - Wing.  
Reprint from Aircraft Engineering, Dec. 1969 - April 1970 issues, Bunhill Pubns.
2. C. L. Bore                    Post-stall aerodynamics of the "Harrier G.R.1"; in Fluid Dynamics of Aircraft Stalling,  
AGARD-CP-102, 1972
3. S. F. Stapleton &        Comments on some windtunnel and flight experience of the post-buffet behaviour  
B. V. Pegram                of the Harrier aircraft;  
in Flight/Ground Testing Facilities Correlation, AGARD-CP-187, 1975.
4. E. J. Blackburn            A strain multiplier for fatigue sensors.    Strain, Vol. 4, no. 4, Oct. 1968.  
W. R. Symmons
5. E. J. Blackburn            Direct measurement of fatigue damage in aircraft.    Strain, vol. 7, no. 1, Jan. 1971.
6. T. W. Brown                Intake surge loads on Concorde.    Unpublished note, BAC Filton, 18 June 1976.



## SECTIONAL LOADS TECHNIQUE

## Part 1: TEST TECHNIQUE

H.P. Franz \*

Vereinigte Flugtechnische Werke-Fokker GmbH, Bremen, West Germany

## Part 2: TEST RESULTS

B. Ewald \*

Vereinigte Flugtechnische Werke-Fokker GmbH, Bremen, West-Germany

## SUMMARY

During the development of the VSTOL Fighter VAK 191 B wind tunnel measurements were carried out on some different forward fuselage configurations.

In comparison with the wing alone characteristic the configuration presented a very favorable wing-body interference effect. Most of this effect was lost with a shorter forward fuselage.

These results finally led to the invention of the Sectional Load Model Technique described in part 1 of this paper, since the well known technique of pressure distribution measurement technique was too expensive for tests on various configurations. With this technique the aerodynamic loads of nearly arbitrarily split sections of the model are measured separately by means of strain gage balances.

This technique proved very effective in several test programs because the loads on several exchangeable parts could be measured directly together with the total aerodynamic forces on the model in the wind tunnel.

The following configurations have been tested:

- Original VAK 191 B configuration
- Derivatives of VAK 191 B forward fuselage configuration
  - forward fuselage of less width
  - short forward fuselage
- VAK 191 B fuselage with a larger wing in three different longitudinal positions and additional small forward fuselage strakes
- Schematic model of fighter configuration with large wing and strake

In all cases the Sectional Load Model Technique allowed the evaluation of load distribution along the fuselage and detailed information on the wing body interference.

In the case of the original VAK 191 B configuration it was found that the wing induces a strong additional lift on the fuselage. It mainly acts on its central part and is insensitive to the configuration of the forward fuselage.

A much larger additional lift is induced by the fuselage on the wing and this lift is very sensitive to the forward fuselage length and width. The non-linearity of the fuselage-alone lift indicates the existence of fuselage generated vortices which are responsible for the favorable fuselage-wing interference.

It is well known that the advantageous lift characteristics of strake configurations (like the YF 16 e.g.) are the results of strong vortices generated by the strake leading edge. A sectional load test was carried out on such a model. Herein the strake was mounted on a separate internal balance, making an exceptionally detailed analysis of the body-strake-wing load interference possible.

It is shown that the interference mechanism of the strake configuration is not unsimilar to the behavior of the VAK 191 B configuration generated by its forward fuselage with intakes at the fuselage sides and that in this sense the VAK configuration is a forerunner of the modern strake configuration

## NOTATION

## Symbols:

A	m <sup>2</sup>	area
b	m	span
E	kg/mm <sup>2</sup>	module of elasticity
f	mm	bending of a balance beam
p	kg/m <sup>2</sup>	static pressure
q	kg/m <sup>2</sup>	dynamic pressure
D	kg	drag
L	kg	lift
M	kg m	pitching moment
N	kg	normal force
T	kg	axial force
$\alpha$	°	angle of attack

## Subscripts

$\infty$	free stream conditions
i	internal
B	body
W	wing
(B)	in presence of the body
(W)	in presence of the wing
B1, B2 ... B5	body sections
St	strake

## Coefficients:

$C_D, c_D$	drag coefficient (total, sectional)	$c_{LB2}, c_{LB2(W)} \dots$	<div>sectional loads</div> <div>(model parts)</div>
$C_L, c_L$	lift coefficient	$c_{MW}, c_{MB4} \dots$	
$C_M, c_M$	pitching moment coefficient		
$C_N, c_N$	normal force coefficient	$\Delta c_{LB(W)} \dots$	<div>overall interferences</div> <div>(total model)</div>
$C_T, c_T$	axial force coefficient	$\Delta c_{MW(B)} \dots$	
$C_L, c_{LB(W)} \dots$	<div>overall loads</div> <div>(total model)</div>	$\Delta c_{LB3(W)} \dots$	<div>sectional interferences</div> <div>(model parts)</div>
$C_M, c_{MW(B)} \dots$		$\Delta c_{MW(B)} \dots$	

## Part 1: TEST TECHNIQUE

## 1.1 INTRODUCTION

In the early sixties the VAK 191 B was designed as a part of the VTOL/VSTOL activities in Europe (FIG 1). The VAK 191 B is a transonic fighter of the lift-lift/cruise category (2 lift engines and 1 lift/cruise engine), fitted with a high-wing of small aspect ratio, thin profile section, large sweep and large wing load.

It is commonly known that for this wing arrangement the profile does not play a significant part; in this case the flow is for the most determined by the planform. The influence of the slender wing planform does, however, include the influence of the fuselage on maximum lift. This influence increases the smaller the wing span is in comparison to fuselage width and the larger the fuselage is in comparison to the wing chord. The addition of the lift on the wing alone and the lift on the fuselage nowhere nearly yields the lift actually measured for the wing-fuselage combination with large angles of attack. This means that strong lift interference forces must still be active.

The conventional method used for an analysis of the interference influences of the individual aircraft components is the pressure distribution measuring technique. The obvious advantage of this method is that the pressure at each point is known. The high costs for the model, the small variation potential, the necessary density of the measuring points and the extremely large accumulation of test data are on the other hand negative aspects. Furthermore, the pressure data must be reduced and integrated for valuation of the final test result.

A new experimental technique which we call the "Sectional Loads Technique" was introduced to reduce the extent of these disadvantages (FIG 2).

The basic principle of this method is that individual sections are assembled to form that structural member which is to be examined, e.g. the fuselage. These sections are independently supported on a central beam via internal strain gage balances. Therefore the aerodynamic loads on these sections can be measured separately. The overall loads are synchronously measured by the external wind tunnel balance via the central beam to which e.g. the wing and tail planes can also be connected. (FIG 3)

The particular advantage of this test method is the direct measurement of integral loads on easily exchangeable, preselected parts.

One disadvantage of the Sectional Loads Technique might be that minute gaps are required between the components so as not to disturb the contour and air flow course, although more flexible balances would be of value to have more sensitive balances. Unfortunately, a higher flexibility effects larger gaps between the parts. Furthermore, an air flow separation, in particular at the tail section, can cause the associated part to oscillate. These oscillations have to be damped, separately. Finally, the pressure which is acting in the interior of the model due to the gaps must be measured and used for corrections.

The procedure of the Sectional Loads Technique as described above, has in the meantime been successfully applied in various stages of extension on various model configurations. The initial breakdown of the basic fuselage of the VAK into five sections with five strain gage balances, each containing the three components. normal force, pitching moment and axial force, has in the course of time been extended and altered as follows: four fuselage sections on four balances each with five components. normal force, pitching moment, axial force, side force and yawing moment — as well as a separate pair of strakes on a special four component strain gage balance (without axial force).

The largely universal design of the model skeleton and of the strain gage balance ensure that this test technique can be easily applied.

The contour shells of the selected structural members of the model can be relatively easily manufactured, modified and measured.

There is also enough space for the ducting lines of boundary layer control, span-wise blowing, engine realization etc. in the hollow interior of the model fuselage.

## 1.2 CONCEPT

Extremely large interferences were seen to occur between the fuselage and the wing of the VAK 191 B, and this gave rise to the wish for a more detailed analysis of the flow mechanism. Modifications on the forward fuselage section were to serve as geometrical aids in changing the length/width ratio of the forward fuselage; the slender wing, however, staying the same. An investigation of the aerodynamic loads on these exchangeable fuselage segments seemed to be an obvious way. The concept led to the following model design: A model skeleton is connected to the external wind tunnel balance by means of a conventional wire suspension in wing tips and fuselage nose. The skeleton consists of a wing spar and a rigid fuselage longeron. The almost arbitrarily split components — such as the fuselage "slices", wing sections, strakes, fair surfaces and external loads — are then individually connected to the skeleton via separate strain gage balances.

The model set-up as described here and the measuring equipment with internal and external balances are used to establish the interference pattern taking the wing-body lift coefficients as an example (FIG 4). For other forces and moments and for configurations with tails, strakes and external loads the interference pattern would be similar, of course.

The three most important interferences:

$$\Delta C_L = C_{LWB} - (C_{LW} + C_{LB})$$

$$\Delta C_{LB(W)} = C_{LB(W)} - C_{LB}$$

$$\Delta C_{LW(B)} = C_{LW(B)} - C_{LW}$$

are pictured as they are obtained, taking the differences of the test results. The same procedure applied for determination of the total loads at the fuselage can also be applied for individual fuselage sections, as the following discussion of the test results will show.

## 1.3 REALIZATION

We started the application of the SECTIONAL LOADS TECHNIQUE on a 1/10 scale model of the VAK 191 B, designed for the VFW-Fokker low speed wind tunnel (max. velocity 70 m/sec, test section 2.1 m x 2.1 m). The fuselage of the model was divided into five sections and the exchangeable wing attached directly to the model skeleton. (FIG 5)

With consideration for the proposed modifications, the breakdown of the fuselage was such that the fuselage could be shortened by removing section B2 from the basic configuration and the fuselage width reduced in the region of the LCE inlet ducts by exchanging the fuselage shells B1, B2 and B3. Thus the wing-body combination was realized by varying width and length of the forward fuselage but leaving the wing unchanged, for the first test phase. In a subsequent test program a second wing with smaller loading and sweepback was mounted to the basic model fuselage and tested in three longitudinal positions. A comparison of the geometrical model wing data is given in the table below.

Wing	I	II
LE sweep	45°	30°
span	0.536 m	0.794 m
area	0.125 m <sup>2</sup>	0.179 m <sup>2</sup>
aspect ratio	2.3	3.5
taper ratio	0.346	0.342

In both these test phases the installed strain gage balances (FIG 6) were manufactured from a steel alloy. They comprise a balance unit for the normal force  $N$  and the pitching moment  $M$  and another unit for the axial force  $T$ . Single-beam balances are used for the  $N/M$  system within the limits

$$N_{\max} = 5 \text{ kg}$$

$$M_{\max} = 0.125 \text{ kg m.}$$

Only the fuselage tail section B5 is provided with a double-beam  $N/M$  unit which is less sensitive to torsional oscillations. This balance system is dimensioned for

$$N_{\max} = 10 \text{ kg}$$

$$M_{\max} = 0.25 \text{ kg m}$$

The axial force balance units are all of the double-beam type with

$$T_{\max} = 2 \text{ kg}$$

The surface of cut between two adjoining fuselage sections must be provided with gaps to prevent contact. The size of the gaps must, however, not be larger than required for the static deflection of the loaded strain gage balances. Preceding investigations have shown that these gaps range between 1 and 2 mm. The comparison of the overall force measurement with the sum of the partial loads gives a reliable possibility to check the gap influence. It was found out that no noticeable measuring errors occur at a horizontal gap width up to 2 mm and a vertical step gap up to nearly 1 mm for the model size discussed here. (The vertical step between adjoining sections is the result of the flexibility of the balances loaded with a homogenous pitching moment.) If, however, the vertical step exceeds approximately 1 mm it will no longer be within the local boundary layer thickness, a disturbance flow develops which tries to counter rotate the associated sections and thus leads to a non-correctable fault. The gap between adjoining sections has another effect apart from the possible geometrical disturbance of the outer flow: a pressure  $p_i$  is formed in the hollow interior of the model which can differ from the ambient pressure  $p_{\infty}$ . Depending on the shape of the individual sections, additional forces act on the fuselage sections, in particular on nose and rear sections. These additional forces are also measured by means of the associated balances. The balance output signal therefore has to be corrected by subtraction of the pressure load  $\Delta p_i \times \Delta A$ . The interior pressure  $p_i$  is determined by pressure holes in several small pipes inside of the model. If these measuring points indicate different pressures it is obvious that an air flow exists in the hollow model fuselage. This especially arises when the gaps between the sections are too big or the local pressure at the gaps differ very much. In this unfavorable case the included error in measurement can not be corrected, and therefore one has to try to avoid this "air passage" by means of labyrinth seals at the gaps or something else.

It has been mentioned that the optimum gap width must account for the static deflection of the loaded balances, only. Dynamic deflections, as they occasionally occur when measurements of this kind are made, must be avoided, generally. We encountered just these difficulties at the fuselage tail section of the VAK model during the first application of the sectional loads technique. The excitation caused by the periodicity of the separating boundary layer at the fuselage tail section as well as the natural frequencies of the mass spring system adjacent to the excitation frequency resulted in a strong vibration, which at first was limited only by the impact of the tail section against the neighboring part. This vibration tendency then was totally eliminated by installing a simple mechanical oil damper at the largest possible lever arm. After that all four and five-component balances were equipped with oil dampers. Only the nose section balance was not provided with an oil damper since tests have shown that there is no excitation which might cause vibrations here.

The model shown in FIG 7 has a symmetrical fuselage, because this makes comparative analytical calculations easier and a useful experimental variation of wing high position possible. The principal data of the wing III are.

LE sweep	32°
aspect ratio	3.2°
taper ratio	0.3

This wing can also be provided with a pair of strakes, which is individually mounted on a four-component strain gage balance.

These new four- and five-component balances are manufactured from a copper-beryllium alloy "Cu Be 2". A comparison of the most important characteristics

- modulus of elasticity
- machining properties
- weldability (electron beam welding)
- heat treatment
- hysteresis and
- resistance to corrosion

proved this spring material most suitable.

The lower modulus of elasticity of "Cu Be 2" in comparison with steel is favorable in this case. If the cross-section of a cantilever beam is not limited by a maximum balance diameter requirement, under the assumption of fixed load, length and sensitivity the stiffest balance will be the balance whose material has the smallest modulus of elasticity.

$$f = \text{const.} \times E^{1/3}$$

Of course, the balance with the highest modulus of elasticity then will be the stiffest balance when the cross-sections are fixed

$$f = \text{const.} \times E^{-1}$$

The modulus E of "Cu Be 2" is only approximately 65 % of that of steel alloys and therefore in the case of selectable cross-sections the deflection of the "Cu Be 2" is only about 86 % of the steel balance deflection, that means the material "Cu Be 2" is more favorable with respect to the gaps between the sections which cannot be avoided. Although the modulus of elasticity of aluminium or titanium alloys would be even more favorable, some of the other characteristics, such as weldability and hysteresis are comparatively poor.

#### 1.4 CONCLUSIONS

Application of the Sectional Loads Technique to wind tunnel models provides both the overall aerodynamic loads acting on the model and the integral partial loads on those structural components of the airplane which are of particular interest. These components can be exchanged with relative ease. The design of an aircraft and its components can be optimized by this method and through proper layout of the sections.

Tests conducted up to now have shown that

- copper beryllium alloy is the most suitable material for the strain gage balances
- all the balances should be of the six-component type, so that the partial loads can be totally transformed in the aerodynamic system of coordinates
- simple hydraulic dampers are quite sufficient to avoid vibrations
- the gap width between sections can be 1 to 2 mm without disturbing the air flow and the results
- the step height of the gap under load must not exceed about 1 mm for the size of model
- pressure measurements in the interior model are required for watching the air flow passage and for correcting the partial loads depending on pressure.

After the initial difficulties were overcome the Sectional Loads Technique has all in all proved to yield a very good efficiency due to the expenditure of cost.

## Part 2 TEST RESULTS

### 2.1 VAK 191 B CONFIGURATION

The VAK 191 B is a VTOL Ground Attack Fighter, of which three prototypes have been built and flight tested (see FIG 1). It has a small low aspect ratio wing with 45 degrees leading edge sweep.

The aerodynamic characteristics of this configuration with its original fuselage configuration (fuselage contour "A") are shown in FIG 8. Compared with the clean wing lift ( $CL_W$ ) the wing-body combination develops much more lift above  $16^\circ$  angle of attack. At large angles of attack the lift increment is larger than the lift of the body alone ( $CL_B$ ), so there must be a positive wing-body lift interference.

The lift curve of the body alone shows a nonlinear increase beginning at  $12^\circ$  incidence combined with a reduction of the unstable moment. The reason for this behavior may be a vortex separation at the fuselage sides. At the same angle of attack the linear lift curve slope of the wing-body suddenly decreases. The influence of the body vortices on the behavior of the wing-body combination is thus obvious.

In subsequent investigations of VAK derivatives with shorter and smaller forward fuselages the favorable wing-body lift interference was lost and this finally gave rise to the development of the test technique described in part 1 of this paper.

The results of this test technique for the original VAK 191 B configuration are shown in FIG 9. This figure shows the lift increments induced on the body and the wing due to the presence of the wing and the body respectively. The wing-body interference ( $\Delta CL_{B(W)}$ , increment on body lift due to presence of the wing) shows an almost linear increase with angle of attack. The body-wing interference shows a steep decrease with angle of attack. Above  $12^\circ$  angle of attack the slope changes and becomes positive, above  $27^\circ$  angle of attack there is a positive body-wing interference. The sum of both interference effects  $\Delta CL$  has a negative slope at low angles of attack. The interference becomes positive at  $22^\circ$  and reaches large positive values at high angles of attack.

FIG 10 shows the local lift on five parts of the fuselage. The measurement was carried out with the fuselage alone and with the fuselage in presence of the wing. The difference between the two curves is therefore the influence of the wing on the fuselage parts.

Without the wing the main lift acts on the front part of the fuselage. The nonlinear behavior of the fuselage total lift (see FIG 8) above  $12^\circ$  degrees is obviously produced by the third and the fourth section. At this location the vortex separates at the fuselage flanks.

The main lift increment due to presence of the wing occurs at the wing location, e.g. at the fourth section and at the sections in front of and behind the wing.

### 2.2 FORWARD FUSELAGE VARIATIONS

As already mentioned above, the favorable lift behavior of the wing-body combination was lost, when shorter and more slender forward fuselages were tested during VAK-derivative studies. FIG 11 shows a comparison of the interference behavior of three different forward fuselage combinations.

At angles of attack below  $14^\circ$  the fuselage has no influence on the lift curve. At high angles of attack the lift of the slender fuselage configuration is slightly lower than the basic configuration lift. The lift of the shorter configuration is much lower, there is almost no positive interference effect.

The bottom diagram in FIG 11 shows the interference effects. The wing-body interference is not affected by the different fuselage configurations. The body-wing interference is largely affected at angles of attack larger than  $20^\circ$  degrees.

The large influence of the forward fuselage contour on the body-wing interference indicates the importance of the vortex development at the fuselage flanks for the lift increment on the wing. Obviously the large fuselage side-mounted intakes of the basic VAK 191 B configuration promote the vortex development. On the other hand the forward fuselage must have a certain length for this vortex development as shown by the poor result of the short fuselage.

### 2.3 WING PLANFORM VARIATIONS

During further VAK 191 B derivative development configurations with larger wings were investigated. FIG 5 shows such a configuration, designated configuration II in this paper. Fuselage and fuselage variations A, B and C are the same as in the original VAK configuration I.

The influence of the forward fuselage length on lift and lift interference is shown in FIG 12. By comparison with FIG 11 it is obvious that the effects are similar to the effects of the small wing, but the total interference as well as the wing-body and body-wing interferences are much smaller. The large wing more or less suppresses the interference effects. This becomes even more evident by a direct comparison of the large and the small wing both with fuselage "A". FIG 13 shows that:

- The small wing has -- due to its larger leading edge sweep and its lower aspect ratio -- a higher  $CL_{max}$  and a higher  $\alpha CL_{max}$ .
- The total lift interference of the small wing-body configuration is much larger at angles of attack larger than  $24^\circ$  degrees.
- Even in terms of absolute force the interference effect of the body on the wing is much smaller in the case of the larger wing. This is demonstrated in the bottom diagram of FIG 13 by a recalculation of the body-wing interference  $\Delta CL_{W(B)}$  for the large wing with the small wing reference area, see dotted line.

## 2.4 STRAKE CONFIGURATION

The former partial load tests with VAK derivatives described above clearly showed the possibility of increasing the lift of small aspect ratio swept wings by vortex separation at the fuselage flanks. Extremely stable vortices are produced at the leading edges of highly swept wings. This led to the development of the "strake"-configuration which is realized e.g. in the F 16.

To obtain a deeper understanding of the interference mechanism and the optimisation possibilities of this configuration, a partial load wind tunnel model was tested. The dimensions are given in FIG 7. In this model the fuselage was cut into four parts as indicated in FIG 15, and the strake was mounted on a separate strain gage balance. The necessary cut between wing and strake was sealed as good as possible.

The overall interference effects of this configuration are shown in FIG 14. The interference effect of the wing body configuration is only moderate as was to be expected with the size of the wing and the fuselage cross section. The behavior is very similar to that of the large wing-VAK fuselage combination, see FIG 13. The addition of the strake largely increases the overall lift at angles of attack larger than  $12^\circ$ . At  $\alpha = 24^\circ$  the increase in lift due to the strake is  $\Delta C_L = 0,47$ .

Approximately 8 % of this increase are induced by the strake on the fuselage. The main contribution, about 54 % is induced on the wing. About 38 % of the lift increment act directly on the exposed strake area.

The VAK 191 B fuselage with its round flank intakes needs greater angles of incidence for the development of vortices at the fuselage sides than the sharp leading edge of a strake. So, the positive strake-wing interference becomes evident at  $\alpha = 12 - 14^\circ$  already, while the VAK 191 B fuselage needs more than  $14^\circ$  degrees of incidence to develop its full interference effect on the wing. This difference can be seen by comparison of the bottom diagrams in FIG 13 and FIG 14.

The distribution of lift on the four fuselage segments and on the exposed strake area is shown in FIG 15. In the diagram partial lifts and moments are plotted for fuselage alone, fuselage in presence of wing and fuselage in presence of wing and strake. The behavior of the fuselage alone is not unsimilar to that of the VAK 191 B fuselage. The interference effect of the wing on the fuselage also concentrates on the wing intersection part of the fuselage and to a smaller extent on the fuselage part in front of the wing.

The positive interference effect of the strake on the fuselage concentrates on the strake intersection part of the fuselage. A further small additional lift is induced on the front fuselage.

On the wing intersection part of the fuselage the strake induces a lift decrement, which in its trend corresponds exactly to the lift increment on the wing due to the strake (see Fig. 14, difference between the curves  $\Delta C_{LW}(B)$  and  $\Delta C_{LW}(B,St)$ ). This leads to the conclusion that in parallel to the lift increase due to the strake the lift distribution is shifted towards the outboard part of the wing span.

The far right diagram in FIG 15 shows the lift force on the exposed strake area, which contributes about 38 % to the total strake effect. This exposed strake area is heavily loaded, which is demonstrated by a recalculation of the lift coefficient with the exposed strake area as a reference area (see the scale  $C_{L_{St}}$  on the right side of this diagram!). The maximum lift coefficient reaches 1,95 at  $\alpha \approx 28^\circ$ .

A general impression of the strake influence is given in FIG 16, in which the relative lift is plotted against angle of attack. The reference lift is the lift of the clean wing and is set to unity for all angles of attack. All the values correspond very well with the slender body theory below  $\alpha \approx 9^\circ$ , if the fuselage width is used as fuselage diameter for this theory.

The hatched areas represent the strake influence on the body and the wing respectively. Together with the direct strake lift they give the total strake influence.

## 2.5 CONCLUSIONS

The results of the examples for the VFW Fokker Sectional Loads Technique demonstrate the mechanism of wing-body interference and the influence of fuselage side or strake generated vortices on this interference.

The results further demonstrate the possibilities this test technique provides for a better understanding of such phenomena and the advantages for further optimisation work. Changes in strake planform, for instance, are simple; they result in cheap changes on the model described above and allow very useful wind tunnel work.

## REFERENCES

- [1] Barche, J. "Zur Interferenz schlanker Flügel und Rumpfe bei hohen Anstellwinkeln in Unterschallströmung (Experimental-Studie)" VFW-Fokker Rep. No. Ea 391, June, 1972
- [2] Krahl, H. "Klarung realisierbarer Möglichkeiten des Hochauftriebes" VFW-Fokker Rep. No. Ea 301 (published as ZTL-FAG 4, Final Report 1970, VFW 4.01/70, Dec. 1970).
- [3] Krahl, H. "Klarung realisierbarer Möglichkeiten des Hochauftriebes" VFW-Fokker Rep. No. Ea-377 (published as ZTL-FAG 4, Final Report 1971, VFW 4.01/71, Dec. 1970)
- [4] Krahl, H. "Klarung realisierbarer Möglichkeiten des Hochauftriebes" VFW-Fokker Rep. No. Ex1 430 (published as ZTL-FAG 4, Final Report 1972, VFW 4.01/72, Dec. 1972).
- [5] Krahl, H. "Klarung realisierbarer Möglichkeiten des Hochauftriebes – Untersuchung der Interferenz und der Lastenverteilung bei Kampfflugzeugen mit Strakes" VFW-Fokker Rep. No. Ef-566 (published as ZTL-FAG 4, Final Report 1974, VFW 4.01/74, Dec. 1974).



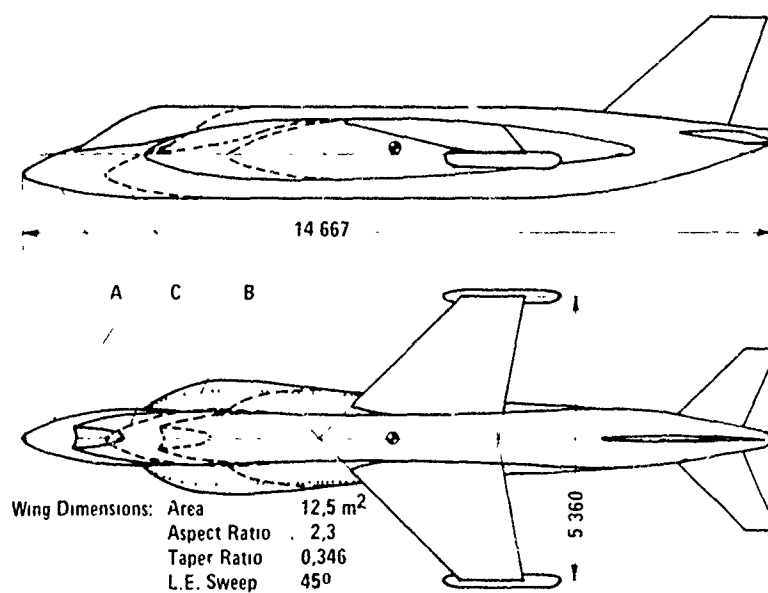


Fig 1 VAK 191B CONFIGURATION WITH FORWARD FUSELAGE VARIATIONS  
Configurations I A, I B, I C

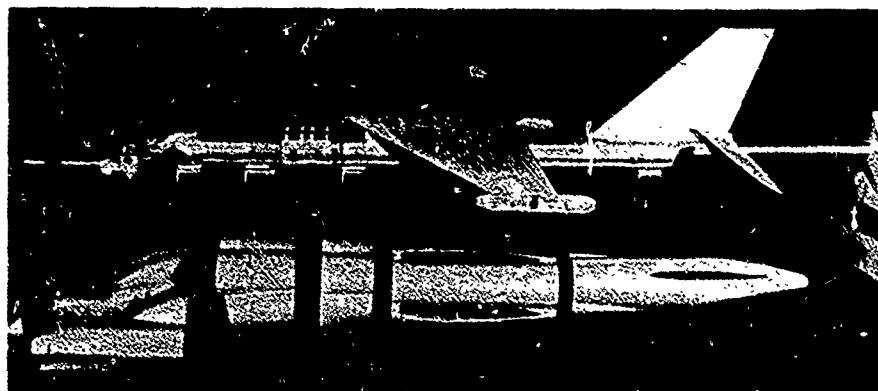
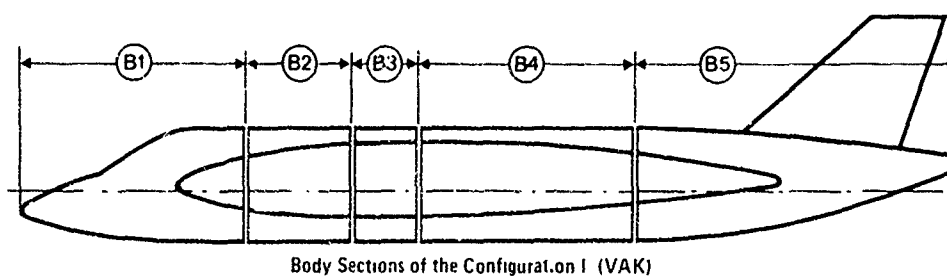


Fig. 2 MODEL PARTS OF CONFIGURATION I

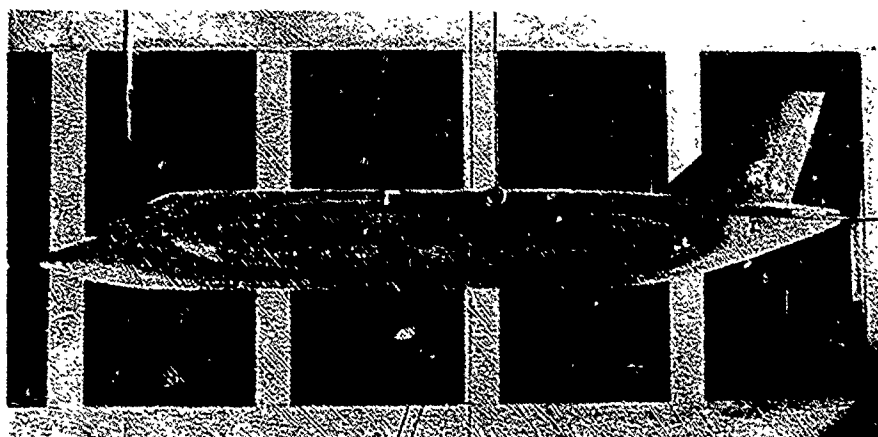


Fig. 3 CONFIGURATION I A IN THE VFW-WINDTUNNEL






Component	Coefficient	Sketch	Determined by :
Lift of the total model	$C_{LWB}$		external balance
Lift of the body only	$C_{LB}$		external balance and/or strain gage balance
Lift of the wing only	$C_{LW}$		external balance
Lift of the body, in presence of the wing	$C_{LB(W)}$		strain gage balances
Lift of the wing, in presence of the body	$C_{LW(B)}$		difference of external balance and strain gage balances
Total interference	$\Delta C_L$	$= \left[ \text{Sketch of total model} \right] - \left[ \text{Sketch of wing} + \text{Sketch of body} \right]$ $= C_{LWB} - (C_{LW} + C_{LB})$	
Wing body interference	$\Delta C_{L(W)}$	$= \left[ \text{Sketch of body with wing} \right] - \left[ \text{Sketch of body} \right]$ $= C_{LB(W)} - C_{LB}$	
Body wing interference	$\Delta C_{LW(B)}$	$= \left[ \text{Sketch of body with wing} \right] - \left[ \text{Sketch of wing} \right]$ $= C_{LW(B)} - C_{LW}$	

Fig. 4 SCHEME OF INTERACTING COMPONENTS  
(Shown with Total Lift Behaviour)

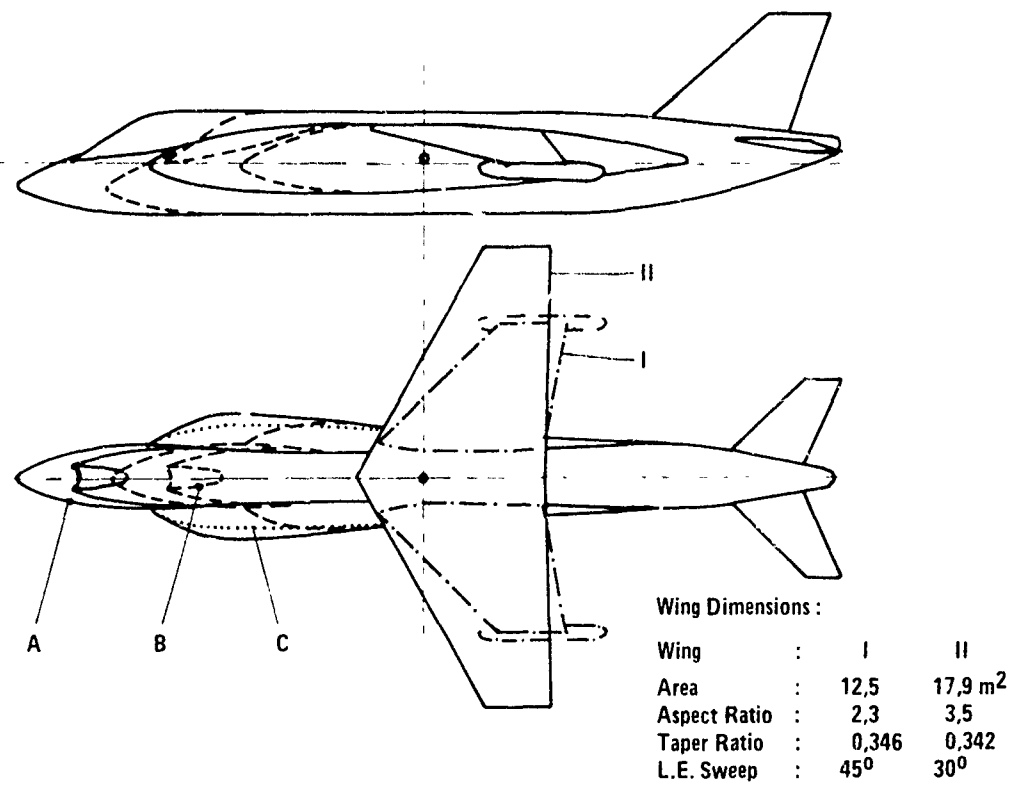


Fig. 5 VAK 191 B DERIVATIVE WITH LARGER WING AND FORWARD FUSELAGE VARIATIONS  
Configurations IIA, IIB, IIC

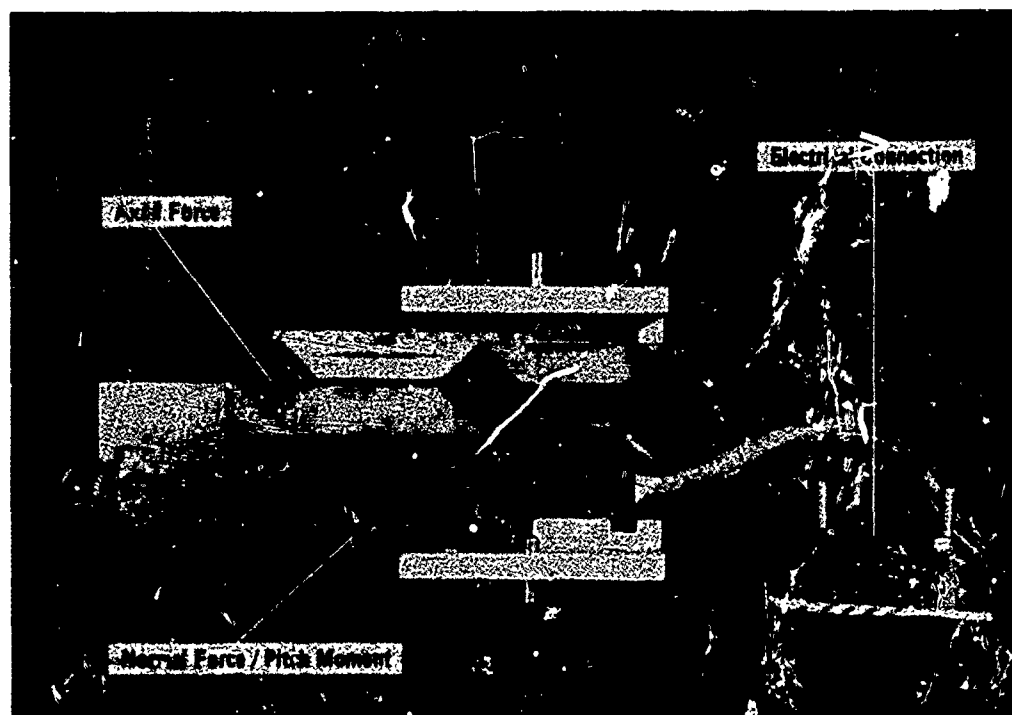


Fig. 6 INTERNAL STRAIN GAGE BALANCE

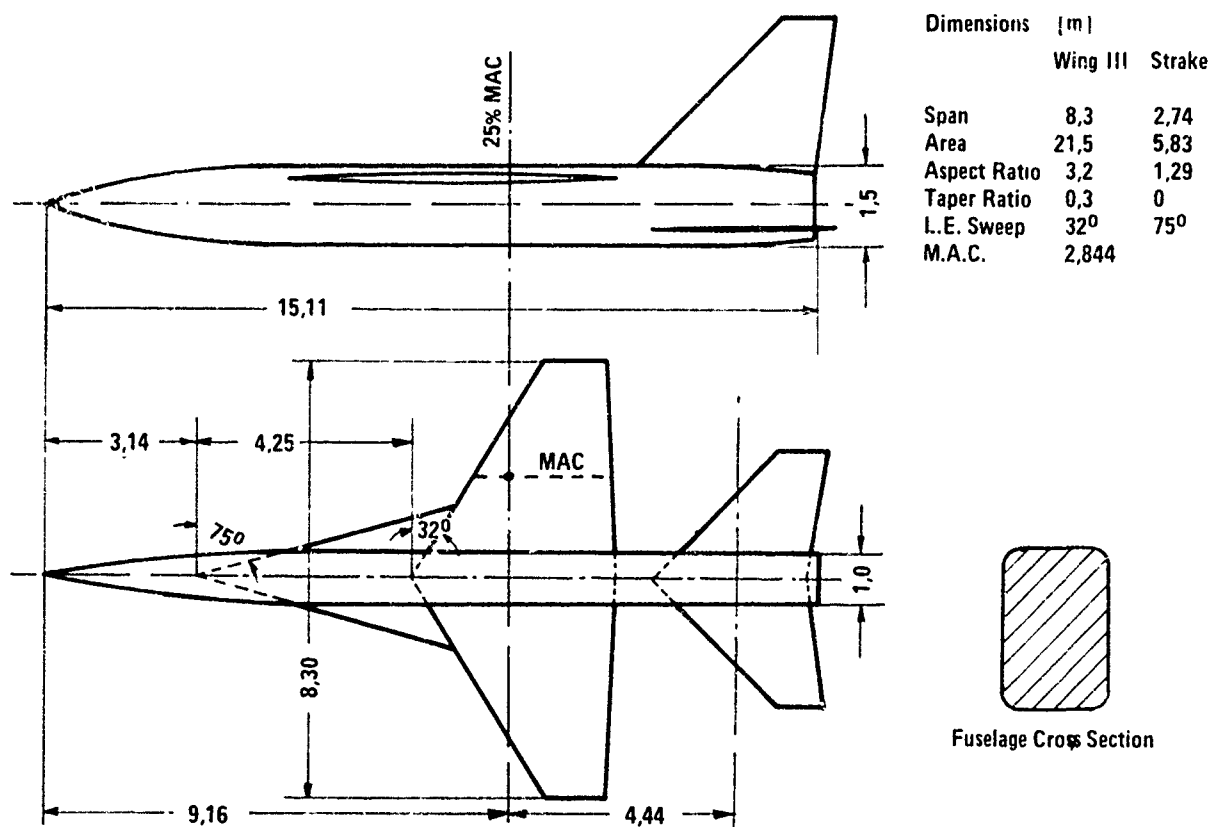


Fig. 7 STRAKE CONFIGURATION III  
Reference [5]

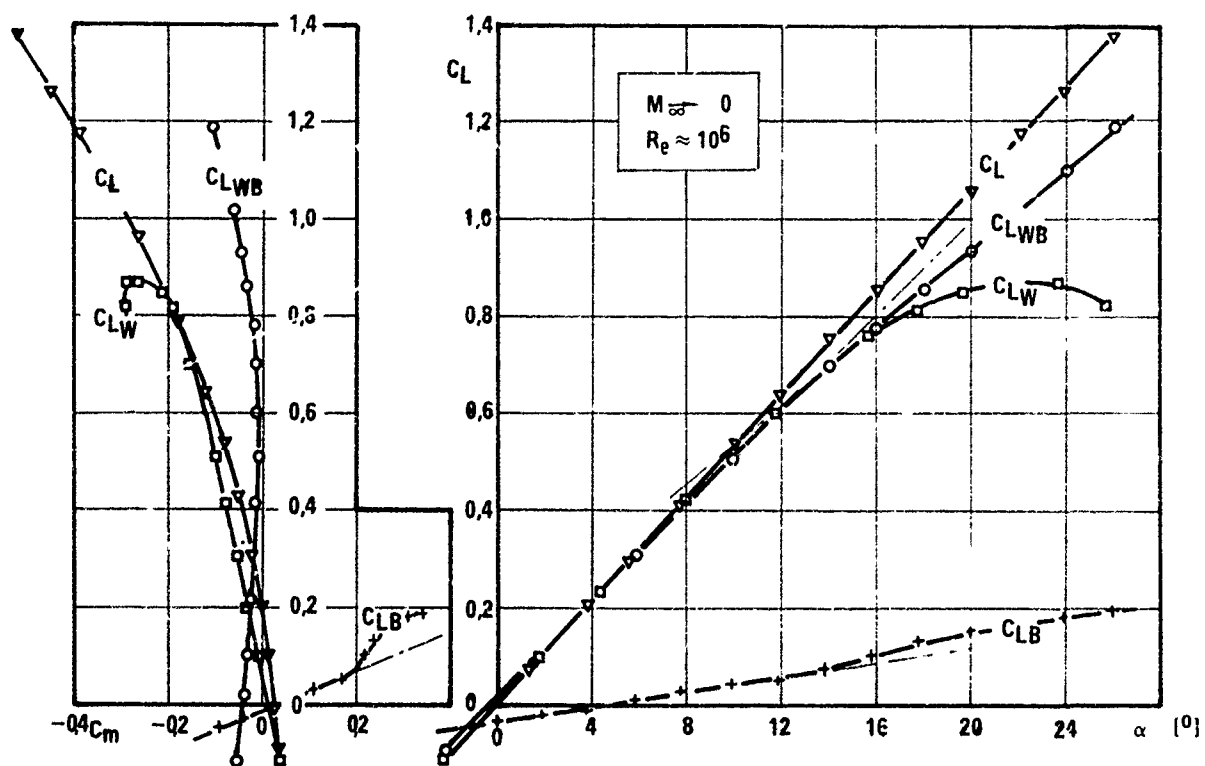


Fig. 8 LIFT AND PITCHING MOMENT BREAK-DOWN  
(Reference [1])

Configuration I A

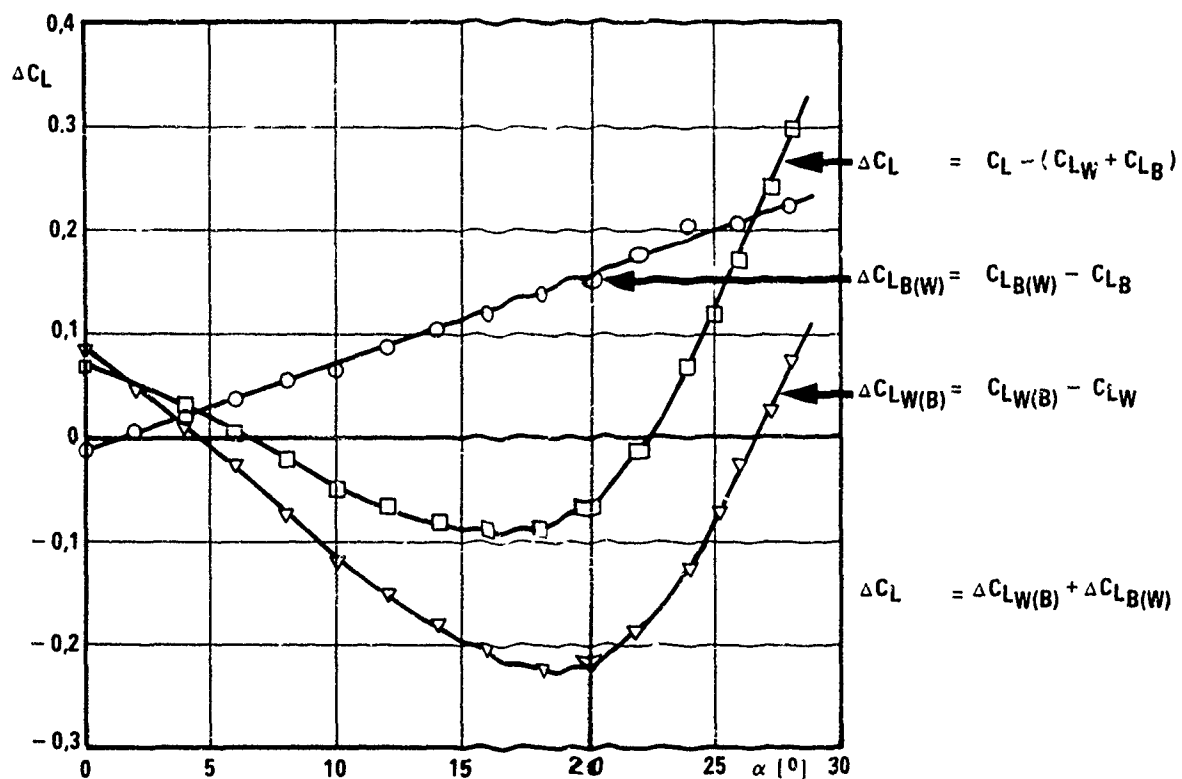


Fig. 9 WING-BODY INTERFERENCE BREAK-DOWN  
Configuration 1 A

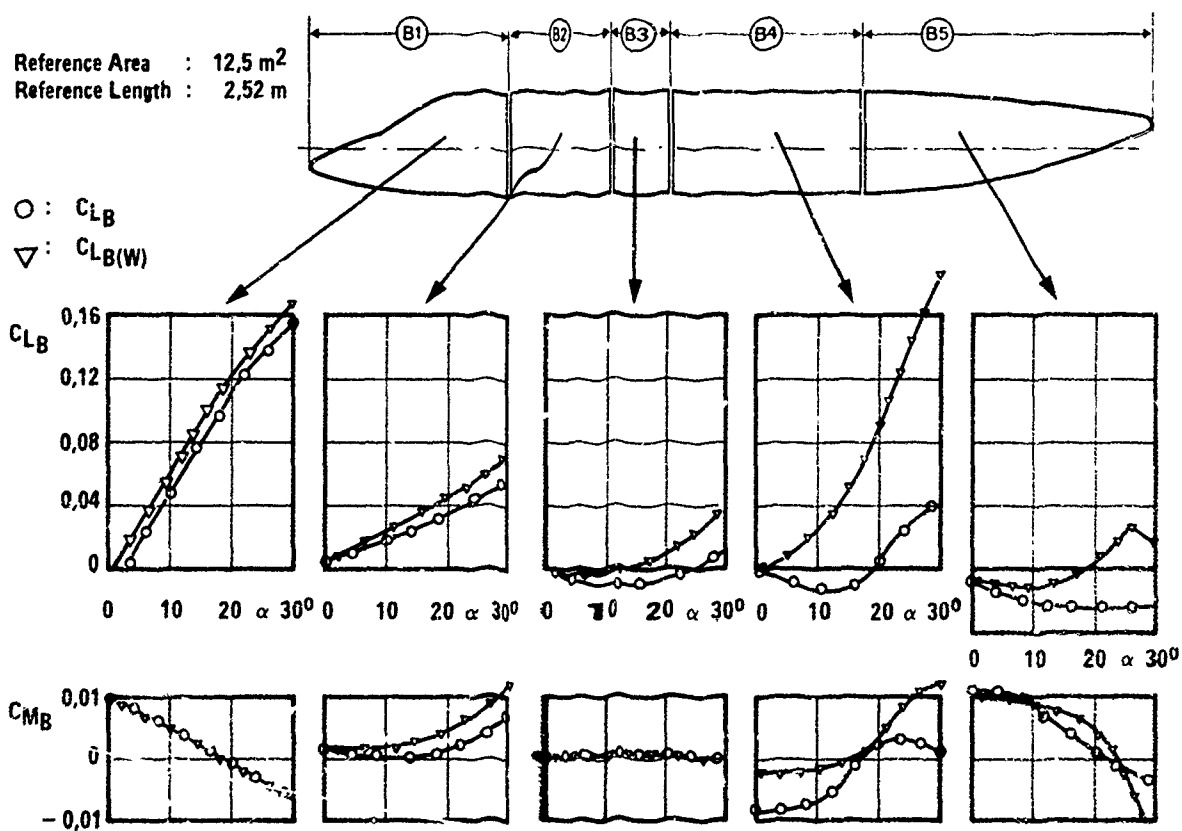


Fig. 10 FUSELAGE PARTIAL LIFTS AND MOMENTS.  
Configuration 1 A

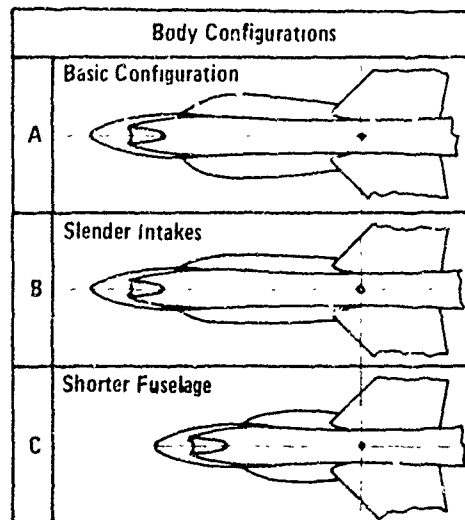
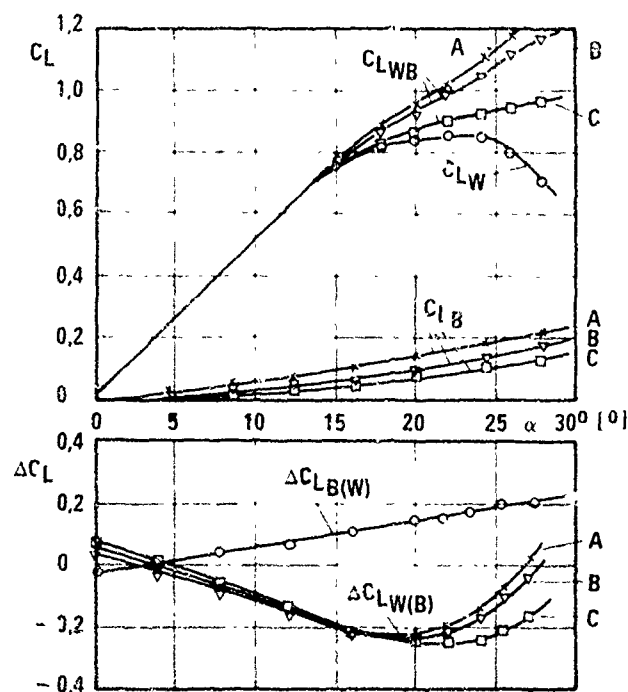


Fig. 11 INFLUENCE OF FORWARD FUSELAGE CONFIGURATION ON LIFT INTERFERENCE  
Reference [1], [3]

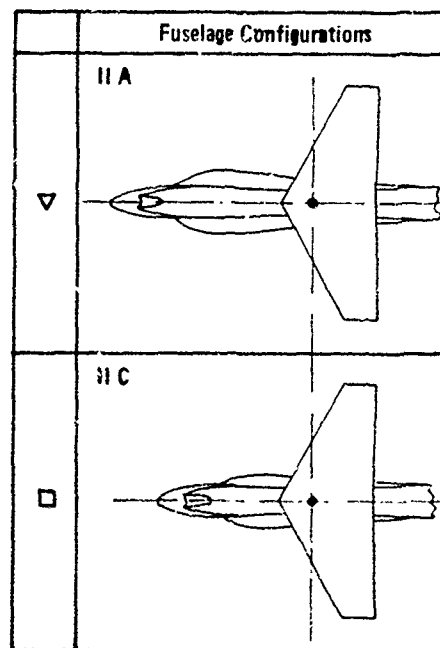
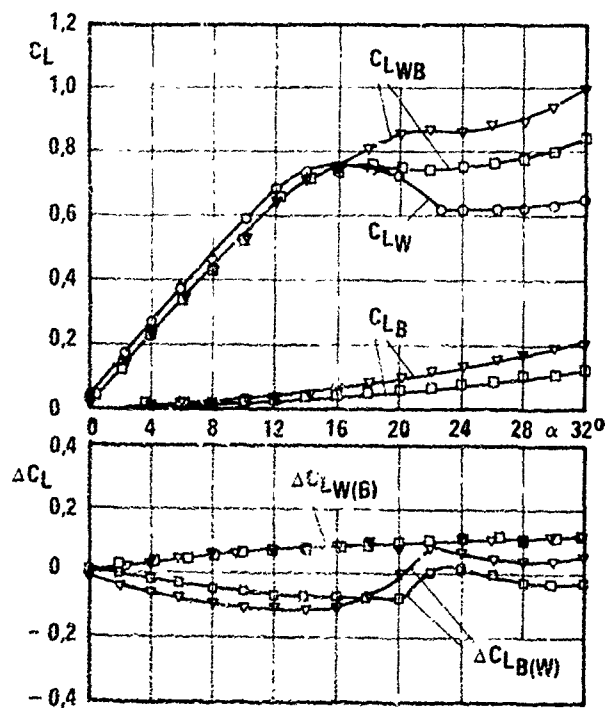


Fig. 12 INFLUENCE OF FORWARD FUSELAGE CONFIGURATION ON LIFT INTERFERENCE  
Reference [4]

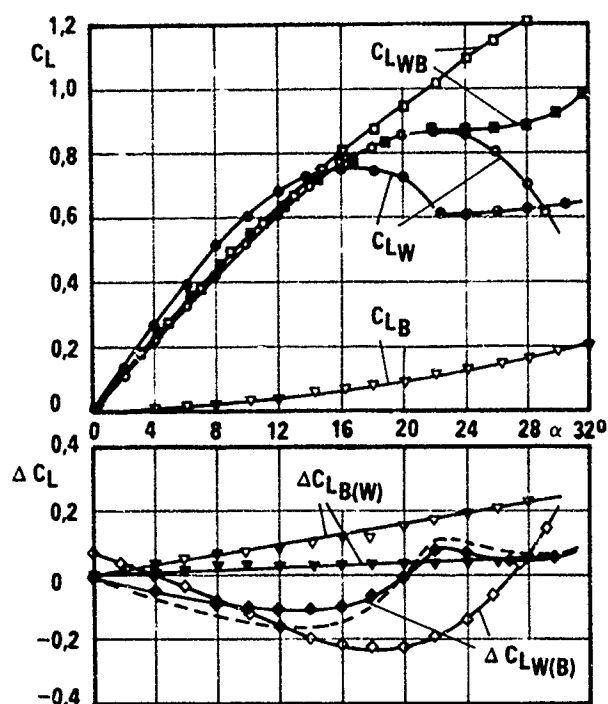


Fig. 13 INFLUENCE OF WING PLANFORM AND SIZE ON LIFT INTERFERENCE

Wing Dimensions See Fig 5

Reference: [4]

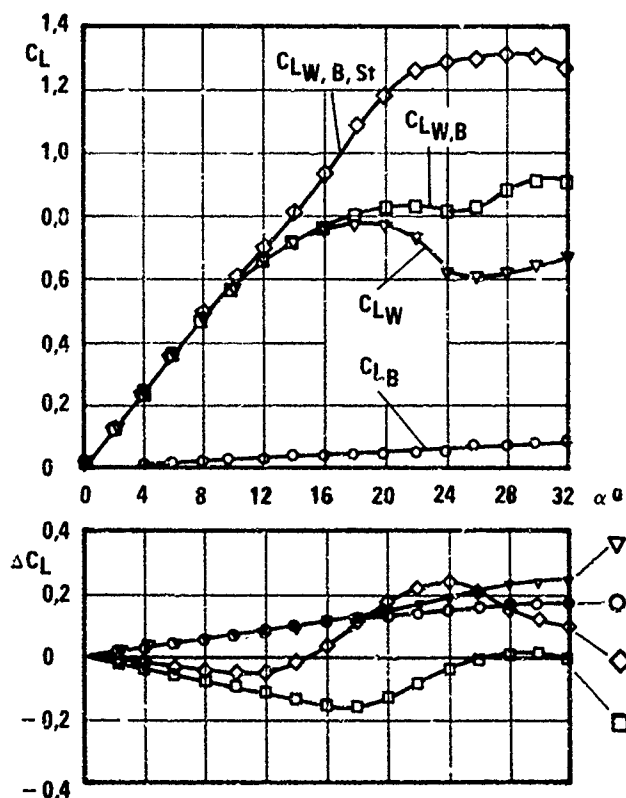
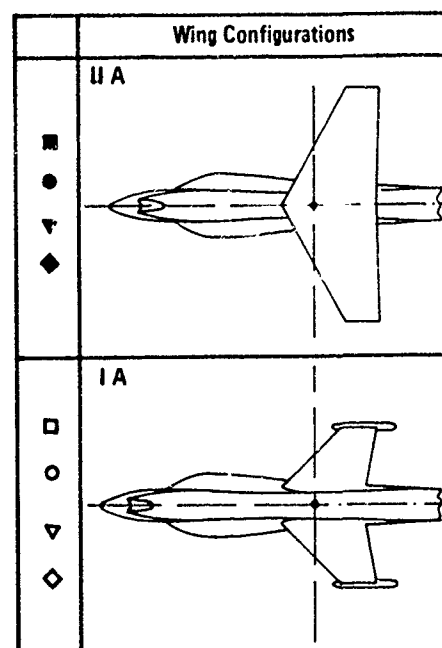
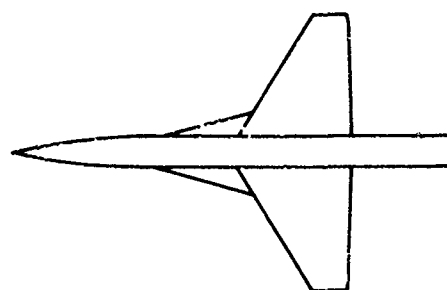


Fig. 14 INTERFERENCE EFFECTS OF STRAKE CONFIGURATION III

Reference [5]

Body Wing and Strake Dimensions see Fig 7

Reference Area: 21,5 m<sup>2</sup> $\Delta C_{LB}(W, St)$  $\Delta C_{LB}(W)$  $\Delta C_{LW}(B, St)$  $\Delta C_{LW}(B)$

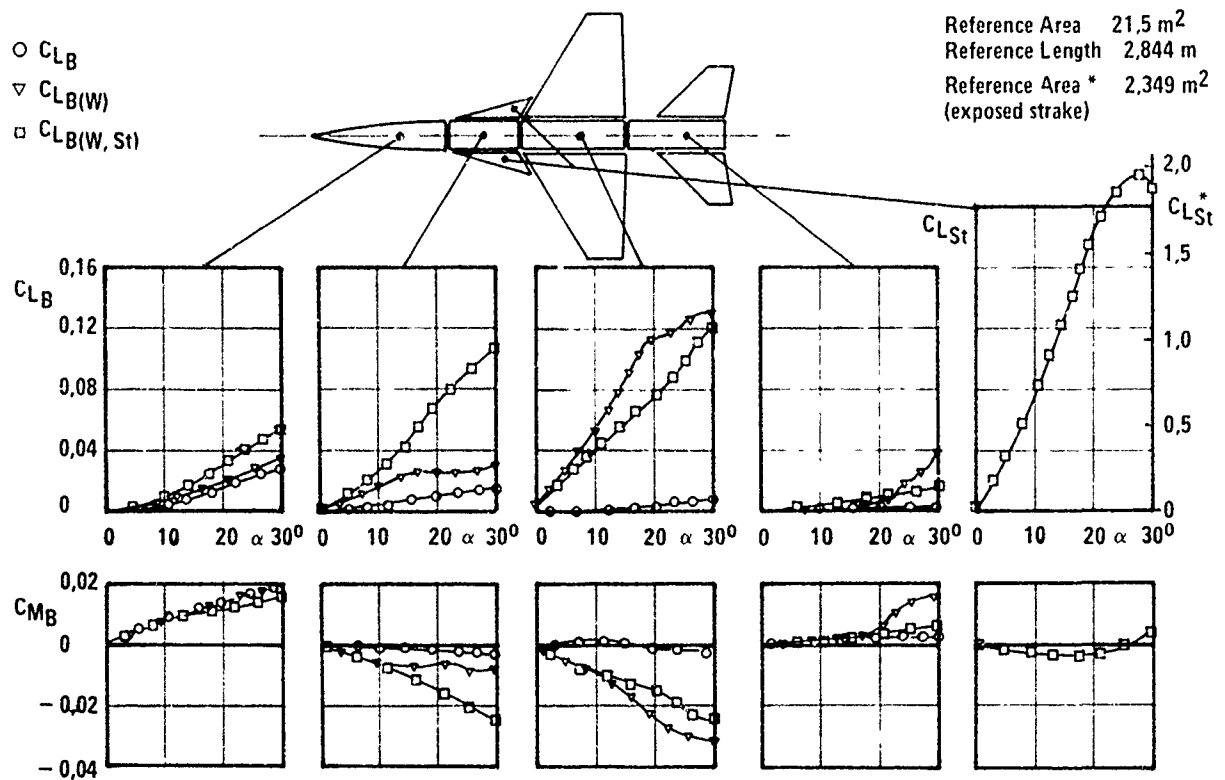


Fig. 15 FUSELAGE AND STRAKE PARTIAL LIFTS AND MOMENTS, CONFIGURATION III  
 Reference [5]

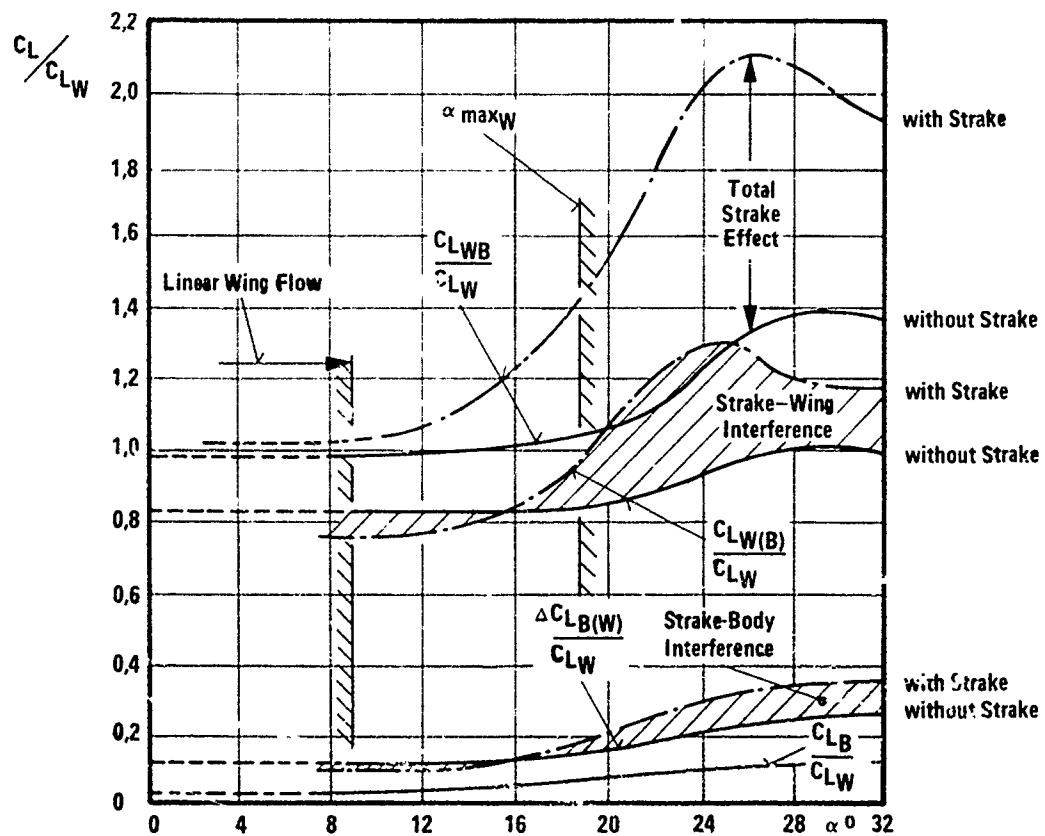


Fig. 16 RELATIVE LIFT BREAK-DOWN, STRAKE INFLUENCE  
 Reference [5]



PREDICTION OF AERODYNAMIC LOADINGS ON  
THE LEADING-EDGE SLATS OF THE FOKKER F 28 AIRLINER

by  
F. de Poer  
Aerodynamics dept.  
Fokker-VFW BV.  
POB 7600  
Schiphol Oost  
The Netherlands.

# SUMMARY

Prediction of aerodynamic loadings on leading-edge slats of modern airliners is a very complicated process. For passive components, the isolated critical load cases on the boundaries of the field of flight conditions as dictated by airworthiness requirements are readily recognizable and their loadings need only to be specified for these conditions. For lift carrying components, however, matters are much more complicated and a load case analysis covering the complete field of flight conditions must be conducted.

Component load data must be specified for this, which are based on wind tunnel data; test conditions thereof cover only a part of the complete field. This discrepancy is bridged by data extrapolation, but this procedure may well result in off-design component loadings which are no longer physically sound, in particular in case of shock effects.

Determination at the relevant conditions of more realistic loadings is then an elaborate second phase of the prediction process.

The whole procedure is illustrated for the slats, introduced on later versions of the F 28 airliner, with some discussion on problems for that particular case.

# LIST OF SYMBOLS

$\alpha$	aircraft or section angle of incidence, °
$c$	section chord
$C_L$	aircraft lift coefficient, related to wing area $S$
$C_{L_s}$	section lift coefficient, related to section chord $c$
$C_{m_s}$	section moment coefficient, related to 25 % section chord
$C_p$	pressure coefficient
$C_{N_s}$	slat normal force coefficient, related to airfoil section chord
$C_{T_s}$	slat tangential force coefficient, related to airfoil section chord
$C_{m_s}^+$	slat moment coefficient, related to airfoil section chord +
$\delta_f^m$	flap deflection, °
$\delta_s$	slat deflection, °
$M$	Mach number
$n$	aircraft acceleration factor
$q$	dynamic pressure
$Re$	Reynolds' number
$S$	wing area
$V$	aircraft speed, kts. EAS
$V_A$	$1.58 V_S$
$V_{u_s}$	speed, at which aircraft reaches stall in 66' per sec. EAS gust encounter
$V_D$	diving speed (390 kts. EAS)
$V_S$	stalling speed with slats and flaps retracted
+	$C_{m_s}$ with subscript 0 or 25 to indicate reference point at 0 or 25 % slat chord

# 1. INTRODUCTION

Prediction of aerodynamic loadings on leading-edge slats of a modern airliner is a very complicated process. For passive components, the isolated critical load cases on the boundaries of the field of flight conditions as dictated by airworthiness requirements are readily recognizable and their loadings need only to be specified for these conditions. For lift carrying components, the lift distribution over the component and the weight and c.g. position of the aircraft are co-determining factors, usually yielding different critical flight load cases at different stations; in particular for slats, matters are even more complicated because the deformation relative to the wing greatly affects the support loads.

In such cases, the load case analysis must cover the complete field of flight conditions. Component load data must be specified, as functions of  $M$  and  $\alpha$ , which are based on wind tunnel data. The field of conditions thereof is restricted

- with respect to  $\alpha$  because of scale effects,
- with respect to  $M$  because it is impractical to conduct investigations at all values of  $M$  which may finally be of interest.

These restrictions may be overcome by data extra- and inter- polations on some analytical basis, but this procedure may well result in off-design component load predictions which are no longer physically sound, in particular due to occurrence of shock waves, and may adversely affect the conclusions to be drawn.

Reconsideration - rather construction - of physically sound component loadings at such conditions is then an elaborate second phase of the prediction process.

This will be illustrated for the slats, introduced on later versions of the F 28.

Physical aspects of the general load data will be discussed. For deflected slats at low speeds problems, specific to the aircraft or the prediction method applied, will also be considered. An in-flight verification of the load predictions was possible and yielded a satisfactory correlation.

For retracted slats at high speeds, the main lines of the loading construction process at off-design conditions will be indicated.

## 2. THE AIRCRAFT

The Fokker F 28 twin jet short haul airliner is available in six versions indicated in tabel 1. The increased aspect ratio of the later versions was obtained by addition of larger wing tips to the original design. The F 28 family is shown in fig. 1.

Some remarks are desirable with respect to the wing, which features a distinct kink in the leading edge at some 40 % of half span. The wing section at this station is thus relatively heavily loaded; it furthermore features a lower lift divergence Mach number than the other sections defining the wing shape and a precisely determined amount of inverse camber. By these measures it proved possible to provide the aircraft with flight characteristics eliminating the need for Mach trim compensation at speeds in excess of the maximum operating Mach number ( $M_{MO} = .755$ ).

This subject is brought up here because

- . a section close to the kink is discussed in chapter 5 to clarify a peculiar aspect of retracted slat loads at transonic speeds, in casu at  $M = .77$  just over  $M_{MO}$ ,
- . in view of its generally satisfactory behaviour, it was decided to maintain the shape of the clean wing when slats were introduced. As a result, high-speed wind tunnel testing for the Mk. 5/6,000 could be restricted to a bare minimum; consequences of this fact are commented upon in chapter 5.

Next to the clean wing shape, the front spar position of the original design was maintained for obvious reasons. This advances from 16 % chord outboard of the kink to 12½ % chord at the root, where, consequently, the slat chord became small and the slot behind the deflected slat pronounced oblique. A part of the wind tunnel efforts towards slat development was devoted to this deviating situation at the root.

## 3. THE WIND TUNNEL MODELS

Two wind tunnel models provided the load data to be discussed.

Tests in the 1.6 by 2 m. NLR high speed wind tunnel on a 1 : 20 scale pressure model of the F 28 Mk. 1.000 yielded pressure distributions over the clean wing, for the full aircraft M-range of .19 to .83 and the Q-range as far as realizable at the relevant Re-numbers. Within these limits, fairly accurate spanwise lift distributions were thus obtained as well as leading-edge pressure distributions for the retracted slat load data required later on. The Q-range at  $M = .19$  could be substantially extended, because the relevant wind tunnel can be operated at that speed with a 4 atm. stagnation pressure.

The lift distributions thus obtained were supplemented by results of lifting line theory (Weissinger/de Young) to account for effects of span extension and, at  $M = .19$ , of flap deflection.

The other model is the section model shown in fig. 2, originally applied to develop optimum type, shape and positions for the trailing-edge flaps. It was tested in the NLR 2 by 3 m. low speed tunnel. The test section was provided with wall blowing to suppress otherwise large wall interference effects at larger angles of incidence.

Two test slat/fixed leading-edge combinations are of interest here; one - the "normal" - is characteristic for a section at about 55 % half span of the F 28 wing, the other - the "shortened" - more or less representative for the root section commented upon in chapter 2.

Pressure recordings in the tunnel center plane over the several model components - slat, main section, vane and flap - were integrated to yield the forces on these components as functions of  $Q$  (or  $C_L$ ) and section configuration.

## 4. AIR LOADS ON DEFLECTED SLATS

### Prediction method.

Predictions of aerodynamic loadings on deflected slats were based on the probably familiar assumption, that the relation of any slat load coefficient at a given wing station to the local  $C_L$  is the same as to the  $C_L$  of the section model with the same slat and flap deflections.

This assumption is subject to somewhat less obvious restrictions.

In the section tests, variations in  $C_L$  are caused by variations in either  $\alpha$  or  $\partial_f$ . On the aircraft, other causes are possible for local variations in  $C_L$ , in particular interference of the fuselage-mounted nacelles and of discontinuities in  $\partial_f$  at flap ends. The different character of the latter should be accounted for, a subject to be discussed later.

The slot flow might affect slat section load data. On the section model, a locked vortex originates in the slat excavation. On the aircraft (model) this takes the shape of a core flow, spiralling outboard with a pitch, about proportional to (local) sweep back. For the F 28, the attendant lateral speed is too small to lower the excavation pressures significantly, but on aircraft with larger sweep its effect may become of

interest.

The flow pattern in the slot is indicated in fig. 3. Fig. 4a. shows a day-glo visualization of the core flow, fig. 4b. one of the disturbance traces over the wing slightly outboard behind the slat suspension brackets; these originate by the interaction of the core flow with these brackets and indicate some, largely inevitable, parasite drag of the slat suspension.

#### General load data.

Sets of deflected slat load data for three flap deflections on the "normal" section model are shown in fig. 3. They are shifted to feature effective  $Q$  rather than  $C_L$  as a parameter and as such are virtually identical, in representing the characteristics of the slat section as an air foil in an unusually deformed flow field, varying mainly with incidence. This fact is convenient when data are needed for a section configuration not covered by wind tunnel tests; it facilitates the construction of such data.

The data for the "normal" model section were applied on the F 28 wing outboard of the kink, those of the "shortened" section at the root, with linear interpolation between. The difference between the two sets was, otherwise, small.

The slope of all curves increase with  $Q$  and this tendency is such that, for constant lift ( $C_L q S$ ), the heaviest upward loads on the slats ( $C_L q S$  etc.) invariably occur immediately before the stall. In view of the relative identity of the data for different flap deflections, the largest slat loads will occur immediately before the stall with the highest speed, i. e. with retracted flaps. The shape of the curves is also such, that the situation with the lowest  $C_L$  to be considered will yield the other limitation to the slat loads.

Airworthiness requirements dictate consideration of flight conditions with deflected high-lift devices up to  $\alpha_f = 2$  and down to  $\alpha_f = 0$ . Hence the stall just mentioned is the 2<sup>nd</sup> stall with  $\alpha_f = 0$  and the other limitation is related to  $C_L = 0$  at a relevant placard speed, either for slat deflection (220 kts. EAS), for flap deflection up to  $\alpha_f = 25^\circ$  (200 kts.) or for landing flaps (160 kts.); it was not difficult to trace the second one as critical.

All this may be done without a real load case analysis, but then it concerns only the slats as such. For the suspension, matters are less simple since the deformation of the slats with respect to the wing is an important parameter in the structural analysis; this latter is so difficult to oversee that a comprehensive slat load data specification is still indispensable. Thus, the subject of local  $C_L$ -variation due to downstream influences now enters into the discussion.

#### Interference effects.

The nacelle interference effect on the flow field is most evident at the wing root trailing edge and gradually damps off upstream and in spanwise direction. Sectionwise, it causes a lift drop by inducing a virtually constant small overpressure at the upper surface. Direct application of the decreased  $C_L$ 's found on the pressure model with nacelles, in combination with section data from the other model (i.e. attributing the decrease to a change in  $Q$ , which is essentially in peak suction) would yield a too low local slat load. This difficulty may be overcome by neglecting the nacelle interference effect, which is slightly conservative; on the F 28 this was also logical since the effect is different on the Mk. 5,000 and 6,000.

Slat load predictions were thus based on the wing lift distributions established on the aircraft pressure model without nacelles. See fig. 6.

Incidentally, this effect tends to shift further outboard the lift resultant on each half wing the closer the nacelles stand to the wing. Insertion of a fuselage plug between the wing trailing edge and the nacelles on a stretched version thus brings with it some wing load alleviation. This fact kept the structural modifications, resulting from the span extension and required for the heavier Mk. 6,000, to a minimum.

The lift carry-over effect at the flap ends is also most evident at the adjacent t.e. region, but not neglectable at the l.e. region upstream. As in the case of the nacelles, the interference effect cannot be considered in terms of local  $C_L$  in the sense of section  $C_L$ . Here, one is led to consideration of the change in incidence of the section ( $\Delta Q$ ), required to yield the same change in leading-edge suction peak as is caused by the flap deflection in its lift carry-over effect.

On the "normal" model section, it was found that - independent of  $\alpha_f$  and  $\alpha_s$  as well as  $C_L$  and within remarkably narrow tolerances ( $\pm 1.5\%$ ) -

$$\Delta Q_p = .40 \Delta Q_L$$

where  $\Delta Q_L$  is the change in section incidence equivalent to the change in local  $C_L$ . On the aircraft pressure model, which featured deflectable ailerons, the aileron lift carry-over effect could be studied, albeit on a wing without slats. Since the aileron-to-wing chord ratio here was about the same as the flap-to-chord ratio of the section model with all high-lift devices deflected, it nevertheless yielded a worthwhile contribution. It confirmed the .40 ratio for the three-dimensional case.

Fig. 7 shows one of the cases analyzed from section model results, fig. 8 one from aircraft pressure model results.

Consequently, 40% of the theoretically derived flap lift carry-over effect was taken into account in the  $C_L$ -distributions applied for slat load derivation (see fig. 9). This

simple correction eliminated the need for far more complex and expensive analyses of the subject problem.

It was difficult to foresee the impact of the adjustments discussed in the structural analyses. Since slat deformation - and thus primarily bending moment - is an important parameter, they would most probably affect the support forces of the slat tracks closest to the wing root (nacelle interference) and the stations where the flaps end (flap lift carry-over effects).

#### Reynolds' effects.

On the F 28 section model, some research was conducted at reduced tunnel speeds. This mainly indicated some Re-effect on pitching moments, a finding of interest with respect to the 1 : 12 scale force model, figuring in figs. 4.

No effects on the load specifications were established for  $Re > 2.4 \times 10^6$  and since the normal value was  $2.8 \times 10^6$ , no particular problems arose here. In view of the increase in slope of all slat load curves with  $C_L$ , the prediction method could be somewhat vulnerable to underestimation of local  $C_L$  immediately before the stalls, but for the F 28, the high-pressure low speed tests on the pressure model (see ch.3) practically eliminated this as a problem.

In the section tests at very low Re evidence was found of interference in the lift development due to occurrence of a laminar separation bubble behind the upper surface discontinuity inherent to slat deflection; fig. 10 shows an example of relevant data. This effect must play a role when use is made of a low-speed aircraft pressure model provided with deflected high-lift devices. Such a model, when not very large and then very expensive to build and to test, will feature lower Reynolds' numbers than those in fig. 10 over a substantial part of the wing. The test results must then be difficult to interpret correctly when there is no section model test material at sufficiently high Re; when there is, the need for the relevant aircraft model is subject to discussion.

#### Verification.

Load predictions for deflected slats have been checked against results of in-flight strain-gauge measurements on suspension components and spigots of the slats. Summation of the internal forces thus measured to provide external loads on the slats yielded a very good agreement with the predictions, as shown in fig. 11. Note, that the scale for the moments is very large to make correlation points better distinguishable.

The relevant agreement was considerably better than that between calculated and measured structural stresses. Of course, the stress calculations were kept on the conservative side.

The correlation of the slat load predictions is not really good at very low loads and thus not with respect to specifications for the deflection/retraction cycle. This is probably a common problem, though one of relatively low order.

#### 5. AIR LOADS ON RETRACTED SLATS

##### Prediction method and general load data.

Load predictions on retracted slats were obtained by direct integration of the appropriate wind tunnel data from the aircraft pressure model, a relatively simple process, though elaborate in view of the amount of input data. Furthermore, chordwise  $C_p$ -plots were found to be necessary for data checking and extrapolation purposes.

The major feature of these load data is connected to leading-edge suction peaks and coherent forward shock waves.

At high Mach numbers, peak suction increases linearly with  $C_L$  only as long as local M remains below some 1.25, at least for the "peaky" sections on the F 28. Any further increase in lift goes together with widening of the peak with limited further growth of  $C_{p_{min}}$ . This obviously causes a quite sudden increase in the rate of change of  $C_N$  and in particular  $C_{m_N}$  with  $C_L$  at a specific wing station; both coefficients increase sharply until the shock wave, by now terminating the suction peak downstream, reaches the local slat trailing edge.

With further increase in  $C_L$  it crosses over to the wing. The consequent sudden drop in pressure in the narrow gap between the retracted slat and the wing causes a sharp decrease in both coefficients mentioned. This course of events is illustrated for the F 28 pressure model section nr. 3 in figs. 12 and 13, at  $M = .77$  distinctly over-critical for this section (see ch. 2).

Occurring only locally at a specific moment, this phenomenon does not cause sudden changes in over-all slat loads, but merely a somewhat unexpected relation with  $\alpha$ . At the wing root, fuselage interference ties the forward shock wave to the leading edge; there the load variations noted above do not occur, but the development of the shock wave can be seen in the load-versus- $\alpha$  curves for test section 1 (close to the root), which show up discontinuities at its beginning. This can be seen in fig. 14, which also shows idealized shock wave pattern on the wing at three characteristic  $\alpha$ 's.

At sufficiently high M, the described phenomenon occurs within the test  $\alpha$ -range. Then, determination of the condition at which it occurs (per section) is arbitrary only within narrow limits. Firm data are obtained on the relation between M and the  $C_p$  at which the suction peak starts widening and on the slope of  $C_p$  with  $C_L$  with further increase in  $\alpha$ . These may well be extrapolated to lower Mach numbers on theoretical basis.

As will be discussed next, the main problems arise when the phenomenon occurs beyond the wind tunnel test  $\alpha$ -range.

#### Load cases.

The load case analysis scans the  $n$ - $V$ -fields for manoeuvring and gusts described in the airworthiness requirements. The case, initially predicted to be most critical for the slats was

$$M = .560, \alpha = 8^\circ$$

which occurs when the aircraft, after take-off at maximum weight, flies at 18,000' altitude with a speed  $V_B$  and is hit by an upward limit gust (66' per sec. EAS), which brings it to the point of stalling. The adjacent wind tunnel test limits were

$$M = .45, \alpha = 7.5^\circ \text{ (shock-free)}$$

$$M = .65, \alpha = 3.2^\circ$$

In this case, the  $M$ -margin was very wide, since the intermediate range was of minor interest for the original design; as was mentioned in chapter 2, no further tests on the aircraft pressure model were conducted on behalf of the slat development. However, the real problem lies not in interpolation with respect to  $M$ , but in extrapolation with respect to  $\alpha$ .

The construction of the slat loads at off-test conditions of the sort is well possible. Sources of information available for construction of the relevant  $C_p$ -distributions over the wing leading-edge are:

- . high-speed airfoil section data, collected during the original F 28 development,
- . general wind tunnel data of the aircraft pressure model, from which the characteristic variation of the suction peak shape at any Mach number can be derived,
- . the lift distribution, predicted by the load case analysis, which should be in harmony with the  $C_p$ -distribution to be constructed.

In the subject  $V_B$ -case, where shock waves were found to be mainly behind the slat trailing-edge, slat loads were substantially lower than predicted beforehand over most of the span. Then, two "next critical" conditions emerged from the load case analysis, i.e.

- .  $V_D$ ,  $n = 2.5$  at sea level ( $M = .590, \alpha = 2.60^\circ$ ),
- .  $V_A$ ,  $n = 2.5$  at 20,000' altitude ( $M = .504, \alpha = 7.95^\circ$ ).

Both were found to be indeed critical over part of the span. Similar analyses were conducted for load cases with downward limit gusts and with gust encounters at  $M_{MO}$ .

#### Notes on the high-speed load construction processes.

1. Slat load extrapolation should be in harmony with extrapolation of  $C_p$  test data, to account for
  - . stagnation point travel with  $\alpha$ ; in the over-pressure region the  $C_p$ - $\alpha$ -relation is far from linear,
  - . hysteresis effects on the  $C_p$ 's close to the slat trailing-edge in transient conditions; these may well result in substantially lower slat loads than for static conditions.
2. On the F 28 - slat construction limitations together with anti-icing hot air discharge requirements - the slot seal position is at some 35 % slat chord, well aft of the optimum for minimum loads on the retracted slats. However, for the case of failed (removed) seal, the same level of critical slat loads was found as for the case with effective seal. This will be coincidental for the F 28.
3. Contacts between slats and wing due to different bending of the two prevents checking of retracted slat load predictions against in-flight strain-gauge measurements as was done for deflected slats.
4. Comparison between the general prediction methods discussed in chapters 4 and 5 was possible for the "common" case of retracted slats at  $M = .19$ , a subject also covered in the section tests to survey the deflection/retraction cycle. Given the sober character of the method - based on data for only two sections - used in chapter 4, the agreement, as shown in fig. 15, can be considered as very satisfactory.

#### 6. CONCLUDING REMARKS

The prediction process described may be used when a restricted amount of wind tunnel test data is available. The models required to collect these data are usually planned for development purposes and not specifically needed for load prediction.

There appear to be no elements, essentially restricting the process to small angles of sweep, provided that for the case of deflected slats the influence of the core flow in the slot is accounted for.

#### Notes.

1. An adjustment process as described for the flap lift carry-over effect in chapter 4 can also be derived for the tip alleviation effect. In this case a slightly higher loading is found for the far outer part of the slats.
2. A minor, but intriguing problem is connected with  $C_{ms}$ , which is found as the sum

$$\int C_p \times dx + \int C_p \times dz$$

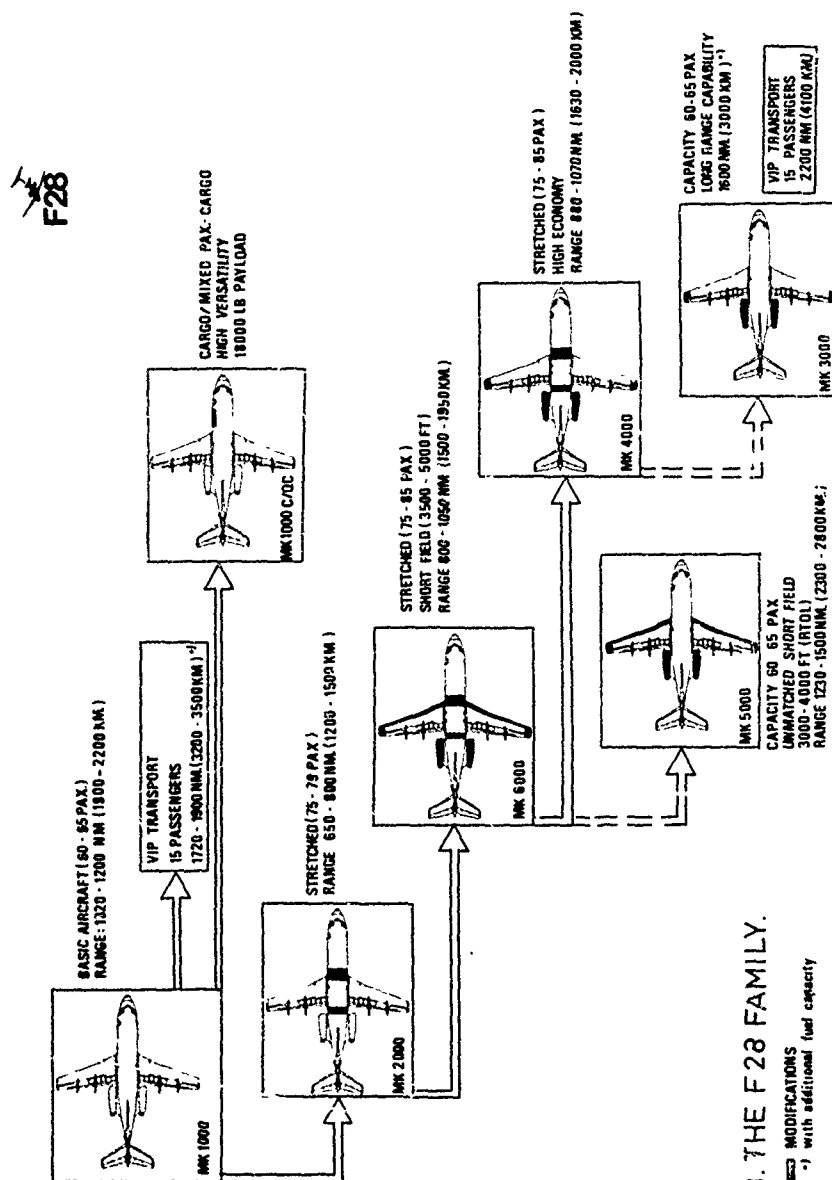
It is in a plane in flight direction, whereas the structural analysis works with planes perpendicular to the elastic axis of the slats. With an angle of sweep  $\beta$  of this axis, the local torsion moment coefficient around it becomes

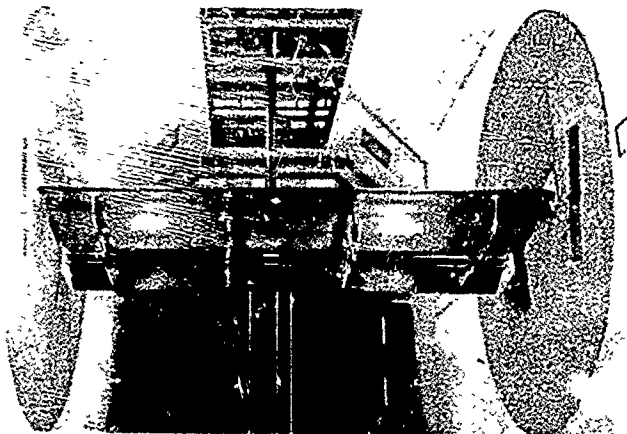
$$/ C_p \times dx \cos \beta + / C_p z dz$$

and not the smaller  $C_{m_s} \cos \beta$ . The apparent contradiction in this statement disappears at the tips of each slat segment.

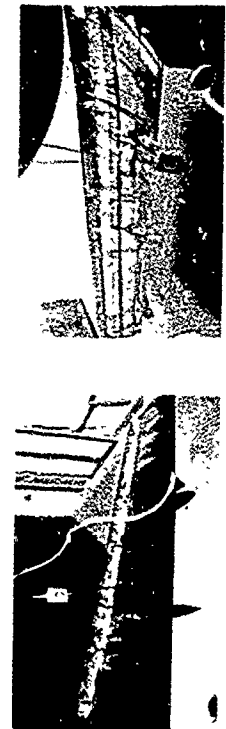
Mark nr.	seating ( pass. )	certified in	wing aspect ratio	l.e slats	t.e flaps
1,000 2,000	65 79	1969 1972	7.27	no	double slotted
5,000 6,000	65 79	- 1975	7.98	yes	
3,000 4,000	65 79	1976 1976	7.98	no	

Tabel 1.

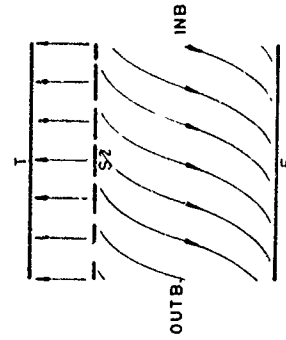
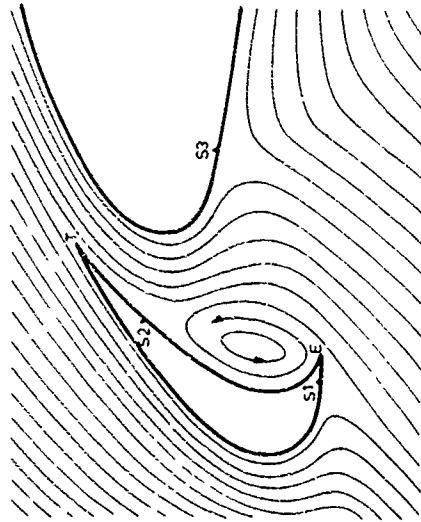




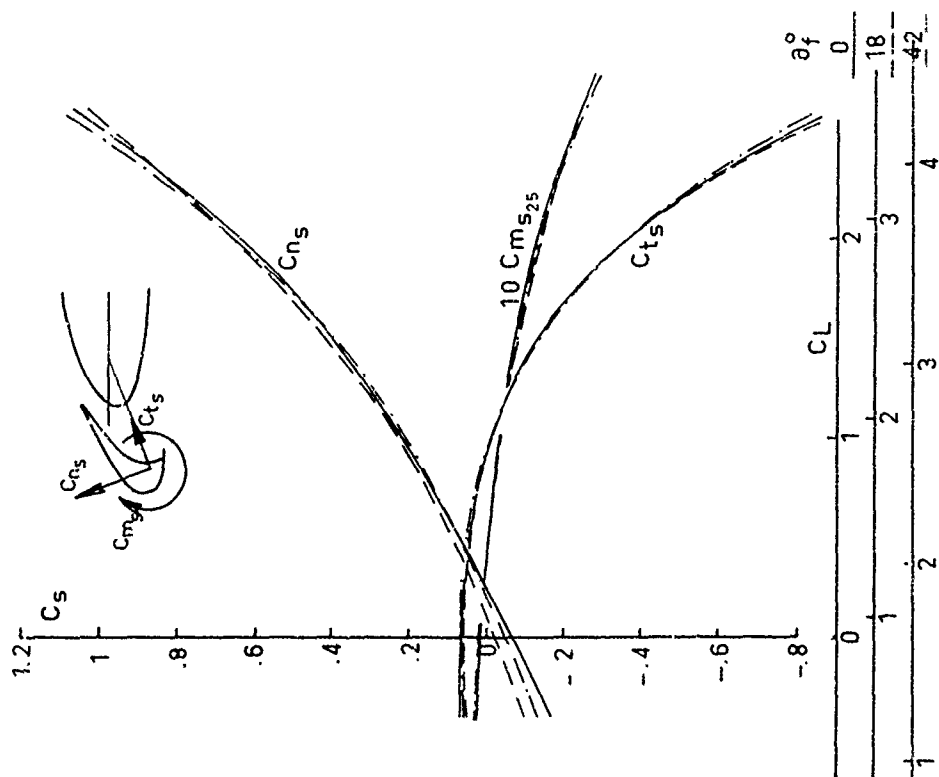
2 FLAP AND SLAT SECTION MODEL



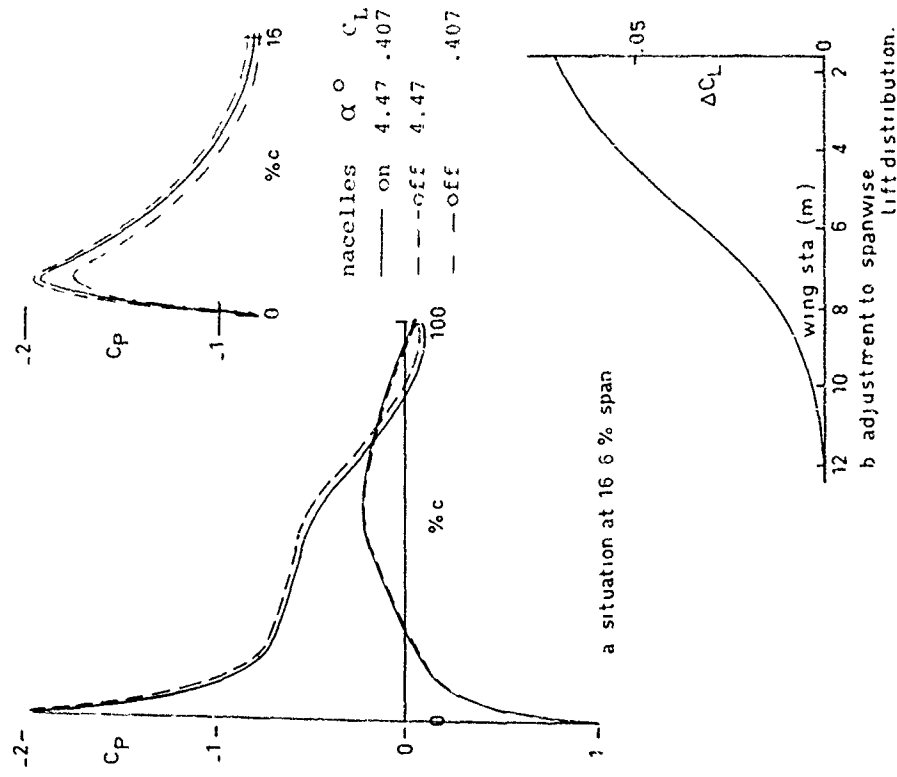
4 DAYGLO VISUALIZATIONS



3. THREE-DIMENSIONAL SLAT FLOW PHYSICS.

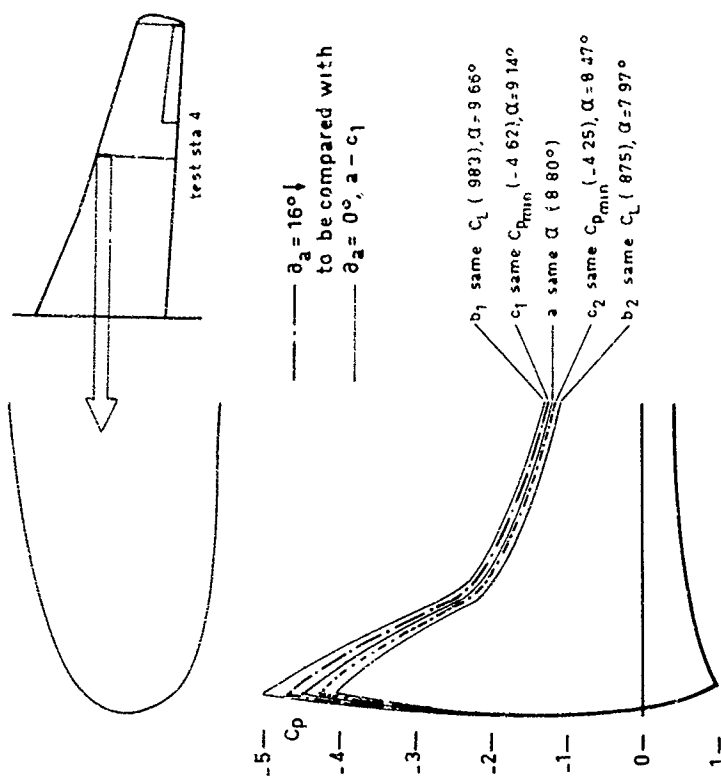


5. EXTENDED SLAT LOAD DATA.



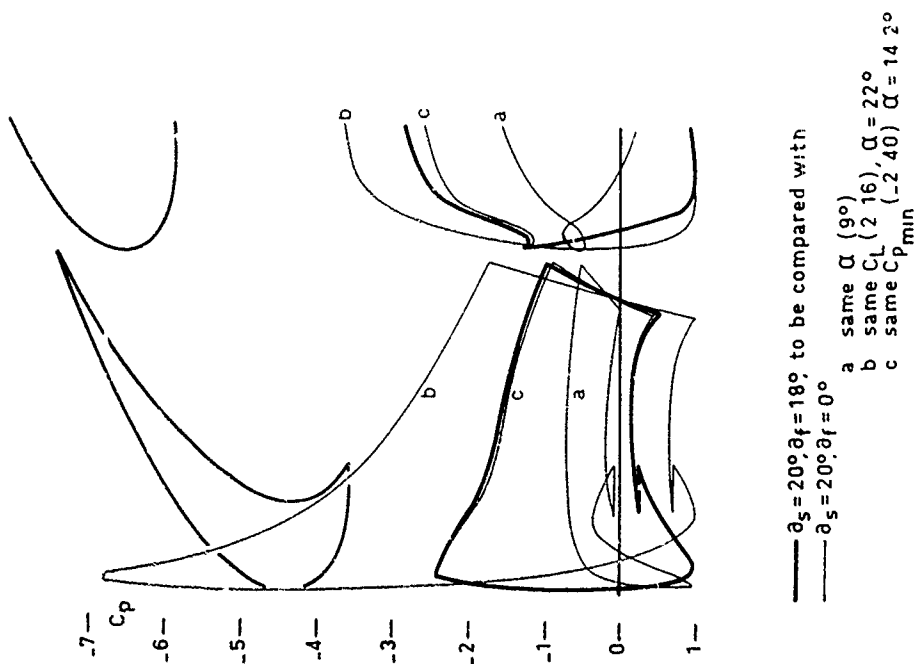
6 NACELLE INTERFERENCE EFFECT





---  $\alpha_a = 16^\circ$   
to be compared with  
—  $\alpha_a = 0^\circ$ ,  $a - c_2$

8. THREE-DIMENSIONAL AILERON LIFT CARRY-OVER.



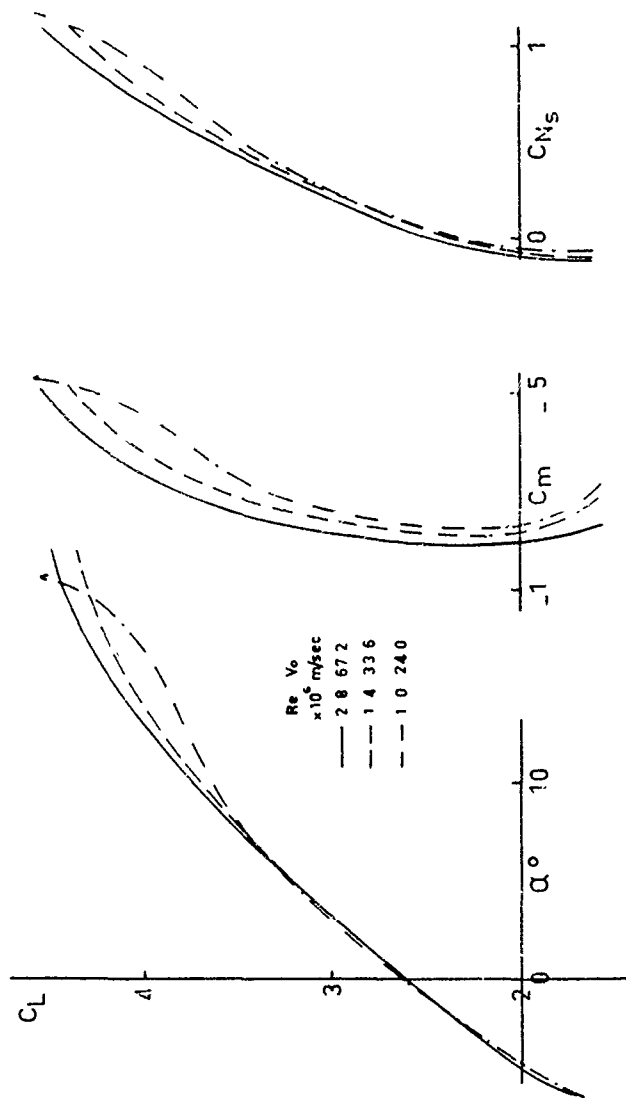
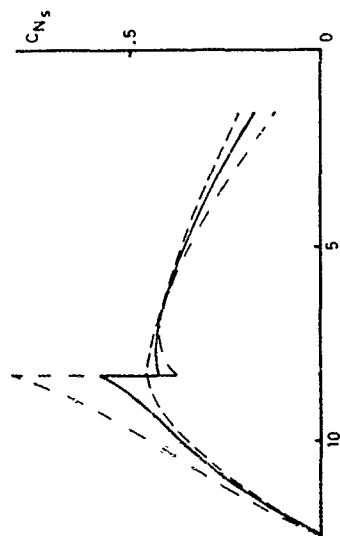
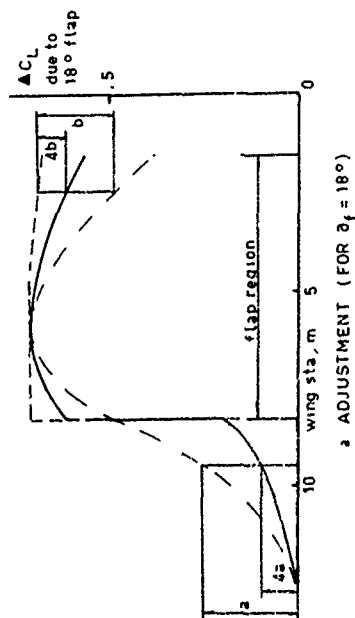
7. TWO-DIMENSIONAL FLAP LIFT CARRY-OVER

# ADDITIONAL LIFT DUE TO FLAP DEFLECTION

— ADJUSTED FOR SLAT LOAD PREDICTION

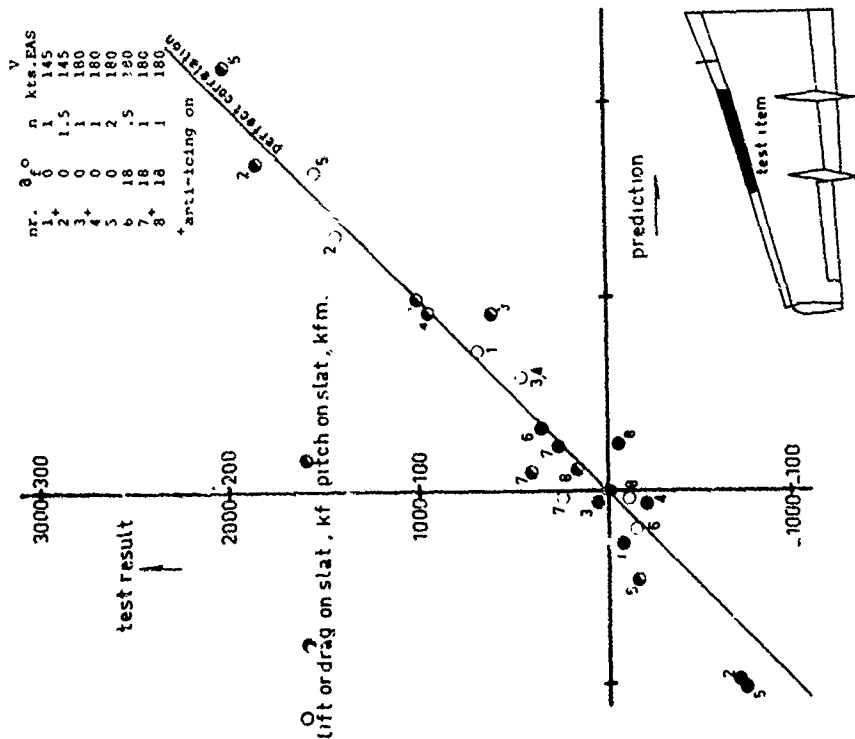
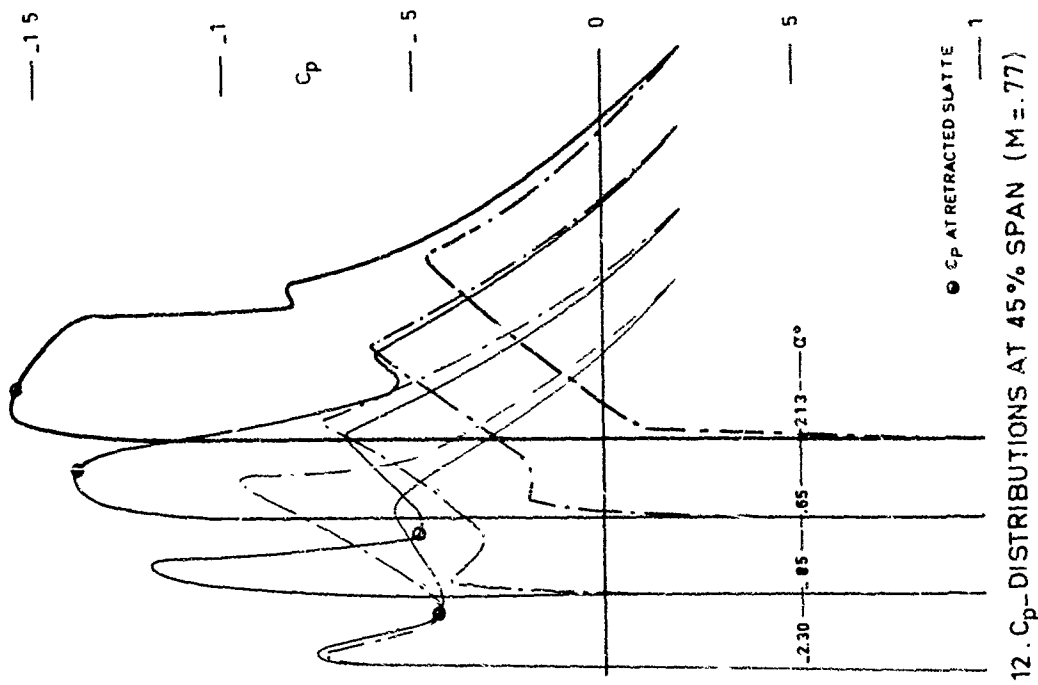
— 3-DIMENSIONAL

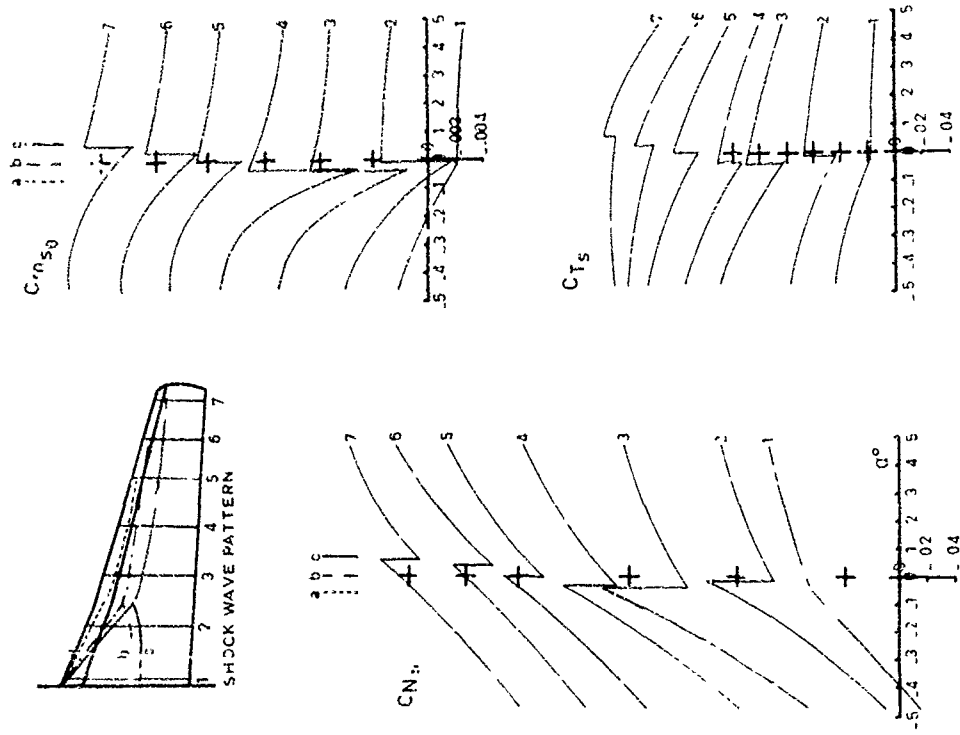
--- 2-DIMENSIONAL



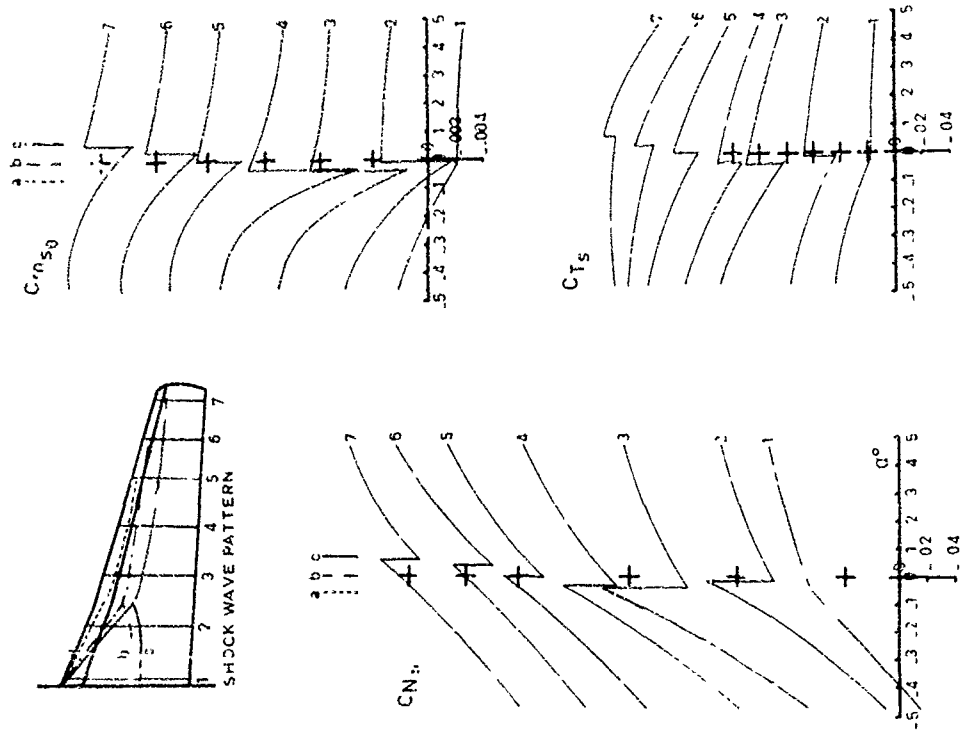
10 REYNOLDS' EFFECTS (NACA 0012-64 mod,  $\alpha_s = 25^\circ$ ,  $\alpha_f = 42^\circ$ ).

## 9. CORRECTION FOR FLAP LIFT CARRY-OVER

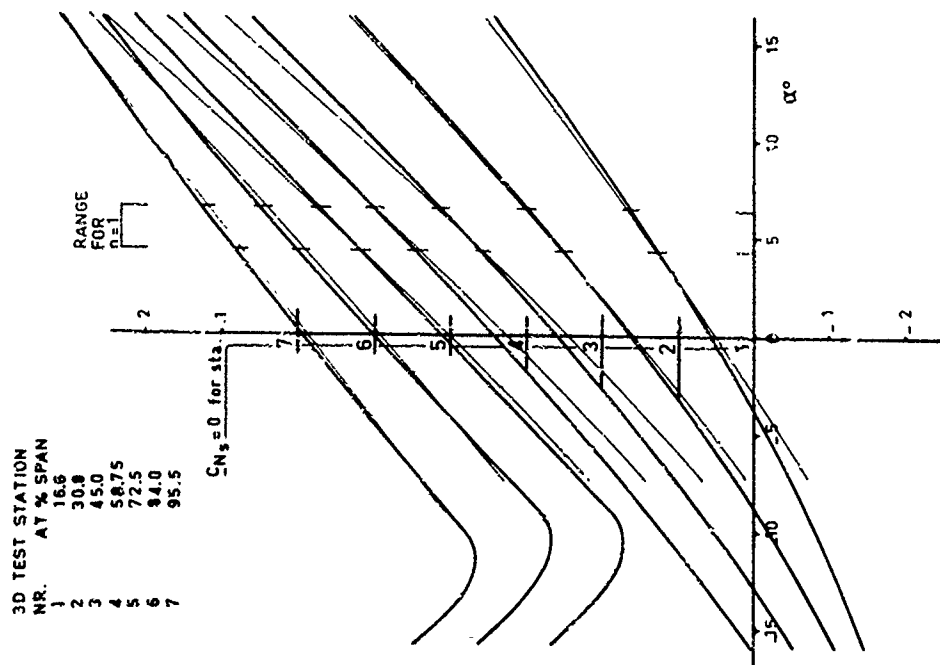
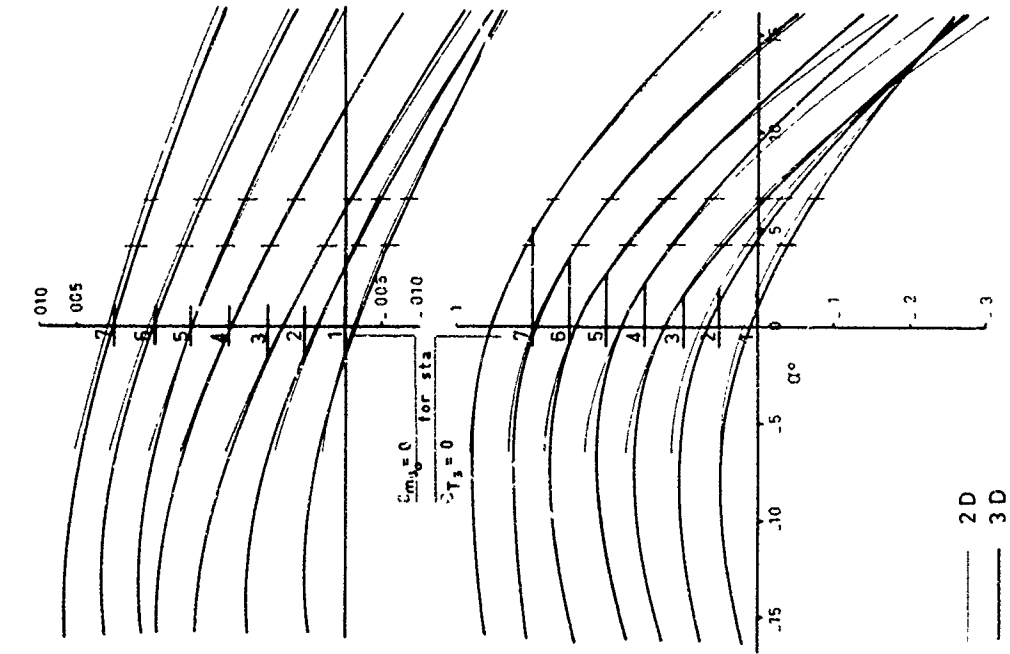




13 INTEGRATED RESULTS AT 45% SPAN ( $M = 77$ )



14 INTEGRATED RESULTS ( $M = 77$ )  
+ ORIGIN SHIFTING WITH SECTION



15. COMPARISON BETWEEN 2D- AND 3D-PREDICTIONS WITH SLATS RETRACTED AT  $M=0.19$ .

## PREDICTION OF AERODYNAMIC EFFECTS OF SPOILERS ON WINGS

by

G.V. Parkinson\* and P. Tam Do†  
 Department of Mechanical Engineering  
 The University of British Columbia  
 Vancouver, B.C. V6T 1W5 Canada

## SUMMARY

In work from the authors' laboratory reported at an AGARD Conference on VSTOL Aerodynamics in 1974, three theoretical methods were described for the prediction of aerodynamic loading on two-dimensional airfoils with spoilers. Two were thick-airfoil theories for steady-state pressure distribution, one analytic and the other numerical, and the third was a thin-airfoil theory for steady and transient lift. In the present paper, the above work is extended to an experimental study of effects of base venting on two-dimensional spoiler performance, and to a theoretical and experimental study of effects of finite span of spoilers and wings. The effects of realistic amounts of base venting on lift and pressure distribution proved small, so that unvented-spoiler theory can be used with acceptable accuracy. Lifting-line theory, requiring the sectional values of lift-curve slope and zero-lift angle as inputs, was used for the finite-span study, and the theoretical predictions were compared with experimental data from reflection-plane wind tunnel tests. Results are presented for lift and rolling moment, and agreement is good. The overall result is that the performance of finite-span, base-vented spoilers on finite-span wings can be predicted with acceptable accuracy, with only the spoiler base pressure as an empirical input.

## SOMMAIRE

Dans un travail du laboratoire des auteurs présenté à une conférence de l'AGARD sur l'aérodynamique des avions à décollage et à atterrissage court ou vertical (V/STOL), trois méthodes théoriques ont été décrites concernant l'évaluation de la charge aérodynamique sur les profilés d'aile bidimensionnels munis d'aérofreins. Deux de celles-ci, l'une analytique et l'autre numérique, relèvent de la théorie des profilés épais pour un état permanent de la répartition des pressions tandis que la troisième s'inspire de la théorie des profilés minces pour déterminer la portance en régime permanent et transitoire.

Dans la présente communication ces travaux ont été étendus à une étude expérimentale bidimensionnelle de l'effet d'une fente à la base de l'aérofrein sur les performances du profil d'aile de même qu'à l'étude théorique et expérimentale des effets dus aux aérofreins sur une aile d'envergure finie. Les effets sur la portance et la répartition des pressions se sont avérés minimes de sorte que la théorie développée pour les aérofreins sans fente peut être utilisée avec un degré de précision acceptable. La théorie de Prandtl sur l'aile d'envergure finie a servi de tremplin à l'étude tridimensionnelle. Cette approche requiert comme paramètres d'entrée l'incidence de portance nulle ainsi que la pente de la courbe de portance pour les différentes sections constituant l'aile. Les prédictions de cette théorie ont été comparées avec les résultats expérimentaux obtenus au moyen d'une maquette utilisant les propriétés de réflexion du mur du tunnel à vent.

Cette communication inclut une présentation des résultats concernant la portance et le moment de roullis. L'accord entre l'essai et le calcul semble bon. À titre de conclusion, la performance des ailes d'envergure finie munies d'aérofreins avec fente à la base peut être prédite avec une précision acceptable avec comme seule donnée empirique requise la pression de base derrière l'aérofrein.

## NOTATION

c	airfoil section chord	$\rho$	air density
b	wing semi-span	U	free-stream velocity
S	planform area for half wing	$\Gamma$	airfoil section circulation
$b_s$	spoiler span	$L'$	sectional lift
h	spoiler height	L	half-wing total lift
E	chordwise spoiler position	R	half-wing rolling moment
$\delta$	spoiler erection angle	$C_L$	sectional lift coefficient
$\alpha$	airfoil geometric angle of attack	$C_L$	half-wing lift coefficient
$\alpha_{L0}$	airfoil zero-lift angle	$C_R$	half-wing rolling moment coefficient
$\alpha_a = \alpha - \alpha_{L0}$	absolute angle of attack	$C_p$	pressure coefficient
x	chordwise distance from leading edge	$m_o$	sectional lift curve slope
y	spanwise distance from mid-span	$A_n$	Fourier coefficient
$\theta = \cos^{-1} y/b$	spanwise variable	( ) <sub>s</sub>	values for spoilered sections

\* Professor of Mechanical Engineering.

† Graduate Student, Department of Mechanical Engineering.

## 1. INTRODUCTION

In the prediction of aerodynamic loading on aircraft surfaces, the occurrence of separated flow creates great difficulties, because of the inadequacies of aerodynamic theory in dealing with such flows. As a result, design information on the aerodynamic effects of spoilers on wings has been obtained entirely from ad hoc testing, and prediction of loading has only been possible approximately, on the basis of experience with similar configurations. Yet spoilers are currently of great importance as control devices, whether deployed symmetrically for lift and drag control, or asymmetrically for roll control, and the development of prediction methods would clearly be beneficial.

For the past eight years, there has been a research program in the Mechanical Engineering Department at The University of British Columbia on the aerodynamics of spoilers. In the first phase of this program, three new theoretical two-dimensional potential flow methods were developed for the prediction of sectional characteristics of airfoils with spoilers, and wind tunnel experiments were conducted to correlate with the theoretical predictions. The results of these studies were reported at an earlier AGARD Symposium on V/STOL Aerodynamics [1]. Two of the above three theoretical methods were for the prediction of pressure distribution. One was an analytic method involving a combination of Theodorsen's [2] conformal mapping of an arbitrary profile with Parkinson's [3] wake source model. It could be used for any single-element airfoil with a normal spoiler, and a typical comparison of predicted and measured pressure distribution is shown in Figure 1.

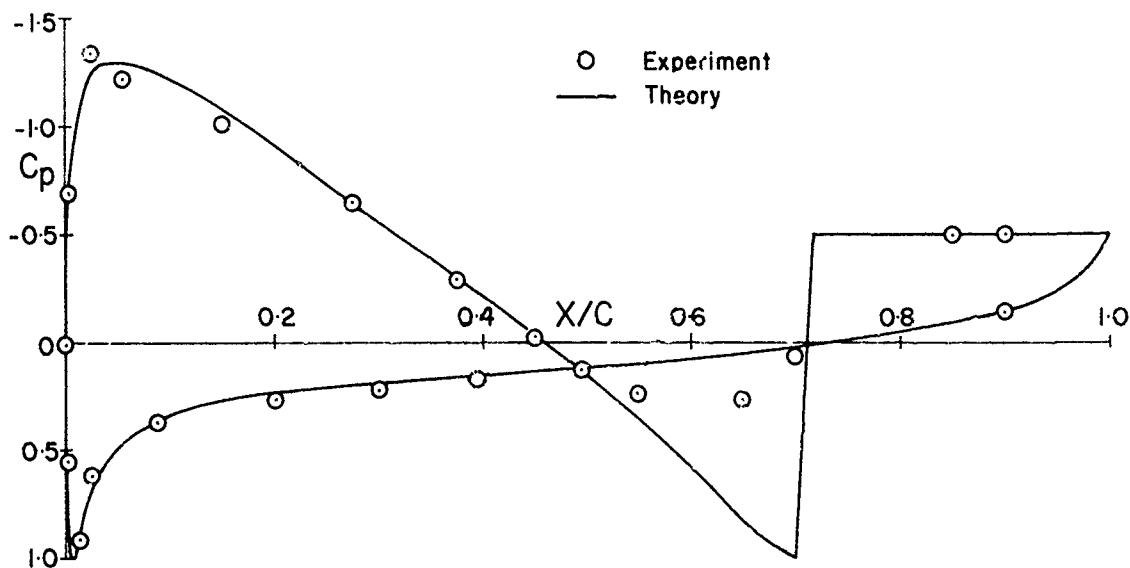


FIGURE 1. Pressure Distribution on Clark Y Airfoil with Spoiler.

The airfoil is a 14% thick Clark Y with an 8.4% normal spoiler at 70% chord. Angle of attack  $\alpha = 10.19^\circ$ , and the experimental Reynolds number was  $5.3 (10)^5$ . The experimental data were corrected for tunnel wall effects, and the resulting agreement with the theoretical curve is seen to be excellent, except for the usual disagreement just upstream of the spoiler. Here the theory predicts a stagnation point, whereas the actual flow separates and forms a constant-pressure bubble. The second method replaced the conformal mapping by the surface source distribution method of A.M.O. Smith and his colleagues [4], and as a result could be applied to multi-element airfoils with inclined spoilers.

The third method used linearized free-streamline theory, and was for the prediction of lift and moment on an arbitrary single-element airfoil with spoiler, under either steady-state or transient conditions following spoiler actuation. A typical comparison of predicted and measured steady-state lift as a function of angle of attack is shown in Figure 2. The airfoil is again a 14% thick Clark Y, in this example with a 10% spoiler inclined at  $60^\circ$  and located at 70% chord. The test Reynolds number was  $4(10)^5$ . Agreement of the theoretical curve with the experimental data is seen to be good. The nonlinear increase of the experimental lift at high  $\alpha$  is a result of the growth of the separation bubble seen in Figure 1. In the above theories, the only empirical input needed is the spoiler base pressure coefficient.

However, in these theories the spoilers are impervious, and the flows are two-dimensional, whereas in aircraft practice spoilers are vented at the base and cover only part of the finite span of wings. The current phase of the research program is therefore investigating the effects of base venting and finite span of spoilers.

## 2. BASE VENTING EXPERIMENTS

Two-dimensional flow conditions were retained for experimental investigations of spoiler base venting, so that direct comparisons could be made with the two-dimensional theories, and with previous sectional measurements for unvented spoilers [1]. The experiments were performed in a low-speed, low-turbulence wind tunnel with a test section 915 mm wide and 687 mm high. The test airfoil was a Joukowski section 11% thick with 2.4% camber, of 307 mm chord. It was constructed mainly of wood, with an aluminum section at mid-span containing 37 pressure taps, of which 24 were distributed on the upper surface. It was built with end plates on which spanwise metal spoilers could be mounted. The spoilers were normal to the airfoil surface, and of 10% airfoil chord in height above the surface. They were located at 50, 60, 70, or 80% chord. The spanwise base vent was 10, 20, 30, 40, or 50% of the spoiler height.

The test airfoil spanned the tunnel test section vertically, with small clearances at floor and

ceiling, and was mounted on the yaw turntable of the tunnel balance, located under the test section. For each spoiler location and degree of base venting, lift, drag, and pitching-moment measurements were made over a full range of angle of attack, using the tunnel balance. For some angles of attack, pressure distributions were measured using a multitube manometer. The test Reynolds number was  $4.4 (10)^5$ .

Figures 3 and 4 show some of the results of these measurements for the tests with the spoiler located at 70% chord. Table 1 identifies the symbols used in the Figures for the different base vent depths expressed as percentages of the spoiler height.

Figure 3 shows airfoil pressure distributions at  $\alpha = 8^\circ$ , and Figure 4 gives the variation of lift coefficient  $C_L$  with  $\alpha$ , for the various degrees of spoiler base venting. The most significant result is that over the range of positive  $C_L$ , there is very little difference in airfoil loading from that of the unvented configuration for vents of up to 20% of the spoiler height - the range of practical interest. This is implied by the close agreement of the  $C_p$ -distributions for 10 and 20% vents in Figure 3 (the unvented  $C_p$ -distribution was not measured at  $\alpha = 8^\circ$ ), and confirmed by the  $C_L$  data of Figure 4. As the size of the vent is increased above 20%, the airfoil upper-surface suction increases ahead of the spoiler, and the lower-surface pressure becomes more positive, so that the lift slowly approaches the value for the basic airfoil without spoiler. The base pressure behind the spoiler remains fairly constant for vents of 10 and 20%, but shows the effect of flow through the vent for 40 and 50% depths.

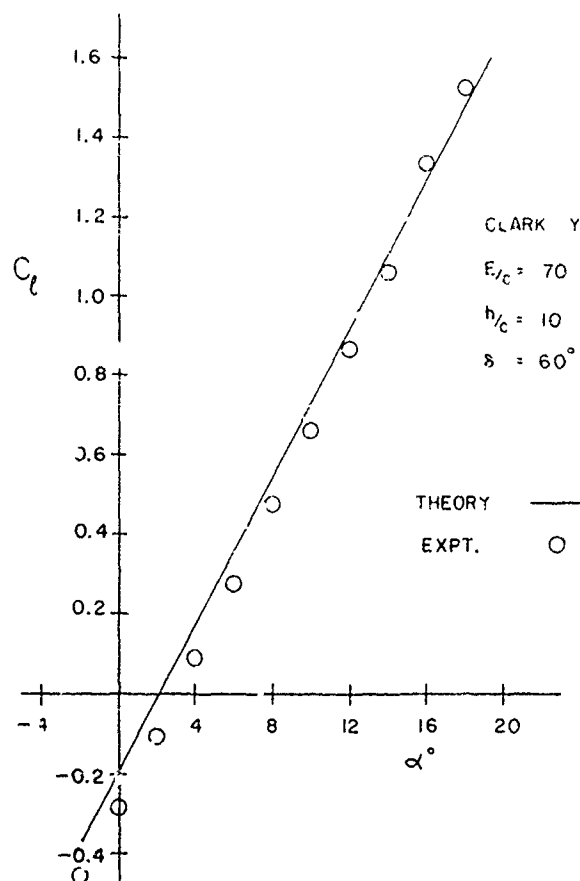


FIGURE 2. Lift on Clark Y Airfoil with Spoiler.

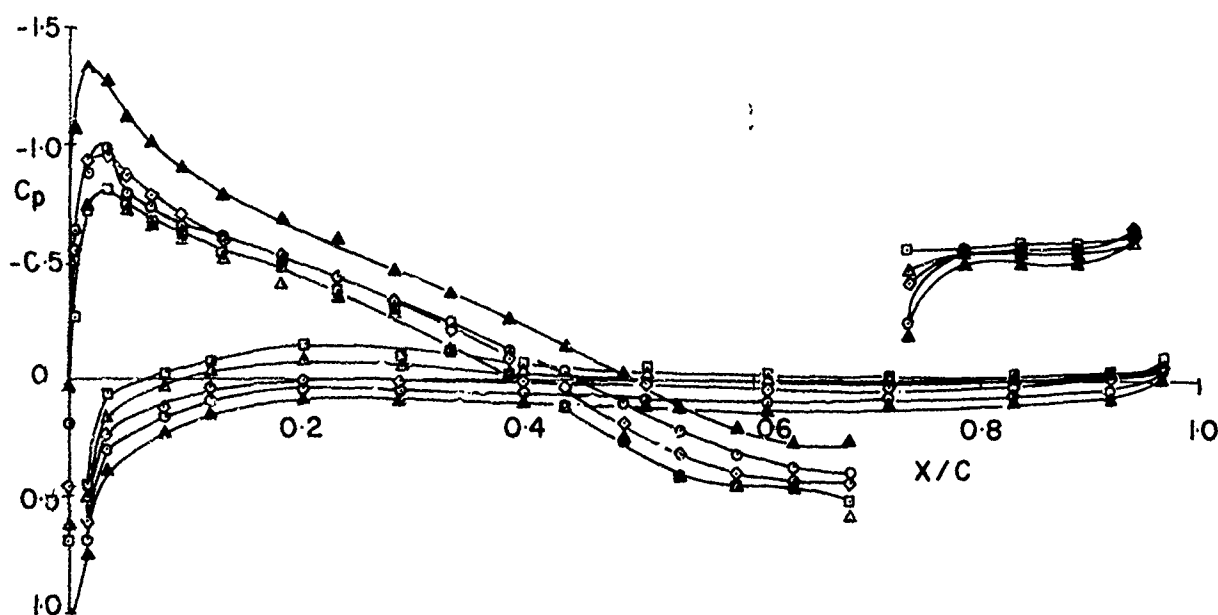


FIGURE 3. Pressure Distributions on Joukowski Airfoil with Base-vented Spoiler.



TABLE 1.

Symbol	Base Vent %
●	0
□	10
△	20
◇	30
○	40
▲	50

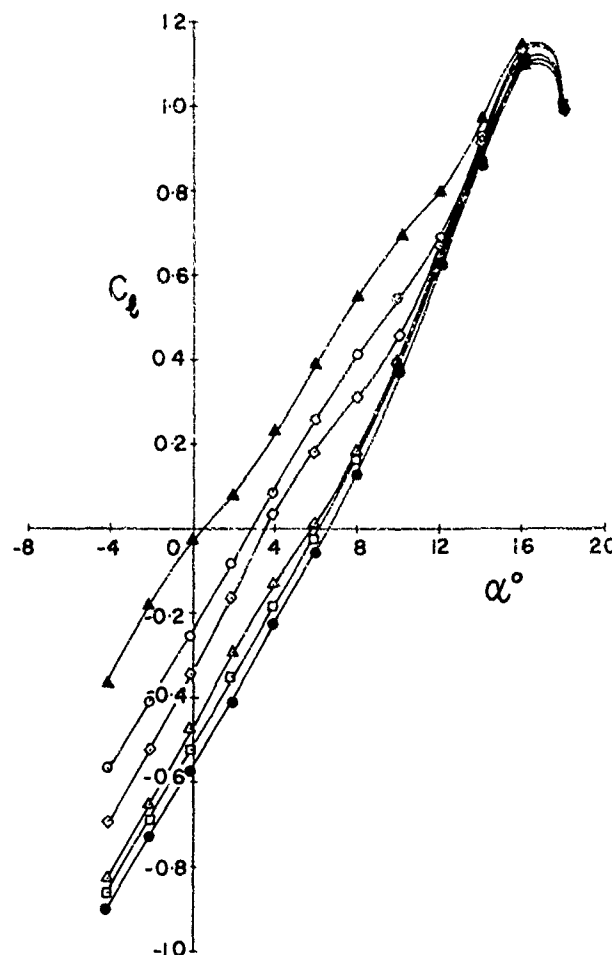


FIGURE 4. Lift on Joukowski Airfoil with Base-vented Spoiler.

### 3. SPOILERS OF FINITE SPAN

#### 3.1 Reflection-plane Experiments

For experimental investigation of effects of finite span of spoilers and wings, it was decided to use half models, as shown in Figure 5, in order to accommodate a good range of wing aspect ratios (4 to 8) with as large a chord and Reynolds number as possible. For such tests, the floor is properly a plane of symmetry for cases of symmetrical spoiler deployment, but not for the asymmetric deployment used in roll control. The use of the reflection-plane data for prediction of rolling moment is considered theoretically later.

The wings were tested in the same wind tunnel and mounted on the same balance system as described in § 2. They were machined from solid aluminum, in spanwise sections 51 and 13 mm long, and of 131 mm chord, so that half-model wings of equivalent full aspect ratio 3.9, 4.8, 5.8, 6.8, and 7.7 could be assembled. Wings spanning the height of the test section could also be assembled for two-dimensional tests. The airfoil section was NACA 0015, and the wings could be fitted with 10% unvented normal spoilers located at 48, 58, 68, 77, or 87% chord. Spoiler spans were 20, 30, 40, or 50% of the span of each half wing, with the spoiler inboard tip always at mid-span of the half wing. Test Reynolds number was  $3(10)^5$ . Force and moment measurements were made for all configurations over a full range of angle of attack.

#### 3.2 Lifting-line Theory - General Formulation

The lifting-line theory as formulated by Prandtl [5], is applicable to unswept wings of large aspect ratio. In this theory, the wing is replaced by a lifting line of bound vortex filaments at the one-quarter-chord position, and a sheet of trailing vortices lies in the plane of the wing and the free-stream velocity. The trailing vortices induce a downwash over the wing, which alters the direction of the flow approaching the wing downward by an induced angle of attack. The effective angle of attack and the corresponding sectional lift are thus reduced below their two-dimensional values, although the relationship between them is unchanged. Also, the sectional lift  $L'$  is still given in terms of local circulation  $\Gamma$  by the Kutta-Joukowski law,

$$L' = \rho U \Gamma \quad (3.1)$$

so that the unknown spanwise distributions of downwash and circulation are related. An additional relation between them is found by using the Biot-Savart law.

Next, it is assumed, in the manner of Glauert [6], that the circulation is given by the infinite Fourier series,

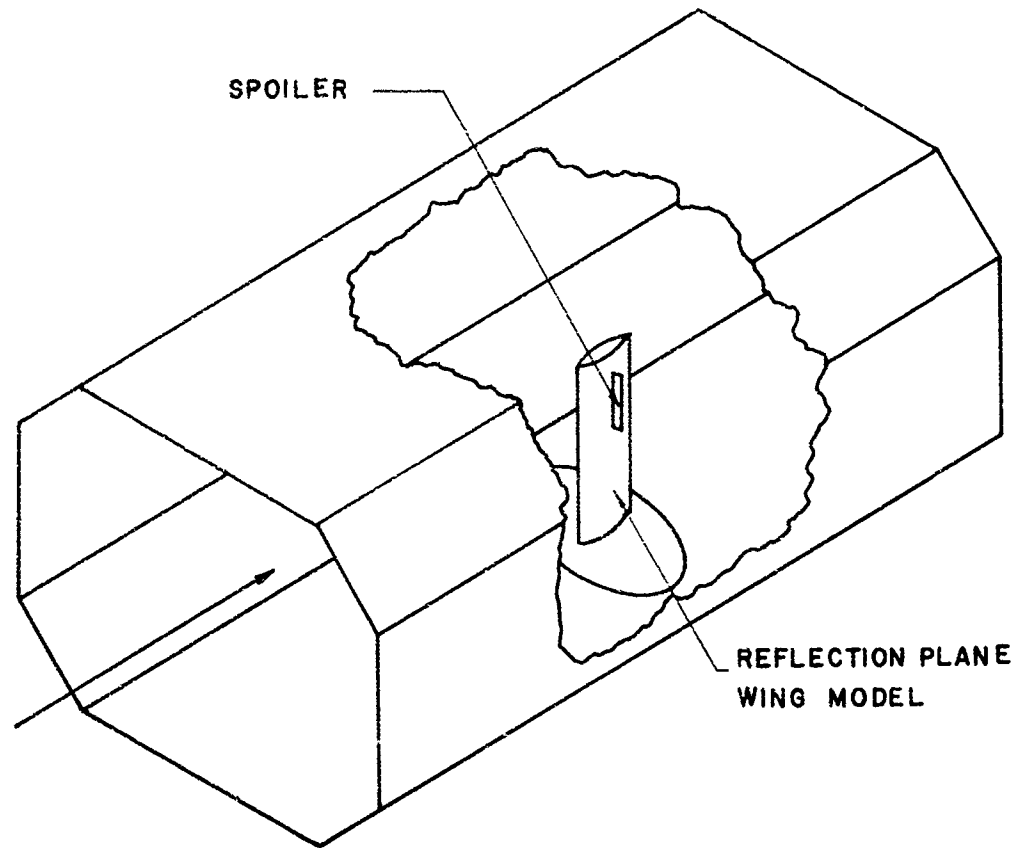


FIGURE 5. Wind Tunnel Test Configuration for Finite-span Spoilers.

$$\Gamma = 4bU \sum_{n=1}^{\infty} A_n \sin n\theta \quad (3.2)$$

where  $U$  is the free-stream velocity,  $b$  the wing semispan, and  $\theta$  is defined in terms of spanwise coordinate  $y$  by

$$y = b \cos \theta \quad (3.3)$$

Substitution of Equation (3.2) in the previous relations leads to the fundamental equation for the unknown coefficients  $A_n$ :

$$\sum_{n=1}^{\infty} A_n \sin n\theta \left[ \frac{8b}{m_0 c} \sin \theta + n \right] = \alpha_a \sin \theta \quad (3.4)$$

where  $c$ ,  $m_0$ , and  $\alpha_a$  are the sectional chord, lift-curve slope, and absolute angle of attack. Parameters  $c$ ,  $m_0$ , and  $\alpha_a$  may vary along the span depending on whether or not the wing has section changes, taper or twist. The equation must be satisfied for all points,  $0 \leq \theta \leq \pi$ .

Solution for the unknown  $A_n$ 's is accomplished by considering a finite number of terms of the Fourier series, say  $m$  terms. By choosing the number of values of span variable  $\theta$  equal to  $m$ , the number of terms in the truncated Fourier series, and by substituting these  $m$  values of  $\theta$  into Equation (3.4), a system of  $m$  equations in  $m$  unknowns is obtained, and hence a solution for the  $A_n$ 's. Since only  $m$  terms of the Fourier series are considered, Equation (3.4) is satisfied only at the  $m$  positions of  $\theta$ .

Wieselsberger [7] has pointed out the necessity of including the wing tips in calculations for flapped wings. Since Equation (3.4) is degenerate at the tips where  $\theta = 0$  or  $\pi$ , L'Hôpital's rule must be applied to obtain the result

$$\left. \begin{aligned} \alpha_a(0) &= \sum_{n=1}^m n^2 A_n \\ \alpha_a(\pi) &= \sum_{n=1}^m n^2 A_n (-1)^{n+1} \end{aligned} \right\} \quad (3.5)$$

The lift  $L$  and rolling moment  $R$  can be calculated once the Fourier coefficients are known. Since

$$dL = \rho U \Gamma(y) dy$$

and

$$dR = y dL,$$

by integrating across the span, the lift and rolling moment for the wing can be obtained. Since the theoretical results were to be compared with symmetric reflection-plane experimental results, the integrations were made over the semi-span. Thus,

$$C_L = \frac{L}{\frac{1}{2} \rho U^2 S} = \frac{\int_0^b \rho U \Gamma(y) dy}{\frac{1}{2} \rho U^2 S} \quad (3.6)$$

and

$$C_R = \frac{R}{\frac{1}{2} \rho U^2 S b} = \frac{\int_0^b \rho U \Gamma(y) y dy}{\frac{1}{2} \rho U^2 S b} \quad (3.7)$$

where  $S$  is the planform area of the half wing. Upon integration, we get

$$C_L = \frac{2\pi b^2}{S} A_1 \quad (3.8)$$

$$C_R = \frac{8b^2}{S} \sum_{i=1}^m A_{2i-1} \frac{(-1)^i}{(2i-3)(2i+1)} \quad (3.9)$$

In Equation (3.9), use is made of the fact that only the odd terms of the Fourier series contribute to a symmetric loading distribution.

### 3.3 Application to Wing with Part-span Spoilers

Experimental and theoretical investigations of two-dimensional airfoils with spoilers [1] have shown that the effect of a spoiler on section characteristics is to alter both the lift curve slope  $m_o$  and zero-lift angle of attack  $\alpha_{LO}$ . (The absolute angle of attack  $\alpha_a$  is related to the geometric angle of attack  $\alpha$  by  $\alpha_a = \alpha - \alpha_{LO}$ .) Let  $m_{o_s}$  and  $\alpha_{a_s}$  be the sectional lift curve slope and absolute angle of

attack of the spoiled sections. Then in applying the lifting-line Equation (3.4) to a wing with a part-span spoiler,  $\alpha_{a_s}$  and  $m_{o_s}$  must replace  $\alpha_a$  and  $m_o$  over that portion of the wing which is spoiled.

This results in a discontinuity in the angle of attack and lift curve slope distributions across the wing. For an infinite Fourier series, the position of this discontinuity may be exactly fixed, since all values of the span variable  $\theta$  are covered by the series. For a Fourier series with a finite number of terms, however, the values of lift curve slope and angle of attack will change from one value to another between two adjacent values of  $\theta$ . This represents a gradual change in sectional lift curve slope and angle of attack over a finite range of the span variable  $\theta$ , and is an approximation of the real situation. The position of each discontinuity may then be arranged to lie midway between two consecutive values of the span variable  $\theta$ .

Either experimental or theoretical values of  $m_o$ ,  $m_{o_s}$ ,  $\alpha_a$ , and  $\alpha_{a_s}$  may be used as inputs to

Equation (3.4). In this paper, experimental data was used, since it was available. The two-dimensional experimental data must first be linearised, as Equation (3.4) is linear. Straight line regressions were made on the data and the resultant values of  $m_o$  and  $\alpha_{LO}$  are given in Table 2. An example of the linear approximation to the experimental sectional data is shown in Figure 6, for the NACA 0015 section with 10% normal spoiler at 48% chord.

Lift coefficient  $C_L$ , rolling moment coefficient  $C_R$ , and spanwise lift distribution in the form  $(\Gamma/4Ub)$  were calculated for symmetric cases corresponding to the reflection-plane experiments. Calculations were also made for asymmetric cases of full wings with spoiler erected on only one half. A comparison of calculated spanwise lift distributions for unspoiled, asymmetrically spoiled, and symmetrically spoiled rectangular wings of aspect ratio 7.7 is shown in Figure 7. The airfoil section is again NACA 0015 and, for convenience, calculations were made for an angle of attack of 1 radian. Spoilers were of length  $b_s$  equal to 40% of the wing semispan  $b$ , and mounted between 50 and 90% semispan. The chordwise location  $E$  of the spoilers was at 48% chord  $c$ .

Examination of the curves shows that the symmetric loadings differ by less than 2% from the asymmetric loading at the wing root, and the two spoiled cases are in progressively closer agreement away from the root. This suggests that the reflection-plane tests can be used with small error to predict the characteristics of an asymmetrically spoiled wing.

### 3.4 Comparison of Theoretical Predictions with Experimental Results

Theoretical values of half-wing  $C_L$  and  $C_R$  were calculated for all wing-spoiler configurations tested in the wind tunnel. A typical comparison is shown in Figures 8 and 9 for the rectangular half-wing of equivalent full aspect ratio 7.7. The airfoil section is NACA 0015 as before, and the spoiler parameters are  $\delta = 90^\circ$ ,  $h/c = 0.10$ ,  $E/c = 0.48$ ,  $b_s/b = 0.20$ , with the inboard spoiler tip at mid-span of the half-wing.

The agreement of the predicted and measured values is seen to be quite good, both for  $C_L$  and  $C_R$ , although the sectional input data for the NACA 0015 (both spoiled as in Figure 6 and unspoiled), for which a linear approximation is used in the theory, is more nonlinear with  $\alpha$  than usual. The same non-linearity appears in the experimental finite-span data of Figures 8 and 9, and accordingly limits the degree of agreement with the linear theory.

Another comparison of interest is that of the variation of the predicted and measured effective moment arm of the incremental rolling moment caused by spoiler erection. Such a comparison is presented in Figure 10 in the form  $\Delta C_R / \Delta C_L$  as a function of relative spoiler span  $b_s/b$ . Again the half-wing is rectangular, of equivalent full aspect ratio 7.7, with NACA 0015 section and spoiler parameters  $\delta = 90^\circ$ ,  $h/c = 0.10$ ,  $E/c = 0.48$ . The spoiler inboard tip is again at mid-span of the half-wing for all cases. The experimental points for each value of  $b_s/b$  represent an average  $\Delta C_R / \Delta C_L$  over the range  $-4^\circ \leq \alpha \leq 14^\circ$ .

TABLE 2. Values of Lift-curve Slope and Zero-lift Angle from Linear Regression of Data for NACA 0015.

E/C	$m_o$ or $m_{oS}$ per rad.	$c_{L0}$ or $\alpha_{L0S}$ rad.
unspoilered	5.40	0
.48	4.45	0.182
.58	5.02	0.172
.68	5.70	0.160
.77	6.15	0.159
.87	7.00	0.157

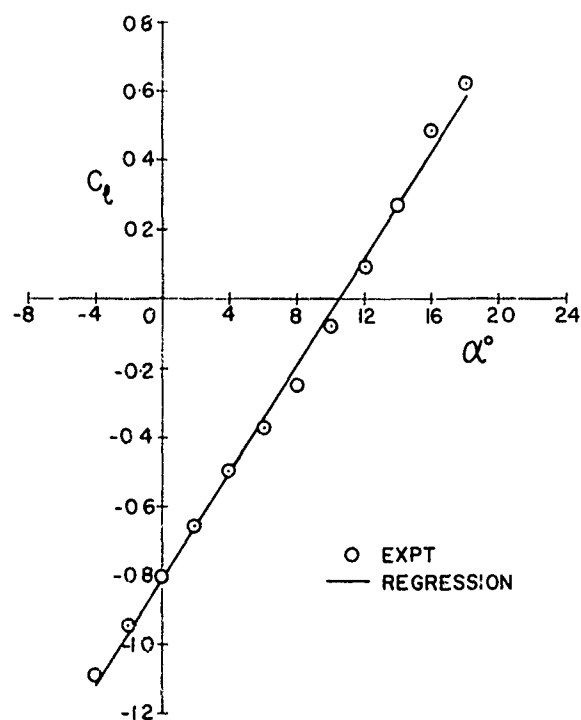


FIGURE 6. Linear Approximation to Lift Variation of NACA 0015 Airfoil with Spoiler.

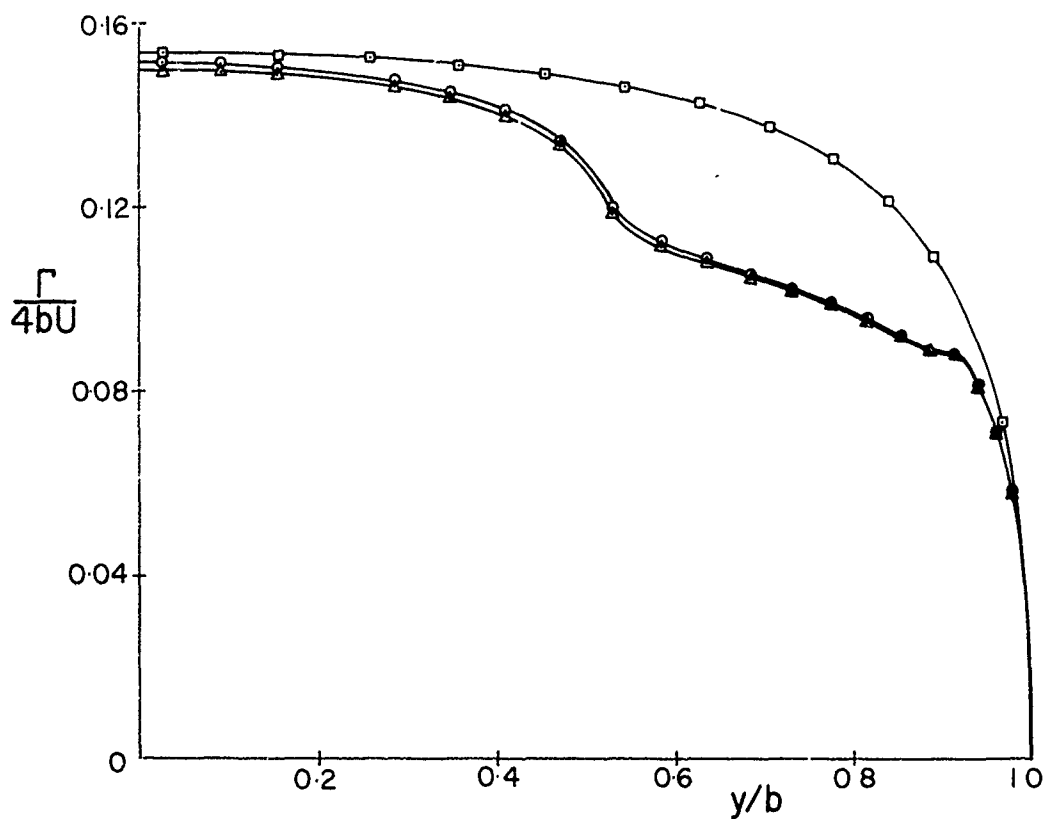


FIGURE 7. Spanwise Lift Distributions for Symmetric and Asymmetric Spoiler Configurations on a Rectangular Wing of Aspect Ratio 7.7.

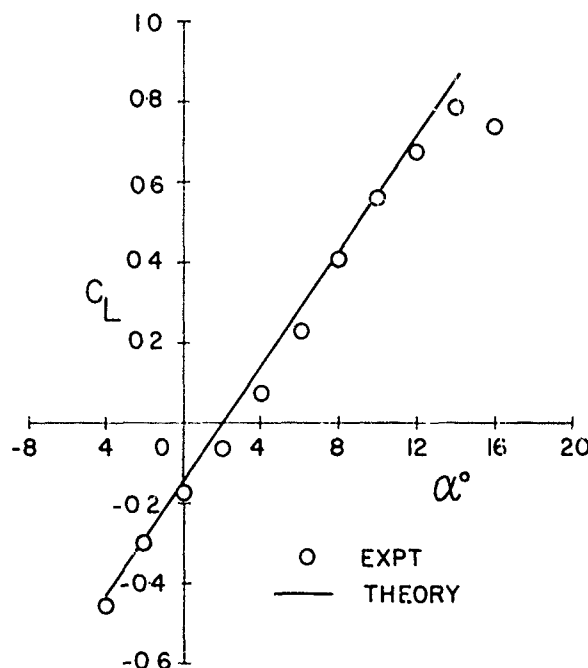


FIGURE 8. Half-wing Lift for Wing of Aspect Ratio 7.7.

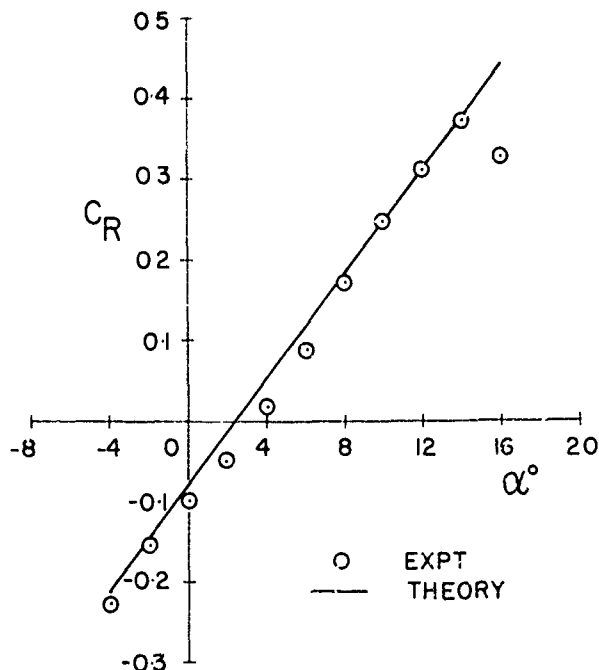


FIGURE 9. Half-wing Rolling Moment for Wing of Aspect Ratio 7.7.

The dashed line in the figure represents the variation that would occur if the incremental lift acted at mid-span of the spoiler.

The agreement between predicted and measured values is seen to be good, with the effective center of incremental lift lying between 1/3 and 1/2 the distance from the spoiler mid-span to its inboard tip.

#### 4. DISCUSSION

Figures 8, 9, and 10 indicate that good prediction of the lift and rolling moment characteristics of finite-span wings with spoilers can be achieved using sectional input data in a lifting-line theory. As usual with lifting-line theory, the loading is somewhat over estimated, but the agreement between predicted and measured values is good, and would have been still better if an airfoil section with a more linear basic  $C_L - \alpha$  variation than that of the NACA 0015 had been used.

Also, as Figure 2 indicates, the thin-airfoil theory of Reference 1 would give at least as good predictions of  $\alpha_{0s}$ ,  $\alpha_{LOs}$  as the linear

approximation to experimental sectional data used here. This thin-airfoil theory of course takes no account of the nonlinear effect of the separation bubble upstream of the spoiler, and so would produce better agreement for the lifting-line theory at the lower angles of attack. The thin-airfoil theory wasn't used in this paper because it hasn't been worked out yet for the NACA 0015 section with spoiler.

Figure 4 shows that  $C_L$  at a given  $\alpha$  is only slightly higher for an airfoil with spoiler containing a 10 to 20% base vent than for the same configuration unvented. Since the value of  $C_L$  predicted by the thin-airfoil theory, as in Figure 3, also tends to be slightly higher than the experimental value for the unvented

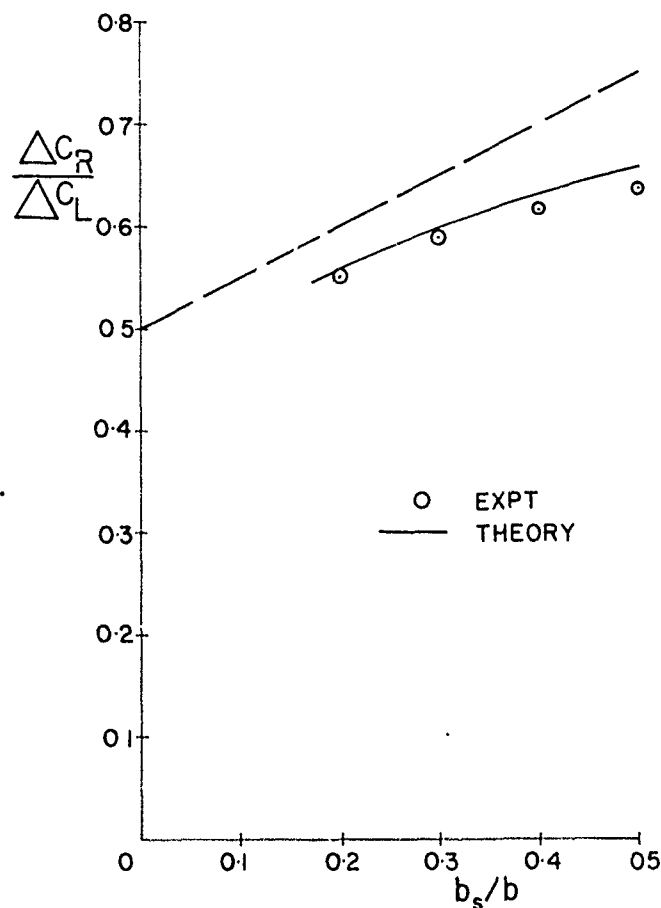


FIGURE 10. Effective Moment Arm of Incremental Rolling Moment from Spoiler.

configuration, it appears that the sectional lift of actual vented configurations will be accurately predicted by the thin-airfoil theory. Figure 3 indicates that practical amounts of spoiler base venting do not change the spoiler base pressure significantly.

The theoretical results of Figure 7 suggest that reflection-plane wing experiments will be satisfactory for wind-tunnel investigations of asymmetric wing-spoiler configurations. It should be noted that the half-wing rolling moment coefficient  $C_R$  used here is not the rolling moment coefficient as usually defined for a wing or complete aircraft. Figure 10 indicates that the effective center of the incremental lift from the spoiler lies well inboard of the spoiler mid-span.

The overall result of the paper is that for a finite-span wing without slotted flaps, the effect of base-vented part-span spoilers on lift and rolling moment can be predicted accurately with only the spoiler base pressure coefficient as a required empirical input. It seems likely that an adequate empirical recipe can be devised for predicting this base pressure coefficient as a function of wing geometry and incidence, since it has a very limited range of values.

For the more interesting case of a wing with spoilers in the presence of slotted flaps, a sectional thin-airfoil theory for predicting  $m_{o_s}$  and  $\alpha_{LO_s}$  is not available. However, the numerical thick-airfoil theory of Reference 1, in its so-called 2-source model, can be used to calculate  $C_L$  as a function of  $\alpha$  for an airfoil with spoiler and slotted flap, so that  $m_{o_s}$  and  $\alpha_{LO_s}$  can be determined, and the lifting-line theory can then be used as in this paper. This form of theory has still to be worked out and tested against experimental data.

#### ACKNOWLEDGEMENT

The work described here was supported by the Defence Research Board of Canada under Grant 9551-13, and by the National Research Council of Canada under Grant 67-0586.

#### REFERENCES

1. Parkinson, G.V., Brown, G.P., and Jandali, T.; 'The Aerodynamics of Two-dimensional Airfoils with Spoilers', Proc. AGARD Conf. on V/STOL Aerodynamics, Delft, April, 1974, pp. 14-1 to 14-10.
2. Theodorsen, T.; 'Theory of Wing Sections of Arbitrary Shape', NACA Rep. 411, 1931.
3. Parkinson, G.V. and Jandali, T.; 'A Wake Source Model for Bluff Body Potential Flow', Jour. Fluid Mech., 40, 3, 1970, pp. 577-594.
4. Hess, J.L. and Smith, A.M.O.; 'Calculation of Potential Flow About Arbitrary Bodies', Prog. in Aero. Sci., 8, Pergamon, 1966.
5. Prandtl, L.; 'Applications of Modern Hydrodynamics to Aeronautics', NACA Rept. No. 116, 1921.
6. Glauert, H.; 'Elements of Airfoil and Airscrew Theory', Cambridge University Press, 1927.
7. Wieselsberger, C.; 'Theoretical Investigation of the Effect of the Ailerons on the Wing of an Airplane', NACA TM510, 1928.

# A TECHNIQUE FOR PREDICTING EXTERNAL STORE AERODYNAMIC LOADS

A. R. Rudnicki, Jr.  
E. G. Waggoner, Jr.  
R. D. Gallagher  
Vought Corporation  
Systems Division  
Dallas, Texas 75222

## SUMMARY

A technique has been developed under U.S. Air Force sponsorship for predicting six-component airloads on captive stores for single and multiple carriage configurations. The prediction method includes techniques for predicting the basic airload as well as the incremental airloads due to aircraft yaw and adjacent store interference. The single carriage prediction technique is valid for the Mach number range 0.5 to 2.0 while the multiple carriage technique was developed for the Mach range 0.5 to 1.6.

The basic approach to the prediction technique was an empirical correlation of a large experimental data base consisting of literature survey data and data obtained from a parametric wind tunnel test.

This paper summarizes the study program, presents the approach and major variables considered in the technique development, and discusses the prediction results achieved. Comparisons between experimental data and predictions for the six airload components are included for both subsonic and supersonic flight conditions.

## NOTATION

b	Aircraft wing span, in.	$X_B, Y_B, Z_B$	Store body axis coordinate system
$C_y$	Side force coefficient, $\frac{SF}{qS_{REF}}$	$\frac{x}{c}$	Fraction of wing chord
d	Store maximum diameter, in.	Z	Distance from lower surface of wing to bottom of pylon at the mid-lug point, in.
K	Generalized factor used to represent an empirically derived correction. Descriptive subscript will be associated with this factor.	$\alpha$	Angle of attack, deg.
$K_{CSF}$	Side force correlation factor	$\alpha_L$	Local angle of attack, deg.
$K_{INTF}$	Interference correction factor	$\beta, \beta_s$	Store yaw angle, positive nose outboard, deg.
$K_{L/C}$	Correction factor based on store length and aircraft wing local chord	$\Delta$	Increment
$K_{NOSE}$	Store nose lift efficiency factor	$\eta$	Fraction of wing semi-span, $\frac{Y_{BL}}{b/2}$ , where $Y_{BL}$ is the distance from the aircraft centerline to the centerline of the pylon, measured in the wing plan view.
$K_{WING}$	Store wing/fin lift efficiency factor	$\Lambda$	Aircraft wing quarter-chord sweep angle, deg.
$K_Z$	Pylon height correction factor	$\sigma$	Sidewash angle, positive outboard, deg.
$K_\eta$	Wing spanwise correction factor	$\psi$	Aircraft yaw angle, positive aircraft nose right, deg.
$K_{\Lambda_1}$	Aircraft wing sweep correction factor, $\frac{\sin \Lambda}{\sin 45^\circ}$	<u>Subscripts</u>	
$K_\sigma$	Partial derivative of sidewash with respect to $\alpha$ , $\frac{\partial \sigma}{\partial \alpha}$	A/C	Aircraft
L	Store length, in.	C	Aircraft local wing chord
M	Mach number	INTF	Interference
q	Free-stream dynamic pressure, $\frac{1}{2} \rho V^2$	ISOL	Isolated
SF	Side force, lbs	PRED	Predicted
SPA	Side projected area, in. <sup>2</sup>	$\alpha$	Differentiation with respect to angle of attack
$S_{REF}$	Store reference area, $\frac{\pi d^2}{4}$ , ft <sup>2</sup> .	$\psi$	Differentiation with respect to yaw angle

## 1.0 INTRODUCTION

Determination of the aerodynamic forces and moments acting on individual components of an aircraft is a part of the design process to assure that adequate load carrying structure is provided for all design flight conditions. Accurate information on the aerodynamic loads is important to achieving aerodynamic compatibility between the aircraft and stores. The flow environment in which external stores are immersed is generally highly complex and affected by many variables; e.g., flight conditions and physical characteristics of the aircraft, store installation, and adjacent stores. Successful theoretical prediction of quantitative data has proven to be difficult, although some techniques have been used successfully to predict qualitative trends. The strong influence of viscous flow, particularly at transonic speeds with multiple carriage store arrangements, has made current methods inadequate for many applications. The most reliable method by which the engineer can provide store airloads continues to be through wind tunnel testing. This latter process is normally complex and expensive and too often provides airloads data late in the design effort, after many decisions influencing aircraft/store compatibility have already been made.

A study program was conducted by Vought Corporation, Systems Division under sponsorship of the Air Force Armament Laboratory (DLJC), Eglin AFB, Florida to develop a generalized technique to predict aerodynamic loads acting on airborne external stores. As a consequence of the relatively low effectiveness and inherent limitations of present theoretical methods, an experimental data correlation approach was selected for developing the prediction technique. The major objective of this program was to provide a prediction technique that is rapid and easy to use, versatile in application to various aircraft and store configurations, applicable to maneuvering flight conditions at subsonic, transonic, and low supersonic speeds, and sufficiently accurate for store/store installation design purposes.

Objectives of this program were accomplished in two phases. The initial phase involved the collection, documentation, and correlation of existing airloads data upon which to initiate the technique development and preparations for wind tunnel testing. The second phase of the program consisted of conducting the wind tunnel test program to complete the required supporting data, performing detailed data correlations, and developing the final prediction technique.

This paper describes the work performed and the results obtained during all phases of the study program. The various sections delineate specific tasks which were performed. Descriptions of both the technical information survey and wind tunnel test planning and preparations are included. A discussion of the approach to the prediction technique including the dominant parameters is also presented. Finally, the capabilities and nominal accuracies of the method are assessed, including some comparisons with experimental data.

## 2.0 TECHNICAL INFORMATION SURVEY

An extensive data survey was performed by Vought Corporation to locate and acquire data and related information on captive store and store installation airloads. Acquiring these data was necessary to develop correlations essential to the prediction technique development and to provide guidelines in planning the wind tunnel test program. Although data were known to exist on numerous store types and store installations, problems in acquiring useful airloads data were apparent. These problems included: the inter-industry and inter-service dispersion of data, the diverse origin of airloads data, and the assorted approaches used in measuring airloads. The following paragraphs explain the general survey approach, the type of data solicited and the broad survey results.

### 2.1 Survey Procedure

Early survey planning indicated three primary avenues by which the required technical data could be identified. Selection of these avenues, which were chosen to encompass the majority of data sources, also provided a built-in cross-reference system which minimized the possibility of overlooking pertinent data. Listed below are the primary approach avenues followed:

- o Airframe and weapon contractors and government agencies
- o Aircraft/weapon system program offices
- o Technical literature surveys

Vought had compiled a comprehensive stores data bank through continuing in-house efforts and systematic surveys under contract. Hence, data sought through the survey were the most recently generated data available in the technical community. Although all the data identified through the survey were not obtained, efforts to acquire those data deemed most relevant to the program were highly successful.

### 2.2 Nature of Data Solicited

Aerodynamic data and information as summarized in this section were requested to support the study. The desired data involved stores, store installations, and parent aircraft. This information is classified in three broad categories: experimental data, existing prediction methods and data correlations, and related literature on the subject. A further breakdown of the experimental data includes aerodynamic force and moment data, both wind tunnel and inflight, and flow field information. The aerodynamic force and moment data include those obtained for individual stores, racks, pylons, or aircraft, such that airloads on individual installed stores can be defined. Free-stream store data were also sought to be used as a base in isolating store-aircraft interference effects. Data for all types of store loading arrangements were solicited. These included data for stores mounted singly or on MER or TER racks, single and multiple rail launchers, conformal pallets, etc., on both wing and fuselage stations.

Techniques capable of predicting airload components for stores carried in the flow field of aircraft were also solicited. In general, these prediction methods were found too limited to meet the objectives for preliminary design. However, most techniques present an approach to the treatment of certain parameters which are considered primary independent variables influencing the store airloads. These include such parameters as aircraft attitude and flight condition, store geometry, location and installation, and



adjacent interference. Hence, these correlation and prediction techniques were a useful aid in the formulation of the general prediction method.

## 2.3 Survey Results

The data survey resulted in the acquisition of a considerable amount of data pertaining to stores and store installations which was not in the original Vought data bank. Much of the experimental data acquired provides total aircraft airloads due to the combined aircraft-store configuration. While useful in determining general store effects, it is difficult to isolate individual store or store installation airloads from these data. Extensive individual store and store installation airloads data were made available on the A-7, F-4, and F-111 aircraft. The majority of data on these aircraft consists of metric store and metric pylon airloads where a balance mounted internal to the store or pylon installation measures the applied aerodynamic forces and moments. Other aircraft for which store airloads have been acquired are the A-4, A-6, F-5, F-86, F-105, F-100 and various wing-fuselage combinations.

The following summary observations are made concerning the specific flight condition and geometry variables encompassed by the survey data and the general nature of the data. The significance of these observations is best realized when it is understood that the developed prediction capability for a given variable and the selected conditions/configurations for wind tunnel testing are a direct function of the available data quantity and quality.

Data coverage for the desired subsonic to supersonic Mach number range was generally acquired with lesser quantities being available for the supersonic region. The majority of acquired data defines airloads in the subsonic flight regime. In the supersonic flight regime data are generally limited to single store carriage installations; however, substantial multiple store installation data were obtained well into the transonic region. F-4 and F-111 store airloads data comprise the majority of the supersonic data. The available A-7 store airloads data are limited to subsonic and transonic flight although considerable A-7 supersonic data were acquired in wind tunnel tests conducted as part of this study.

Store and store installation airloads were acquired for a variety of store types. However, there has not been a great quantity of data acquired for any one store type mounted on various aircraft. These data are necessary to isolate the effects of certain variables, or at least to remove the variance in store geometry as an independent variable. Considerable free-stream store aerodynamic data were also obtained which were useful in isolating aircraft/store interference effects. In regard to store installation type, the bulk of the data acquired were for single and multiple stores carried on wing pylons. Limited data are available on fuselage mounted installations, including multiply and singly carried stores, both tangent and pylon mounted. Sparse data exist for TFR, wing tip mounted, fuselage semi-submerged, wing tangent and semi-submerged, and conformal store installations.

## 3.0 WIND TUNNEL TEST PROGRAM

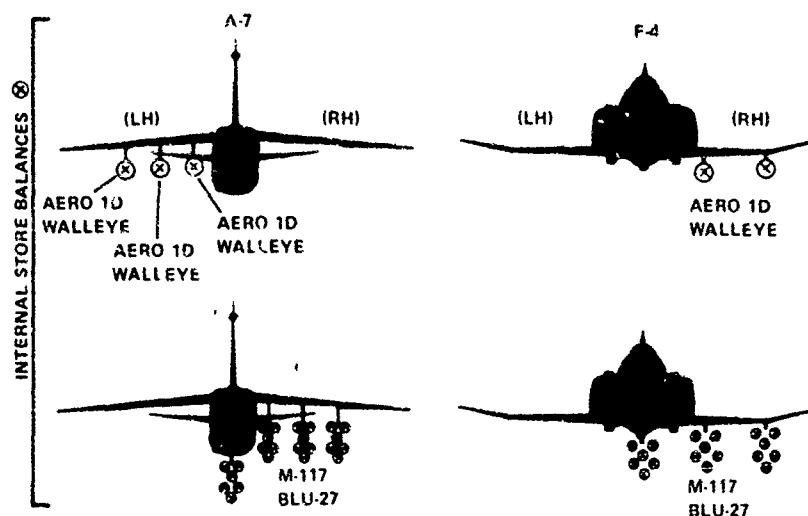
Early in the study it was recognized that sufficient airloads data did not exist for developing the prediction techniques from empirical correlations. Also, it was impractical to expect that data accumulated from the varied sources would be thorough enough to establish predictable trends for all priority variables whose contributions collectively define captive store airloads. The practical solution seemed to be to compile all available airloads data, review these data to identify voids where additional data were needed, and then perform a wind tunnel test program to acquire complementary airloads data through systematic variations in aircraft and store configurations. Vought possesses unique wind tunnel model instrumentation and hardware capable of acquiring extensive store airloads data in a single run. Much of the model hardware needed to test a wide variation of instrumented store arrangements was already available for high speed testing. It was decided to adapt this hardware to existing F-4 and A-7 wind tunnel models for a test program which would technically and economically satisfy the current study needs. The following sections describe the test program and include a description of test hardware, variables encompassed, and related test preparation.

### 3.1 Program Description and Test Capabilities

The wind tunnel test program consisted of instrumenting 0.05 scale models of both the A-7 and F-4 aircraft to measure individual store airloads for both single and multiple carriage stores. In addition, the A-7 parent aircraft model was instrumented to obtain six-component aircraft force and moment data simultaneously with the instrumented store data.

Five component balances (excludes axial force) were used on both F-4 and A-7 test programs to obtain multiple carriage store airloads data. The instrumented MER is designed to carry six of these balances simultaneously, one on each of the six MER stations. Data were obtained at all six MER stations continuously during a run. The M117 (MAU-103A/B fin) and BLU-27/B (finned and unfinned) firebomb stores were utilized in obtaining multiple carriage rack airloads. Instrumented multiple carriage racks were capable of being tested on all right-hand wing store stations and on fuselage centerline store stations on both the A-7 and F-4 aircraft models. All multiple carriage store airloads data for the wind tunnel test program were obtained using an instrumented MER since no instrumented TFR hardware was available. Six component balances were used on both aircraft models to obtain individual store airloads for the single carriage stores. The 300 gallon fuel tank and the Walleye (AGM-62A) store models were used to obtain the single carriage airloads. Instrumented single carriage stores had the capability of being mounted at any wing store station on both the A-7 and F-4 models. The illustrations presented in Figure 1 provide a summary description of instrumented single and multiple store testing capabilities.

Another test capability, which is not obvious from Figure 1, permits  $\pm 12$  inch (full scale) longitudinal shift relative to the pylon in the instrumented F-4 single carriage store position for both inboard and outboard wing pylon stations. It provided additional parametric type store airloads data for the 300 gallon tank and Walleye stores by providing captive airloads data at several chordwise positions. These data were of considerable value to the technique development.



## NOTES

1. INSTRUMENTED MER RACKS CAN BE CARRIED AT EACH OF THE PYLON STATIONS ON THE A-7 AND F-4 AS SHOWN ABOVE, BUT NOT AT MORE THAN ONE STATION SIMULTANEOUSLY
2. THE INSTRUMENTED SINGLE-CARRIAGE STORE CAN BE CARRIED AT THREE A-7 OR TWO F-4 PYLON STATIONS SIMULTANEOUSLY

Figure 1. A-7 and F-4 Instrumented Store Test Capability

with data obtained at the same Mach numbers as single carriage excluding Mach 2.0. Difficulties were encountered with model dynamics when testing multiple carriage configurations at Mach 2.0; therefore, this higher Mach number was deleted from the test program. The angle of attack range for all test data varied from -4 to +12 degrees while the yaw angle range varied from -8 to +8 degrees in four degree increments.

## 4.0 PREDICTION TECHNIQUE

Development of the prediction technique was approached as an empirical correlation of all available airloads data. The parametric type wind tunnel data obtained from tests conducted as part of this study were used to complement the existing data.

The question of how to correlate these data into a prediction method that is both simple and accurate was answered by preliminary comparisons of captive and isolated store data. Aerodynamic characteristics of the captive stores were observed to possess much the same linear nature as isolated stores. The isolated characteristics are presented in Figure 2 for the same store whose captive side force characteristics are shown in Figure 3. The linear approximation is indicated in each figure by a dashed line and is an adequate representation of the actual quasi-linear data.

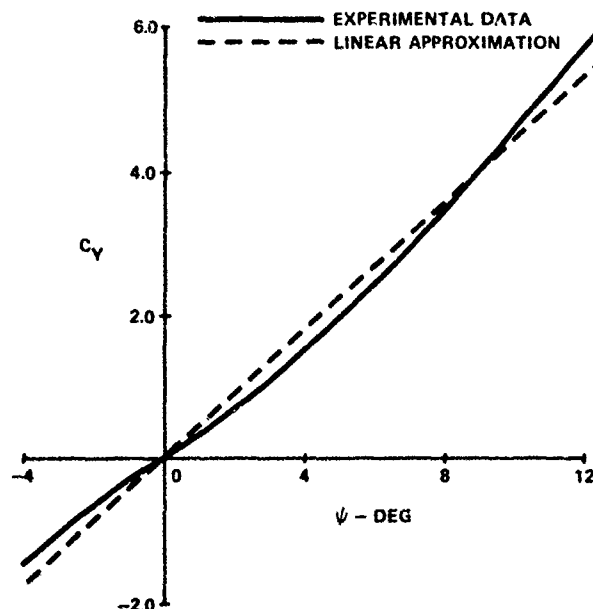


Figure 2. Typical Isolated Store Aerodynamic Characteristics

## 3.2 Test Variables

Any prediction technique derived through an empirical correlation of data requires an adequate data base to be meaningful. The data base must span the range of variables that dominate captive store airloads. These dominant parameters include store configuration; store spanwise, chordwise, and vertical position; aircraft configuration (wing sweep angle, high/low wing, etc.); aircraft attitude; and flight conditions.

Many of the variables examined during the wind tunnel test program concerned with aircraft/store configuration effects were included in the discussion of test capabilities above (aircraft type, chordwise position, spanwise position, etc.). Remaining variables include the range of flight conditions tested. The Mach number range for single carriage configurations varied from 0.5 to 2.0 with data obtained specifically at M=0.5, 0.7, 0.9, 1.05, 1.2, 1.6, and 2.0. The Mach number range for multiple carriage configurations varied from 0.5 to 1.6

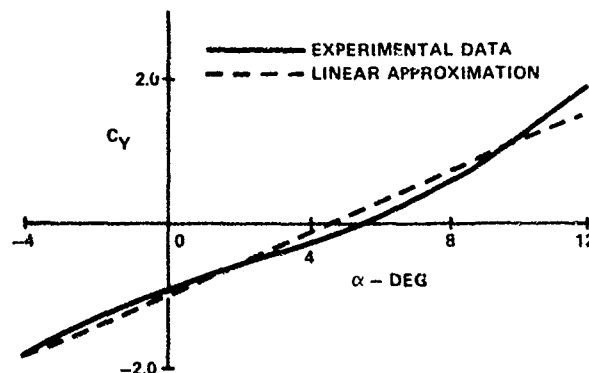


Figure 3. Captive Store Side Force Characteristics

This linear characteristic found in most of the data greatly simplifies the mathematical expressions needed. Unfortunately, the quasi-linear relationship displayed by the side force component does not extend to all components for the angle of attack range desired for the prediction technique (-4/12 degrees). The captive yawing moment component for the subject store is presented in Figure 4 along with the linear approximation covering the largest portion of the

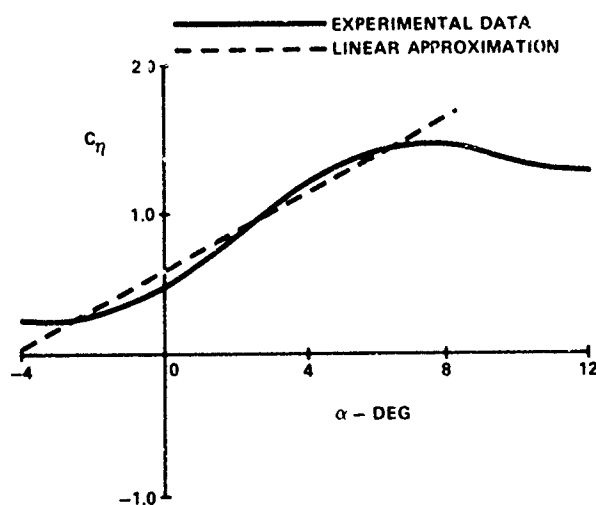


Figure 4. Captive Store Yawing Moment Characteristics

significant errors are likely outside the range of applicability stated for these variables. A summary of nominal method accuracy including some comparisons with experimental data is presented in Section 5.0.

#### 4.1 Basic Approach

A theoretical method must rely on mathematical descriptions of the aircraft components, pylons, racks and stores to implement potential flow solutions of the store airloads. Any corrections for viscous effects must be handled separately. An empirical method allows much simplification to that approach. The basic approach used in this method applies the concept that captive airloads are the result of a free-stream flow plus the interference effects. In this way, work that has been previously accomplished for free-stream aerodynamic predictions can be used as a base on which to relate captive airloads. This permits the prediction procedure to be a summation process as indicated below.

$$\text{Captive Store Airloads} = \text{Isolated Store Airloads} + \text{Interference Effects}$$

Applying the summation approach to interference increments depends first on airloads for some base configuration. Corrections can then be added to these initial airloads to account for differences between the base configuration and the desired configuration. Predicting these initial airloads is called the initial prediction. It involves assuming the store is in the flow field of a base wing with 45° sweep and installed at a specific spanwise, chordwise, and vertical location. The next step is to obtain a final prediction by applying empirically derived corrections to the initial prediction to compensate for aircraft configuration differences and to account for the effects of the store being in the desired spanwise, chordwise, and vertical location.

This approach was used in correlating the experimental data to develop the prediction method presented here. Correlations to identify airloads for the base configuration implement the initial prediction procedure and were basic to the entire development process. These correlations were performed with  $M=0.5$  data to avoid the increased complexity of compressible flow corrections and shock induced effects. This is the lowest Mach number of the test data from the wind tunnel tests of this program. Because compressibility effects are normally small at speeds below  $M=0.5$ , the method is considered valid for low subsonic speeds without Mach number corrections.

Correlations of the data to identify corrections needed to account for Mach number and configuration differences were much more difficult than those for the base data. This greater difficulty results from the many factors which contribute to the aerodynamic differences between the various store installation configurations. Some of these factors are the reason rigorous mathematical solutions are not yet practical for prediction purposes on many installations, particularly for multiple carriage racks. Fortunately, experimental data indicate that some of these differences are either small or compensating so that empirical expressions are possible without including terms which evaluate each contributing parameter. A method has been developed by using the available data to establish predictable trends and these trends are expressed mathematically.

To apply the method, the initial prediction of captive airloads is always made first at  $M=0.5$  by assuming the store is inserted into the flow-field of the base wing (45° sweep). The initial prediction is made for the basic airload case (i.e., the captive store airload generated by a zero-yaw pitch excursion of the parent aircraft). The incremental captive airloads due to aircraft yaw and the effects of adjacent store interference are predicted as increments to be added to the basic airload. The effects of Mach number are treated as an increment to be added to the prediction at  $M=0.5$ . At a particular Mach number the total captive airload experienced by a store can be obtained from the following generalized coefficient expression:

$$C_{x \text{ TOTAL}} = C_{x \text{ BASIC}} + \Delta C_{x_B} + \Delta C_{x \text{ INTF}}$$

desired angle of attack range. As shown in the figure, significant errors will result using the linear approximation above approximately 8 degrees angle of attack. Even so, there is a linear region to represent a significant part of the airplane's flight envelope, and the advantages of using the linear approximation for each component far outweigh the disadvantage of some loss in accuracy in a portion of the desired angle of attack range. It should be noted that if the isolated aerodynamic characteristics of the store are non-linear in nature, then this non-linearity should be expected in the captive airloads. The advantages of linearizing the data base are (1) a simple representation of the component airload by a  $y=mx+b$  type equation and (2) a major variable, aircraft angle of attack, is built into the mathematical component airload representation. As a result, the data base was linearized so that each airload component could be expressed as a slope (force or moment as a function of angle of attack) and an intercept at zero angle of attack. As a result of the linearized data base, air predictions are accomplished in the form of a predicted slope and intercept for each of the airload components. Because of increasing non-linearity at the larger aircraft angles of attack and yaw angles,

where:

- $x$  - can be  $y$ ,  $n$ ,  $N$ ,  $M$ ,  $A$ , or  $\ell$  representing side force, yawing moment, normal force, pitching moment, axial force, and rolling moment, respectively.
- $C_{x\_BASIC}$  - Basic captive airload generated by a zero yaw pitch excursion of the parent aircraft.
- $\Delta C_{x\_B}$  - incremental airload due to aircraft yaw per degree store yaw angle,  $\beta$ .
- $\beta$  - Store yaw angle equal to  $\psi_{A/C}$  for a right wing store installation and  $-\psi_{A/C}$  for a left wing store installation.
- $\Delta C_{x\_INTF}$  - Incremental airload due to the effect of adjacent store interference.

In summary, the total captive airload experienced by a store can be calculated by incrementing the isolated store aerodynamic characteristics through the initial prediction summation procedure for the base wing (45° sweep), applying empirical corrections to arrive at the final prediction for the subject wing, and using the generalized coefficient expression above to sum the major contributions to the installed airload.

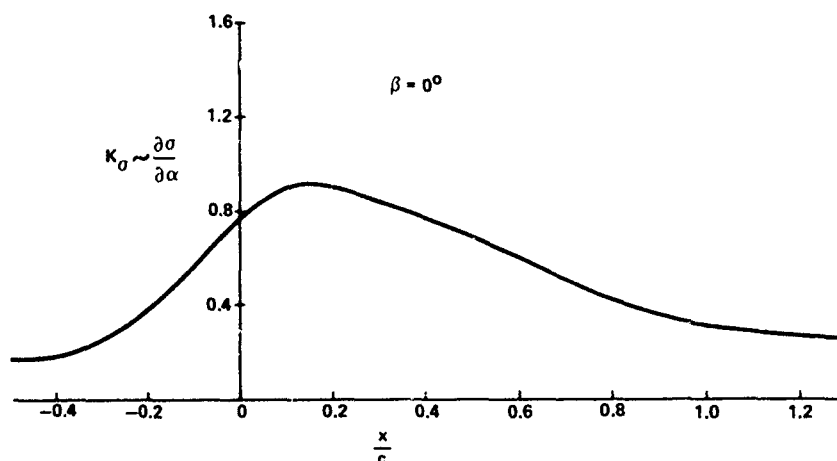


Figure 5. Variation of  $\sigma$  with  $\alpha$  for a 45° Swept Wing

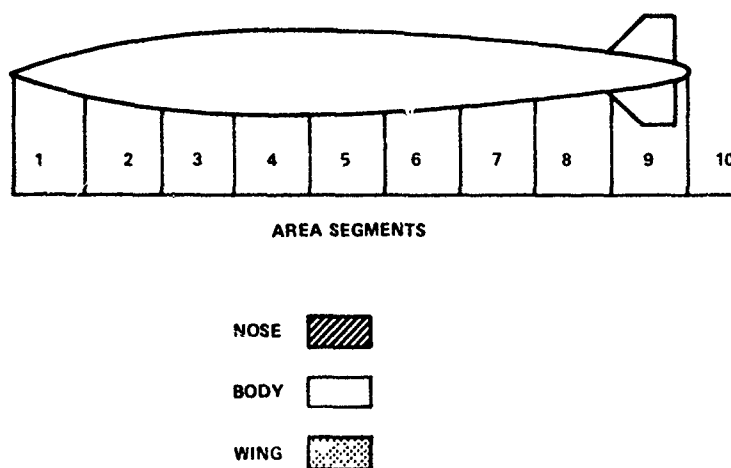


Figure 6. Area Segments for a Typical Store

since aerodynamically the nose and wing are more efficient producing lift (or side force in this case) than the store body. Because of this efficiency distinction, factors have been defined using Reference 2 for

## 4.2 Prediction Equations

The variables used in deriving the final prediction equations for both single and multiple carriage configurations were essentially the same. These variables accounted for: store configuration characteristics (both physical and aerodynamic); store spanwise, chordwise, and vertical location in the aircraft flow-field; the interference effect of the aircraft fuselage and adjacent stores; parent aircraft attitude (pitch and yaw); and Mach number.

As a result of the similarities in the equation forms, only the single carriage  $M=0.5$  side force slope prediction equation is presented and discussed here. The intent is to describe typical procedures used in developing the prediction method.

### 4.2.1 Initial Airload Prediction

Initial prediction calculations begin by assuming the store is inserted into the flow field of the base wing (45° sweep) at the mid-semispan ( $\eta=0.5$ ) position. Longitudinally the store is placed at the true captive position and the local wing chord is assumed to be the same as the captive position for the subject aircraft wing. The sidewash characteristics of the base wing are known from an analysis of the flow field data presented in Reference 1. This analysis yielded the rate of change of sidewash angle,  $\sigma$ , with respect to angle of attack,  $\alpha$ . This term,  $\frac{\partial \sigma}{\partial \alpha}$  is known as a function of  $x/c$  for the base wing, Figure 5.

Several definitions concerning the store and aerodynamic characteristics must also be made. The total store planform area is divided into nose area, body area, and wing area as shown in Figure 6. The distinction in planform areas is required

for the store nose,  $K_{NOSE}$ , and wing(s),  $K_{WING}$ , to weight their respective planform areas in relation to the store body planform area.

With a knowledge of the store geometric and isolated aerodynamic characteristics, a summation procedure is performed along the store in the aircraft flow-field to obtain an initial prediction of side force slope. The store is positioned in the aircraft flow field as shown in Figure 7. The planform area of the store is projected into the  $X_B, Z_B$  plane and is defined as side projected area, SPA. The store is divided into constant length segments from nose to tail, Figure 6, and the SPA is computed for each of the segments with distinction made as to nose, body, or wing areas.

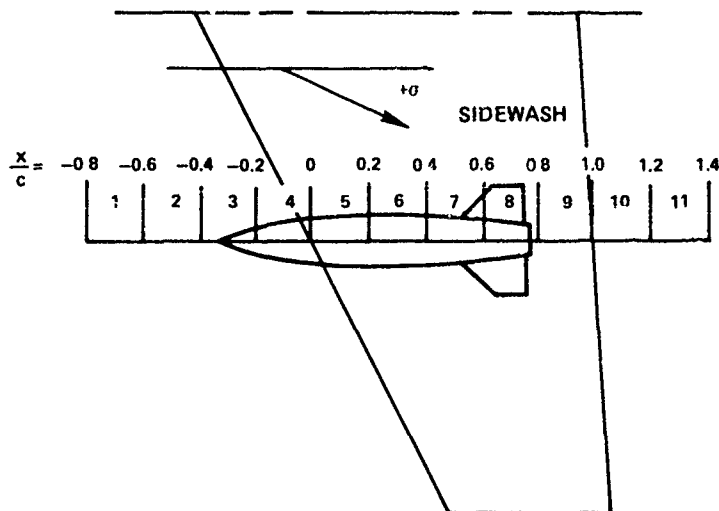


Figure 7. Typical Store Immersed in Aircraft Flow-Field

With the segmented side projected areas defined and the store inserted into flow field of the base wing, the summation procedure is given by the following relationship.

$$\text{ADJUSTED SPA} = \sum_{n=1}^m K_{\sigma_n} K_{NOSE_n} K_{WING(TAIL)_n} SPA_n$$

where:

- $m$  - Number of constant length area segments as computed from store nose to tail.
- $K_{\sigma}$  - Rate of sidewash variation with angle of attack,  $\frac{d\sigma}{d\alpha}$ , Figure 5.
- $K_{NOSE}$  - Store nose lift effectiveness.
- $K_{WING(TAIL)}$  - Store wing or tail lift effectiveness.
- $SPA$  - Store side projected area,  $\text{in}^2$ , Figure 6.

then:

$$K_{CSF} = \frac{\text{ADJUSTED SPA}}{SPA_{TOTAL}}$$

where:

- ADJUSTED SPA - Adjusted side projected area of the store as given by the summation equation above.
- $SPA_{TOTAL}$  - Total side projected area of the store. The sum of nose, body, and wing side projected areas.

The initial side force slope prediction is given by the following equation:

$$\frac{d\left(\frac{SF}{q}\right)}{d\alpha}_{INITIAL PRED} = K_{CSF} \frac{d\left(\frac{SF}{q}\right)}{d\psi}_{ISO}$$

where:

$$\frac{d\left(\frac{SF}{q}\right)}{d\psi_{ISO}} - \text{Isolated aerodynamic characteristics of the subject store. Equal to } C_{L\alpha_{ISO}} S_{REF} \frac{ft^2}{deg}.$$

Computed from the method of Reference 2.

It should be noted that if experimental isolated store characteristics are used in the above equation, the user must still perform most of the computations of Reference 2 since many of the terms of the computation are used in defining the store nose and wing weighting factors.

The discussion in this section has been limited to the single carriage side force slope initial predictions. Initial predictions of normal force, pitching moment, and yawing moment slopes for both single and multiple carriage, are similar. An additional term is added to the summation procedure for the moment terms to account for the displacement of the area segment with respect to the moment reference point. Initial predictions of axial force and rolling moment are somewhat different with a complete discussion included in Reference 3.

#### 4.2.2 Aircraft/Store Interference Prediction

The single carriage side force slope prediction equation is presented below.

$$\left(\frac{SF}{q}\right)_{\alpha_{PRED}} = K_{CSF} \left(\frac{SF}{q}\right)_{\psi_{ISO}} K_{\eta} K_{INTF} \frac{K_L}{C} K_Z K_{A_1}$$

The initial term,  $K_{CSF} \left(\frac{SF}{q}\right)_{\psi_{ISO}}$ , in the above equation is the initial prediction discussed in Section

4.2.1. The remaining factors are empirical corrections to the initial prediction to compensate for the effects of the parameters previously mentioned in this section.

The first empirical correction, term,  $K_{\eta}$ , is a factor to compensate for the spanwise position of the subject store. This factor was derived from three independent data sources, all of which were contained in the data base consisting of the survey data and the wind tunnel test data. In order to derive a spanwise correction factor, it is desirable to have captive airloads data for several store types on all wing pylons for as many parent aircraft as possible. Two of the previously mentioned data sources came from the survey. One source, Reference 4, contained the BULLPUP "A" missile on F-4 inboard and outboard wing pylons. A second source, Reference 5, came from the test program in which the 300 gallon tank and Walleye stores were tested on all wing pylons of both the A-7 and F-4 aircraft. The third and final data source was a flow-field investigation of a wing-body combination at low subsonic speeds reported in Reference 1. The flow-field investigation reported flow angularities both in the lateral and vertical planes for semi-span stations  $\eta=0.25$ ,  $.50$ , and  $.75$  for a number of chordwise and vertical locations beneath the test wing. Ratioing the sidewash flow angularities from the flow-field data, assuming the mid-semispan position,  $\eta=0.5$ , as the base, the solid curve in Figure 8 was derived. Through a similar analysis the data points represented by symbols were derived as also shown in Figure 8. Hence, from three independent data sources, essentially the same spanwise trends were obtained for single carriage side force slope. The final correlation curve presented for this term is the best fairing of the data presented in Figure 8.

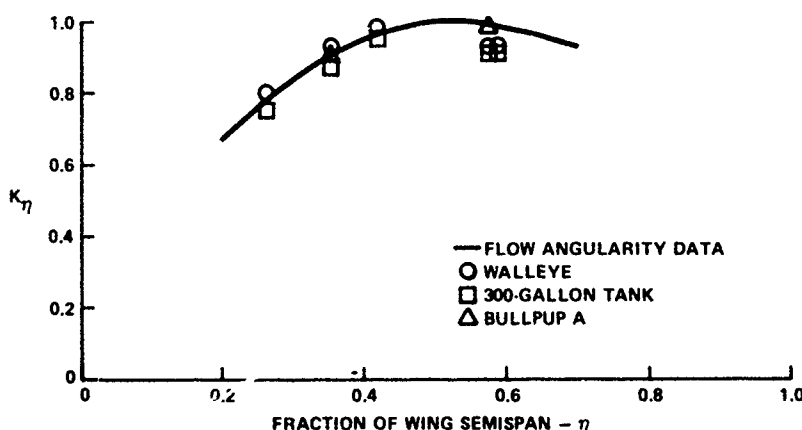


Figure 8. Derivation of Side Force Slope Spanwise Correction

The next empirically derived correction to the initial prediction is the factor  $K_{INTF}$ . This term accounts for the interference effect of the fuselage on the captive store side force slope for high-wing aircraft. The presence of the fuselage near the installed store prevents the full development of a sidewash flow-field and, therefore, modifies the spanwise trends established earlier.

The term  $K_L/C$  is an empirical factor based on the length of the store divided by the local aircraft wing chord. In addition to the chordwise location of the captive store, this factor gives an indication of the amount of the store contained in the non-uniform wing flow-field.

The next term,  $K_Z$ , in the side force slope equation is a factor to account for pylon height variation.

Sidewash angularity beneath a swept wing is strongest near the wing surface and decays to zero at some distance, on the order of a local wing chord length, beneath the wing. Experimental flow-field data indicate that the decay is exponentially shaped. Other investigators (Reference 6) have developed an empirical pylon height correction factor for side force slope which is presented in Figure 9 as a function of vertical distance beneath the wing surface to the store longitudinal axis. Figure 9 also presents the pylon height correction factor for side force slope developed from the present study for comparative purposes and is presented as a function of vertical displacement from the wing lower surface to the pylon rack mid-lug point. The exponential variation with pylon height is apparent in both cases.

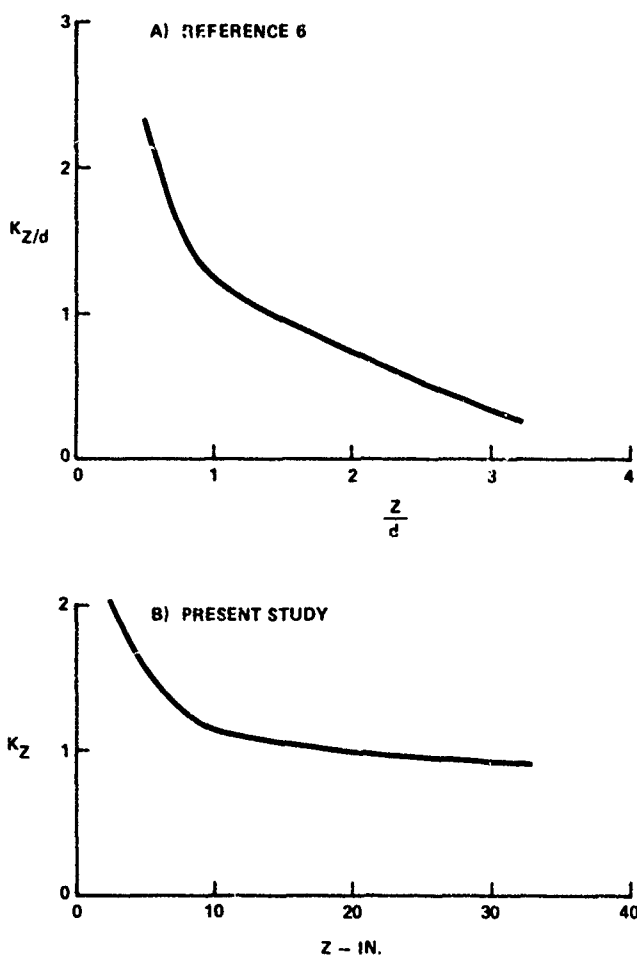


Figure 9. Comparison of Pylon Height Correction Factors

purposes. The results reported in Reference 3 indicate that this goal was achieved. One of the important factors influencing these results was the quantity and quality of data used in the correlation. Because of the limited data obtained in the survey, the wind tunnel data produced as part of the program made possible the versatility which was accomplished.

Simplicity was achieved in the sense that there are no complicated steps required to apply the method. There are many factors to be evaluated, but the process is outlined in a systematic sequence of simple steps. Because there are numerous calculations required for a complete prediction of six component airloads for multiple store installations, computerization of the method for practical applications appears appropriate.

The method has a wide range of applications and capabilities. The method is capable of predicting the captive airloads for single carriage and multiple carriage store configurations for a generalized aircraft including the basic airload (that airload generated by a zero-yaw pitch excursion of the parent aircraft) and the incremental airloads due to aircraft yaw and adjacent store interference. Establishing absolute limits of applicability is difficult since this is often a function of the accuracy that is acceptable. Recommended limits are submitted and sufficient data are presented to implement the method for those limits. Applications beyond the stated limits will normally mean a decay in accuracy.

The single carriage method is valid over the Mach number range 0.5 to 2.0 while the multiple carriage Mach range is from 0.5 to 1.6. Both single and multiple carriage prediction techniques are valid over the angle of attack range of  $-4$  to  $+12$  degrees and the aircraft yaw angle range of  $-8$  to  $+8$  degrees although best accuracy for the increments due to aircraft yaw are for the range  $-4$  to  $+4$  degrees. The aircraft wing sweep angle (quarter chord) range of validity is from 30 to 60 degrees although the method can be applied to a wider sweep angle range (say 20 - 70 degrees) with decreased accuracy. The method is applicable to all wing/pylon and fuselage centerline carriage configurations. It is not intended for fuselage configurations off the centerline nor to semi-submerged or conformal carriage.

An assessment of the accuracy of the method has been conducted through comparisons with the data base used in the technique development. The first accuracy check, and possibly the most meaningful, was a comparison of predicted values of individual airload components with the linearized representation of the data obtained from the test of that configuration in the wind tunnel. This check is meaningful because accurate linearized representations, like those shown in Figures 2 and 3, are adequate for most engineering applications. Wind tunnel tests for airloads data can often be avoided if this type prediction has sufficient accuracy. The accuracy comparisons with the linearized data base indicate that all components for both single and multiple carriage configurations are nominally within  $\pm 10\%$  of the base value.

The final empirical factor,  $K_{\Lambda_1}$ , is a first order correction for aircraft wing sweep angle. The factor is defined as  $\sin \Lambda / \sin \Lambda_{BASE}$  where  $\Lambda$  is the quarter chord sweep of the subject aircraft wing. The base sweep angle,  $\Lambda_{BASE}$ , for this factor is  $45^\circ$  since the initial prediction discussed in Section 4.2.1 was made for a base wing with  $45^\circ$  sweep angle. This factor has been suggested by several investigators including those of Reference 6 and is adequate for wing sweep angles that do not vary significantly from the base wing sweep ( $45^\circ$ ). For this reason the range of sweep angles for which the technique is recommended is limited to quarter chord sweep angles between 30 and 60 degrees.

The discussion in this section has been limited primarily to those empirical factors pertaining to the single carriage side force slope prediction for  $M=0.5$ . Presented in Reference 3 are the prediction equations for all applicable rack types, store carriage locations, and aircraft speed regimes. Inspection of these equations reveals a large number of empirical correction factors which have not been discussed here. However, the development of those terms was similar to those presented here, and detailed descriptions of these terms are included in Reference 3.

## 5.0 ASSESSMENT OF APPLICABILITY AND ACCURACY OF THE PREDICTION METHOD

In undertaking this research program, there was some question regarding the degree of success that could be expected from a data correlation approach to developing a store airloads prediction technique. Experience in developing other empirical methods gave reasonable assurance that a method was possible. However, the goal for this program was a method that was easy to use and would provide sufficient accuracies to make the predictions suitable for preliminary design

Additional comparisons were made to check predicted values with specific data points. This check does include the effects of scatter in the wind tunnel data which is not necessarily a true test of the method. However, it does indicate something of the data non-linear effects on accuracy. Comparisons with the experimental data base for two single and one multiple carriage configuration are presented in Figures 10 through 15. These comparisons allow the reader to see the effects of data non-linearity on accuracy in portions of the angle of attack range.

## 6.0 CONCLUSIONS AND RECOMMENDATIONS

With the conclusion of the program we are left with a few summary comments and observations which are mentioned here.

- o It is possible to take experimental captive store airloads data and correlate these data into mathematical expressions for predicting store airloads for the generalized aircraft/store configuration.
- o Accuracy is sufficient for preliminary design.
- o The number of steps required for a six component airloads solution suggests that computerization of the method is desirable.
- o Better accuracy is attained for the force components than the moment components due to the sensitivity of the moment components to the factors affecting the local flow-field such as viscous effects and adjacent store installations
- o Further work should include parametric data obtained on a generalized wing/body aircraft model utilizing generalized store shapes to generate larger ranges of data for the most influential variables. An improvement in accuracy should naturally result.
- o Additional work should consider using higher order curve fits of the data base for possible accuracy improvements.

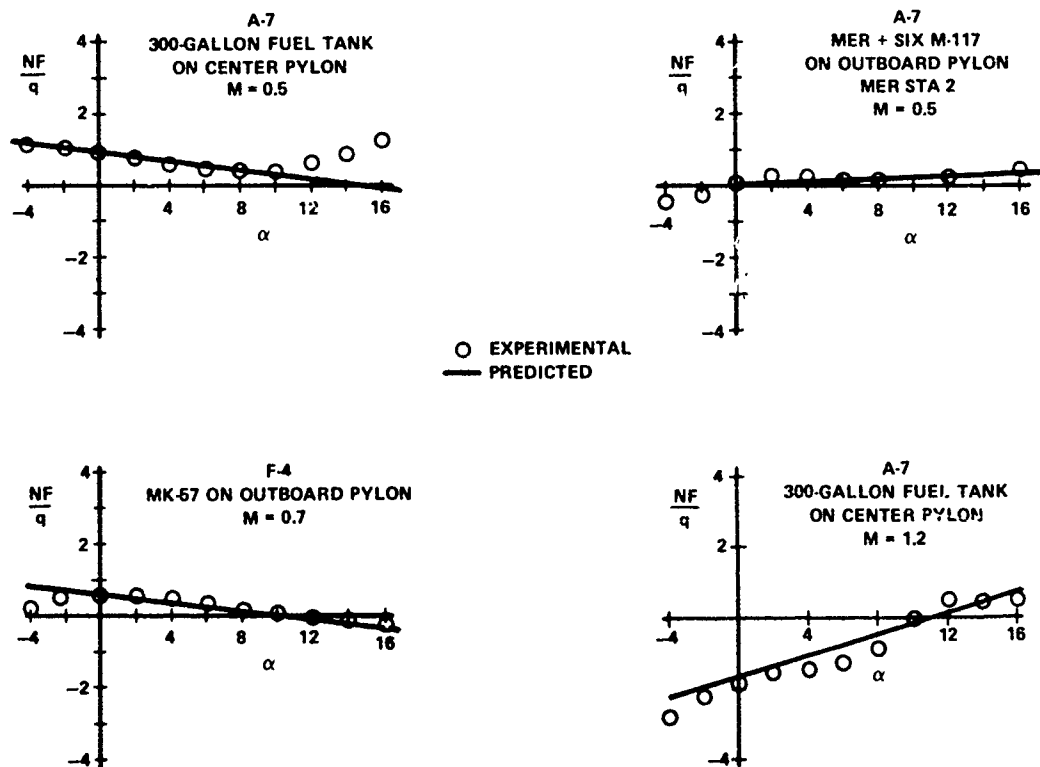


Figure 10. Normal Force Prediction Results



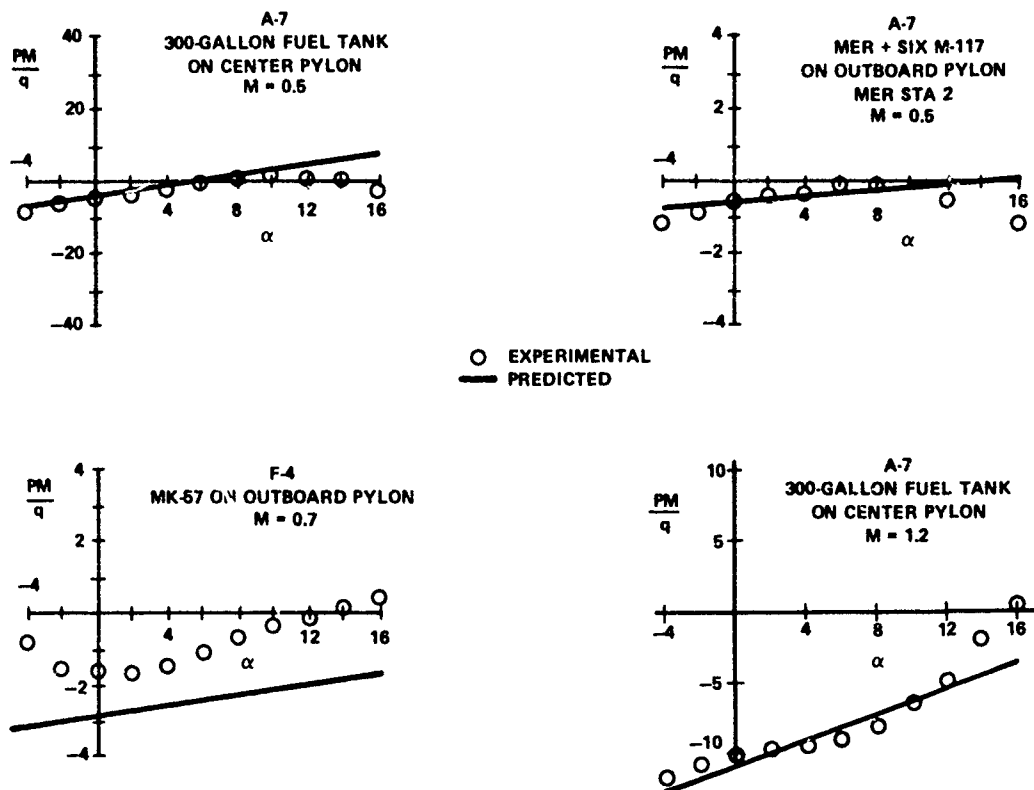


Figure 11. Pitching Moment Prediction Results

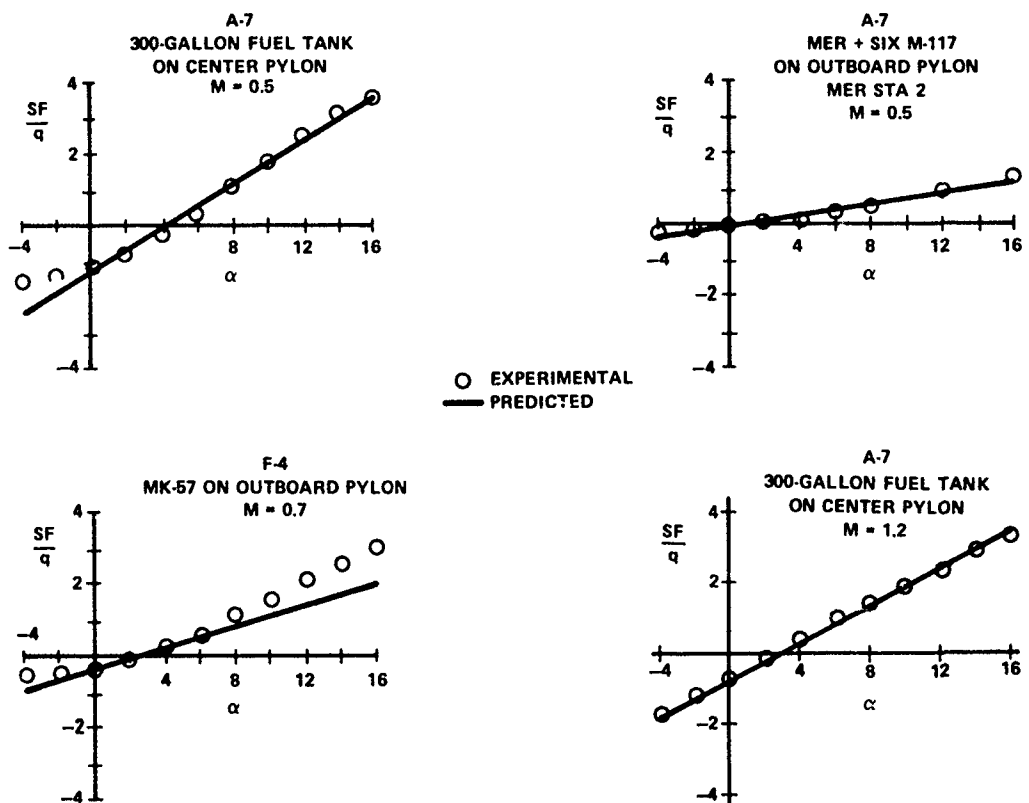


Figure 12. Side Force Prediction Results

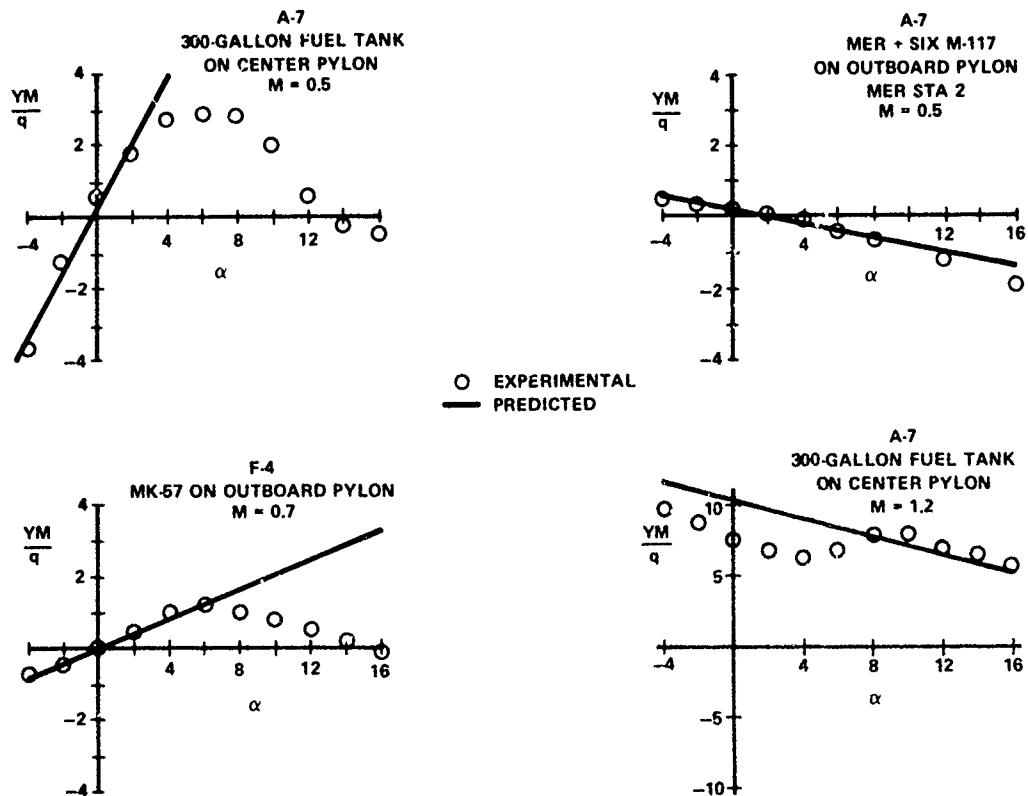


Figure 13. Yawing Moment Prediction Results

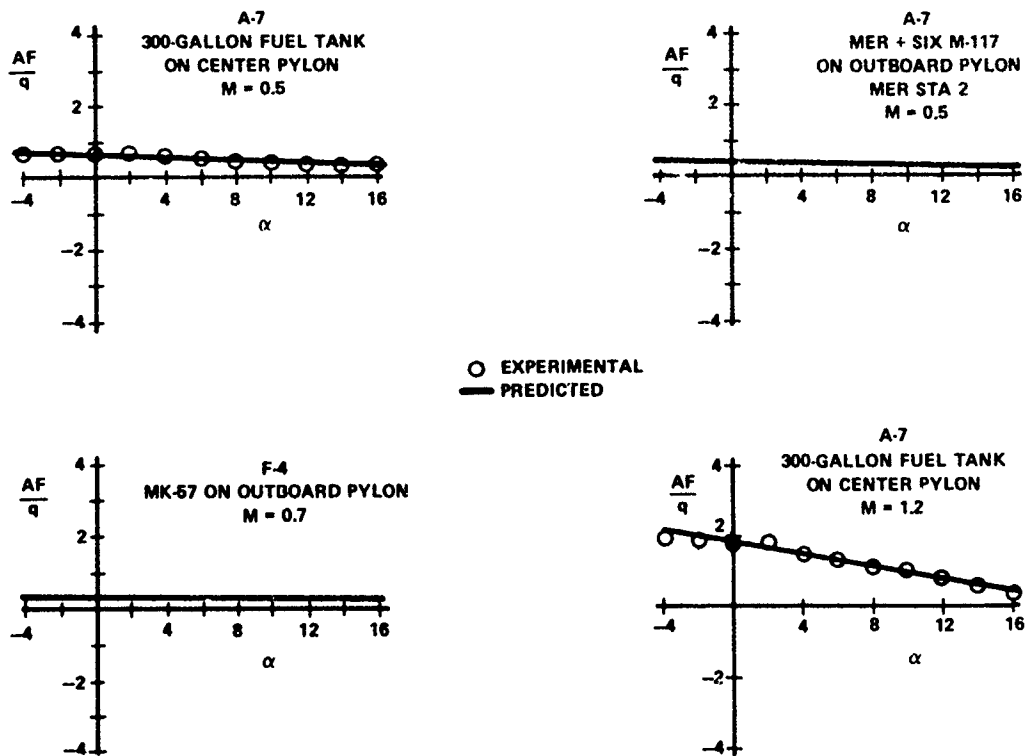


Figure 14. Axial Force Prediction Results

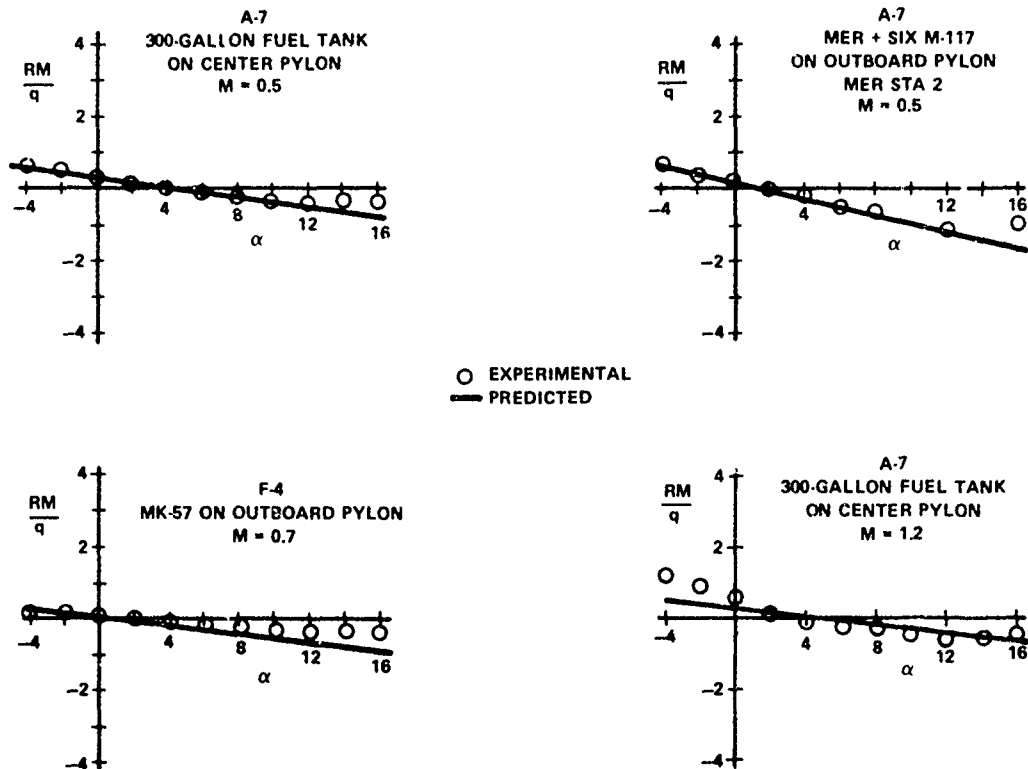


Figure 15. Rolling Moment Prediction Results

## REFERENCES

1. Alford, W. J. Jr., "Theoretical and Experimental Investigation of the Subsonic Flow-Fields Beneath Swept and Unswept Wings with Tables of Vortex - Induced Velocities," NACA Report 1327, 1957.
2. Nielsen, J. N., Pitts, W. C., and Kaattari, G. E., "Lift and Center of Pressure of Wing-Body-Tail Combinations at Subsonic, Transonic and Supersonic Speeds," NACA Report 1307, 1957.
3. Rudnicki, A. R. Jr., Waggoner, E. G. Jr., Alexander, C. T., and Gallagher, R. D., "External Store Airloads Prediction Technique," Air Force Armament Test Laboratory Technical Report 75-87, July 1975.
4. Gregoire, J. E., "Wind Tunnel Tests on the 7.5% F-4C Store Loads Model in the McDonnell Polysonic Wind Tunnel, Series II, "Report A879, McDonnell Aircraft Corporation, January 1965.
5. Hill, D. W. Jr., and Mattasits, G. R., "Aerodynamics Loads on Four External Stores in the Carriage Position on the A-7D and F-4C Aircraft at Mach Numbers from 0.5 to 2.0," AEDC-TR-74-29, AFATL-TR-74-64, Arnold Engineering Development Center, May 1974.
6. Marsden, P. and Haines, A. B., "Aerodynamic Loads on External Stores: A Review of Experimental Data and Method of Prediction," R. & M. No. 3503, November 1962.

## PREDICTION OF EXTERNAL-STORES AND TIP-TANK LOADS ON WING-FUSELAGE CONFIGURATIONS

S.R. Ahmed \*

## SUMMARY

An evaluation of a first order "panel" method to predict the six-component aerodynamic forces and moments on captive stores and tip-tanks mounted on a wing-fuselage configuration is presented. The method has been tested on two accounts: prediction of surface pressure distribution, and estimation of the resulting forces and moments.

In view of the large number of parameters involved, the main investigation dealt with three geometric parameters: store chordwise and spanwise location below the wing, and the wing mid-chord sweep. Influence of Mach number was investigated separately over a range of 0 to 0.9. Store/pylon/fin and wing/tip-tank interactions were studied on basis of calculated surface flow patterns.

The method was next applied to calculate the forces and moments acting on an extreme forward, central and extreme rearward located tip-tank on the swept wing-fuselage configuration.

Comparisons between wind-tunnel data and results of inviscid flow analysis are included for high subsonic speeds.

## NOTATION

$b$	wing span
$c$	local wing chord
$c_a$	local lift coefficient, based on store maximum frontal area $F_A$
$C_A$	lift coefficient, based on store maximum frontal area $F_A$
$C_M$	pitching moment / $q_0 F_A l_A$ , positive nose upwards, referred to store mid-point
$C_N$	yawing moment / $q_0 F_A l_A$ , positive nose inwards, referred to store mid-point
$C_p$	static pressure coefficient = $(p - p_0)/q_0$
$C_y$	local side force / $q_0 F_A$ , positive towards fuselage
$C_Y$	side force / $q_0 F_A$ , positive towards fuselage
$d_A$	store maximum diameter
$F_A$	store maximum frontal area = $\frac{\pi d_A^2}{4}$
$l_A, l_T$	store and tip-tank overall length
$l_P$	pylon chord
$Ma$	free stream Mach number
$P, P_0$	local and freestream static pressure
$q_0$	freestream dynamic pressure
$V_\infty$	freestream velocity
$v_x, v_y, v_z$	velocity components in $x, y$ and $z$ directions
$V_{xy}, V_{xz}$	resultant velocity of $v_x, v_y$ and $v_x, v_z$ components
$x, y, z$	distance measured along horizontal, lateral and vertical axis of right-handed coordinate system
$x_A, y_A, z_A$	distance along store axis from nose, lateral and vertical distance between fuselage centreline and store axis
$x_P$	distance along pylon chord from pylon leading edge
$x_S$	chordwise position of store mid-point from local leading edge, fraction of local wing chord, positive aft
$y_S$	spanwise position of store mid-point from fuselage centreline, fraction of semispan
$x_{TS}$	chordwise position of tip-tank mid-point from leading edge, fraction of wing-tip chord, positive aft
$\alpha$	angle of incidence (degrees), positive nose up
$\varphi_m$	wing mid-chord sweep

\* Dr.-Ing., Research Scientist, Institut für Aerodynamik der DFVLR, Braunschweig, Germany.

## 1. INTRODUCTION

With the increasing demands made on the manoeuvrability and store carrying capacity of combat aircraft, the aerodynamic forces and moments acting on individual components tend to be relatively large compared to the aircraft size and inertia forces. To achieve compatibility between aircraft and stores, as well as for a safe structural design, a physical insight into the details of the flow field and accurate prediction of component loads are needed at an early design stage. Information about carriage loads forms also the basis for the initial conditions at the time of store release.

Most of the present day combat airplanes have stores or similar bodies mounted externally beneath the aircraft wing and are thus placed in a non-uniform flow field of curved streamlines, varying velocity and dynamic pressure. The highly complex interference phenomena between aircraft and store assembly components induce sidewash, up- and downwash, and angular flow displacements. These in turn cause normal- and side-forces, and pitching, yawing and rolling moments on the components. The mutual superimposition of the component pressure fields and that of the parent aircraft has a corresponding influence on the boundary layer development, often enhancing the adverse effects leading to its separation.

The complexity of the problem, the strong influence of viscous effects particularly at transonic speeds and by multiple store arrangements, makes theoretical prediction of store loads in real flow extremely difficult. Earlier effort in this field has been mainly experimental in nature. A comprehensive review of both experimental and theoretical work till 1962 was given by Marsden and Haines, Ref. 1. Based on this they developed an empirical method to calculate aerodynamic loads, which was later substantiated by more measurements, Ref. 2, and updated, Ref. 3.

Existing theoretical methods for estimating store/pylon and tip-tank loads use approximate analytical techniques to allow for the interaction among configuration components. The flow field around the wing-fuselage is most commonly determined by linear theory. Fernandes (Ref. 4) computes the load along store axis by applying the so determined local field conditions to the load distribution obtained in uniform flow. His method is developed for subsonic compressible and supersonic flow. Grose and Bristow (Ref. 5) use singularities to satisfy boundary conditions on store surface. Effects of pylon and fins is not included in the reported results. Nielsen, Goodwin and Dillenius (Ref. 6) evaluate store loads from slender body theory and fin loads from linear theory. Viscous crossflow effects are included, the results however seem to be sensitive to the assumed location of separation point. Chadwick (Ref. 7) uses non-planar lifting surface theory to calculate pylon loads from wing/pylon analysis for incompressible flow. Interference carryover loads between pylon and store are calculated assuming a constant sidewash.

The present approach, the so called "panel" method, permits a detailed simulation of the aircraft and store geometry, with the result that the whole can be considered from the outset as a complete entity.

Both the displacement effect of shape thickness and lift generation is accounted for within the framework of potential theory. The mutual interference of all configuration components is simultaneously considered, and exact, not linearized, boundary conditions for attached flow are fulfilled on body surface. The validity of the analysis is extended to the high subsonic flight regime by the application of Göthert rule. The method is discussed in detail in Ref. 8.

Output data of a calculation are flow quantities over the entire body surface. Integration of pressure over the surface, part or whole, yields the forces and moments required.

## 2. BASIC CONCEPTS OF THE METHOD

The incompressible potential flow around an arbitrarily shaped three dimensional body is considered to be formed by a linear superposition of a known uniform onset flow and an unknown perturbation flow. The perturbation flow represents the amount that the onset flow is changed by the presence of the body to produce the actual flow field. The perturbation flow fulfils the condition of irrotationality and continuity; it can therefore be expressed as gradient of a scalar potential function. This potential function represents a solution of the Laplace equation.

In the flow field, perturbation effects vanish at distances far from body and on the body surface, flow tangency is prevalent everywhere. These two boundary conditions are imposed on the solution sought.

The solution of the Laplace equation is constructed by arranging a distribution of basic singularities on the body and wake surfaces. Each of these singularities represents by itself a solution of the Laplace equation. Effect of this singularity distribution producing disturbance velocities at a point on body surface is evaluated as an integral, employing Green's theorem. This integral expresses the induced velocity at a body point in terms of the known body geometry and the unknown perturbation singularity strength. Satisfying condition of zero normal velocity (i.e. flow tangency) at a surface point yields a determining equation for the singularity strength. The procedure has been developed originally by Hess and Smith, Ref. 9. Rubbert and Saaris (Ref. 10) added the capability to handle problems with circulation and lift. Detailed description of the formulation and experience gained with the computing routine used in this paper are given in Refs. 8 and 11.

### 3. DESCRIPTION OF THE THEORETICAL MODEL AND SOLUTION IMPLEMENTATION

Simulation of flow about lift generating bodies should include representation of trailing vorticity, which for the present case consists of contributions from wing, fuselage, pylon, store, fin and tip-tank. As the trailing surface is treated in the method in a similar manner as the body surface, its geometry needs to be known in advance. The definition of a trailing surface, especially for bluff bodies, and its disposition with change of aerodynamic parameters is extremely difficult to describe quantitatively.

A simplified procedure, meeting practical purposes, is adopted to enable the computation. All trailing surfaces are assumed to be planar, their relative position with body geometry remaining constant with change of, for example, incidence. Wing, pylon, and fin trailing surfaces emanate from trailing edge and extend planar, in direction of trailing edge bisector, downstream. Fuselage and store trailing surfaces start at the bluff aft end, fuselage trailing surface coplanar with that of the wing, and store and pylon trailing surfaces perpendicular to each other (see Figs. 1 and 2).

With these assumptions body and trailing surface is approximated by plane quadrilateral panels, each carrying a constant singularity distribution over its surface. Solid surface is represented by a source panel network. Lift and sideforce generation is accounted for by multihorseshoe vortex system on the camber surface of wing, fuselage, pylon, store, fins and tip-tank. The trailing surface is represented by the trailing vorticity of the multihorseshoe vortex system arranged inside the body, and emanating at the trailing edges. The numerical model so developed is detailed in Figs. 1 and 2.

The integral equation for perturbation potential, mentioned in Section 2, reduces through the surface discretisation described above, to a sum of integrals, each belonging to a panel. The integrals are essentially functions of panel singularity strength and its geometry. Fulfilment of boundary condition at a point on body or wake surface yields a linear equation relating the unknown panel singularity strengths with the known body and trailing surface geometry. Solution of the integral equation means therefore, the solution of a large system of linear equations, the number of unknowns being equal to the number of points where boundary conditions are satisfied.

Output data available after a computation, are flow quantities at a characteristic point of each panel, six-component forces and moments of each panel obtained from integrated surface pressure, and finally flow quantities and streamlines in flow field outside the body.

### 4. EXPERIMENTAL INVESTIGATIONS

#### 4.1 Pressure measurements

The experimental pressure distributions for comparison with theory were obtained on wind-tunnel models shown in upper half of Fig. 3. The straight and the 45° sweptback wing were alternatively mounted symmetrically on a fuselage of fineness ratio 8. Both wings, of aspect ratio 6, were untapered, unwarped, and had a 9% thick RAE 101 Section profile. Unswept pylons with blunt leading and trailing edge were fixed vertically without skew on the wing. Stores and tip-tanks had identical geometry.

Closely spaced static pressure orifices were provided on the wing, fuselage, pylon, store and tip-tank surface. All test data was obtained at a wing chord based Reynolds number of about  $3.3 \cdot 10^5$ . A fuller description of the experiments conducted at Deutsche Forschungs- und Versuchsanstalt für Luft- und Raumfahrt e.V. (DFVLR), in Germany, is given in Ref. 11.

#### 4.2 Store/Pylon load measurements

Principal dimensions of the wing-fuselage model used at Aeronautical Research Association (ARA) in England, for store/pylon load measurements is shown in lower half of Fig. 3. The results, reported in Ref. 2, have been utilised in the present study to check the load predictions of the theory.

The wing of aspect ratio 2.8, taper ratio of 0.33, a mid-chord sweep of  $45^\circ$  and a 6% thick RAE 102 section was mounted symmetrically on a fuselage of relatively large diameter. Wing planform and thickness/chord ratio are typical of aircraft design for which store assembly loads are required. Store used in the tests was a simple streamlined body of revolution of fineness ratio 8.3. The swept forward pylon of constant chord could be placed at 0.3, 0.5 and 0.75 semispan locations beneath the wing. Slots were machined at these positions on the wing underside allowing a chordwise displacement of store/pylon assembly to positions with  $x_s = 0, 0.15$  and  $0.5$ . For all test locations, the store centreline was 1.4 store diameters below the wing chordal plane.

Side forces and yawing moments, for the store in the presence of pylon, and for the full store/pylon assembly, were measured at Mach numbers between 0.6 and 1.4. The store was tested with and without its cruciform fins. No tests were conducted with a tip-tank arrangement.

### 5. RESULTS OF THEORY AND COMPARISON WITH EXPERIMENT

#### 5.1 Surface Pressure Distribution

Fig. 4 and Fig. 5 show a representative result of the comparison between computed pressure distribution and experimental data on the pylon, store and tip-tank of the straight wing and swept wing-fuselage configurations. The case chosen is that of mid-semispan location of store under the wing, the tip-tank mounted flush with wing tip, its axis lying in wing chordal plane and parallel to fuselage axis.

Notwithstanding the idealisation of flow in the theoretical model used, the overall agreement between the measured and calculated pressure distribution is good. The deceleration of flow in sections 1 and 8 along store meridians and the superimposition of wing pressure distribution on the distributions in sections 3 and 4 along tip-tank meridians, is predicted very well. The pylon, store and tip-tank models used exhibited regions of separated flow at the aft end so that discrepancies occur in this region.

#### 5.2 Surface Flow Pattern on Store, Pylon and Tip-tank

Fig. 6 and Fig. 7 show examples of the theoretical study that explored the detailed variation of flow on the store and pylon surface with incidence and store chordwise position. The theoretical velocity vector plot for the inboard side view in Fig. 6 depicts the strong influence of incidence on the flow pattern of the store and pylon. Results shown are for store on port wing. Except in the vicinity of the fins, the entire surface flow is affected by the incidence of the freestream. With positive incidence the pylon leading edge experiences a flow from the inboard to outboard face as evident from the velocity distribution seen from top. With negative incidence this flow pattern is reversed. Displacement of store along the wing chord induces change of the sidewash below the wing. The resulting change in surface flow over store and pylon is depicted in Fig. 7. Starting with the store chordwise position of  $x_s = 0$ , a rearward movement to  $x_s = 0.15$  brings the store pylon intersection apparently in a region of higher sidewash as seen in the top view. With a further displacement to  $x_s = 0.5$ , the flow over the main store body is "straightened", the store nose experiencing now the region of high sidewash.

The chordwise movement of a tip-tank relative to the wing-tip and the subsequent velocity pattern which develops is represented in the illustrations of Fig. 8. Shown are the inboard side view, tip-tank on starboard side, and topview, tip-tank on port side, for the tip-tank chordwise locations  $x_{TS} = 1, 0.5$  and  $0$ . The superimposition of wing flow field on the tip-tank flow pattern is clearly depicted in the sideview. In the top view, the wing induced inward flow over the tip-tank periphery can be seen.

#### 5.3 Variation of Side force and Lift distribution with various parameters

The influence of incidence  $\alpha$ , store chordwise position  $x_s$ , store spanwise position  $y_s$  and wing mid-chord sweep  $\phi_m$  on side force and lift distribution along store axis is investigated in Fig. 9. For the sake of clarity only the distribution for store is considered with pylon and fins present.

When the store is positioned beneath the wing, the induced side force on the store at  $\alpha = 0^\circ$  is already of considerable magnitude and positive, Fig. 9a. As was indicated in velocity pattern of Fig. 6, a slight negative sidewash is present at zero incidence which causes this positive side force. The load is greatest in a region corresponding to the store/pylon intersection. The store side force distribution changes its sign between  $\alpha = 0^\circ$  and  $\alpha = 10^\circ$ ; the negative load at  $\alpha = 10^\circ$  is associated with the large positive sidewash induced, as seen in the corresponding velocity plot of Fig. 6. Most of the side force in this example considered is induced near the store mid-point, so that the resultant store yawing moments would be small.

The case with negative incidence is characterized by a reversal of side force over a sizable rear portion of the store.

Store side force distribution is sensitive to the store chordwise position, as demonstrated by the curves of Fig. 9b. The greatest load is experienced when the store mid-point lies below the wing leading edge ( $x_s = 0$ ). A drastic reduction in side force is evident for the rearmost store location of  $x_s = 0.5$ . This behaviour is confirmed by the experimental results summarized in Ref. 1.

The nature of variation of store side force with spanwise location is shown in Fig. 9c. The trend is for the side force to increase with distance out along the span, the greatest change being effected on the rear half of the store. The curves shown are for the same chordwise store location of  $x_s = 0$ , so that with store moved out along the span, the trailing edge of the tapered wing comes closer to the store aft end. This behaviour of side force change with store spanwise location stands in qualitative agreement with the analysis of experimental results of Ref. 1.

The variation of store side force distribution suggests that the store yawing moment may vary most with spanwise position.

Variation of wing mid-chord sweep between the values of  $0^\circ$  and  $45^\circ$  appears to have minor influence on the side force distribution of the store at the chosen chordwise and spanwise location, Fig. 9d.

The illustrations 9e to 9h depict the influence of the four investigated parameters on the lift distribution along store axis. Also here the greatest changes are visible in the region of store/pylon intersection. It is interesting to note that the store induces a flow acceleration on wing underside at zero incidence, causing a negative lift on store nose and a positive lift on store aft portion, Fig. 9e. This trend is maintained also for negative incidence. The major effect of a positive incidence is evident on the store nose and aft regions which causes corresponding variations in the store pitching moment.

Effects of store chordwise and spanwise displacement on lift distribution as seen in Figs. 9f and 9g are similar to those on the side force distribution. As noted earlier for the yawing moment, the changes in lift distribution in Fig. 9f and 9g entail changes in the store pitching moment.

The lift distribution over a major part of the store rear varies with the wing sweep, changing its sign as the sweep increases from  $0^\circ$  to  $45^\circ$ , Fig. 9h. Although in this investigation the relative position of store mid-point to local wing leading edge is retained, the change in  $\varphi_m$  decreases the wing leading edge and trailing edge sweep, the latter becoming negative for  $\varphi_m = 0^\circ$ . This drastic change in wing plan geometry overshadowing the store aft part is responsible for the lift distribution change with  $\varphi_m$ . An interesting insight into the side load distribution over the pylon height is afforded by the parameter study in Fig. 10. As earlier in Fig. 9 the influence of the 4 parameters:  $\alpha$ ,  $x_s$ ,  $y_s$  and  $\varphi_m$  is investigated. The side force values are minimum near the pylon/store intersection ( $x/z_A = -0.64$ ) which for potential flow could be explained by the "straightening" effect of the pylon/store intersection on the surface flow. The values of pylon side force are invariably much smaller than the values for the store. The most pronounced change on pylon side loads is seen from Fig. 10 to be effected by incidence and spanwise location. Pylon side loads which are present even at zero incidence increase and change sign with  $\alpha$ . The relative increase in  $c_y$  is much stronger with negative incidence as for the positive values of  $\alpha$ . Another important parameter which leads to a rapid increase in pylon side loads is the spanwise positions. However, the spanwise position effects are of consequence for values of  $y_s$  above about 0.75. Chordwise displacement of store/pylon assembly on the wing or change of wing sweep have, as indicated in Fig. 10, little influence over pylon side loads.

The force distribution on the tip-tank is strongly influenced by wing pressure distribution as borne out by the curves in Fig. 11 which show the effects for an extreme rearward, central and extreme forward placed tip-tank. The tip-tank geometry chosen in the study is identical to that of the ARA store without fins, which has a slenderness ratio of 12%, compared to wing thickness/chord ratio of 3%.



Highest values of side force and lift are obtained for the extreme forward location of the tank, whereby the maximum is located near the tip-tank mid-point which for this case also lies in the vicinity of wing leading edge. As the maximum is located near tip-tank mid-point, the corresponding yawing and pitching moments can be expected to be small. Moving the tip-tank rearward to the central position shifts the location of  $c_y$  and  $c_a$  maximum towards the tip-tank nose which is a direct consequence of the location of wing leading edge. As the maximum store diameter is shifted now aft of wing leading edge, the absolute values of  $c_y$  and  $c_a$  maximum also decrease. The curves for  $c_y$  and  $c_a$  for the central tip-tank location are asymmetric so that the yawing moment and pitching moment values would be high. For the extreme rearward location of the tip-tank, the side force over the whole tip-tank axis remains negative (nose outwards) with a fairly constant value over the rear half.

#### 5.4 Variation of forces and moments with various parameters

The force and moment distributions as discussed in Figs. 9, 10 and 11 can be integrated to evaluate the force and moments acting on the store, pylon and fins. A comprehensive representation of the influence of the four parameters  $\alpha$ ,  $x_S$ ,  $y_S$  and  $\phi_m$  on the store, pylon and fin forces and moments is shown in Fig. 12. The values plotted for a component include the induction effect of the other two components of the store/pylon and fin assembly. The physical quantity most sensitive to a parameter change turns out for the store to be the side force  $c_y$  as inferred from Figs. 12a to d. The variation of store  $c_y$  with the parameters  $\alpha$  and  $y_S$  is non-linear, especially for the negative incidence range and for outboard locations exceeding  $y_S = 0.7$ . Lift coefficient for the store remains practically constant between the values of  $\alpha = -3^\circ$  to  $3^\circ$ . Moving the store rearwards along chord, outboard along span or decreasing the mid-chord wing sweep decreases the store lift. The store pitching moment  $c_M$  is essentially a function of  $\alpha$  and to lesser extent of  $x_S$  and  $y_S$ . Except for a change of sign for high  $y_S$  values, the yawing moment  $c_N$  for store is relatively little influenced by the parameters under study. Variation of the rolling moment  $c_L$  for the store was negligible and its absolute value very near zero, so that the result has been omitted in the Figs. 12a to d.

Sizable variation was observed in the case of the pylon for the side force, for the parameters  $\alpha$  and  $y_S$ , Figs. 12e to h. It is interesting to note the high value of pylon side force for negative incidence. Pylon yawing moment ( $c_N$ ) behaviour seems to be of consequence for high values of  $y_S$  where its value changes from negative to positive.

The last column in Fig. 12 shows the forces and moments acting on the four store fins. Except the rolling moment  $c_L$ , whose value remains very small, the contribution of the fins to all other forces and moments is very high. Major part of the lift  $c_A$ , pitching moment  $c_M$  and yawing moment  $c_N$  of the store/pylon/fin assembly would, according to the result of Figs. 12i to l, be contributed by the fins.

Fig. 13 shows the variation of loads and moments on the tip-tank configuration studied earlier in Fig. 11. As indicated before, the central tip-tank location results in lowest side force value but highest values of pitching and yawing moments. Low values of pitching and yawing moments are obtained for the forward tip-tank location, with the side force attaining a high negative value for the rearward position.

#### 5.5 Comparison with experiment

The theoretical prediction method has been tested by comparing the computed forces and moments with the results of a series of wind-tunnel tests conducted at the ARA in England (Ref. 2). Fig. 14 shows a representative example of the agreement obtained between the theory and experiment. The first set of results are for three chordwise positions  $x_S = 0, 0.15$  and  $0.50$ , and the second set for the two spanwise positions of  $y_S = 0.5$  and  $0.75$ . In the first set, the spanwise store location was  $y_S = 0.5$  and in the second set the chordwise store location  $x_S = 0$ .

Except for the high incidence range and the rearmost store location, agreement between theory and experiment is good. Even though the values for the case of  $x_S = 0.5$  and negative incidence are overestimated, the non-linear behaviour of experimental results is also exhibited by the theory. A rather severe test for the theory is the comparison of yawing moment results. The basis of the calculation of forces and moments in the prediction method is the assumption of constant pressure over the panel surface and that the resultant force be acting at a characteristic central point on the panel surface. The approximation of the continuous surface by plane surface elements, the ensuing error due to misalignment of resultant force direction and the

error caused by the assumption of the force acting concentrated at a point on the panel, lead to discrepancies especially in the prediction of moments.

A typical result of the agreement between the predicted yawing moments for the store assembly components and experiment is shown in Fig. 15. The results for store plus pylon and store alone are for the fins off case, whereby the computation was done without fins in the theoretical model, to conform with the experiments. Fin yawing moment was obtained as the difference between fins on and fins off cases.

Theoretical prediction of store plus pylon and store alone yawing moments is for not too high incidence satisfactory. The non-linear trend of  $C_N$ -variation is essentially reproduced by the theory.

The real flow over the sharp-edged fins bears little similarity with the attached potential flow. Side-wash produces separation regions near the sharp fin leading edges, which is one of the main causes of the discrepancy between the experiment and predicted results.

Effect of compressibility in the subcritical Mach number range is allowed for in the method by the G6thert rule. Although it is speculative to expect a reasonable prediction beyond a Mach number of say 0.6 by this method, a sample calculation was performed for a configuration at zero incidence between Mach numbers of 0 and 0.9. The values of computed side force are compared with experimental data in Fig. 16. Agreement of theory with experiment is quite satisfactory. Increase of side force with Mach number is, in its trend, correctly predicted.

## 6. CONCLUSIONS

Six-component aerodynamic loads and moments have been calculated for a wing/fuselage/pylon/store/fin and a wing/fuselage/tip-tank configuration with the help of "panel" method for high subsonic Mach numbers. Some results of pressure distribution on a straight wing and swept wing-fuselage configuration with pylon, store and tip-tank are also included.

Parameters considered are incidence, store chordwise and spanwise locations, tip-tank chordwise location, and Mach number. The study reveals that pylon loads and moments are mainly influenced by incidence, chordwise, and spanwise location. For the store, the wing mid-chord sweep affects, in addition, the loads and moments. Contribution of fins to value of total loads and moments is high and exceeds in most cases that of store and pylon.

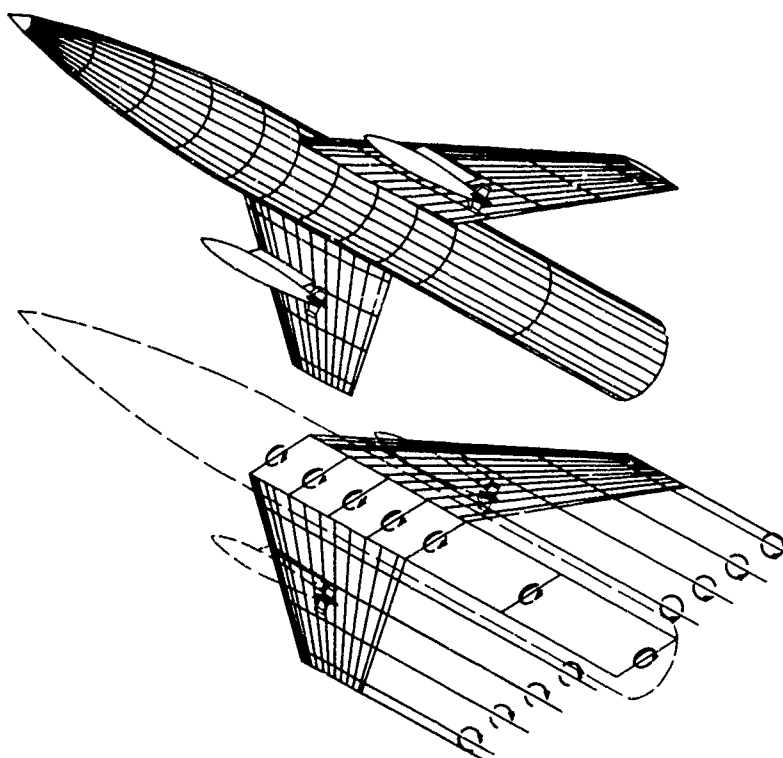
Comparison with experiment shows that for attached flow conditions the estimation of forces and moments by this potential flow analysis yields adequate agreement. Accuracy of results obtained suffices for preliminary design. Viscous effects present in the real flow cause a non-linear behaviour.

The predicted force and moment results for store assembly components exhibit non-linear behaviour, so that non-linearity observed in experimental data is not the result of viscous effects alone.

## REFERENCES

- 1     Marsden, P. and  
       Haines, A.B.             Aerodynamic loads on external stores. A review of experimental data and method of prediction.  
                                      ARC R.&M. No. 3503 (1967).
  
- 2     Marsden, P. and  
       Haines, A.B.             Measurements at transsonic speeds of the side force and yawing moment on various store arrangements mounted beneath a 45° swept wing-fuselage model.  
                                      ARC C.P. No. 955 (1964).
  
- 3     Berry, J.B.                 Example of airframe-store interference.  
                                      AGARD-CP-71-71, (1971), 27, 1-10.
  
- 4     Fernandes, F.D.            A method for predicting interference forces and moments on aircraft stores.  
                                      AGARD-CP-71-71, (1971), 33, 1-7.
  
- 5     Grose, G.G. and  
       Bristow, D.R.            Evaluation of the prediction of airplane/store interference by linear theory.  
                                      AGARD-CP-71-71, (1971), 28, 1-10.
  
- 6     Nielsen, J.N.  
       Goodwin, F.K. and  
       Dillenius, M.F.E.        A calculative method for predicting store separation trajectories at speeds up to the critical speed.  
                                      AGARD-CP-71-71, (1971), 26, 1-12.
  
- 7     Chadwick, W.R.            External-store loads using nonplanar lifting surface theory.  
                                      J. Aircraft, (1974), 11, 181-188.
  
- 8     Ahmed, S.R.                Calculation of the inviscid flow field around three dimensional lifting wings, fuselages and wing-fuselage combinations using the panel method.  
                                      European Space Agency, Rep. No. ESATT-210, (1975)  
                                      (Translation of DLR-FB 73-102, 1973).
  
- 9     Hess, J.L. and  
       Smith, A.M.O.            Calculation of non-lifting potential flow about arbitrary three-dimensional bodies.  
                                      Douglas Aircraft Report No. E.S. 4C622, (1962).
  
- 10    Rubbert, P.E. and  
       Saaris, G.R.             A general three-dimensional potential-flow method applied to V/STOL aerodynamics.  
                                      SAE Air Transportation Meeting, New York, (1968).
  
- 11    Ahmed, S.R.                Prediction of the optimum location of a nacelle shaped body on the wing of a wing-body configuration by inviscid flow analysis.  
                                      AGARD-CPP-150, (1974), 25, 1-12.

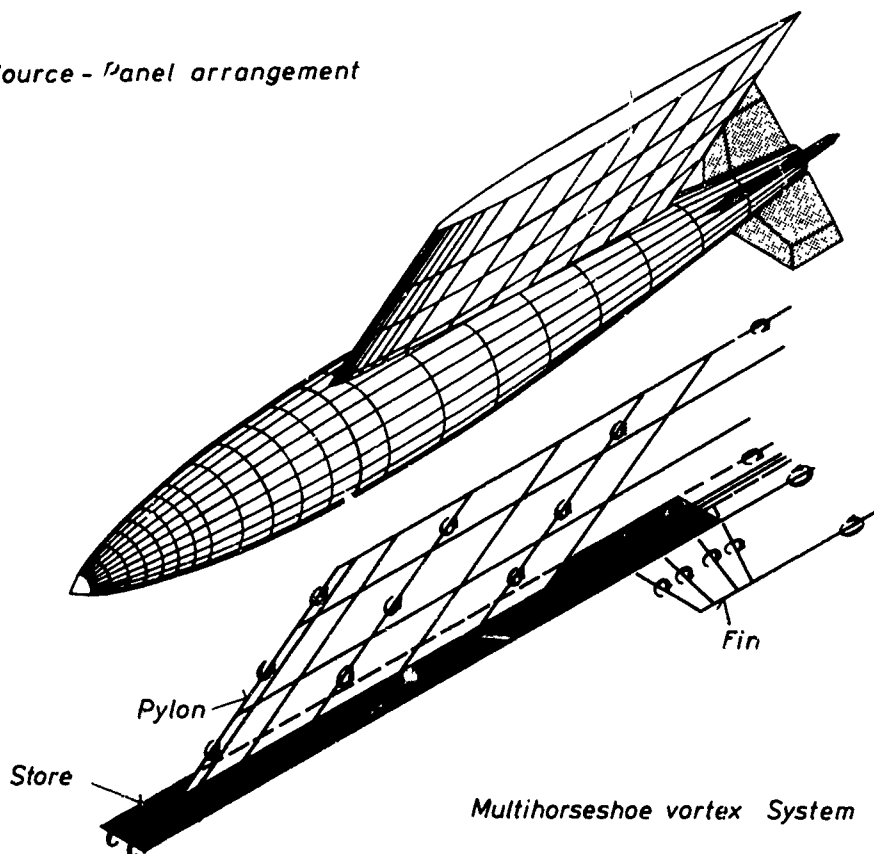
*Source - Panel arrangement*



*Multihorseshoe vortex system*

Fig 1 Numerical model of swept wing-fuselage

*Source - Panel arrangement*



*Multihorseshoe vortex System*

Fig.2 Numerical model of pylon and store with fins

# DFVLR Models for pressure measurements

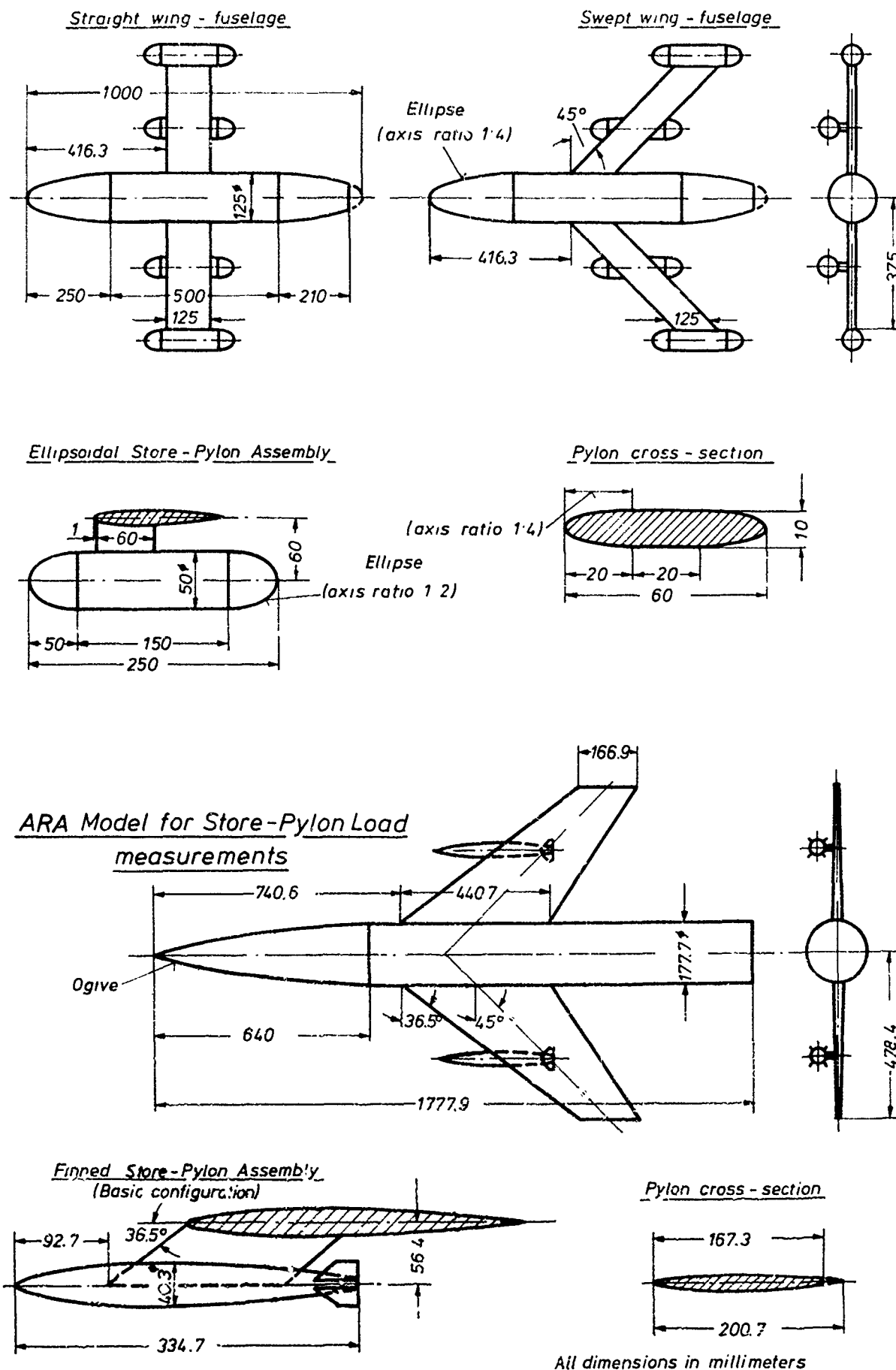


Fig.3 Model configurations

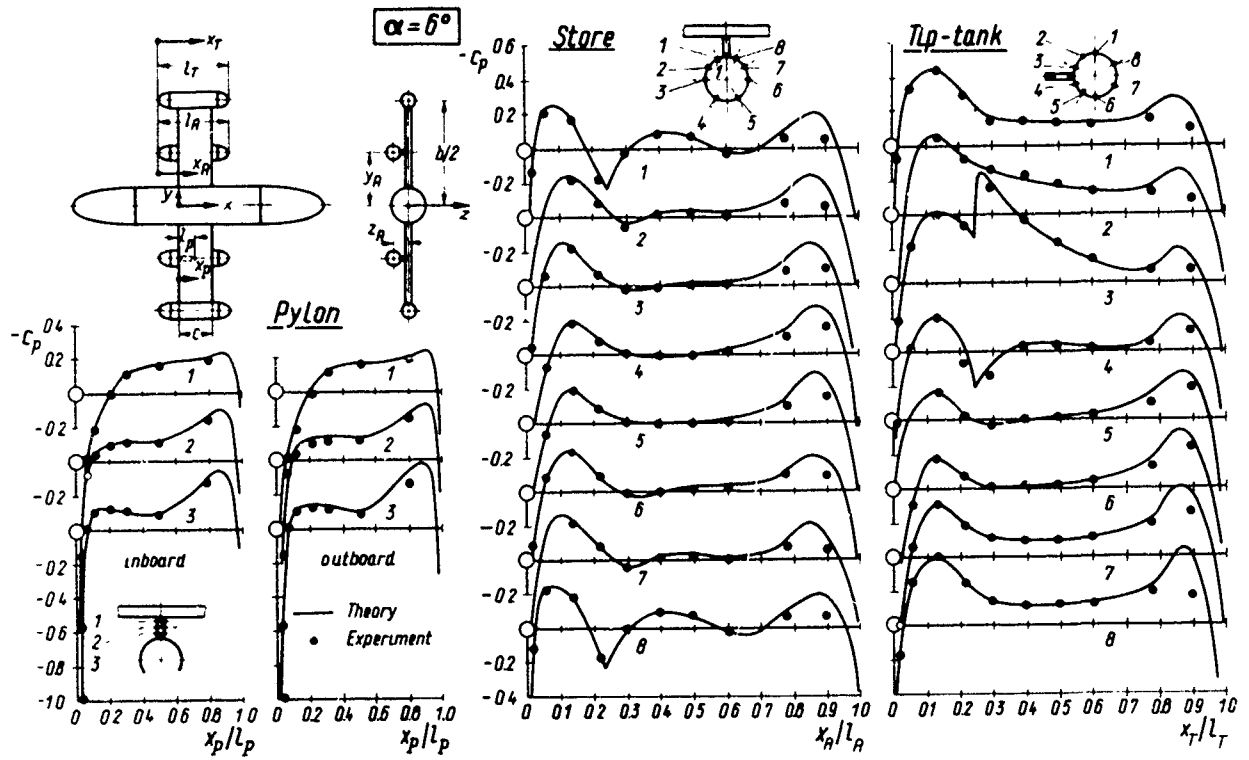


Fig.4 Pressure distribution on pylon, store and tip-tank surface (straight wing-fuselage)

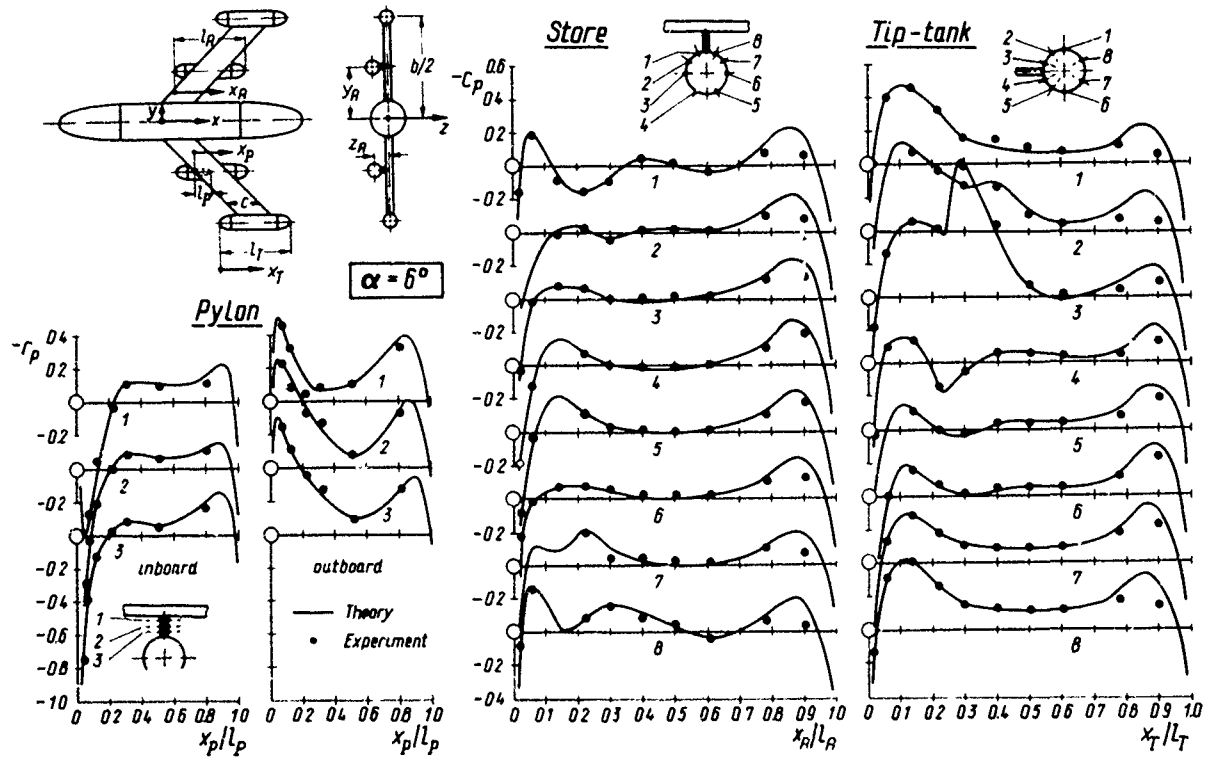


Fig.5 Pressure distribution on pylon, store and tip-tank surface (swept wing-fuselage)

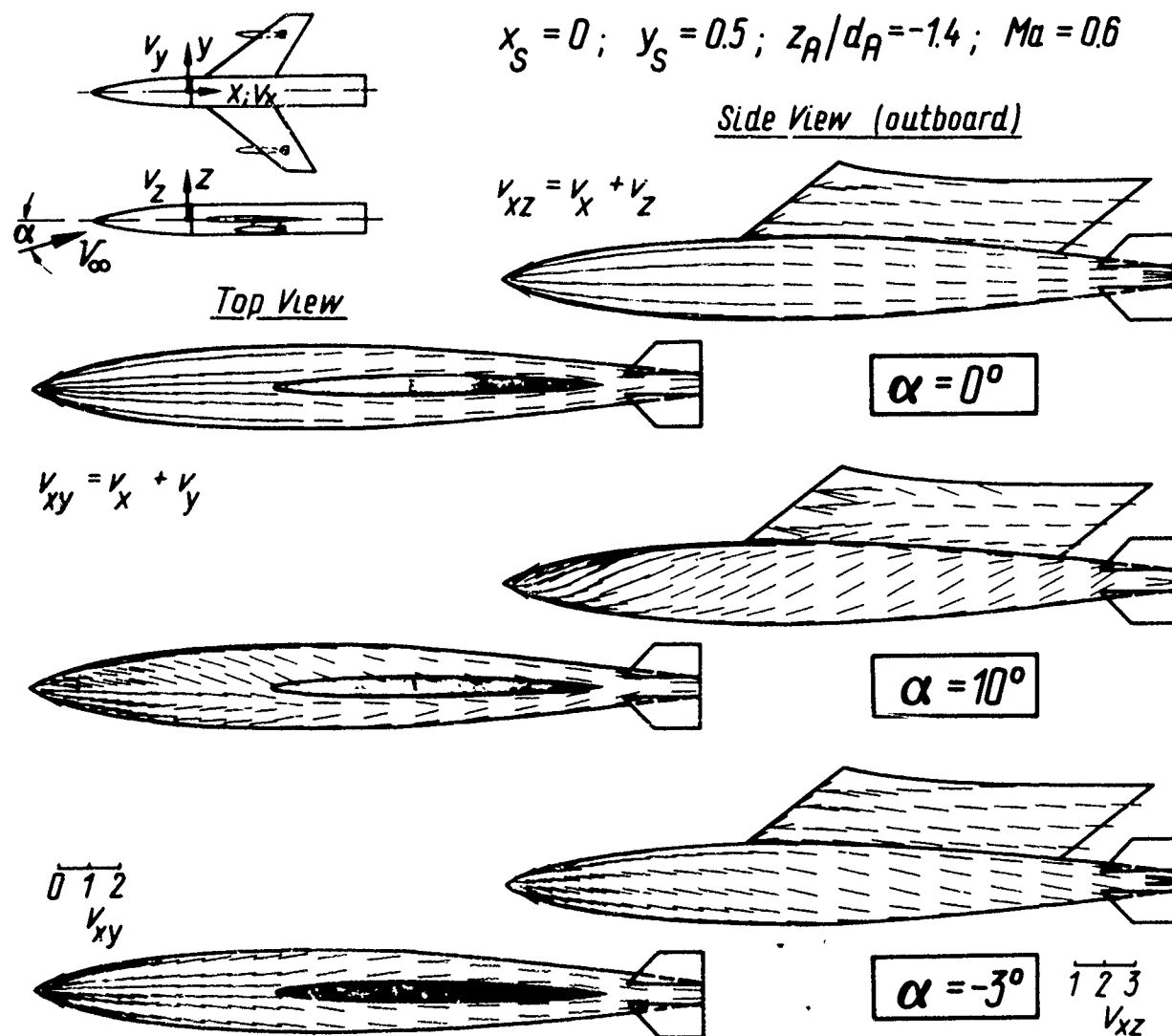


Fig.6 Variation of velocity distribution with incidence  
(Store on port wing)

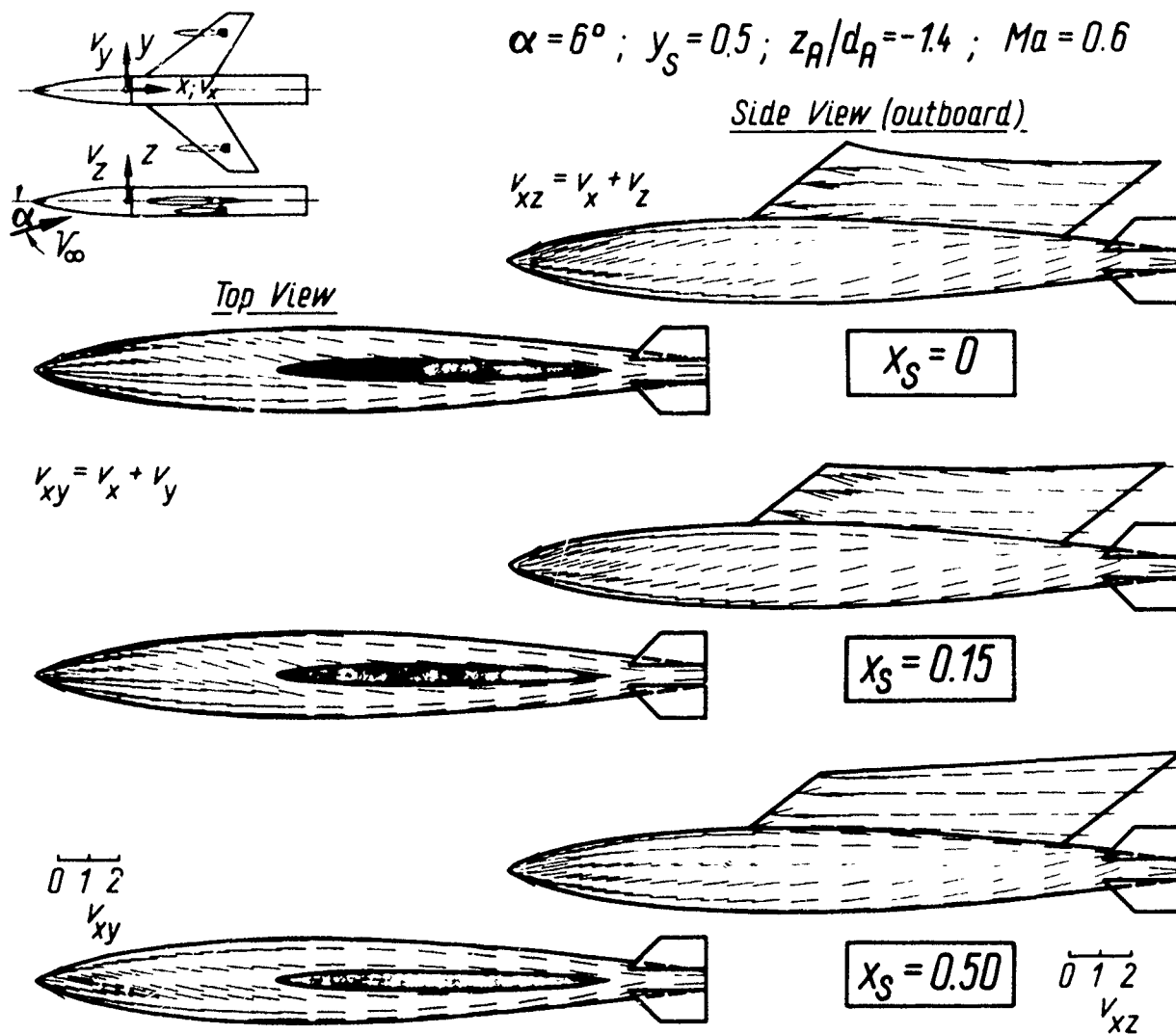


Fig 7 Variation of velocity distribution with store chordwise position  
(Store on port wing)



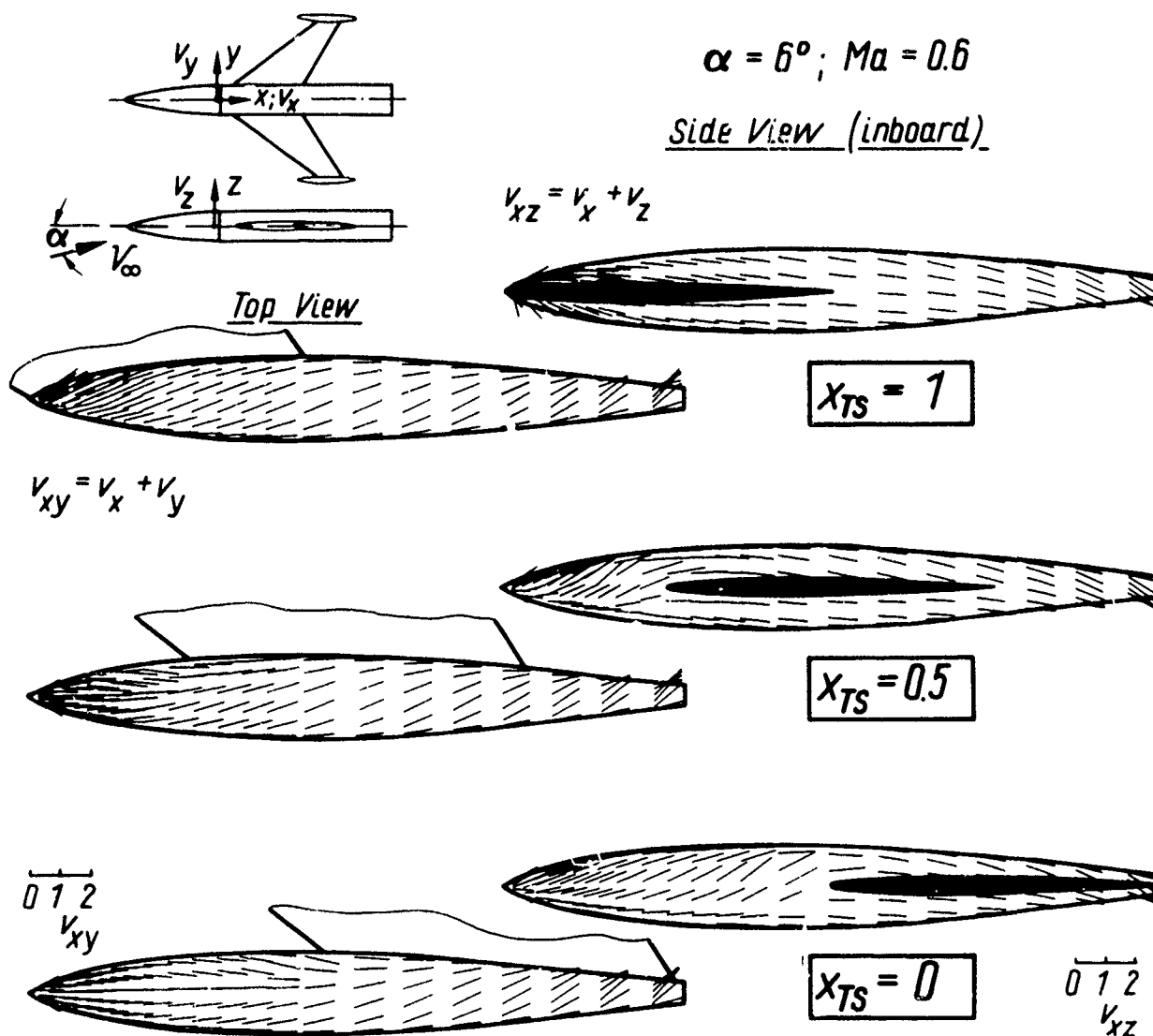


Fig.8 Variation of velocity distribution with tip-tank chordwise position  
(Side view: tip-tank on starboard wing, top view: tip-tank on port wing)

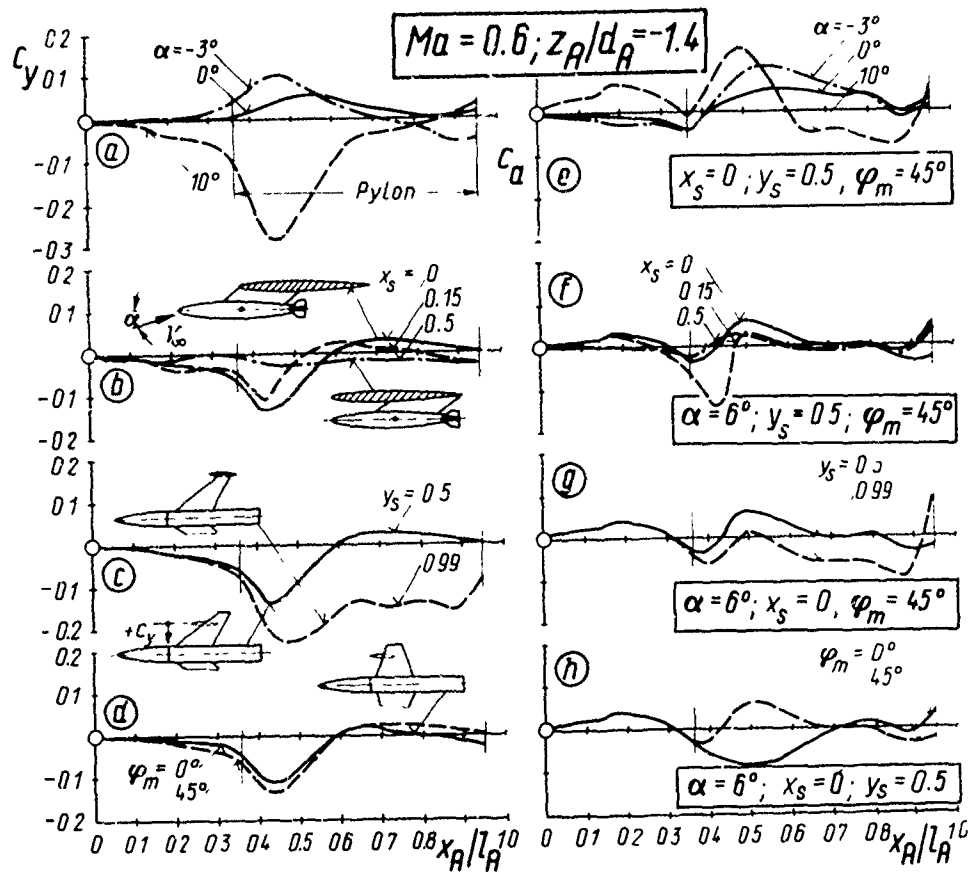


Fig.9 Variation of store side force and lift distribution with various parameters

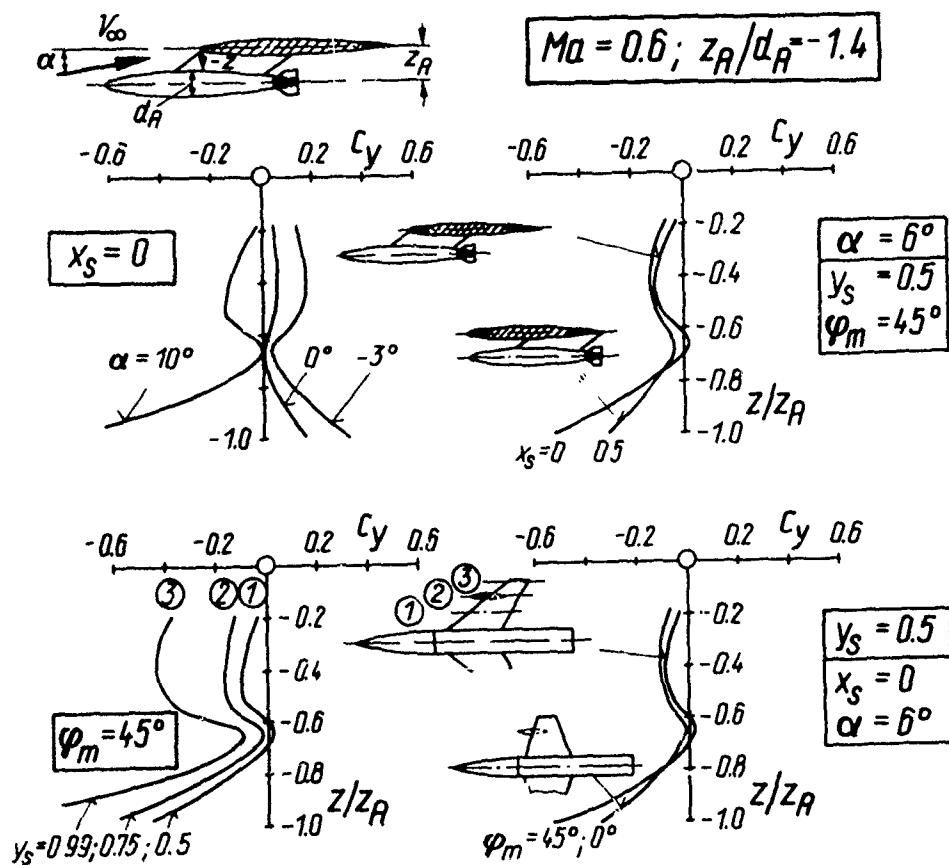


Fig.10 Variation of pylon side force distribution with various parameters

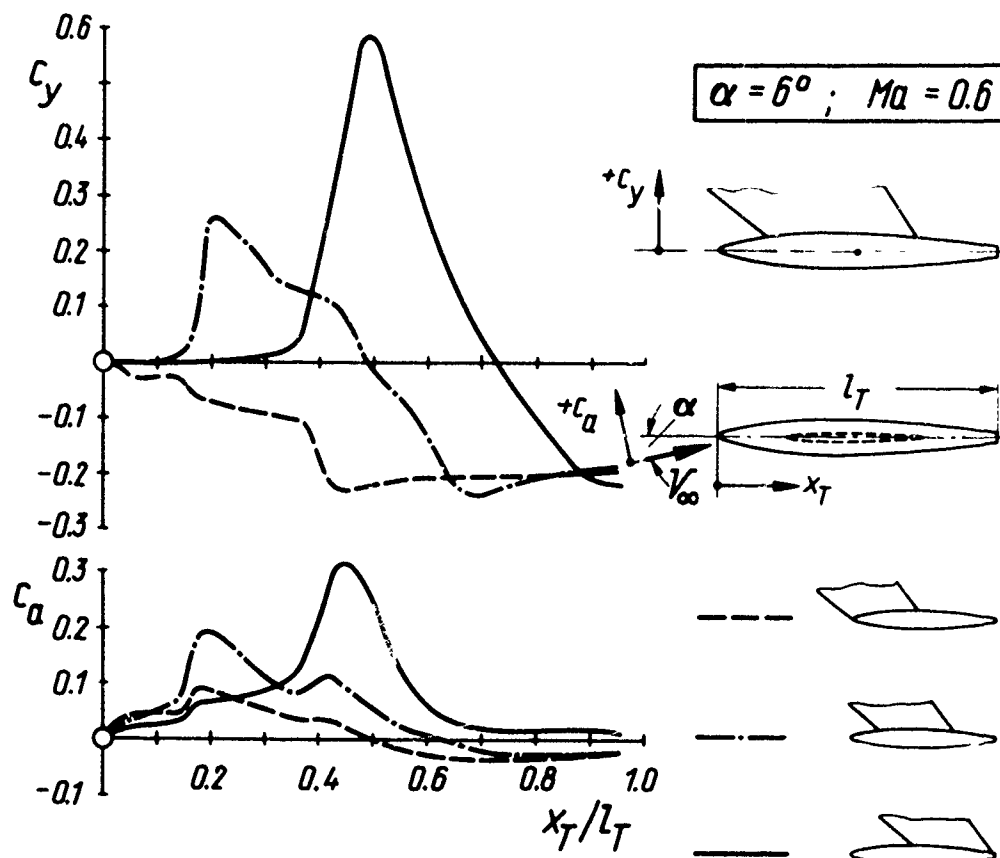


Fig.11 Variation of tip-tank side force and lift distribution with chordwise position

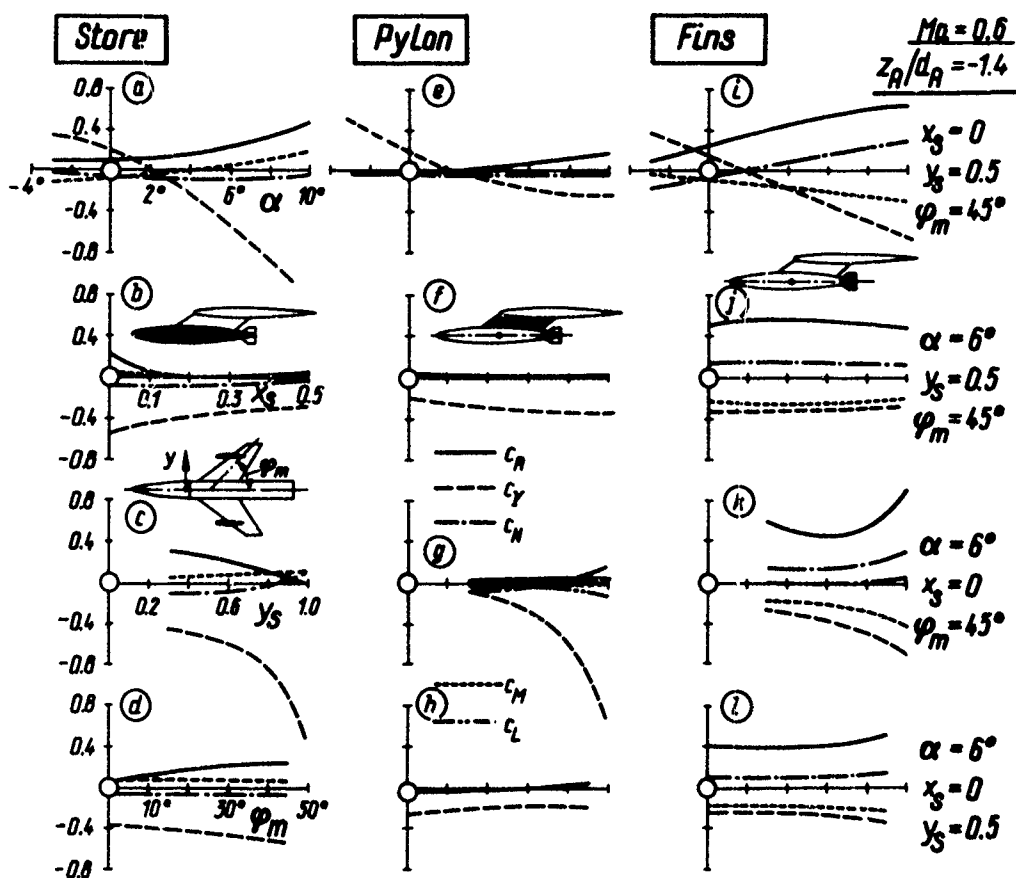


Fig.12 Variation of forces and moments with various parameters

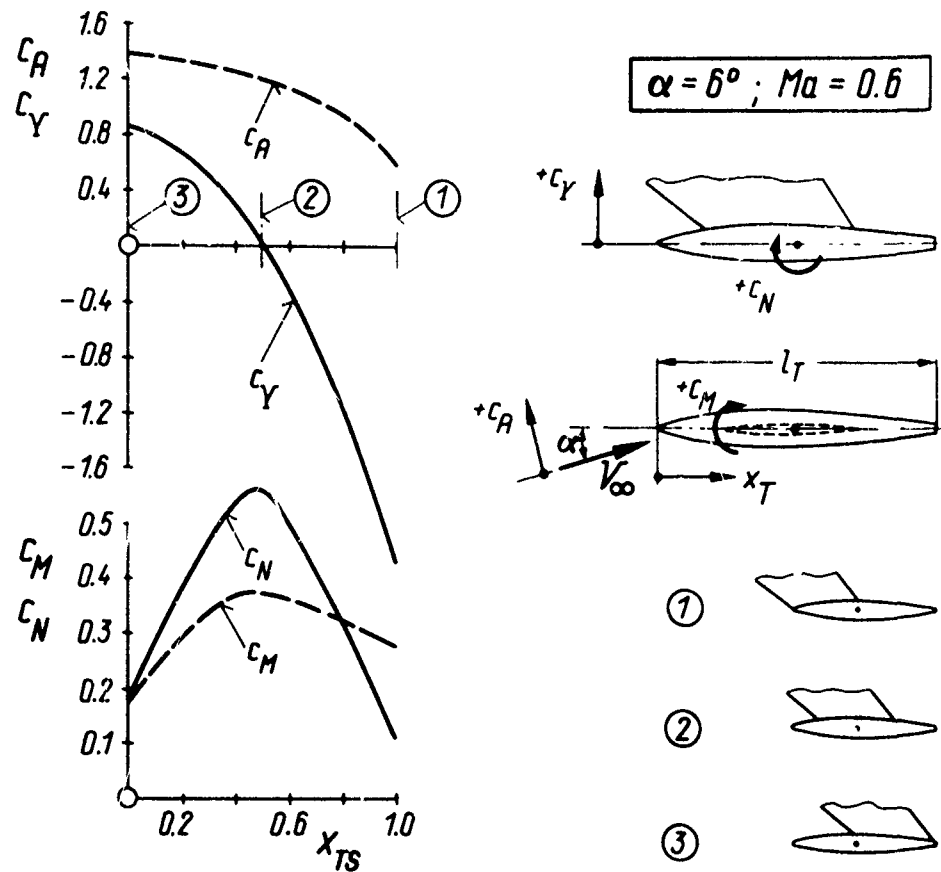


Fig.13 Variation of tip-tank forces and moments with chordwise position

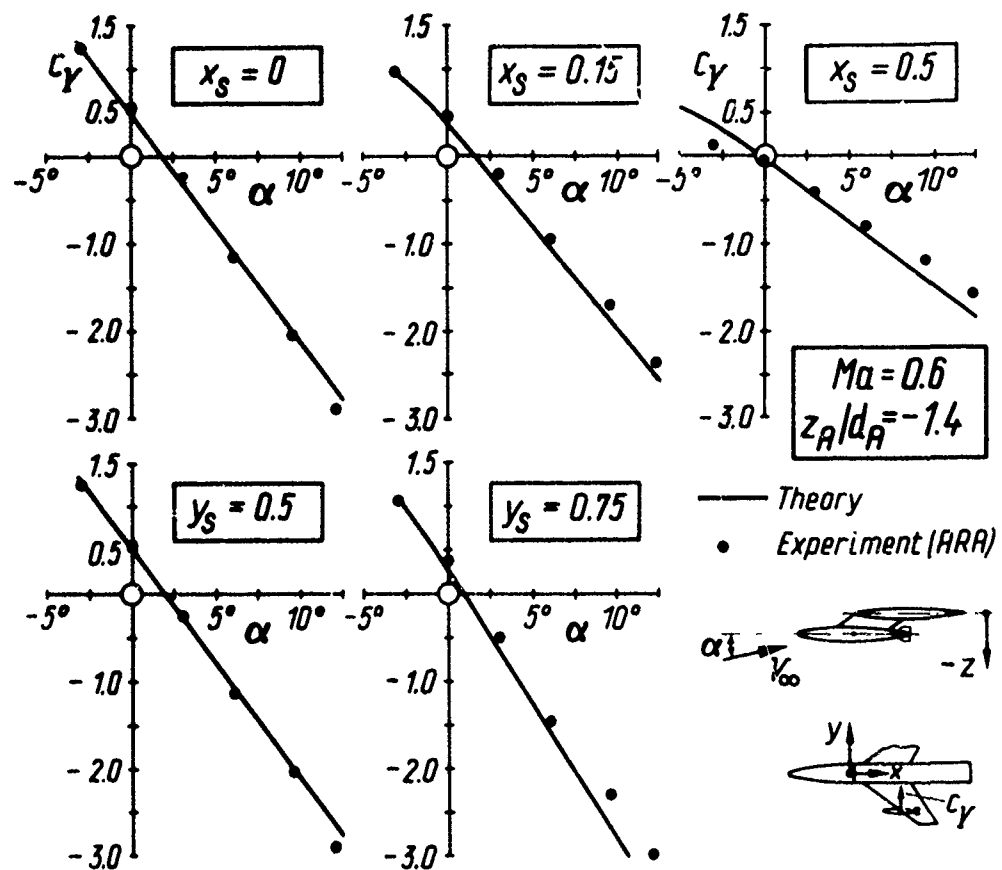


Fig.14 Variation of side force with incidence for various chordwise and spanwise locations

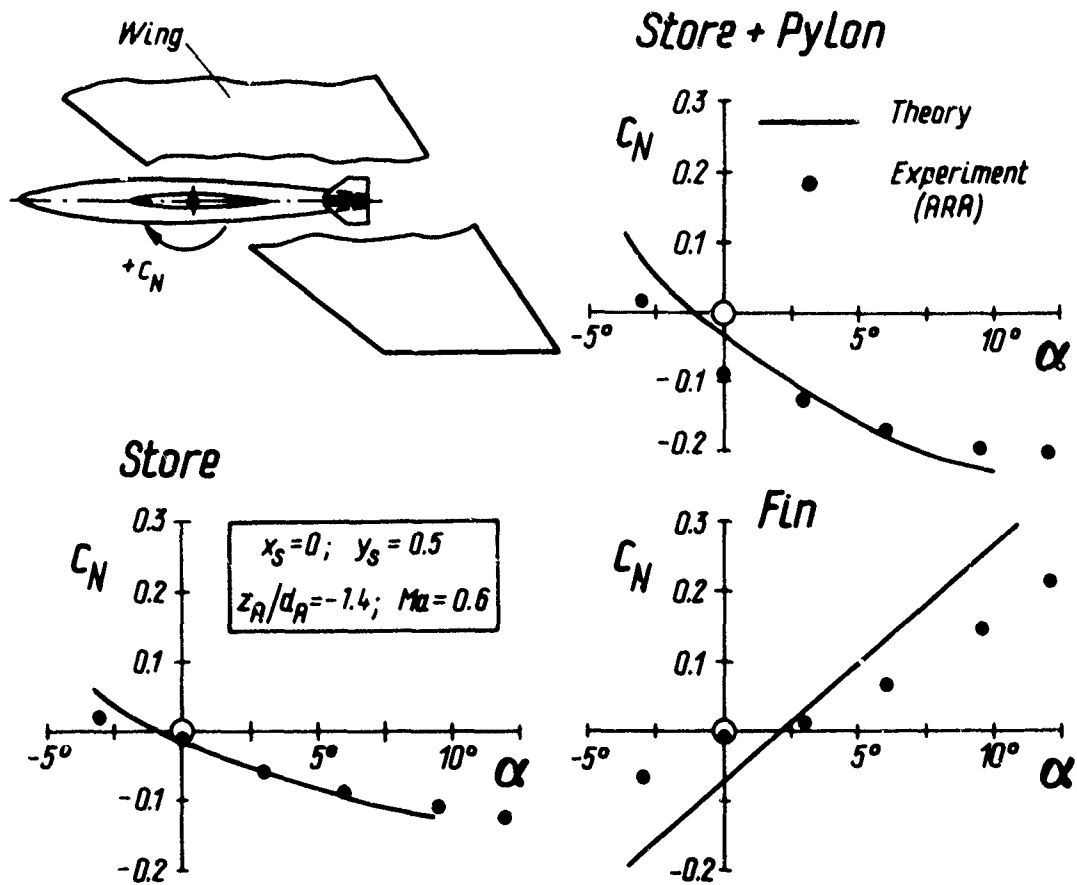


Fig. 15 Variation of store, pylon and fin yawing moment with incidence

$$x_s = 0; y_s = 0.5; z_R/d_R = -1.4 \quad \underline{\alpha = 0^\circ}$$

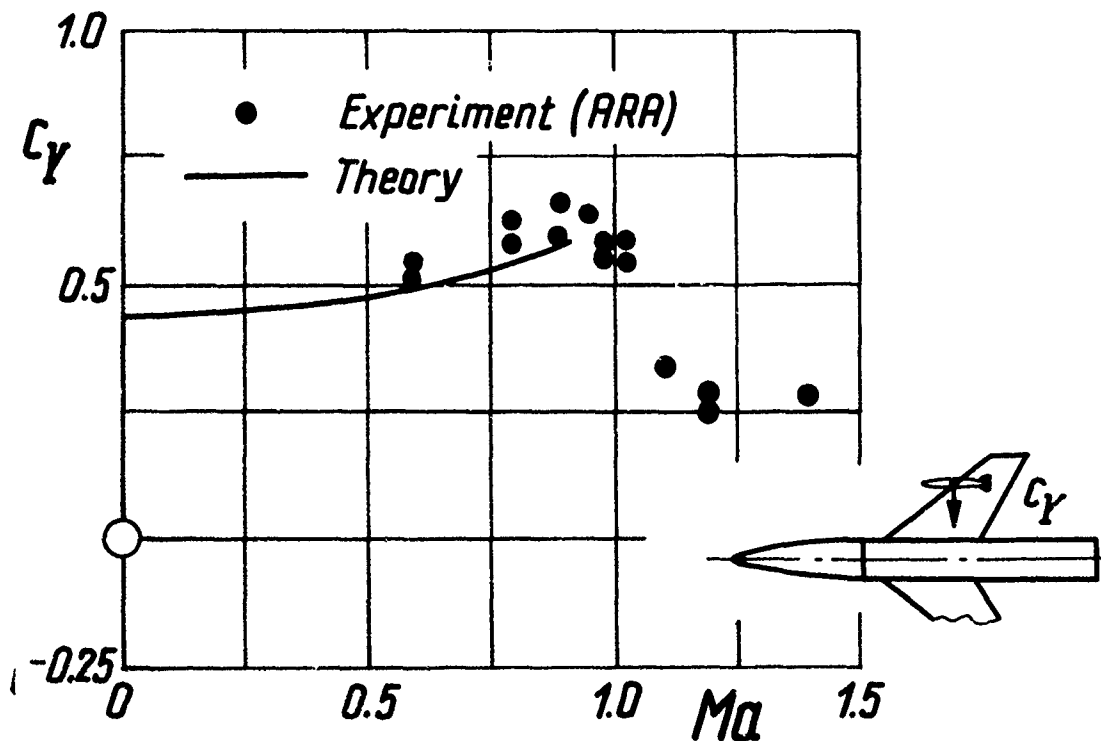


Fig. 16 Variation of side force at zero incidence with Mach number

## COMPARISON OF PREDICTED AERODYNAMIC LOADING WITH FLIGHT TEST RESULTS

by

Jan Kloos

SAAB-SCANIA AB

S 58188 Linköping, Sweden

## SUMMARY

Four load prediction problems of the more intricate kind are treated in this paper. In the first three cases,

- prediction of loads on wing mounted external stores during rolling pull-outs,
- prediction of fin loads during fast rolling manoeuvres,
- effect of airframe elasticity on load distribution,

it is shown how windtunnel data, combined with fairly simple computation procedures, can provide adequate load predictions that are in good agreement with flight test results.

In the fourth problem area,

- loads due to encounter with wing-tip vortices from aircraft at high load factors,

results from the first stage of a flight test program that has been started, are shown.

## INTRODUCTION

The importance of having reliable load predictions available in an early stage of the design and of avoiding subsequent flight testing, is obvious. The aim of this paper is to give an account of a number of cases in which Saab-Scania's experience indicates that load predictions of adequate reliability can be obtained by windtunnel testing and to show examples of the agreement with flight test results.

## LOADS ON EXTERNAL STORES

Comparison between windtunnel tests and flight tests

The aerodynamic load on the Rb 27 (Falcon) missile, wing mounted on the Saab 35 Draken aircraft, see figures 1 and 2, was measured in the  $1 \times 1 \text{ m}^2$  transonic-supersonic windtunnel at the FFA, Aeronautical Research Institute of Sweden. The tests were done on a 1:18 scale model at Mach numbers, .5 to 1.9, using a five component strain gauge balance inside the missile, connected to the pylon by means of a vertical strut. The opposite wing station was utilised for a simultaneous measurement of the loading on missile plus pylon by attaching the pylon to the missile and attaching the strut, through an opening in the pylon, to the wing.

In a later stage of the program, loads were measured in flight tests with a special dummy missile containing a six component strain gauge balance. The variation of the air loads with angle of attack, angle of sideslip and Mach number showed good agreement with the windtunnel test results.

The critical loading case for a wing mounted pylon and its attachment usually is a rolling pull-out. The reason for this is that on the downward moving wing the most important loading components, side loads and rolling moments, due to several factors all act in the same direction. Loads due to

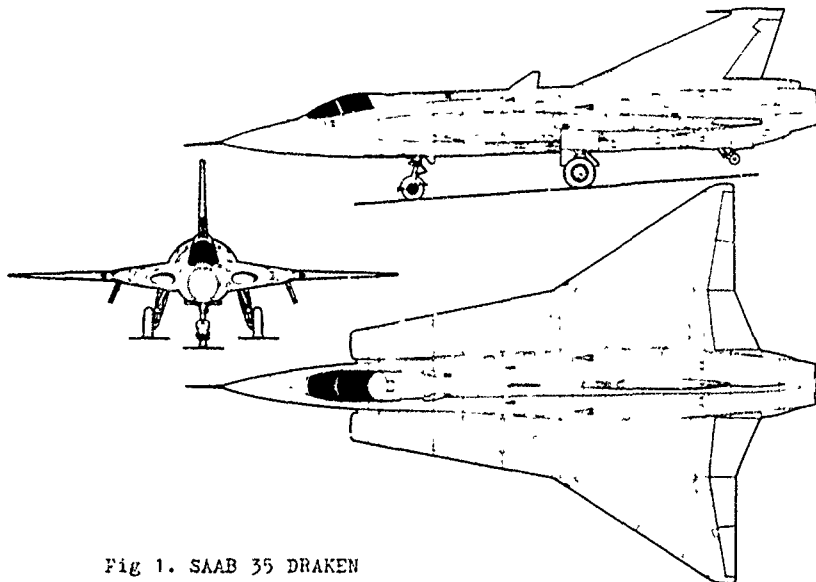


Fig 1. SAAB 35 DRAGEN

- angle of attack, inducing sidewash,
- rolling velocity, inducing mass loads and a increase in local angle of attack
- angle of sideslip, induced by aerodynamic and inertia coupling,

all add up to critical loads.

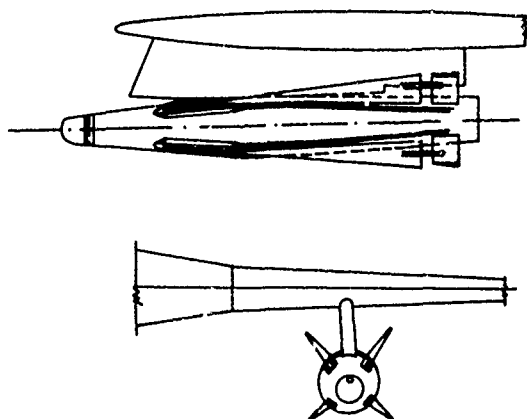


Fig. 2. Rb 27 missile.

It would be a distinct advantage if missile loads during a rolling pull-out could be predicted adequately from windtunnel results without recourse to complicated computational methods. Therefore, flight test measured missile loads during rolling pull-outs were compared with loads, calculated from windtunnel tests by using the flight test values of Mach number and angle of sideslip and using as angle of attack the local angle of attack at the missile station

$$\alpha_{\text{missile}} = \alpha_{a/c} + y \omega_x / V.$$

An example of the result of this comparison is shown in figure 3 for a  $360^\circ$  rolling manoeuvre at a load factor  $n_z = 2.5$  for the missile on the downward moving wing. Completely satisfactory agreement was obtained consistently for the missile on the downward moving wing. The loads on the upward moving wing did not show quite such good agreement. During a part of the rolling manoeuvre better agreement is obtained with a calculation in which the  $y \omega_x / V$  - contribution to  $\alpha_{\text{missile}}$  is neglected, but the reason for this is not clear. As the loads on the downward moving wing are more critical than those on the upward moving wing, this lesser degree of agreement is not of great importance.

As a consequence of the good prediction that was obtained for missile loads, even during complicated manoeuvres, the amount of flight load testing of external stores at Saab-Scania has been drastically reduced and replaced by windtunnel tests which can be done in an earlier design stage. A later check of windtunnel-measured loads on the Rb 04 on the Saab 37 Viggen, for which especially reliable loading data was considered desirable, confirmed the agreement between windtunnel and flight test results.

#### Effect of gap between missile and pylon

It has been mentioned above that the strain gauge balance in the Rb 27 windtunnel model was attached to the pylon and not to a separate sting. Although the torsional flexibility of such a strut has occasionally caused excessive deformation in yaw of the missile model, the strut-attachment has the important advantage that accurate control of the gap between missile and pylon is possible. A separate sting almost inevitably implies a larger gap in order to avoid contact between missile and pylon and considerable variation of gap size due to flexibility under the varying loads during the windtunnel tests.

The importance of the size of the gap between missile and pylon is illustrated by figure 4 which shows missile rolling moment as a function of gap size for the wing-mounted Rb 71 (Sparrow) on the Saab 37 Viggen at different angles of attack. Figure 5 shows missile rolling moment as a function of missile forward travel for different gap sizes. Because of the gap size effect, the Saab-Scania windtunnel test programs that use sting mounted missile models for the measurement of aircraft-missile interference for separation calculations are usually complemented by measurements with the missile model strut-mounted in several fixed positions to obtain accurate loading data for stressing purposes as

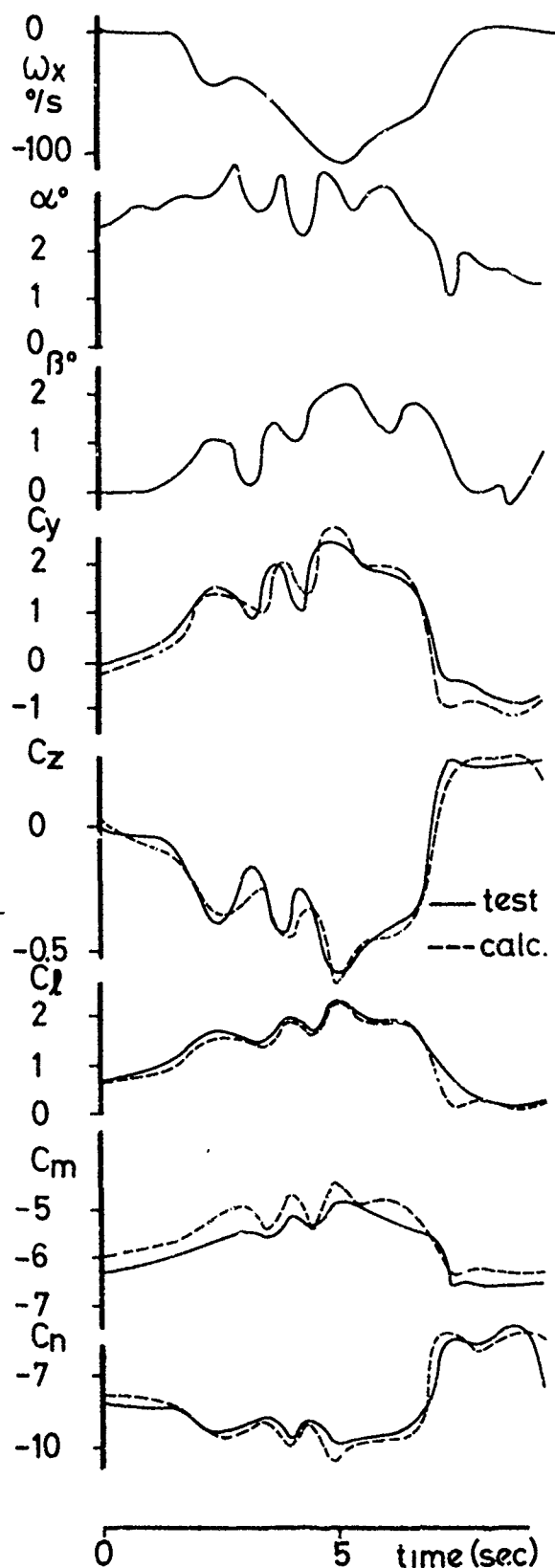


Fig. 3. MISSILE LOADS DURING A  $360^\circ$  ROLLING MANOEUVRE AT  $M=0.9$ ,  $n_z=2.5$

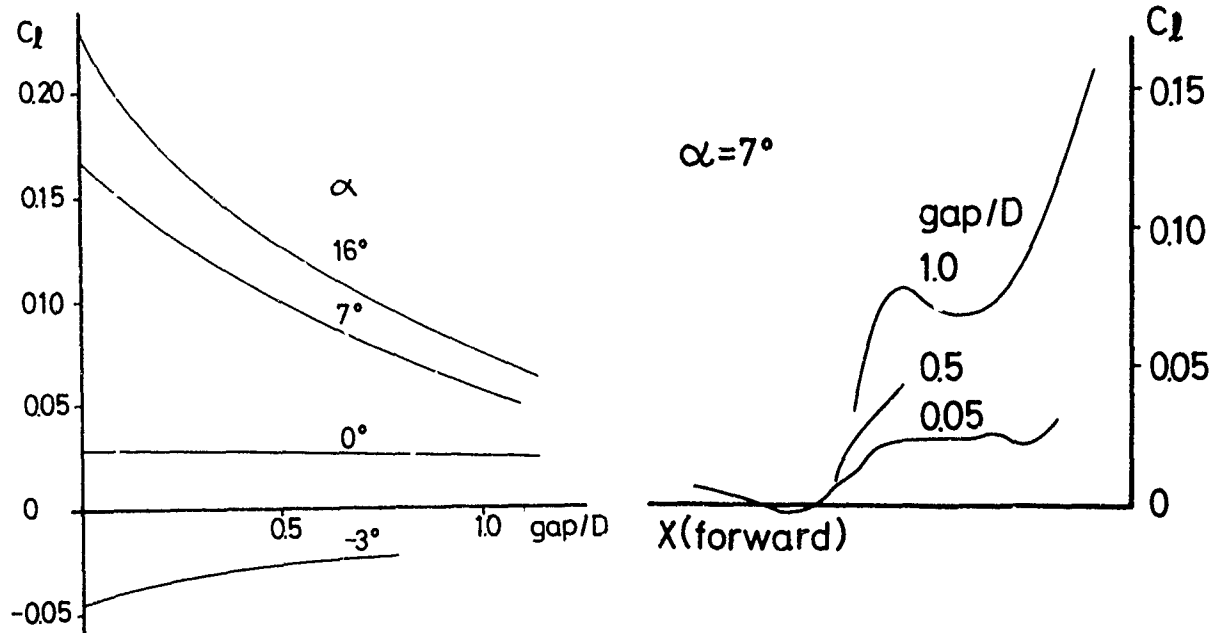


Fig. 4. EFFECT OF GAP/D ON MISSILE ROLLING MOMENT,  $M = 0.95$

Fig. 5. VARIATION OF MISSILE ROLLING MOMENT DURING MISSILE TRAVEL

well as accurate interference data for the very first part of the missile path, where interference effects are most important.

#### FIN LOADS

##### Comparison between windtunnel tests and flight tests

On slender delta wing configurations such as the Saab 35 Draken and 37 Viggen, appreciable angles of sideslip occur during fast rolling manoeuvres due to inertia and aerodynamic coupling. An important cause of aerodynamic coupling on these aircraft is the side load on the fin which is caused by different elevon angles on port and starboard elevon during a rolling manoeuvre.

On the Saab 35 Draken, fin loads were measured on a 1:18 scale model at Mach numbers .5 to 1.5 in the FFA 1 x 1 m<sup>2</sup> transonic-supersonic windtunnel by mounting the fin on a separate three-component strain gauge balance. Beside the usual parameters, angle of yaw, angle of attack and rudder angle, that define fin loading, the effect of aileron and elevator angle (superimposed to elevon angles) on fin loading was determined.

Fin load measurements in flight were executed in a manner very similar to the windtunnel tests, the normal fin attachments being replaced by measuring elements with strain gauges. After some initial calibration difficulties caused by the fairings carrying more load than was expected, good agreement was obtained with the windtunnel test results during steady sideslip and yawing oscillations.

The main aim of the flight test program was the measurement of fin loads during fast rolling manoeuvres as a check on fin design loads. Subsequently, an attempt was made to calculate the fin loads during such rolling manoeuvres with the help of the windtunnel data, using the test flight conditions as a basis. The fin loads, side force, bending moment and torsion moment, were determined from the windtunnel data for the flight test measured angle of sideslip at the corresponding Mach number, angle of attack and elevator angle. Corrections were then applied, for the effect of aileron angle and rudder angle, determined from windtunnel data, and for the effect of roll rate, determined by a simple calculation of the load distribution.

An example of the resulting comparison is shown in figure 6 for fin bending moment during a  $160^\circ$  roll at  $M = .93$ ,  $h = 6.5$  km,  $n_z = 3$ . A slight zero shift of the calculated value seems to be present, which is due to rudder angle. As the cause of this shift could not be determined it was preferred to use the measured values as read from the flight tests without arbitrary corrections, although these would improve the result.

The same degree of agreement that is shown in figure 6 was obtained in other cases. For each rolling manoeuvre for which fin loads were calculated, the maximum load for each manoeuvre was compared with the flight test value. In figure 7 the cumulative probability distribution of calculated fin load divided by flight test measured fin load has been plotted on normal distribution paper. The distribution is seen to be normal with a mean value of .96 and a standard deviation of .075, which must be considered satisfactory.

##### Sideslip during rolling manoeuvres

For both missile load and fin load calculations, flight test measured values of angle of attack and sideslip during the rolling manoeuvres have been used. It would of course be advantageous if the angle of attack and sideslip variation during rolling manoeuvres could also be predicted. Our experience shows, however, that these variations only can be computed when very accurate aerodynamic data are available. The degree of accuracy that is necessary has thus far not been achieved without the extensive use of flight test results.



The fastest way to obtain the necessary data is therefore often to measure angle of attack, sideslip etc during rolling manoeuvres in flight tests. The fact that flight tests must be used does to some degree decrease the advantage of being able to calculate missile loads and fin loads, but the saving of the time and expense involved in the flight test measurement of these loads is still considered to be a worthwhile advantage.

#### Reynolds number effects

The agreement between windtunnel and flight test results indicate that no significant Reynolds number effects are present on the missile and fin arrangements that are considered here, even though the Reynolds number, based on aircraft m.a.c., is below  $5 \times 10^6$  in the windtunnel tests and around  $65 \times 10^6$  in the flight tests. Missile configurations like the Rb 27 are usually not very sensitive to Reynolds number and delta wings like the Saab 35 Draken have been shown in ref 1 to exhibit good agreement between aerodynamic data from flight tests and from low Reynolds number windtunnel test.

Possible Reynolds number sensitive has certainly to be kept in mind, while on the other hand critical loading cases often occur at high speeds and low or medium altitudes, which entails moderate angles of attack and sideslip where Reynolds number effects may be neglectable.

#### AEROELASTIC EFFECTS ON LOAD DISTRIBUTION

The effects of airframe elasticity on the aerodynamics of the Saab 37 Viggen (figure 8) are appreciable, see ref 2, which makes aeroelastic corrections of the load distributions necessary.

The basis for the determination of all aerodynamic loading distributions is a windtunnel pressure measurement in approximately 280 points, distributed over the entire aircraft model. The correction for aeroelastic effects was computed, using a vortex lattice method for subsonic speeds and a panel method for supersonic speed as described in ref 2, in the following way.

Load distributions were calculated on the rigid aircraft for the required load factor, Mach number, altitude etc, including the necessary (rigid) control surface angles to trim the aircraft. Then the same procedure was repeated for the elastic aircraft, thus resulting in the same load factor but different angle of attack and control surface angles. The difference between these two load distributions, constituting a load distribution that, integrated, yields neither loads nor moments, was applied as a correction to the distribution derived from windtunnel data.

Although reductions of up to nearly 70 % in elevon effectiveness compared to the rigid aircraft do occur, the load distribution corrections are small due to the opposing effect of elevon angle and angle of attack. The smallness of the corrections causes simplifications in the computation model to be of less importance, thus rendering the most accurate result for the effort involved. An example of the correction of the load distribution on the main wing in a symmetric pull up at  $M = .9$ ,  $H = 0$  is shown in figure 9.

Wing and canard loads were checked in flight tests by strain gauge measurements. Main wing bending moment vs. load factor according to the prediction is compared in figure 10 with flight test results, confirming that the windtunnel pressure measurements with the computed aeroelastic corrections predict correct load distributions.

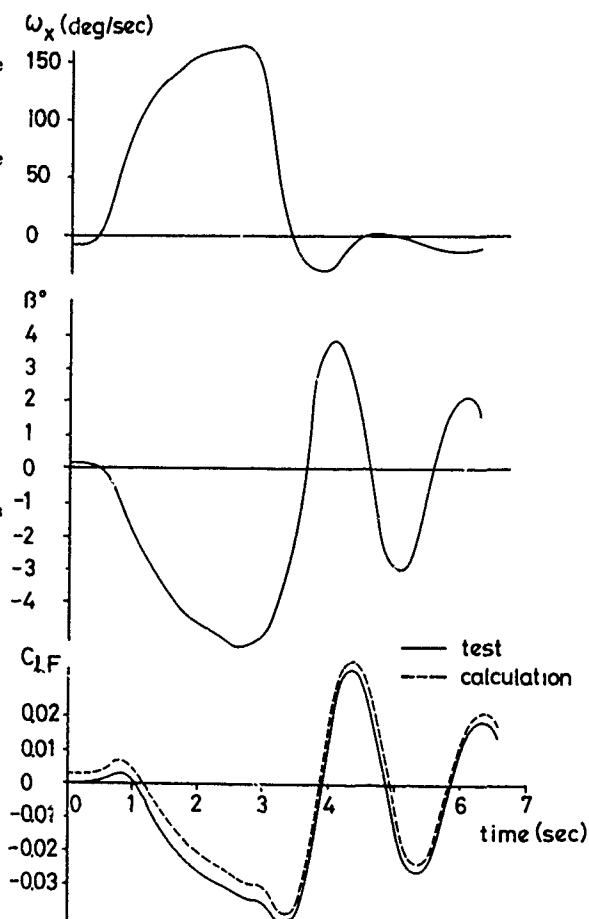


FIG 6. FIN BENDING MOMENT DURING A 360° ROLLING MANOEUVRE AT  $M=.93$ ,  $h=6.5$  km,  $n_z=3$

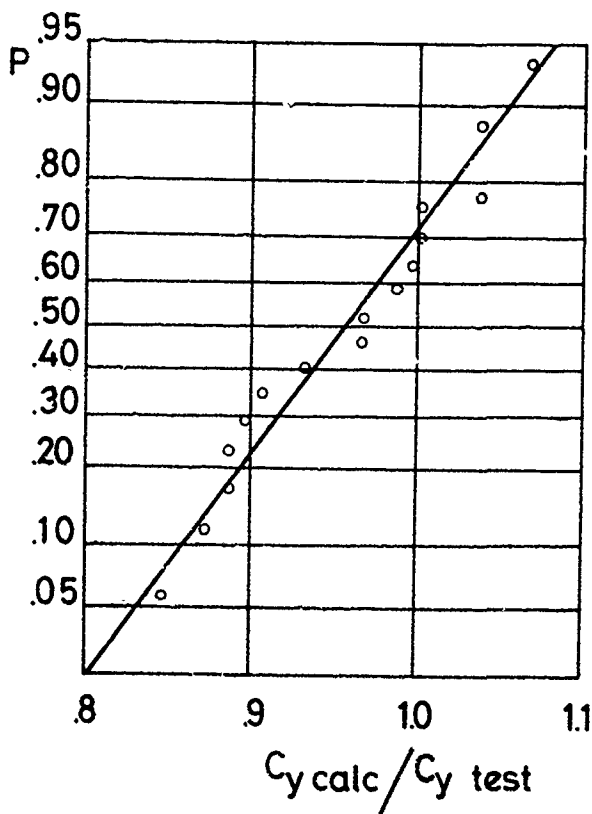


FIG 7. PROBABILITY DISTRIBUTION OF CALCULATED FIN LOAD DIVIDED BY FLIGHT TEST MEASURED FIN LOAD

## LOADS DUE TO ENCOUNTER WITH WING TIP VORTICES

An estimate of the vertical velocity of the air between the wing tip vortices of an aircraft shows that this velocity gives rise to a load factor increment on a second aircraft (same type at same speed) approximately equal to the preceding aircraft's load factor if the encounter is relatively symmetrical.

During dog fights, resulting load factors can thus be very high, which is confirmed by overload reports from Saab 35F Draken operation. Although high load factors do occur, the probability of their occurrence is sufficiently low. The probability of exceeding ultimate load factor due to vortex encounter is well below  $10^{-6}$  per flight hour.

Another simple analysis shows that the sidewash of one tip vortex may cause appreciable side load if the second aircraft's fin tip is near the vortex core long enough for a yawing oscillation to develop.

In order to check these calculations, a few test flights were conducted in which the leading aircraft flew at load factors 1, 2 and 3 while the second aircraft, at the same speed  $M = .8$  at  $H = 4$  km made slow and fast, downward and upward symmetrical passages

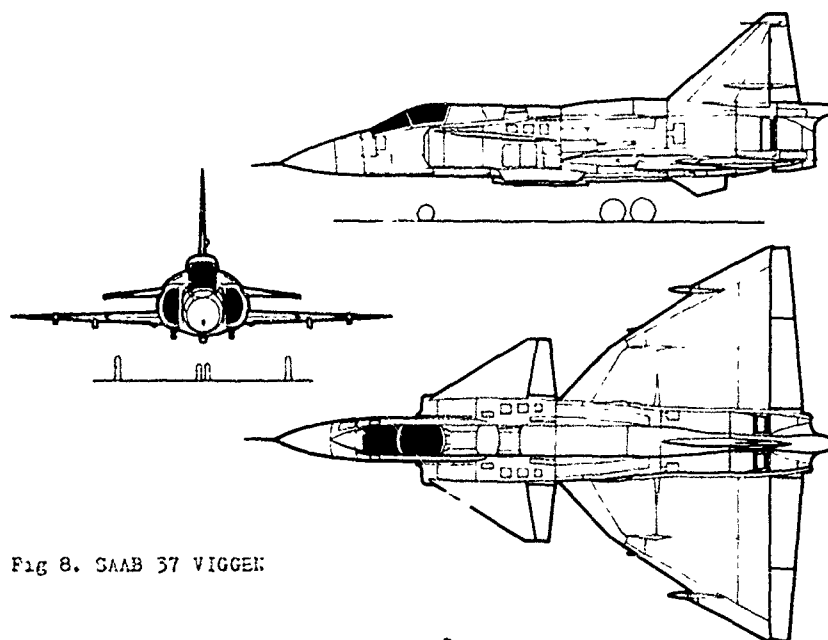


Fig 8. SAAB 37 VIGGEN

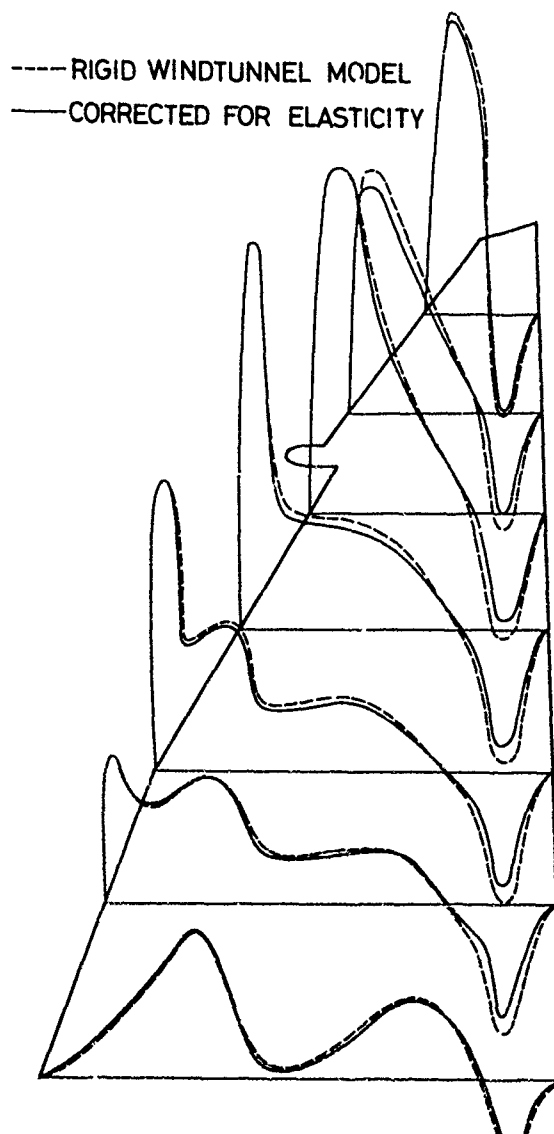
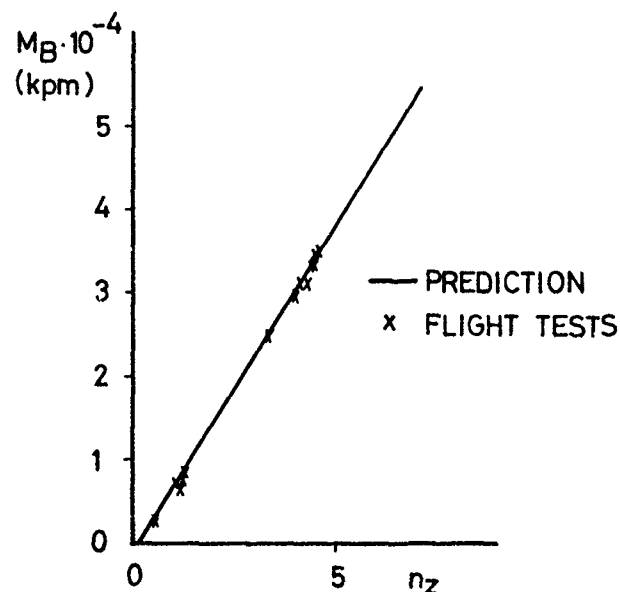


Fig 9. LOAD CORRECTIONS DUE TO AERO-ELASTIC EFFECTS, MAIN WING SAAB 37 VIGGEN

Fig 10. COMPARISON OF MAIN WING BENDING MOMENT, PREDICTION AND FLIGHT TEST RESULTS,  $M=.8-.9$ ,  $H=.5$  km

of the tip vortices and also tried to put the fin into one of the vortices.

The test results are shown in figures 11 and 12. The results show appreciable scatter because the leading aircraft's vortices were not visualized by smoke. The envelopes of the points for downward passage and upward passage in figure 11 show that the simple rule  $\Delta n_z \approx n_{z, \text{leading a/c}}$  is reasonably correct, although higher load factors do occur. The fast passages tend, naturally enough, to result in the highest load factors. The occasional very high load factor during a slow passage is due to the pilot keeping the aircraft in the vortex field until it, according to his report, was thrown out. The effect of the autopilot is, as could be expected for such high-gradient disturbances, negligible. The normal load factor increments in the fin-in-vortex case are, as could be expected, lower than during the symmetrical passages.

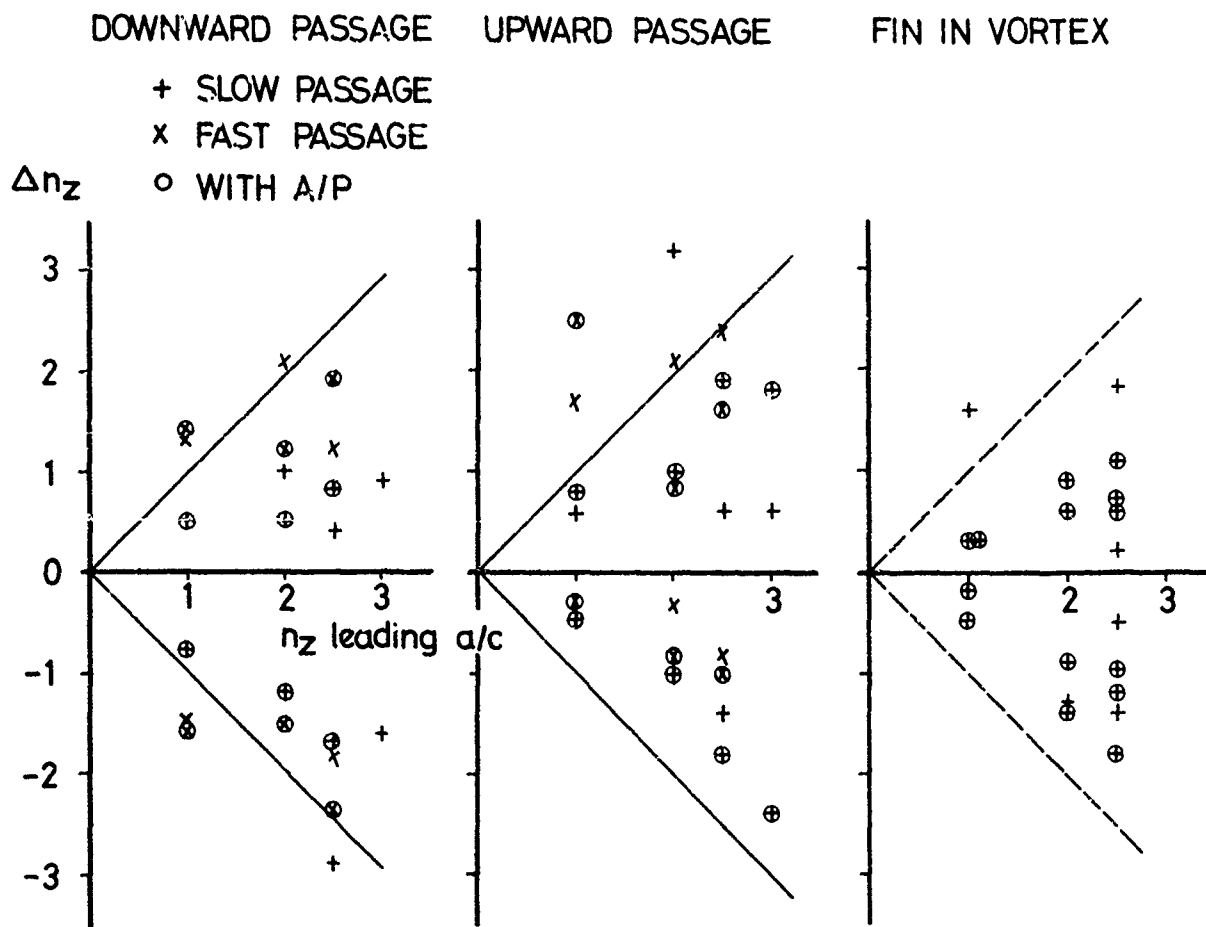


Fig 11. NORMAL LOAD FACTOR INCREMENT DUE TO VORTEX ENCOUNTER

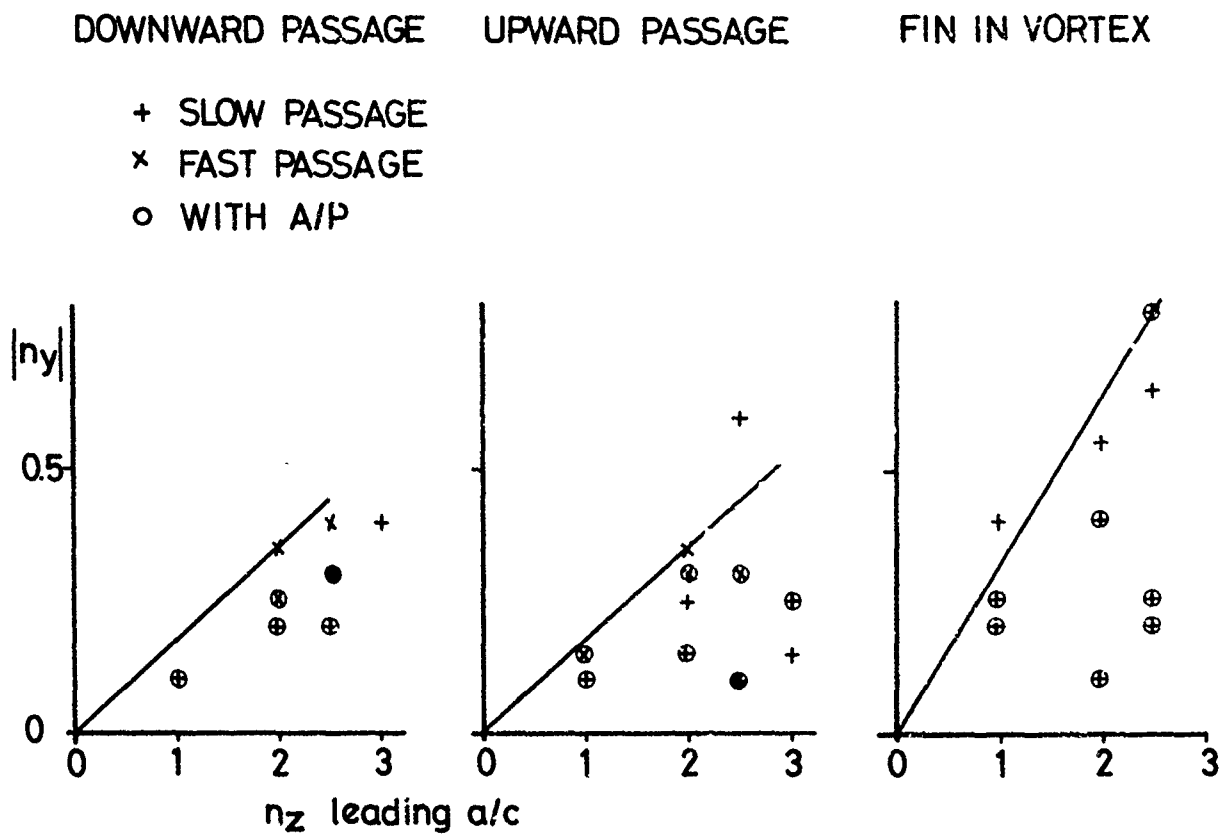


Fig 12. LATERAL LOAD FACTOR DUE TO VORTEX ENCOUNTER

Figure 12 shows moderate lateral load factors during the (attempted) symmetrical passages, but appreciably more vigorous disturbances in the fin-in-vortex case. In fact, the envelope gradient indicates that the fin-in-vortex case may result in damage to the second aircraft. During these preliminary flight tests the second aircraft's test equipment was, however, not suitable to determine the loads with sufficient accuracy. Therefore, preparations have been started for additional flight tests during which loads will be measured at the main fuselage joint, at the main fin bracket and at the external tank pylon.

#### REFERENCES

1. G. Strang, Flugzeugkennndaten der AJ37, Vergleich von Windkanal- und Flugversuchsergebnissen. DLR-Mitteilung 73-25
2. J. Kloos and L. Elmeland, Static aeroelastic effects on the aerodynamics of the Saab 37 Viggen aircraft, a comparison between calculations, windtunnel tests and flight tests. ICAS Paper 74-55

# WING-VORTEX LIFT AT HIGH ANGLES OF ATTACK

Richard P. White, Jr.\*  
Systems Research Laboratories, Inc.  
RASA Division  
1055 J. Clyde Morris Boulevard  
Newport News, Virginia 23602

## SUMMARY

The beneficial effects of attached vortex flows on the aerodynamic characteristics of swept tapered wings at high angles of attack is being investigated by theoretical and experimental techniques under a continuing research program.†

It has been determined from the results of the experimental investigations that the maximum lift generated by a low aspect ratio swept wing can be increased by 60 percent due to the suction and induced effects of attached vortex flows. The manner in which the vortex flows effect the performance characteristics of the lifting surface will be discussed in terms of the measured performance characteristics, surface pressure distribution and the results of flow visualization studies. On the basis of the results obtained during this research investigation methods of further enhancing the performance characteristics of low aspect ratio wings by means of controlled vortex flows will also be discussed briefly. In addition, the correlation of theoretical predictions based on a refined theoretical analysis technique, now under development, with experimental results will be presented.

## 1.0 INTRODUCTION

In the past, emphasis has been placed on maintaining the flow over lifting surfaces fully attached in order to achieve benefits in the performance and maneuvering characteristics of high performance aircraft. It has been found, however, that leading edge separation and the resulting nonlinear incremental lift contribution of concentrated vortices can, if properly generated and controlled, be of great benefit to the overall performance characteristics of a low aspect ratio lifting surface. Control of the concentrated vortex flow by devices such as snags, strakes, and canards has been found to stabilize the local flow, to increase the maximum lift coefficient, and to increase the subsonic and transonic maneuvering capabilities of the lifting surface. These type of concepts have been cited for the superior performance characteristics of the YF-16, YF-17 and Saab A37 aircraft.

Under the sponsorship of the Office of Naval Research (ONR), the RASA Division of Systems Research Laboratories, Inc. has been investigating the effects of vortex flow and vortex flow interactions on the aerodynamic performance characteristics of various types of lifting surface configurations. Initial efforts in this research were focused on the fundamental interaction mechanisms of concentrated vortex filaments with a finite wing (Ref. 1). In this initial study, a simplified potential flow analysis was developed to predict the incremental lift and drag contributions resulting from the interaction of a lifting surface with a concentrated vortex filament of specified strength, orientation and geometry. The basic theory, which included nonlinear effects, showed positive correlation only in predicting the trends of the available measurements of the incremental lift and drag resulting from wing/vortex interaction when snags, strakes, and canard devices were utilized with lifting surface configurations. On the basis of the results that were obtained during the initial effort, it was concluded that the efficiency of a vortex formed in the pressure field of a lifting surface in generating incremental lift was by far the best approach as the suction field generated by this type of wing/vortex interaction is far in excess of the suction field associated with a free vortex of the same strength interacting with a lifting surface.

Subsequently, an experimental research program has been carried out, in part to demonstrate and to verify that beneficial incremental lift can be obtained from a controlled vortex generated by and interacting with a lifting surface and also to determine the mechanism by which the favorable performance gains were achieved. In this program, which is summarized herein, studies were conducted using an F-4 type of wing planform with and without leading edge vortex-control devices including a strake, a snag and combinations thereof. Measurements were obtained of the pressure distributions and the total forces and moments on the lifting surface. Flow-visualization studies were also carried out using the helium-bubble technique of flow visualization.

In conjunction with the experimental program, effort has been directed toward developing a suitable analysis procedure for predicting the development of vortex flows, the

\*Division Manager

†The research effort is being sponsored by the Office of Naval Research (ONR) under Contract No. N00014-74-C-0091

interaction of these vortex flows with the lifting surface and their subsequent effects on the performance characteristics. Since the prediction technique, by necessity, must consider mixed flow regions of potential flow, separated flow and vortex induced and suction flow effects, its successful development, while a challenge, is showing great promise as a useful design tool.

This paper will describe the results of both the theoretical and experimental phases of the research program and will focus on the advancement of vortex-control technology as a step toward its successful development and wide-scale application on existing and future aircraft.

## 2.0 DESCRIPTION OF MODEL AND TEST

The model used in the program was a swept, tapered, semispan lifting surface similar in geometry to, and approximately a 1/4-scale version of the F-4 Phantom wing planform. While many different individual and combinations of leading edge vortex generating and control devices were tested in the program, this paper will deal primarily with the results that were obtained by the use of an outboard leading edge snag and an inboard strake both separately and in combination. A summary of the results obtained for all of the configurations that were tested can be found in References 2 and 3. Figure 1 shows a photograph of the model, with the strake attached, mounted in the wind tunnel as well as a planform sketch of the model showing the dimensions (in inches) of the basic wing and leading edge vortex generation devices. The basic wing planform is shown by the solid lines in the figure and the dashed lines show the removable leading edge snag at the outboard section of the wing, and the removable strake at the wing root.

The inboard strake modification consisted of a triangularly-shaped, leading edge extension which increased the planform area of the model by 6%. The strake was constructed of 1/4-inch thick metal plate with a wedge-shaped leading edge. The leading edge wedge of the strake had a 6.4° included angle, and was swept 75° with respect to the free stream. The strake also had the capability of being oriented with a relative angle of attack with respect to the chordplane of the wing.

The snag consisted of a 6% extension in the local chord starting at the 68% semispan location. The snag was tapered linearly from this point to the tip chord. The snag changed the profile of the wing slightly and the extended chord was faired smoothly to the normal wing profile. The snag increased the planform area of the wing by 0.7% and was similar in geometry to the wing snag found on the F-4 Phantom aircraft.

In order to measure the detailed pressure distributions on the semispan model, pressures were obtained from a total of 255 static pressure taps on one side of the airfoil. Pressure measurements were taken at both positive and negative angles of attack and the combined measurements were then used to compute the differential pressure coefficients and/or the loads.

Forces and moment on the semispan model were measured by a six-component, yoke-type balance located beneath the floor of the test section. The balance measurements were monitored on-line prior to off-line computer processing into the lift, drag and side force, and the pitch, roll, and yawing moment coefficients. The pitching moment was taken about an axis which passed through the quarter chord line of the mean aerodynamic chord, and the rolling and yawing moments were referenced to the wing root.

Flow visualization of the vortex flow in the vicinity of the model was provided by neutrally-buoyant helium bubbles which were released upstream of the model. The bubbles were illuminated by a collimated beam of light and were observed visually and photographed. A detailed description of the flow-visualization system and technique for its use can be found in Reference 4. Visualization of the surface flow was obtained by means of tufts attached to the wing at each of the pressure tap locations.

## 3.0 DISCUSSION OF TEST RESULTS

The experimental results that were obtained will be presented and discussed in two different groupings, first the measured performance results which are the integrated results of the surface pressure distributions, and second, the surface pressure distributions, which give some insight as to why the measured integrated performance characteristics were obtained, will be discussed in conjunction with the results of the flow visualization studies which provide an understanding as to how the wing vortex flows interact to generate the measured pressure distribution.

### 3.1 Performance Characteristics

The basic performance results which are additive across the wing span and are of general interest are the lift, drag and pitching moment which are presented for three of the configurations which were tested in Figures 2, 3 and 4 respectively. In this grouping of results the only configuration of interest for which data has not been presented is that for the basic wing with the snag. The reason that it has not been presented is that while the snag created significantly different loading distributions than those for the basic wing over the lifting surface below the stall angle, the integrated performance characteristics were almost identical to those of the basic wing. Above the stall angle of attack, the snag vortex separated from the wing surface and again the performance characteristics of the wing with the snag added were almost identical to those presented for the basic wing.

The addition of the beveled flat plate strake to the lifting surface, while not affecting the performance characteristics significantly below the onset of leading edge separation ( $\sim 13$  degrees) had a very large effect on the performance characteristics at higher angles of attack. As can be seen from the results that are presented in Figure 2, the effect of the strake and its vortex flow was to maintain the slope of the lift curve obtained at angles of attack below the inception of leading edge separation, up to an angle of attack of approximately 28 degrees. The lift coefficient at this angle of attack is approximately 1.45 times the maximum value that was measured for the basic wing. Since the lift coefficient has been normalized with the respect to the appropriate wing planform areas, this demonstrated increase in lifting capabilities is due to a difference in the aerodynamic flow characteristics of the two configuration. It is believed that the significant difference in the flow characteristics is due to the control obtained by the strong coupling of the strake and leading edge vortex.

The addition of the snag to the wing-strake configuration had a beneficial effect in the high angle of attack range in that it increased the lift at a given angle of attack and yielded a maximum lift coefficient that is approximately 1.6 times that of the basic wing configuration, which is 10 percent higher than that measured for the wing-strake configuration. It is believed that the reason the snag had a beneficial effect for this configuration and not for the basic wing, is that the interaction of the stronger leading edge vortex with the snag vortex strengthened and stabilized the leading edge vortex whereas for the basic wing the leading edge vortex had separated and burst in this angle of attack range and thus the favorable influence of the snag-vortex could not be realized.

The effect of the strake and snag on the drag characteristics of the basic lifting surface are shown in Figure 3. The results presented in this figure show that the increased lift obtained by the vortex flows also increased the drag, but not to the degree that would be expected based on a quadratic variation of induced drag with lift.

While the lift to drag ratio  $L/D$  for the various configurations are approximately the same at a given angle of attack in the angle of attack range of 20 to 35 degrees, the amount of lift obtainable with the controlled vortex configurations at a given value of aircraft drag (power) is higher than the basic wing. This benefit can be illustrated by using the data presented in Figures 1 and 2. As an example, at the same drag coefficient measured for the basic wing at an angle of attack of 28 degrees the lift coefficient of the strake-snag configuration is 1.36 times that of the basic wing. This result indicates that if an aircraft configuration has sufficient installed power for the basic aircraft configuration at an angle of attack of 28 degrees then, with the addition of a suitable strake and snag the aircraft would develop 36% more lift, for the same installed power. Since the turning radius is inversely proportional to the lift coefficient, the increased lift available would significantly decrease the turning radius. This performance benefit is obviously very desirable as regards the maneuverability characteristic of an aircraft.

The pitching moment coefficients about the M.A.C. for the various configurations are shown in Figure 4. As can be seen the vortex-generating surfaces have a very pronounced effect on the pitching moment about the M.A.C. For the basic wing the nose down pitching moment increases in a somewhat linear fashion until the angle of attack at which leading edge separation and the attendant formation of the leading edge vortex is reached at which point the rate of increase in the pitching moment with angle of attack becomes much less. As the angle of attack is increased further, however, the rate of increase of pitching moment with angle of attack becomes larger until it becomes approximately equal to that obtained below the initiation of the leading edge separation. Since the leading edge vortex is formed when leading edge separation occurs, it is believed that the break in the pitching moment curve of the basic wing is caused by the formation of the leading edge vortex. As the angle of attack of the lifting surface is increased further the effect of the weak leading edge vortex diminished due to the separation from the wing surface and is completely gone at an angle of attack of approximately 22 degrees.

With the strake, and the strake and snag added to the basic wing planform the trend of the pitching moment with angle of attack is approximately the same below an angle of attack of 13 degrees as that of the basic wing. Above 13 degrees, however, the trends of the pitching moment with increasing angle of attack is opposite to that of the basic wing. It is believed that the reason for the change in the pitching moment characteristics is that when the leading edge vortex is formed, its interaction with the strake vortex causes it to be strengthened and stabilized and thus it continues to grow in strength as the angle of attack is increased instead of separating from the lifting surface. Since the leading edge vortex is formed over the inner half of the span, ahead of the M.A.C., it creates a nose up pitching moment and because of its increased strength, it dominates the pitching moment. For example, at 30 degrees angle of attack, the data indicates that the pitching moment generated by the leading edge vortex is 1.5 times greater than that generated by the entire lifting surface. It is noted that with the snag added to the strake configuration the leading edge vortex moves slightly aft and the pitching moment variation is not as pronounced as it was for the just wing-strake configuration.

Even though the pitching moment is destabilizing in the post-leading edge stall region, its maximum magnitude is less than one-third of that which was measured for the basic wing and should therefore be controllable with a properly placed horizontal tail surface. The proper placement of the horizontal tail surface, however, may be significantly different for this configuration than it would be for the basic wing because of the vortex induced flow field on the horizontal tail due to the vortex wake of the wing. It is of interest to note that since the vortex lift seems to dominate the pitching moment characteristics of the lifting surface, that with the use of proper wing planform tailoring to obtain

an optimum vortex placement, it might be possible to maintain a constant pitching moment at all angles of attack in the post stall region which would be highly advantageous as regards the stability and control characteristics of the aircraft.

In summarizing the performance results that have been measured for a low aspect ratio lifting surface, the addition of a strake and snag to the basic wing planform, a significant increase in the maximum  $C_L$  was obtained with a less than anticipated increase in the drag coefficient. Since this increase in the lift is believed to be associated with a strong leading edge vortex, the pitching moment about the M.A.C. while becoming destabilizing is significantly less in magnitude than that of the basic wing and should be easily overcome by a properly placed horizontal stabilizer. It is concluded that the reason for the noted gains in the performance characteristics is probably due to the fact that the vortices generated by these additional surfaces seem to strengthen and stabilize the leading edge vortex and the complex mutually interacting vortex flow field tends to control and stabilize the flow field of the lifting surface above the stall angle of attack.

### 3.2 Analysis of the Wing-Vortex Flow Characteristics

The manner by which the attached vortices control the flow over the wing surface and thus the lift at angles of attack below and above the angle of attack at which leading edge separation occurs can be deduced from the measured pressure distribution and associated visualized external and surface flows. The surface pressure distributions will therefore be compared for the various configurations at an angle of attack at which the flow is fully attached (13.1 degrees) and at an angle of attack near that at which the maximum lift was obtained with the modified wing configurations (27.7 degrees). At this high angle of attack the majority of the lifting surface is operating in separated flow.

Figure 5 presents the spanwise distributions of the surface pressures along constant chord lines for the three configurations of interest at an angle of attack of 13.1 degrees. It is interesting to note that while the total lift generated by each configuration is almost identical to the other at this angle of attack (Figure 2) it can be seen that the spanwise loading distributions are significantly different for the three configurations. As will be discussed it can be shown that these differences in the loading distributions are caused by the vortex flows that are generated by the lifting surface and the attached vortex generators.

In analyzing the effect of the attached vortex flows on the pressure distribution over the surface of the wing, both the induced and the suction effect of the vortex flows must be considered. While the induced effect is generally generated at spacial locations greater than the core diameter, the vortex suction effect occurs at spacial locations associated with dimensions on the order of the vortex core diameter.

The sparwise pressure distributions presented in Figure 5 for the basic wing at an angle of attack at 13.1 degrees indicate that there is the semblance of a leading edge vortex which, after its formation as a coordinated vortex along the 5% chord line, trails outward and aft and leaves the trailing edge near the wing tip. (The path of the centerline of the vortex can be traced by the peaks in the pressure distribution). The pressure distributions also indicate that a small secondary leading edge vortex is formed at the leading edge at about 75% span location. This secondary vortex, which is probably formed by the induced effect of the primary leading edge vortex as it turns in the chordwise direction, is quickly separated from the surface of the wing by the induced upwash of the primary vortex flow. Due to the broadness of the peaks in the pressure distribution and the rather low value of the suction pressure of the main leading edge vortex, it is obvious that the leading edge vortex at this angle of attack is rather weak and diffuse. This conclusion is supported by the external flow visualization pictures that were taken using helium bubbles as only a slight large diameter swirling flow, that might be associated with a leading edge vortex, was indicated in the pictures. The induced effect of the leading edge vortex, although relatively weak at this angle of attack, tended to reduce the angle of attack over the inboard sections of the lifting surface which in turn reduced the chordwise gradient of potential lift in this region.

The pressure distribution for the configuration with the strake added while showing some overall similarity to those obtained with the basic lifting surface, are significantly different in detail. The effect of the strake vortex, while small, is clearly evident near the wing root. By tracing the peak pressures associated with the strake vortex it can be deduced that the path of the strake vortex over the surface of the lifting surface is basically in the chordwise direction. Since the magnitude of the pressure peak associated with the strake vortex decreases as it traverses the chord indicates that the vortex is moving away from the lifting surface as it moves across the chord. Both of these conclusions regarding the path of the strake vortex are shown to be valid by the photographs presented in Figure 6. The photographs of the strake vortex, visualized by helium filled bubbles, show that the strake vortex goes directly across and away from the wing surface as it moves downstream. The induced effect of the strake vortex on the lifting surface, while relatively weak, is such as to create a spanwise loading gradient near the location at which the leading edge vortex has its initial formation. The induced effect of the strengthened leading edge vortex tends to reduce the potential lift over the inboard sections of the lifting surface as it did to a lesser degree for the basic wing planform. In addition, the upwash induced by the leading edge vortex over the outboard section of the wing seems to have separated the flow as the surface pressures are less than they were for the basic wing in this region. Due to the induced and suction effect of the strake vortex and the stabilized flow over the inboard sections of the lifting surface, the leading edge vortex not only becomes slightly stronger but much more concentrated and thus



the suction peak it creates over the outboard sections of the lifting surface, while narrower, is larger in magnitude. It can also be seen by comparing the pressure distributions of the wing with and without the strake, that once the leading edge vortex of the wing strake configuration becomes a "semi-free" vortex it is turned in the free stream direction much more rapidly than it was for the basic wing configuration thus creating a rather effective aerodynamic wing fence across the chord at approximately the 80% span location.

The surface flow for this configuration as depicted by tufts is shown in Figure 7. The centerline of the paths of both the strake and leading edge vortices have been indicated on those photographs. As indicated by the tufts the flow inbetween the streamwise positions of the two vortices is in the spanwise direction indicating that potential flow and lift are being developed in this area. While there is some effect of vortex induced flow inboard of the strake vortex location, the flow is basically potential in nature over that region as well. Outboard of the leading edge vortex as it crosses the chord, however, it is noted that the flow is basically in the spanwise direction. A closer look at the tufts along the leading edge outboard of the leading edge vortex indicated that this area is stalled and the flow is separated. It is believed that the large induced effect of the leading edge vortex, which creates an upwash in this region, is responsible for the flow separation. Once the flow over the surface of the wing has been separated, the induced velocity of the leading edge vortex creates the spanwise flow in the low velocity region of the separated flow. While the pressure distributions presented for the wing with both the strake and outboard snag added is considerably different than those of the other configurations, the same total lift is obtained. The pressure peaks associated with the strake, leading edge, and snag vortex are clearly evident in the distributions that are presented in Figure 5. As can be seen, the characteristics of the strake vortex remains about the same as they were for the previous configuration and the leading edge vortex has been weakened and moved inboard due to its interaction with the rather strong snag vortex. Since the strake vortex is rather far removed from either the leading edge or snag vortex, there is little evidence of interacting effects of the strake vortex with the outboard vortices. In fact the pressure distributions for this configuration, except for the independent effects of the strake vortex are almost identical to those of the basic wing with just the snag added. On the basis of the pressure distributions obtained for the various configurations at a relatively low angle of attack, it is concluded that while the influence of the rather weak vortex flows did not alter the total lift that was generated, they did alter significantly the loadings distributions.

At angles of attack much greater than the angle at which the basic wing stalls, the influence of the vortex flows on the total lift that is generated is much more significant as is shown by the pressure distributions presented in Figure 8. The pressure distributions shown for the basic wing indicate that except for a weak pressure peak due to the leading edge vortex near the wing root, the entire lifting surface is completely stalled as indicated by pressure coefficients of near unity. In contrast, the pressure distributions obtained for the wing with the strake added indicate that large pressure peaks are obtained. It can also be seen that not only has the peak pressure associated with the leading edge vortex increased but the position of the vortex has moved inward. It is believed that both of these effects are due to the interaction of the two vortices and the strengthening of the leading edge vortex by the loading gradients generated by the strake vortex.

As indicated by the pressure distribution, the strake vortex has an entirely different path over the surface of the wing at 27.7 degrees than it did at 13.1 degrees angle of attack. This difference in the paths of the strake vortex can be seen by comparing the visualized strake vortices in Figure 9 with those in Figure 6. While the initial rate of movement away from the surface of the strake vortex is greater at 27.7 degrees than it was at 13.1 degrees, the strong induced effect of the leading vortex moves the strake vortex back towards the surface of the wing as well as outward along the 75% chordline. As shown in Figure 10, the leading edge vortex moves out along the leading edge as well as away from the lifting surface due to the induced effect of the strake vortex until it bursts. After bursting the leading edge vortex becomes turbulent and turns in the streamwise direction. Although not shown in these pictures the strake and burst leading edge vortex could be seen to mix near the trailing edge of the lifting surface near the 70% span location as they both moved in the downstream direction.

The tuft picture visualizing the surface flow for this configuration at an angle of attack at 27.7 degrees is shown in Figure 11. The small areas of potential flow generated by the induced effect of the leading edge and strake vortices can be seen in the picture. It can also be seen that the strong induced effect of the leading edge vortex as it moves over the chord of the wing has completely stalled the tip region and generates a strong spanwise flow in the separated flow region over the mid span portion of the lifting surface between the two vortices.

The pressure distributions presented for the wing with the strake and snag added indicate that at this high angle of attack the primary effects of the snag vortex have disappeared but the effects of the strake and leading edge vortices have remained about the same as they were for the wing-strake configuration.

It is believed that the pressure distribution presented for the various configuration at 27.7 degrees clearly indicates the strong influence of the vortex flows on the lift that is generated by the wing. As will be verified later in this paper, the majority of additional lift obtained from the vortices is due to the low pressures within the core of

the vortices and not due to their induced effects on the lifting surface. This conclusion was drawn as at all locations outside of the regions of the influence of the vortex flow the wing is completely stalled.

During the tests the conventional leading edge snag having an airfoil section was replaced with a sharp edge plate to determine its effect on the loading distributories over the tip region. Flow pictures taken in the tip region for this configuration are shown in Figure 12. As can be seen from these flow pictures, a concentrated leading edge vortex is formed at a relatively low angle of attack over the flat plate snag and that the flow on the wing surface behind the snag vortex is unseparated. As the angle of attack was increased the leading edge and turbulent vortex at the leading edge discontinuity get stronger but at an angle of attack of 27.7 degrees the vortices no longer exist because of complete flow separation caused by the sharp leading edge on the snag. On the basis of what was observed for this configuration it was deduced that a sharp edge separator plate along the leading edge of the wing might generate a leading edge vortex at angles of attack lower than those at which the leading edge of the contoured airfoil separated. If this could be accomplished, it was reasoned that the lift at low angles of attack should be increased due to the vortex that would be generated by the separator plate. To test this hypothesis a 5% chord sharp leading edge separator plate was attached to the wing-strake configuration and the performance characteristics of this configuration was determined over a range of angle of attack. The lift coefficient as a function of angle of attack for this configuration, is compared to that obtained for wing with just the strake in Figure 13. It can be seen from the data presented in this figure, that in the angle of attack range of 5 to 24 degrees an increase in the lift coefficient was obtained with the maximum increase being obtained at approximately 16 degrees. While there was an associated increase in drag, it is believed that the increased lift can be obtained without the attendant drag increase by using a small boundary layer trip instead of the separator plate to initiate the formation of the leading edge vortex.

#### 4.0 BRIEF OUTLINE OF THE THEORETICAL PREDICTION TECHNIQUE

The low aspect ratio swept wing-vortex system that is modeled allows for six vortices over the surface of the wing and because of the range of angles of attack of interest, the analysis considers mixed potential and separated-flows over the surface. The phenomenon of "vortex bursting" is included in the analysis as is the prediction of the important effects of the suction pressures generated by the vortices over the wing surface. The strengths of the various vortices that are formed by the lifting surface as well as their force free positions with respect to the wing are obtained by an iterative procedure. In general, the calculation of wing loads in the presence of vortices generated by the lifting surface (e.g. strake vortex-leading edge vortex, tip vortex, etc.) involves the computations of the following lift components:

1. Potential flow lift including the induced effects of the vortices
2. Lift due to separated flow
- and 3. Vortex suction lift.

The definition of each of these lift components and the general procedures followed for their determination are briefly described below:

1. Potential flow lift is the lift generated by the wing where the flow remains attached even at relatively high angles of attack due to the induced effect of the vortices. A modified potential flow theory (Surface Lattice-Doublet Method) is utilized for the computation of this component of the lift. Since the areas of potential flow vary from one iteration to another, the computation of the potential lift must be part of the iterative procedure.

2. Lift due to separated flow is the component of the lift where the flow is fully separated from the upper surface of the wing. The program computes the regions of the separated flow on the wing surface by calculating the total aerodynamic angle of attack at each control point and testing to determine if the local stall angle has been exceeded. This is accomplished through the following relationship:

$$U \sin \alpha_a = U \sin \alpha - \sum_p \sum_k B_{mnk}^p \Gamma_k^p$$

Where  $U$ , is free-stream velocity

$\alpha_a$ , is local aerodynamic angle

$\alpha$ , is geometric angle

$B_{mnk}^p$ , is the influence coefficient of the  $k^{\text{th}}$  element of  $p^{\text{th}}$  vortex at the control point  $mn$

$\Gamma_k^p$ , is the strength  $k^{\text{th}}$  element of the  $p^{\text{th}}$  vortex.

If  $\alpha_a$  exceeds the specified stall angle at any control point, the box corresponding to that control point is considered separated and  $\Gamma_k^p$  corresponding to that control box is taken to be zero. The pressure coefficient at the separated points are then determined

by utilizing empirically obtained cross-flow force coefficients for a three-dimensional lifting surface.

It should be noted that, at the start of the computation, the strength of the vortices ( $\Gamma$ ) are unknown quantities and therefore an iterative procedure must be followed for the determination of the separated flow boundaries utilizing the above relation.

3. Suction lift is the component of the lift generated by the vortices when they are in the proximity of the wing surface. The suction effect is created by two different flows within the vortex core. The first is the suction created by the axial flow and the second is that suction required to balance the centrifugal forces developed by the swirling flow.

The amount of suction lift achieved is very dependent on the axial flow in the core of the vortex as well as the strength of the vortex. Since the magnitude of the axial flow in the vortex core is very sensitive to the distance of the vortices from the wing surface, it is necessary to include the thickness and curvature of the airfoil for the adequate determination of the suction lift. In the present formulation the calculation of the suction lift is the only lift component in which the finite thickness effects of the lifting surface have been included.

As noted previously, for the correct prediction of the wing loading distribution in the presence of vortex flows, it is essential that the force free positions of the vortices with respect to the lifting surface be determined. In the present analysis control points, in addition to those on the lifting surface, are located along the length of the vortex. At each of these control points all the following components of velocities are predicted:

- a. the velocities induced by the wing loads
- b. the self-induced velocities due to vortex curvature
- c. the axial velocity in the core of the vortex, and
- d. the free-stream velocity component

Since a force-free vortex can only remain in a stationary position when the total flow is along its axis, this criterion is utilized to determine when the vortex has reached a stationary position during the iteration procedure. As might be expected, it was found that the axial velocity in the core of the vortex was of primary importance for the determination of the force-free positions of the vortices, and therefore it must be computed accurately. Because of this requirement it is believed important, because of its effect on the axial velocity, that the radial component of velocity in the vortex core be included in the improved version of the analysis.

As previously noted, the effects of bursting of the vortex is included in the analysis since it greatly affects the vortex suction characteristics. A simple criterion is used in the present analysis to account for this effect, that is, it is assumed that the vortex bursts when the core velocity is in a stagnation condition with the free stream. While this simple criterion seems to agree reasonably well with experimental observations of vortex bursting and also with the bursting of the leading edge and tip vortex, it is believed that a more refined representation of vortex bursting based on core stagnation or finite transition will yield more realistic vortex bursting criteria.

## 5.0 CORRELATION OF PREDICTED AND MEASURED RESULTS

The analysis in its present form was utilized to predict the performance characteristics of the wing strake configuration at three angles of attack: 13.1, 19.4, 27.7 degrees. A comparison of the predicted and measured  $C_L$ 's at these three angles of attack are presented in Figure 14. The various components of the lift at each angle of attack are indicated in the Figure. At 13.1 degrees it can be seen that, as might be expected, the lift is wholly potential in nature and is predicted very well by the lattice-doublet potential flow analysis. At an angle of attack of 27.7 degrees the total predicted lift agrees very well with the measured results and of the total lift, approximately 2/3 is due to cross flow and the other third is due to vortex suction. While the cross flow and potential lift have been lumped together, over 90% of this lift was that due to separated cross-flow. At an angle of attack of 19.4 degrees, it can be seen that the various components of lift are about equal in magnitude and that the total predicted lift is approximately 8% less than the measured lift. It is in this angle of attack range in which there is a strong interaction of the mixed flows that the analysis procedure is somewhat lacking at the present time.

A more demanding comparison is between the predicted and measured pressure distributions over the surface of the wing. Comparison of the pressure distributions along 5 different constant chordlines at an angle of attack of 19.4 degrees are presented in Figure 15. As can be seen the correlation between the predicted and measured results is rather good although the areas of potential lift and the transition to separated flow are not being predicted as accurately as desired. It is believed that the reason for this underestimation of the potential lift is that the number of control points within the area of influence of the vortex was not sufficient and therefore the separated flow criterion was applied over too large an area in the areas of the vortex flows.

Figure 16 shows the areas over which the wing flow is predicted to be separated as well as the predicted paths of the vortices. It is noted that both of these predicted characteristics are close to those that were measured.

It is believed that the correlation that was obtained between the predicted and measured performance characteristics and pressure distributions indicates that with the noted improvements in the theoretical representation, a relatively accurate, practical, and useful prediction technique will be available for use for optimizing the beneficial effects of attached vortex flows by wing planform tailoring.

#### 5.0 CONCLUDING REMARKS

It is believed, on the basis of the results of the experimental investigations, that the potential of attached vortex flows in creating beneficial aerodynamic performance benefits has been conclusively demonstrated for low aspect ratio swept wings operating in the moderate to high angle-of-attack range. It remains to be evaluated, however, what effects these vortex flows, generated by the primary lifting surface, might have on the stability and control characteristics of the entire aircraft because of their induced effects on the tail surfaces. In addition, the effects of compressibility on the attached vortex flow remains to be evaluated before they can be utilized with confidence to improve the transonic maneuvering capabilities of high performance aircraft.

While the experimental investigations have demonstrated the potential of attached vortex flows, they did not determine the manner by which the wing-vortex flow characteristics can be optimized. It is suggested that seeking this optimum by wing planform tailoring can be more effectively accomplished by the use of a reliable prediction technique rather than by means of an experimental approach. It is believed that the prediction technique that has been discussed herein, once the noted improvements have been made, can be effectively utilized to seek the desired optimum for a given aircraft configuration.

#### 6.0 REFERENCES

1. White, R. P., Jr. and Zalay, A. D., "High Lift Generation by the Use of Vortices", ONR Contract No. N00014-74-C-0091, RASA/SRL Report No. 74-12, December 1974
2. White, R. P., Jr. and Balcerak, John C., "An Experimental Investigation of Vortex Flow Control for High Lift Generation", ONR Contract No. N00014-74-C-0091, RASA/SRL Report No. 74-12, Interim Report, December 1975 (AD-A027524)
3. Gangwani, Santu T. and Balcerak, J. C., "A Theoretical and Experimental Investigation of Vortex Flow Control for High Lift Generation", ONR Contract No. N00014-74-C-0091, RASA/SRL Report No. 74-12, Final Report to be Published
4. Hale, R. W., Tan, P., Stowell, R. C. and Ordway, D. E., "Development of an Integrated System for Flow Visualization in Air Using Neutrally-Buoyant Bubbles", ONR Contract No. N00014-74-C-0934, SAL-RR-7107, December 1971

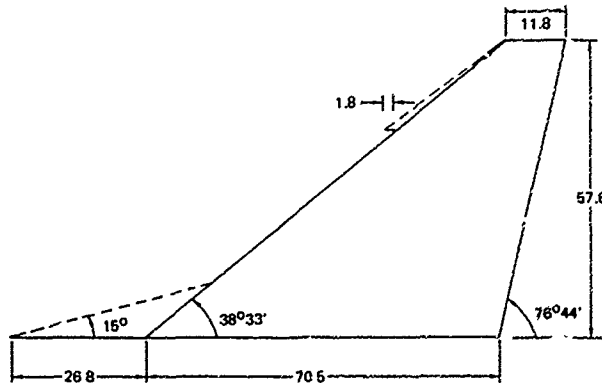


Figure 1. Wind Tunnel Model.

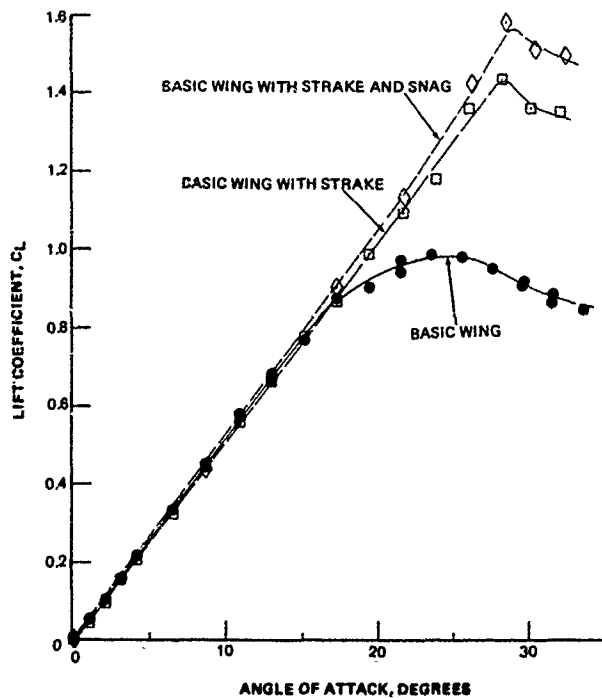


Figure 2. Lift Coefficient vs. Angle of Attack.

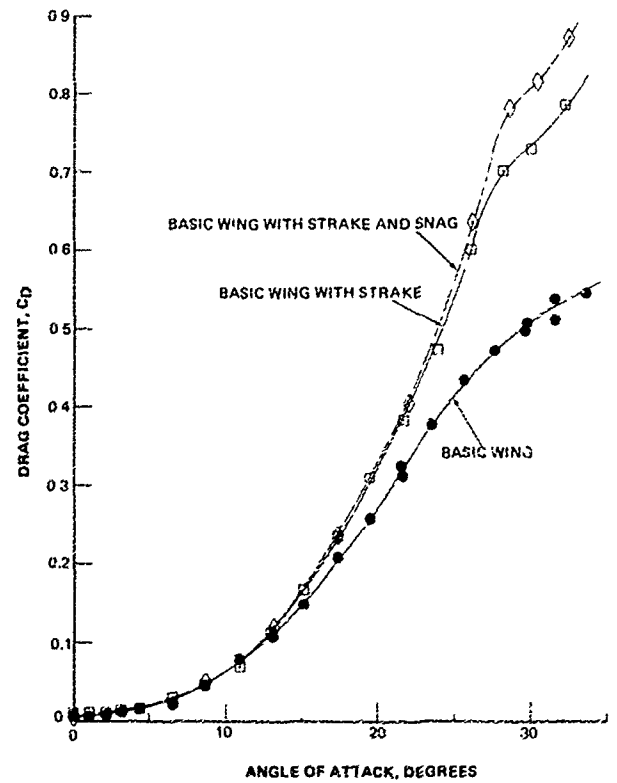


Figure 3. Drag Coefficient vs. Angle of Attack.

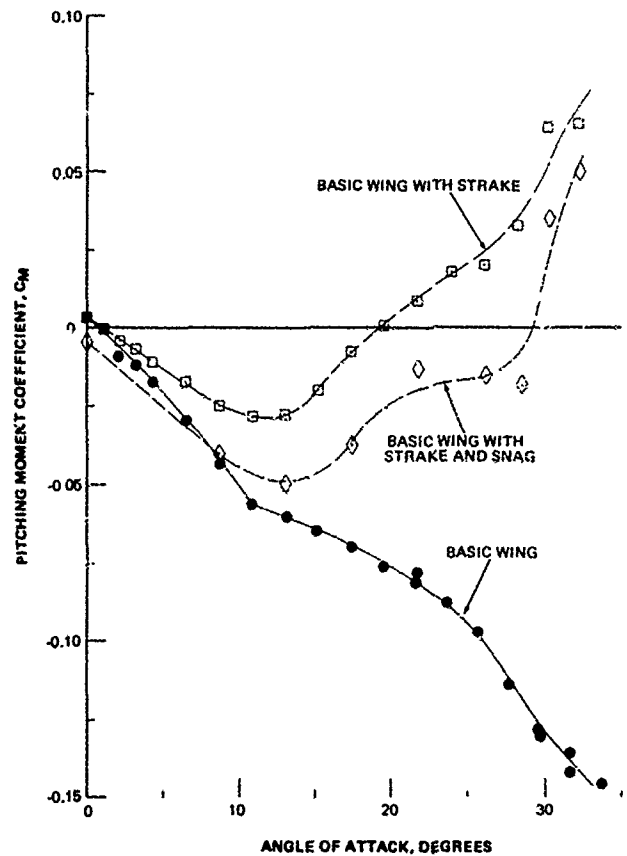
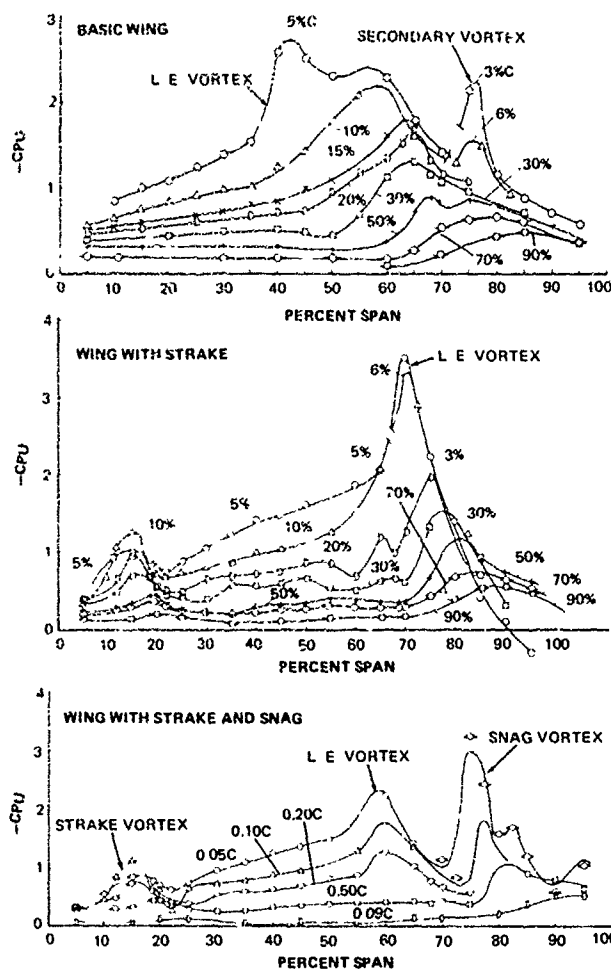
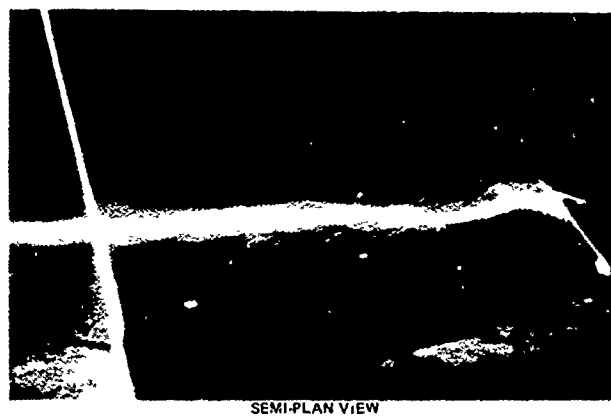


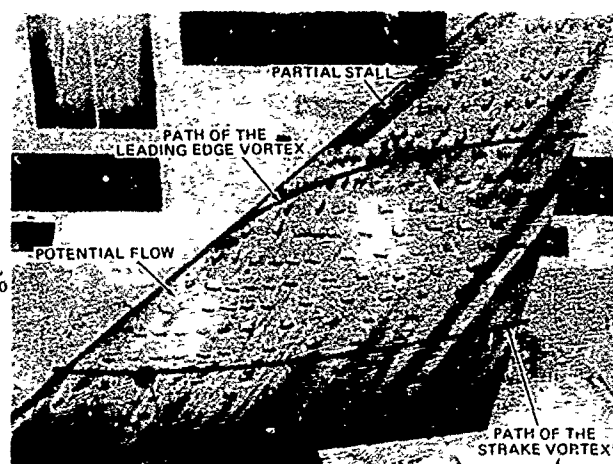
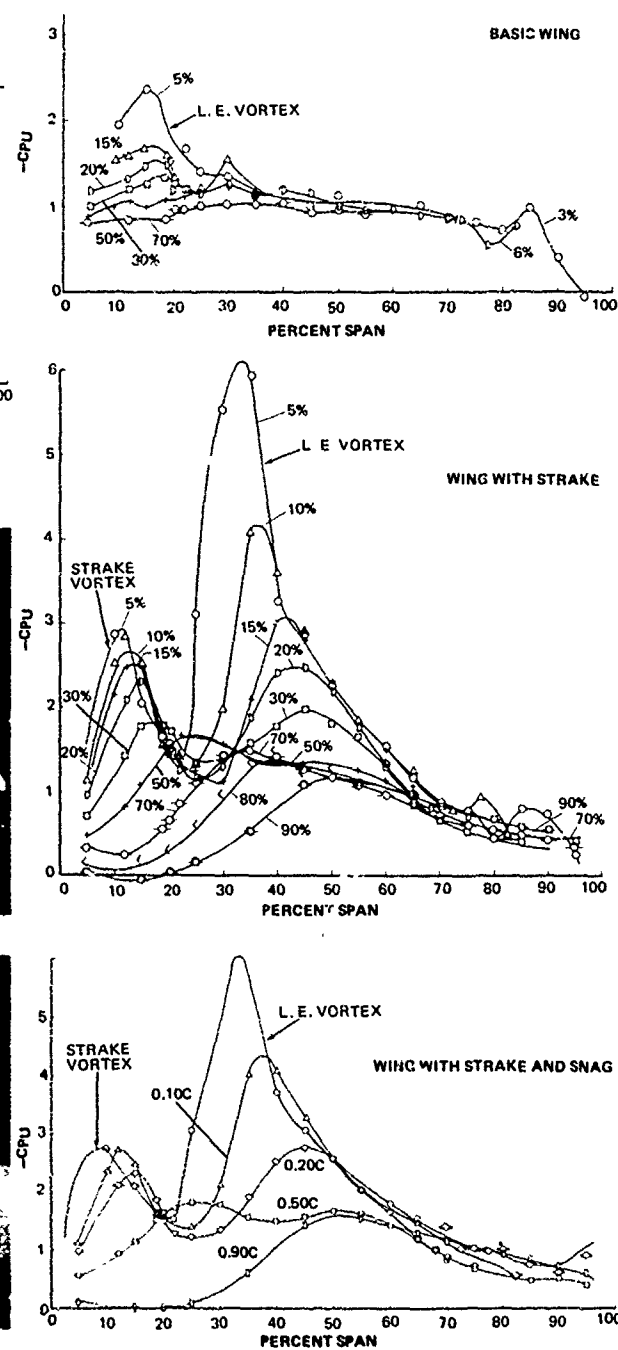
Figure 4. Pitching Moment Coefficient vs. Angle of Attack.

Figure 5. Upper Surface Pressure Distributions  $\alpha = 13.1$  Degrees.

SEMI-PLAN VIEW



LOOKING TOWARD ROOT

Figure 6. Strake Vortex,  $\alpha = 13.1$  Degrees.Figure 7. Surface Flow for Wing-Strake Configuration,  $\alpha = 13.1$  Degrees.Figure 8. Upper Surface Pressure Distributions,  $\alpha = 27.7$  Degrees.

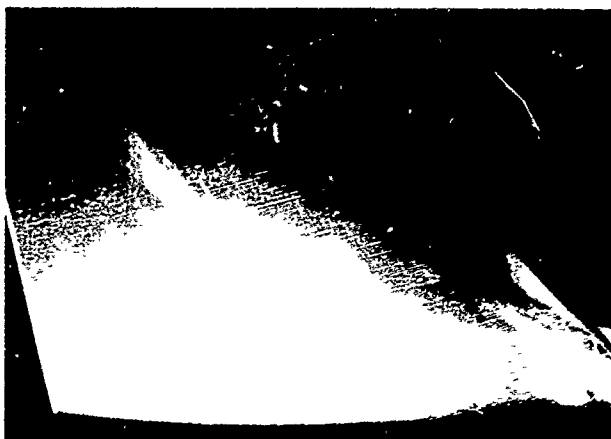


Figure 9. Strake Vortex  $\alpha = 27.7$  Degrees

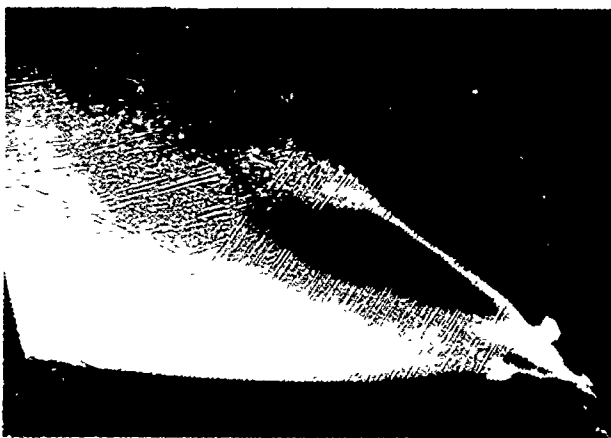
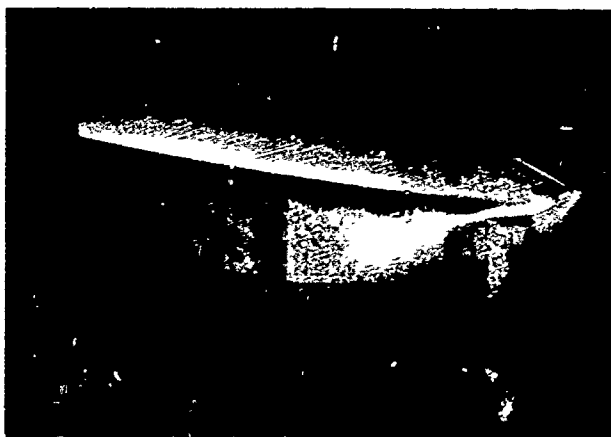


Figure 10. Leading Edge Vortex  $\alpha = 27.7$  Degrees.

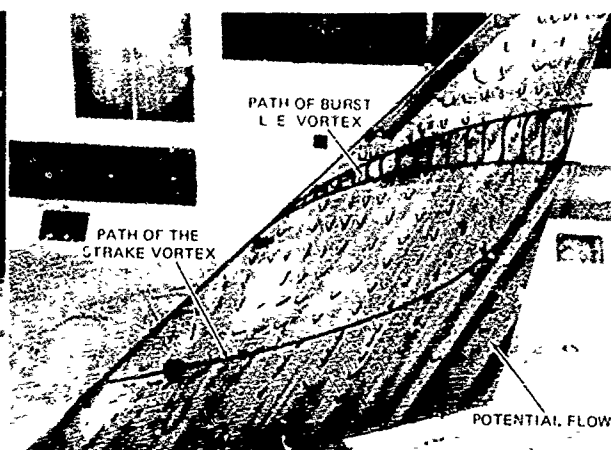


Figure 11 Surface Flow for Wing-Strake Configuration  $\alpha = 27.7$  Degrees

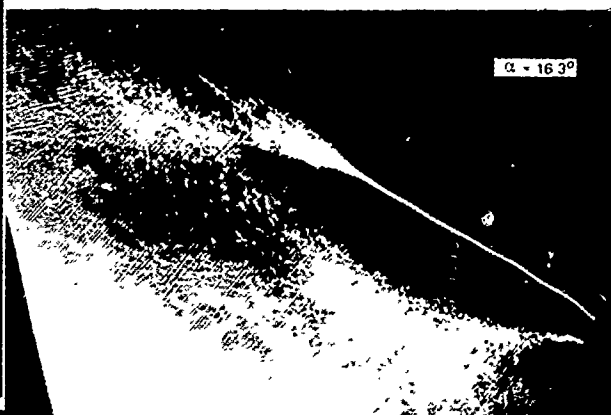


Figure 12. Flow pictures for Flat Plate Snag

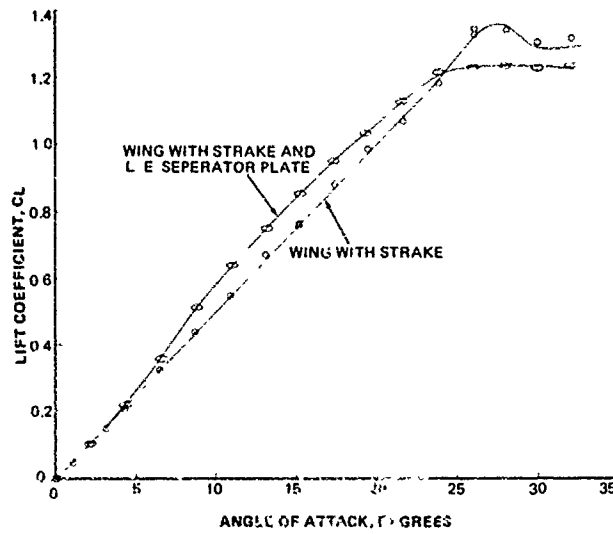


Figure 13. Comparison of Lift Coefficient vs. Angle of Attack With and Without Separator Plate.

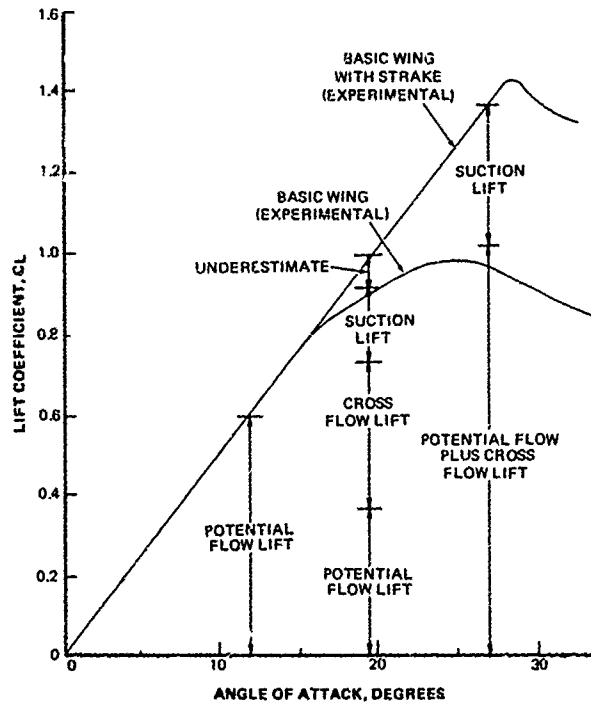


Figure 14. Lift Coefficient vs. Angle of Attack.

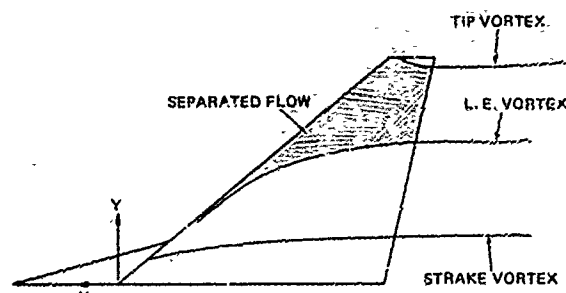


Figure 16. Predicted Flow Patterns  $\alpha = 19.4$  Degrees.

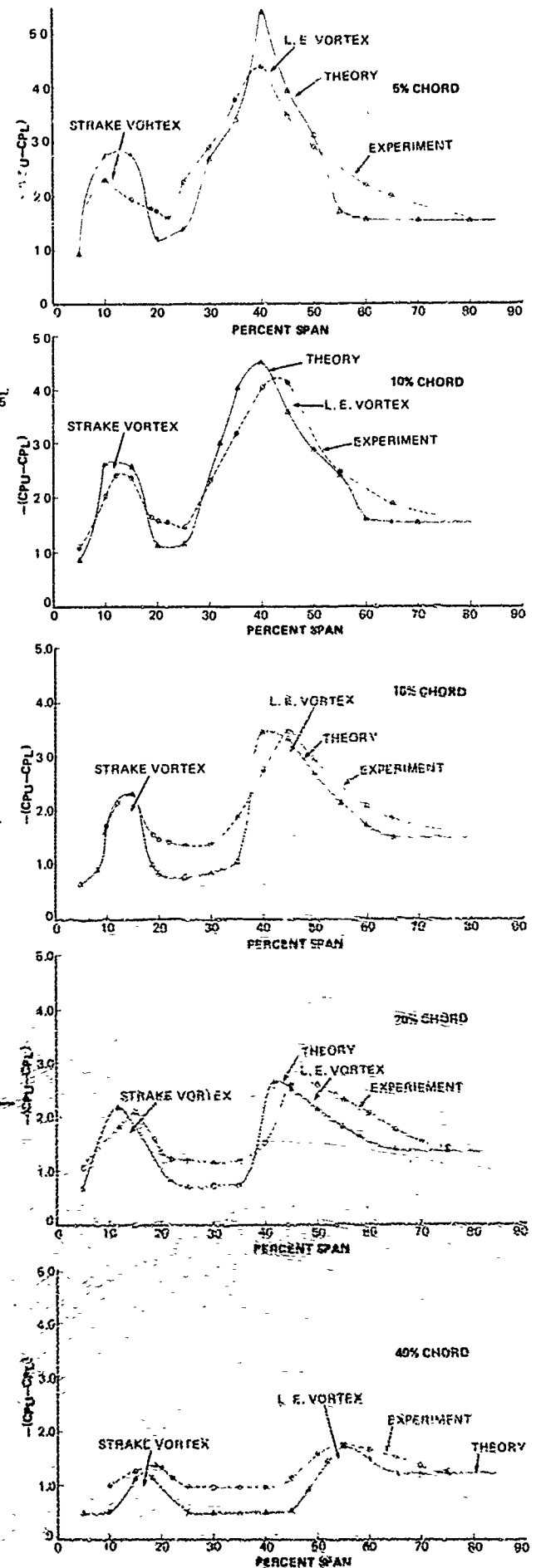


Figure 15. Comparison of Predicted and Measured Spanwise Pressure Distributions  $\alpha = 19.4$  Degrees.



## VORTEX/JET/WING INTERACTION BY VISCOUS NUMERICAL ANALYSIS\*

by

R. M. Scruggs and J. F. Nash  
 Sybucon., Inc., Atlanta, Georgia 30339  
 Charles J. Dixon  
 Lockheed-Georgia Co., Marietta, Georgia 30063  
 U.S.A.

## SUMMARY

A computational model has been developed for analyzing the flow mechanism of vortex/wing/jet interactions. The model is applicable to a wide class of viscous flows but is particularly suitable for calculating vortex-type flows near no-slip or solid boundaries. Examples are leading edge vortices formed on highly swept delta wings or on moderately swept wings with active control by jets or passive control by "strakes." The model is based on reducing the full Navier-Stokes equations to parabolic form with respect to one of the three space coordinates. Computing time is in minutes rather than hours bringing the solution of the Navier-Stokes equations into the engineering realm. Examples of computations for various vortex/wing/jet interactions are presented in the report. Experimental pressure, laser velocimeter, and flow visualization data are presented for an unswept wing with leading edge vortex control by spanwise blowing. These data are used to analyze the formation and strength of the leading edge vortex and as examples of typical input/output data for the computational model.

## LIST OF SYMBOLS

$\bar{u}, \bar{v}, \bar{w}$	Mean velocities in x, y, and z directions, respectively	$V_0$	Velocity of vortex normal to line through vortex center
x, y, z	Spanwise, normal to chord and chordwise coordinates, respectively	$\dot{w}/g$	Jet mass flow
$\xi, \eta, \zeta$	Vorticity in x, y, and z directions, respectively	$\hat{z}$	Variable of integration on $Y=0$ in Green's function integral
AR	Aspect ratio	$C_{l_v}$	Lift coefficient, vortex lift
C	Wing chord	$C_N$	Wing normal force coefficient
q	Free stream dynamic pressure	$C_n$	Local normal force coefficient
$R_0$	Region of integration containing vorticity	$C_p$	Pressure coefficient
S	Wing area or Strouhal number	$C_\mu$	Momentum coefficient - $\dot{w}V_j/gqs$
s	Length of vortex feeding sheet	$\alpha$	Angle of attack of wing
t, T	Time	$\Gamma$	Circulation
$V_j$	Fully expanded isentropic jet velocity	$\delta$	Boundary layer thickness
$V_0$ or $V$	Free stream velocity	$\lambda$	Taper ratio
$\vec{V}$	Total velocity vector (x, y, z)	$\nu$	Kinematic viscosity
		$\rho$	Density of flow in wind tunnel
		$\vec{\omega}$	Vorticity vector

## 1.0 INTRODUCTION

The favorable lifting effects of leading edge vortices on delta wings have been under investigation for many years. More recently, other types of favorably interfering vortices have been noted. These consist of streamwise vortices formed from leading edge "strakes," outboard leading edge extensions ("snags") as on the F-4 (aircraft) and trailing vortices from canard configurations. Now that interfering vortices are recognized as aids, as well as detriments, to lift and stability augmentation, considerable emphasis is being placed on gaining knowledge concerning their formation and stability.

There have been many attempts to model the flow for delta wings with leading edge vortices. Matsui (Ref. 1) has provided a good survey of many of these attempts. The efforts of most have been limited to potential flow models, assuming rotational elements for viscous effects such as the leading edge feeding sheet. The basic assumptions of slender body, conical flow have been followed by most investigators such as Mangler and Smith (Ref. 2). Results of these early investigators have laid a good foundation for further research, but they are not successful in obtaining forces and moments over a general range of configurations. Polhamus (Ref. 3), with the leading edge suction analogy, has good success in predicting vortex lift and, in later efforts, the moments. His method does not describe the pressures or flow mechanism. Good results were obtained most recently by Weber et al (Ref. 4) and Rao and Jones (Ref. 5), where the trailing edge conditions of delta wings are included in the boundary conditions. The latter are still not considered satisfactory for an arbitrary range of configurations and flow conditions. Both note the need for including the secondary vortex formation in their methods.

The secondary vortex, along with leading edge separation, and the vortex core are all highly viscous flow areas. Also, the vortex axial velocity and its gradient are considered very important in determining

\*The research reported herein was conducted by the Lockheed-Georgia Company under contract from the Office of Aeronautical Research. Co-authors from Sybucon, Inc., are consultants to Lockheed-Georgia Company.

the stability of the vortex. There are no satisfactory analytical treatments of these areas. Neither are there any experimental results that provide the assurance of not having experimental probe interference. Knowledge of these viscous flow areas is essential to defining any model of the flow, since the characteristics of these viscous flow areas will affect portions of the flow field such as the feeding-sheet shape, the location and size of the primary vortex core, and the vortex "decay" or "burst" (vortex instability); all affect the overall force and moments.

The Lockheed-Georgia Company is currently developing under contract with the Office of Naval Research, a viscous model for leading edge and other interfering vortex concepts. Current development of this viscous model is presented in this paper. The viscous model will provide knowledge of the vortex feeding sheet, such as position and strength, while vortex position and core size can be determined as a function of input conditions. Contrary to the potential flow solutions, the viscous model has a no-slip condition at the wing surface. This should have significant effect on vortex shape and position. The viscous model can include effects of a spanwise blowing jet (discussed in this paper) or other axial velocity along the axis of the vortex core. It can be used to investigate the flow for "over-wing" blowing jets also.

A vortex lattice lifting surface theory may be used to determine input for the viscous vortex model by iteration procedure. In fact, the desired end result of this vortex analysis program is a combination of the vortex lattice model (potential flow model) with the viscous numerical model. This should be an iterative procedure in which the vortex lattice model contains free line vortices connected by feeding sheets to the bound vortex lattice with sources and sinks representing the span blowing jet, if there is one. Location and strength of the free vortices and sources and sinks are determined by iteration. Universal parameters may be determined from a parametric study of the input characteristics to the viscous vortex model. The parameters such as vortex locations and strength may be used directly in the potential flow-vortex lattice model. Input for the viscous model may also be obtained by laser velocimetry, which is discussed subsequently.

## 2.0 THEORY

The theory is based on the assumption that for a certain class of flows the rate of change of viscous stresses in one direction is small compared with those in the two orthogonal directions. Limited development of this concept was accomplished in earlier work (Ref. 6), wherein momentum transport normal to the surface was neglected. The present approach, which remedies this weakness, is to proceed from the vorticity transport equations for incompressible, three-dimensional, steady flow. These equations are obtained from the Navier-Stokes equations and the continuity equation by noting that

$$\bar{\omega} = \text{curl } \bar{V} \quad (1)$$

and performing differentiations appropriate to steady flow to produce

$$\bar{i} \cdot \text{grad } \bar{\omega} = \bar{\omega} \cdot \text{grad } \bar{V} + \nu \nabla^2 \bar{\omega}. \quad (2)$$

The velocity is determined from

$$\nabla^2 \bar{V} = - \text{curl } \bar{\omega}. \quad (3)$$

Equation (3) is derived from a vector operation on Eq. (1), utilizing the continuity condition for incompressible flow:  $\text{div } \bar{V} = 0$ . The vorticity  $\bar{\omega}$ , and  $\bar{V}$ , compose six unknowns governed by the six scalar equations represented by Eqs. (2) and (3). Putting the equations in rectangular cartesian coordinates, a direction, say the x-direction, may be taken as the one having minimum rate of change of viscous stresses. Then, the last term in Eq. (2) may be approximated as  $\nu(\bar{\omega}_{yy} + \bar{\omega}_{zz})$ . Equation (2), written in scalar form, now appears as

$$\xi_x = \frac{1}{\nu} \{ u_x \xi + u_y \eta + u_z \zeta - w \xi_z - v \xi_y + \nu(\xi_{yy} + \xi_{zz}) \} \quad (4)$$

$$\eta_x = \frac{1}{\nu} \{ v_x \xi + v_y \eta + v_z \zeta - w \eta_z - v \eta_y + \nu(\eta_{yy} + \eta_{zz}) \} \quad (5)$$

$$\zeta_x = \frac{1}{\nu} \{ w_x \xi + w_y \eta + w_z \zeta - w \zeta_z - w \zeta_y + \nu(\zeta_{yy} + \zeta_{zz}) \} \quad (6)$$

where  $(\xi, \eta, \zeta)$  are the components of  $\bar{\omega}$  and  $(u, v, w)$  are the components of  $\bar{V}$ . Equations (4) through (6) may be conveniently represented in matrix form.

$$F_x = AF - BF_z + CF_y + DF_{zz} + DF_{yy}, \quad (7)$$

where  $F = (\xi, \eta, \zeta)^T$  and the three-by-three matrices A through C contain the velocity coefficients. D is the identity matrix times  $\nu$ . The partial differential system represented by Eq. (7) is parabolic in the x-direction and elliptic in the local y-z plane. This permits the use of forward-marching techniques to perform the numerical integration, wherein the solution is stepped progressively in x using information from the previous x-step and the prescribed boundary values.

Figure 1 depicts the arrangement of the coordinate system and the domain of integration. The solution is started in some initial plane,  $x=0$ . For every point  $(y, z)$  of the initial domain or "cross-flow" plane, a value is prescribed for the vorticity components and for the velocity components. The velocity components are, of course, derivable to within a constant from the vorticity and must be thus compatible. In order to integrate Eq. (7) for vorticity, it is necessary to simultaneously solve for the velocities. The procedure for obtaining velocities will be discussed subsequently. The finite differencing procedure finally adopted for Eq. (7) uses the following:

For x-derivatives,

$$F_{x_{m,n}}^k = \frac{1}{\Delta x} (F_{m,n}^k - F_{m,n}^{k-1}) \quad (8)$$

(m indexes the y-direction, n the z-direction, and k denotes current x-location)

For the first-y-derivatives,

$$F_{y_{m,n}}^k = \frac{1}{\Delta y} (F_{m+1,n}^k - F_{m,n}^k), \quad v < 0, = \frac{1}{\Delta y} (F_{m,n}^k - F_{m-1,n}^k), \quad v > 0 \quad (9)$$

For first z-derivatives,

$$F_{z_{m,n}}^k = \frac{1}{\Delta z} (F_{m,n+1}^k - F_{m,n}^k), \quad w < 0, = \frac{1}{\Delta z} (F_{m,n}^k - F_{m,n-1}^k), \quad w > 0 \quad (10)$$

For second y-derivatives,

$$F_{yy_{m,n}}^k = \frac{1}{(\Delta y)^2} (F_{m+1,n}^k - 2 F_{m,n}^k + F_{m-1,n}^k) \quad (11)$$

and similarly for second z-derivatives. All first differences are first order accurate and the second differences are second order accurate. The "locally upwind" first differences in Equations (9) and (10) were chosen because the resulting finite difference equations are unconditionally stable. Centered first differences may be used to improve accuracy, but a stability limit exists in that case in the form of a cell Reynolds number.

Substituting Eqs. (8) through (11) into Eq. (7) leads to a set of simultaneous algebraic equations involving the unknown vorticity vectors at the five forward node points shown in Figure 1. The procedure used for solving these equations is an Alternating Direction Implicit (ADI) sweeping technique. The method proceeds as shown in Figure 2. Points along a line  $z = \text{constant}$  are solved simultaneously where, if  $M$  denotes the number of mesh points in the y-direction, the equations take the form

$$\begin{bmatrix} a_{11} & a_{12} & 0 & \dots & 0 \\ a_{21} & a_{22} & a_{23} & 0 & \dots & 0 \\ 0 & a_{32} & a_{33} & a_{34} & 0 & \\ & & & & & \\ 0 & \dots & \dots & \dots & a_{i,i-1} & a_{ii} \end{bmatrix} \begin{Bmatrix} F_1 \\ F_2 \\ \vdots \\ F_i \end{Bmatrix} = \begin{Bmatrix} G_1 \\ G_2 \\ \vdots \\ G_i \end{Bmatrix} \quad (12)$$

The  $a$ 's are  $3 \times 3$  matrices, the  $F$ 's are  $3 \times 1$  matrices, and the  $G$ 's are  $3 \times 1$  and are known on any solution. The subscript  $i$  has the value of  $M-2$  when solving implicitly with respect to  $y$ . When the solution is implicit with respect to  $z$ , i.e. along  $y = \text{constant}$  as shown in Figure 2, then  $i$  has the value  $N-2$ , where  $N$  is the number of mesh points in the  $z$ -direction. As shown in Figure 2, a solution is obtained sequentially at each  $z$ -station and then at each  $y$ -station. The process of sweeping once with respect to  $z$  and once with respect to  $y$  constitutes one iteration on the solution in the local cross-flow plane. The values of vorticity either to the left and right or above and below a local solution line, evident from the molecule in Figure 1, are obtained from the previous iteration. Each implicit solution follows from Eq. (12) in the form,

$$F = a^{-1}G, \quad (13)$$

where  $a^{-1}$  is the inverse of either an  $(N-1)$  or an  $(M-2) \times (M-2)$  matrix. The  $a$ -matrix is solved by an efficient successive elimination algorithm.

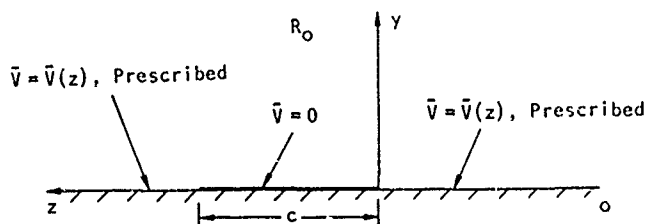
In order to close the iterative loop at a new  $x$ -station, it is necessary to have starting values of vorticity and velocity. The values are input as initial conditions at the starting plane; at successive planes they are either arbitrarily guessed or taken as the values from the previously converged plane. Having obtained new vortices on an iteration, it is necessary to obtain updated velocities on the whole plane and establish appropriate values of boundary vorticity. Vorticity is prescribed on all sides of the integration domain except the solid boundary. On that boundary the vorticity cannot be specified directly but must be that value which is consistent with zero velocity at the wall.

Since the flows of primary concern in the research are those over rounded flat surfaces, it was found convenient to formulate a Green's function integral solution for velocity in terms of vorticity. The advantage in this approach is that velocity boundary values do not have to be prescribed on the free boundaries of the computing mesh, since the integral solution is asymptotic to a constant at infinity. The solution appropriate to a bounded no-slip surface with  $\bar{V}$  asymptotic to  $\bar{V}_\infty$  for  $(y^2 + z^2)^{1/2} \rightarrow \infty$  is a Green's function solution. The sketch below depicts the boundary value problem. It is required to solve Eq. (3) subject to the conditions in the sketch, regarding  $\bar{\omega}$  as a known point function. The integral solution satisfying no-slip on the surface is

$$\bar{V}(y,z) = \frac{1}{2\pi} \int_{R_0} \int \ln \left( \frac{\bar{r} - \bar{r}_0^*}{\bar{r} - \bar{r}_0} \right) \text{curl } \bar{\omega} d R_0 + \frac{1}{\pi} \left[ \int_0^0 \frac{y \bar{V}(0,\bar{z}) d\bar{z}}{y^2 + (z - \bar{z})^2} + \int_0^\infty \frac{y \bar{V}(0,\bar{z}) d\bar{z}}{y^2 + (z - \bar{z})^2} \right] \quad (14)$$

where  $\vec{r}_0 = (y_0, z_0)$  and  $\vec{r}_0^* = (-y_0, z_0)$ .

Thus on each iteration, Eq. (14) may be used in a straightforward manner to determine a velocity field. It was found, however, that exclusive use of the integral form for all mesh points led to excessive computing time, so the method is only used on the boundaries. Having thus established boundary values for the velocity, the ADI procedure is then used in the interior of the domain. With a velocity field known after each iteration, a new value of wall vorticity is found by using a first order accurate, one-sided difference on the velocities. The integral method is ideal for converging the critical wall vorticity since the velocity is forced on each iteration to satisfy no-slip. Other methods require simultaneously converging wall vorticity to its correct value and velocity to zero.



Numerous tests have been run on the convergence behavior for flows of varying degrees of complexity. In general, for planes after the initial one, the number of iterations required is 6 or less. For the initial plane, up to 12 iterations were found to be necessary. This apparently is due to the assumed initial values not being compatible with the three-dimensional requirements of the flow. Generally, it has been found that a finer mesh requires more iterations for convergence on the first step but not on later steps. It is also noted that an apparent difference exists for the value of vorticity obtained with different mesh sizes. A finer mesh reduces the error due to artificial viscosity. The error as a function of mesh size has yet to be fully explored. Most of the calculations reported here were performed with an  $11 \times 21$  mesh, for which it is believed that inaccuracy has not destroyed the general validity of the results.

Except for the effect of artificial viscosity, the method is relatively insensitive to step length in the x-direction, since both the theory and the numerical integration method are first-order accurate in x. Consequently, most of the results presented were computed for a  $\Delta x$  of 1. unit, while  $\Delta y$  and  $\Delta z$  were .1 units. The method has been used extensively on a CDC 6600 machine. For this machine, using a cross-flow mesh of  $11 \times 21$ , approximately 20 cpu seconds are required per x-step after the first step. The first step generally will require more time because more iterations are required to converge. For a cross-flow domain of size 1. unit by 2. units ( $11 \times 21$  and  $\Delta y = \Delta z = .1$  units), stepping 5. units in  $\Delta x$  requires approximately 100 cpu seconds when the number of iterations on the first step is 12 and on successive steps 6. The computing time per second increases approximately linearly with the number of mesh points in the cross-flow plane.

The velocities off the edge of the plate can either be arbitrarily prescribed or be obtained by some coupling scheme whereby the flow in the region exterior to the vorticity box is calculated by some other method.

#### Theoretical Results for Typical No-slip Flows:

The computational method has been used to calculate a number of complex vortical flows during the development stage. Figure 3 shows the interaction of a pair of streaming, counter-rotating vortices with a parallel wall. This figure, depicting the velocity vectors in the cross-flow plane, demonstrates clearly that much more than potential flow is involved when the vortices and the wall interact. High-energy fluid is entrained from the irrotational outer flow and then is ejected upward between the vortices, having suffered an energy loss due to interaction with the outer wall. The effect of this energy loss is reflected as well in the streamwise component of velocity. Figure 4 shows the wake development in the streamwise velocity. The low-energy flow between the vortices is reflected in a progressively retarded U-profile, similar in appearance to a boundary-layer profile approaching separation.

### 3.0 EXPERIMENT

The primary objectives of the experimental efforts have been to obtain additional knowledge of leading edge vortex formation and realistic input values for the viscous numerical model. Quantitative and qualitative information is obtained to compare with the theoretical output.

The model used for the investigation is a semi-span, aspect ratio 3, rectangular wing of zero sweep. The airfoil section is an advanced transonic airfoil, 12% thick. The airfoil was chosen because of its characteristic leading edge separation and its relatively flat upper surface which corresponds with the flat surface used in the theory. A spanwise blowing nozzle is installed at the wing root for active control of this leading edge vortex formed at high angle of attack. Fifteen surface static pressure taps are installed in the model at each of four spanwise stations.

Tests conducted with this model include measurements of surface pressures, flow visualization with a Sage action helium bubble generator, and flow field velocities measured with the Lockheed-Georgia laser velocimeter. Surface pressure data were obtained at angles of attack from  $-3$  to  $30^\circ$  at various jet momentum coefficients. Laser velocimeter data were obtained at angles of attack of  $-3$  and  $30$  degrees only and one jet momentum coefficient. The laser velocimeter is capable of obtaining two component velocity time histories and all the resulting statistical analyses of turbulent flow. Reference 6 describes the laser system in detail and presents results for the turbulence characteristics of the wing at  $-3$  degrees angle of attack with the spanwise blowing jet on.

#### 3.1 Experimental Results and Analysis

This paper is concerned primarily with the results for the wing at  $30$  degrees angle of attack where a strong leading edge vortex is formed. At this angle a limited amount of laser data were obtained (mean

velocities only), but with the pressure data and flow visualization, considerable insight to the vortex formation is provided.

Surface static pressures for the wing at 30 degrees angle of attack and a  $C_{lu}$  of 0.769 are shown in Figure 5. The artistic concept of the leading edge vortex illustrated in the figure is approximately in the right position, but later data indicate the shape is different. Figure 6 shows the leading edge vortex which forms with spanwise blowing as reflected by the helium bubble flow visualization. Velocity vectors obtained by the laser velocimeter are shown in Figure 7, which is discussed in the following.

Figure 7 illustrates a composition of the results as just discussed for the flow at 33% span and the wing at 30 degrees angle of attack. Based on these available data, position, size, and strength of the primary and secondary vortices are approximated; the vortex feeding sheet shape and strength can be determined; and total circulation available from the leading edge vorticity and its relation to wing lift is deduced. Vorticity contours are indicated by relating the experimental results with available theoretical results.

Development of the vorticity lines (isovors) of Figure 7 is based on linking all the experimental and available theoretical data in a logical manner. The vortex position in percent chord is approximated from both the pressure data and flow visualization. Size of the vortex comes primarily from flow visualization. The oval shape of the vortex and the tilting of the top edge is based on flow visualization and the vorticity contours of the theoretical method. Figures 9 and 11, discussed in Section 4.0, show vorticity contours for two of the theoretical cases.

Laser data shown in Figure 7 provides the slope of the edge of the shear layer (or feeding sheet) and the height of the edge above the wing surface. These conditions, the height of the vortex, and the leading edge proximity allow the logical approximation of the edge of the shear layer which is shown by a line as  $\xi \rightarrow 0$ .  $\xi$  rapidly approaches zero outside of this layer.

The thickness of the vortex sheet is linked to the position of zero velocity along the vertical ordinate from the wing surface. A line through the lowest laser data point could logically pass through the zero velocity at the line of maximum vorticity. The level for this zero velocity should be about halfway across the positive vorticity layer. This latter criteria allows a reasonably shaped line to be drawn from the separation point through the zero velocity point and into the primary vortex. Also, straight lines through the zero velocity point and the lower laser data points for  $w/V_0$  and  $V/V_0$  are nearly the same line over most of the length of the lines. This would be a logical result.

The separation point is based on the pressure distribution for which a portion is plotted on Figure 7. At the leading edge the velocity has increased from stagnation to  $V/V_0 = 2.86$ . It then decreases due to adverse pressure gradient until separation occurs at  $Z\cos\alpha = .25$ . From this point to  $Z\cos\alpha = 0.44$ , the velocity indicated by the pressure is relatively constant. It begins to rise at the point corresponding to the intersection of the airfoil surface and the line on which laser data were taken, i.e.  $Z\cos\alpha = 0.50$ .

It is probable that the pressure is coming under the influence of the secondary vortex at this point; therefore, it is reasoned that zero vorticity should occur at or near this point. To substantiate this, it can be shown that at the wall the change in pressure with chordwise direction is a direct function of the change in vorticity with direction normal to the chord, i.e.

$$\frac{\partial}{\partial z} \left( \frac{p}{\rho} \right) = v \left( \frac{\partial \eta}{\partial x} - \frac{\partial \xi}{\partial y} \right) = \frac{v \partial \xi}{\partial y} \Big|_{\text{wall}}$$

As shown in Figure 7, the vorticity does not change much with  $Y$  at the wall, between the separation point and a small distance forward of the zero vorticity line; therefore, the pressure should not change much. Since the pressure is beginning to decrease at  $Z\cos\alpha = 0.50$ , it is probable that the zero vorticity line should be slightly forward and the secondary vortex slightly aft where  $\partial \xi / \partial Y$  is negative and the pressure decreases.

It should be noted that  $V/V_0$  from the pressure distribution at  $Z\cos\alpha = 0.50$  agrees quite closely with laser velocity at the outside edge of the shear layer. This implies very little, if any, change in pressure across the entire shear layer. This is probably true only for the flow ahead of this  $Z/C$  station.

The pressure distribution shows that the maximum velocity occurs at  $Z/C = 0.117$  or  $Z\cos\alpha = 1.32$ . This should occur at a position where the  $\partial \xi / \partial Y$  is changing from negative to positive, i.e. as shown in Figure 7. The lower part of the primary vortex should be near this point since the maximum velocity due to the primary vortex is at the outer edge of the vortex (the bottom of the oval shape).

### 3.2 Vorticity and Vortex Strength

With the geometry of the vortex established, some useful quantitative values can be estimated. The values can then be used as input to the theoretical model as well as checks on the output of the model.

#### 3.2.1 Leading Edge Vorticity

How much leading edge vorticity makes a primary vortex? This can be estimated, but first the value of the leading edge vorticity must be estimated. From the geometry of Figure 7, the thickness,  $\delta$ , of the boundary layer just ahead of the separation point is determined to be approximately 0.30 inch or 2.8% of the wing chord. Assuming a laminar boundary layer, a linear velocity profile allows a convenient calculation of the slope of the velocity profile  $\partial V / \partial n$ , where  $n$  is the distance from the surface along a line approximately normal to the velocity vectors in the boundary layer, and  $V$  is the magnitude of the velocity vectors. Now  $V$  at the edge of the boundary layer is obtained from the pressure distribution at the point of separation, i.e.  $C_p = -6.7$ . Therefore,  $V/V_0 = 2.77$  and the normalized slope is:

$$\frac{\partial(V/V_o)}{\partial(n/c)} = \frac{2.77}{.028} = 99.10$$

The above is also the value of vorticity across the boundary layer, since

$$\zeta = \frac{\partial w}{\partial y} - \frac{\partial v}{\partial z} \approx \frac{\partial V}{\partial n}$$

As will be shown later, the value of the vorticity and the boundary layer thickness at the leading edge separation point are needed for input to the viscous numerical model.

### 3.2.2 Vortex Strength

It is interesting to analyze the primary vortex strength as a function of the leading edge vorticity. To do this, some assumptions based on vortex shedding from a circular cylinder are made. First, as shown in Ref. 7, the strength of the vortex shed from a cylinder is a function of the length of the feeding sheet. As the vortex sheds from the surface, its strength grows until the feeding sheet separates from the cylinder. At this point, the vortex and feeding sheet have approximately equal circulation strengths and the feeding sheet is about 4.8 cylinder diameters long. The total circulation in the vortex and sheet is approximately equal to the circulation emitted from the boundary layer during one cycle of vortex shedding.

Circulation is described as a function of boundary layer vorticity as follows:

$$(1) \quad d\Gamma = \left( \frac{\partial w}{\partial y} - \frac{\partial v}{\partial z} \right) dz dy, \quad (2) \quad \frac{d\Gamma}{dt} = \left( \frac{\partial w}{\partial y} - \frac{\partial v}{\partial z} \right) w dy \quad \text{or} \quad \frac{\partial V}{\partial n} \cdot V dn, \quad (3) \quad \Gamma = \int_0^T \int_0^\delta \frac{\partial V}{\partial n} V dn dt$$

where  $\Gamma$  is the circulation available from the boundary layer for a given time,  $T$ . For a laminar boundary layer

$$(4) \quad n/V = \delta/V_1$$

where  $\delta$  is the boundary layer edge and  $V_1$  is the velocity at the edge. Also, where  $T$  is the time for one cycle of vortex shedding and  $S$  is the Strouhal number for laminar separation,

$$T = \frac{1}{f}, \quad \text{and} \quad f = \frac{V_o S}{d'} = \frac{V_o S}{C \sin \alpha}, \quad (5) \quad \text{Now } \Gamma = \frac{C \sin \alpha}{V_o} \int_0^{V_1} \frac{V_1}{\delta} \cdot V \cdot \frac{\delta}{V_1} dV, \quad (6) \quad \text{or} \quad \frac{\Gamma}{V_o C} = \frac{\sin \alpha}{2 S} \left( \frac{V_1}{V_o} \right)^2$$

The value of  $\Gamma/V_o C$  is the total strength of the vortex and sheet combined. This value provides an end point for computing the leading edge vortex strength as a function of feeding sheet length. It can be shown from Ref. 7 that the vortex strength growth follows a relation as follows:

$$(7) \quad \frac{\Gamma}{V_o C} = \frac{1}{2} \cdot \frac{\sin \alpha}{2 S} \cdot \left( \frac{V_1}{V_o} \right)^2 \left( \frac{s}{s_p} \right)^{1.2}$$

The growth relation  $(s/s_p)^{1.2}$  is valid over the range  $0 \leq s/s_p \leq 0.42$ , where  $s$  is the actual length of the feeding sheet, and  $s_p$  is the length of the feeding sheet at the time of vortex shedding. Since  $s_p = 4.8$ ,  $d' = 4.8 C \sin \alpha$ , and this is many times the distance for the leading edge vortex sheet on an airfoil, the limit  $s/s_p \leq 0.42$  is well above that for a leading edge vortex formation.

Geometry in Figure 7 shows the feeding sheet length along the line of maximum vorticity produces a value of  $s/s_p = 0.089$ . For  $\alpha = 30^\circ$ ,  $S = .2$ , and  $V_1/V_o = 2.77$ , the strength of the primary vortex is approximately

$$\frac{\Gamma}{V_o C} = 0.26 \quad \text{or} \quad \Gamma = 14.9 \text{ ft}^2/\text{sec.}$$

This is only a fraction of the full potential vortex strength, e.g. if  $s/s_p = 1.0$ , then  $\Gamma$  would be 272 ft.<sup>2</sup>/sec.

A check of the order of magnitude for  $\Gamma$  can be made by referring back to the geometry of Figure 7. It is logical that the peak pressure coefficient,  $C_p = -9.7$  corresponds to the peak velocity due to the primary vortex (assuming negligible total pressure loss). Assuming a distance from the center of the vortex to a point near the airfoil on a line through the  $z/c = 0.117$  ordinate, the radius of the vortex is approximately 0.071 feet. The velocity at this point based on the peak  $C_p$  is 208 ft/sec.; therefore, assuming this point is outside the vortex core:

$$\Gamma = V_\theta r = 208 \times 0.071 = 14.7 \text{ ft}^2/\text{sec.}$$

This is amazingly close to the previously computed value of  $\Gamma$ , and of course it does confirm the order of magnitude strength of the primary vortex.

As a further check on the order of magnitude vortex strength, vortex lift is extracted from lift obtained by integrating the pressure distributions shown in Figure 5. Total lift is obtained. Then, the potential flow lift, less leading edge thrust effect at  $\alpha = 30^\circ$ , is subtracted to get an approximate value for vortex lift. At 33% semi-span the rectangular wing vortex lift is  $C_{lv} = 1.02$ . Since  $C_{lv} = 4\pi \Gamma V_o C$ ;

$V_0 = 63.6$  ft/sec., and  $C = .892$  ft.;  $\Gamma_v = 4.60$  ft<sup>2</sup>/sec. This value must represent the combined circulation strength of primary and secondary vortex and any negative circulation effect of the jet. In order for the primary vortex strength to be 14.9 ft<sup>2</sup>/sec., the combined secondary and jet circulation must be of order -10.30 ft<sup>2</sup>/sec. It is not unlikely the secondary vortex is of this magnitude since the jet does create negative vorticity primarily by its expansion and surface shear towards the wing leading edge.

### 3.4.3 Parameters Affecting Vortex Strength

From the preceding discussion, it is indicated that the vortex strength is primarily a function of the space within which it is allowed to grow or the length of its feeding sheet and the vorticity shed at the leading edge. It indicates that once these confines are met the vortex no longer grows, and the excess vorticity is converted downstream. It would appear that due to reduced local angle of attack on the outboard stations of the unswept, untapered wing the value of  $V_1/V_0$  decreases causing a decrease in vortex strength, but this is compensated with increased vortex sheet length and probably by jet vorticity as well.

All of the above reasoning assumes the two-dimensional effect only. Unfortunately, the leading edge vortex is a three-dimensional phenomena and the vortex cannot exist in a stable condition without spanwise flow. It has been shown by Campbell (Ref. 8) and in unpublished works of Dixon that the local section lift coefficient increases with increasing spanwise blowing momentum. This might be explained as an effective increase in the feeding sheet length due to the helix angle created by spanwise blowing. The remaining effect of spanwise velocity is the stabilizing effect on the vortex. Also, the velocity gradient in the spanwise direction can cause decay or growth of the vortex (decreasing velocity decays and increasing velocity causes growth). The case from Ref. 9 for outboard blowing shows an increase in vortex strength with span. Based on the above analyses, this is due to accelerating jet flow (under-expanded jet) and vortex feeding sheet increasing in length as it marches spanwise.

Even though three-dimensional effects can be significant, the two-dimensional analysis provides valuable insight. First, the value of  $V_1/V_0$  depends not only on angle of attack, but on the shape of the leading edge and trailing edge recovery. Reference 7 and others have shown the value of  $V_1/V_0$  to be approximately 1.4 at the separation point of blunt bodies. A lifting body with leading edge separation and flow recovery at the trailing edge causes  $V_1/V_0$  to be much higher and a function of angle of attack; therefore, the vortex lift is a function of angle of attack due both to increasing  $V_1/V_0$  and length of the feeding sheet.

In conclusion, the analyses of experimental results have resulted in both a hypothesis and quantitative values to be used in the viscous numerical analysis. Primarily, the order of magnitude for leading edge vorticity and an approximate shape of the input velocity is determined. The theory should then produce primary and secondary vortices with strengths of magnitude as computed above. The analyses also indicate parameters that could favorably increase vortex strength and wing lift. These are: (1) appropriately shaped leading edge, (2) large cavity for vortex to grow or longer feeding sheet, and (3) positive spanwise velocity gradient.

Shape of the pressure distribution and therefore the pitching moment with a leading edge vortex will be a strong function of the position and strength of the secondary vortex. This evolves since the secondary vortex causes the negative value of  $\partial\epsilon/\partial y$ , i.e. a reduction of the pressure. With a tight, strong secondary vortex,  $\partial\epsilon/\partial y$  at the wall is negative and relatively large in the area of the secondary vortex.

### 4.0 EVALUATION OF THEORY

While it is possible to compute, via the numerical method, a wide class of flows of practical interest such as delta wing leading edge flows and fillet flows, it is the primary intent here to address the flow associated with a laterally blown jet. In this case the primary or outer irrotational flow is not parallel to the jet direction but approximately normal to it. It is known from experimental observation that at angles of attack where spanwise blowing is effective, there is leading edge detachment of the streaming flow over the wing. The jet then penetrated far out the span and a spanwise vortex forms in the vicinity of the jet. It is valid in this circumstance to apply the forward marching procedure in the spanwise direction. The integration is confined to the detached, rotational region of flow over the surface, where second derivatives with respect to  $x$  are much smaller than those with respect to  $y$  and  $z$ .

As noted earlier, the method of Eq. (14) leaves arbitrary the specification of the velocity vector along  $y=0$  for all points not on the no-slip surface. Thus, it is possible, via the integral method, to represent the effect of the outer irrotational flow on the viscous flow nearer the surface. For the streaming flow past a surface with leading edge separation, the velocity distribution is not generally known. In fact, the outer potential flow and the inner viscous flow are strongly coupled. This larger problem is not addressed in the present investigation, so that it is necessary to approximate the affects of the surrounding flow field on the jet/vortex formation region. The angle of attack in the cross-flow plane is fixed by specifying  $w_\infty$  and  $V_\infty$ . The manner in which these velocities approach zero near the plate from upstream and downstream along  $y=0$  serves (as discussed in Section 2.0) to specify the streaming flow. The idea is that the outer flow should exhibit sharp turning near the leading edge and should slowly recover freestream conditions downstream. Thus,  $w$  and  $v$  are as follows:

$$\text{for } z \leq 0: \quad w = w_\infty \left(1 - \frac{1}{1-z}\right), \quad \text{and } v = v_\infty \left(1 - \frac{1}{z}\right), \quad \text{for } z < z_k, \quad \text{and } v = -\frac{1+z_k}{z_k^2} v_\infty z, \quad z_k \leq z \leq 0.$$

$$\text{for } z \geq c: \quad w = \frac{w_\infty}{z_1 - c} (z - c), \quad \text{and } v = \frac{v_\infty}{z_1 - c} (z - c), \quad \text{for } c \leq z \leq z_1 \quad \text{and } w = w_\infty, v = v_\infty \quad \text{for } z > z_1$$

By varying  $z_k$  and  $z_1$  a range of conditions in the surrounding flow can be imposed on the integration domain, thus allowing a sensitivity evaluation. Having a fixed angle of attack and the surrounding flow,

the remaining parameters relate to the initial data, or conditions imposed in the plane  $x=0$ , and the boundary values of vorticity.

As noted earlier, the mathematical method as now posed, requires the vorticity to be given on the free sides of the cross-flow plane. The upper face and the downstream face were fixed in all cases at zero vorticity. The face along the leading edge however requires a representation of the vorticity associated with leading edge separation. This region of flow is important in any coupling with potential flow representation, and its criticality will be revealed in the example calculations to follow.

For all cases presented here, the integration domain was fixed at two units of length chordwise and one unit of depth normal to the surface. The mesh is  $11 \times 21$  so that  $y=z=.1$ . In the initial plane, the  $u$ -profile of the jet, when it is used, is of the form

$$u = u_{\max} e^{-r^2/a_j^2}$$

where  $r$  is the distance from the jet center and  $a_j$  is a constant fixing the initial jet diameter. The initial vortex is assumed to have the form of a Lamb vortex. If  $V_0$  denotes the axisymmetric velocity vector, the vortex is of the form,

$$V_0 = \frac{k_v a_v}{r^2} (1 - e^{-r^2/a_v^2}),$$

where  $k_v$  fixes the strength of the vortex and  $a_v$  its core diameter. The angle of attack for all cases is approximately  $25^\circ$ , with  $w=1$ ,  $v=.47$ , and  $u_\infty=.1$ . The small value of  $u_\infty$  is necessary to ensure no flow reversal occurs in the  $x$ -direction. The value assigned to  $u_\infty$  may be considered to represent a wing sweep angle. Unless otherwise noted, the following values apply for the various cases:  $u_{\max}=1.0$ ,  $a_j=.15$ ,  $a_v=.15$ ,  $k_v=20$ . Using the freestream values of velocity and the two-unit chordlength as references, the Reynolds number is approximately 2200 for all the examples in this section.

It became apparent after a few trials and analysis of the experimental data that the initial estimate of leading edge vorticity distribution was a critical factor. Using  $z=2$  units as a length scale for chord and appealing to experimental results, it became clear that the leading edge vorticity should not extend upward more than .1 or .2 units and should have a maximum value very near the surface. The separation profile distributes vorticity too diffusely for effective capture to be made by the initializing vortex. Thus, the vortex, in proceeding outboard, loses strength rather than holding constant or increasing in strength.

Figure 8 shows an interesting result obtained with no downstream recovery (i.e.  $z_1$  very large). The vorticity distribution at the leading edge has a maximum of  $\xi=45$ , at  $y=0.1$ . The initial position of the jet is at  $z=1$  and that of the vortex at  $z=5$ .

At three units outboard a secondary, counter-rotating vortex has formed behind the jet. At this point the jet is still centered very near  $z=1$ . Apparently, since very little convection exists downstream of the jet, vorticity of opposite sign builds up in an otherwise stagnant region and forms its own vortex flow field. This vorticity of opposite sign is generated at the wall, induced by the primary vortex, and is then convected by the primary vortex and the outer flow into the stagnant region. The anomalous behavior of the leading edge velocity at  $y=0.1$  appears to be due to numerical inaccuracy caused by the large gradients of vorticity in the neighborhood of the leading edge.

Figure 9 presents the results for a flow with recovery of freestream conditions 4.5 chordlengths downstream of the trailing edge. Maximum leading edge vorticity,  $\xi=25$ , is at  $y=0.1$ . The  $\xi$ -component vorticity contours indicate, at least for the  $x=3$  spanwise location, that the vortex is capturing leading edge vorticity. This is approximately sustained at least through  $x=5$ .

Since  $\partial(P/\rho)/\partial z = v\partial\xi/\partial y$ , an examination of the sign and strength of  $\partial\xi/\partial y$  presents an interesting result assuming the  $\partial P/\partial x$  is not significant. Starting with the leading edge, there is a low pressure due to the flow around the leading edge (a high negative  $C_p$ ), then a rapid increase to about  $Z=0.2$  where the pressure continues to increase, but slowly until  $Z=0.6$  where the increase becomes slightly more rapid because  $\partial\xi/\partial y$  becomes more positive. About  $Z=1.0$  the pressure reaches a high and thus starts decreasing rapidly under the jet at  $Z=1.1$ . The decrease continues to  $Z=2.0$ , therefore, the jet has an effect of increasing lift. This has been noted in experimental data.

Figure 10 depicts the  $u$ -component contours imposed on the vector plot of Figure 9. This defines the location of the jet relative to the vortex. The mutual interaction of the vortex and jet is obvious. Note the  $\partial u/\partial z$  across the vortex center is small, but  $\partial u/\partial y$  is not and peak  $u$  occurs below the center of the vortex.

All examples so far presented have been initialized with a vortex and then allowed to develop spanwise. While this allows more control in studying the interaction between the various flow components, the question still remains whether a vortex is induced by the combined action of separated flow and jet or whether at least a small vortex is already present and is merely amplified through these mechanisms. A series of runs were made to search for conditions leading to the natural formation of a vortex. Figure 11 shows one of the better results obtained. It was found that strong recovery to freestream was required (two chordlengths), along with an increased vorticity at the leading edge. The leading edge vorticity in this case is  $\xi=45$  at  $y=.1$ . It is noted that the results of Figure 11 are for five units outboard. This was the first station for which a vortex-like structure appeared. Presumably this structure would become better defined further outboard, but the calculations were not carried beyond five units of span. A drastic loss of jet velocity is apparent, the initial jet peak velocity having been 20, thus the jet is swept more rapidly off the surface. For the given starting and boundary conditions then, the jet may not remain over the surface much more than five units outboard.



Further examination of the leading edge criteria produced the results of Figures 12 and 13. It was determined from analysis of the experimental data that a strong positive value of vorticity should occur on the surface at the leading edge. Figures 12 and 13 show this to be true. All input is the same for these two figures except the vorticity at  $z=y=0$ . Figure 12 has a value of vorticity,  $\xi$ , = 43 at  $z=y=0$  and Figure 13 has  $\xi=0$  at  $z=y=0$ . The strong recovery of flow behind the jet (input at  $z=1.0$ ,  $y=.4$ ) in Figure 12 contrasts significantly with the vortex roll-up in Figure 13. The strong value of leading edge vorticity decays to zero on the surface within less than 0.1 unit of  $z$ , but its influence over the whole flow field is large. It must be noted that the value of  $\xi=43$  has been chosen to have the same value as  $\partial V/\partial z$  for  $Z_K \leq Z \leq 0$ . This is a compatible relation as is discussed in Section 3.2.1 of this report, and agrees in order of magnitude with the value deduced from experimental data.

This latter analysis emphasizes the need for accurate values of input velocity and slopes at the leading edge, i.e. across the boundary layer at the point of leading edge separation.

## 5.0 CONCLUSIONS

1. A computational fluid mechanical model based on reducing the full Navier-Stokes equations to parabolic form, with respect to one of the three space coordinates, has been developed to a level to prove its feasibility.
2. The viscous model can be applied to a wide class of flows: in particular vortex flows and interacting jet flows over no-slip lifting surfaces. The method allows the computation of large viscous flow regions without approximations of the boundary layer type.
3. The method has been developed with economical computing time, reducing computing time for such methods to minutes rather than hours. Full capability and accuracy limitations of the model need further investigation, however.
4. The model is sensitive to boundary conditions at the leading and trailing edges. These conditions must be obtained from a potential flow model which interfaces with the viscous model.
5. Analysis of experimental laser velocimeter data, surface pressure data, and flow visualization has provided a relation between the strength of the primary leading edge vortex, the vorticity shed at the leading edge separation, and the length of the vortex feeding sheet.
6. Data from the laser velocimeter is required to provide knowledge of the sensitive leading and trailing edge input quantities during the early exploration of this problem.
7. Analysis of the experimental data has indicated the shape of the pressure distribution and therefore the pitching moment is a strong function of the location and strength of the secondary leading edge vortex.

## REFERENCES

1. Matoi, Thomas K.: On the Development of a Unified Theory for Vortex Flow Phenomena for Aeronautical Applications. Massachusetts Institute of Technology Report, 1 November 1973 through 31 October 1974, for Office of Naval Research, April 14, 1975.
2. Mangler, K. W.; and Smith, J. H. B.: Calculation of the Flow Past Slender Delta Wings with Leading Edge Suction Analogy. NASA TN D-3767, 1966.
3. Polhamus, E. C.: A Concept of Vortex Lift of Sharp-Edge Delta Wings Based on a Leading Edge Suction Analogy. NASA TN D-3767, 1966.
4. Weber, James A.; Guenter, W. Brune; et al: A Three-Dimensional Solution of Flows over Wings with Leading Edge Vortex Separation. AIAA Paper No. 75-866, Presented at AIAA 8th Fluid and Plasma Dynamics Conference, Hartford, Conn., June 16-18, 1975.
5. Rao, B. M.; and Jones, W. P.: Theoretical Prediction of Airload on Thin Delta in Incompressible Flow. Texas A&M University, TEES-3029-75-01, January 1975.
6. Scruggs, R. M.; and Dixon, C. J.: Theoretical and Experimental Investigations of Jet Parallel to Wing in Cross Flow. Final Report, Office of Naval Research Contract, Lockheed-Georgia Engineering Report LG75ER0028, April 30, 1975.
7. Sarpkaya, Turgut; and Garrison, C. J.: Vortex Formation and Resistance in Unsteady Flow. Transactions of the ASME, March 1963.
8. Campbell, J. F.: Effects of Spanwise Blowing on the Pressure Field and Vortex-Lift Characteristics of a 44° Swept Trapezoidal Wing. NASA TN D-7907, 1975.
9. Dixon, C. J.; Theisen, J. G.; and Scruggs, R. M.: Theoretical and Experimental Investigation of Vortex Lift Control by Spanwise Blowing. Vol. 1, Experimental Research; Vol. II, Three Dimensional Theory for Vortex-Lift Augmentation. Final Report, Office of Naval Research Contract, Lockheed-Georgia Engineering Report LG73ER0169, September 15, 1973.

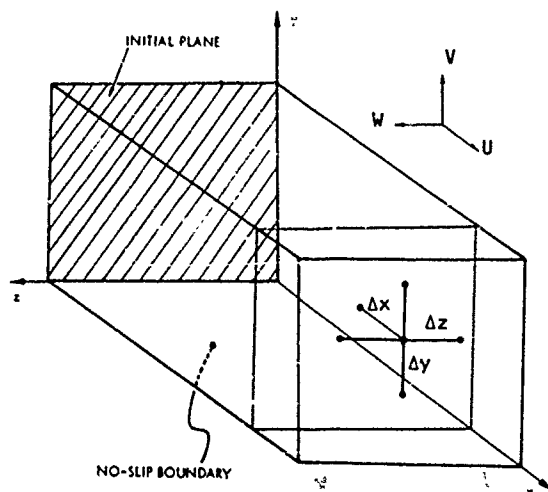


Figure 1. Coordinate System and Domain of Integration

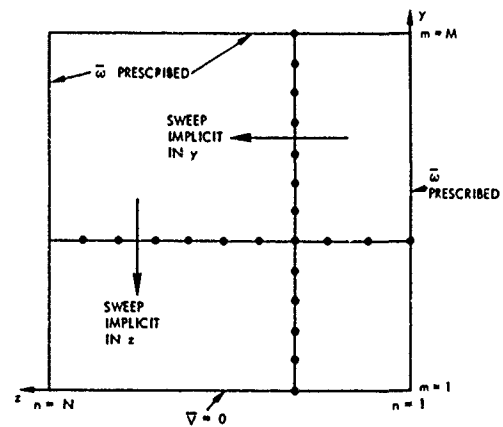


Figure 2. Alternating Direction Implicit Sweeping Procedure

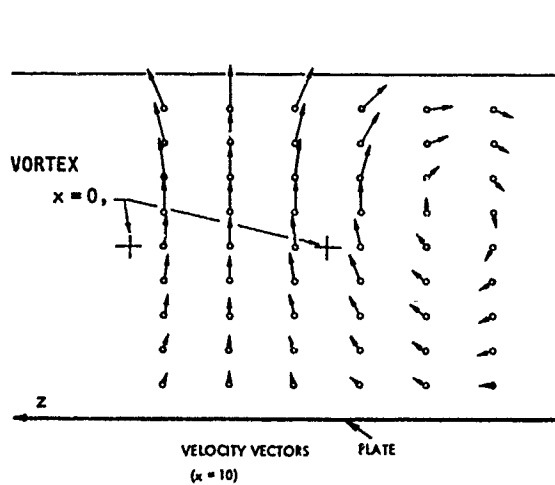


Figure 3. Pair of Counter-Rotating Vortices Over a Plate

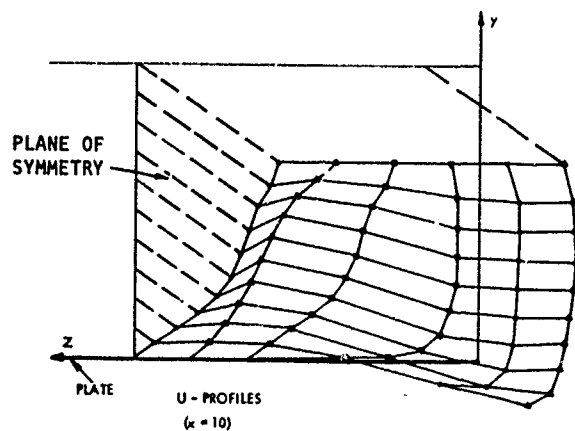


Figure 4. Wake Defect Due to Pair of Vortices in Figure 3

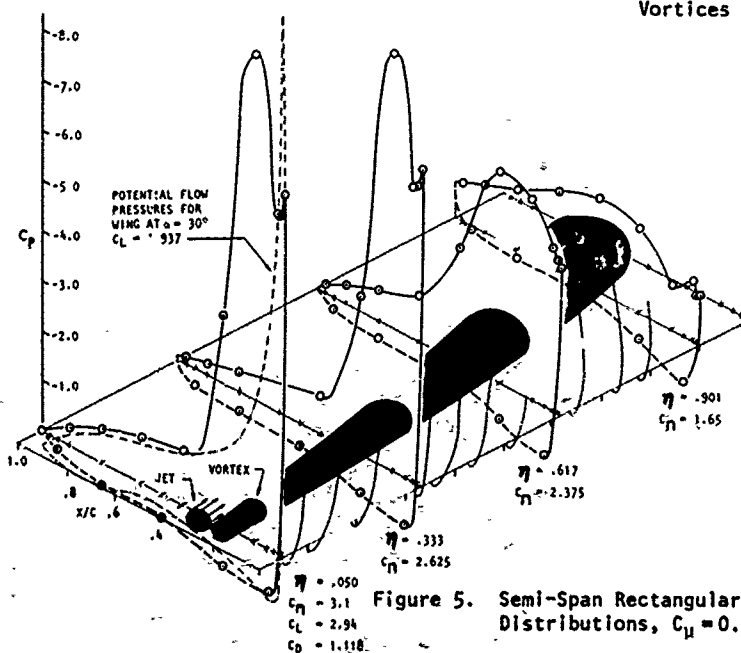
Figure 5. Semi-Span Rectangular Wing Pressure Distributions,  $C_{u1} = 0.769$ ,  $\alpha = 30^\circ$



Figure 6. Flow Visualization of Vortex on Rectangular Wing with Spanwise Blowing

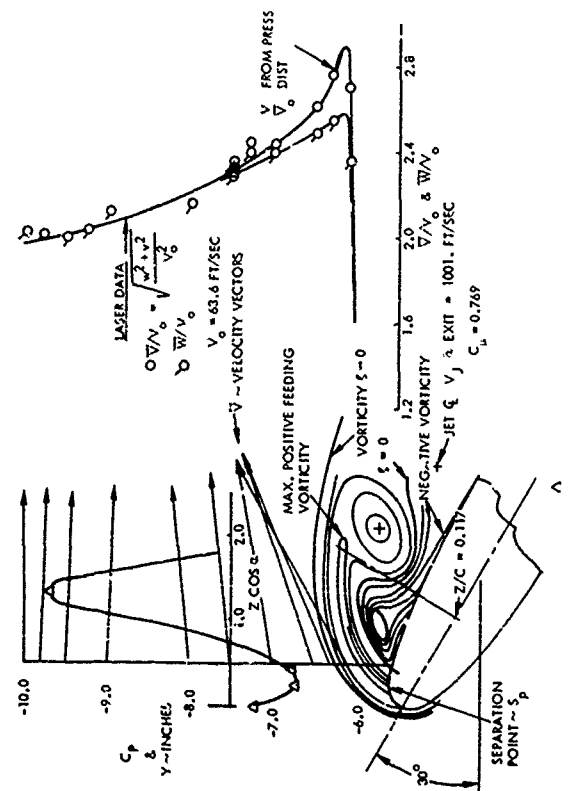


Figure 7. Composite of Experimental Results,  $\eta = 33.3\%$

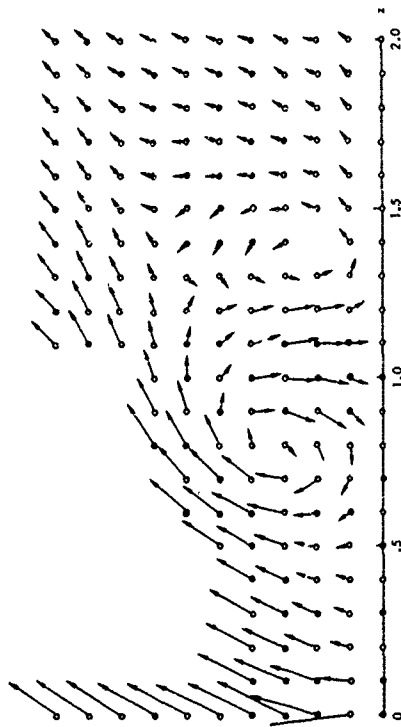


Figure 8. Stable Flow with Counter-Vortex,  $x = 3$ ,  $\alpha = 25^\circ$ , No Downstream Recovery; Initial Positions:  $(y_j, z_j) = (.4, 1.0)$ ,  $(y_v, z_v) = (.4, .5)$

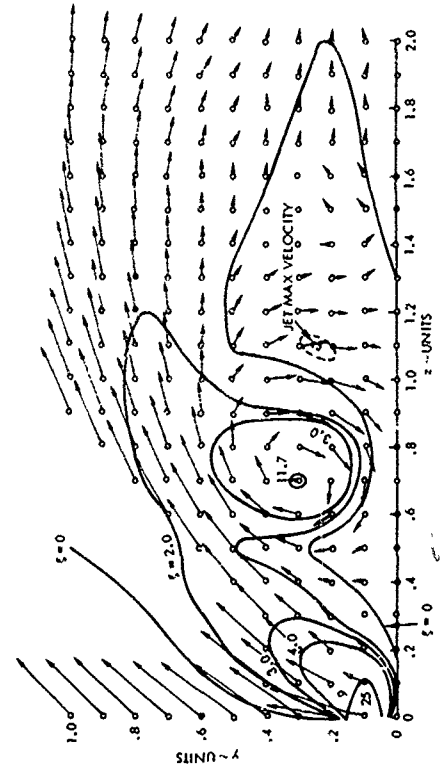


Figure 9. Relation of Isovorticity and Velocity Vectors @  $x = 3.0$ ,  $\alpha = 25^\circ$ . Recovery @ 4.5 Chordlengths Downstream. Vortex Input @  $x = 0$ ,  $y = .4$ ,  $z = 0.5$ ; Jet Input @  $y = .4$ ,  $z = 1.0$

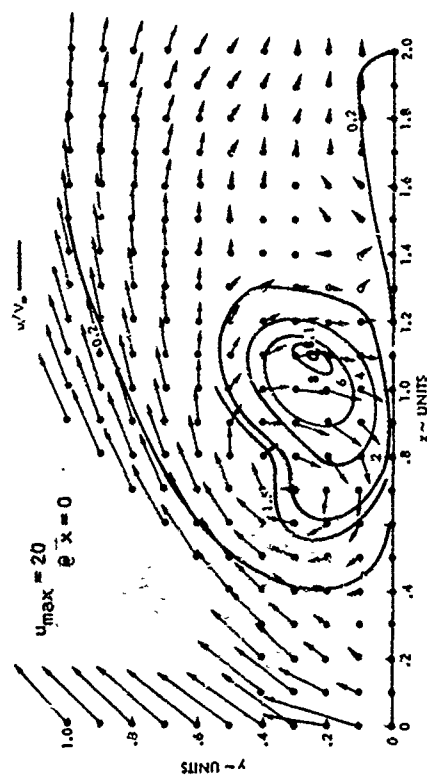


Figure 10. Relation of  $u$  Isovels and  $yz$  Velocity Vectors @  $x = 3.0$ ,  $\alpha = 25^\circ$ . Recovery @ 4.5 Chordlengths Downstream. Vortex Input @  $x = 0$ ,  $y = .4$ ,  $z = 0.5$ ; Jet Input @  $y = .4$ ,  $z = 1.0$ .

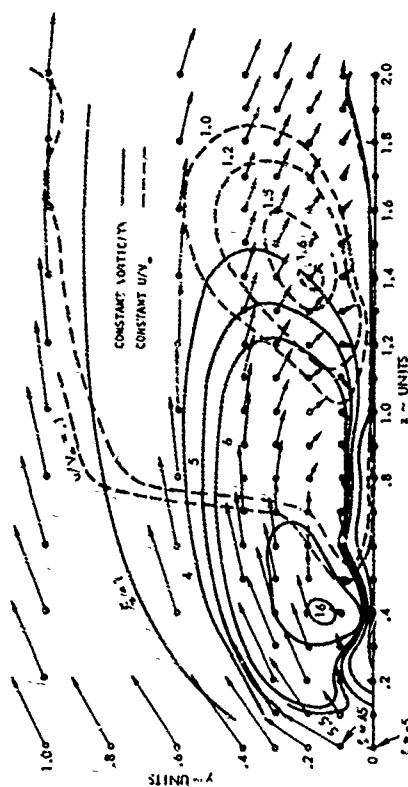


Figure 11. Vortex Formation Without Vortex Input,  $x = 5.00$ ,  $\alpha = 25^\circ$ . Jet Input @  $y = .4$ ,  $z = 1.0$   $u_{max} = 20$

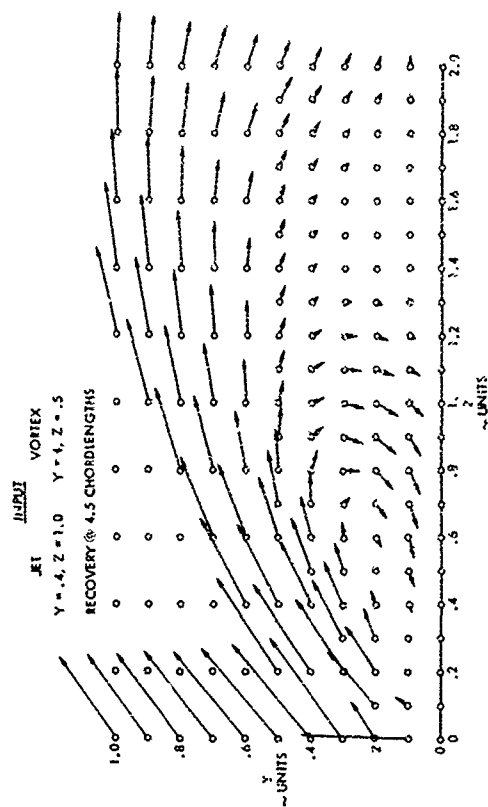


Figure 12. Effect of Leading Edge Input Vorticity,  $\xi = 4.3$  @  $Y = Z = 0$ ,  $X = 3.0$ ,  $\alpha = 25^\circ$

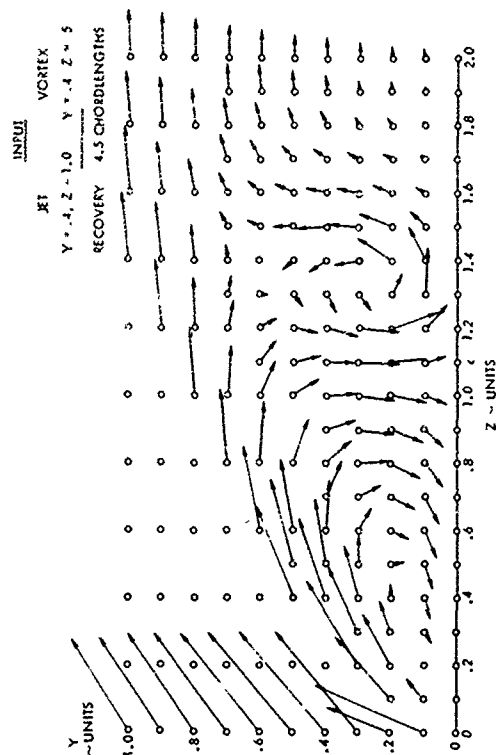


Figure 13. Effect of Leading Edge Input Vorticity,  $\xi = 0$  @  $Y = Z = 0$ ,  $X = 3.0$ ,  $\alpha = 25^\circ$

# COMPARISONS OF THEORETICAL AND EXPERIMENTAL PRESSURE DISTRIBUTIONS ON AN ARROW-WING CONFIGURATION AT SUBSONIC, TRANSONIC, AND SUPERSONIC SPEEDS

by

Marjorie E. Manro, Senior Specialist Engineer, Loads Research Group, M.S. 73-33,  
Boeing Commercial Airplane Company, Seattle, Washington 98124, U.S.A.

Percy J. Bobbitt, Head, Theoretical Aerodynamics Branch, M.S. 360,  
NASA Langley Research Center, Hampton, Virginia 23665, U.S.A.

John T. Rogers, Head, Loads Research Group, M.S. 73-33,  
Boeing Commercial Airplane Company, Seattle, Washington 98124, U.S.A.

## SUMMARY

A wind-tunnel test of an arrow-wing body configuration consisting of flat and twisted wings, as well as a variety of leading- and trailing-edge control surface deflections, has been conducted at Mach numbers from 0.40 to 2.50 to provide an experimental data base for comparison with theoretical methods. Theory-to-experiment comparisons of detailed pressure distributions have been made using current state-of-the-art attached- and separated-flow methods. The purpose of these comparisons was to delineate conditions under which these theories are valid for aeroelastic calculations and to explore the use of empirical methods to correct the theoretical methods where theory is deficient. It was determined that current state-of-the-art attached-flow and empirical methods were inadequate to predict aeroelastic loads for this configuration. The separated-flow theories now under development show promise of being a possible tool to solve this problem.

## ABBREVIATIONS AND SYMBOLS

b	wingspan	$C_N$	normal-force coefficient	MS	model station
BL	buttock line	$C_n$	section normal-force coefficient	T.E.	trailing edge
c	chord length	$C_p$	pressure coefficient	x, y, z	orthogonal coordinates
$\bar{c}$	reference chord	L.E.	leading edge	$\alpha$	angle of attack
$C_{M.25}$	pitching-moment coefficient	M	Mach number	$\delta_{T.E.}$	trailing-edge control surface deflection

## INTRODUCTION

Accurate analytical techniques for predicting the magnitude and distribution of aeroelastic loads are required in order to design, in an optimum manner, the structure of large, flexible aircraft. Uncertainties in the characteristics of loads may result in an improper accounting for aeroelastic effects, leading to understrength or overweight designs, performance penalties, and unacceptable fatigue life. Moreover, correct prediction of loads and the resultant structural deformations is essential to the determination of control power requirements, control surface moments, and aircraft stability and control characteristics. The alternative to the development of satisfactory analytical techniques is the employment of expensive, time-consuming wind-tunnel tests for each aircraft configuration. In addition, the ability to perform meaningful parametric or tradeoff studies is severely limited by the lack of accurate prediction techniques.

The problem of accurate load prediction becomes particularly difficult for aircraft with highly swept wings and critical design conditions in the transonic speed regime. Highly swept leading edges precipitate flow separation and the formation of a leading-edge vortex; transonic flight is synonymous with mixed-flow regions and embedded shocks. The degree to which our best state-of-the-art theoretical techniques can account for these flow conditions is known in only a few circumstances. Obviously, attached-flow theories, including those that properly treat mixed-flow regions, cannot be expected to do well at moderate and large angles of attack when the leading-edge vortex is a dominant factor. However, theories that do account for the leading-edge vortex, and yield detailed pressure distributions, are often limited as to the wing geometries they can treat. Several methods, now under development, are far more versatile in terms of wing shape and show promise of improved accuracy as well. Clearly, if we are to continue to improve our predictive techniques, the limitations of all these methods need to be quantified through detailed comparisons of theoretical and experimental pressures for configurations of current interest.

In the structural design of an aircraft, wind-tunnel pressure tests on a single wing shape (with twist and camber) are extrapolated by means of an aeroelastic solution to obtain the load distributions for all other elastically deformed shapes of that wing. In this process, equations are used that relate the changes in local pressure to changes in structural deformation. Methods for doing this for high-aspect-ratio wings at subsonic speeds are well developed and have been substantiated by flight tests. However, for highly swept wings and/or transonic flight conditions where various nonlinear phenomena become important, no satisfactory methods are available. Until such tools are developed, the need will remain for wind-tunnel test programs simulating each flight design condition on the flexible airplane.

The purpose of this paper is to report on the results of a comprehensive study carried out to define the ability of current state-of-the-art linear and separated-flow techniques to predict detailed pressures over a highly swept arrow-wing configuration with flat and twisted wings. The wings were provided with both leading- and trailing-edge controls, and the flat wing could be fitted with either a sharp or rounded leading edge. The ability of theory to predict the detailed pressures associated with control-surface deflection or leading-edge shape was examined. Comparisons will be shown of theoretical and

experimental pressures for the flat wing as well as for the incremental pressure changes due to twist. The latter is of interest since this calculation is similar to that often made to correct basic rigid-model wind-tunnel results for aeroelastic effects on the full-scale airplane.

The results of the subsonic and transonic program are summarized in NASA SP-347 (ref. 1) and discussed at greater length in reference 2.

### MODEL AND TEST DESCRIPTION

The wind-tunnel-model configuration selected for this study is a highly swept ( $71.2^\circ$ ) thin wing on a slender body. The planform and basic geometry of the model are shown in figure 1. Two complete wings were constructed, one with no camber or twist and one with no camber but a spanwise twist variation (see fig. 1). Both wings were designed to permit deflection of either partial- or full-span, 25-percent chord, trailing-edge control surfaces with brackets to allow streamwise deflections of  $\pm 4.1^\circ$ ,  $\pm 8.3^\circ$ ,  $\pm 17.7^\circ$ , and  $\pm 30.2^\circ$ , as well as  $0^\circ$ . In addition, the flat wing was provided with removable leading-edge segments that extended over 15 percent of the streamwise chord. These segments permitted testing of the leading edge drooped  $5.1^\circ$  and  $12.8^\circ$  as well as undeflected. A leading-edge segment was constructed with a sharp leading edge to examine the effects of leading-edge shape. Figure 1 shows the basic rounded leading edge with the sharp leading edge superimposed.

The 217 pressure orifices on the wing were equally divided into 7 streamwise sections on the left wing. Pressure taps were located on both the top and bottom surfaces at the chordwise locations shown in figure 2. The body orifices were arranged in 5 streamwise rows of 15 orifices each. An additional 8 orifices in the area of the wing-body junction made a total of 83 orifices on the left side of the body.

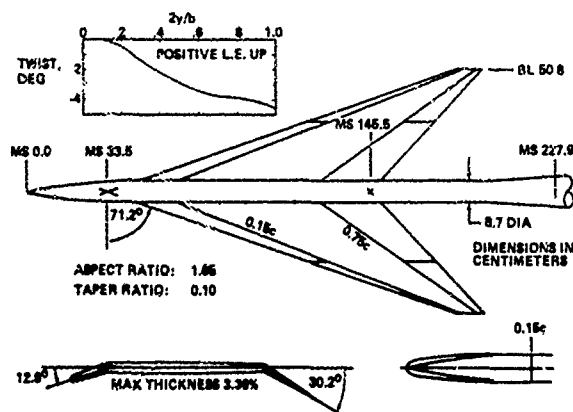


Figure 1. — General Arrangement and Characteristics

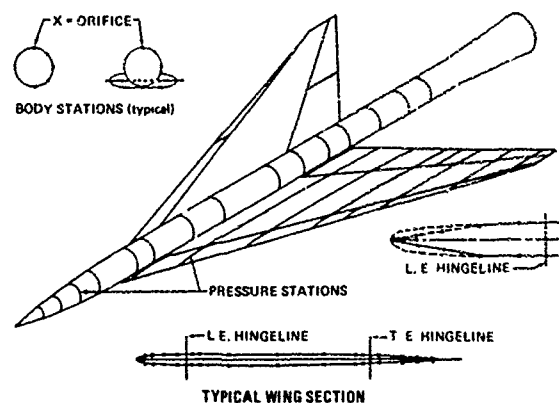


Figure 2. — Pressure Orifice Locations

The model was constructed of steel to minimize aeroelastic deflections. To ensure close control of the model dimensions, a computerized lofting program was used to provide data for machining the model components using numerically controlled operations.

The model was tested in the Boeing Transonic Wind Tunnel (BTWT) and in the supersonic 9-by 7-foot leg of the NASA Ames Unitary Wind Tunnel. The former is a continuous-flow, closed-circuit, atmospheric facility with a 12.5-percent porosity test section measuring 8 by 12 by 14.5 feet; the latter is a continuous-flow, closed-circuit, variable-density facility with a test section measuring 7 by 9 by 18 feet. Seven Mach numbers from 0.40 to 1.11 were tested in the BTWT, with angle of attack varying from  $-8^\circ$  to  $+16^\circ$ . In the Ames facility, data were obtained primarily at Mach numbers of 1.7, 2.1, and 2.5. The major configurations tested are shown in tables 1 and 2.

Table 1. — Summary of Conditions Tested in Boeing Transonic Wind Tunnel

WING	TRAILING EDGE	LEADING EDGE DEFLECTION, DEGREES	TRAILING EDGE DEFLECTION, DEGREES
ROUNDED LEADING-EDGE FLAT WING	FLAT	0	$0, \pm 4.1, \pm 8.3, \pm 17.7, \pm 30.2$
			PARTIAL SPAN $\pm 8.3, \pm 17.7$
			PARTIAL SPAN $\pm 8.3, \pm 17.7$
			$0, \pm 4.1, \pm 8.3, \pm 17.7$
SHARP LEADING-EDGE FLAT WING	FLAT	0	0
ROUNDED LEADING-EDGE TWISTED WING	TWISTED	0	$0, \pm 4.1, \pm 8.3, \pm 17.7, \pm 30.2$

MACH NUMBERS: 0.40, 0.70, 0.85, 0.95, 1.00, 1.05, 1.11  
ANGLE OF ATTACK:  $-8^\circ$  TO  $+16^\circ$  ( $2^\circ$  INCREMENTS)

Table 2. — Summary of Conditions Tested in NASA Ames Unitary Wind Tunnel

WING	TRAILING EDGE	LEADING EDGE DEFLECTION, DEGREES	TRAILING EDGE DEFLECTION, DEGREES
ROUNDED LEADING-EDGE FLAT WING	FLAT	0	$0, \pm 4.1, \pm 8.3$
		5.1	0
SHARP LEADING-EDGE FLAT WING	FLAT	0	0
		5.1	0
ROUNDED LEADING-EDGE TWISTED WING	TWISTED	0	$0, \pm 8.3$

MACH NUMBERS: 1.70, 2.10, 2.50  
ANGLE OF ATTACK:  $-8^\circ$  TO  $+14^\circ$  ( $2^\circ$  INCREMENTS) +  $15^\circ$

### THEORETICAL METHODS

Theoretical calculations utilized in this study are based on inviscid theories for both attached and detached flows. Results from two attached-flow theories are discussed: one uses the linear, subsonic/supersonic, constant-pressure-panel formulation, and the second uses a panel solution of the exact incompressible-flow equation satisfying the exact boundary condition on the configuration surface.

The separated-flow method is based on distributions of quadratically varying doublet panels. Since this approach is still under development, and only tentative results are available, the term "state-of-the-art" used in the Introduction is not strictly applicable. However, the older separated-flow methods can handle only simple wing geometries, and theory-experiment comparisons for an arrow wing would be of limited usefulness.

As noted in the Introduction, attached-flow theories can be expected to yield good agreement with experiment only at low angles of attack. The strong influence of the leading-edge vortex flow for angles of attack greater than a few degrees clearly indicates the need for detached-flow theories for detailed loads prediction. These theories should be able to more closely predict loading trends at the higher angles of attack even though the geometry they can handle is less general than that of the more mature attached-flow methods. Additional details of the analytical methods are discussed below.

#### Attached-Flow Theories

The primary analysis method used for pressure calculations in this study was the unified subsonic/supersonic panel technique of FLEXSTAB, which was developed by Boeing under NASA Ames sponsorship (see refs. 3 and 4). The FLEXSTAB system of digital computer programs uses linear theory to evaluate the static and dynamic stability, the inertial and aerodynamic loading, and the resulting elastic deformations of aircraft configurations. The aerodynamic module contained in the FLEXSTAB system is based on the constant-pressure-panel method developed by Woodward (refs. 5 and 6) to solve the linearized potential-flow equations for supersonic and subsonic speeds with planar boundary conditions. The method is also used at transonic speeds, where the nonlinear terms not accounted for may be important.

Figure 3 shows the distribution of panels used in this analysis. Line sources and doublets are distributed along the longitudinal axis of the body to simulate its thickness and lifting effects. Similarly, source and vortex panels are placed in the plane of the wing to simulate its thickness and lifting effects. To account for the interference effects between the wing and body, constant-pressure vortex panels are placed on a shell around the body. This "interference" shell serves to cancel the normal velocity components on the body induced by the wing.

At subsonic Mach numbers and the high supersonic Mach numbers, 60 line singularities, 168 interference panels, and 160 wing panels were used to represent the configuration. For the very low supersonic Mach numbers (1.05 and 1.11), the number of interference panels had to be greatly increased (to 330) to overcome instabilities associated with the solution. The edges of the wing panels were chosen to coincide with the control surface hingelines and breaklines. Note on figure 3 that the panels are of nearly equal width and, in the chordwise direction, panel edges are at constant percent chord with closer spacing at the leading edge and the hingelines.

The second attached-flow method used was the general method of Rubbert and Saaris (refs. 7, 8, and 9) for the numerical solution of nonplanar, three-dimensional boundary-value problems. The method solves the exact incompressible potential-flow equation (Laplace's equation), with compressibility effects incorporated via the Göthert rule. In contrast to FLEXSTAB, the Rubbert-Saaris (hereafter referred to as TEA-230) solution is not encumbered by the small perturbation approximation and is capable of treating problems of far more detail and generality than the linearized theories.

Figure 4 shows a typical paneling scheme used for the TEA-230 representation of the arrow-wing body model. The source panels are placed on the configuration surface; consequently, new paneling was required for each configuration. The linearly varying internal and trailing vortex panel networks are not shown.

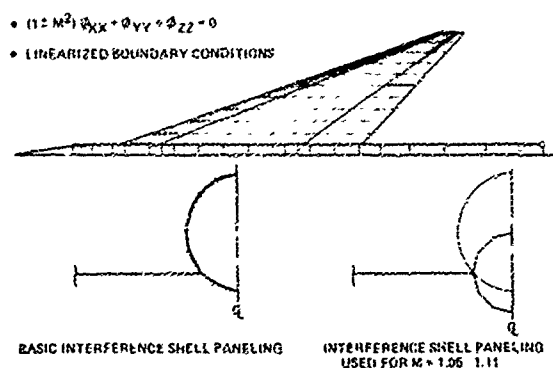


Figure 3. — FLEXSTAB Paneling Scheme

#### Detached-Flow Theories

The method chosen to predict the effect on wing pressures of the leading-edge spiral vortex was that of Weber, Brune, Johnson, Lu, and Rubbert (refs. 10 and 11). This method is capable of predicting forces, moments, and detailed surface pressures on thin, sharp-edged wings of arbitrary planform. The wing geometry is arbitrary in the sense that leading and trailing edges may be swept as well as curved or kinked.

The governing equations are the linear flow differential equation and nonlinear boundary conditions which require that the flow be parallel to the wing surface and that the free vortex sheet, springing from the leading and trailing edges, be aligned with the local flow and support no pressure jump. The Kutta condition is imposed and satisfied along all wing edges. This problem is solved numerically by an aerodynamic panel method. The configuration is represented by quadrilateral panels on all surfaces with quadratically varying doublet singularities distributed on them. The vortex core is modeled as a simple line vortex that receives vorticity from the free sheet through a connecting kinematic sheet. The set of nonlinear equations is solved by an iterative procedure, starting with an assumed initial geometry.

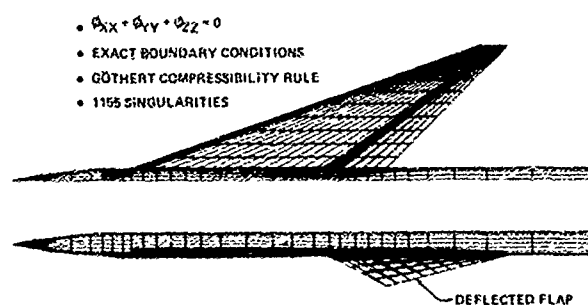


Figure 4. — TEA-230 Paneling Scheme

Figure 5 shows the paneling arrangement used on the wing. Note that the leading and trailing edges are extended to a point rather than chopped off to form a finite tip. This should have only a trivial effect on the answers obtained. The fuselage was not a part of the current model; instead, the wing external to the body was moved inboard to obtain a more realistic model of the wing alone. A total of 212 panels were used for this solution: 63 panels to describe the wing, 108 panels to describe the rolled-up vortex, and 41 panels to describe the wake. The current version of the program is restricted to incompressible flow.

The separated-flow computer program described above is still in its early stages of development. The capability for handling wing thickness, camber, and twist as well as a fuselage representation are now being added. In addition, the effects of compressibility (Göthert correction) and a new vortex model are being incorporated.

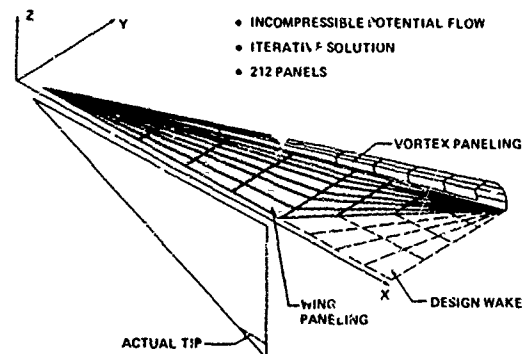


Figure 5. — 3-D Vortex Program Paneling Scheme

### TEST-THEORY COMPARISONS

The utility of any aerodynamic theory is judged by its ability to accurately predict flight or wind-tunnel results. Of course, these judgments should be made on the basis of theory-to-experiment comparisons for configurations and flight conditions similar to those to which one expects to apply the theory. With this in mind, and recognizing the limited amount of detailed pressure data available for arrow-wing configurations, the present program was initiated to provide basic experimental data and to examine the ability of some of our more common, and promising, theoretical techniques to correlate with experiment.

Theory-to-experiment comparisons were made over a range of Mach numbers from 0.40 to 2.50 using the FLEXSTAB system and at Mach numbers of 0.40 and 0.85 with the TEA-230 program. Both the flat- and twisted-wing configurations were analyzed, including the effect of deflecting control surfaces. This paper concentrates on results for the flat untwisted wing. Calculations using the separated vortex method are limited to the flat wing at a Mach number of 0.40.

To get an idea of the gross aerodynamic properties, a comparison is shown in figure 6 of experimental and theoretical normal force and pitching moment coefficients over the range of Mach numbers. Both the FLEXSTAB and TEA-230 calculations are in good agreement with experiment throughout the Mach number range at low and moderate angles of attack. However, at moderate angles of attack the agreement is fortuitous, and detailed comparisons of surface pressures are necessary to evaluate the adequacy of these theoretical solutions in describing the load distribution on the surfaces.

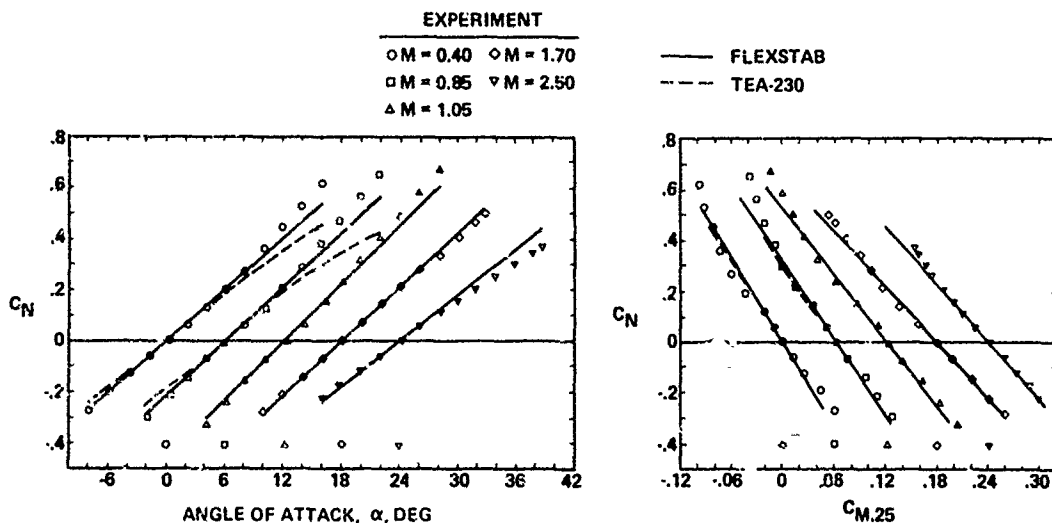


Figure 6. — Total Normal Force and Pitching Moment Coefficients, Flat Wing

A comparison of experimental and theoretical surface pressures on the flat-wing configuration is shown in figures 7 through 10 for four Mach numbers. Wing surface pressures at three spanwise wing stations and at angles of attack of approximately  $4^\circ$  and  $12^\circ$  are shown. At the low angle of attack, generally good agreement with experimental results was obtained by the use of either attached-flow theory. However, the lack of agreement of the upper-surface pressures at the most outboard station at Mach numbers of 0.85 and 1.05 is due to the start of vortex formation. The TEA-230 predictions are somewhat better near the leading edge than the FLEXSTAB results, which exhibit the typical linear theory leading-edge singularity.



At the higher angle of attack in figures 7 through 10, good agreement of the predictions with the experimental data is obtained only at the most inboard wing section ( $2y/b = 0.20$ ). At the two outboard stations, neither the FLEXSTAB nor the TEA-230 results compare well with experimental data. One final point of interest with respect to these chordwise pressure distributions is the diminishing effect of the leading-edge vortex as Mach number increases from 1.05 to 2.50.

○ UPPER EXPERIMENT    ▽ LOWER EXPERIMENT    — FLEXSTAB    --- TEA-230

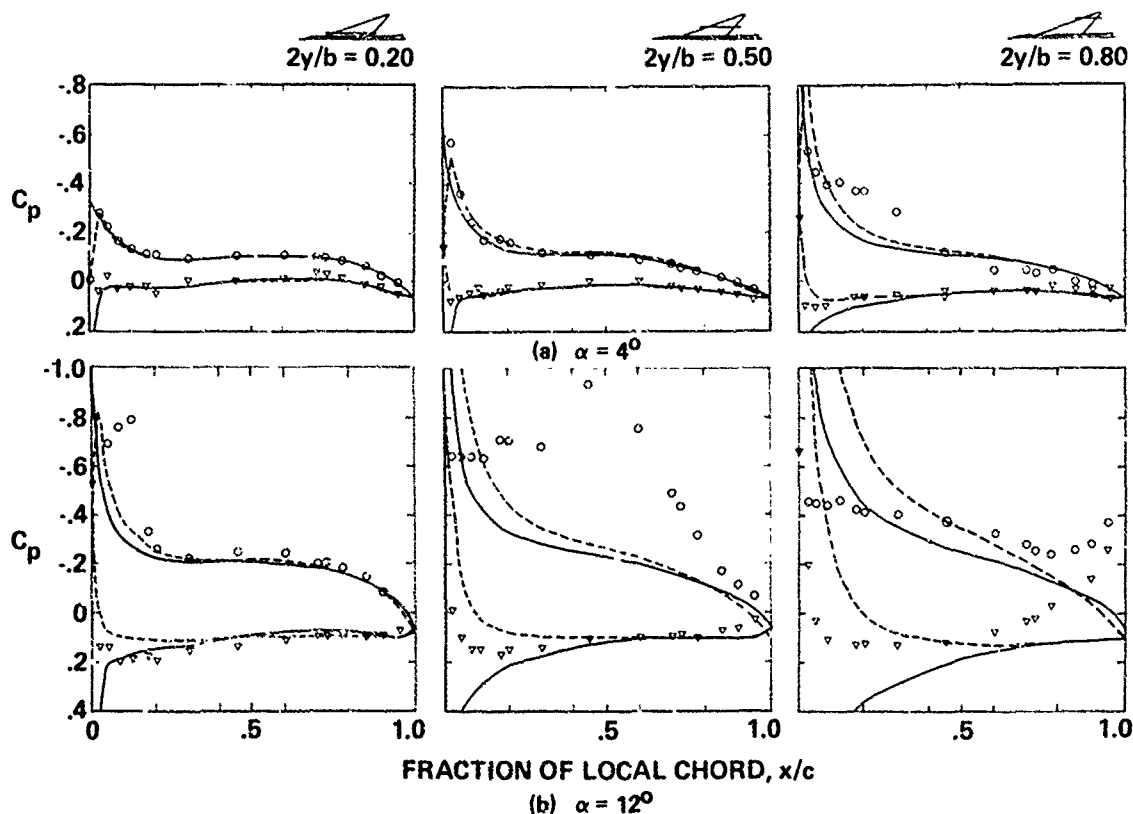


Figure 7. — Surface Pressure Distributions, Flat Wing,  $M = 0.85$

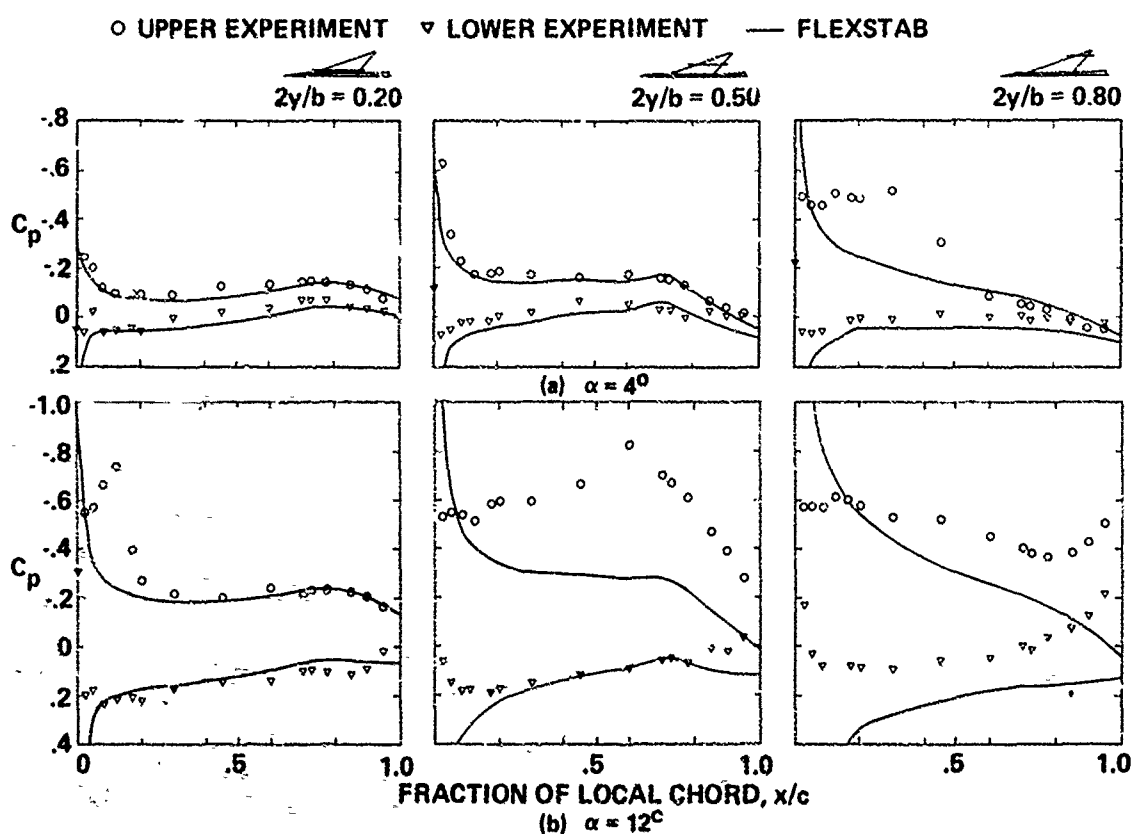
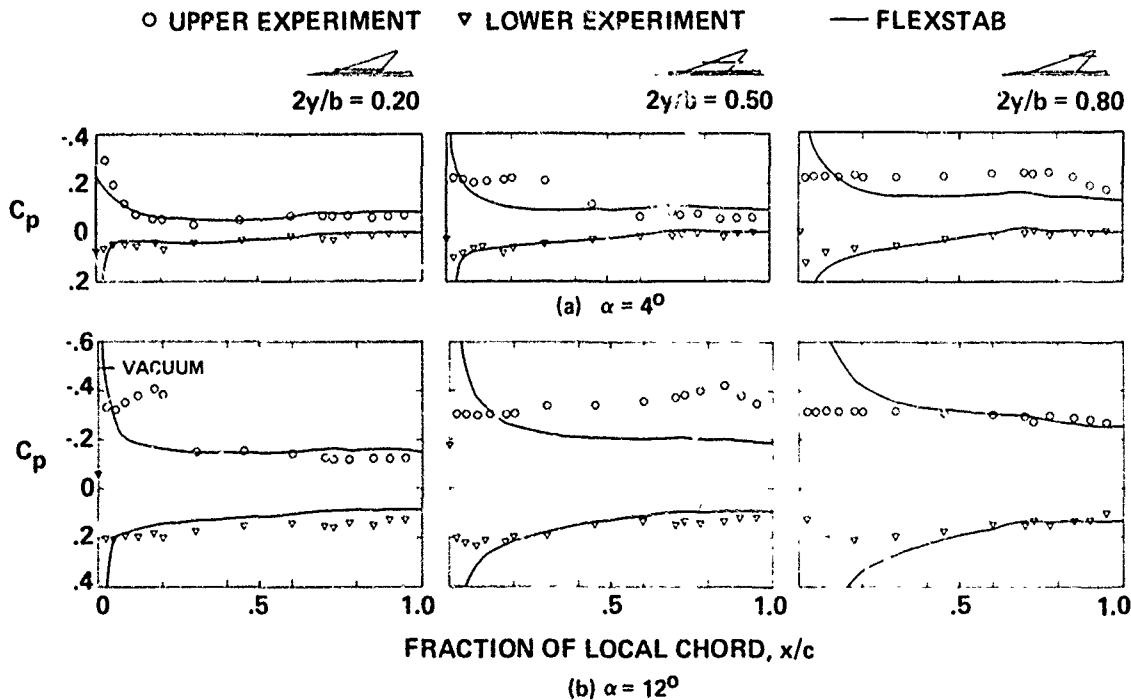
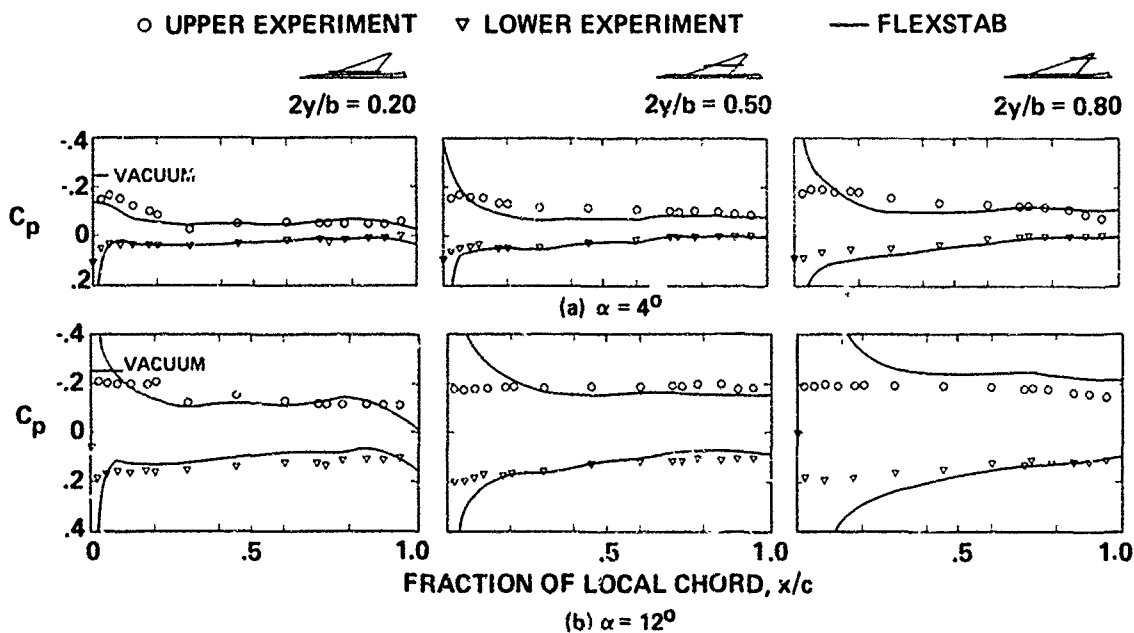


Figure 8. — Surface Pressure Distributions, Flat Wing,  $M = 1.05$

Figure 9. — Surface Pressure Distributions, Flat Wing,  $M = 1.70$ Figure 10. — Surface Pressure Distributions, Flat Wing,  $M = 2.50$ 

The spanwise load distributions shown in figure 11 demonstrate the same points made earlier with respect to the chord load distributions. The agreement is best at small angles of attack and near the wing root. At high angles of attack, the theory generally underpredicts the load level over the inboard half of the wing and overpredicts it outboard.

The discrepancies between theory and experiment in both chordwise and spanwise loading are obviously caused by the development of a spiral vortex above the wing leading edge at relatively low angles of attack. Plots of upper-surface isobars at Mach 0.40 can be used to better illustrate this. Figure 12 shows the formation of the vortex on the rounded leading-edge flat wing. Evidence of the vortex formation is first seen at an angle of attack of  $4^\circ$  and is clearly evident at  $8^\circ$ .

The development of this vortex with angle of attack is influenced by both the sharpness of the leading edge and the wing twist. The first of these influences can be seen by comparing the isobars of figure 12 with those of figure 13, which are for the sharp leading-edge flat wing. The vortex is more developed at  $4^\circ$  for the sharp leading edge than it was for the rounded one at  $6^\circ$  and continues to develop more rapidly with angle of attack. This phenomenon is less evident at the higher Mach numbers.

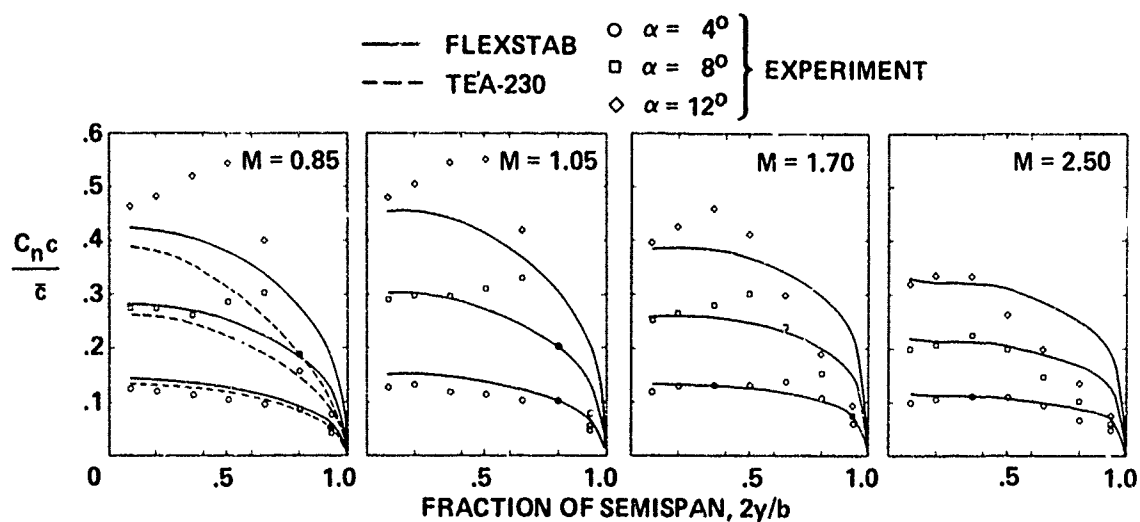


Figure 11. — Spanload Distributions, Flat Wing

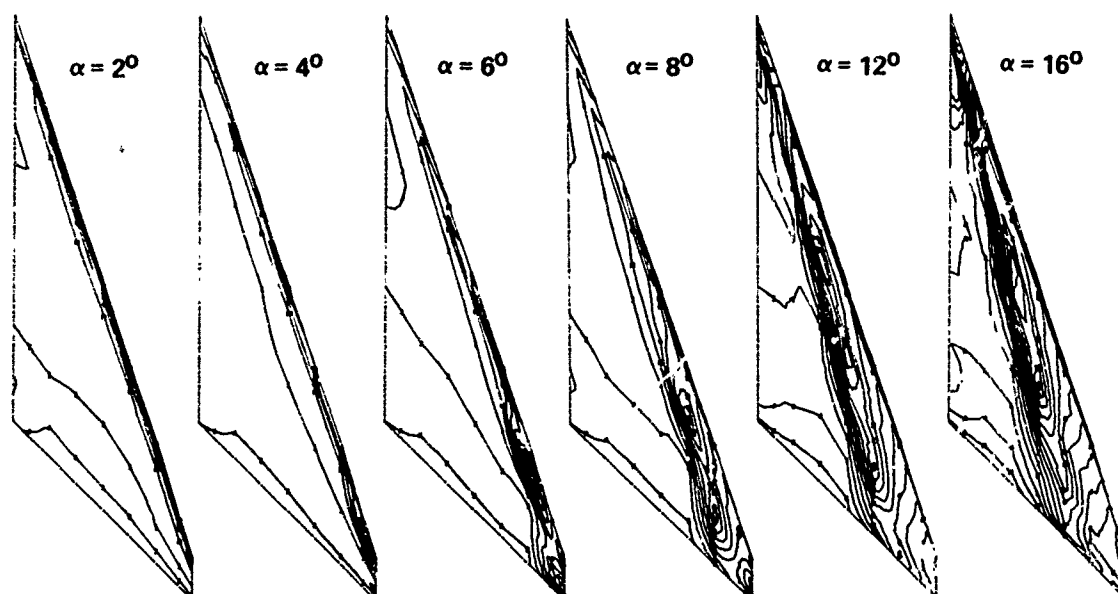
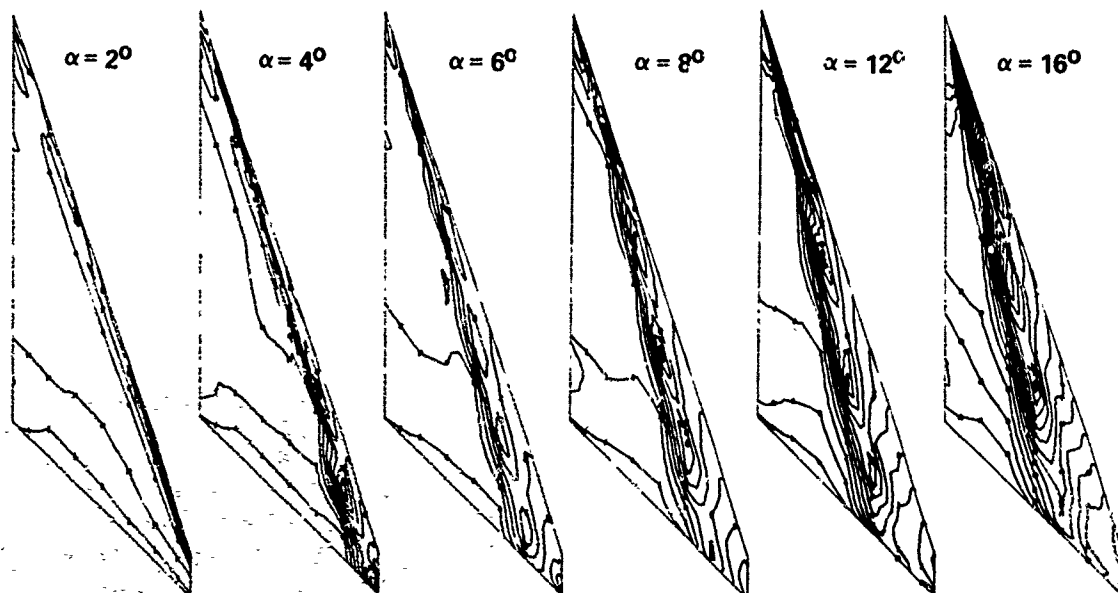
Figure 12. — Upper-Surface Isobars, Flat Wing, Rounded Leading Edge,  $M = 0.40$ Figure 13. — Upper-Surface Isobars, Flat Wing, Sharp Leading Edge,  $M = 0.40$ 

Figure 14 illustrates the effects of wing twist on vortex formation. An angle of attack of nearly  $8^\circ$  is required to produce the same kind of isobar configuration as was evident at  $4^\circ$  on the flat wing. Since the local angles of attack for the twisted wing are less than those of the flat wing, this behavior is expected.

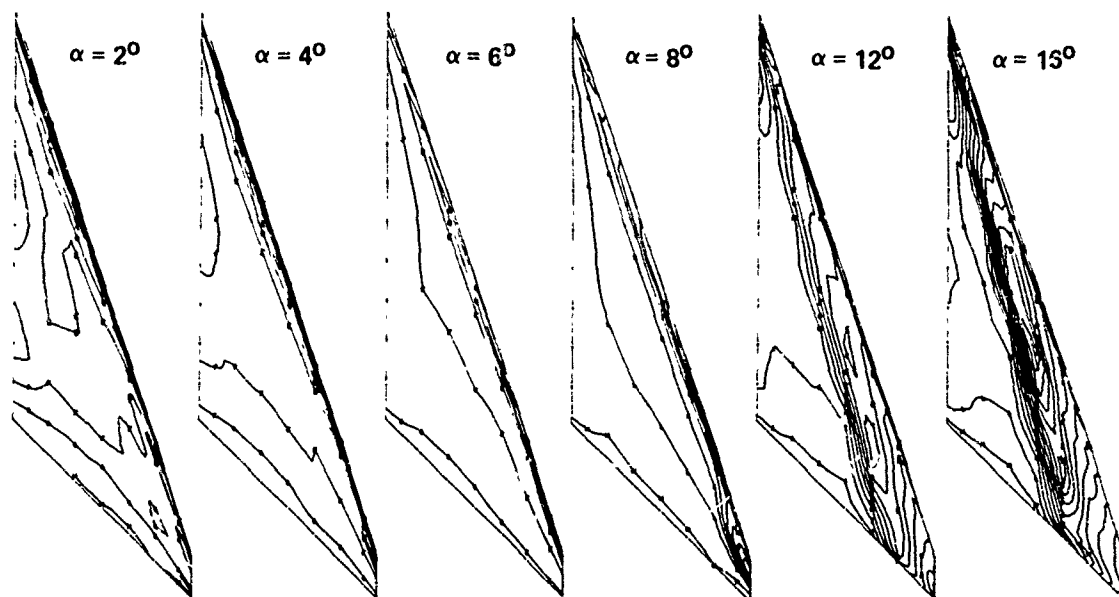


Figure 14. — Upper-Surface Isobars, Twisted Wing, Rounded Leading Edge,  $M = 0.40$

It is abundantly clear by now that the flow on the model is dominated by a separated leading-edge vortex except at small angles of attack and that the attached potential-flow theories do not adequately predict the effects of the vortex. It is of interest then to determine what improvements one can achieve if this vortex is accounted for in the theory. Figure 15 has been constructed for this purpose. Calculations carried out using the method of reference 10 are compared with experimental data and results of the FLEXSTAB program for a nominal angle of attack of  $12^\circ$  for the flat wing with sharp leading edge.

The comparison between experimental data and 3-D vortex results is surprisingly good, particularly considering the absence of the body in the theoretical model. Since the level of the peak lifting pressure is generally overpredicted, it is likely that the vortex is actually further from the surface than the theory is predicting. Nevertheless, the results are encouraging and the accuracy of the method should improve through further development.

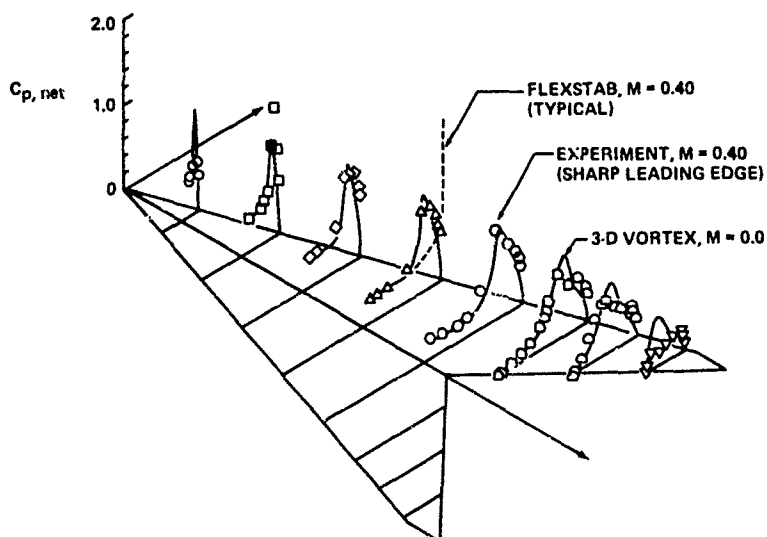


Figure 15. — Net Pressure Distributions, 3-D Vortex Program, Flat Wing,  $\alpha = 12^\circ$

The effects of full-span trailing-edge control deflection on the pressure distributions are particularly interesting. At low deflections and angles of attack, the pressure distributions at transonic speeds look typical of those for wing-flap combinations of moderate to low sweep. For the higher deflections and angles of attack, the loadings at the inboard wing sections are still similar to those of moderately swept wings with controls but, on the outboard sections, the distributions resemble those of the flat wing at an angle of attack. The increased wing circulation due to control deflection apparently causes the formation of vortex flow, and it in turn causes the incremental loading due to outboard control-surface deflection to be obscured.

Figure 16 (Mach 0.95) shows the effects of deflecting either the inboard or outboard portion of the trailing-edge control surface, as compared to zero deflection and full-span deflection. Only the upper-surface pressures are shown since they are the most important. Two particularly interesting items are the carryover effect on the outboard loading caused by deflecting only the inboard trailing-edge control surface and the loss in effectiveness at  $12^\circ$  angle of attack when the outboard portion of the trailing-edge control surface is deflected. This loss of effectiveness is due to the vortex that completely dominates the flow on the outboard region of the wing.

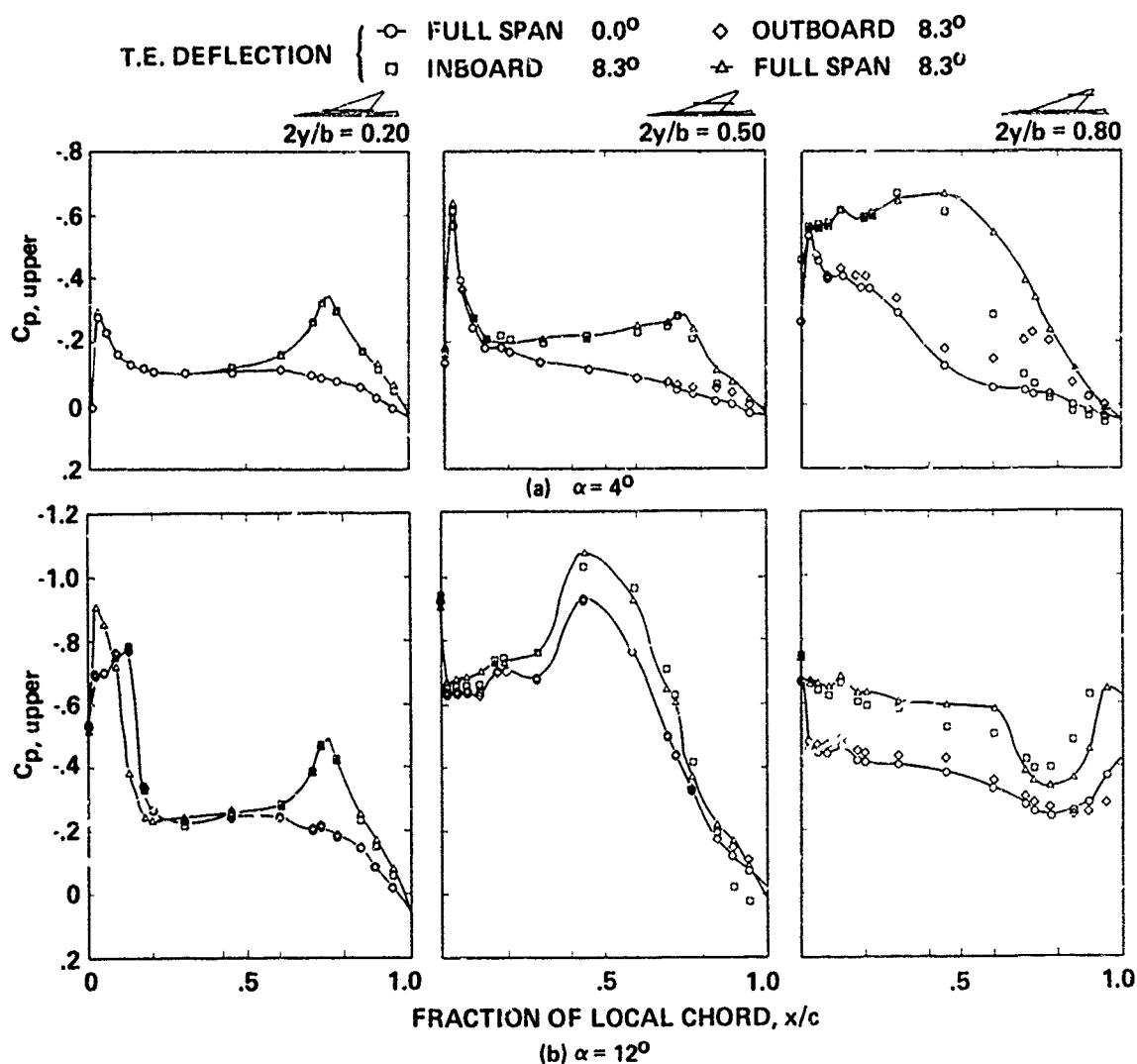


Figure 16. — Upper-Surface Pressure Distributions, Effect of Trailing-Edge Control Surface Deflection,  $M = 0.85$

The phenomena just described may perhaps be grasped more easily from the spanload plots given in figure 17. It clearly shows the incremental loading due to inboard, outboard, and full-span control surfaces at  $4^\circ$  angle of attack whereas at  $12^\circ$  the curves for zero and outboard control-surface deflection are essentially the same. The fact that the inboard and full-span control-surface deflections yield the same spanload distributions is clear evidence of the ineffectiveness of the outboard control surface at high angles of attack.

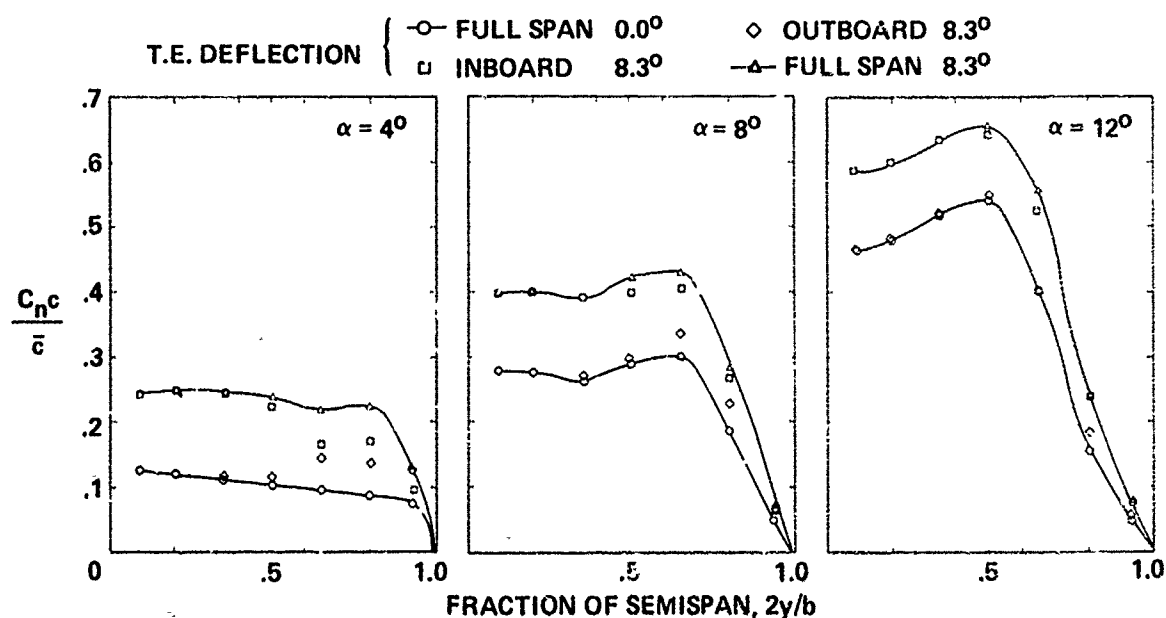


Figure 17. — Spanload Distributions, Effect of Trailing-Edge Control Surface Deflection,  $M = 0.85$

Data similar to that described for the subsonic Mach number is shown in figures 18 and 19 for Mach 2.1. As in the lower Mach number case, the inboard control surface is much more effective than the outboard at all angles of attack. However, in contrast to the low Mach number results, the outboard control surface still retains some of its effectiveness at higher angles of attack. A reduction of the induced lift over the forward portion of the wing due to control-surface deflection coupled with the natural weakening of the leading-edge vortex with increasing Mach number are probably responsible for this effect.

The attached-flow theories have been used to predict pressure distributions with the trailing-edge control surface deflected. The data shown in figure 20 for three Mach numbers (0.40, 0.85, 2.10) are for the control surface deflected  $2.3^\circ$  and the model at  $0^\circ$  angle of attack. The station at  $2y/b = 0.65$  is used, since the agreement between theory and experiment is typical of that obtained at other spanwise stations. The calculations from TEA-230 are included only for Mach 0.40. It is apparent that the prediction of the pressures at the leading edge and at the hingeline are much better with this method. FLEXSTAB overpredicts the pressures on the control surface at all Mach numbers shown, although at this angle of attack the distribution forward of the hingeline is quite good except at the leading edge.

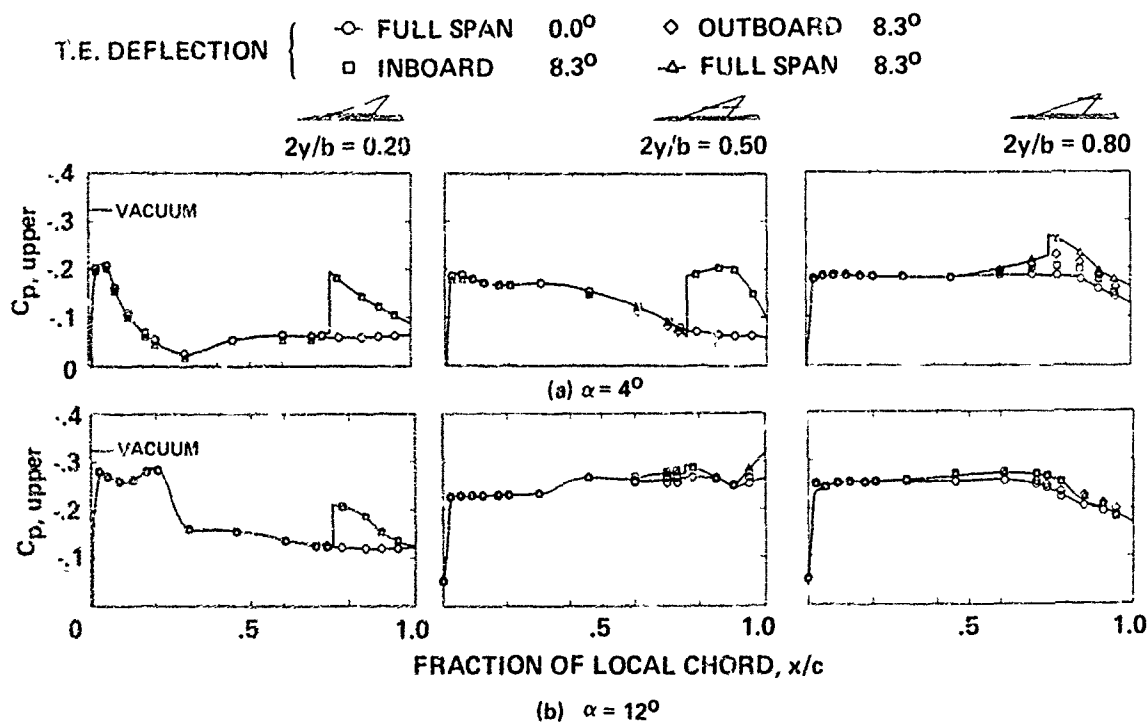


Figure 18. — Upper-Surface Pressure Distributions, Effect of Trailing-Edge Control Surface Deflection,  $M = 2.10$

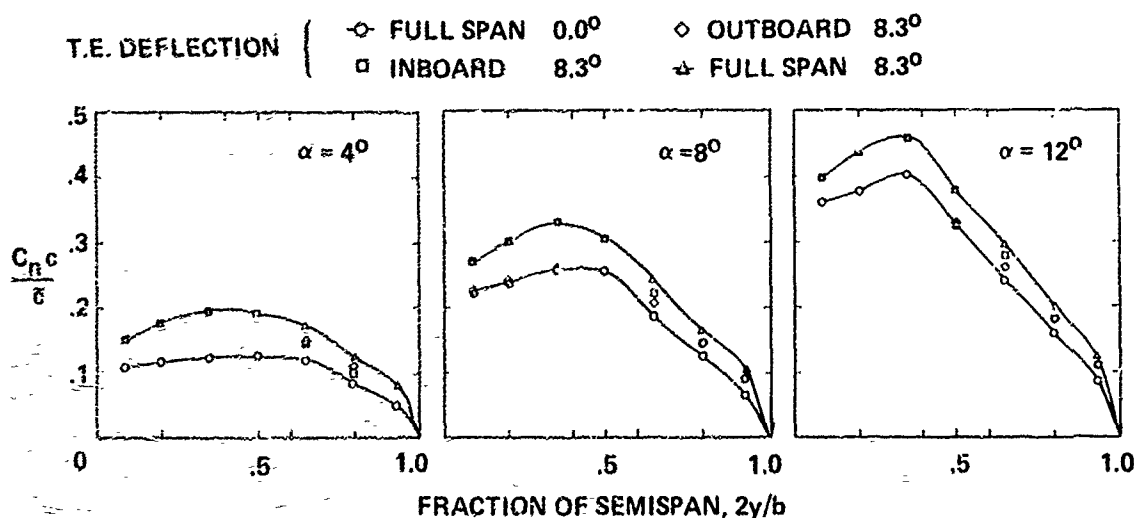


Figure 19. — Spanload Distributions, Effect of Trailing-Edge Control Surface Deflection,  $M = 2.10$

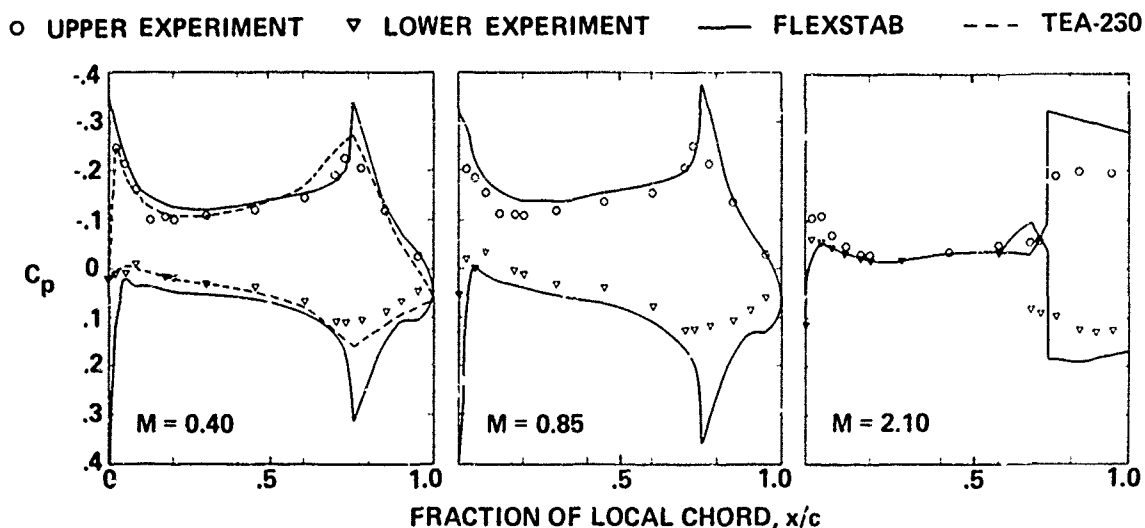


Figure 20. — Surface Pressure Distributions, Flat Wing,  $2\gamma/b = C.65$ ,  $\delta_{T.E.} = 8.3^\circ$ ,  $\alpha = 0^\circ$

The preceding comparisons have shown that the attached-potential-flow theories are able to predict experimental pressures for this configuration at only small angles of attack and control-surface deflections. The effects of Mach number do not appear to be particularly noticeable in the data at Mach 1.05 and below. However, it is quite evident for Mach numbers of 1.7 and above that the character of the experimental chordwise pressure distributions are changing as the strength of the leading-edge vortex diminishes. The test-theory comparisons at Mach 1.05 were generally as good as those at the subsonic Mach numbers.

There were no large differences between the TEA-230 and the FLEXSTAB results in comparison with experiment. TEA-230 with its on-the-surface paneling and boundary conditions predicted more closely the correct pressures near the wing leading edge and on the deflected control surface than did the linearized FLEXSTAB. For configuration development at subsonic speeds, the TEA-230 method is preferred to the FLEXSTAB method because of its ability to better predict detailed surface pressures. For calculating load distributions, the FLEXSTAB method is generally as adequate as the TEA-230 method and is easier to implement. It is also applicable at supersonic speeds and includes the required aeroelastic solution.

### EMPIRICAL CORRECTIONS

For many conditions the available theories do not give adequate results for detail design. The aeroelastic solution provides the means for translating the aerodynamic load distributions obtained from wind-tunnel tests on a single shape to the load distributions on the elastically deformed airplane. Equations are used that relate the changes in local aerodynamic pressure to changes in structural deformations. It is desirable to introduce aerodynamic corrections based on experimental data that would improve the accuracy of the theoretical estimate of elastic increments. The range and scope of these corrections vary greatly in complexity and, for low-aspect-ratio configurations, their utility has not been established.

The simplest type of elastic correction is to scale experimental aerodynamic parameters by the ratio of theoretically calculated elastic-to-rigid values of the parameter in question. This scheme has limited value for structural design because it does not provide an improvement of the load distribution. A very successful method that has been well developed for high-aspect-ratio surfaces at subsonic speeds has been to scale wing section characteristics along the span of the wing. Ideally, a method to correct low-aspect-ratio aerodynamics should influence both chordwise and spanwise loadings.

Since many low-aspect-ratio aerodynamic methods used for elastic predictions are based on some sort of aerodynamic influence coefficient (AIC) matrix, a method that modifies elements of the AIC matrix should prove useful. However, in such a matrix correction scheme, there are always more unknown correction factors than equations available, requiring a number of assumptions to obtain a solution. Table 3 summarizes schemes used for matrix corrections.

For this configuration, matrix correctors do not solve the problems. At small angles of attack, where the experimental data are most nearly linear, attached-flow theory without modification predicts the pressure distributions quite well. At higher angles of attack, the flow is nonlinear and linear corrections to the theory do not improve the prediction.

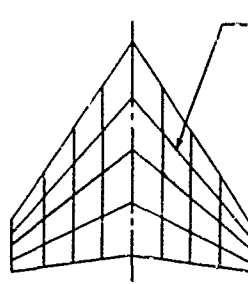
Examples of the variation of upper-surface pressure coefficients with angle of attack for several Mach numbers are shown in figure 21. Several chordwise locations on a typical spanwise station illustrate the region of linearity at low angles of attack and why linear corrections will not improve the match at higher angles of attack. The pressure coefficients on the lower surface, as well as the resulting net pressures, are just as nonlinear.

In practice, theoretical results are used mainly to correct experimental data from a rigid wind-tunnel model for the effects of the elastic deformation of the flight airframe. Examples of this procedure are shown in figures 22 and 23 for Mach 0.85 and 2.1 at an angle of attack of  $8^\circ$ . Here experimental data is taken for the flat wing (rigid model). A theoretical increment calculated for the known twist of the model (supposed elastic deformation) is added to obtain the predicted distribution. This result is compared with the twisted-wing data at the same angle of attack (deformed airframe). Three spanwise locations are shown. The section at  $\gamma/b = 0.35$  is typical of the other inboard stations. The error in predicting the pressure distribution is small,

primarily because the relative twist in this region is small. However, there are significant differences at the midspan and outboard stations between the experimental flat-wing data theoretically corrected for twist and the experimental twisted-wing data. This is because the twist has changed the location and strength of the leading-edge vortex. The theoretical corrections are linear and work only on those cases where the actual flow changes are also linear.

This example is indicative of the type of problems that must be overcome before a reliable prediction scheme for aerodynamic increments due to elasticity is available. These results also indicate that the use of empirical corrections in the aeroelastic solution to calculate flexible airplane loads is extremely risky, and much research is necessary to develop a practical method of using such corrections.

Table 3. - Experimental Corrections to Aerodynamic Influence Coefficient (AIC) Matrix



Panel load,  $L = f$  (incidence of all panels)

$$\{L\} = q [A] \{\alpha\}$$

$A_{jk}$  = analytically derived coefficients of the AIC matrix, effect of panel  $k$  on panel  $j$ ,  $L/q$  per radian

$P = \frac{L}{q}$  = experimental panel load coefficient, area

$\alpha$  = panel angle of attack, radians

$C$  = correction factors

General problem	$\frac{dP_1}{d\alpha} = C_{11}A_{11} + C_{12}A_{12} + \dots + C_{1N}A_{1N}$ $\frac{dP_2}{d\alpha} = C_{21}A_{21} + C_{22}A_{22} + \dots + C_{2N}A_{2N}$ $\frac{dP_N}{d\alpha} = C_{N1}A_{N1} + C_{N2}A_{N2} + \dots + C_{NN}A_{NN}$	<ul style="list-style-type: none"> <li>• <math>N</math> equations available</li> <li>• <math>N^2</math> unknowns</li> <li>• Assumptions are necessary to solve</li> </ul>	
Types of simplified equations	Equations	Type of solution	Assumptions
Scaling	$\left\{ \frac{dP}{d\alpha} \right\} = [C] [A] \{1\}$	One equation $C = \frac{C_{L\alpha} \text{ (experimental)}}{C_{L\alpha} \text{ (analytical)}}$	Distribution is correct, magnitude may be in error, equal correction at all panels
Row correction	$\left\{ \frac{dP}{d\alpha} \right\} = [C] [A] \{1\}$	Separate linear equations $C_j = \left( \frac{dP_j}{d\alpha} \right) / \sum_{k=1}^N A_{jk}$	Equal corrections apply to loads induced on panel $j$ by both local and remote points
Column correction	$\left\{ \frac{dP}{d\alpha} \right\} = [A] [C] \{1\}$	Simultaneous linear equations $\{C\} = [A]^{-1} \left\{ \frac{dP}{d\alpha} \right\}$	Equal corrections apply to loads induced by panel $j$ on both local and remote points
Product correction	$\left\{ \frac{dP}{d\alpha} \right\} = [C] [A] [C] \{1\}$	Simultaneous nonlinear equations  Iterative solution	Correction applied to both local and remote points proportional to product of local factors  Combination of row and column methods

- $\circ$   $M = 0.40$      $\triangle$   $M = 1.70$   
 $\square$   $M = 0.85$      $\nabla$   $M = 2.50$   
 $\diamond$   $M = 1.05$

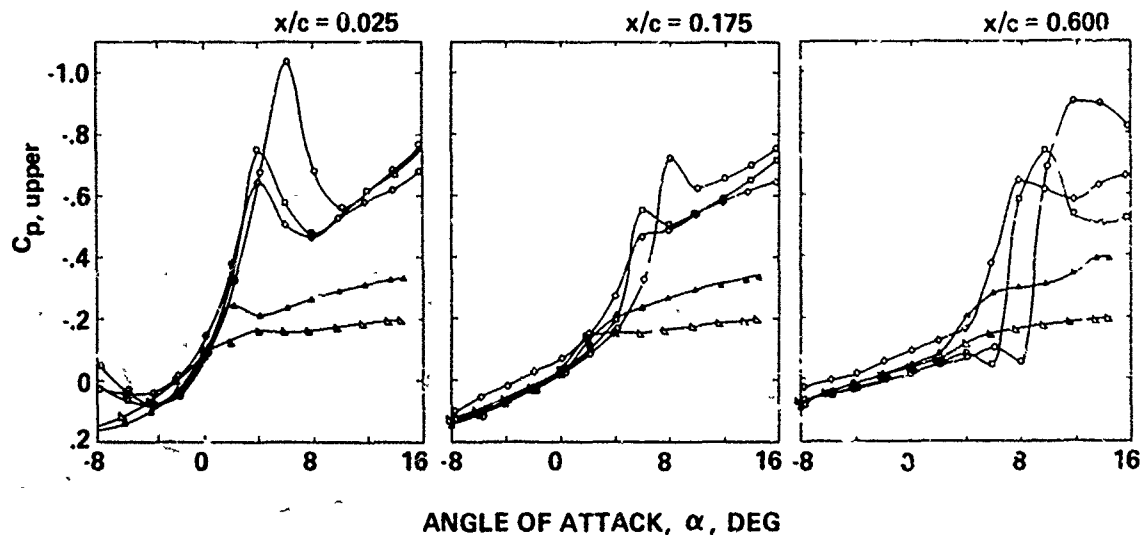


Figure 21. - Typical Variation of Upper-Surface Pressure Coefficients With Angle of Attack,  $2y/b = 0.65$



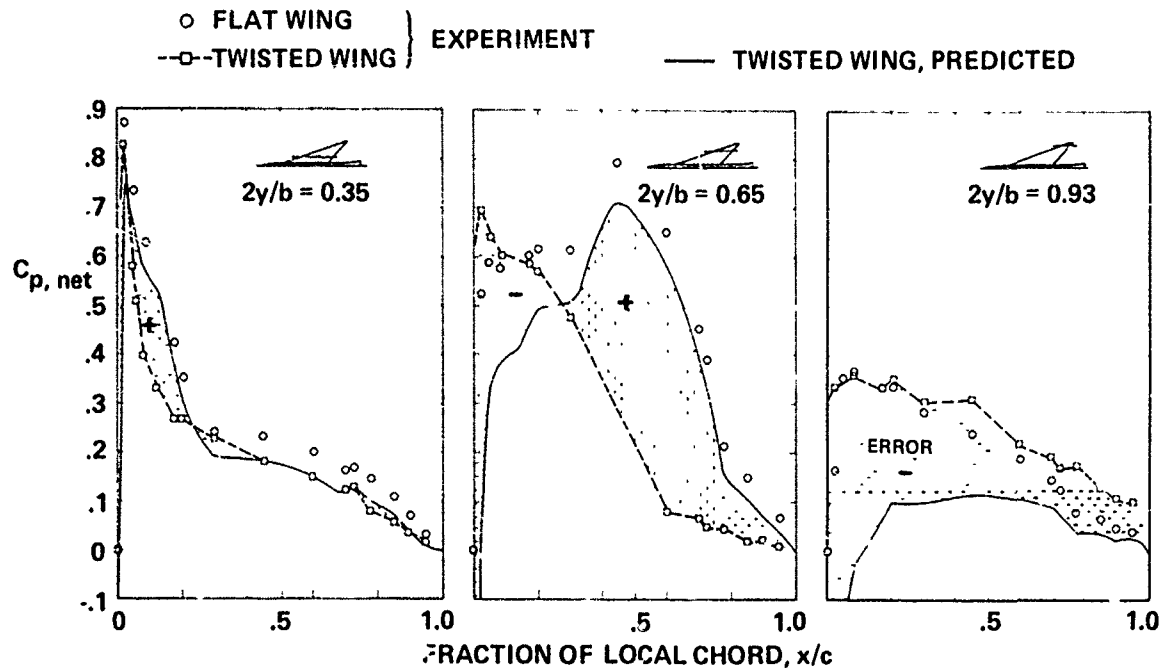


Figure 22. — Pseudo-Aeroelastic Predictions,  $M = 0.85$ ,  $\alpha = 8^\circ$

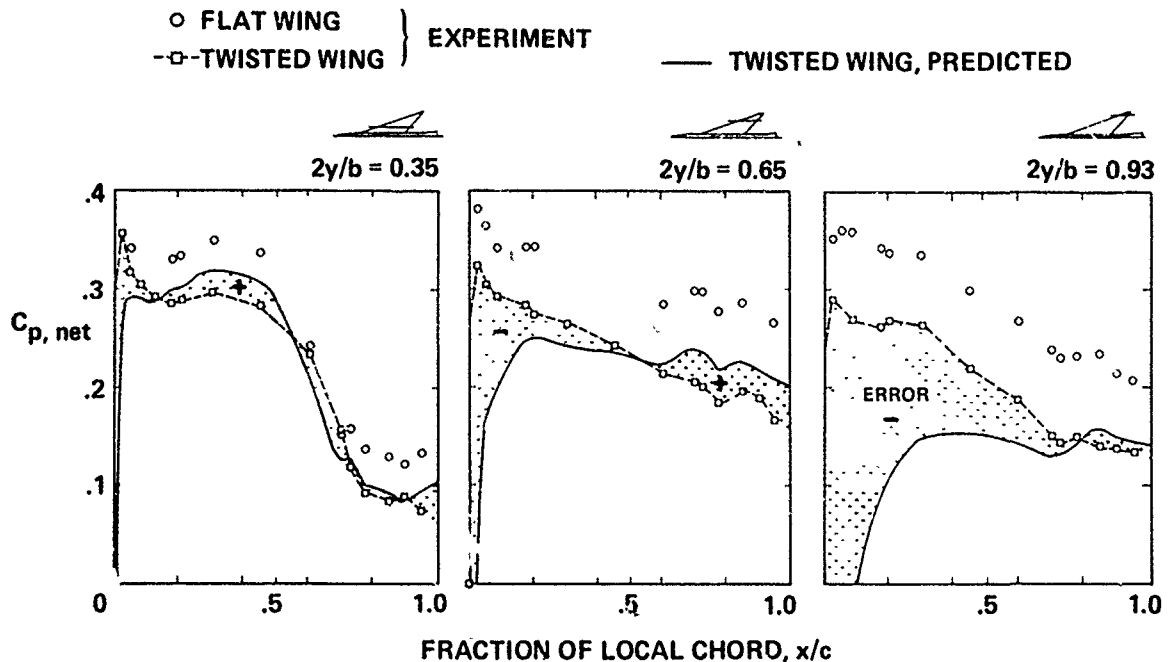


Figure 23. — Pseudo-Aeroelastic Predictions,  $M = 2.10$ ,  $\alpha = 8^\circ$

#### CONCLUDING REMARKS

It has been shown that the attached-potential-flow methods can yield good agreement with experimental data for this type of configuration at low angles of attack only. These analyses are generally adequate for the evaluation of a configuration at cruise conditions (load factor one). At critical structural and control design conditions, which usually involve large angles of attack and/or large control-surface deflections, the attached-flow theories are completely inadequate. Attempts to introduce empirical corrections to improve this situation have been unsatisfactory.

The one comparison ( $M = 0.4$ ) of experiment with a detached-flow theory indicates much better agreement than the attached-flow theories. Further development of this type of analysis technique appears to be the only hope for predicting the aerodynamic loads on highly swept, low-aspect-ratio, flexible airplanes with the accuracy required.

## REFERENCES

1. Marjorie E. Manro, Edward N. Tinoco, Percy J. Bobbitt, and John T. Rogers, "Comparison of Theoretical and Experimental Pressure Distributions on an Arrow-Wing Configuration at Transonic Speed," *Aerodynamic Analyses Requiring Advanced Computers*, 1975, NASA SP-347, pp. 1141-1188.
2. Marjorie E. Manro, Kenneth J. R. Manning, Thomas H. Hallstaff, and John T. Rogers, *Transonic Pressure Measurements and Comparison of Theory to Experiment for an Arrow-Wing Configuration. Summary Report*, 1975, NASA CR-2610.
3. E. N. Tinoco and J. E. Mercer, Boeing Commercial Airplane Company, *FLEXSTAB-A Summary of the Functions and Capabilities of the NASA Flexible Airplane Analysis Computer System*, October 1974, NASA CR-2664.
4. A. R. Dusto et al., *A Method for Predicting the Stability Characteristics of an Elastic Airplane. Volume 1, FLEXSTAB Theoretical Manual*, 1974, NASA CR-114712.
5. F. A. Woodward, E. N. Tinoco, and J. W. Larsen, *Analysis and Design of Supersonic Wing-Body Combinations, Including Flow Properties in the Near Field. Part 1, Theory and Application*, 1967, NASA CR-73106.
6. F. A. Woodward, "Analysis and Design of Wing-Body Combinations at Subsonic and Supersonic Speeds," *J. Aircraft*, vol. 5, no. 6, Nov.-Dec. 1968, pp. 528-534.
7. P. E. Rubbert, G. R. Saaris, M. B. Scholey, N. M. Standen, and R. E. Wallace, *A General Method for Determining the Aerodynamic Characteristics of Fan-in-Wing Configurations. Volume I, Theory and Application*, 1967, USAAVLABS technical report 67-61A.
8. P. E. Rubbert and G. R. Saaris, "A General Three-Dimensional Potential-Flow Method Applied to V/STOL Aerodynamics," *SAE J.*, vol. 77, Sept. 1969.
9. P. E. Rubbert and G. R. Saaris, "Review and Evaluation of a Three-Dimensional Lifting Potential Flow Analysis Method for Arbitrary Configurations," 1972, AIAA paper 72-188.
10. James A. Weber, Guenter W. Brune, Forrester T. Johnson, Paul Lu, and Paul E. Rubbert, "Three-Dimensional Solution of Flows Over Wings With Leading Edge Vortex Separation," *Aerodynamic Analyses Requiring Advanced Computers*, 1975, NASA SP-347, pp. 1013-1032.
11. G. W. Brune, J. A. Weber, F. T. Johnson, P. Lu, and P. E. Rubbert, *A Three-Dimensional Solution of Flows Over Wings With Leading Edge Vortex Separation. Part 1, Engineering Document*, 1975, NASA CR-132709.

## THREE DIMENSIONAL SUPERSONIC FLOW ABOUT SLICED BODIES (\*)

Guido Colasurdo, Assistant  
Maurizio Pandolfi, Professor  
Istituto di Macchine e Motori per Aeromobili, Politecnico di Torino  
Torino, 10129, Italy.

## Summary

Three dimensional supersonic flows about aircrafts or re-entry vehicles are computed by a marching technique along the body axis. Beside the well known features of these flows (3D bow and imbedded shocks, entropy layers...) difficulties arise when the body surface presents lines of discontinuous variations of its slope (as for example in the case of a cone sliced with a plane). It is here shown that the numerical prediction of the pressure at the body comes out quite wrong if the slope discontinuities of the surface of the body are not taken in the proper consideration. A methodology is given in order to implement easily the capabilities of existing computer programs in case of these kinds of bodies. It is based on the explicit computation of the flow properties on the two sides of the discontinuity at the body by using there a local analysis. Comments on this matter are given and supported by the results of numerical experiments.

## 1) INTRODUCTION

Attention is paid today to a family of reentry vehicles which may be controlled in their trajectory by means of very simple lifting devices. The geometry of these vehicles is quite simple; they are shaped as blunted and relatively short cones (generally circular), which, in the after body section, present flat surfaces (obtained by intersecting the original cone with planes parallel to the cone axis).

Part of the flat surfaces may be moved in a flap fashion, in order to generate the required aerodynamic forces needed for controlling the vehicle. The sketch of Fig. 1 shows a typical configuration.

It should be outlined that the computational methods, used in evaluating the surface pressure on these vehicles, must be quite accurate. In fact small errors in the predicted pressures may give a wrong prediction of the maneuvering capabilities of such vehicles.

If we look at the cross-section in the afterbody of such a vehicle, we may see a discontinuity in the slope of the contour; just where the flat surface intersects the cone surface. We will call hereafter "discontinuity line" (d.l.), the line representing this intersection.

If the usual 3D computational methods are carried on, without any provision about the d.l., it will be shown in the following that the predicted results are far from what it should be expected. This is in agreement with a general concept, supported in many papers (see for example Ref. 1,2): shock waves, contact discontinuities, discontinuities at the boundaries and others, need a local analysis and the explicit numerical treatment, in order to get accurate and reliable results.

However, the more complicated is the discontinuity (as for example 3D imbedded shocks), the more sophisticated and cumbersome turns out to be the procedure in writing the computer code. In the present case, the "discontinuity line" pertains to the group of relatively simple discontinuities, so that the explicit treatment does not require complicated features in the code. The purpose of this paper is the presentation of an algorithm (explicit treatment of the discontinuity line), which may be applied quite easily to existing computer codes. The price to be paid in implementing the code capabilities, consists only in few Fortran statements, added here and there. However the results come out definitely as more reliable.

## 2) PRELIMINARY CONSIDERATIONS

In order to understand the perturbations originated at the d.l. we start with a simple problem.

With reference to Fig. 2, we imagine a uniform supersonic flow over a flat plate. At the station  $z_0$ , a groove has been cut into the plate. By looking at the longitudinal section (Fig. 2a) we expect a Prandtl-Meyer expansion fan generated at  $z_0$  (more precisely, a quasi P.M. fan, because of the 3D effects). Moreover, so far the component of the flow velocity, upstream of the d.l. and normal to it, is supersonic ( $M > 1$ ), we expect expansion fans centered all over along the d.l. The isobars pattern in a cross section (normal to  $z$ ), should look as in Fig. 2b. The top view is shown in Fig. 2c.

The flow on the d.l. appears then to be described by a set of double value points (the upstream ones, and the ones immediately downstream of the d.l.).

When we tried to compute this flow field (geometry of Fig. 2), without any particular numerical provision related to the d.l., we got the pressure distribution at the body, which looks as the dotted line in Fig. 3. No numerical oscillations appear in the results, despite the existence of the d.l. Of course this fact should not lead to the wrong

(\*) This research has been supported by the "Centro Nazionale delle Ricerche" (Contract n.115.6799.CT75. 01369.07)

conclusion that the results are good. In fact, let us anticipate the results obtained with the proper numerical treatment at the d.l., which we think as correct and which are reported in Fig. 3 by the solid line. The difference is really remarkable.

In order to emphasize what kind of mistake one does, by neglecting the d.l., we would like to show some further results about an oversimplified example: the 2D flow expanding over a sharp corner. In this case we know the theoretical pressure distribution along  $z$ .

We did two series of computations; we started the integration by marching along  $z$ , just ahead of the corner (uniform undisturbed flow) and just behind it (uniform flow, except at the body where the velocity, tangent to the wall, and the pressure are computed according to the P.M. analysis).

Furthermore we assumed  $Dz$  intervals at each step of the integration reduced, with respect to the  $(Dz)_{FCL}$  determined from the stability criterion, by the factor  $\alpha$  ( $Dz = \alpha \cdot Dz_{FCL}$ ). The plots of Fig. 4,5 show the pressure distributions along  $z$  for supersonic ( $M_\infty = FCL_2$ ) and hypersonic ( $M_\infty = 10$ ) flows. Because the reference length is given by the mesh interval along  $x$ , we have reported  $z^* = z/Dx$  being  $Dx$  the interval at the starting station).

The results obtained by starting just ahead of the corner, without any explicit treatment, are reported by the solid lines in Fig. 4,5, whereas the points refer to the case computed with the P.M. analysis. We may observe that a large delay in  $z^*$  is needed, in order to adjust the pressure level at the wall, in the first case. The delay tends to decrease by marching with smaller  $Dz$ ; however no improvement is practically achieved for  $\alpha$  less than 0.2. The pressure evolution may be monotonic (hypersonic flow) or may show remarkable undershoots (supersonic flow). In any case the prediction of pressure at relatively short distance from the corner is completely wrong. Different conclusions are drawn when the P.M. analysis is used; except for  $\alpha = 1$  at  $M_\infty = 10$  the agreement with the theoretical value is quite good.

We think that these preliminary considerations make clear that a good computation must include the proper treatment at the d.l., by putting there a double value point.

### 3) EQUATIONS AND NUMERICAL APPROACH

We present in this paper numerical results for supersonic flow over a plate with a groove and about a sliced cone. Just for the sake of simplicity, we give hereafter the equations for the first geometrical configuration (where a cartesian frame of reference is assumed). The extension to the sliced cones geometry (cylindrical frame) is obvious.

First we write the equations used in the integration of the grid computational points. We give then the equations used for computing the flow properties on the upstream side of the d.l. Finally the local analysis is shown, in order to relate the flow properties on the two sides of the d.l.

#### 3.1. Grid Points

The Euler equations are written in the cartesian frame  $(x, y, z)$ , and the stream line slopes ( $\sigma = u/w$ ,  $\tau = v/w$ ) are introduced, instead of the usual components of the velocity. All the variables have been normalized as reported in Ref. 3.

We consider the flow field in the region bounded by the upper limit  $c(z)$ , the body contour  $b(y, z)$ , the symmetry line (at the left) and the undisturbed right boundary (see Fig. 6).

Then we introduce the computational frame  $(X, Y, Z)$ , defined as:

$$X = \frac{x - b}{c - b}; \quad Y = y; \quad Z = z$$

The equations of motion come out as:

$$(1) \quad \begin{aligned} & \left(1 - \frac{a^2}{w^2}\right) P_Z + BP_X + \tau P_Z + \gamma D\sigma_X + \gamma \tau_Y + F\tau_X = 0 \\ & \sigma_Z + A\sigma_Z + \tau\sigma_Y + CP_X - \frac{\sigma}{Y} \frac{a^2}{w^2} P_Z = 0 \\ & \tau_Z + A\tau_X + \tau\tau_Y + EP_X + \frac{1}{Y} \frac{a^2}{w^2} P_Y - \frac{1}{Y} \frac{a^2}{w^2} P_Z = 0 \end{aligned}$$

where:

$$P = \ln p; \quad a = \sqrt{\gamma T}; \quad T = \exp\left(\frac{\gamma-1}{\gamma} P\right)$$

$$D = 1/(c-b)$$

$$C = (X-1)b_Y - Xc_Y; \quad H = (X-1)b_Z - Xc_Z$$

$$A = D(\sigma + \tau G + H); \quad B = A - \frac{a^2}{w^2} DH$$

$$E = \frac{D}{Y} \frac{a^2}{w^2} (1 - \sigma H); \quad F = \frac{D}{Y} \frac{a^2}{w^2} (1 - \tau H); \quad F = \gamma DG$$

Eq. 1 are used for evaluating the derivatives  $P_X, \sigma_Z, \tau_Z$  at the interior points; the integration is carried on by a marching technique along  $z$ , according to a two-level (predic

cor-corrector) scheme (Mac Cormack). At the left boundary we used the same procedure as at interior points, because of the symmetry condition. At the right boundary the undisturbed flow conditions are imposed (we will confine the computation to the value of  $z$ , where the d.l. reaches this boundary). The same is done at the upper boundary  $c$ , which is supposed here to move along  $z$  as a characteristic surface, which will be never reached by the waves generated on the d.l. At the body we follow the same procedure as reported in Ref. 3. A compatibility equation is obtained from Eq. 1, which allows to evaluate the pressure derivative with respect to  $z$ :

$$(2) \quad P_z = -\lambda P_X + \{\gamma\lambda(\sigma_X + Gr_X) + \gamma(b_{zz} + 2\tau b_{yz} + \tau^2 b_{yy}) + \\ + (\tau \frac{\lambda}{D} + G \frac{a^2}{w^2}) + \gamma \frac{\lambda}{D} \tau_Y\} / (\frac{a^2}{w^2} \beta)$$

where:

$$\lambda = \frac{D}{(1 - \frac{a^2}{w^2})} (-(\sigma + \tau G) + \beta)$$

$$\beta = \sqrt{\frac{w^2}{a^2} (\sigma + \tau G)^2 + (\frac{w^2}{a^2} - 1) (1 + G^2)}$$

The pressure at the body is computed by integrating Eq. 2, according to the two-level scheme as at the interior points.

We defined at the body the two components  $\hat{u}$ ,  $\hat{v}$ , of the velocity contained in the cross-section plane (see Fig. 7):

$$\hat{u} = \frac{w}{v_1} (\sigma - \tau b_y); \quad \hat{v} = \frac{w}{v_1} (\sigma b_y + \tau); \quad v_1 = \sqrt{1 + b_y^2}$$

The momentum equation in the direction tangent to the body contour (in the cross-section plane) gives:

$$(3) \quad \hat{v}_z = -(\tau \hat{v}_y + \frac{1}{\gamma v_1} \frac{a^2}{w^2} P_Y - \frac{\hat{u}}{v_1^2} (\tau b_{yy} + b_{yz}))$$

By integrating Eq. 3, one gets the updated value of  $\hat{v}$ . By the decoding procedure, which is based on the tangency condition ( $A = 0$ ) and on the conservation of the total temperature ( $T^0$ ), one has:

$$u = \frac{1}{\gamma v_1} (\hat{v} b_y + b_z \sqrt{q^2 - \hat{v}^2}); \quad v = v_1 \hat{v} - u b_y$$

$$w = \sqrt{q^2 - u^2 - v^2}; \quad q^2 = \frac{2\gamma}{\gamma-1} (T^0 - T); \quad v = \sqrt{1 + b_y^2 + b_z^2}$$

### 3.2. The upstream point on the d.l.

We have already anticipated that the present treatment of the d.l. holds, provided that the flow normal to the d.l. is supersonic. It follows that the computation of the flow properties at the point U (Fig. 3) is only depending on the flow at the right side of the d.l. We compute the flow here by writing the equations of motion in the frame of reference  $(\xi, \eta, \zeta)$  moving along the d.l.:

$$\xi = \frac{r-b}{c-b}; \quad \eta = y - y_s; \quad \zeta = z$$

where the d.l. location is given by  $y_s(z)$ .

A set of equations, similar to Eq. 1 may be then written. The compatibility equation, which provides the variation of pressure along the upstream side of the d.l., is:

$$(4) \quad P_\zeta = -\lambda P_X + \{\gamma\lambda(\sigma_X + Gr_X) + \gamma(b_{zz} + 2\tau b_{yz} + \tau^2 b_{yy}) + \\ + ((\tau - y_{sz}(1 - \frac{a^2}{w^2})) \frac{\lambda}{D} + \frac{a^2}{w^2} (G + y_{sz}(\sigma + \tau G))) P_Y + \\ + \gamma \frac{\lambda}{D} \tau_Y\} / (\frac{a^2}{w^2} \beta)$$

The momentum equation, corresponding to Eq. 3, results now as:

$$(5) \quad \hat{v}_\zeta = -((\tau - y_{sz}) \hat{v}_y + \frac{1}{\gamma v_1} \frac{a^2}{w^2} P_Y - \frac{\hat{u}}{v_1^2} (\tau b_{yy} + b_{yz}))$$

By using the same procedure as at the body grid points, one may compute the flow properties at U. In the presented examples, being zero the Y-derivatives in the flowfield upstream of the d.l., we may avoid this procedure, and just set at U the undisturbed flow conditions.

However, in different cases (for example sliced cones at incidence), we need the integration of Eq. 4,5. One may even think to determine the flow at U, by extrapolating the values from the grid points at the right side of the d.l.; our experience has shown that this simple procedure may give some numerical problems.

### 3.3. Local analysis at the d.l.

We define the unit vector,  $\vec{\tau}$ , tangent to the d.l. We consider then the component of the upstream velocity ( $\vec{V}$ ) along  $\vec{\tau}$  ( $v^*\vec{\tau}$ ), and the normal component ( $\vec{u}^*$ ). We have:

$$\vec{\tau} = \tau_1 \vec{i} + \tau_2 \vec{j} + \tau_3 \vec{k} \quad (\text{given by the geometry})$$

$$v^* = \vec{V} \cdot \vec{\tau} = u\tau_1 + v\tau_2 + w\tau_3$$

$$\vec{u}^* = \vec{V} - v^*\vec{\tau}; \quad u^* = \sqrt{V^2 - v^{*2}}$$

So far the Mach number of the upstream flow normal to the d.l. ( $M_n$ , Fig. 2c) is larger than one, we may apply the Prandtl-Meyer analysis to this normal flow, which experiments the deflection  $\Delta v$  and the abrupt expansion over the sharp corner:

$$\Delta v = \alpha \cos(\vec{N} \cdot \vec{N}_1)$$

where  $\vec{N}$  and  $\vec{N}_1$  denote the unit vectors normal to the surfaces upstream and downstream of the d.l. From the P.M. analysis, one gets the pressure  $P_1$  at the downstream point D, and the velocity component  $u_1^*$ , normal to the d.l. and directed along the unit vector ( $\vec{N}_1 \times \vec{\tau}$ ). The velocity  $\vec{V}_1$ , at the point D, is then:

$$\vec{V}_1 = u_1^* (\vec{N}_1 \times \vec{\tau}) + v^*\vec{\tau}$$

Because  $u_1^*$  and  $v^*$ , and the component of the vectors  $\vec{N}_1$  and  $\vec{\tau}$  are known, one may soon evaluate the velocity components ( $u, v, w$ ) and the streamline slopes ( $\sigma, \tau$ ) at D.

The computational points U and D move in the fixed grid of computational points at  $X = 0$  (fig. 6).

Special formulas have to be taken in order to evaluate the Y-derivatives at the point U (Eq. 4,5) and at the grid points MSM, MS (Eq. 2,3), in order to avoid derivatives across the discontinuity and to save the accuracy, whatever is the position of the points U, D in the fixed grid (given by  $\epsilon$  in Fig. 9). The formulas we have used have been suggested in Ref. 5 in the case of computation of shocks floating in fixed grids.

### Numerical results

We have carried on computations for two different cases: uniform flow over a flat plate with a groove and about a sliced cone (pointed nose).

As regards the first case, we refer to Fig. 2. The d.l. has been chosen as the hyperbola:

$$y_s = z_0 \tan \mu \sqrt{\left(\frac{z}{z_0}\right)^2 - 1}$$

The groove profile in the (x,z) plane at  $y = 0$  (left boundary in Fig. 6) is assumed as:

$$g = n_s (z - z_0)$$

The groove profile in the cross section (plane x,y) is given by a second order parabola:

$$b = g \left( \frac{y^2}{y_s^2} - 1 \right)$$

We have based the computations on the following data:

$$z_0 = .2; \quad \mu = 38.66^\circ; \quad n = -.2$$

The results have been plotted (Fig. 10, 11) as the pressure distribution along y at different stations z, for  $M_\infty = 2$  and  $M_\infty = 10$ .

The solid and the dotted lines refer to the computations respectively with and without the explicit treatment of the d.l.

The difference between the two computations is remarkable for  $M_\infty = 2$  (fig. 10) and awfully large for  $M_\infty = 10$  (Fig. 11). This fact may be justified by looking at the results got for the 2D flow (Fig. 4, 5) where the delay in z, for readjusting the pressure at the right level, is larger at higher Mach number.

We have then computed the flow about a  $5^\circ$  cone (pointed nose) with the slice as shown in Fig. 1, for  $M_\infty = 8$ . The results (pressure at the body along  $\theta$ ) are reported in

Fig. 12. We find here the same trend shown in the first example. The fact that at larger  $z$ , the dotted line denotes rather low pressure levels, may be easily related to the undershoot shown in Fig. 4. This is put in evidence in Fig. 13, where the pressure evolution along  $z$  is given, at the symmetry plane ( $\theta = 0$ ). Once again the delay is quite remarkable for the dotted line; whereas for the solid lines is negligible (as in Fig. 4); the weak and smooth pressure increase may be ascribed to the 3D flow effects.

Finally we would like to mention that all these computations have been repeated, by doubling the number of the computational points in the  $Y$  direction. The results are practically the ones got with few points, except small improvements in some case, due to the better flow description in regions of sharp gradients (in  $Y$ ).

#### REFERENCES

- 1) MORETTI G., "The Choice of a Time-Dependent Technique in Gas Dynamics", Polytechnic Institute of Brooklyn, PIBAL, Report, n. 69-26, 1969.
- 2) MORETTI G., "Complicated One-Dimensional Flows", Polytechnic Institute of Brooklyn, PIBAL Report n. 71-25, 1971.
- 3) PANDOLFI M., "Supersonic Flow About Elliptic Cones with Large Semiaxis Ratio", Istituto di Macchine, Politecnico di Torino, Report n. 172; 1975.
- 4) MORETTI G. and PANDOLFI M., "Analysis of the Inviscid Flow About a Yawed Cone. Preliminary Studies", Polytechnic Institute of Brooklyn, PIBAL Report n. 72-18, 1972.
- 5) MORETTI G., "Thoughts and Afterthoughts About Shock Computations", Polytechnic Institute of Brooklyn, PIBAL, Report n. 72-27, 1972.

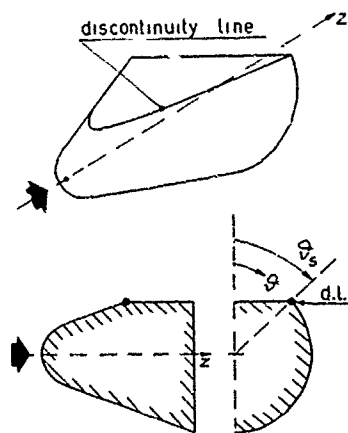


FIG. 1

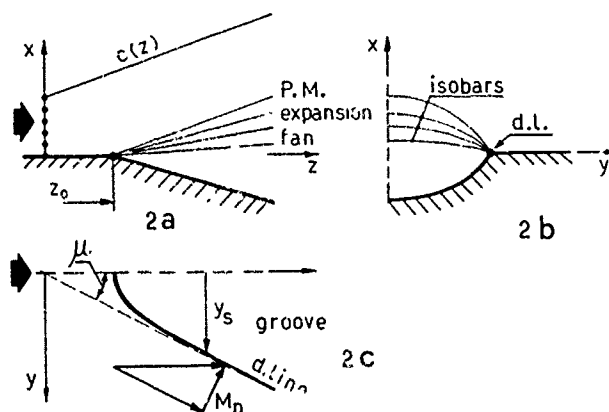


FIG. 2

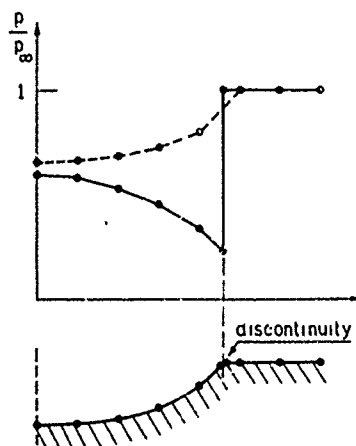
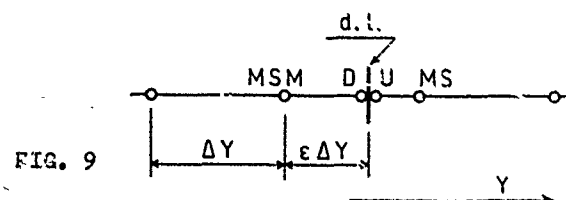
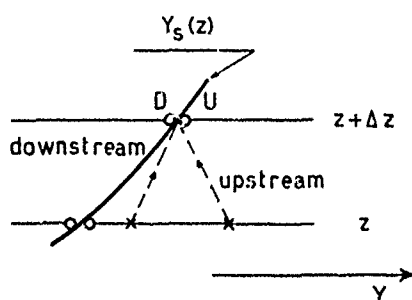
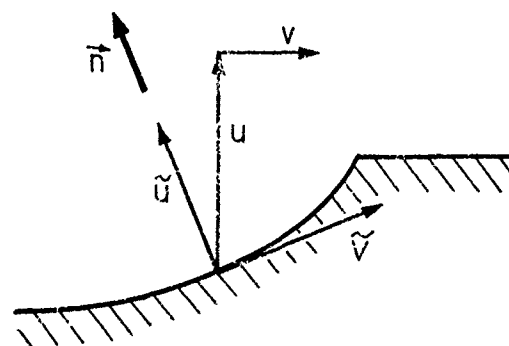
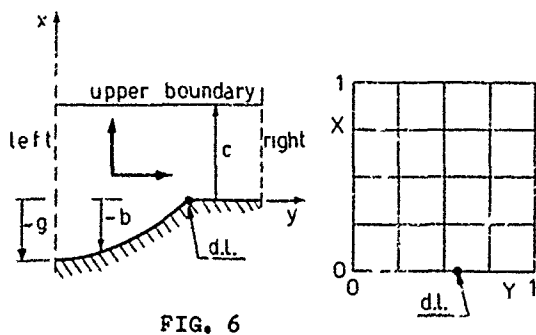
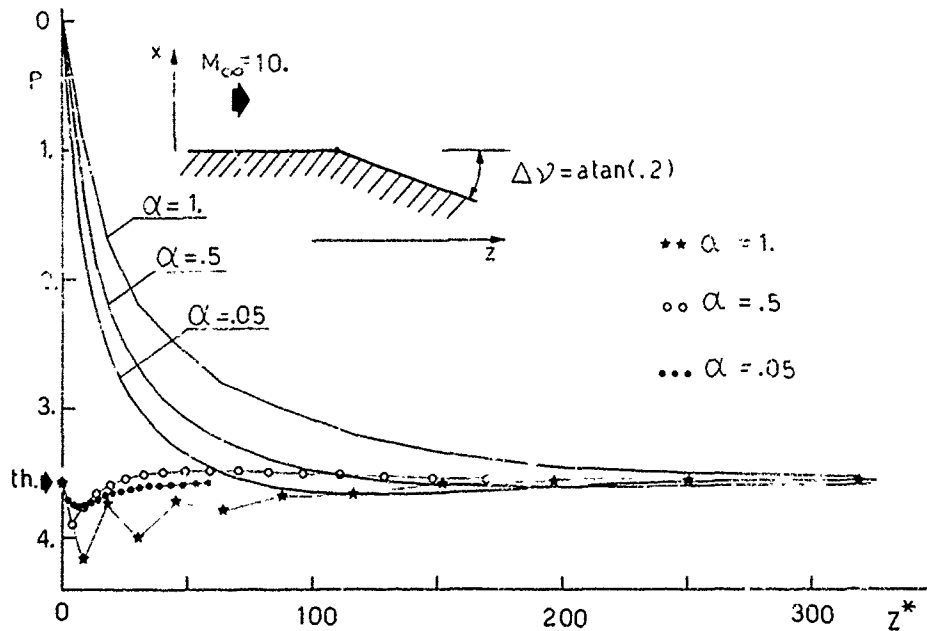
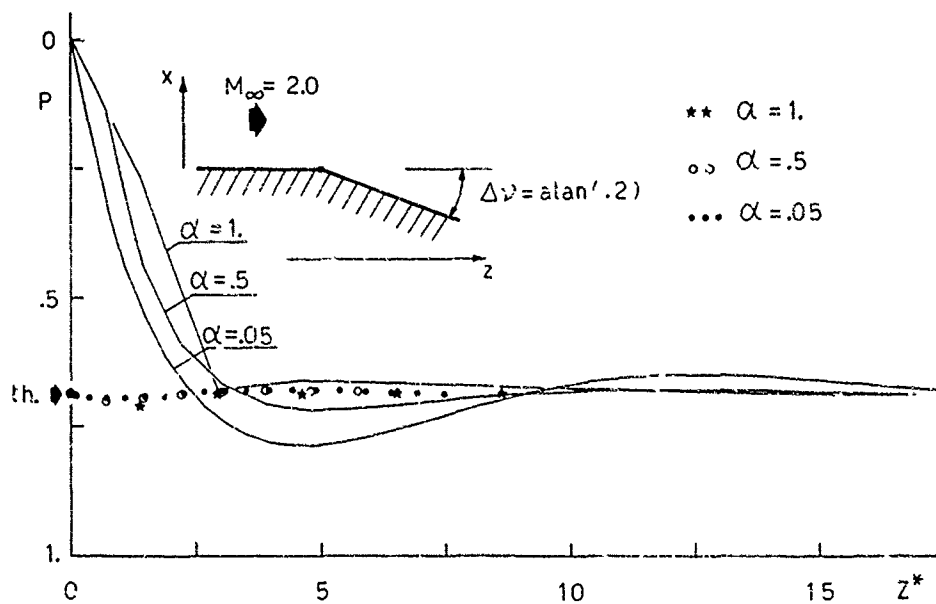


FIG. 3





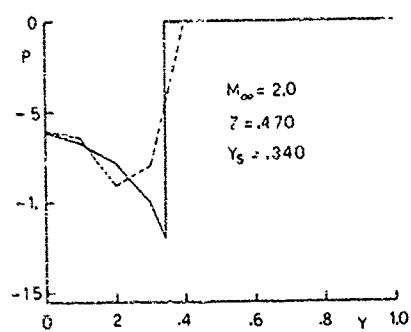


FIG. 10a

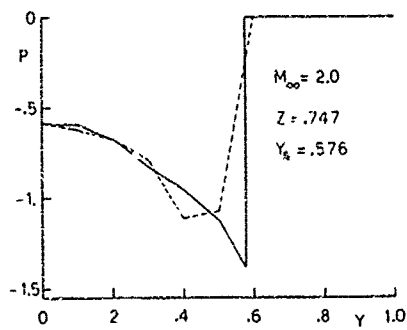


FIG. 10b

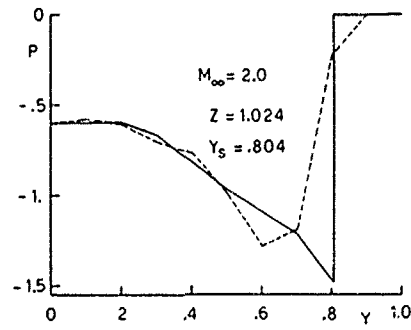


FIG. 10c

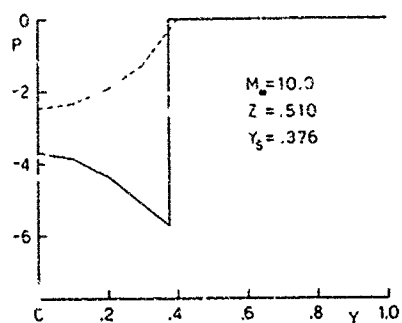


FIG. 11a

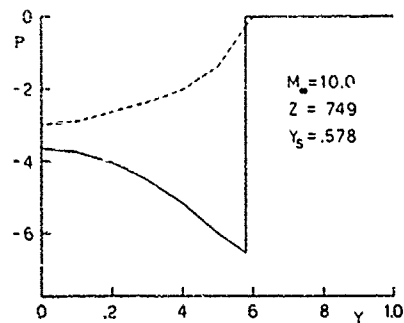


FIG. 11b

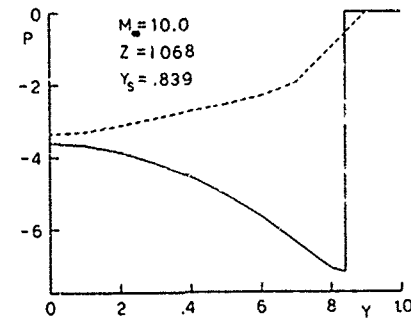


FIG. 11c

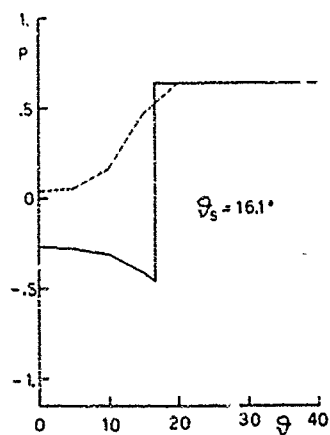


FIG. 12a

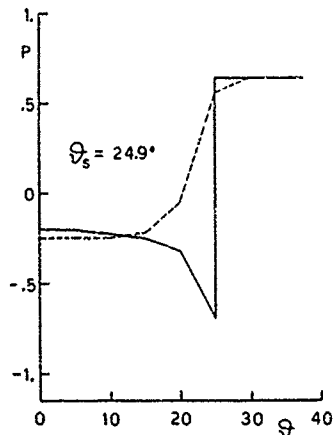


FIG. 12b

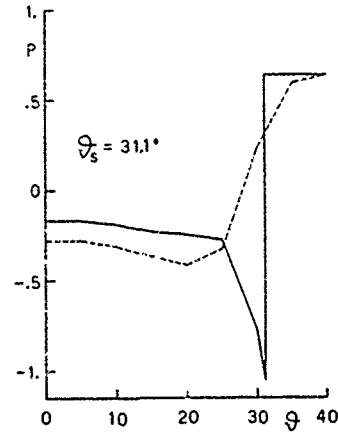


FIG. 12c

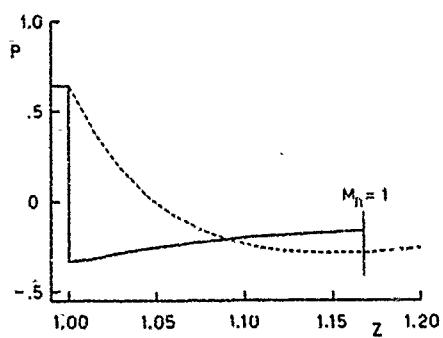


FIG. 13

A METHOD FOR ESTIMATING THE LOADING DISTRIBUTION  
ON  
LONG SLENDER BODIES OF REVOLUTION  
AT  
HIGH ANGLES OF ATTACK  
IN  
INCOMPRESSIBLE FLOW

by  
E. ATRAGHJI  
National Research Council, National Aeronautical Establishment  
OTTAWA, ONTARIO, CANADA  
K1A 0R6

#### SUMMARY

The three-dimensional flow over long slender bodies of revolution at high angles of attack is treated by relating it to the oscillatory two-dimensional flow over a circular cylinder normal to the stream. The approach, which can be considered as a re-interpretation of Allen and Perkins' description of the cross-flow, leads to simple algebraic expressions for the local normal and side forces as functions of the cross-flow Strouhal number and the ratio  $d/l$  (where  $d$  is the body diameter and  $l$  is the pitch length of the Karman vortex street observed in the cross-flow plane). A Fortran IV computer program has been generated for determining these forces, once a proper value is specified for the ratio  $d/l$ . Sample solutions have been computed and are compared with experiment.

The analysis reveals that small changes in the applied value of the ratio  $d/l$  can result in large changes in the predicted magnitude of the forces, particularly, of the normal force. The effects of boundary-layer displacement thickness, location of the point at which separation of the shear layers begins, and the impulsiveness of vortex shedding are studied and discussed.

Comparisons with experimental data, obtained at Mach 0.5 at a Reynolds number  $1.4 \times 10^4$  based on maximum diameter and free stream flow conditions, show good predictions of the normal force coefficient and its centre of pressure location for a variety of body lengths and nose shapes when a specific value of the ratio  $d/l$  is applied. Some explanation is offered where discrepancies are encountered in predicting the normal force coefficient.

Qualitatively good agreement is obtained between theoretical and experimental values of the side force. Quantitatively, the agreement can only be described as fair. The cause is linked with the inability of the present method to determine the location of the onset of flow separation accurately since, in practice, this point appears to be influenced by microscopic surface non-uniformities or blemishes. Furthermore, all contributions due to the skin-friction forces have been neglected. While such contributions constitute only a small portion of the normal force they may form a significant part of the side force. This latter deduction is supported by the experimental evidence of the existence of a not inconsiderable rolling moment which, on a body of revolution, can only arise from the action of surface shear stresses.

#### LIST OF SYMBOLS

$d, d(x)$	body diameter as a function of $x$
$d_{max}$	maximum body diameter
$\alpha$	model angle of attack relative to free stream at infinity- degrees
$x, y, z$	orthogonal system of body axes (See Figure 1)
$U$	free stream velocity at infinity
$\rho$	free stream density at infinity
$\Gamma_0$	strength of a fully developed vortex shed into the wake
$\Gamma, \Gamma(x)$	local circulation at station $x$
$\omega = 2\pi n$	shedding frequency- radians/sec
$n$	shedding frequency -vortices of like sense/sec
$h$	width of the Karman vortex street
$l$	pitch length of the Karman vortex street
$d/l$	ratio of the body diameter to the pitch length of the Karman vortex street
$m = 1, 3, 5, \dots$	integer representing the impulsiveness of vortex shedding

$d\eta/dx$	average rate of vortex shedding (see Section 2.1)
$N, Y$	overall normal and side forces
$CY(x)$	local side force coefficient = $Y(x) \cdot d_{max}/qS$
$CY=Y/qS$	overall side force coefficient
$N(x)$	local normal force
$CN(x)$	local normal force coefficient = $N(x) \cdot d_{max}/qS$
$CN=N/qS$	overall normal force coefficient
CPN	location of the centre of pressure of the normal force from the apex- $d_{max}$
$\phi$	roll angle- degrees
$P(x)$	Munk's potential contribution to the local normal force
$S = \pi d_{max}^2/4$	maximum cross-sectional area of body
$q = \rho U^2/2$	dynamic pressure
D1	skin friction contribution to the cross-flow force
D2	impulsive vortex shedding contribution to the cross-flow force
D3	Karman vortex street contribution to the cross-flow force
$U_2$	advance velocity of the Karman vortex wake- see Section 3.4
$\lambda$	weighting factor defined in section 3.1
$Re = U_1/\nu$	Reynolds number based on diameter of body and free stream conditions
$s=nd/U$	Strouhal number
$s'$	cross-flow Strouhal number defined in Eq. 3.3-3
$Re'$	cross-flow Reynolds number defined in Eq. 3.3-4
$\psi, k1$	parameters defined in Section 4.1
$x1$	distance from the apex at which station flow separation begins
$\xi = x-x1$	distance along the x-axis from the station at which flow separation begins
LB	overall length of body
LN	length of nose section
$d'(x)$	indicates differentiation of $d(x)$ with respect to $x$
$d^*, d1^*, d2^*$	boundary-layer displacement thickness- see Section 4.3
$\dot{\phi}$	roll rate -deg/sec.

#### Abbreviations

c.f.	cross-flow
2D	two-dimensional flow
3D	three-dimensional flow

#### 1.0 INTRODUCTION

Experiments on long slender bodies of revolution<sup>1-4</sup> show that in certain cases depending on angle of attack, Reynolds number, body length, mach number and nose apex angle, a large side force - i.e. a force which acts normal to the plane of symmetry containing the axis of the body and the free stream velocity vector- may develop in addition to the normal force in the plane of symmetry. The present investigation is an attempt at formulating a mathematical model of the flow field that can account for the asymmetric side force and provide a basis for estimating the magnitude of both the normal and side forces.

Allen and Perkins<sup>9</sup> extended the fully-attached linear flow theory of Munk<sup>10</sup> by developing the cross-flow drag concept. Their prediction of the normal force as the sum of Munk's potential term and an average cross-flow drag term agrees well with some experiments as shown in Reference 9. The cross-flow drag term originates from the separation and subsequent roll-up above the body of the shear layers developing from the windward generator. Kelly<sup>11</sup> improved the above method by substituting an expression for the cross-flow drag derived from Schwabe's experiments<sup>12</sup> on cylinders impulsively set in motion from rest instead of applying the steady state value used by Allen and Perkins. Kelly further suggested using the respective cross-flow drag coefficient pertaining to laminar or turbulent flow. A second correction adopted by Kelly, used also by Hill<sup>13</sup>, was the addition of a term to the potential flow solution to account for the boundary-layer growth. Kelly and Hill argued that the growth of the boundary layer increases the effective cross-sectional area of the body and results in increased lift.

The above analyses predict, with varying degrees of accuracy, the non-linear variation of the normal force with angle of attack. However, none gave any consideration to the process of development or estimation of the side force.

More recently, Thomson<sup>14</sup> developed a formula for predicting the maximum and minimum side force which could act on an inclined body of revolution. However, the effects of the various parameters that give rise to the normal or side forces have not been separated to enable evaluating their individual contributions.

In the present paper, an attempt is made at isolating the effects of such parameters as the Reynolds number, the impulsiveness of vortex shedding, the axial station at which vortex shedding begins, body length, boundary-layer growth and, most importantly, the relationship between the dimensions of the wake and those of the body on the development of the normal and side forces.

As mentioned earlier, the mathematical model used herein stems from the description of the physical flow outlined in Reference 9. Allen and Perkins noticed the existence of a certain analogy between the cross-flow at various stations along an inclined body of revolution and the development with time of the two-dimensional flow about the impulsive normal cylinder, i.e. a cylinder impulsively set in motion from rest in a direction normal to its axis. To quote, "...this analogy may be seen by considering the development of the cross-flow with respect to a co-ordinate system that is in a plane normal to the axis of the inclined body moving downstream with a velocity  $U \cos \alpha$  (See Figure 1). The cross-flow velocity is  $U \sin \alpha$ . At any instant, during the travel of the above plane from the nose towards the base of the body, the trace of the body in this plane is a circle and the cross-flow pattern within the plane may be compared with the flow pattern about a circular cylinder normal to the flow. Neglecting, for the moment, the effect of taper over the nose portion, it might be anticipated that over successive downstream sections the development of the cross-flow with distance along the body as seen in the moving plane would appear similar to that which would be observed with the passage of time for a circular cylinder impulsively set in motion from rest with a velocity  $U \sin \alpha$ . Thus the flow in the cross-plane for the most forward sections should contain a pair of symmetrically disposed vortices on the lee side. These vortices should increase in strength as the plane moves rearward and eventually, if the body is long enough or the angle of attack is sufficiently high, should discharge to form a Karman vortex street as viewed in the moving cross-plane, but viewed with respect to the stationary body the shed vortices would appear fixed."

It is argued, therefore, that the important flow characteristics in any cross-plane of the inclined body of revolution may be obtained directly from those of the two-dimensional flow over the impulsive normal cylinder, if the time,  $t$ , is expressed as  $x/(U \cos \alpha)$  and the free stream velocity is substituted by the cross-flow velocity  $U \sin \alpha$ .

The origin of the side force is seen to be the result of interactions between the cross-flow component of the free stream velocity and the residual local circulation on the body arising from the staggered vortex formation observed in the wake of the body. To determine the magnitude of this circulation, recourse is made to Karman's two-dimensional vortex street stability analysis<sup>15</sup> and Roshko's experimentally found relationship<sup>16</sup> between the Strouhal number and the Reynolds number for a cylinder normal to the free stream. Even so, the local residual circulation can only be expressed in terms of one remaining unknown parameter, the ratio  $d/l$ , where  $d$  is the body diameter and  $l$  is the pitch length of the Karman vortex street. Expressions for the local normal and side force distributions are developed in terms of this ratio, which, in the absence of any existing acceptable method to evaluate it, makes further assumptions necessary. A control configuration is first selected. Trial values are substituted for  $d/l$ . The value of  $d/l$  that yields an overall normal force coefficient which matches that found experimentally, over a range of angle of attack, is the one chosen. This value is then used to predict the detailed normal and side force distributions for other configurations.

## 2.0 THE CIRCULATION $G(t)$ OVER THE CYLINDER NORMAL TO A STREAM

A considerable number of experimental investigations<sup>17-21</sup> were conducted to determine the shedding frequency of vortices from cylinders normal to the stream. These investigations indicate that there exists a 'stable' and 'regular' vortex street in the

Reynolds number range  $40 < Re < 7 \times 10^6$  where predominant shedding frequencies can be detected. The data from some of the above experiments are summarised in Figure 2. The regular vortex shedding is manifest by the experimentally measured oscillatory lift forces on the cylinder<sup>18-20</sup>. If the assumption of a uniform vortex street is accepted, although strictly this is not true<sup>23-24</sup> except close to the cylinder, one may interpret the existence of oscillatory lift forces as the result of an oscillatory change with time of the bound circulation,  $G(t)$ , over the cylinder of the form

$$G(t) = \pm G_0 \sin^m(\omega t) \quad \dots 2.0-1$$

where  $\omega = 2\pi n$   
 $n$  = the fundamental shedding frequency of vortices of similar sense  
 $= (1/2) \cdot (d\eta/dt)$   
 $\eta$  = the total number of vortices present in the wake at time  $t$   
 $G_0$  = the strength of each shed vortex  
 $m$  = impulsive index of vortex shedding - an odd integer  
 $t$  = the time  
 and the  $\pm$  signs account for the starting direction of vortex shedding.

In the two-dimensional case, the shedding frequency,  $n$ , may be estimated directly from the empirically-found relationship between the Strouhal number and the Reynolds number (See Reference 16). Roshko concluded from his experiments<sup>16</sup> that the Strouhal number,  $s$ , for the normal cylinder can be expressed as a function of the Reynolds number,  $Re$ , in the form:-

$$\begin{aligned} s = n d / U &= 0.212 - 4.5 / Re & 50 < Re < 140 \\ \text{and} & & \\ s &= 0.212 - 2.7 / Re & 140 < Re < 2000 \end{aligned} \quad \dots 2.0-2$$

In the present investigation it is assumed that the range of application of the second equation is valid up to  $Re = 10^7$ .

Evaluation of the impulsive index,  $m$ , and the amplitude,  $G_0$ , of the circulation  $G(t)$  will be discussed in Sections 3.2 and 3.4.

## 2.1 Corresponding Expression for the Circulation $G(x)$ over the Inclined Body

Let us turn back to consider the flow field over a slender body inclined to the main stream.

In this case the bound circulation at any axial station of the inclined body will vary with distance  $x$  from the apex. Let this circulation be denoted  $G(x)$ ; it is calculated using Eq. 2.0-1 by substituting  $x/(U \cos \alpha)$  for  $t$  and  $(\pi \cdot U \cos \alpha \cdot d\eta/dx)$  for  $\omega$ . Thus,

$$G(x) = \pm G_0 \sin^m(\pi \cdot x \cdot d\eta/dx) \quad \dots 2.1-1$$

noting that

$$\begin{aligned} n &= (1/2) \cdot (d\eta/dt) = (1/2) \cdot (d\eta/dx) \cdot (dx/dt) \\ &= (1/2) \cdot (d\eta/dx) \cdot U \cos \alpha \end{aligned}$$

where  $\eta$  defines the sum of fully-formed vortices and part of, or nascent, vortex observed in the cross-plane at station  $x$ , and is treated as a continuous function of  $x$ .

It should be noted that the bound circulation,  $G(x)$ , has its axis coincident with the  $x$ -axis of the inclined body.

Expressions for the local side and normal force distributions may now be developed as shown in the following section.

## 3.0 THE LOADING DISTRIBUTION $Y(x)$ and $N(x)$

The interaction of the local circulation,  $G(x)$ , at station  $x$ , with the cross-flow component of the free stream velocity gives rise to a side force,  $Y(x)$ , whose magnitude is given by Kutta-Joukowski's formula as

$$Y(x) = \rho \cdot U \sin \alpha \cdot G(x) \quad \dots 3.0-1$$

And, following the approach of Allen and Perkins, the normal force,  $N(x)$ , is calculated as the sum of two basic terms:-

1. Hunk's potential term, denoted here as  $P(x)$ , whose magnitude at a given angle of attack depends solely on the rate of change with distance  $x$  of the cross-sectional area,  $S(x)$ , of the body, and,
2. A cross-flow drag term,  $D(x)$  | c.f., whose magnitude depends on the surface shear stress, the impulsive rate of change of the circulation over the body, and the state of development of the Karman vortex street in the wake of the body.

The normal force may be expressed as:-

$$N(x) = \underbrace{P(x)}_{\text{Munk's potential term}} + \underbrace{D(x)|c.f.}_{\text{cross-flow drag term}} \quad \text{.....3.0-2}$$

$$\text{where } P(x) = q \cdot \sin(2\alpha) \cdot \cos(\alpha/2) \cdot [dS(x)/dx] \quad \text{.....3.0-3}$$

The term  $\cos(\alpha/2)$  is due to Ward<sup>25</sup>, who showed that the net force on a slender body acts mid-way between the normal to the free stream and the normal to the body. This term has been included in the computations, but it should be emphasised that its maximum effect, on the computed values of the overall normal force coefficient of the various configurations discussed below, amounts to less than 1% up to angles of attack as high as 30°.

The cross-flow drag term,  $D(x)|c.f.$ , is expressed as the sum of three terms in the form

$$D(x)|c.f. = \underbrace{D1}_{\text{surface shear stress viscous}} + \underbrace{D2}_{\text{impulsive potential}} + \underbrace{D3}_{\text{Karman vortex street}} \quad \text{.....3.0-4}$$

where the abbreviation |c.f. denotes cross-flow.

In the following analysis the contribution from the surface shear stresses to the normal or side force is neglected. Hence  $D1=0$ .

### 3.1 Determination of $D2$ and $D3$

In order to determine the potential components of the cross-flow force,  $D2$  and  $D3$ , we turn to the analysis<sup>12</sup> of the flow over the cylinder normal to the stream. The impulsive force,  $D2(t)|2D$ , is given by the following formula:-

$$D2(t)|2D = d.p. |dG(t)/dt| \quad \text{.....3.1-1}$$

The equivalent expression in three-dimensional flow for the inclined body of revolution is obtained by substituting  $x/U \cdot \cos\alpha$  for the time  $t$  in the above formula to get  $D2(x)|3D$  as:-

$$D2(x)|3D = d.p. |dG(x)/dx| \cdot U \cdot \cos\alpha \quad \text{.....3.1-2}$$

where the abbreviations |2D and |3D denote two-dimensional flow over a cylinder normal to the free stream and three-dimensional flow over an inclined body of revolution, respectively.

Also from Reference 15, the contribution  $D3|2D$ , in two-dimensional flow, due to the existence of the Karman vortex street is given by

$$D3|2D = \rho \cdot G_0^2 / (2 \cdot \pi \cdot l) - \rho \cdot G_0 \cdot U^2 \cdot h/l \quad \text{.....3.1-3}$$

In two-dimensional flow, the term  $D3|2D$  is the drag due to a semi-infinite Karman vortex street; i.e. a street extending from the cylinder downstream to infinity. This would correspond to the cross-flow drag on the inclined body of revolution at a station far downstream at infinity where the wake in the cross-flow has fully developed. At all other stations ahead of this 'asymptotic' station the cross-flow drag component  $D3(x)$  would clearly be different. Therefore, an appropriate weighting factor,  $\lambda$ , is applied such that in the limits as  $x$  tends to infinity ( $\alpha \neq 0$ ), or as the angle of attack tends to 90°, the limit of  $D3(x)|3D$  becomes identically equal to the two-dimensional value  $D3|2D$ . Of course, the factor  $\lambda$  must satisfy the additional constraint that, as the angle of attack is reduced to zero, the limit of  $D3(x)|3D$  must become identically equal to zero.

Consider the following form for  $\lambda$

$$\lambda = (1 - \exp(-x \cdot d\eta/dx)) \quad \text{.....3.1-4}$$

$$\text{In the limit } \lim_{\substack{x \rightarrow \infty \\ \alpha \neq 0}} \lambda = 1$$

As will be seen from Section 3.3 the limit of  $d\eta/dx$  as the angle of attack tends to 0° or 90° is 0 or infinite respectively, giving the limit of  $\lambda$  as 0 or 1 respectively. Hence, the contribution of the Karman vortex wake to the local cross-flow force is a function of the distance  $x$  from the apex and may be expressed as:-

$$D3(x)|3D = [\rho \cdot G_0^2 / (2 \cdot \pi \cdot d \cdot (d/l)) - \rho \cdot G_0 \cdot U^2 \cdot (h/l)] \cdot (1 - \exp(-x \cdot d\eta/dx)) \quad \text{.....3.1-5}$$

Since  $\eta(x)$ ,  $D2(x)$  and  $D3(x)$  are all functions of  $G(x)$ , which, in turn, is a function of  $\alpha$ ,  $d\eta/dx$  and  $G_0$ , these three parameters need to be evaluated before the local forces can be determined.

### 3.2 Determination of the Index $m$

The value of  $m$ , see Eq. 2.0-1, gives a measure of the impulsiveness of vortex shedding. For  $m$  equals unity, the vortex shedding is sinusoidal. As  $m$  increases, the vortex shedding becomes progressively more impulsive. If we argue along physical lines, we observe that the action of viscosity is one that generally tends to smooth out discontinuities. Therefore, in practice, it is not unlikely that  $m$  is either equal to 1 or 3. Although this analysis is developed for a general value of  $m$  the bulk of the computations is executed using  $m=1$ . However, the effect of varying  $m$  on the magnitude of the predicted forces will be illustrated and discussed. It is worth noting that the index  $m$  can only assume an odd integer value since the oscillatory lift force measured on a cylinder normal to the free stream shows generally equal amplitudes in both directions.

### 3.3 Determination of the Rate of Vortex Shedding $d\eta/dx$

By definition, the Strouhal number,  $s$ , for a cylinder of diameter  $d$  normal to a free stream of velocity  $U$  is

$$s = nd/U = d \cdot (d\eta/dt) / (2 \cdot U) \quad \text{.....3.3-1}$$

For a body of revolution at an angle of attack, a cross-flow Strouhal number,  $s'$ , is defined here as

$$s' = (d/2) \cdot (d\eta/dx) \cdot (dx/dt) / (U \cdot \sin\alpha) \quad \text{.....3.3-2}$$

$$d\eta/dx = 2 \cdot s' \cdot \tan\alpha / d$$

The relationship between the Strouhal number and the Reynolds number for a cylinder normal to the stream, see Eq. 2.0-2, is assumed here to hold in form for the inclined body of revolution also. However, a cross-flow Reynolds number,  $Re'$ , based on the local diameter and the cross-flow component of the free stream velocity, is substituted in the expressions proposed by Roshko. Thus,

$$\begin{aligned} s'(x) &= 0.212 - 4.5/Re'(x), & 50 < Re'(x) < 140 \\ \text{and,} & & \\ s'(x) &= 0.212 - 2.7/Re'(x), & 140 < Re'(x) < 10^7 \end{aligned} \quad \text{.....3.3-3}$$

$$\text{where } Re'(x) = U \cdot \sin\alpha \cdot d(x) / \nu \quad \text{.....3.3-4}$$

The above formulae for the cross-flow Strouhal number,  $s'(x)$ , include general cases where the body diameter is changing with distance along the body axis. Similarly, Eq. 3.3-2 above would, in general, read

$$d\eta/dx = 2 \cdot s'(x) \cdot \tan\alpha / d(x), \quad 0^\circ < \alpha < 90^\circ \quad \text{.....3.3-5}$$

A knowledge of the cross-flow Reynolds number enables evaluating  $s'(x)$  and hence  $d\eta/dx$ .

An interesting special case solution is obtained from Eq. 3.3-3 above. It is noted that at a certain station  $x_1$  the Strouhal number  $s'(x_1)$  may become zero. A possible physical interpretation for this solution is that there is no flow separation in the region ahead of this point. In other words, the flow is fully attached over the portion of the body extending from the apex to the station  $x_1$ . The fixing of the point of separation in this manner is perhaps artificial but it appears to give good results at high angles of attack as will be discussed in Section 5.0.

Noteworthy also is that, since both  $s'(x)$  and  $d(x)$  are finite, the limit of  $d\eta/dx$  as  $\eta$  tends to  $0^\circ$  or  $90^\circ$  is 0 or infinite respectively.

### 3.4 Determination of $Go$

Von Karman's vortex street analysis<sup>15</sup> yields the following expressions:-

$$n = (U/2l) (1 - U_2/U) \quad \text{.....3.4-1}$$

and

$$U_2/U = (Go/2U \cdot l) \cdot \tanh(\pi h/l) \quad \text{.....3.4-2}$$

For stability of the vortex street:  $\tanh(\pi h/l) = 1/\sqrt{2}$  or  $h/l = 0.281$

where  $U_2$ ,  $Go$ ,  $h$  and  $l$  are defined in Figure 3 and  $n$  is the frequency of vortex shedding.

Eliminating  $U_2$  between the above two equations and noting that  $r = su/d$ , the expression for  $Go$  becomes

$$Go = U \cdot d \cdot 2\sqrt{2} [1 - s/(d/l)] / (d/l) \quad \text{.....3.4-3}$$

In the case of the inclined body, the equivalent expression for  $G_0$  becomes

$$G_0 = \pi \sin \alpha \cdot d(x) \cdot 2\sqrt{2} [1 - s'(x)/(d/l)] / (d/l) \quad \dots 3.4-4$$

In Eq. 3.4-4, the diameter  $d(x)$  and the pitch length,  $l$ , of the Karman vortex street are allowed to vary with distance,  $x$ , along the axis of the body. However, the ratio  $d/l$  is assumed to remain constant, i.e.  $l$  varies in direct proportion to  $d(x)$ .

The problem of determining  $G_0$  reduces to the problem of evaluating the ratio  $d/l$ . This is not a simple matter.

In a relatively unknown paper by Heisenberg<sup>26</sup>, an attempt was made to determine the dimensions of the wake,  $h$  or  $l$ , in terms of the dimensions of the body producing it. By assuming the back pressure to be equal to the free stream static pressure, the ratios  $d/l$  and  $h/d$  for a flat plate of width  $d$  were found to be 0.1835 and 1.54 respectively. Heisenberg's analysis predicts that these ratios will always be the same no matter what shape the body has, i.e. whether it is a flat plate or a wedge. Doubts were raised by Prandtl regarding the validity of the approach and the latter's criticism was included in the same Reference.

The absence, at present, of an acceptable method for determining the ratio  $d/l$  results in the final expressions for the normal and side forces containing this ratio as the explicit unknown variable. The value of  $d/l$  is found, for the time being, by a trial and error process through matching the predicted normal force coefficient of a control configuration with experimentally obtained data.

#### 4.0 THE LOCAL NORMAL AND SIDE FORCE COEFFICIENTS

##### 4.1 The Local Side Force Coefficient $C_Y(x)$

The local side force coefficient,  $C_Y(x)$ , is obtained by substituting for  $G(x)$  in Eq. 3.0-1 using Eqs. 2.1-1, 3.3-3, 3.3-4, 3.3-5 and 3.4-4. Thus,

$$C_Y(x)/d_{\max} = \{ \rho \cdot U^2 \cdot \sin^2(\alpha) \cdot k_1 \cdot d(x) \cdot \sin^m(\psi \xi) \} / q_S \quad \dots 4.1-1$$

where  $\xi = x - x_1$ ,

$$k_1 = 2\sqrt{2} [1 - s'(x)/(d/l)] / (d/l) \text{ and}$$

$$\psi = 2 \cdot \pi \cdot s'(x) \cdot \tan \alpha / d(x)$$

##### 4.2 The Local Normal Force Coefficient $C_N(x)$

The local normal force coefficient,  $C_N(x)$ , is obtained by substituting for  $P(x)$ ,  $D_2(x)$  and  $D_3(x)$  into Eq. 3.0-2 using Eqs. 3.0-3, 3.0-4, 3.1-2, 3.1-5, 3.3-3, 3.3-4, 3.3-5 and 3.4-4. Thus,

$$\begin{aligned} C_N(x)/d_{\max} = & \{ (1/2) \rho \cdot U^2 \cdot \sin(2\alpha) \cdot \cos(\alpha/2) \cdot \pi \cdot d(x) \cdot d'(x) / 2 \\ & + \rho \cdot U^2 \cdot \sin \alpha \cdot \cos \alpha \cdot m \cdot \psi \cdot k_1 \cdot d^2(x) \cdot |\sin^{m-1}(\psi \xi)| \cdot \cos(\psi \xi) | \\ & + 0.06 \rho \cdot U^2 \cdot \sin^2(\alpha) \cdot k_1^2 \cdot d(x) \cdot (d/l) [1 - \exp(-\xi d \eta / dx)] \} / q_S \quad \dots 4.2-1 \end{aligned}$$

The first term exists only while the local slope of the profile,  $d'(x)$ , is non-zero. The last two terms are present for  $0 < \xi < (LB - x_1)$ , where  $LB$  is the body length.

In deriving Eq. 4.2-1 the differential of  $G(x)$  with respect to  $x$  is required. When doing so, in order to avoid undue complexities, each axial station of the body is treated as if it were part of a cylinder of the same diameter extending downstream to infinity so that neither  $d(x)$  nor  $s'(x)$  are differentiated. However, in Eq. 4.2-1 the local values for  $s'(x)$  and  $d(x)$  are used when computing  $C_N(x)$ . This procedure would not lead to significant errors since the differentials of  $s'(x)$  and of  $d(x)$  with respect to  $x$  exist only over the limited region of the nose.

##### 4.3 Boundary-Layer Displacement Thickness Effects on $C_N$ and $C_Y$

As mentioned earlier in the introduction, the effect of boundary-layer growth increases the effective cross-sectional area of the body thereby giving rise to increased lift. The effects of boundary-layer displacement thickness,  $d^*$ , are included by adding twice  $d^*$  to the local diameter of the body.  $d^*$  is calculated here as the sum of two terms,  $d_1^*$  and  $d_2^*$ . The first term,  $d_1^*$ , is based on the growth of the axially developing boundary layer while the second term,  $d_2^*$ , is based on the growth of the circumferential boundary layer. Schlichting<sup>27</sup> provides the following expressions for evaluating the boundary layer displacement thickness on a flat plate:-

$$\begin{aligned} d^* &= (5/3) \cdot x \cdot Re_x^{-1/2} & Re_x < 3 \cdot 10^5, & \text{ for a laminar boundary layer} \\ \text{and } d^* &= (0.37/8.0) \cdot x \cdot Re_x^{-4/5} & Re_x > 3 \cdot 10^5, & \text{ for a turbulent boundary layer} \end{aligned} \quad \dots 4.3-1$$



In calculating  $d1^*$ ,  $x$  and the Reynolds number  $Re_x$  are based on the axial distance from the apex and the axial component of the free stream velocity, i.e.  $U \cos \alpha$ , while for  $d2^*$ ,  $x$  is replaced by  $\pi \cdot d(x)/4$  and  $Re_x$  is based on the cross-flow component of the free stream velocity, i.e.  $U \sin \alpha$ . It should be pointed out that, in practice, the boundary layer over the nose of a body of revolution is thinner than one that would develop on a flat plate at the same Reynolds number. The above procedure, therefore, overestimates the magnitude of  $d^*$ .

Except where specified, the effect due to  $d^*$  is included in all cases computed and discussed in Section 5.0 below. However, the effect on the predicted forces, when this term is omitted, will be illustrated. It should be noted that this correction affects the non-linear terms as well as the linear term of Munk (See Eqs. 4.1-1 and 4.2-1).

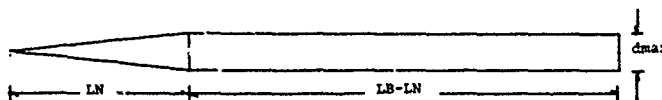
## 5.0 DISCUSSION AND COMPARISON WITH EXPERIMENT

All experimental data referred to in the following were obtained at Mach 0.5 at a Reynolds number of 1.4 million based on maximum body diameter and free stream conditions. These experimental data form part of the results obtained during wind tunnel tests conducted in 1967 in the National Aeronautical Establishment's (NAE) 1.5 metre square trisonic blowdown wind tunnel. The aerodynamic characteristics were determined for a series of long slender bodies of revolution varying in overall fineness ratio from  $LB/d_{max}=17$  to 9 and having nose profiles with semi-apex angle,  $\theta_c$ , varying from  $5^\circ 43'$  to  $18^\circ 26'$ . The following Table provides details on the scope of the test, important dimensions of the configurations tested and the code used to identify each configuration in the Figures referred to below. The raw data were effectively filtered to 3 Hz and all plotted results are individual samples reduced from wind tunnel recorder outputs digitized and punched on cards.

TABLE I TEST SCOPE AND IMPORTANT DIMENSIONS OF MODELS

CONFIGURATION CODE	J	$\theta_c$ degrees	LN $d_{max}$	LB $d_{max}$	644 COMPONENT BALANCE MEASUREMENTS AT MACH			SURFACE PRESSURE MEASUREMENTS AT MACH			FLOW VISUALIZATION AT MACH		
					0.5	2.0	3.5	0.5	2.0	3.5	0.5	2.0	3.5
1001	1	5° 43'	5	17	x	x	x	x++	x	x	x		x
2001	4/3	7° 36'	5	17	x	x	x						
3001	5/3	9° 28'	5	17	x	x	x	x+	x	x+	x		
4001	2	11° 19'	5	17	x	x	x						
5001	1	9° 28'	3	15	x+	x	x	x	x	x	x		x
6001	4/3	12° 31'	3	15	x	x	x						
7001	5/3	15° 31'	3	15	x+	x	x	x	x	x+	x		
8001	2	18° 26'	3	15	x	x	x						
1002	1	5° 43'	5	11	x	x	x	at $\alpha = 0, 3, 7, 11$ deg.			$\alpha = 3, 7, 11, 18, 25$		
2002	4/3	7° 36'	5	11	x	x	x						
3002	5/3	9° 28'	5	11	x	x	x	additional			$\alpha = 7, 11, 18, 25$		
4002	2	11° 19'	5	11	x	x	x						
5002	1	9° 28'	3	9	x	x	x	+ $\alpha = 18$ and $25$			$\alpha = 7, 11, 18, 25$		
6002	4/3	12° 31'	3	9	x	x	x						
7002	5/3	15° 31'	3	9	x	x	x	+ $\alpha = 15$					
8002	2	18° 26'	3	9	x	x	x						
					*, + additional balance measurements while model is being rolled			+ $\alpha = 0$ at $M=4.25$					
					( $\theta \alpha = 0, 2, 5, 11, 18, 25$ )								
					(+ $\alpha = 7, 11, 18, 25$ )								

$$\text{Nose Profile given by the Equation } \frac{d}{d_{max}} = 1 - \left(1 - \frac{x}{LN}\right)^J$$



In attempting to predict the loads, it is helpful to know a priori the extent to which the flow over an inclined body of revolution is stable or repeatable. To achieve a measure of the flow stability and repeatability, the forces on one of the models, Configuration 1001, were measured at fixed angles of attack while rolling the model through 360 degrees. The normal force coefficient,  $C_N$ , its centre of pressure,  $CPN$ , and the side force coefficient,  $C_Y$ , are shown in Figure 4 plotted versus roll angle. Clearly, both normal and side forces are dependent on roll orientation; the spread in the data increases with increasing incidence. A possible explanation for this is that small surface imperfections may be causing a substantial change in the development of the boundary layer as the roll angle is changed, resulting in a shift of the point of flow separation, hence a change in the position of the rolled-up shear layers, to thereby affect the vortex-induced normal and side forces. (See also Reference 28). Under these circumstances, any attempt, based solely on the assumption of boundary-layer development on a perfectly uniform surface, to predict the location of separation,  $x_1$ , especially for angles of attack above say  $10^\circ$  for this Configuration, would be wrought with uncertainties. For this reason, it is perhaps more practical to use available boundary-layer methods to predict the most suitable axial station at which flow separation can be artificially induced. In the meantime, it was decided to apply Eq. 3.3-3 throughout the angle of attack range  $0^\circ < \alpha < 90^\circ$ , when calculating the distance,  $x_1$ , by equating  $s'(x)$  to zero, even though, at the high Reynolds number of this test ( $Re=1.4$  million), the calculated value for  $x_1$  is zero in all cases examined for incidences

as low as  $1^\circ$ , i.e. the separation is predicted to start at the apex at practically all incidences for all the configurations investigated. The effect of varying  $x_1$  will be analysed but first let us discuss how the ratio  $d/l$  is determined.

It is seen from Eqs. 4.1-1 and 4.2-1 that the final solutions for the local forces could only be expressed in terms of the unknown ratio  $d/l$ . To determine this ratio a control configuration is selected such that by matching its predicted normal force coefficient for a range of angles of attack with that measured experimentally the value of  $d/l$  giving the best fit would be chosen. The choice of Configuration 1001 in this case as the control configuration is based on the experimental evidence that flow separation occurs on this Configuration at lower angles of attack than it does on the others.

Computations were made using three values for the ratio  $d/l$  and  $m=1$ . The computed values of  $C_N$ ,  $C_Y$  and  $C_{PN}$  for the Control Configuration are compared with experimental data and are shown in Figure 5. Clearly, the best fit is obtained when  $d/l$  is accorded the value 0.220. In passing, it is worth noting the large effect that a small change in  $d/l$  exerts on the magnitude of the normal force. This is not altogether surprising since the induced suction pressure caused by a vortex is proportional to the square of the inverse of the distance from the vortex: so that as  $l$  decreases, i.e.  $d/l$  increases, the normal force increases.

Even with the best choice for the ratio  $d/l$ , i.e.  $d/l=0.220$ , there is some discrepancy between theory and experiment in the low angle of attack range. It will be remembered that the application of Eq. 3.3-3 yields a value  $x_1=0$  at the test Reynolds number investigated. It was observed from flow visualisation runs on this Configuration, however, that separation over the nose-section does not in fact occur until about  $\alpha=11^\circ$ . It is possible that the noted discrepancy is due to the unrealistic location of the point of separation at  $x_1=0$ . When  $x_1$  is allowed to vary as a function of the angle of attack, see Figure 6, closer agreement with experiment is achieved in the range  $0^\circ < \alpha < 11^\circ$  even though none of the functions employed are the result of a consideration of the development of the boundary layer. A more suitable boundary-layer method to determine  $x_1$ , or to fix  $x_1$  by predicting the most favourable location at which flow separation may be artificially induced, would prove useful. Of course such a method can be readily incorporated into the existing computer program.

Let us now assess the effects of changing the value of the index  $m$ .

The predicted values of  $C_N$ ,  $C_Y$  and  $C_{PN}$ , for the Control Configuration, are calculated using  $m=1, 3$  and  $5$ , and  $d/l=0.220$ . These values are compared with measured data as shown in Figure 7. There is little doubt that  $m=1$  provides the best fit. Therefore, this value of  $m$  will be adopted.

With  $d/l=0.220$ ,  $m=1$  and  $x_1$  calculated with the aid of Eq. 3.3-3, we may now proceed to determine the effectiveness of this theory to predict the normal and side forces acting on other configurations at the same Mach number.

A comparison between the computed values of  $C_N$ ,  $C_Y$  and  $C_{PN}$  with those measured experimentally is shown in Figure 8 for the selected Configurations identified in the same Figure. It is seen that the normal force and its centre of pressure location are, in general, fairly well predicted. Again, the minor discrepancies are attributed to the non-representative location of the point of separation at the apex.

The side force coefficient is less well predicted and only qualitative values are provided by this theory. It is possible that this is the result of two factors. The first is the unrealistic location of the onset of separation at the apex. The second is the exclusion of the surface shear stress contribution from the side force. As an indication of the magnitude of these shear stresses, the experimentally measured rolling moment coefficient,  $C_l$ , is plotted against  $\alpha$  - as  $4.C_l$  versus  $\alpha$ , marked thus  $x$ - and shown in Figure 8. It is seen that there exists a not inconsiderable rolling moment. As all the configurations examined here are bodies of revolution, the source of this rolling moment can only be the action of surface shear stresses; the surface pressure forces cannot produce a rolling moment. Estimation of these stresses and their contribution to the normal or side force is a task outside the scope of this paper.

Application of this method to estimate  $C_N$  or  $C_Y$  at high angles of attack is illustrated in Figure 9. The predicted values of  $C_N$  and  $C_Y$  for Configuration 1001 are shown in the range  $1^\circ < \alpha < 85^\circ$ . It is observed that there are minor 'kinks' in the  $C_N$  curve for angles of attack below  $40^\circ$ . At an angle of attack around  $45^\circ$  there appears a phenomenon similar to the stalling process of the flow over an airfoil. At angles of attack above  $55^\circ$ , sizeable excursions of  $C_N$  are noted. These three regions are perhaps indicative of the reason behind the existence of the three types of flow - steady and stable, steady and bi-stable, and unsteady or periodic - described by Thomson<sup>14</sup> and often observed in practice as the angle of attack is increased. The variation of  $C_Y$  with  $\alpha$  displays a similar behaviour at high angles of attack.

In all cases thus far computed, the influence of the boundary-layer displacement thickness,  $d^*$ , has been included. The effect of omitting  $d^*$  on the predicted values of  $C_N$ ,  $C_Y$  and  $C_{PN}$  for Configuration 1001 is shown in Figure 10. It is seen that the omission of the effect of  $d^*$  reduces slightly the normal force. The effect on  $C_Y$  and  $C_{PN}$  is also quite small. Thus, it is not expected that a more refined boundary-layer method for calculating  $d^*$  would significantly change the calculated results.

Finally, a comparison is made between the predicted normal force distribution,  $CN(x)$ , and that measured experimentally. The circumferential pressure distributions for the control configuration were measured at 24 axial stations located along a generator, by rolling the model continuously through a  $360^\circ$  roll angle at a fixed angle of attack\*. These pressures were integrated at each station to yield the local normal force coefficient  $CN(x)$ . The comparisons are presented in Figure 11. It should be re-emphasized here that the mere act of rolling the model, especially at the higher angle of attack,  $\alpha = 11^\circ$ , can sufficiently change the flow picture over the model resulting in the measurement of a changing pressure distribution. At best, such a pressure measurement can be described as the average of what the flow is like at all roll orientations between  $0^\circ < \phi < 360^\circ$ . The comparison shows that over the nose portion the predicted local normal force is higher than is measured experimentally. As pointed out earlier, this may be due to the assumption of the presence of separation over the nose which, in practice, does not take place until the angle of attack exceeds  $11^\circ$ .

The computer program is written in Fortran IV programming language. Various input flags have been incorporated into the program to make it quite flexible. A typical run on an IBM 360/67 computer to solve for a configuration at angles of attack between  $1^\circ$  and  $30^\circ$  using  $1^\circ$  steps requires less than one minute of CPU time.

## 6.0 CONCLUSIONS

A method for estimating the loading distribution on inclined long slender bodies of revolution is formulated. It is based on the analogy that exists between the two-dimensional flow on a cylinder impulsively set in motion from rest normal to its axis and the flow in the cross-plane normal to the axis of the inclined body moving downstream with a velocity  $U \cos \alpha$ . A feature of this method is that prediction of the side force distribution, which occurs as a result of the asymmetric vortex shedding, can be made simply and economically.

The derived forces, particularly the normal force, depend critically on the vortex spacing ratio expressed as  $d/l$ . This ratio is obtained, for the time being, by matching the measured and predicted normal force for a control configuration. Detailed normal and side force distributions can then be computed for other configurations.

The theory predicts reasonably well the normal force and its centre of pressure location. Qualitatively good prediction of the side force is also achieved.

## 7.0 RECOMMENDATIONS

1- There is a need for a proper boundary layer approach to estimate the distance  $x_l$  from the apex of the station at which separation of the shear layers first occurs.

2- More accurate experimental data on the variation of the Strouhal number with Reynolds number at various Mach numbers would be required for any future extension of this method to predict the loading on inclined slender bodies of revolution in cases where compressibility effects are significant.

3- There is a likelihood that the ratio  $d/l$  is Mach number dependent. Since this ratio is critical for estimating the loading distribution some experimental verification of its magnitude at various Mach numbers would be desirable.

4- Since there appears to be a valid analogy between the two-dimensional flow over the cylinder normal to a stream and the three-dimensional flow in the moving cross-plane perpendicular to the axis of the inclined body of revolution, an alternative and unorthodox approach may be taken in cases where the induced effects from the presence of an organized pattern of vortices are detrimental. It is suggested that in such cases this organized pattern be deliberately disrupted using techniques already applied successfully to achieve this end in the two-dimensional case of the cylinder normal to a stream. A highly diffused wake would be produced resulting in a small or no side force and little or no induced forces on lifting surfaces such as wings or tail.

## 8.0 REFERENCES

- 1- "Proceedings of the Meeting on Ground Wind Load Problems in Relation to Launch Vehicles" Compilation of papers presented at the NASA Langley Research Centre, 7-8 June, 1966.
- 2- "Handbook of Supersonic Aerodynamics" Bodies of Revolution Section-8 NAVWEPS Report 1488, Vol. 3, October, 1961.
- 3- Dixon, R.C. and Ohman, L.H. "Black Brant II and V Wind Tunnel Tests" NAE Data Report 5X5/0011, November, 1965.
- 4- Brown, R.C. "On the Asymmetrical Aerodynamic Forces of Slender Bodies of Revolution" Unpublished Report McDonnell Aircraft Corporation, St. Louis, Missouri.

- 5- Peake, D.J., Rainbird, W.J. and Atraghji, E. "Three Dimensional Flow Separation on Aircraft and Missiles" AIAA Journal, Vol.10, No.5, pp 567-580, May, 1972.
- 6- Thomson, K.D. and Morrison, D.P. "On the Asymmetric Shedding of Vortices from Slender Cylindrical Bodies at Large Angles of Yaw" W.R.E. HSA TN 106, May, 1965.
- 7- Atraghji, E. "Influence of Mach Number, Semi-Nose Angle and Roll Rate on the Development of the Forces and Moments over a Series of Long Slender Bodies of Revolution" NAE Data Report 5X5/0020, September, 1967.
- 8- Atraghji, E. "Pressure Distribution Over a Family of Inclined Long Slender Bodies of Revolution at  $M=0.5$ , 2.0 and 3.5" NAE Data Report 5X5/0029, August, 1968.
- 9- Allen, H.J. and Perkins, W. "A Study of the Effect of Viscosity on the Flow over Slender Inclined Bodies of Revolution" NACA Report 1048, 1951.
- 10- Munk, M. "The Aerodynamic Forces on Airship Hulls" NACA Report 184, 1924.
- 11- Kelly, H.R. "The Estimation of Normal Forces, Drag and Pitching Moment Coefficients for Blunt-Based Bodies of Revolution at Large Angles of Attack" J.Ae.Sc. pp 549-565, August, 1954.
- 12- Schwabe, M. "Pressure Distribution in Non-Uniform Two Dimensional Flow" NACA TM 1039, 1943
- 13- Hill, J.A.F. "Forces on Slender Bodies at Angles of Attack" Naval Supersonic Laboratory, MIT, R-a 100-59, May, 1950.
- 14- Thomson, K.D. "The Estimation of Viscous Normal Force, Pitching Moment, Side Force and Yawing Moment on Bodies of Revolution at Incidence up to  $90^\circ$ " WRE-Report-782, October, 1972.
- 15- Durand "Aerodynamic Theory, Karman Vortex Streets" Vol. II, page 342 Dover publication, 1963.
- 16- Roshko, A. "On the Development of Turbulent Wakes from Vortex Streets" NACA Report 1191, 1954.
- 17- Delany, N.K. and Sorensen, N.E. "Low Speed Drag of Cylinders of Various Shapes" NACA TN 3038, November, 1953.
- 18- Jones, G.W. "Unsteady Lift Forces Generated by Vortex Shedding About a Large Stationary and Oscillating Cylinders at High Reynolds Number" ASME Symposium, 68-FE-36, May, 1968.
- 19- Fung, Y.C. "Fluctuating Lift and Drag Acting on a Cylinder in a Flow at Supercritical Reynolds Numbers" J.Ae.Sc., Vol. 27, N.11, 1960.
- 20- Gerrard, J.H. "An Experimental Investigation of the Oscillating Lift and Drag of a Circular Cylinder Shedding Turbulent Vortices" J.F.M., Vol. 11, 1961.
- 21- Morkovin, M.V. "Symposium on Fully Separated Flows" ASME Fluid Engineering Division Conference, Philadelphia, P.A., May, 1964.
- 22- Bearman, P.W. "On Vortex Shedding from a Circular Cylinder in the Critical Reynolds Number Regime" J.F.M. Vol. 37, Part 3, July, 1969.
- 23- Birkhoff, G. "Formation of Vortex Streets" Journal of Applied Physics, Vol. 24, N 1, January, 1953.
- 24- Wille, R. "Karman Vortex Streets" Progress in Aeronautical Sciences, Vol. 7, 1967.
- 25- Ward, G.N. "Supersonic Flow Past Slender Pointed Bodies" Quarterly Journal of Mechanical and Applied Mathematics, Vol. 2, Part I, pp 75-97, March, 1949.
- 26- Heisenberg, W. "Absolute Dimensions of Karman Vortex Motion" NACA TN 126, January, 1923.
- 27- Schlichting, H. "Boundary Layer Theory" Translated by Dr. J. Kestin, pp 28 and 598, Sixth Edition, McGraw-Hill Book Company, 1968.
- 28- Wardlaw, A.B., Jr. and Morrison, A.M. "Induced Side Forces on Bodies of Revolution at High Angles of Attack" NSWC/WOL/TR75-176, November, 1975.

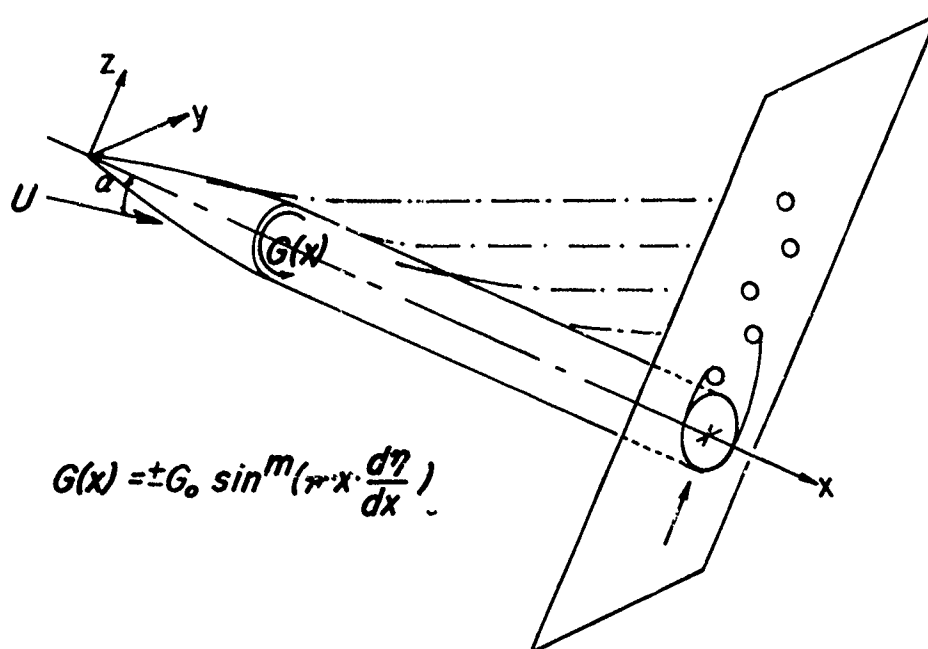


Fig.1 Flow in the cross-plane of an inclined body of revolution

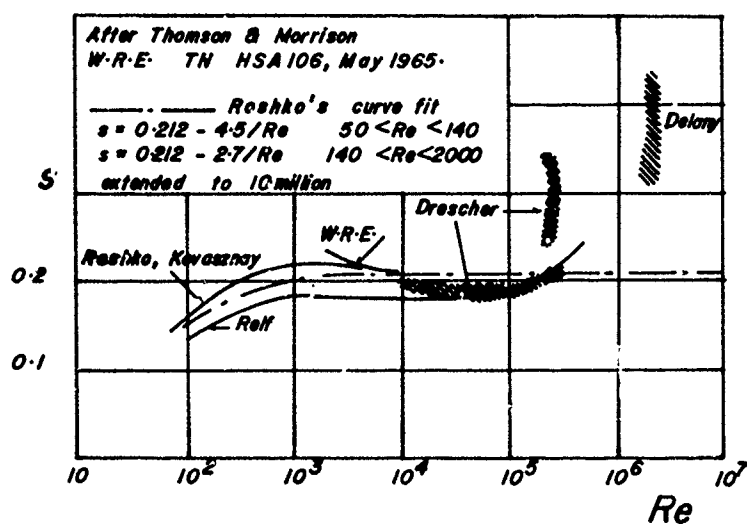


Fig.2 Summary of experimental data on the variation of the Strouhal Number with Reynolds Number

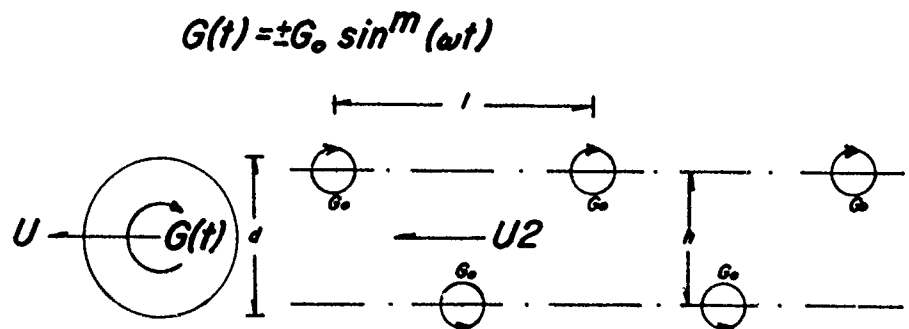


Fig.3 Parameters defining the Karman vortex street behind a circular cylinder normal to the stream

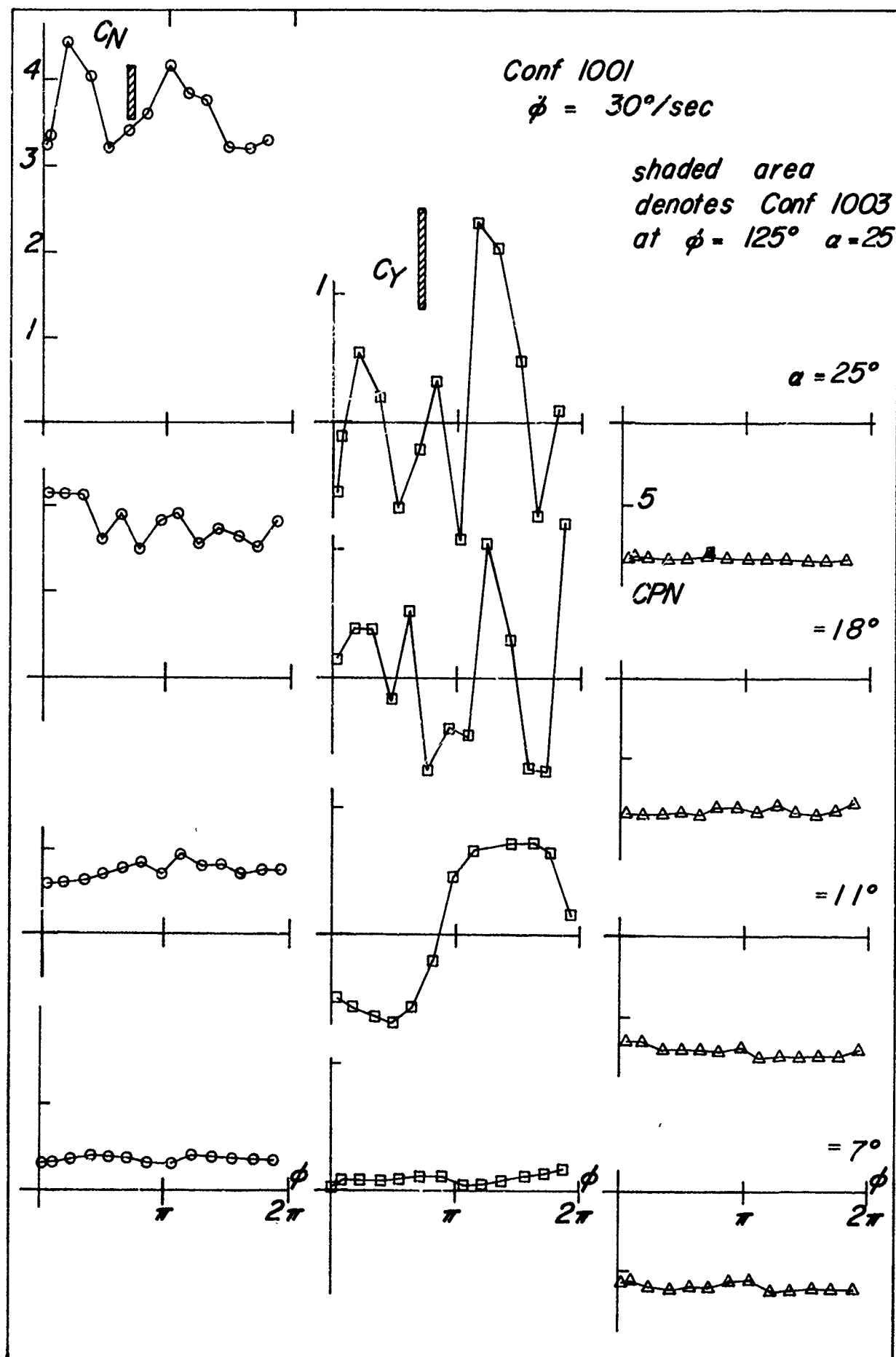
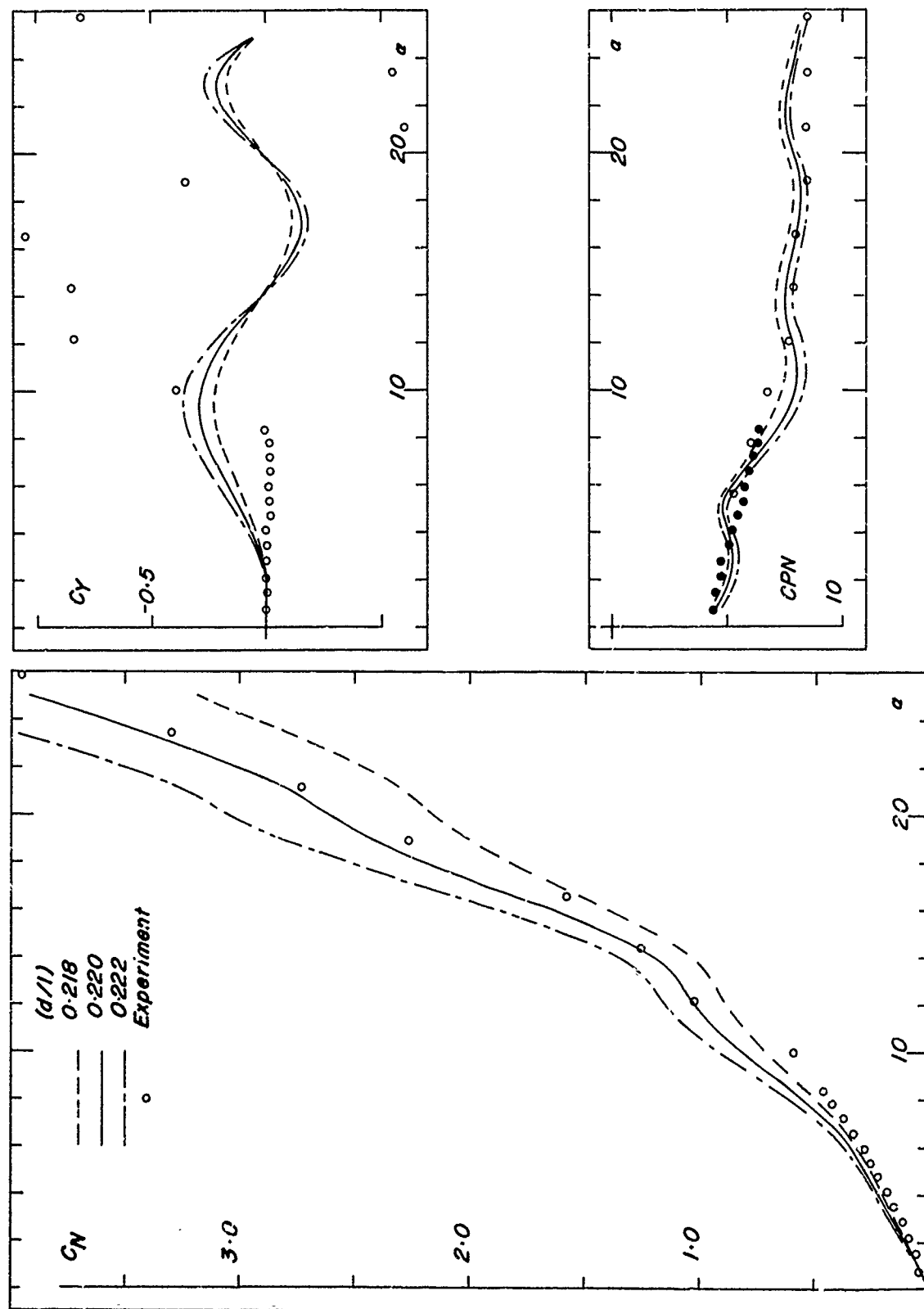


Fig.4 Variation of the measured CN, CY and CPN of configuration 1001 with roll orientation at various angles of attack

Fig.5 Effect of varying the ratio  $d/l$  on the predicted  $C_N$ ,  $C_Y$  and  $C_{PN}$  of configuration 1001

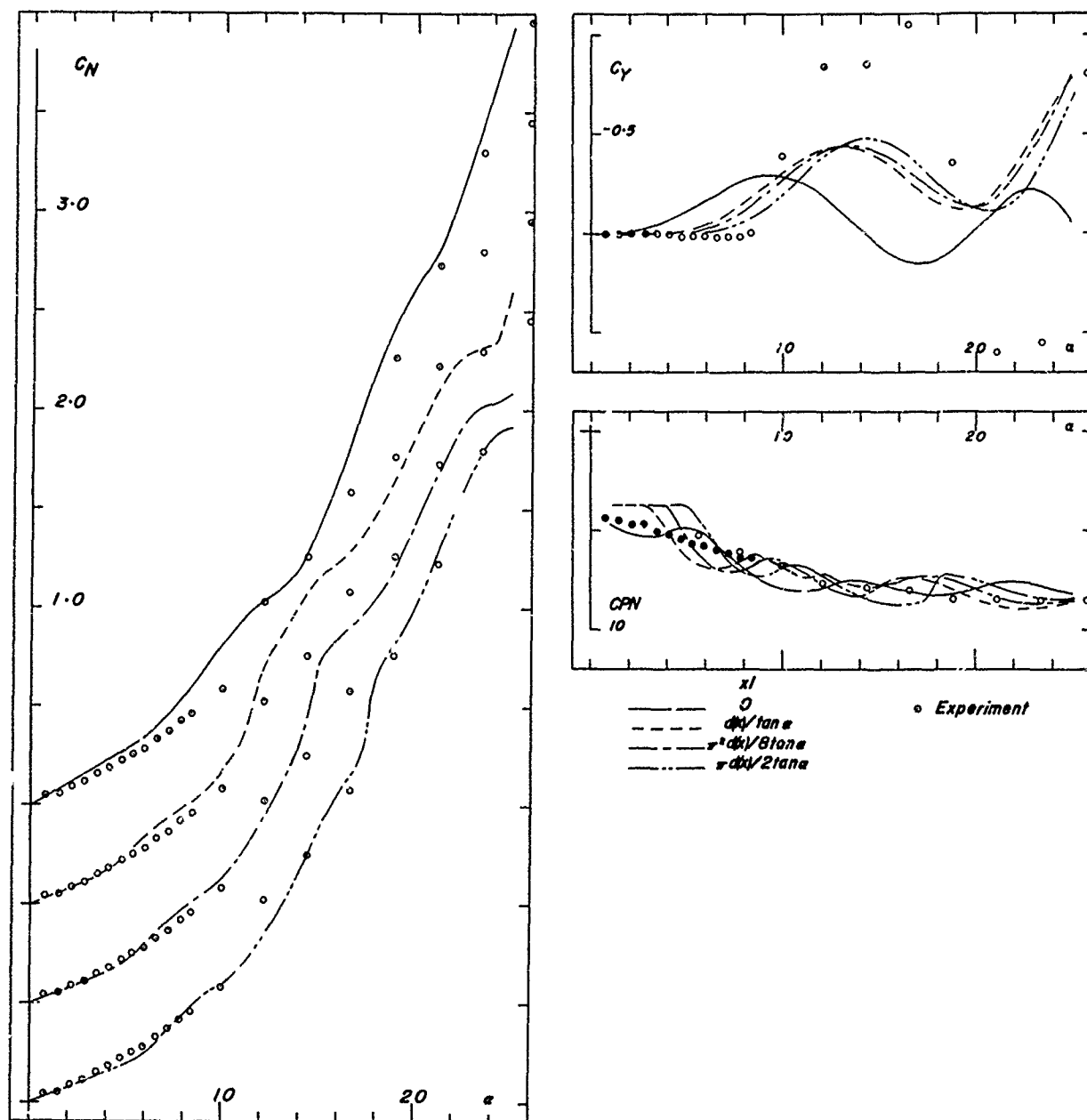
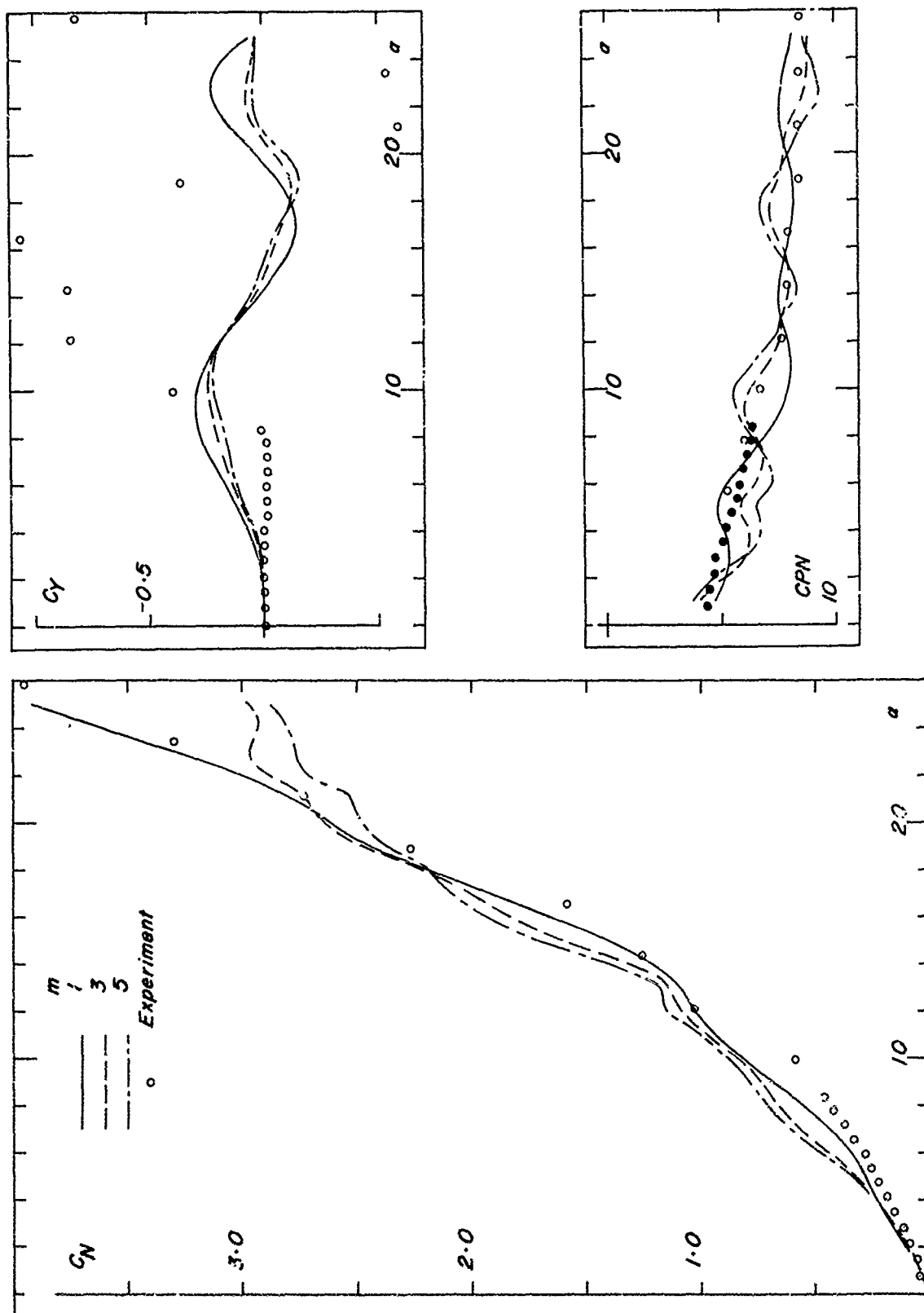


Fig.6 Effect of varying  $x_1$  on the predicted  $C_N$ ,  $C_Y$  and  $CPN$  of configuration 1001



Fig.7 Effect of varying the impulsive index  $m$  on the predicted CN, CY and CPN of configuration 1001

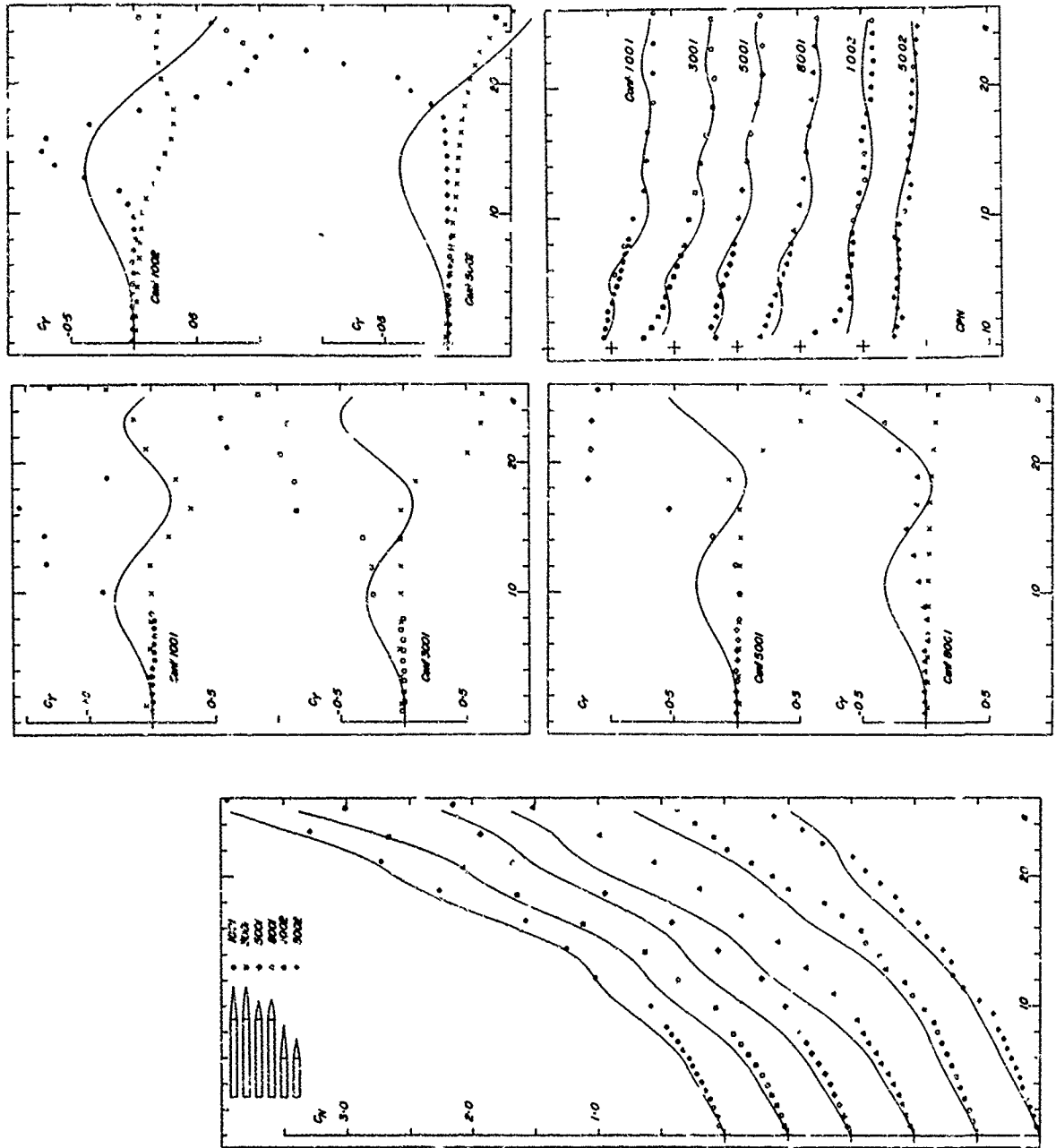
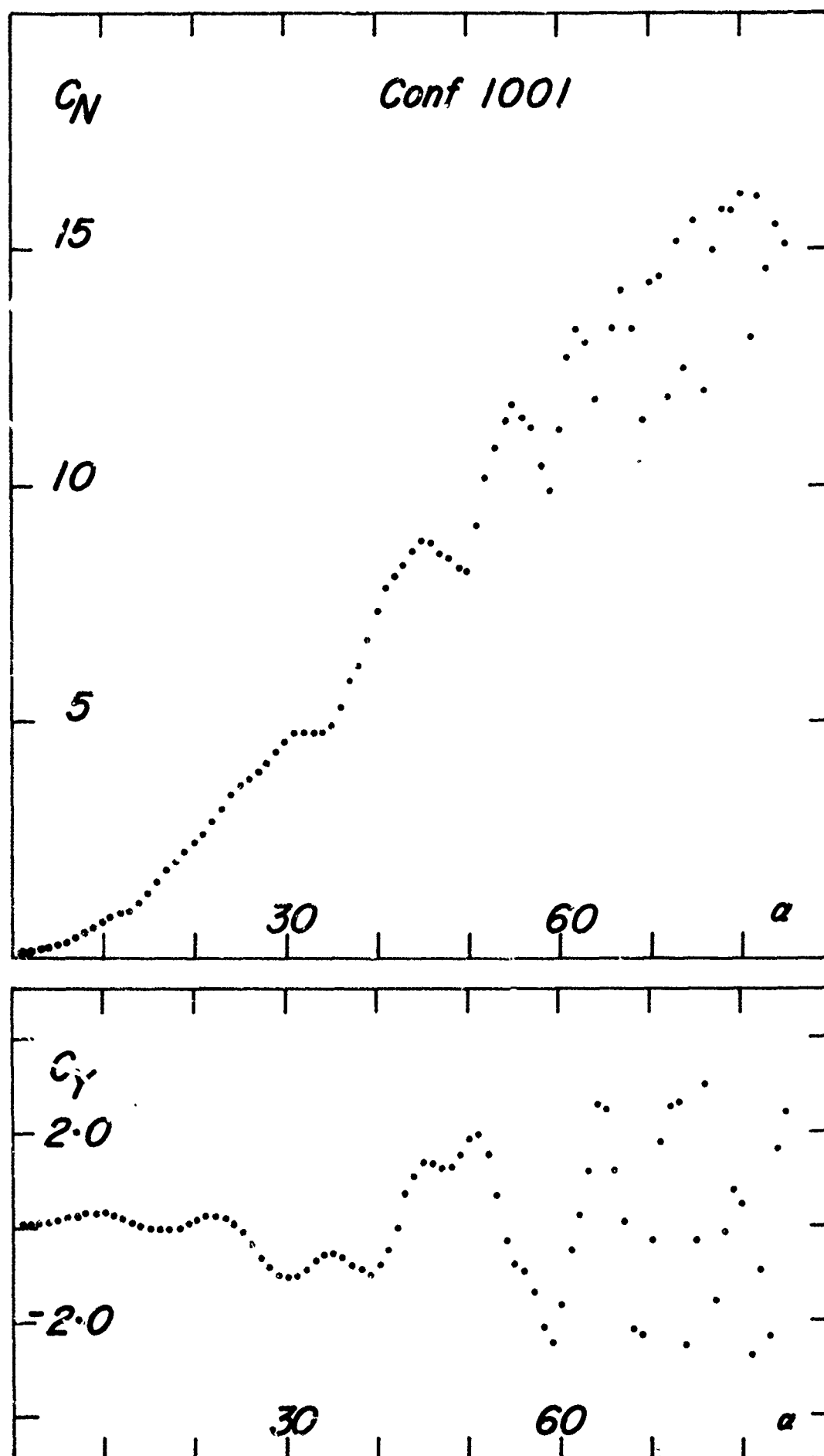
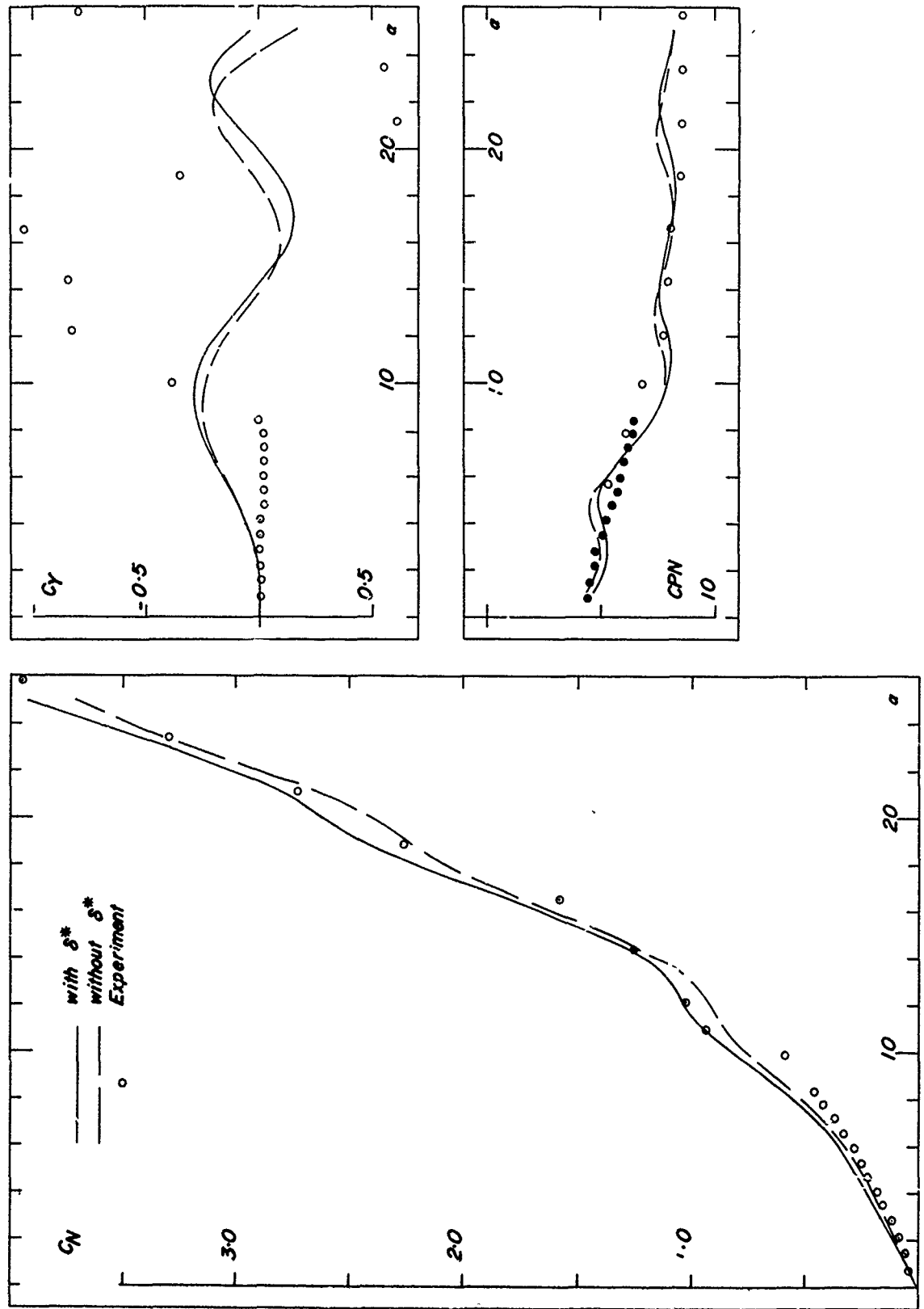


Fig.8 Comparisons of the predicted CN, CY and CPN with experiment for various configurations

Fig.9 Predicted variation of  $C_N$  and  $C_Y$  with  $\alpha$  in the range  $\alpha = 0^\circ \rightarrow 85^\circ$

Fig.10 Effect of boundary-layer displacement thickness  $d^*$  on the CN, CY and CPN of configuration 1001

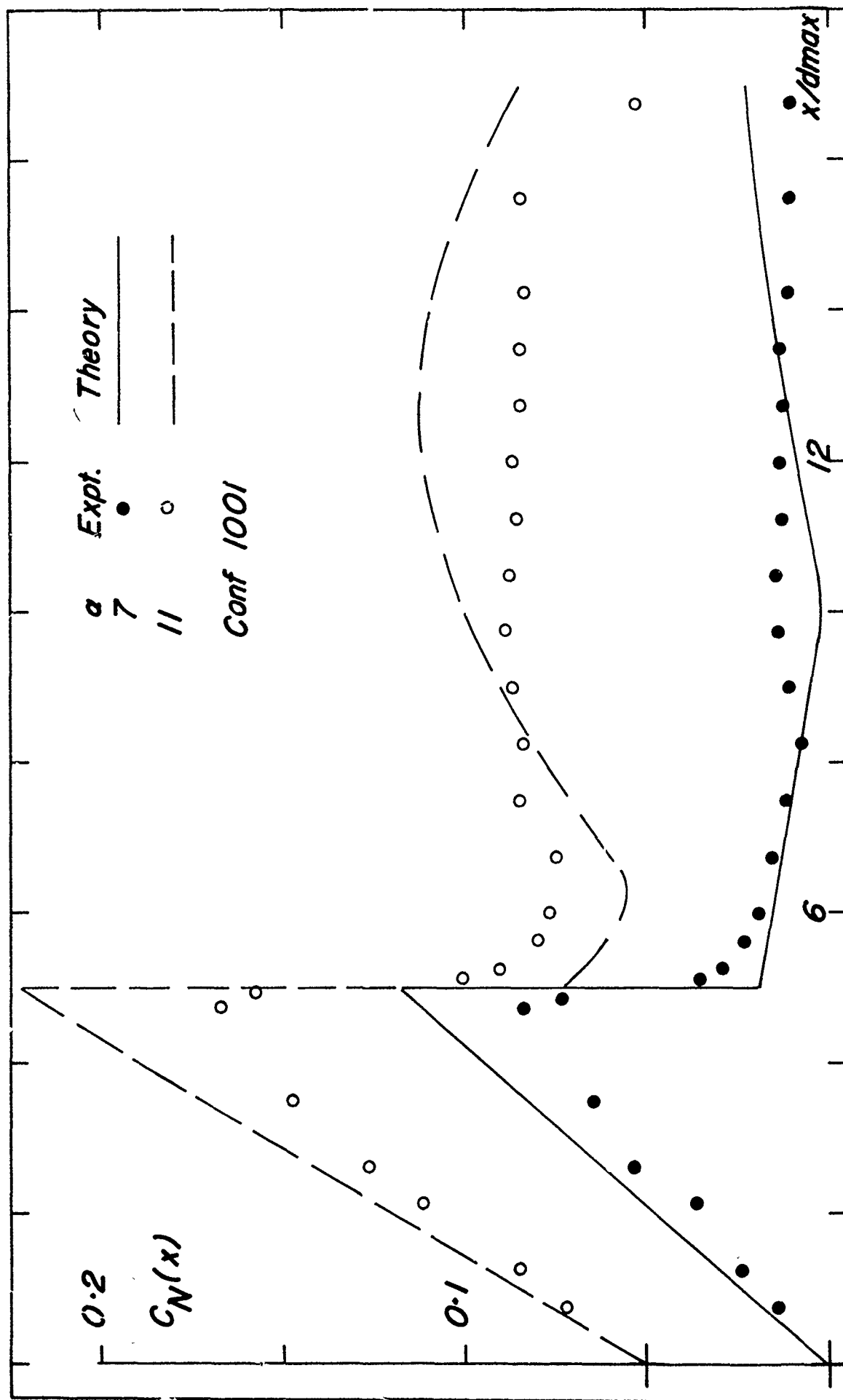


Fig. 11 Comparison between the predicted and measured  $C_N(x)$  distribution at  $\alpha = 7^\circ$  and  $11^\circ$

ASSESSMENT OF EXISTING ANALYTIC METHODS FOR PREDICTION OF HIGH ANGLE-OF-ATTACK LOADS  
ON DELTA WINGS AT SUPERSONIC SPEEDS

Ernest Jean Landrum and James C. Townsend  
NASA Langley Research Center  
Hampton, Virginia 23665

SUMMARY

The purpose of this paper is to provide an assessment of the applicability of four loading prediction methods to high angle-of-attack conditions for simplified wing-body configurations. The methods are: The tangent wedge approximation, the linear theory methods of Middleton and Woodward, and a shock-fitting finite-difference technique. Estimates obtained by these methods were compared with experimental pressure data on delta wings to examine the effects of Mach number, camber, sweep angle, and angle of attack.

Results indicate that all of the methods provided reasonable estimates at moderate angles of attack. At these moderate angles of attack, the methods of Middleton and Woodward provided good estimates at Mach numbers higher than those usually associated with linear theory. Only the finite-difference method provided reasonable load estimates at high angles of attack, where the other methods were unable to predict lower surface pressures.

SYMBOLS

b	Span
c	Local chord
$\bar{c}$	Mean geometric chord
$c_n$	Section normal-force coefficient, $\frac{1}{S} \int_0^1 \frac{c}{\bar{c}} \Delta C_p d\left(\frac{x}{\bar{c}}\right)$
$C_L$	Lift coefficient, $L/q_\infty S$
$C_{L,des}$	Design lift coefficient
$C_p$	Pressure coefficient, $(p - p_\infty)/q_\infty$
$\Delta C_p$	Lifting pressure coefficient, $C_{p,lower} - C_{p,upper}$
L	Lift
M	Mach number
p	Local static pressure
$p_\infty$	Free-stream static pressure
$q_\infty$	Free-stream dynamic pressure
S	Wing reference area
x	Longitudinal distance from model apex
y	Spanwise distance from model center line
$\alpha$	Angle of attack, deg
$\Lambda$	Leading-edge sweep angle, deg

INTRODUCTION

Recent trends toward automation of the airplane design process accentuate the need for analytic techniques for the prediction of aerodynamic loads. Of particular importance is the need for methods applicable to the critical design conditions occurring at high angle of attack and high Mach number.

At this time, there is no analytic technique for the accurate prediction of detailed loadings at high angle of attack for supersonic speeds. An assessment of currently available methods which may apply to this problem is needed. Two such methods are those of Middleton and Woodward both of which are linear theory methods primarily applicable to low angles of attack and moderate supersonic speeds. Another method is the tangent wedge approximation which is frequently used to calculate the pressures on sharp two-dimensional bodies at hypersonic speeds. Useful results can be obtained with this method for angles up to

shock-detachment conditions but all three-dimensional effects are neglected. A numerical technique which should be applicable is an inviscid shock-fitting finite-difference approach represented by the method developed by Moretti.

In order to assess the applicability of prediction methods and to provide guidance in the modification of existing theories or in the development of entirely new methods, there is a need for systematic and detailed experimental data. As part of a test program for the evaluation of the aerodynamic performance of a series of twisted and cambered delta wings designed for a Mach number of 3.5 three pressure models, duplicating three of the force models, were constructed. These pressure models aided in the analysis of the force data and provided systematic and detailed pressure data for comparison with theory.

The purpose of this paper is to use that experimental data for an assessment of the tangent wedge, Middleton, Woodward, and shock-fitting finite-difference methods for the prediction of high angle-of-attack loads.

#### PREDICTION METHODS

The following sections present the four prediction methods to be compared with the experimental pressure distributions. One method uses the local surface slope to predict the surface pressure (tangent wedge), two others use linearized theory (Middleton and Woodward methods), and the last uses a numerical solution of the inviscid flow equations (shock-fitting finite-difference method). See Figure 1.

##### Tangent Wedge

This is a well-known empirical method for predicting surface pressures in hypersonic flow (Ref. 1) included as an option in the computer program of Reference 2. The basic premise of the tangent wedge method is that there is little change in the pressure or flow inclination through the thin shock layer of the hypersonic flow over a two-dimensional surface. This leads to the assumption that the pressure at a point on the surface of a wing is the same as that given by the oblique shock relations for flow over a flat plate at the same inclination and free-stream Mach number. Thus, the pressure at each point on the surface is computed independently, and no interaction with the flow at other points is considered. The method is exact for flow over a wedge with an attached shock wave; it loses validity as the surface curvature increases, as the flow becomes strongly three dimensional, or if the shock wave is detached. Its application to the present configurations is based on the fact that at moderate to high supersonic Mach numbers the shock lies close to a highly inclined surface such as a wing at high angle of attack.

##### Middleton

In this method, which is based on linearized supersonic flow theory, the pressure distribution is calculated by a linear superposition of lifting surface and thickness pressures. For the calculation the planform is divided into a planar grid system of rectangular panels. The lifting surface pressures are obtained by the technique described in References 3 and 4 using refinements given in Reference 5. In this technique the pressure at a point on the surface is related to the local surface slope at that point, taking into account the influence of upstream pressures as defined by a system of elementary horseshoe vortices fitted to the grid. In the computer program used for the present calculations (Ref. 6), there is an option to constrain the lifting pressure coefficient at each point to a specified fraction of the vacuum pressure coefficient. The thickness pressures are calculated by a near-field method, with line sources replacing the horseshoe vortices in the same planar grid system. Both the lifting surface and thickness pressure calculations employ a streamwise marching technique and do not require matrix solutions.

##### Woodward

This linearized theory approach to the aerodynamic analysis of wing-body-tail configurations, presented in References 7 and 8, has been extended in Reference 9 by the introduction of several aerodynamic singularity distributions which improve its capability to represent arbitrary shapes.

The configuration surface is subdivided into a large number of trapezoidal panels, each of which contains an aerodynamic singularity distribution. A constant source distribution is used on the body panels, and a vortex distribution having a linear variation in the streamwise direction is used on the wing and tail. The normal components of velocity induced at specified control points make up the coefficients of a system of linear equations relating the strengths of the singularities to the magnitude of the normal velocities. A matrix inversion procedure is used to solve this system of equations for the singularity strengths which satisfy the boundary conditions of tangential flow at the control points for a given Mach number and angle of attack. From these singularity strengths, pressure coefficients are calculated and the forces and moments acting on the configuration are determined by numerical integration. This method, although it is a linearized theory, does not make the small angle assumptions. It also limits pressures to vacuum after all the pressures have been calculated.

##### Shock-Fitting Finite-Difference Method

The general numerical scheme developed by Moretti (Ref. 10) for solving the Euler equations for supersonic flow about complex configurations has been extended and implemented for digital computation (Ref. 11). This method uses a finite-difference marching technique of second-order accuracy to compute the complete flow field between the body and the bow shock wave. Essentially, the flow equations are recast to give the derivatives of the flow variables in the marching direction (along the body axis) in terms of the quantities and their derivatives in a plane perpendicular to the axial direction. Starting from a given data plane, these derivatives are integrated a single step forward (along the axis) using a MacCormack two-level predictor-corrector finite-difference scheme to obtain a new data plane. This process is repeated until the end of the model is reached. The step size in the marching direction is computed before each step in order to satisfy the Courant-Friedrichs-Lewy criterion for stability. The computational grid is a conformal mapping of the region between the body and the bow shock into a rectangular region. If embedded shock waves

occur in the flow, the mesh is adjusted so the mesh lines coincide with these shocks. Across each of the shock waves the Rankine-Hugoniot relations are satisfied explicitly. In order to provide a smooth surface (continuous second derivative, to avoid generating spurious shock waves) the configuration is defined by analytic functions (generally conic sections) through a relatively few prescribed points.

The only inherent limitation on this finite-difference marching technique is that the velocity component in the marching direction must always be supersonic. However, the present implementation of the technique is somewhat restricted in the configurations it can handle. The most important restriction for the present study is that unless the flow is supersonic normal to the wing leading edge, the leading edge must be blunt. A second restriction is that the configuration cross section must be single valued in polar coordinates; thus, for example, the configuration cannot have a highly cambered wing. In addition, the two methods presently in use for generating the initial data plane for starting the computational process may require modifications to the configuration nose. One method is to begin with a circular cone, whose half angle must be greater than the maximum angle of attack. The other choice is to begin with a blunt nose, which may be very small, but which nonetheless introduces the further complication of an entropy layer at the body surface.

## EXPERIMENTAL INVESTIGATION

### Models

At the design Mach number of 3.5 three sweep angles were selected to cover three basic leading-edge conditions:  $76^\circ$  for a fully subsonic leading edge,  $68^\circ$  for a supersonic leading edge with detached shock (estimated to be detached at angles of attack greater than  $3^\circ$ ), and  $55^\circ$  for a supersonic leading edge with attached shock (estimated to be detached at angles of attack greater than  $15^\circ$ ).

Force models of a flat wing and a twisted and cambered wing designed by the method of Reference 12 to have a minimum drag at  $C_{L,des} = 0.1$  and  $M = 3.5$  were constructed for each sweep angle. In addition, for the  $76^\circ$  sweep angle a twisted and cambered wing designed (by the method of Ref. 13) to have minimum drag at  $C_{L,des} = 0.05$  and  $M = 3.5$  were constructed. Design details are given in Reference 14. In order to provide a housing for the strain-gage balance and mounting sting a body of revolution was added symmetrically about the wing center line. Three of the force models were duplicated as pressure models: the  $76^\circ$  sweep flat, the  $76^\circ$  sweep  $C_{L,des} = 0.1$ , and the  $55^\circ$  flat wings. The pressure models are shown as shaded planforms in Figure 2.

### Tests

Force and moment as well as pressure distribution data were obtained at five Mach numbers: 2.3, 3.0, 3.5, 4.0, and 4.6. Reynolds number was  $8.1 \times 10^6$  per meter. Angle-of-attack range was from  $-5^\circ$  to  $22^\circ$  with some variation from model to model. Oil-flow photographs were taken at selected test conditions.

## COMPARISON OF EXPERIMENT WITH THEORETICAL PREDICTIONS

### Cruise Conditions

The lifting pressure as calculated by each of the prediction methods is compared with experiment in Figure 3 for the  $76^\circ$  sweep flat wing at a Mach number of 3.5 and a nominal cruise condition of  $C_L = 0.1$ . Angle of attack is approximately  $5.7^\circ$ . All of the prediction methods provided reasonable estimates at this Mach number and angle of attack even though the usual applicable range was exceeded in some instances. For example, the tangent wedge method is primarily used for hypersonic speeds where forward regions of influence are relatively narrow and two-dimensional conditions are approached. A Mach number of 3.5 is at the low end of the applicability range so the method might not be expected to work as well as at higher speeds. On the other hand, a Mach number of 3.5 is high for linear theory applications such as those of Middleton and Woodward. Both of these methods tend to overpredict the pressure at the leading edge and at the tip (especially the Middleton theory without pressure limiting). Otherwise, the predictions are reasonable at this angle of attack. As indicated previously, the shock-fitting finite-difference method, as presently implemented, imposes certain requirements on configurations which can be handled. For this  $76^\circ$  sweep flat wing it was necessary to reshape the apex to provide a  $24^\circ$  half-angle conical nose (needed to obtain a starting plane solution). Also, to satisfy the requirement that the leading edge be blunt for subsonic leading edges, the sharp leading edge of the  $76^\circ$  wing was altered. The outboard half of the cross sections normal to the axial (marching) direction were changed to an elliptic arc tangent to the design wing at the 50-percent span station of the cross section resulting in increased thickness in the modified region. As a result, good agreement with experiment is not expected at the leading edge. This leading-edge bluntness effect probably also accounts for a major part of the failure of the theory to predict the pressures near the tip.

### Test Extremal Conditions

Since all the prediction methods show similar trends (Fig. 3), the Woodward method was arbitrarily chosen to compare with experiment for the various ranges of test conditions. These comparisons for sweep angle, angle of attack, camber, and Mach number are shown in Figures 4 to 7, respectively.

The change in sweep angle from  $76^\circ$  to  $55^\circ$  (Fig. 4) represents a change from subsonic to supersonic leading edge at  $M = 3.5$  and  $\alpha = 5.7^\circ$ . Upper surface pressures are generally well predicted although they tend to become too high near the trailing edge of the  $55^\circ$  sweep wing. The lower surface pressures show some departure from expected trends, particularly at the leading edge where the pressures are too high. For a supersonic leading edge, these pressures would be expected to be relatively flat. It should be pointed out that the Middleton theory does predict relatively flat pressure distributions all the way to the leading edge on the lower surface (Ref. 14). The span loading comparisons at each sweep angle show that the total forces and moments would be estimated reasonably well. The bump in the theoretical curves near the root and the tip is probably due to changes in panel span in these regions as well as some body



interference effects at the root. As was indicated earlier, a body of revolution was added symmetrically about the wing center line to provide a housing for the mounting sting. For the theoretical calculations, the configurations were considered to be an all-wing configuration with the body of revolution dimensions included as part of the camber surface description.

In Figure 5 the effect of angle of attack is shown. Here, the  $76^\circ$  sweep comparison at  $M = 3.5$  and  $\alpha = 5.7^\circ$  from the previous figure is repeated as representative of the lower angles of attack and compared with the  $\alpha = 19.7^\circ$  data for the same wing at the same Mach number. The flat theoretical pressure distributions on the upper surface at  $\alpha = 19.7^\circ$  are the result of the pressure limiting feature of the Woodward method which limits the upper surface pressures to 100 percent of vacuum. The theory completely fails to predict the lower surface pressures where the experimental pressures are much higher than the estimates except at the tip. This result is reflected in the span loading which shows that the total forces and moments, as estimated by the theory, would be too low.

Similar results are shown in Figure 6 for the effects of camber at  $\alpha = 19.7^\circ$ . The higher experimental pressures shown at the root of the cambered wing ( $C_{L,des} = 0.1$ ) are probably due to a valley on the lower surface center line. This valley resulted from shearing the camber lines.

The results at  $\alpha = 19.7^\circ$  for the Mach number extremes (Fig. 7) indicate that the same trends with angle of attack as shown for  $M = 3.5$  can be expected. It should be pointed out that the Woodward theory is a linear theory and should not be expected to provide good results at Mach numbers above 3.0 or angles of attack above  $8^\circ$  or  $10^\circ$ . Because of the failure of the Woodward theory to predict the lower surface pressures at high angle of attack, each of the methods will be compared with experimental data at the high angle of attack in the next section.

#### High Angle-of-Attack Comparisons

Comparisons of the various prediction methods with experiment at  $\alpha = 19.7^\circ$ ,  $M = 3.5$  are shown in Figures 8 to 10. In general, upper surface pressures are predicted reasonably well by all of the methods except for the Middleton method without pressure limiting. Only the finite-difference method predicted lower surface pressures with any degree of accuracy at this high angle of attack.

When using the tangent wedge approximation, lower surface pressures are overpredicted across the entire span (Fig. 8). This results in an overprediction of both the lifting pressures and the span loadings and, hence, the integrated total forces and moments. This overprediction of pressure is probably due in part to the fact that interactions between panels are neglected. On the lower surface of a delta wing there is a flow outward toward the tip which would tend to lower the local pressure and thus decrease the pressure coefficient. On the upper surface, on the other hand, the flow behind the leading-edge vortex would flow inward toward the root increasing the local pressure with a resulting increase in pressure coefficient. This would tend to decrease the overprediction at the root as shown in Figure 8.

The linear theory Middleton and Woodward methods are compared with experiment in Figures 9 and 10, respectively. The Middleton method without pressure limiting overpredicts the pressures on the upper surface but grossly underpredicts the lower surface pressures. The lower surface pressures indicate that the force data correlations for this method shown in Reference 14 are fortuitous in that an underprediction of lift at the inboard stations is canceled by an overprediction at the outboard stations (see lifting pressures and span loadings shown in Fig. 9). When using the Middleton method, the user has the option of setting the fraction of vacuum he wishes to use as the minimum possible pressure. This pressure limiting is applied to the lifting pressures as they are being calculated. A vacuum fraction of 0.7 was used to obtain the pressure limited curves shown in Figure 9. The zero-thickness linear theory assumes equal pressure coefficients of opposite sign on the upper and lower surfaces. Thus, the high pressure coefficients measured on the lower surface, which are sometimes more than twice the magnitude of those measured on the upper surface, cannot be predicted. Pressure limiting as applied to the Middleton method tends to magnify further this discrepancy since the limits are applied to the loading parameter  $\Delta C_p$ . Because the limits are applied to  $\Delta C_p$  the assumption of equal pressures of opposite sign on the upper and lower surfaces results in even lower pressures on the lower surface than those obtained without pressure limiting.

The Woodward theory (Fig. 10) also employs pressure limiting. Here, pressures are limited to vacuum but only after all pressures have been calculated. Thus, only the upper surface is affected. As previously indicated, the flat pressure distribution predictions on the upper surface are the result of pressure limiting. As can be seen by comparing with upper surface pressure limited curves in Figure 9 for the Middleton method, the Woodward values are slightly higher because of the difference in percent of vacuum used (70 for Middleton, 100 for Woodward). Since the theory does a totally inadequate job of predicting the lower surface pressures, the lifting pressure estimates are too low. This results in a span loading which, when integrated, provides total forces and moments that are too low.

The shock-fitting finite-difference method (Fig. 11) produces much better agreement with the experimental pressure distributions at high angles of attack than any of the other methods. Along the center line and midspan chord line, this theory is in good agreement with the data. The difference at these locations appears to be caused by the displacement effect of the boundary layer on the model (which is not included in any of these methods). As was the case at the cruise condition, the pressure distribution near the wing tip is poorly predicted on the lower surface because of the leading-edge blunting added to the numerical model in order to obtain the solution. Nonetheless, the span loading prediction is quite good. It should be noted that it was only with considerable effort, involving variations in the nose shape and some changes to the computer code, that the results shown were obtained. In this regard, the shock-fitting finite-difference method cannot yet be considered fully operational in the sense that the Middleton and Woodward linearized theory methods are. Further development is required to allow the routine application of this finite-difference method to a wide range of configurations (including wings with high camber and twist and with sharp subsonic leading edges). However, the results shown here show that finite-difference methods can be particularly useful for calculating the effects of conditions, such as high angle of attack, where the linearized theory methods cannot produce useful results.

## CONCLUDING REMARKS

Comparison of experimental pressure data with predictions based on four theoretical methods indicate that all of the methods will yield satisfactory loads data at moderate angles of attack. At moderate angles of attack the methods of Middleton and Woodward can provide reasonable estimates at Mach numbers higher than those usually associated with linear theory.

Only the shock-fitting finite-difference method yields satisfactory loads estimates at high angles of attack where the other methods examined are unable to predict lower surface pressures. Reasonable estimates of upper surface pressures at high angles of attack were obtained by linear theory when pressures were constrained to vacuum pressure or a percentage of vacuum. The results hold promise that with further development finite-difference methods can meet the need for aerodynamic load prediction at high angles of attack.

## REFERENCES

1. Hayes, Wallace D., Probstein, Ronald F., "Hypersonic Flow Theory," Academic Press, 1959.
2. Gentry, Arvel E., "Hypersonic Arbitrary-Body Aerodynamic Computer Program. (Mark III Version)," Report DAC 61552, Vol. 1.
3. Middleton, Wilbur D., and Carlson, Harry W., "A Numerical Method for Calculating the Flat-Plate Pressure Distributions on Supersonic Wings of Arbitrary Planform," NASA TN D-2570, 1965.
4. Middleton, W. D., and Carlson, H. W., "Numerical Method of Estimating and Optimizing Supersonic Aerodynamic Characteristics of Arbitrary Planform Wings," Journal of Aircraft, Vol. 2, No. 4, July-August 1965, pp. 261-265.
5. Carlson, Harry W., and Miller, David S., "Numerical Methods for the Design and Analysis of Wings at Supersonic Speeds," NASA TN D-7713, 1974.
6. Middleton, W. D., and Lundry, J., "Aerodynamic Design and Analysis System for Supersonic Aircraft," NASA CR-2520, 1975.
7. Woodward, F. A., Tinoco, E. N., and Larsen, J. W., "Analysis and Design of Supersonic Wing-Body Combinations, Including Flow Properties in the Near Field," NASA CR-73106, August 1967.
8. Woodward, F. A., "Analysis and Design of Wing-Body Combinations at Subsonic and Supersonic Speeds," Journal of Aircraft, Vol. 5, No. 6, November-December 1968.
9. Woodward, F. A., "An Improved Method for the Aerodynamic Analysis of Wing-Body-Tail Configurations in Subsonic and Supersonic Flow," NASA CR-2228, 1973.
10. Moretti, G., Grossman, B., and Marconi, F., "A Complete Numerical Technique for the Calculation of Three-Dimensional Inviscid Supersonic Flows," AIAA Paper No. 72-192, 1972.
11. Marconi, Frank, Salas, Manuel, and Yaeger, Larry, "Development of a Computer Code for Calculating the Steady Super/Hypersonic Inviscid Flow Around Real Configurations. Volume I - Computational Technique, Volume II - Code Description," NASA CR-2675, 1976.
12. Carlson, Harry W., and Middleton, Wilbur D., "A Numerical Method for the Design of Camber Surfaces of Supersonic Wings With Arbitrary Planforms," NASA TN D-2341, 1964.
13. Sorrells, Russell B., and Miller, David S., "Numerical Method for Design of Minimum-Drag Supersonic Wing Camber With Constraints on Pitching Moment and Surface Deformation," NASA TN D-7097, 1972.
14. Sorrells, Russell B., III, and Landrum, Emma Jean, "Theoretical and Experimental Study of Twisted and Cambered Delta Wings Designed for a Mach Number of 3.5," NASA TN D-8247, 1976.

## TANGENT WEDGE

- OBLIQUE-SHOCK RELATIONSHIPS
- INTERACTION NEGLECTED

## MIDDLETON

- LINEARIZED THEORY
- UNSWEPT VORTEX LATTICE
- MARCHING TECHNIQUE
- SUPERPOSITION

## WOODWARD

- LINEARIZED THEORY
- SWEEPED TRAPEZOIDAL PANELS
- SIMULTANEOUS SOLUTIONS

## FINITE DIFFERENCES:

- EXACT INVISCID EQUATIONS
- CONTINUOUS SURFACE SHAPE
- MARCHING TECHNIQUE
- SURFACE and FIELD DATA



Figure 1. Prediction methods considered.

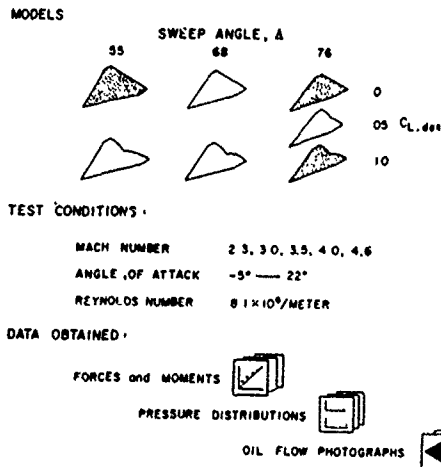


Figure 2. Scope of investigation.

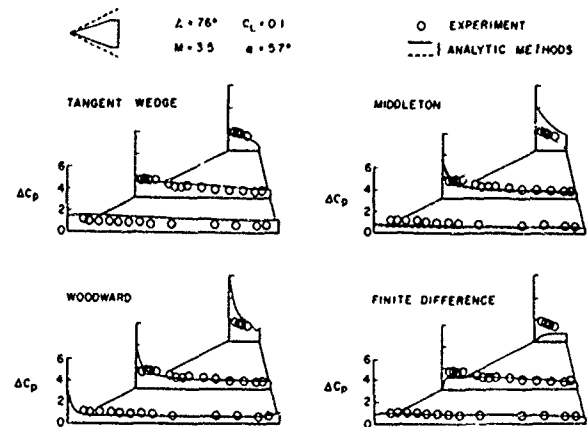
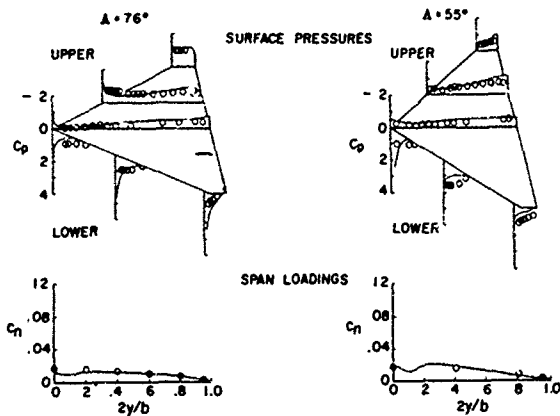
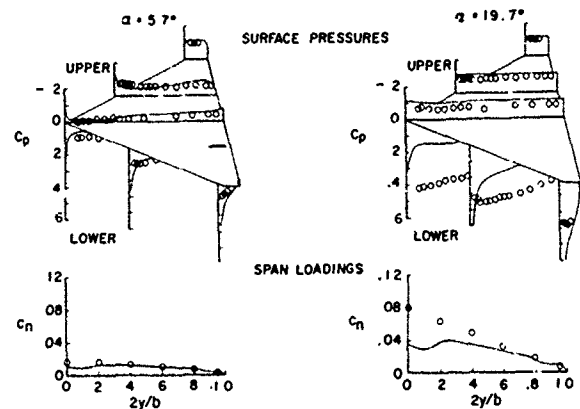
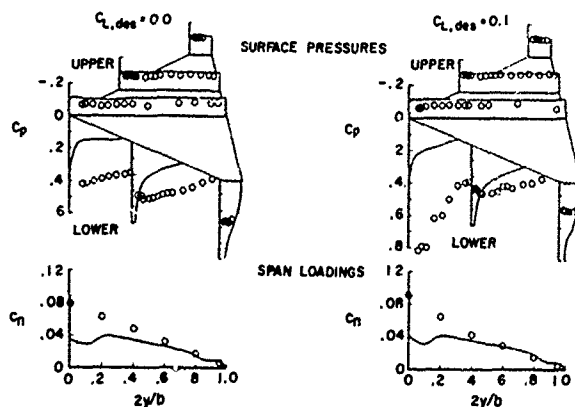
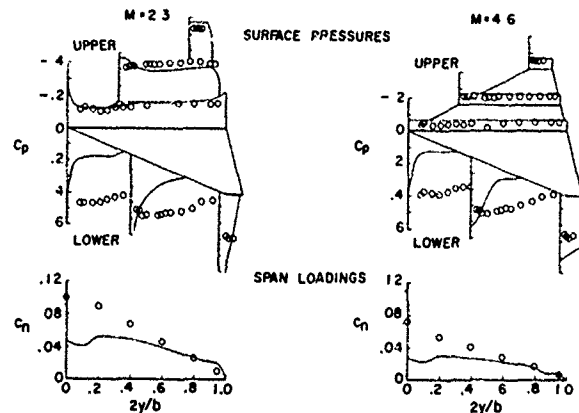


Figure 3. Cruise condition loading prediction by various methods.

Figure 4. Woodward method predictions for sweep angle of extremes.  $M = 3.5$ ,  $\alpha = 5.7^\circ$ .Figure 5. Woodward method predictions for cruise and maximum  $\alpha$ .  $\Lambda = 76^\circ$ ,  $M = 3.5$ .Figure 6. Woodward method predictions for camber extremes.  $M = 3.5$ ,  $\Lambda = 76^\circ$ ,  $\alpha = 19.7^\circ$ .Figure 7. Woodward method predictions for Mach number extremes.  $\Lambda = 76^\circ$ ,  $\alpha \approx 20^\circ$ .

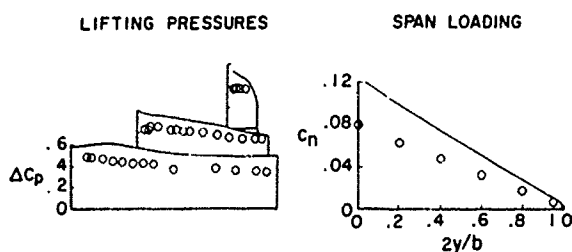
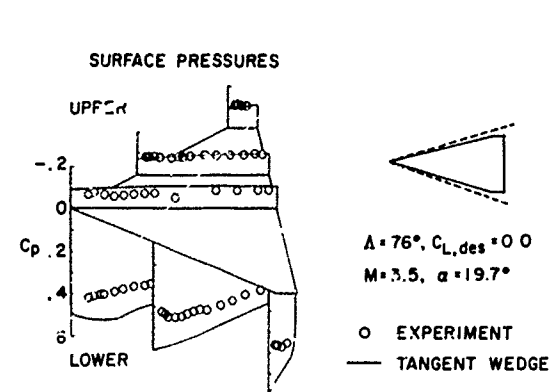


Figure 8. High angle-of-attack loading predictions by tangent wedge method.

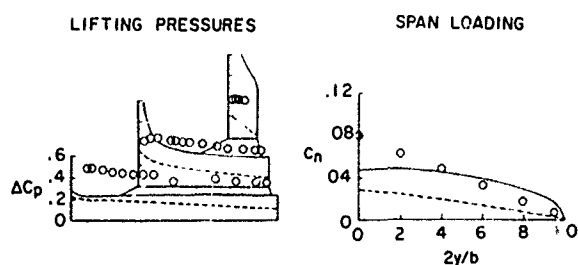
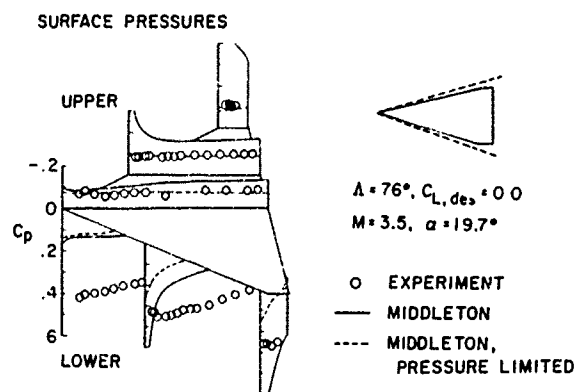


Figure 9. High angle-of-attack loading prediction by Middleton linearized theory method.

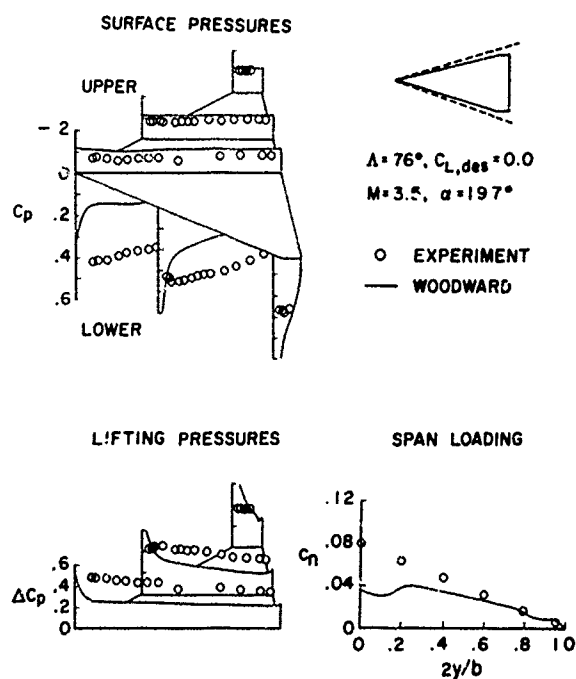


Figure 10. High angle-of-attack loading prediction by Woodward linearized theory method.

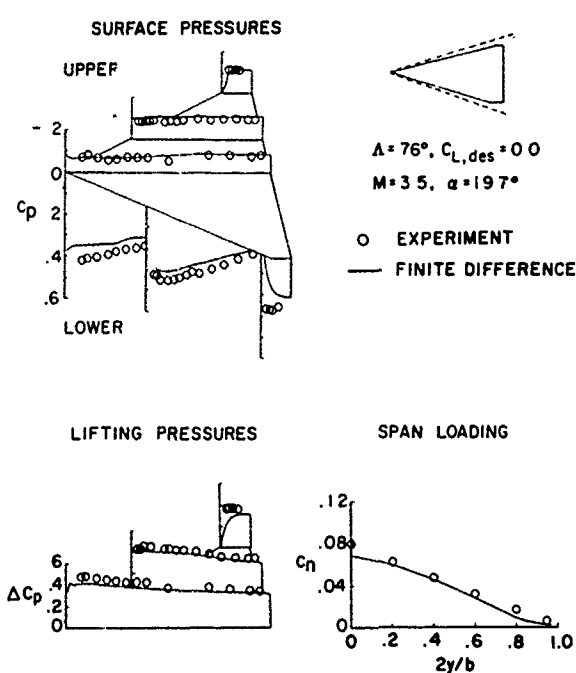


Figure 11. High angle-of-attack loading prediction by shock-fitting finite-difference method.

ON THE CALCULATION OF THE PRESSURE DISTRIBUTION OF WING-BODY  
COMBINATIONS IN THE NON-LINEAR ANGLE OF ATTACK RANGE\*

Gregor Gregoriou  
MESSERSCHMITT-BÖLKOW-BLOHM GMBH  
8000 Munich 80 Postfach 801149  
West Germany

SUMMARY

Based on the potential theory, an iterative singularity method was developed which yields the pressure distribution of symmetric wing-body configurations in the non-linear angle of attack range at subsonic speeds. The body is axis-symmetric and of finite length. The wing is infinitely thin and located at mid-wing position.

The following mathematical model was used.

Wing: Lattice method, free vortices partially inclined to the wing plane by  $\alpha_\infty/2$ .

Body: Ring sources over the body surface

Theoretical results show good agreement with wind tunnel tests.

NOTATION

$\alpha$	Angle of attack	$\bar{x}$	Distance between local force and moment reference point
$\delta$	Inclination angle of the free vortices	$a_i$	Fourier coefficient ( $i = 0, 1, 2, \dots$ )
Ma	Mach number	$\Gamma$	Vortex strength
$U_\infty$	Free-stream velocity	$C_Z$	Normal force coefficient ( $= \frac{\text{Normal force}}{q_\infty S_R}$ )
$x, y, z$	Rectangular coordinates	$C_m$	Pitching moment ( $= \frac{\text{Moment}}{q_\infty S_R D}$ )
$\vartheta$	Polar angle	$C_p$	Pressure coefficient
$u, v, w$	Velocities in x-, y-, z-directions	$\Delta C_p$	Pressure difference between upper and lower wing surfaces
$v_\vartheta, v_m$	Velocities in tangential and meridian directions	<u>Subscripts</u>	
$q_\infty$	Dynamic pressure		
$\bar{q}$	Intensity of the ring sources at $\vartheta = 0^\circ$	$\infty$	Free-stream condition
$q_i$	Intensity of the ring sources ( $i = 0, 1, 2, \dots$ )	W	Wing
D	Maximum body diameter	B	Body
L	Body length	l	Local
l	Wing chord	P	Panel
$S_R$	Reference area	V	Vortex
r	Body local radius	C	Panel control point
		e	Exposed wing
		FC	Fourier coefficient

\* The work is sponsored by the Ministry of Defence of the Federal Republic of Germany

## INTRODUCTION

Over the past years large angles of attack have become more and more important as far as missiles are concerned in consequence of the constantly increasing requirement for greater maneuverability. In the light of this development, aerodynamicists have endeavoured to establish methods with a view to estimating the total coefficients of the normal force and pitching moment in the non-linear angle of attack range. However, investigations permitting the determination of pressure distribution over the missile surface at large angles of attack are lacking. This paper deals with a wing-body configuration in the case of subsonic flow and provides information as to the pressure distribution at the body as well as at the wing. As is well known, knowledge of the pressure distribution is of importance for the dimensioning of the missile structure. The pressure distribution then yields the coefficients of the normal force and the pitching moment for the body, the exposed wing and the total configuration. In the present investigation wing-body configurations were studied, the body being of arbitrary thickness but axis-symmetric, whilst the infinitely thin wing (in mid-wing position) may feature any plan form.

The computing model used is based on singularity distributions which have been applied successfully by other authors to solve similar problems.

Comprehensive wind tunnel measurements conducted by DFVLR were utilised in order to test the results of the computing method.

## BRIEF DESCRIPTION OF THE METHOD APPLIED

Let us consider a wing-body configuration according to Fig. 1

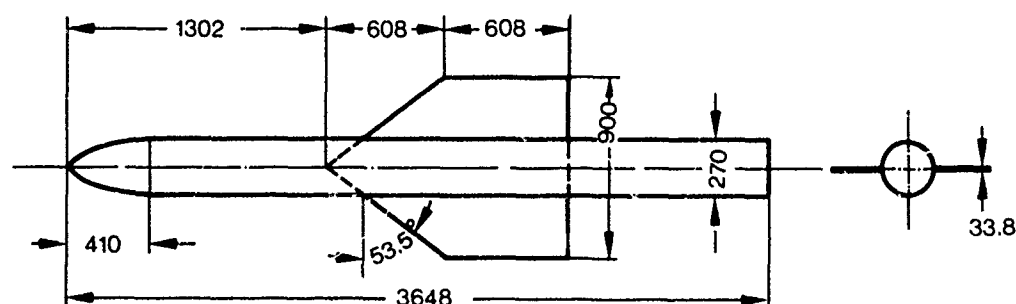


Fig. 1: Tanner wing-body combination [4]

For the sake of clarity we subdivide the computation performed into several steps.

### Step 1 Calculation of the wing potential without body influence

It is first assumed that the wing extends up to the body axis. Its plan form area is divided into several panels and a horseshoe vortex is assigned to each panel. The bound vortex lies on the  $1/4$  line, whilst the inclination of the free vortices to the wing plane can be seen in Fig. 2 (according to the Lattice method, Hedmann [1], Lange [2]). The free vortices with the angle of inclination  $\delta \neq 0^\circ$  are, as is known, responsible for the non-linearity of the wing. Computing the extended wing according to the Lattice method yields the vortex strength  $\Gamma_p$  of each panel.

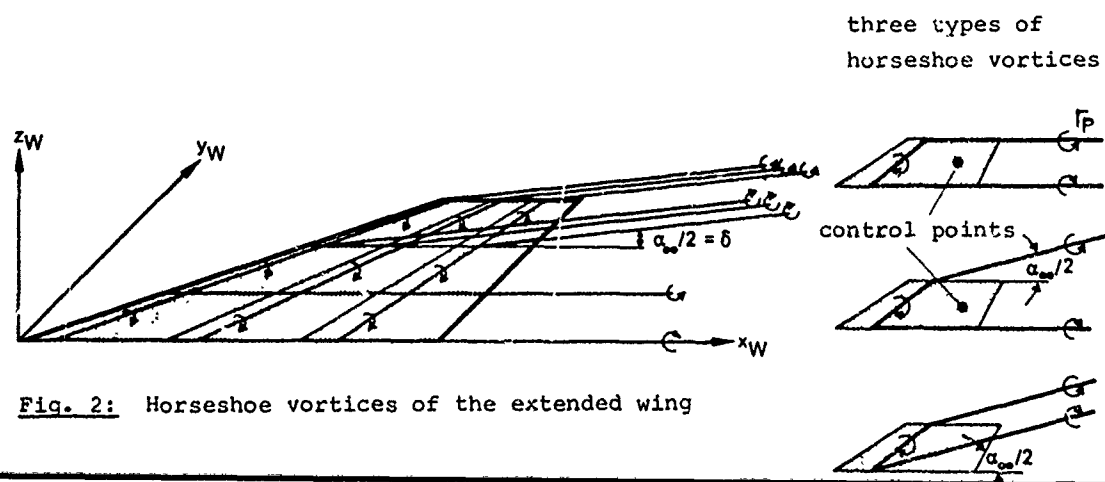


Fig. 2: Horseshoe vortices of the extended wing

### Step 2 Determination of the normal velocities induced on the body

In this step the velocities in y- and z-direction are determined for several body sections (s. Fig. 3), the velocities being induced by the horseshoe vortices of the wing on the body surface. These velocities are computed at 10 points of the circle. Due to symmetry, it is sufficient to consider merely the one half of the circle, for only the angles of attack and not the angles of sideslip are taken into account. The normal velocity  $w_n$  is determined from the velocities  $v$  and  $w$ .

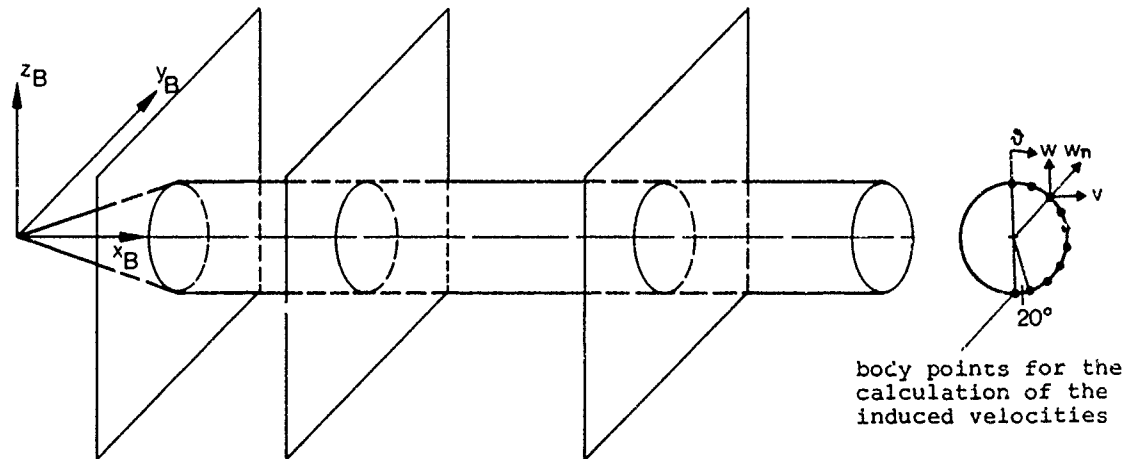


Fig. 3: Sections of the body for the calculation of the induced velocities

### Step 3 Approximation of the normal velocities through Fourier's Series

An important prerequisite for the further computation is the approximation of the normal velocities induced on the body through the following Fourier's series.

$$w_n(\vartheta, x) = a_0(x) + a_1(x) \cos \vartheta + a_2(x) \cos 2\vartheta + a_3(x) \cos 3\vartheta + \dots \quad (1)$$

Fig. 4 gives some examples of this approximation. The number of Fourier terms required depends on the curve of the normal velocities and can vary according to the position of the body section under consideration. Due to the occurrence of normal velocities at 10 points of each body section, maximally 10 Fourier coefficients can be determined. In the course of computations performed according to this method, it has proved adequate to use 6 Fourier terms. Increasing the Fourier terms to 10 did not lead in general to significantly improving the computing results, but increased the computing time and core storage requirements. The reason for the relative nonsusceptibility of the computing results to the number of Fourier coefficients is that the Fourier's series approximates the preestablished curve in an alternating manner.

### Step 4 Calculation of the body potential considering wing influence

In this step computing the flow at the body is effected according to the method whereby the surface is covered with ring sources, which was first practised for a body alone by Lotz [3].

The normal velocities induced on the body by the oncoming flow are compensated for by ring sources which are attached to each body section. Some examples of the shape of these ring sources are shown in Fig. 5. A corresponding ring source is necessary for each term of the Fourier's series, (Eq. 1). The intensity of the ring sources follows from the condition that the sum of all normal velocities must disappear at each point of the body surface (see next section).

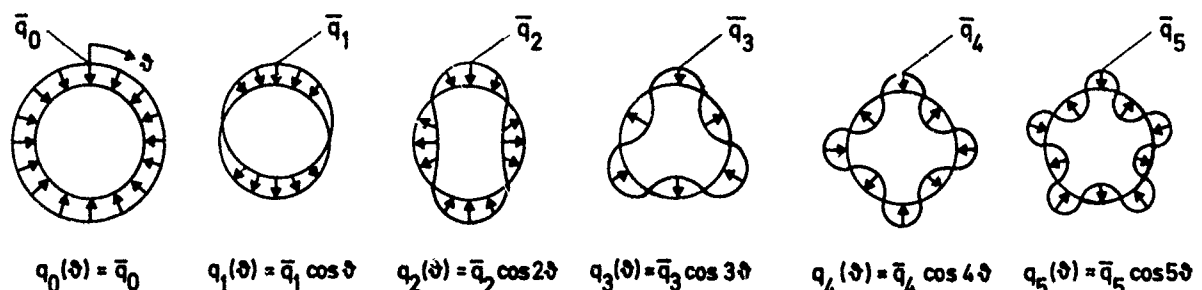


Fig. 5: Shape of the ring sources for the 6 Fourier terms

When computing the body, the normal velocities which occur on considering the body without the wing must be compensated for additionally.

The axial component of the flow ( $=U_{\infty} \cos \alpha_{\infty}$ ) or the vertical component ( $=U_{\infty} \sin \alpha_{\infty}$ ), respectively, are considered by ring sources as follows:

$$q(x) = \bar{q}(x) \cos \theta \quad \text{or} \quad q(x) = \bar{q}(x) \cos \vartheta, \quad \text{respectively.}$$

It is evident that the normal velocities occurring in these 2 cases at the body can be obtained by adding the appropriate coefficients in Eq. 1 as follows:

$$\begin{aligned} a_{0 \text{ axial}} &= U_{\infty} \cos \alpha_{\infty} \frac{dr(x)/dx}{C}, & C &= \sqrt{1 + (dr(x)/dx)^2} \\ a_{1 \text{ cross}} &= -U_{\infty} \sin \alpha_{\infty} \frac{1}{C}. \end{aligned} \quad (2)$$

The result of the computation in this step is the intensity

$$\bar{q}_i(x) \quad (i = 0, 1, 2, \dots, 5) \text{ of the ring sources.}$$

Step 5 The angle-of-attack distribution on the wing considering body influence

The potential of the ring sources induce velocities at the wing in x, y and z-direction. The velocities in x and z-direction (u and w) lead to a change in the local angle of attack  $\alpha_1$  at the wing. The following relations apply to the wing alone:

$$\alpha_1 = \alpha_{\infty} = \text{const.} \quad \text{or} \quad \tan \alpha_1 = \frac{w}{u} = \frac{U_{\infty} \sin \alpha_{\infty}}{U_{\infty} \cos \alpha_{\infty}}. \quad (3)$$

The induction of velocities by the body yields

$$\tan \alpha_1 = \frac{U_{\infty} \sin \alpha_{\infty} + w}{U_{\infty} \cos \alpha_{\infty} + u} \neq \tan \alpha_{\infty}. \quad (4)$$

The local angle of attack  $\alpha_1(x, y)$  is determined for the control point of each wing panel.

Step 6 Calculation of the wing potential considering body influence

Step 1 is now repeated with the changed angle-of-attack distribution, which yields a new intensity  $\Gamma_p$  of the horseshoe vortices.

Steps 2-6 are subsequently repeated until no further change to the body sources or to the wing vortex potential can be determined. The convergence behaviour of this iterative process is extremely good, so that this process can be interrupted after 3-4 steps. Thus the potential of the wing horseshoe vortices and of the ring sources are known.

Step 7 Pressure distribution over the body and the wing

When the individual potentials are known, the velocities in peripheral direction  $v_{\vartheta}$  or in meridian direction  $v_m$  can be determined at each point of the body. According to the prerequisites, the normal velocities should disappear. Thus the pressure coefficient  $C_p$  is yielded as

$$C_p(x, \vartheta) = 1 - \left( \sum v_{\vartheta}(x, \vartheta)^2 / U_{\infty}^2 + \sum v_m(x, \vartheta)^2 / U_{\infty}^2 \right). \quad (5)$$

or

$$\begin{aligned} C_p(x, \vartheta) &= 1 - \left\{ [v_{\vartheta_{2FC}}(x) \sin \vartheta + \dots + v_{\vartheta_{6FC}}(x) \sin 5\vartheta - U_{\infty} \sin \alpha_{\infty} \sin \vartheta + v_{\vartheta_{WV}}(x, \vartheta)]^2 / U_{\infty}^2 \right. \\ &\quad + [v_{m_{1FC}}(x) + v_{m_{2FC}}(x) \cos \vartheta + \dots + v_{m_{6FC}}(x) \cos 5\vartheta + \frac{U_{\infty}}{\sqrt{1 + (dr(x)/dx)^2}} (\sin \alpha_{\infty} \cos \vartheta \frac{dr(x)}{dx} + 1) \\ &\quad \left. + v_{m_{WV}}(x, \vartheta)]^2 / U_{\infty}^2 \right\}. \end{aligned} \quad (6)$$



Determining the pressure difference  $\Delta C_p$  on the wing is simpler. It is yielded from the relation

$$\Delta C_p(x, y) = \Gamma_W(x, y) \frac{1}{(x_C - x_V) U_\infty} \quad (7)$$

#### Step 8 Determination of the total coefficients

The integration of the pressure distribution over the body surface yields the coefficient of the normal force of the body

$$C_{Z_B} = \frac{2r(x)}{S_R} \text{sign}(\cos \vartheta) \int_0^L \int_0^\pi C_p(x, \vartheta) \frac{\cos \vartheta d\vartheta dx}{\sqrt{1+(dr(x)/dx)^2}} \quad (8)$$

Analogously for the coefficient of the pitching moment

$$C_{m_B} = \frac{r(x)}{S_R D} \text{sign}(\cos \vartheta) \int_0^L \int_0^\pi C_p(x, \vartheta) \bar{x} \frac{\cos \vartheta d\vartheta dx}{\sqrt{1+(dr(x)/dx)^2}} \quad (9)$$

With regard to the coefficient of the normal force of the wing, the  $\Delta C_p$  distribution is integrated only in the range of the exposed wing

$$C_{Z_{We}} = \frac{2}{S_R} \int_{D/2}^s \int_0^{l(y)} \Delta C_p(x, y) dx dy \quad (10)$$

Analogously for the coefficient of the pitching moment

$$C_{m_{We}} = \frac{2}{S_R D} \int_{D/2}^s \int_0^{l(y)} \Delta C_p(x, y) \bar{x} dx dy \quad (11)$$

Since the pressure coefficients at discrete points are known and are not available in analytical form, effecting integration in the Eqs. (8 + 11) can be replaced by quadratures.

The coefficients of the wing-body configuration are composed additively of the shares of the body and of the exposed wing.

#### REMARKS CONCERNING THE BASIC MATHEMATICAL APPROACH AND THE CONVERGENCE OF THE METHOD

Several works, e.g. Hedman [1] for the linear angle-of-attack range and Lange [2] for the nonlinear one, have described in detail the wing calculation using the Lattice method which from the mathematical point of view is comparatively simple. It therefore does not seem necessary to repeat the basic mathematical approach.

The Lotz method [3] for calculating a body with the aid of ring sources distributed over its surface is much more difficult from the mathematical viewpoint and less known. It is based on the solution of a Fredholm integral equation:

$$\frac{\bar{q}_i(x)}{2} \cos i \vartheta + \frac{1}{4\pi} \int_0^L \int_0^{2\pi} \frac{\bar{q}_i(x') \sqrt{\frac{1+(dr(x')/dx')^2}{1+(dr(x)/dx)^2}} r(x') \cos i \vartheta' \left[ r-r(x') \cos(\vartheta-\vartheta') - \frac{dr(x)}{dx} (x-x') \right] d\vartheta' dx'}{\sqrt{(x-x')^2 + r(x)^2 + r(x')^2 - 2r(x)r(x') \cos(\vartheta-\vartheta')}} = -w_n(x, \vartheta)$$

$$i = 0, 1, 2, \dots, 5.$$

(12)

where  $\bar{q}_1(x)$  is the function to be found.

The right side of this equation represents the distribution of the normal velocities over the body surface. A total of 6 such integral equations is produced through the approximation of these normal velocities by means of 6 Fourier terms, Eq. ( 1 ).

The numerical solution of equation ( 12 ) calls for substituting a polygon for the body contour, the condition of tangential flow being fulfilled in the middle of each polygon side (Fig. 6).

As far as the solution of equation ( 12 ) is concerned, special care must be taken to determine the singular points. To this end, the Kernal function must be approximated in the vicinity of the singular points with the aid of Taylor series. In this way terms are obtained which can be integrated analytically and result in finite values.

When performing the calculations, the number of wing panels and of body sections was varied. It was found that 60 sections are generally sufficient for the body, whereby said sections must be distributed very densely in the nose region. An increase in the number of body sections does no longer result in any appreciable improvement of the calculated results.

As far as the wing is concerned, approx. 10 panels in span direction and 5 in chord direction are sufficient. The free vortices of the panels in the body area are located in the wing plane. The panels located completely outside the body region feature free vortices inclined by  $\alpha_\infty/2$  with respect to the wing plane.

From the physical point of view the assumption that the free vortices leave the wing at an angle of  $\alpha_\infty/2$  is not quite correct. Therefore, the computing programme includes the angle of inclination as a free parameter. No variation of this angle has so far been effected.

The effect of the Mach number has been considered by applying the Prandtl-Glauert Rule to the wing-body combination.

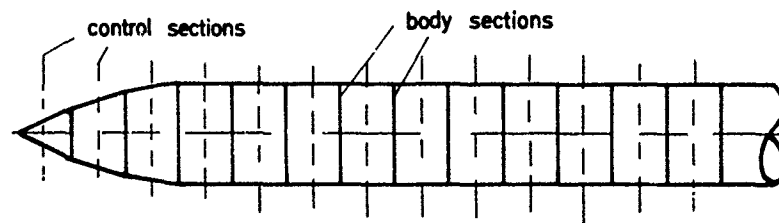


Fig. 6: Approximate representation of the body

#### COMPARISON OF THEORETICAL RESULTS WITH TESTS

The results of the present theoretical method were examined using appropriate experimental data obtained from DFVLR [4], [5].

The wing-body combination subjected to experiment is shown in Fig. 1. Fig. 7 illustrates the coefficients of normal force  $C_z$  and pitching moment  $C_m$  as a function of the angle of attack. For high  $\alpha_\infty$ , the values established theoretically are slightly lower than those obtained from tests. The deviation can be explained by the lack of two body nose vortices in the theoretical model. Presently, the model is being improved by taking these vortices into account. Fig. 8 shows pressure difference  $\Delta C_p$  for specified sections of the exposed wing. Here, large deviations of measured data from theory are evident in the vicinity of the wing tip. They suggest that a concentrated vortex is generated on the upper surface of the wing. This phenomenon cannot be described accurately with the present theoretical model, which is based on the assumption that the free vortices separate from the wing at  $\alpha_\infty/2$  with respect to the wing plane.

In Figs. 9 and 10, the  $C_p$  distribution over various body meridians is shown for two angles of attack.

REFERENCES

- [1] Hedman, S.G. VORTEX LATTICE METHOD FOR CALCULATION OF QUASI STEADY STATE LOADINGS ON THE ELASTIC WINGS IN SUBSONIC FLOW. FFA (FLYG-TEKNISKA FÖRSÖKDANSTALTEN), STOCKHOLM (1966), REP.NO. 105
- [2] Lange, A.G. NONLINEAR LIFTING SURFACE THEORY FOR CAMBERED LOW ASPECT RATIO WINGS OF ARBITRARY PLANFORM. GRUMMAN AIRCRAFT ENGINEERING CORPORATION REP.NO. ADR 01-03-67 (1967)
- [3] Lotz, J. Zur Berechnung der Potentialströmung um quergestellte Luftschiffkörper. ING.-ARCH. II (1931)
- [4] Tanner, M. Druckverteilungsmessungen an einem Flügel mit Rumpf. DFVLR REPORT NO. IB 157-74A21 (1974)
- [5] Tanner, M. Einfluß des Rollwinkels auf Auftrieb, Widerstand und Nickmoment eines Kreuzflügelmodells. DFVLR REPORT NO. IB 157-74A16 (1974)

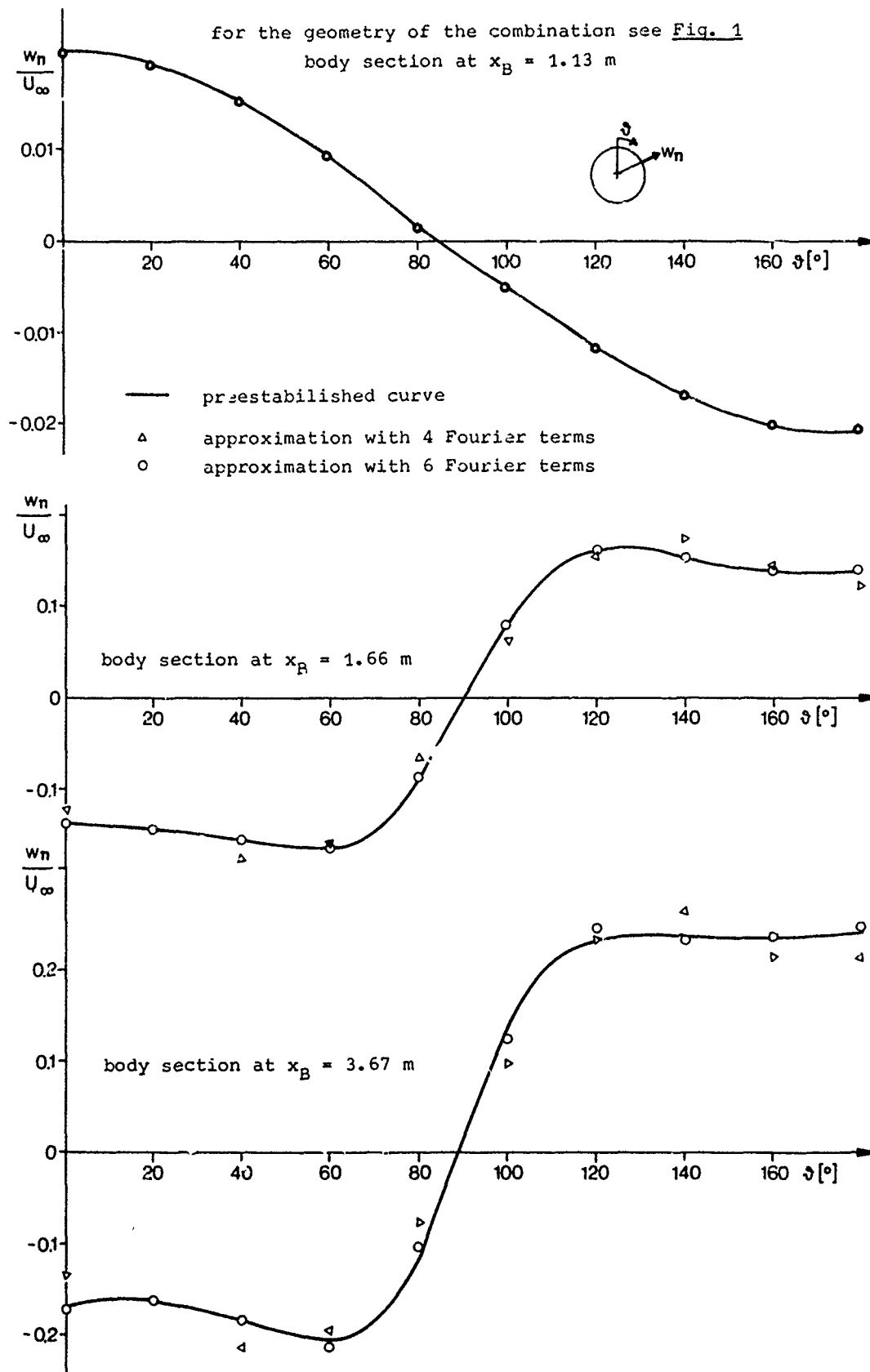


**Fig. 4:** Induced velocities on the body and their approximation through Fourier's series

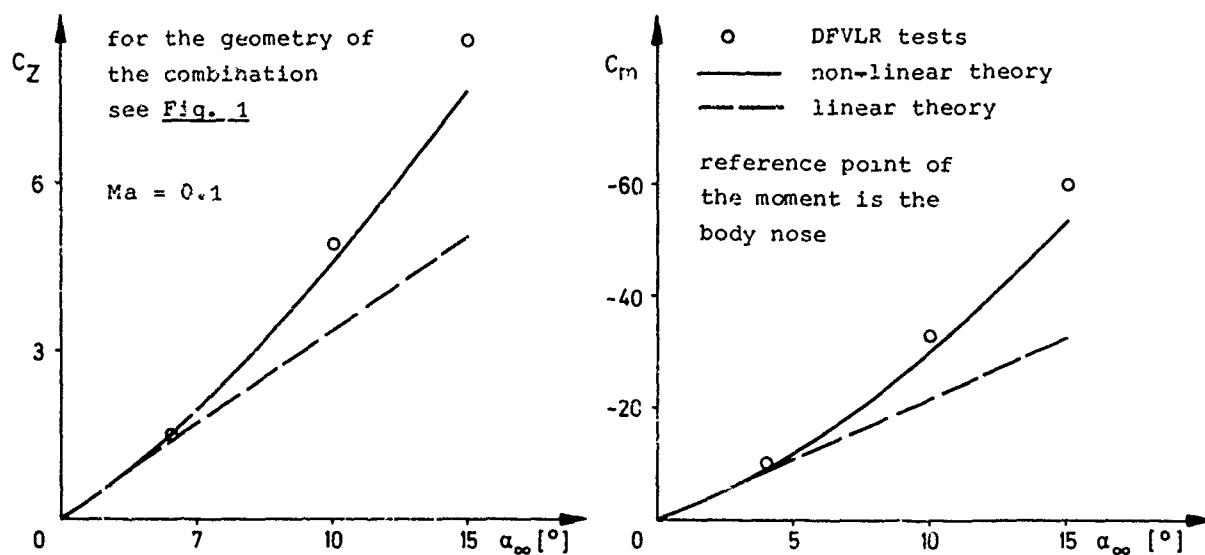


Fig. 7: Comparison between theoretical and test results

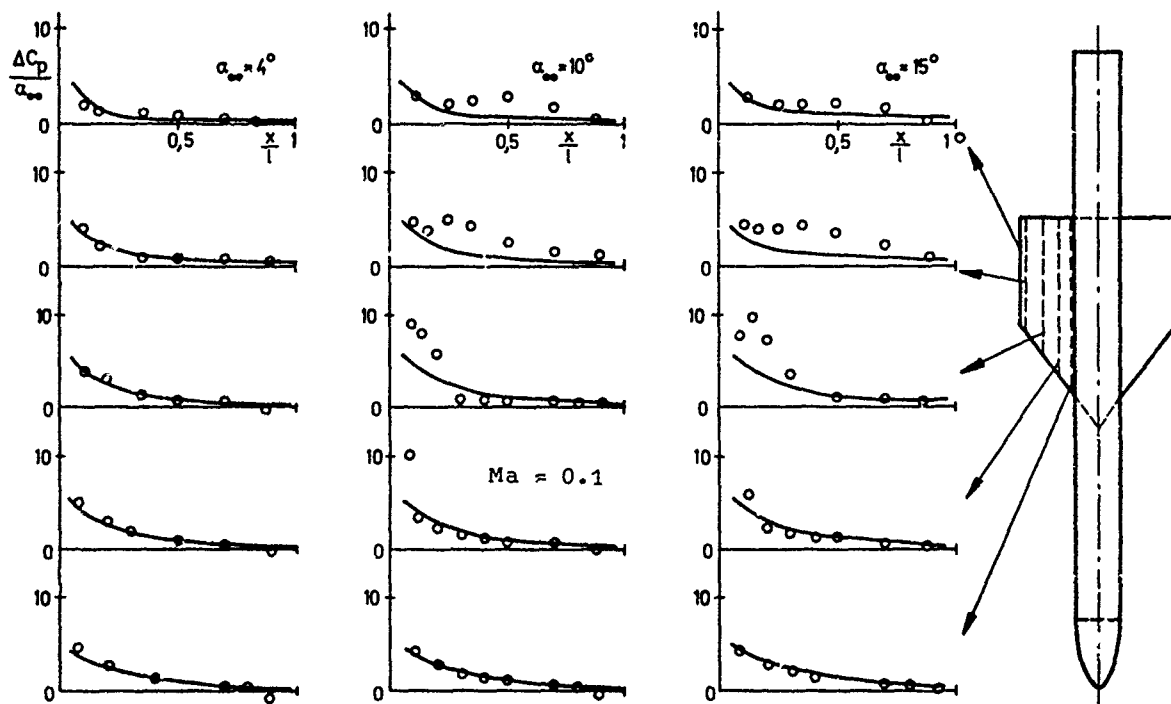
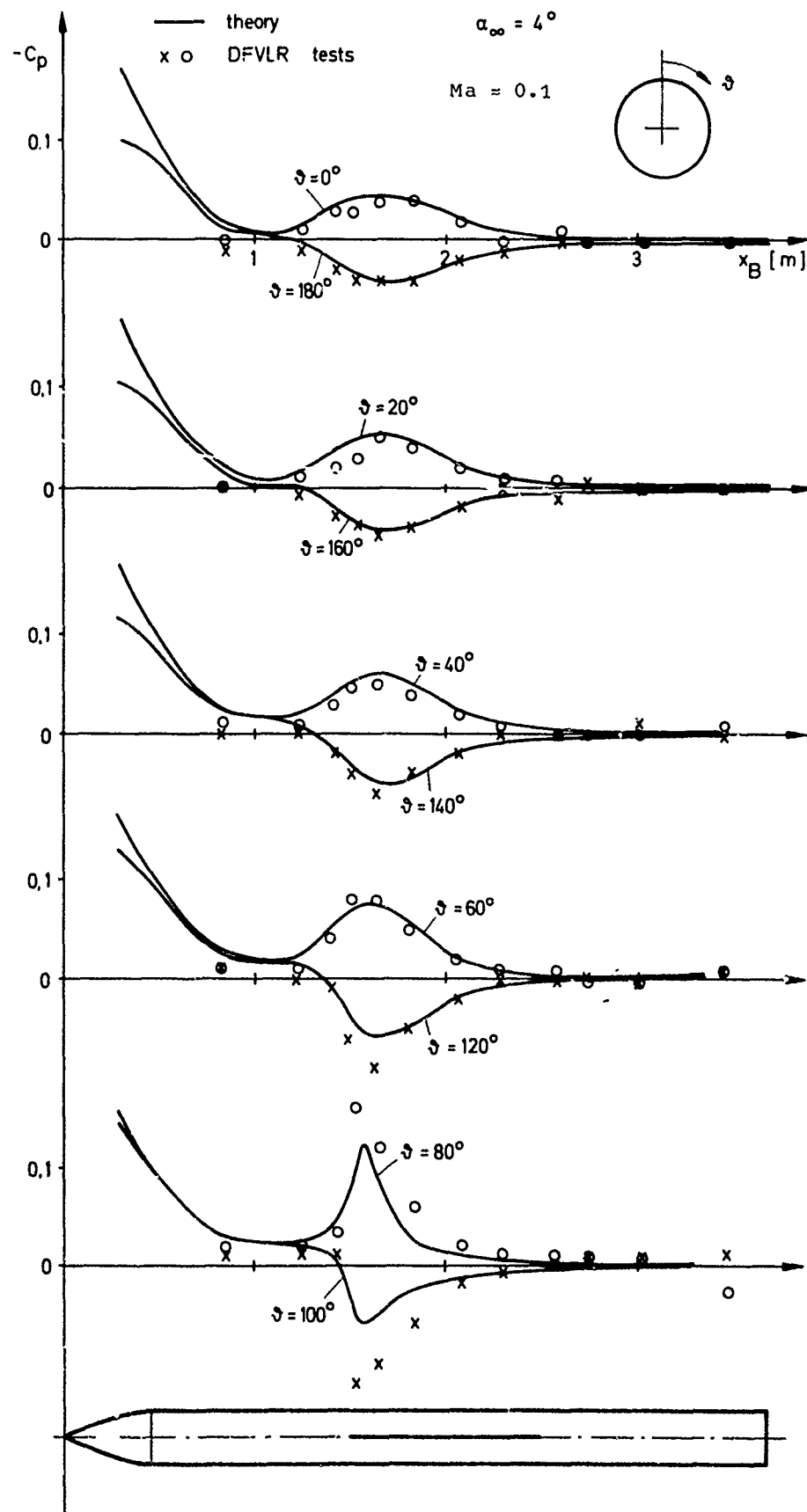


Fig. 8: Load distribution on the exposed wing  
Comparison between theory and tests



**Fig. 9:** Comparison between theoretical and test results

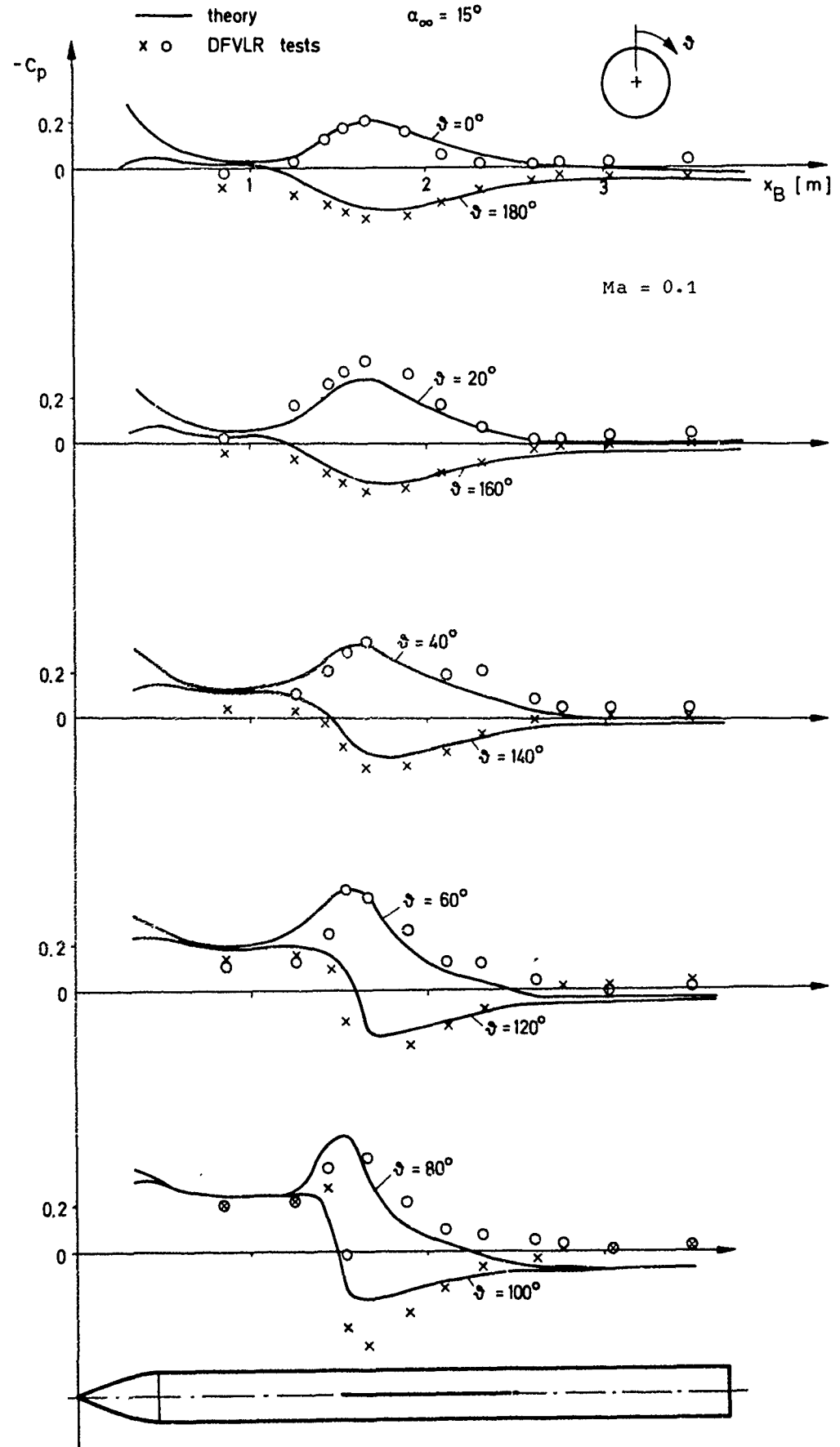


Fig. 10: Comparison between theoretical and test results

# PREDICTION METHOD FOR STEADY AERODYNAMIC LOADING ON AIRFOILS WITH SEPARATED TRANSONIC FLOW

by

P. G. Thiede\*

Vereinigte Flugtechnische Werke-Fokker GmbH  
D 2800 Bremen, Hünefeldstrasse 1-5, Germany

## SUMMARY

A method is outlined for transonic flows on airfoils, extending the boundary layer concept to regions of flow separation by coupling a viscous boundary layer solution with an inviscid external flow solution iteratively. For viscous flow in the separated region an inverse integral method is developed, defining the surface pressure as a dependent variable with a prescribed streamline angle at the boundary layer edge. For the inviscid flow, a finite difference method is used, which satisfies the complete transonic equation.

Two coupling schemes with different boundary conditions for both the interacting flow fields are considered:

1. Tangential coupling along the boundary layer displacement thickness
2. Tangential and normal velocity coupling along the boundary layer edge.

The above method was verified with tests on a two-dimensional bump in a transonic duct, and on a circular arc transonic airfoil, for which results of the Navier-Stokes solutions have been published. Results indicate that with the second boundary condition the present method is accurate enough for practical purposes provided that the separated regions have a moderate extension.

## NOTATION

$a$	speed of sound	$M$	Mach number
$c_D$	dissipation coefficient, $\frac{2 \int_0^\delta \tau_{du}}{\rho_e u_e^3}$	$P$	static pressure
$c_f$	skin friction coefficient, $\frac{2 \tau_w}{\rho_e u_e^2}$	$r$	recovery factor
$c_p$	pressure coefficient	$R$	Reynolds number
$H_{01}$	shape parameter of velocity profile, $\frac{\delta}{\int_0^\delta (1 - \frac{u}{u_e}) dn} - 1$	$s, n$	orthogonal coordinates along the surface
$H_{21}$	shape parameter of velocity profile, $\frac{\int_0^\delta \frac{u}{u_e} (1 - \frac{u}{u_e}) dn}{\int_0^\delta (1 - \frac{u}{u_e}) dn}$	$T$	temperature
$H_{31}$	shape parameter of velocity profile, $\frac{\int_0^\delta \frac{u}{u_e} [1 - (\frac{u}{u_e})^2] dn}{\int_0^\delta (1 - \frac{u}{u_e}) dn}$	$u, v$	velocity components in $s, n$ -coordinates
$H_{01}^*$	shape parameter, $\frac{\delta - \delta_1}{\delta_1}$	$x, y$	Cartesian coordinates
$H_{21}^*$	shape parameter, $\frac{\delta_2}{\delta_1}$	$\beta$	pressure gradient parameter, $\frac{2\xi}{u_e} \frac{du_e}{d\xi}$
$H_{31}^*$	shape parameter, $\frac{\delta_3}{\delta_1}$	$\delta$	boundary layer thickness
$H_{41}^*$	shape parameter, $\frac{\delta_4}{\delta_1}$	$\delta_1$	displacement thickness, $\int_0^\delta (1 - \frac{\rho u}{\rho_e u_e}) dn$
$l$	length	$\delta_2$	momentum thickness, $\int_0^\delta \frac{\rho u}{\rho_e u_e} (1 - \frac{u}{u_e}) dn$
$m$	Mach number coefficient, $\frac{\kappa - 1}{2} M^2$	$\delta_3$	energy thickness, $\int_0^\delta \frac{\rho u}{\rho_e u_e} [1 - (\frac{u}{u_e})^2] dn$
		$\delta_4$	density thickness, $\int_0^\delta \frac{u}{u_e} (1 - \frac{\rho}{\rho_e}) dn$
		$\theta$	streamline angle
		$\xi, \eta$	transformed $s, n$ -coordinates
		$\Pi$	pressure gradient parameter, $\frac{1}{u_e} \frac{du_e}{d\xi} \int_0^\delta (1 - \frac{u}{u_e}) dn$

\*Dr.-Ing., Department of Aerodynamics



$\rho$	density	<u>Subscripts</u>	
$\tau$	shear stress	e	edge of boundary layer
$\varphi$	correction coefficient for compressibility transformation,	equ	equilibrium condition
	$\frac{1}{\Gamma M_e} \left( \frac{1}{\delta_2} \int_0^{\delta} \frac{u}{u_e} \left( 1 - \frac{u}{u_e} \right)^{n-1} \right)$	w	wall surface
		$\delta$	boundary layer thickness
$\phi$	potential function	$\delta_1$	displacement thickness
$\psi$	stream function	$\infty$	free stream condition

## INTRODUCTION

The knowledge of steady supercritical airfoil flows is an important instrument for the calculation and design of transonic wings because of the complexity of transonic wing flows.

The difficulties in predicting the aerodynamic loading of thick rear-loaded supercritical airfoils for transonic flows, especially at off-design conditions, arise due to their sensitivity to viscous effects resulting from both shock and pressure induced separation and their interaction with the potential flow - cf. Pearcey et al. (Ref. 1) and Kacprzynski (Ref. 2), see also Fig. 1. However the existing viscous transonic flow calculation methods (Refs. 3, 4 and 5), wherein the boundary layer displacement thickness is superimposed to the airfoil contour producing an equivalent shape to represent the boundary layer displacement of the inviscid streamlines, are limited to weak viscous-inviscid interactions and hence exclude separated zones.

Therefore, considerable efforts were made for the calculation of separated flows in the past few years, concentrating mainly on the following two areas:

1. Solving the complete Navier-Stokes equations.
2. Solutions incorporating boundary layer concepts.

Although the Navier-Stokes solutions (Refs. 6, 7) represent the direct and exact way for the solution of strong interaction cases, the computer costs are still far too high for engineering applications. In contrast the boundary layer concept is more economical, although for every case a control of the boundary layer assumptions is necessary. Results of separated flows from Ghia et al. (Ref. 8) and Murphy et al. (Ref. 9) for specific examples wherein the boundary layer assumptions are approximately satisfied, show that the boundary layer concept gives results comparable with the complete Navier-Stokes solutions.

In the last few years, considerable success was achieved, beginning with the pioneering contribution of Lees and Reeves (Ref. 10), in treating the separated supersonic laminar flow as a boundary layer problem. However, the technique of locally considering the interaction between the viscous and inviscid flow due to the hyperbolic nature of the inviscid supersonic flow field, resulting in regular solutions of the boundary layer equations for the separated regions, cannot be utilized for subsonic or transonic flows, as pressure at any point of the elliptical inviscid flow is dependent on the entire airfoil the pressure at any point of the elliptical inviscid flow is dependent on the entire airfoil displacement distribution. For the subsonic case, Catherall and Mangler (Ref. 11) were pressure is prescribed, can be avoided by using an inverse solution procedure, wherein the displacement thickness or wall shear stress distribution is prescribed and the pressure is deduced from the resulting solution.

The calculation of separated turbulent boundary layers has not yet achieved the comparable accuracy of the laminar case for three main reasons:

1. The estimation of the Reynolds stresses becomes very difficult with deviations from the equilibrium condition.
2. A suitable family of separated turbulent velocity profiles must exist as reference.
3. A suitable compressibility transformation must be imputed.

An inverse integral method prescribing the wall shear stress distribution was developed by Kuhn and Nielsen (Ref. 12) for predicting separated turbulent boundary layers, fails however in the shock region.

For the calculation of the complete supercritical airfoil flow field, it is necessary to incorporate a description of the inviscid transonic flow. A very effective iterative procedure can be obtained combining an inverse boundary layer method with an inverse inviscid calculation method, in which the pressure calculated from the inverse boundary layer solution is prescribed analogue to the incompressible flow procedure of Carter and Wornom (Ref. 13).

However, due to the absence of a suitable inverse method for inviscid transonic flow, a direct inviscid method was first used by Klineberg and Steger (Ref. 14) to develop an iterative procedure for separated laminar flows and later, for the corresponding turbulent case at transonic speeds by Tai (Ref. 15). The results of the calculation of turbulent transonic viscous-inviscid interactions from Tai are not quite satisfactory as a result of inaccuracies caused by the small-disturbance approximations of the inviscid solution and the thin airfoil boundary conditions as well as the insufficiencies of the reverse flow velocity profiles of the boundary layer solution.

The present paper describes an iterative procedure for transonic airfoil flows with strong viscous-inviscid interactions including separation zones by combining a turbulent boundary layer solution with an inviscid solution. For the separated turbulent boundary layer flow, an inverse integral method is developed, prescribing the streamline flow angle, by using the similar solutions of Alber (Ref. 16) for the reverse flow velocity profiles and an empirical relation for non-equilibrium flows. For the inviscid flow the finite difference method of Klevenhusen (Ref. 17) is used, which satisfies the complete transonic equation in curvilinear coordinates and fulfills the exact boundary conditions. In separated regions the coupling of the interacting flow fields is tested with the following two boundary conditions:

1. Tangential coupling along the boundary layer displacement thickness.
2. Tangential and normal velocity coupling along the boundary layer edge.

A numerical matching procedure for separated regions is developed introducing the second boundary condition. Finally the complete matching procedure is applied to viscous transonic airfoil flows with both shock and/or pressure induced separation, considering primarily flow cases without circulation.

## ANALYSIS

### Viscous flow solution

Assuming the validity of the boundary layer approximations, the separated flow on airfoils can be treated as a boundary layer problem. For the iterative calculation of the viscous transonic airfoil flow it appears most effective at the present moment to apply the parametric integral technique for the boundary layer solution, emphasised by the better information available about the reverse flow velocity profiles than of the turbulence structure in the separated case.

The integral relations, evolved from the boundary layer conservation equations for stationary two-dimensional compressible flows are for

moment

$$\frac{d\delta_2}{ds} + \left(2 + \frac{\delta_1}{\delta_2} - M_e^2\right) \frac{\delta_2}{u_e} \frac{du_e}{ds} - \frac{c_f}{2} = 0 \quad (1)$$

moment of momentum

$$\frac{d\delta_3}{ds} + \left(3 + 2 \frac{\delta_4}{\delta_3} - M_e^2\right) \frac{\delta_3}{u_e} \frac{du_e}{ds} - c_D = 0 \quad (2)$$

and continuity

$$\frac{d\delta_1}{ds} - (\delta - \delta_1) \frac{d}{ds} \ln(\rho_e u_e) - \tan \vartheta_e = 0 \quad (3)$$

In regions of weak interaction the continuity equation is approximated by

$$\tan \vartheta_e = \frac{d\delta_1}{ds} \quad (4)$$

and therefore uncoupled from the remaining equations (1) and (2), which satisfy the description of the boundary layer. Here the boundary layer is computed by a standard procedure (Refs. 18, 19 and 20), prescribing the pressure distribution from the inviscid outer flow solution. In the standard procedure, the shape parameter function of the velocity profiles imputes a saddle-type singularity at the separation and reattachment points, which is avoided by an inverse solution procedure, prescribing the displacement thickness or the wall shear stress distribution and defining the surface pressure as a dependent variable. For the solution of the complete viscous equation system (1) - (3) in the strong interaction case, it is more advantageous to define the streamline flow angle at the boundary layer edge  $\vartheta_e$ .

For the inverse solution procedure the integral equations (1) - (3), introducing the inverse shape parameters  $H_{01}^*$ ,  $H_{21}^*$ ,  $H_{31}^*$  and  $H_{41}^*$ , are transformed into:

$$\frac{dH_{21}^*}{ds} + \frac{1+H_{21}^*(2-M_e^2)}{1+m_e} \frac{1}{M_e} \frac{dM_e}{ds} + \frac{H_{21}^*}{\delta_1} \frac{d\delta_1}{ds} = \frac{c_f}{2\delta_1} \quad (5)$$

$$\frac{dH_{31}^*}{dH_{21}^*} \frac{dH_{21}^*}{ds} + \frac{2H_{21}^* + H_{31}^*(3-M_e^2)}{1+m_e} \frac{1}{M_e} \frac{dM_e}{ds} + \frac{H_{31}^*}{\delta_1} \frac{d\delta_1}{ds} = \frac{c_D}{\delta_1} \quad (6)$$

$$- \frac{H_{01}^*(1-M_e^2)}{1+m_e} \frac{1}{M_e} \frac{dM_e}{ds} + \frac{1}{\delta_1} \frac{d\delta_1}{ds} = \frac{\tan \vartheta_e}{\delta_1} \quad (7),$$

see Ref. (21). Taking into account that the van Driest relation between temperature and velocity profiles (Ref. 22)

$$\frac{T}{T_e} = 1 + m_e \left[ 1 - \left( \frac{u}{u_e} \right)^2 \right] \quad (8)$$

is valid also for separated flows, reduces the compressible boundary layer integral quantities, appearing in the integral equations (5) - (7), to incompressible ones.

The solution of the viscous equation system with a prescribed streamline flow angle at the boundary layer edge  $\vartheta_e$ , requires the following relations for a one-parametric family of turbulent reverse flow velocity profiles:

- shape parameter functions  $H_{31}(H_{21})$ ,  $\frac{dH_{31}}{dH_{21}}(H_{21})$ ,  $H_{01}(H_{21})$
- compressibility transformation coefficient  $\varphi(H_{21}, M_e)$
- skin friction coefficient  $c_{f1}(H_{21})$
- dissipation coefficient  $c_{D1}(H_{21})$ ,

for which the lower branch similar solutions of Alber (Ref. 16) are used as a basis, Fig. 2. The above relations, evaluated in Ref. 23, are also valid for separated non-equilibrium boundary layers, excluding however the dissipation law, wherein the history effects must be considered. From the evaluation of separated turbulent boundary layer measurements, especially from Ref. 24, Fig. 3, the following empirical formula for the dissipation coefficient is established:

$$c_{D1} = c_{D1}(H_{21}) + \Delta c_{D1}(\Pi - \Pi_{equ}) \quad (9),$$

wherein the deviation from the equilibrium conditions is determined. For a better estimation of the characteristics of the reverse flow profiles, further tests with separated turbulent flows are absolutely necessary.

Together with the relations of the reverse flow profiles, the integral equations (5) - (7) form, with the prescribed streamline angle at the boundary layer edge  $\vartheta_e$ , a linear equation system with 3 dependent variables  $dH_{21}^*/ds$ ,  $dM_e/ds$  and  $d\delta_1/ds$ , which can be written with Cramer's rule as

$$\frac{dH_{21}^*}{ds} = \frac{N_1(H_{21}, M_e, \delta_1)}{D(H_{21}, M_e, \delta_1)} \quad (10)$$

$$\frac{1}{M_e} \frac{dM_e}{ds} = \frac{N_2(H_{21}, M_e, \delta_1)}{D(H_{21}, M_e, \delta_1)} \quad (11)$$

$$\frac{1}{\delta_1} \frac{d\delta_1}{ds} = \frac{N_3(H_{21}, M_e, \delta_1)}{D(H_{21}, M_e, \delta_1)} \quad (12).$$

This system of ordinary differential equations can be solved by a Runge-Kutta integration.

The accuracy of the inverse boundary layer method with the above relations suggested for the reverse flow profiles, was compared with measurements of the separated turbulent boundary layer of Alber et al. (Ref. 24) on a two-dimensional bump in a transonic duct. For comparison of the calculated results with the tests, the reduced viscous equation system (5) and (6) is used, prescribing the measured displacement thickness  $\delta_1$ . The calculated boundary layer values  $M_e$ ,  $H_{21}^*$  and  $c_f$  of the separated flow regions in the shock and pressure gradient induced separation cases are compared to the measured ones in Fig. 4 and 5. Deviations between the computed and measured boundary layer values near the reattachment point, arising from the non-equilibrium condition, essentially vanish by considering the non-equilibrium character of the boundary layer in the dissipation law. Further deviations between the computed skin friction coefficients and those evaluated from the measured velocity profiles, despite the good  $H_{21}^*$ -conformity, indicate the strong disturbed turbulence structure of the boundary layer at the reattachment point.

#### Inviscid flow solution

A finite difference method, described in Ref. 17, which satisfies the full non-linear transonic velocity potential equation in curvilinear coordinates and fulfills the exact boundary conditions on the matching line, is adopted for the inviscid transonic airfoil flow solution.

The differential equation for two-dimensional inviscid flow in Cartesian coordinates is

$$\phi_{xx}(a^2 - \phi_x^2) + \phi_{yy}(a^2 - \phi_y^2) - 2\phi_x\phi_y\phi_{xy} = 0 \quad (13).$$

The fulfillment of the boundary conditions for complicated profile contours not contained in the network for the finite difference schemes is the inherent difficulty in solving this differential equation, which, however, can be circumvented by introducing a streamline coordinate system:

$$\varphi = \text{const} \quad \psi = \text{const} \quad (14)$$

with the boundary as coordinate

$$\phi\psi = 0 \quad (15).$$

For the calculation of the streamline coordinates, a panel method with dipole covering is suggested (for unproblematic description of profile contours with viscous effects), to avoid the difficulties discerned in the conformal mapping, as for instance in the method of Garabedian et al. (Ref. 3).

The differential equation (13) in streamline coordinates is

$$2a^2(\phi_{\varphi\varphi} + \phi_{\psi\psi}) = \phi_{\varphi}B_{\varphi} + \phi_{\psi}B_{\psi} \quad (16)$$

with

$$B = (\phi_{\varphi}^2 + \phi_{\psi}^2)A \text{ and } A = \varphi_x^2 + \varphi_y^2$$

Eq. (16) is solved with the Murman finite difference scheme (Ref. 25).

#### Matching of the viscous and inviscid solutions

The two different boundary conditions for coupling both the interacting viscous and inviscid flow fields considered are:

1. Tangential coupling along the boundary layer displacement thickness.
2. Tangential and normal velocity coupling along the boundary layer edge.

The first boundary condition, an approximation of the continuity integral equation (3),

$$\frac{v}{u_*} = \tan \delta = \frac{d\delta_1}{ds} \quad (17),$$

is normally adopted for weak interaction problems. This signifies that the displacement thickness serves as a streamline, which primarily hinders mass transfer and consequently the communication between the inner viscous and the outer inviscid flow.

The second boundary condition, which exactly satisfies the continuity integral equation (3)

$$\frac{v_e}{u_e} = \tan \vartheta_e = \frac{d\delta_1}{ds} - (\delta - \delta_1) \frac{d}{ds} \ln(\rho_e u_e) \quad (18),$$

forces the inviscid solution to match the tangential and normal velocity components  $u_e$  and  $v_e$  given by the viscous solution along the boundary layer edge, verifying that the induced streamline angle at the boundary layer edge  $\vartheta_e$  is a common variable for both the viscous and inviscid solutions. This boundary condition forms the basis for a more realistic flow model for the strong interaction case.

The coupling of the interacting flow fields with both the boundary conditions (17) and (18) is tested with the experimental results of Alber et al. (Ref. 24) in separated turbulent transonic flow. For the test

- case A with pressure-gradient induced separation and
- case B with shock induced separation,

the inviscid flow field is calculated with the above boundary conditions at the bump derived from the measured boundary layer values, Fig. 7 and 8. Although the duct ceiling above the bump approximates the streamline of the unrestrained flow field, the influence of the opposite wall on the bump flow cannot be neglected; therefore the boundary condition (17) is satisfied on the opposite wall for both calculations. In the attached boundary layer flow region a good agreement between the calculated and measured Mach number distributions is reached using both boundary conditions. However, in the separated flow region where the viscous effects are dominant, better results are achieved with the  $u_e, v_e$ -coupling on the boundary layer edge, confirmed by Murphy et al. (Ref. 9). Consequently, only the second boundary condition (18) is used to develop a matching procedure for flows with strong viscous-inviscid interactions.

Matching is the process determining the specific combination of the tangential and normal velocity components on the boundary layer edge,  $u_e$  and  $v_e$  respectively, simultaneously satisfying both the viscous and inviscid flow solution. The inverse solution for the tangential velocity component  $u_e$  of the viscous equation system (5) - (7) at the positions ( $s = \text{const}$ ) of a prescribed airfoil geometry can be written as

$$u_{e,vs} = f_{vs}(\tan \vartheta_{e,vs}) \quad (19)$$

and the direct solution for the normal velocity component  $v_e$  by the inviscid equation (16) as

$$u_{e,is} = g_{is}(\tan \vartheta_{e,is} | \delta) \quad (20),$$

i.e. the induced streamline angle at the boundary layer edge

$$\vartheta_e = \tan^{-1}\left(\frac{v_e}{u_e}\right)$$

is a common variable for both the viscous and the inviscid flow fields. Aim of the matching procedure is to achieve the coincidences

$$u_{e,vs} = u_{e,is} \quad (21)$$

and

$$v_{e,vs} = v_{e,is} \quad \text{or} \quad \tan \vartheta_{e,vs} = \tan \vartheta_{e,is} \quad (22).$$

Assuming that the boundary layer thickness variation as a second-order term in Eq. (20) is negligible, the intersection of the functions  $f_{vs}$  and  $g_{is}$  in the  $u_e, v_e$ -coordinates represent the matched solution of Eqs. (19) and (20). According to Ref. 26, the matched solution can be derived using an initial approximation  $v_e^{(0)}$  by a two-dimensional Newton iteration, see Fig. 9, which leads to a good convergence. The initial approximation  $v_e^{(0)}$  is obtained empirically from  $\delta_1$ - or  $u_e$ -estimation as used in Refs. 3 - 5.

In a modified form this matching procedure can also be applied to weak interaction regions of a transonic airfoil. However special attention must be paid to the sonic point, which is a singularity of the inviscid solution. In the weak interaction case the initial approximation is obtained from the inviscid solution without any boundary layer consideration. The advantage of this procedure for weak interaction problems is the better convergence of the iterative solution compared to the conventional procedure, wherein the displacement thickness is superimposed to the airfoil contour.

## RESULTS

The matching procedure described above is applied to separated turbulent transonic airfoil flow cases for which experimental details were available.

The most suitable example for a comparison is the aforementioned two-dimensional 10-percent thickness bump on the floor of a transonic duct (Ref. 24), where measurements of the wall static pressure distribution and of the boundary layer velocity profiles in the reverse flow region are carried out. The first comparison is made for the test case A ( $M_\infty = .7325$ ) with pressure-gradient induced separation at some distance downstream of the shock. As the influence of the opposite wall on the bump flow cannot be neglected, in addition to the bump contour, the duct ceiling is predefined for the calculations. The displacement contour of the opposite wall was kept constant during the iterative process. Furthermore, as the boundary layer develops before the test section, the inputs of the initial boundary layer parameters are required. For the calculation of the inviscid flow field a mesh with 48 (with 22 in the bump region)  $\times$  15 grid points is used. In the weak interaction region the initial approximation for the matching procedure is the inviscid solution, followed by a boundary layer calculation with the prescribed inviscid pressure distribution. In the strong interaction region beginning upstream of the separation point, a displacement thickness distribution corresponding to the initial values in the weak interaction region is estimated for the initial approximation. Matched results are obtained in the strong interaction regions after 5 iterations, whereby only 2 iteration steps are required in the weak interaction region. The predicted pressure distribution, Fig. 10, shows excellent coincidence with the tests in the attached boundary layer region and little scatter in the separated flow region.

Using the same inputs as case A, the predicted pressure distribution of the test case B ( $M_\infty = .7339$ ) with shock induced separation, Fig. 11, shows more scatter in the separated zone than the pressure induced separation case. Here, because of the larger extension of the separated flow regions (compare Fig. 4 and 5), the boundary layer approximations are less accurate than in case A.

A circular arc airfoil of 18-percent thickness is chosen as a further test case for transonic flows ( $M_\infty = .7425$ ,  $R_\infty = 4 \cdot 10^6$ ) with pressure induced separation, for which pressure measurements are presented from Mc Devitt et al. (Ref. 27). For this case Navier-Stokes solutions with four different turbulence models are published by Delwert (Ref. 7). For the calculation only the airfoil contour was defined, whereby the wind-tunnel wall, contoured to approximate the undisturbed flow conditions, was not considered. The boundary layer was assumed to be turbulent. Profile wake approximations were imputed. The inviscid solution was obtained with a 42 (with 22 on the airfoil)  $\times$  26 grid point mesh. Using the foregoing initial approximation, convergence for the complete flow field including the separated zone is reached after 4 iterations. Good coincidence of the matched solution with the measured pressure distribution in the separated trailing edge flow region is achieved. In the supersonic region deviations occur similar to the Navier-Stokes solutions, which apparently result from the wall interference and the laminar-turbulent boundary layer transition.

## CONCLUDING REMARKS

A prediction method for separated turbulent transonic flow on airfoils is achieved by coupling an inverse integral method with an inviscid finite difference method.

Results of flow cases with both pressure-gradient and shock induced separation indicate, that the present method is accurate for practical purposes, provided that the separated regions have a moderate extension. Although inherently good convergence is reached, further work is necessary to minimize the computing time for the matching procedure.

As there are no fundamental difficulties in extending the present method to flows with circulation, it can, with some additional development, be applied to cambered airfoils with incidence. Furthermore, this method can be extended for supercritical airfoils with flaps.

## REFERENCES

1. Pearcey, H. H.; Osborne, J.; and Haines, A. B.: The interaction between local effects at the shock and rear separation - a source of significant scale effects in wind-tunnel tests on aerofoils and wings. AGARD CP 35, 1968.
2. Kacprzynski, J. J.: Viscous effects in transonic flow past airfoils. ICAS Paper 74-19, 1974.
- 3a. Bauer, F.; Garabedian, P.; and Korn, D.: Supercritical wing sections. Lecture Notes in Economics and Mathematical Systems, Vol. 66, Springer-Verlag, Berlin, Heidelberg, New York, 1972.
- 3b. Bauer, F.; Garabedian, P.; Korn, D.; and Jameson, A.: Supercritical wing sections II. Lecture Notes in Economics and Mathematical Systems, Vol. 108, Springer-Verlag, Berlin, Heidelberg, New York, 1975.

4. Bavitz, P. C.: An analysis method for two-dimensional transonic viscous flow. NASA TN D-7718, 1975.
5. Klevenhusen, K. D.; and Hilbig, R.: Beitrag zur Untersuchung der Überkritischen Profilströmung. WGLR-Jahrbuch, 1974.
6. Mac Cormack, R. W.; and Baldwin, B. S.: A numerical method for solving the Navier-Stokes equations with application to shock boundary-layer interactions. AIAA Paper 75-1, 1975.
7. Deiwert, G. S.: Computation of separated transonic turbulent flows. AIAA Paper 75-829, 1975.
8. Ghia, K. N.; Ghia, U.; and Tesch, W. A.: Evaluation of several approximate models for laminar incompressible separation by comparison with complete Navier-Stokes solutions. AGARD CP 168, 1975.
9. Murphy, J. D.; Presley, L. L.; and Pose, W. C.: On the calculation of supersonic separating and reattaching flows. AGARD CP 168, 1975.
10. Lees, L.; and Reeves, B. L.: Supersonic separated and reattaching laminar flows: I. General theory and application to adiabatic boundary-layer/shock-wave interactions. AIAA Journal Vol. 2, No. 11, 1964.
11. Catherall, D.; and Mangler, K. W.: The integration of the two-dimensional laminar boundary-layer equations past the point of vanishing skin friction. J. Fluid Mech., Vol. 26, Part 1, 1966.
12. Kuhn, G. D.; and Nielsen, J. N.: Prediction of turbulent separated boundary layers. AIAA Paper 73-663, 1973.
13. Carter, J. E.; and Wornom, S. F.: Solutions for incompressible separated boundary layers including viscous-inviscid interaction. NASA SP 347, 1975.
14. Klineberg, J. M.; and Steger, J. L.: Calculation of separated flows at subsonic and transonic speeds. Proc. of the 3rd International Conference on Numerical Methods in Fluid Dynamics, Vol. 2, Paris, 1972. Lecture Notes in Physics No. 66, 1973.
15. Tai, T. C.: Transonic turbulent viscous - inviscid interactions over airfoils. AIAA Paper 75-78, 1975.
16. Alber, I. E.: Similar solutions for a family of separated turbulent boundary layers. AIAA Paper 71-203, 1971.
17. Klevenhusen, K.-D.: Die Berechnung der ebenen und rotationssymmetrischen stationären transsonischen Potentialströmung um Körper beliebiger Form. VFW-Fokker Memorandum, 1976, not published.
18. Felsch, K. O.; Geropp, D.; and Walz, A.: Method for turbulent boundary layer prediction. In: Computation of turbulent boundary layers, 1968 AFOSR-IFP - Stanford conference. Proceedings Vol. I. Edited by Kline, S.J.; Morkovin, M. V.; Sovran, G.; and Cockrell, D. J. Stanford University, California, 1969.
19. Otte, F.; and Thiede, P.: Berechnung ebener und rotationssymmetrischer kompressibler Grenzschichten auf der Basis von Integralbedingungen. Fortschr.-Ber. VDI-Z, Reihe 7, No. 33, 1973.
20. Thiede, P.; and Klevenhusen, K. D.: Theoretische und experimentelle Untersuchungen der Grenzschicht von Transsonikprofilen. ZTL-FAG 4 Final Report, VFW-Fokker 4.03/6/74, 1974.
21. Thiede, P.; and Dargel, G.: Berechnung abgelöster turbulenter Grenzschichten bei transsonischer Profilströmung. ZTL-FAG 4 Final Report, VFW-Fokker 4.03/7/75, 1975.
22. Van Driest, E. R. in Lin, C. C.: Turbulent flows and heat transfer. Sect. Princeton Uni. Press, 1959.
23. Thiede, P.; and Dargel, G.: Untersuchungen von abgelösten turbulenten Geschwindigkeitsprofilen bei transsonischer Strömung. VFW-Fokker Report Ef 606, 1976, not published.
24. Alber, I. E.; Bacon, J. W.; Masson, B. S.; and Collins, D. J.: An experimental investigation of turbulent viscous - inviscid interactions. AIAA Journal, Vol. 11, No. 5, 1973.
25. Murman, E. M.; and Cole, J. D.: Calculation of plane steady transonic flows. AIAA Journal, Vol. 9, No. 1, 1971.
26. Brune, G. W.; Rubbert, P. E.; and Nark, T. C.: New approach to inviscid flow/boundary layer match. AIAA Journal, Vol. 13, No. 7, 1975.

27. Mc Devitt, J. B.; Levy, Jr., L. L.; and Deiwert, G. S.: Transonic flow about a thick circular-arc airfoil. AIAA Paper 75-878, 1975.

#### ACKNOWLEDGEMENT

This work was encouraged and financed by the Ministry of Defence of the Federal Republic of Germany under ZTL contracts T/R 720 / R 7600 / 52003 and T/R 420 / 60 003 / 62 006.

The assistance of Mr. G. Dargel in developing computer codes and performing calculations is gratefully acknowledged.



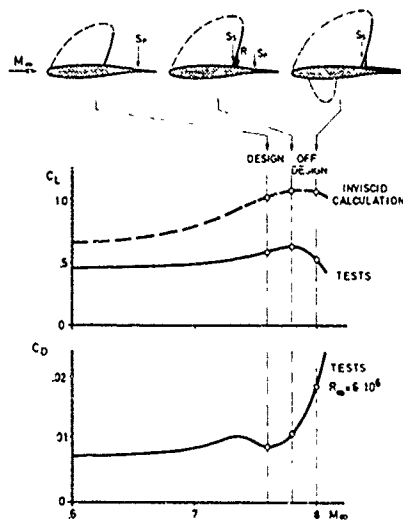


Fig. 1 Viscous effects of a rear-loaded supercritical airfoil in separated transonic flow

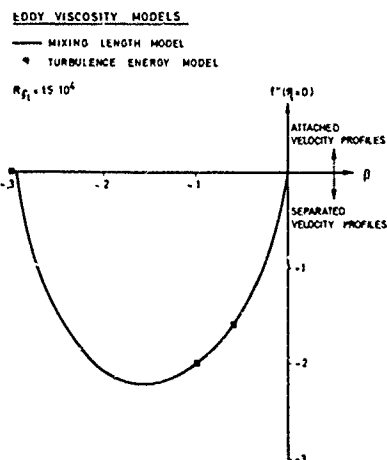


Fig. 2 Similar solutions for a family of separated turbulent boundary layers of Alber (Ref. 16)

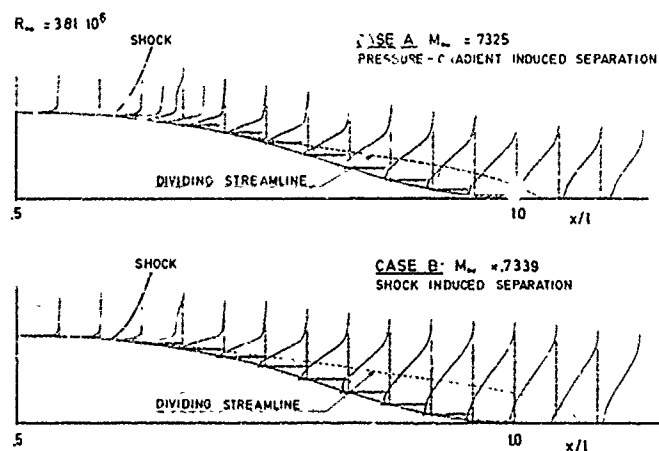


Fig. 3 Velocity profiles of separated turbulent transonic flow measurements of Alber et al. (Ref. 24)

$M_\infty = 7.325$   $R_\infty = 3.81 \cdot 10^6$   
 • DATA OF ALBER ET AL (REF 24), CASE A  
 --- EQUILIBRIUM RELATIONS  
 --- NON-EQUILIBRIUM RELATIONS } PRESENT INVERSE METHOD

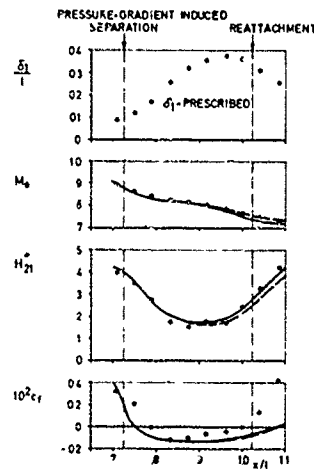


Fig. 4 Comparison of predicted separated turbulent boundary layer data with measurements

$M_\infty = 7.339$   $R_\infty = 3.81 \cdot 10^6$   
 • DATA OF ALBER ET AL (REF 24), CASE B  
 --- EQUILIBRIUM RELATIONS  
 --- NON-EQUILIBRIUM RELATIONS } PRESENT INVERSE METHOD

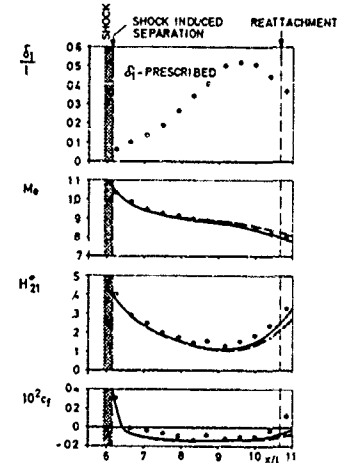


Fig. 5 Comparison of predicted separated turbulent boundary layer data with measurements

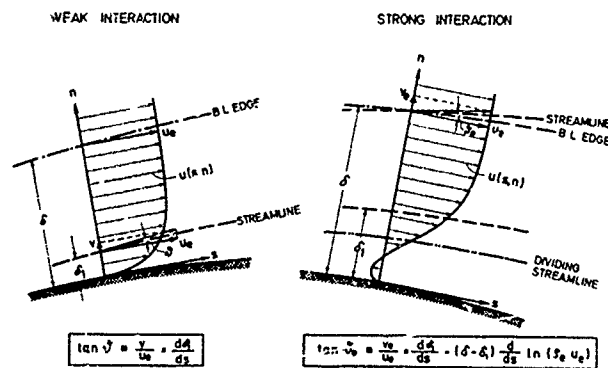


Fig. 6 Boundary conditions for coupling of the viscous and inviscid flow fields

• DATA OF ALBER ET AL (REF 24), CASE A  
 --- BOUNDARY CONDITIONS  
 ---  $v=0$  ON BODY CONTOUR  
 ---  $v=0$  ON DISPLACEMENT CONTOUR  
 ---  $u, v_0$  ON B.L. EDGE } PRESENT INVISCID METHOD

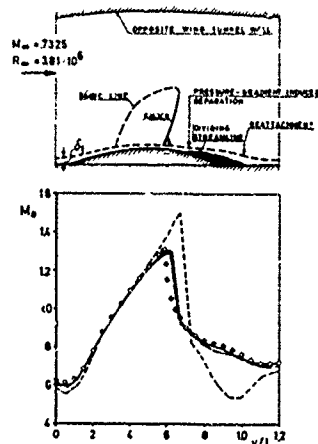


Fig. 7 Comparison of different boundary conditions with measurements

• DATA OF ALBER ET AL (REF 24), CASE B  
 --- BOUNDARY CONDITIONS  
 ---  $v=0$  ON BODY CONTOUR  
 ---  $v=0$  ON DISPLACEMENT CONTOUR  
 ---  $u, v_0$  ON B.L. EDGE } PRESENT INVISCID METHOD

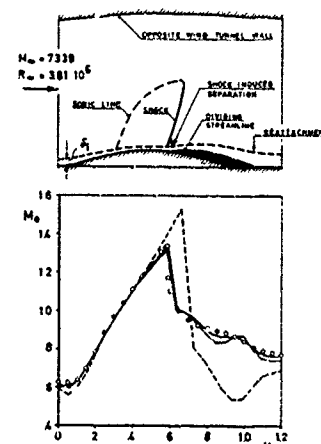


Fig. 8 Comparison of different boundary conditions with measurements

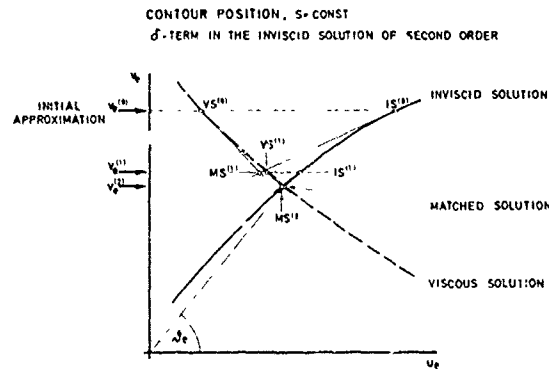


Fig. 9 Matching procedure for strong interaction regions

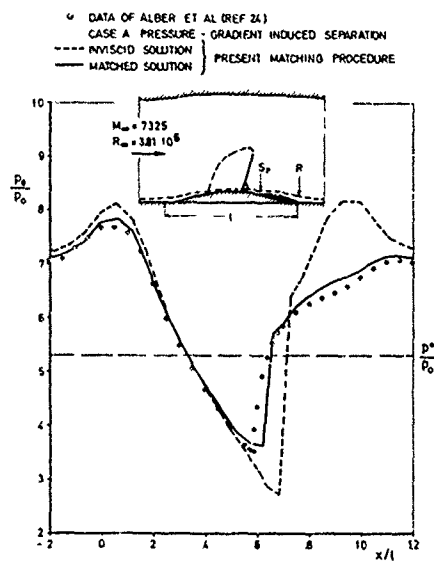


Fig. 10 Comparison of the predicted pressure distribution with measurements

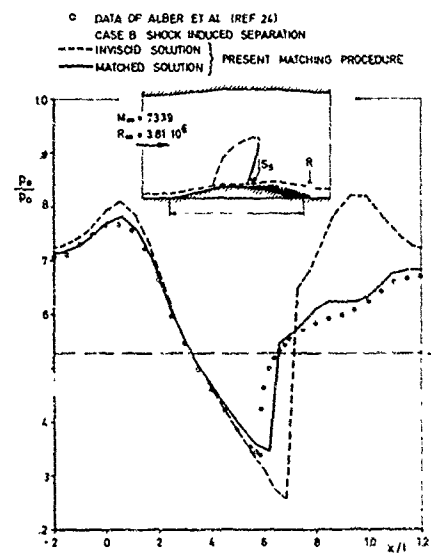


Fig. 11 Comparison of the predicted pressure distribution with measurements

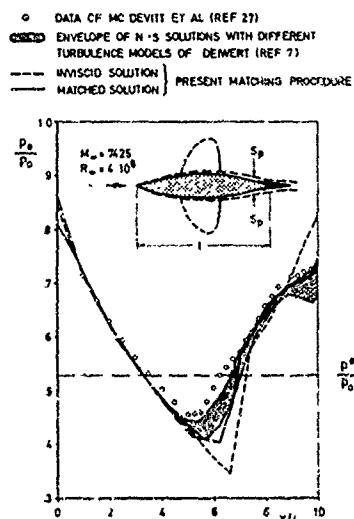


Fig. 12 Comparison of predicted pressure distributions with measurements and Navier-Stokes solutions

PRESSURE DISTRIBUTIONS FOR A SWEEP WING BODY CONFIGURATION  
OBTAINED FROM COUPLING TRANSONIC POTENTIAL FLOW CALCULATIONS  
AND BOUNDARY LAYER CALCULATIONS

Sven C. Hedman  
The Aeronautical Research Institute of Sweden (FFA)  
S - 161 11 Bromma, Sweden

SUMMARY

In a study of the aerodynamics of swept wings at transonic speed a series of wings on cylindrical bodies has been designed, tested and analyzed. The wings have a common planform, a  $35^\circ$  swept quarter chord line, an aspect ratio of 4, and a taper ratio of 0.4. The relative thickness of the wings generally exceeds 8.5%. For comparison, pressure distributions were obtained on an uncambered wing with NACA 64 series sections.

In this paper comparisons will be described between calculated and measured pressure distributions at two supercritical flow conditions  $M = 0.8$ ,  $\alpha = 6^\circ$  and  $M = 0.9$ ,  $\alpha = 0^\circ$ . The pressures were calculated with a relaxation method based on the transonic small disturbance equation. Boundary layer displacement thicknesses were calculated both with an integral method and a finite difference method for three dimensional turbulent flow.

It was found that use of the simplified or the full boundary condition and of including the  $\phi$ ,  $\phi_{xy}$  and  $\phi_z$ ,  $\phi_{xz}$  terms in the potential flow calculations affected the results only slightly. Addition of the boundary layer thickness to the wing thickness into an equivalent wing surface improved the agreement between calculated and measured pressures.

1. NOTATION

b	wing span	$\alpha$	angle of attack
$C_f$	friction coefficient	$\Gamma$	circulation
$C_p$	pressure coefficient	$\gamma$	specific heat ratio
$C_L$	lift coefficient	$\delta$	boundary layer thickness, airfoil thickness ratio
c	local chord	$\delta^*$	displacement thickness
$c_{ref}$	wing root chord	$\eta$	spanwise station $y/b/2$
H	shape factor, $\delta^*/\theta$	$\theta$	momentum thickness
M	Mach number	$\epsilon$	scaling factor, $\delta^*/M$
R	defined in Eq.(5)	$\phi$	velocity potential function
Re	Reynolds number	$\varphi$	disturbance velocity potential
$Re_\theta$	Reynolds number based on momentum thickness		
$U_\infty$	freestream velocity	Indices	
u,v,w	disturbance velocity components	$te$	trailing edge
x,y,z	Cartesian coordinates	ff	far field

2. INTRODUCTION

In a study of the aerodynamics of swept wings mainly for small lift coefficients at transonic Mach numbers, FFA has designed and tested a series of swept wings mounted on cylindrical bodies and analyzed the results. The work has been performed in cooperation with Dornier GmbH in Germany, NAE in Canada and Saab-Scania in Sweden.

The wings have a common planform defined by a  $35^\circ$  swept quarter chord line, an aspect ratio of 4.0. The relative thickness of the wings taken in the chordwise direction varies slightly between configurations but generally exceeds 8.5%. Tests of total force on an uncambered wing with NACA 64A010 section perpendicular to the quarter chord line and fitted with leading and trailing edge flaps were reported in [1]. A first cambered wing was designed with a subsonic panel method to have a sonic roof-top pressure distribution at its design point,  $M = 0.9$ ,  $C_L = 0.1$ . Comparisons were reported in [2] between pressures computed both with the panel method and with a transonic small disturbance finite difference method and with pressure distributions obtained experimentally. A second cambered wing was designed using a supercritical airfoil section. Total force balance tests for that configuration were published in [3]. A fully supercritical roof-top wing designed by the finite difference method will be reported in [4].

The wings were designed to have pressure gradients such that two-dimensional turbulent boundary layer calculations [5] showed to be free from separations. No three-dimensional boundary layer calculations were done. Lately several calculation procedures for that purpose have been published [6].

The pressures on wings in a real flow without separation can be predicted by potential flow calculations performed on an equivalent wing geometry that includes the boundary layer displacement thickness. Two methods for computing the displacement thickness and for prediction of separation of turbulent boundary layers have been selected, one is an integral method by Stock in [7] and the other a finite difference method [8]. The pressures obtained are compared with experimentally attained values for the above-mentioned plane wing. For this wing, pressure measurements are available for a wide range of incidence and Mach number,  $0 < \alpha < 9^\circ$ ,  $0.5 < M < 0.975$ ,  $7 \cdot 10^5 < Re < 16 \cdot 10^5$  [9].

## 3. METHODS OF CALCULATION

3.1 Potential flow method

The method will be described in detail in [4] and [7].

The perturbation potential  $\phi$  is defined in terms of the full velocity potential  $\phi$ .

$$\phi(x, y, z) = U_\infty [x + \epsilon \phi(x, y, z)]$$

where  $\epsilon$  is the scaling factor, here put  $\epsilon = \delta^{2/3}/M$ . The potential equation is generally simplified into the transonic flow small disturbance formulation.

$$[(1-M^2) - (\gamma+1)M^2 \epsilon \phi_x] \phi_{xx} + \phi_{yy} + \phi_{zz} = 0 \quad (1)$$

For calculations of pressures the x-component of the velocity plays a dominant role, for three dimensional boundary layer calculations the spanwise component is also important. For swept wings with round leading edges considerable crossflow velocities  $v, w$  can appear. To take these into account two more terms are retained in the potential equation.

$$[(1-M^2) - (\gamma+1)M^2 \epsilon \phi_x] \phi_{xx} + \phi_{yy} + \phi_{zz} - 2M^2 \epsilon (\phi_y \phi_{xy} + \phi_z \phi_{xz}) = 0 \quad (2)$$

The boundary condition on wing and body surfaces states that the product of surface slope and velocity at the surface should vanish. The equation of the surface is written,  $z = f(x, y)$ , and thus the boundary condition becomes

$$\phi_z = \frac{1}{\epsilon} f_x + \phi_x f_x + \phi_y f_y \quad (3)$$

This relation is used for the body together with either potential equation (1) or (2), and also for the wing when Eq.(2) is applied. However, the wing boundary conditions are simplified in connection with Eq.(1).

$$\phi_z = \frac{1}{\epsilon} f_x \quad (4)$$

The potential jump across the wake is assumed to vary linearly from the wing trailing edge  $x_{te}(y)$  to the downstream end of the computation domain  $x_{ff}$ . At intervals the far field circulation  $\Gamma_{ff}(y)$  is updated to the wing value  $\Gamma_{te}(y)$ .

$$\phi(x, y, +0) - \phi(x, y, -0) = \Gamma_{te}(y) + [\Gamma_{ff}(y) - \Gamma_{te}(y)] [x - x_{te}(y)] / [x_{ff} - x_{te}(y)]$$

In the first two grids used for preliminary calculations special far field expressions are used for the outer sides of the volume of grid points. For the surface furthest upstream and that furthest downstream the potential equation is reduced to the cross flow equation

$$\phi_{yy} + \phi_{zz} = 0$$

For the remaining three exterior surfaces far field expressions by Klunker for the potential are used.

$$\phi(x, y, z) = \frac{z}{4\pi} \left(1 + \frac{x}{R}\right) \int_{-b/2}^{b/2} \frac{\Gamma_{te}(y') dy'}{(y-y')^2 + z^2} \quad (5)$$

$$R^2 = x^2 + (1-M^2)(y^2 + z^2)$$

In the first calculations the potential on the boundaries of the computation grid is interpolated from values of the preliminary calculations.

Calculations of body surface pressures and wing pressures in connection with Eq.(2) are made with the isentropic pressure relation.

$$C_p = \frac{2}{\gamma M^2} \left\{ \left[ 1 - \frac{\gamma-1}{2} M^2 (2\epsilon \phi_x + \epsilon^2 [\phi_x^2 + \phi_y^2 + \phi_z^2]) \right]^{\frac{\gamma}{\gamma-1}} - 1 \right\}$$

When the potential equation in Eq.(1) is used, the pressure coefficient expression is linearized.

$$C_p = -2\epsilon \phi_x$$

3.2 Boundary layer methods

The boundary layer flow on the wing was assumed to be turbulent, three-dimensional, and compressible.

The aim of the calculations is primarily to determine the displacement thickness to be added to the wing geometry. The flow over the equivalent wing will then be recalculated and the pressures compared to the ones obtained without boundary layer addition. Two methods have been employed for the determination, an integral method for the major part of the work and a finite difference method to check some of the results.

The integral method.

The method was first developed by Smith [10] and later by Stock in [7]. It is based

on the boundary layer momentum integral and the entrainment equation. For the cross flow velocities Mager profiles are used. In the program there is an option for Johnston profiles. The skin friction is taken from the Ludwig-Tillmann relation. Consideration of compressibility is taken according to Eckert's reference temperature concept. The entrainment coefficient depends on the shape factor  $H$  and the exterior Mach number  $M$ .

Starting values are calculated in a laminar flow across a cylinder approximating the wing leading edge. The flow is computed over one surface at a time.

The finite difference method.

This is an extension of the Bradshaw-Ferriss transport equation method applicable to tapered swept wings [8]. A cylindrical polar coordinate system is used with its center in the node of the wing's generators. The isobars are assumed to follow the generators.

Initial values of  $\theta$ ,  $Re_\theta$  and  $C_f$  at 10 % chord have been given by the integral method. From these values a starting velocity profile is synthesized from Coles' and Mager profiles. Finite difference solutions of the transport equations then proceed along a circular arc and the solution is transformed to an adjacent wing section. One section is computed at a time.

The main advantage of the integral method is its ability to treat a front line that sweeps past the wing surface, while the salient feature in the finite difference method lies in the absence of assumed velocity profiles.

### 3.3 Calculation procedures

The program for potential flow has the two main alternatives for operation listed below. A third hybrid alternative was used in one case.

Operation alternative	Crossterms in potential equation	Boundary conditions	Pressure coefficient expression
1	Yes	Full	Isentropic
2	No	Linearized	Linearized
3	No	Full	Linearized

The calculations of the flow fields utilized three grids.

Grid	Calculations	Number of points			Size in root chords		
		x	y	z	x	y	z
1	Preliminary	26	19	28	-2.5/2.6	0./4.0	-4.8/4.8
2	Preliminary	41	28	28	-2.3/2.5	0./3.9	-4.3/4.3
3	Final	48	28	29	-.6/1.8	0./1.6	-1.2/1.2

The number of points on the unit length root chord was 7, 14 and 20 respectively. In each grid iterations were continued until a maximum change of the potential in the field was less than 0.0005. Relaxation factors when approaching convergence were 1.8 and 0.9 for subsonic and supersonic columns in the grid respectively. The number of iterations for convergence in the different grids were approximately 160, 70 and 40. The program with storage for the final grids 38,976 points nearly filled the available CDC 6600 computer. Execution time for the final calculation was approximately 4 seconds per iteration when alternative 2 was used and approximately twice that time for alternative 1.

The boundary layer calculations required less time and storage. The integral method takes both surfaces in one computer run, it uses two thirds of the CDC 6600 storage and gets the answers within one minute. The finite difference method takes one wing-station per run. It needs very little core, the computation time is approximately 8 seconds.

### 4. CASES INVESTIGATED

For the investigation on the performance of the procedures to compute potential flow and boundary layer flow two test cases with steep pressure gradients were selected, one with high suction peaks at the leading edge,  $M = 0.8$ ,  $\alpha = 6^\circ$ , and one with shocks further aft,  $M = 0.9$ ,  $\alpha = 0^\circ$ . It was hoped that boundary layers would be thick enough to effect the pressure distributions significantly.

A sketch of the model showing the pressure tap stations appears in Fig. 1 (see next page). In the calculations the fuselage was an infinitely long cylinder.

### 5. RESULTS

Pressures calculated without and with consideration of the boundary layer displacement will be shown and compared with measured values. The influence of the different program alternatives referred to in Section 3 will be demonstrated. Velocity distributions will be given and comparisons between displacement thicknesses calculated with the integral method and the finite difference method will be made.

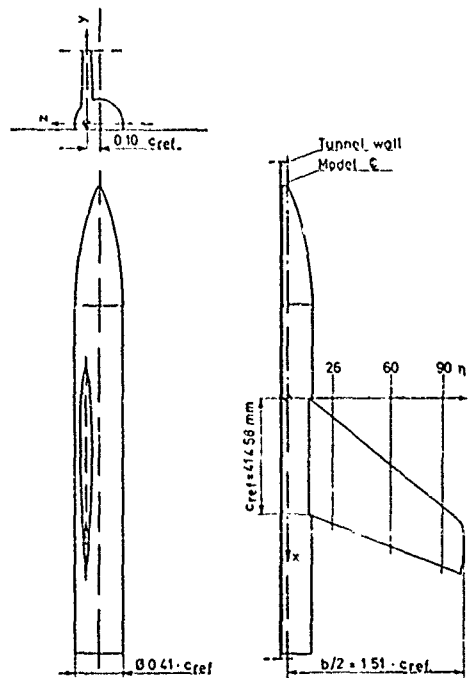


Fig. 1. The model.

#### 5.1 Pressures calculated with no consideration of the boundary layer

Fig. 2 contains data for  $M = 0.8$ ,  $\alpha = 6^\circ$ . The calculated values show the general trend of the experimental ones. However the upper surface leading edge expansion is underestimated. Downstream of the leading edge shock the pressures obtained with alternative 1 show too low values, which is not surprising as the shock strength was too small. Alternative 2 gives slightly more positive pressures that happen to come closer to experiments.

The first grid point on each chord was situated at 3.6 %. To improve the agreement would require grid points closer to the leading edge.

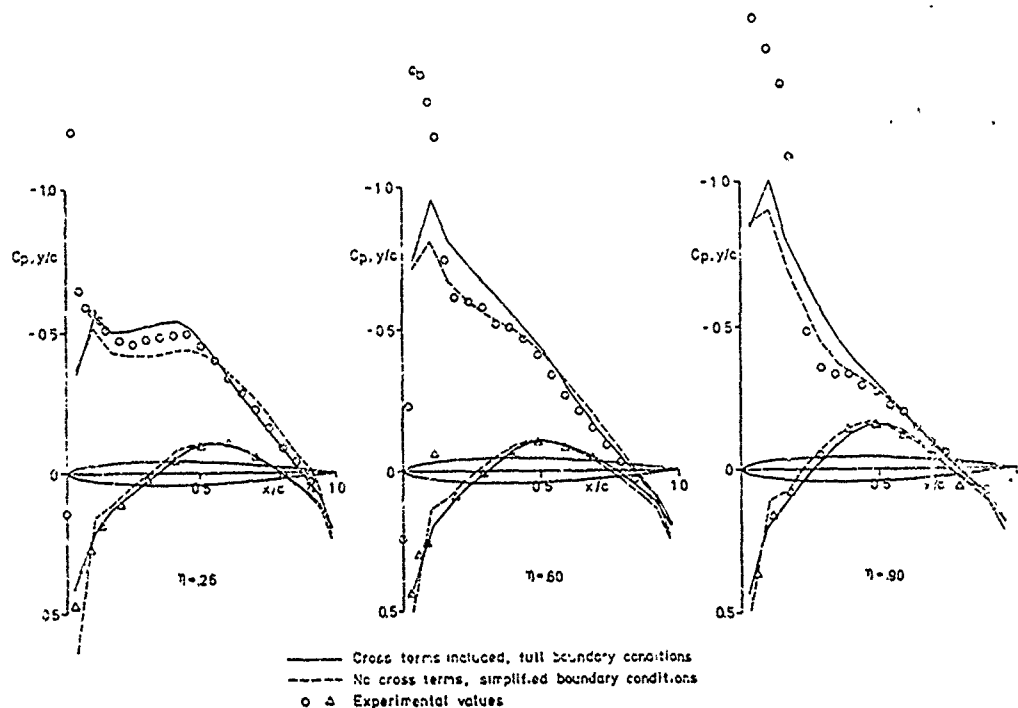


Fig. 2. Pressure distributions.  $M = 0.8$ ,  $\alpha = 6^\circ$   
comparison between calculated and measured data.

The other flow condition investigated  $M = 0.9$ ,  $\alpha = 0^\circ$  gives so little difference in pressure on the wings' two sides that for clarity the results are shown separately in Fig. 3. There is a fair agreement in the results here also. There are some features worthy of note. The linearized boundary conditions cause an expansion peak in the second grid points. In the region of the lowest pressures the pressures are lower both due to the full boundary conditions and due to the cross terms in the potential equation. In this region  $v$  and  $w$  are small, see Section 5.2, so no appreciable effect of choice of pressure coefficient expression occurs. The lower surface shock is predicted to be stronger in its inboard portions than is observed in the wind tunnel. However, in Section 5.3, the boundary layer calculations will indicate separation on the inboard section which explains this over-estimation. The tip shock is predicted too far aft.

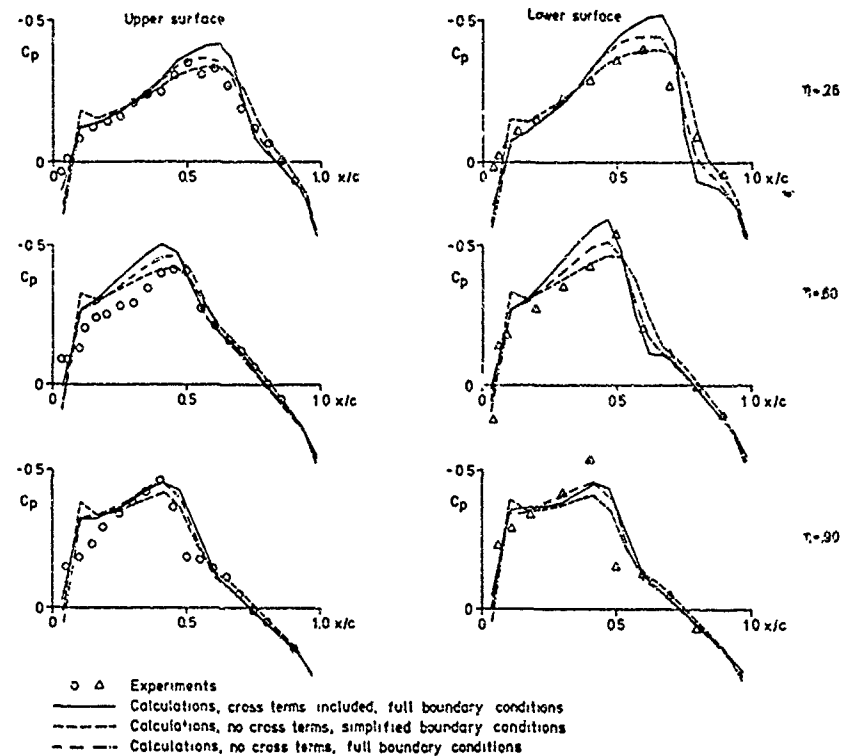


Fig. 3. Pressure distributions.  $M = 0.9$ ,  $\alpha = 0^\circ$ , comparison between calculated and measured data.

## 5.2 Velocity distributions

The integral method uses velocity components as input. The upper surface values will be illustrated. Fig. 4 contains the high incidence case,  $M = 0.8$ ,  $\alpha = 6^\circ$ , as calculated by the two al-

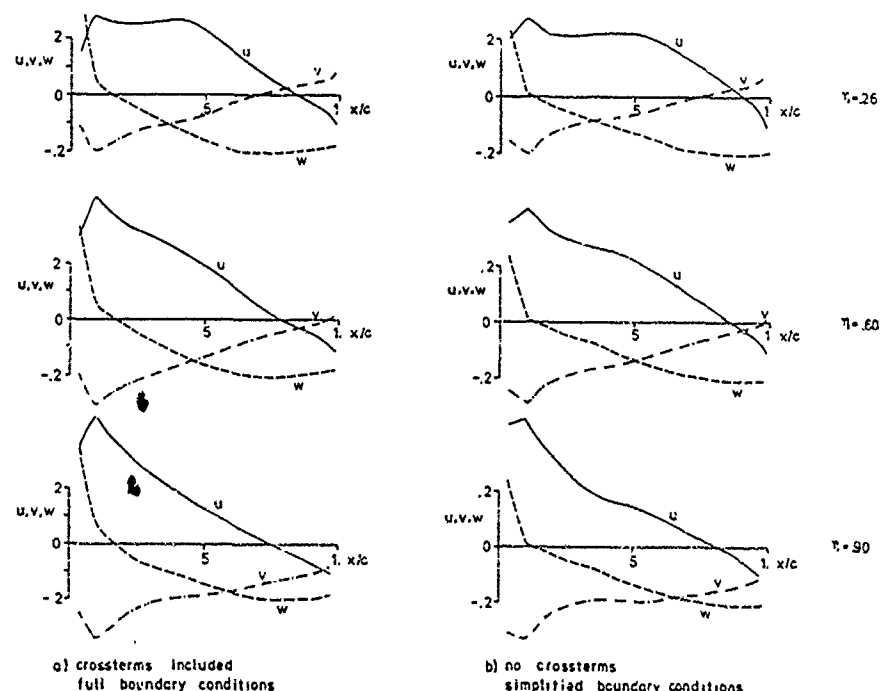


Fig. 4. Disturbance velocity components upper wing surface.  $M = 0.8$ ,  $\alpha = 6^\circ$ .



ternatives 1 and 2.  $u$  of course looks like the  $C_p$ -values from Fig. 2.  $w$  equals  $dz/dx$ , when the simplified boundary condition is applied, but otherwise it resembles the surface slope.  $v$  is directed towards the centerline over most of the upper wing surface, with larger values towards the tip. The potential flow at the surface is converging.

The high Mach number case  $M = 0.9$ ,  $\alpha = 0^\circ$  is shown in Fig. 5. The velocity components are generally smaller.

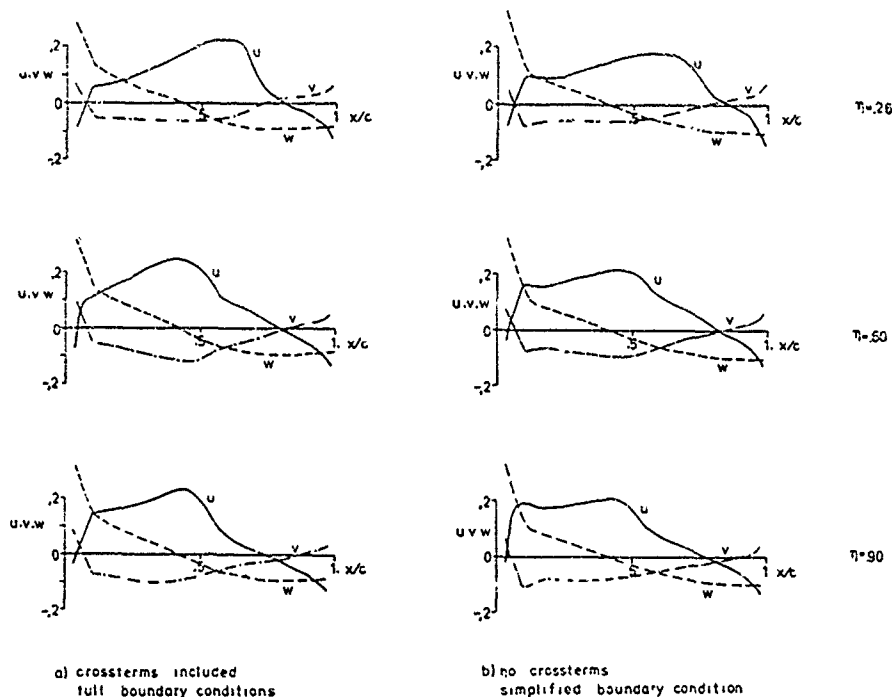


Fig. 5. Disturbance velocity components upper wing surface.  $M = 0.9$ ,  $\alpha = 0^\circ$ .

### 5.3 Boundary layer characteristics

Calculations were carried out for  $Re = 7 \cdot 10^6$ , referred to the root-chord,  $c_{ref}$ .

Displacement thicknesses  $\delta^*/c$  for the two flow conditions  $M = 0.8$ ,  $\alpha = 6^\circ$ , and  $M = 0.9$ ,  $\alpha = 0^\circ$  are shown in Fig. 6 and Fig. 7. They were calculated on velocities obtained with the potential flow program using both alternatives 1 and 2. The major portion of data was obtained using the integral method.

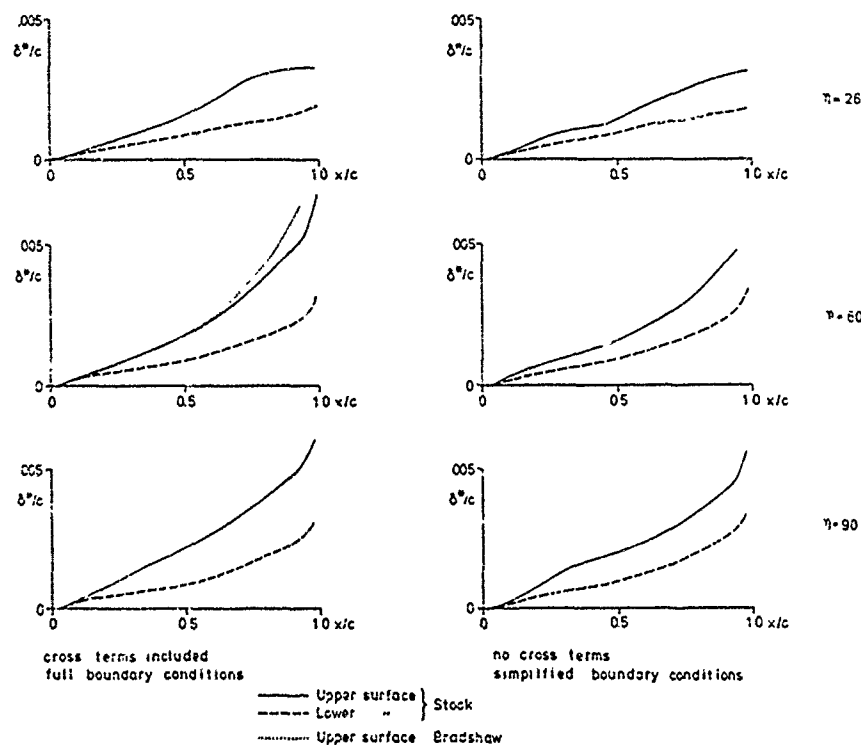


Fig. 6. Displacement thickness.  $M = 0.8$ ,  $\alpha = 6^\circ$ ,  $Re = 7 \cdot 10^6$ .

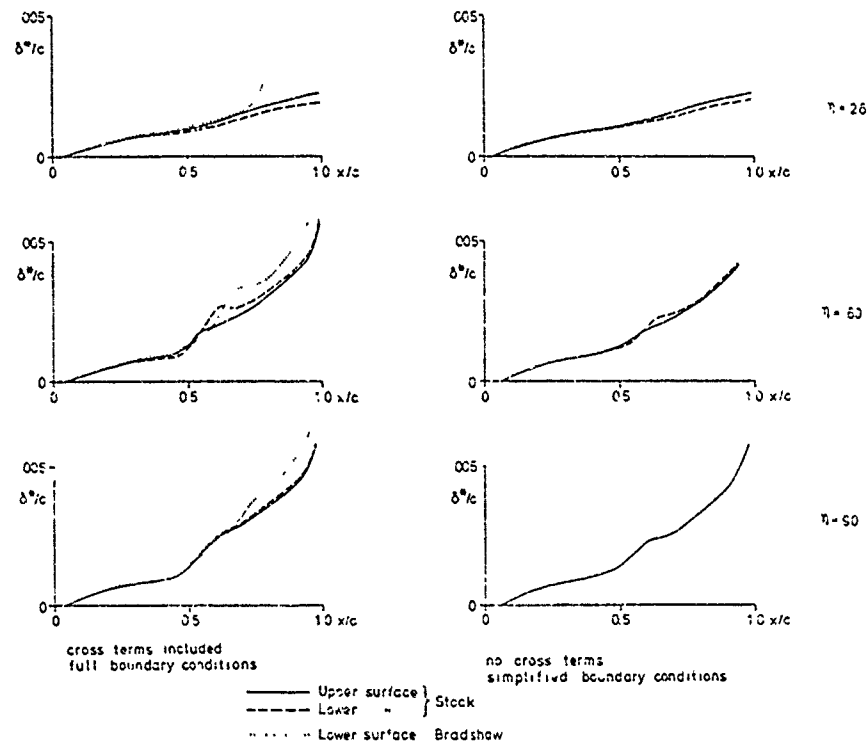


Fig. 7. Displacement thickness.  $M = 0.9$ ,  $\alpha = 0^\circ$ ,  $Re = 7 \cdot 10^6$ .

In the high incidence case,  $M = 0.8$ ,  $\alpha = 6^\circ$  the displacement thickness grows undramatically as the flow proceeds towards the trailing edge. There is no significant difference between the thicknesses obtained from the two sets of velocity components. The data from the integral method agree very well with the finite difference method data.

The boundary layer development in the high Mach number case is more important. The integral method predicts rapid growth of the displacement thickness for the two outboard stations in fair agreement with the finite difference method. However, the former recognizes no serious situation

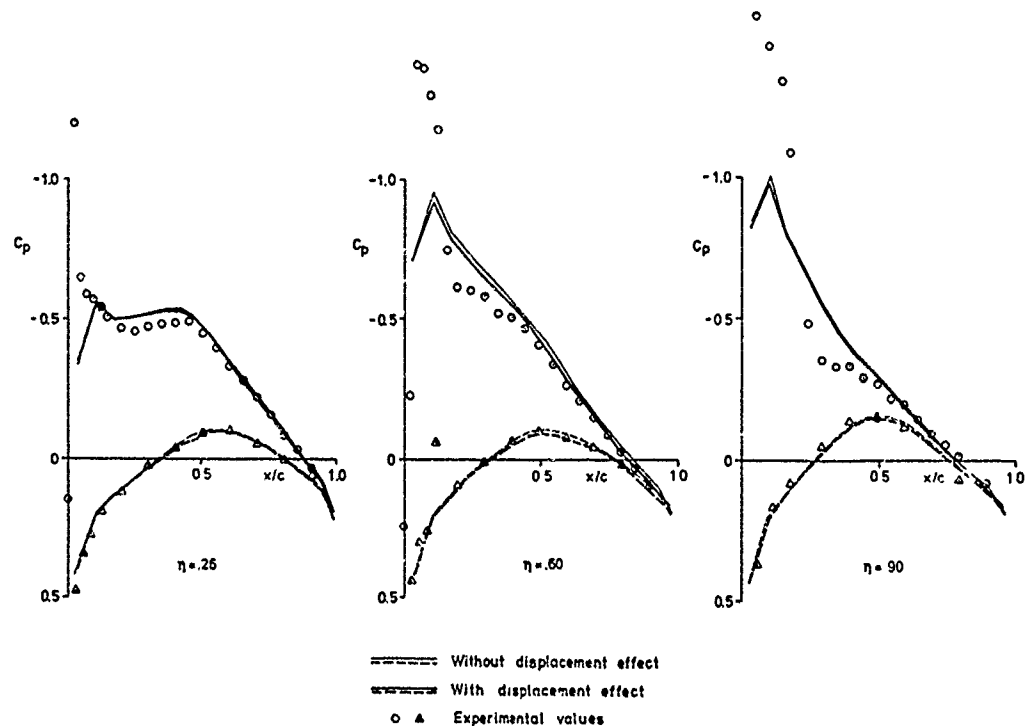


Fig. 8. Effect of displacement thickness on calculated pressure distributions (cross terms included, full boundary conditions).  $M = 0.8$ ,  $\alpha = 6^\circ$ ,  $Re = 7 \cdot 10^6$ .

at the root section whereas the latter method signals separation. According to the finite difference method the boundary layer cross flow angle changes sign at the shock, but not so according to the integral method using prescribed cross flow velocity profiles.

#### 5.4 Pressures calculated on equivalent wing

The displacement thicknesses were added to the wing ordinates to give an equivalent wing. As the overall changes in slope due to this addition were of the order of 0.005 only minor flow field changes were expected and the pressure calculations were made in the final grid without recalculation of the potential at the exterior of the calculation domain. Program alternative 1 was used.

For the high incidence case,  $M = 0.8$ ,  $\alpha = 6^\circ$  the calculated pressure gradient was much lower than the experimental value as has been shown in Fig. 2. Thus the true displacement thickness should be larger than the computed one. Fig. 8, showing the effect of the displacement thickness on the pressure distribution, shows that the pressures are indeed improved but that the effect is too small.

For the high Mach number case,  $M = 0.9$ ,  $\alpha = 0^\circ$  there was no agreement between the two boundary layer methods regarding the flow on the inboard section, as shown in Fig. 7. The displacement thicknesses computed by the integral method almost certainly are too thin. In Fig. 9 can be seen the effect of adding the displacement thickness. At the inboard section the pressure modification is too small around the shock. At the mid-semi-span station the pressure around the shock is shifted towards the experimental values but on the forward portion the pressure increase due to inboard section displacement is missing. At the tip section the changes are in the right direction.

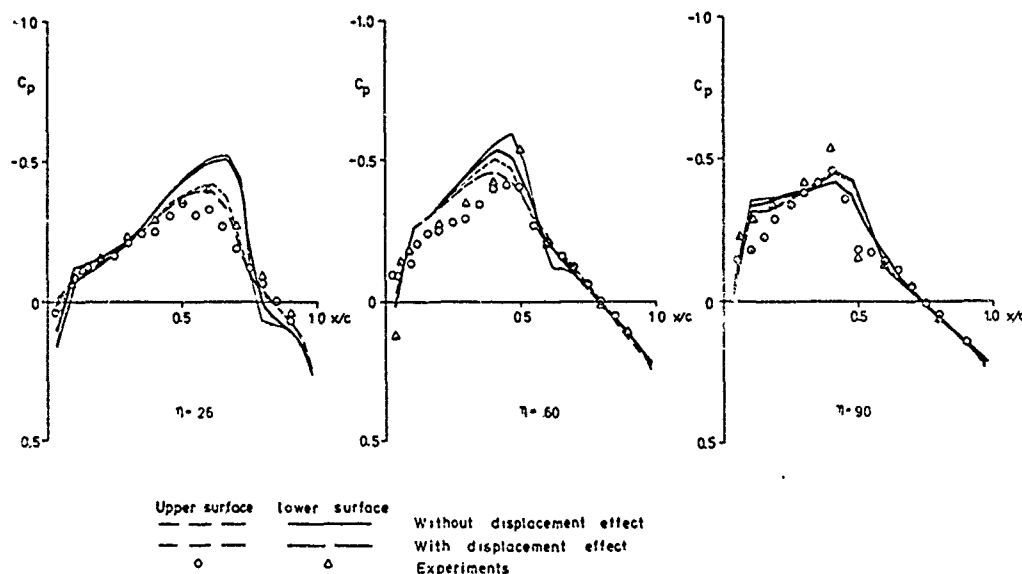


Fig. 9. Effect of displacement thickness on calculated pressure distributions (cross terms included, full boundary conditions).  $M = 0.9$ ,  $\alpha = 0^\circ$ ,  $Re = 7 \cdot 10^6$ .

#### 6. CONCLUSION

Calculation of the effect of including the boundary layer displacement thickness in the potential flow pressure distribution on a swept wing at two transonic flow conditions, one at high incidence and one at no incidence showed that the effect was small and that its inclusion brought calculated values towards experimental values. The effect was small probably because the estimated displacement thickness was too small. In the high incidence case the leading edge pressures were not calculated to be as low as the experimental values, the smaller pressure gradient should give a thinner boundary layer. In the low incidence case the two boundary layer methods give different answers and the smallest thickness was used because it indicated no separation.

#### REFERENCES

1. Atraghji, E. Reynolds number effects on swept-wing-body configurations in transonic flow. NAE LTR-HA-5x5/0066, 1974.
2. Gustavsson, A.L. Hedman, S.G. Design and test of a sonic roof top pressure distribution wing. Proc. Symp. Transonicum II, Göttingen, 1975.
3. Gustavsson, A.L. Vanino, R. Entwurf und Windkanalmessung einer Flügel-Rumpf-Kombination mit überkritischem Profil. Z. Flugwiss. 23 (1975), Heft 7/8.
4. Schmidt, W. Hedman, S.G. Recent explorations in relaxation methods for three dimensional transonic potential flow. Proc. ICAS 1976 (to be published).

5. Mc Nally, W.D. Fortran program for calculating compressible laminar and turbulent boundary layers in arbitrary pressure gradients. NASA TN D-5681, 1970.
6. East, L.F. Computation of three-dimensional turbulent boundary layers. Euromech 60, Trondheim 1975. FFA TN AE-1211, 1975.
7. Hedman, S.G.  
Stock, H.W.  
Fritz, W.  
Schmidt, W. Entwurfsvorfahren für dreidimensionale reibungsbehaftete transsonische Strömung. Dornier FB 75/45 B, 1975.
8. Bradshaw, P.  
Mizner, G.A.  
Unsworth, K. Calculation of compressible turbulent boundary layers with heat transfer on straight-tapered swept wings. I.C. Aero Report 75-04, 1975.
9. Atraghi, E.  
Sörensen, H. Report to be published.
10. Smith, P.D. An integral prediction method for three-dimensional compressible turbulent boundary layers. RAE TP 72 228, 1972.

# AERODYNAMIC LOADS NEAR CRANKS, APEXES, AND TIPS OF THIN, LIFTING WINGS IN INCOMPRESSIBLE FLOW

Richard T. Medan  
Ames Research Center, NASA  
Moffett Field, Calif. 94035, U.S.A.

## SUMMARY

The calculation of the incompressible and irrotational flow in the vicinity of tips and corners of thin, lifting wings is considered. It is shown that the important characteristics of the flow are governed by an eigenvalue problem, which is nonlinear at the trailing edge because of the shed wake (assumed to be in the wing plane). It is also shown that previously proposed solutions for the trailing-edge case are incorrect because they neglect the wake and because they do not, in general, satisfy the Kutta condition. A new solution method was devised because either the existing methods were not valid for the trailing-edge case or they would have required excessive amounts of computer time. The new method, which is fundamentally different than the previous ones, was used to calculate solutions for a number of cases, including some for which correct answers had not previously been obtained. Two of these solutions were used to determine the validity of drag and leading-edge-suction distributions near the tips of a delta wing and a swept wing as calculated by using both the vortex lattice method and a kernel function method. The calculations for the swept wing resolved the question of whether or not the induced drag should be zero at the wing tip.

## NOTATION

$A(k), B(k)$	Fourier coefficients of $\psi(\frac{\pi}{2} - \varphi)$ or $\psi_1(\varphi)$	VLM	acronym for standard vortex lattice method (Ref. 12)
$b$	wingspan	VLMI	acronym for vortex lattice method with tip inset (Ref. 12)
$C_n$	coefficients in expansion for $\psi(\frac{\pi}{2} - \varphi)$ defined by Eq. (39)	$x, y, z$	Cartesian coordinates with center at the origin of any of five regions shown in Fig. 1
JJ	number of spanwise integration stations in KFM	$n$	nondimensional spanwise wing coordinate with left tip at -1 and right tip at +1
KFM	acronym for kernel function method for lifting surfaces (Ref. 11)	$\gamma$	lift per unit span divided by product of dynamic pressure and twice the span
$M$	number of spanwise control points or vortices on wing half span	$\phi$	velocity potential
$N$	number of modes used to represent $\psi(\frac{\pi}{2} - \varphi)$ ; see Eq. (39)	$\varphi$	spherical polar coordinate
PP	number of chordwise control points or vortices on wing	$\varphi_1, \varphi_2$	values of $\varphi$ at edges of wing; see Fig. 2
$P_s^k$	associated Legendre function of the first kind and of degree $s$ and order $k$	$\psi$	factor in velocity potential; see Eq. (1)
$r$	radial distance from origin of any of five regions shown in Fig. 1	$\psi_1$	potential mode in expansion of $\psi(\frac{\pi}{2} - \varphi)$ ; see Eq. (39)
$s$	eigenvalue and characteristic exponent of $r$	$\theta$	spherical polar coordinate
$T(k, s)$	[see Eq. (15)]	$\tau_d$	drag per unit of spanwise distance divided by product of dynamic pressure and twice the wingspan
		$\tau_t$	leading edge thrust per unit of spanwise distance divided by product of dynamic pressure with twice the wingspan

## 1. INTRODUCTION

The calculation of properties of wings idealized as thin and nearly planar and in incompressible and irrotational flow at small angles of attack and with flat wakes is an important and difficult aspect of aerodynamics, despite the numerous simplifications. Accordingly, there have been a large number of methods devised for this calculation. The validity of these methods with respect to solving the given, idealized problem is, however, questionable near the tips and corners of the wing planforms. Therefore, a number of investigations, including the present one, have been undertaken to determine the nature of the flow in such regions, which are illustrated in Fig. 1. In general, the wing side edge in region IV may also be a leading edge (e.g., region IV may be the tip of a delta wing.) All of these regions are special cases of the general case illustrated in Fig. 2, in which the only restriction on  $\varphi_1$  and  $\varphi_2$  is that  $\varphi_1 \leq \varphi_2$ . Shed wakes generally occur when  $\varphi_1 > 0$  or  $\varphi_2 > \pi$ . To facilitate the study, these regions are idealized as being infinite in extent. That is, they are considered to be flat, angular sectors. Solutions so obtained will thus be local solutions that require patching into global solutions valid on the remainder of the planform.

Because of the assumptions of irrotationality and incompressibility, the flow can be described by a velocity potential,  $\phi$ , that satisfies Laplace's equation. The thin-wing assumptions allow the boundary

conditions to be simplified and satisfied in the  $z = 0$  plane. On the wing, the boundary condition is that the velocity in the  $z$ -direction must satisfy a prescribed distribution. In wake regions, the boundary condition is basically that there can be no pressure jump across the wake. This condition is equivalent to requiring the jump in  $\phi$  across the wake to be a function of  $y$  only. In addition to these conditions, the potential must be finite, except at infinity, and the pressure difference between the upper and lower surfaces must vanish at trailing edges.

Solutions satisfying the preceding conditions can be easily found. These solutions are in the form of linear combinations of analytic solutions to Laplace's equation. For example, uniform flow along the  $z$ -axis is a solution for all of the regions in Fig. 1 when the wing is a flat plate.

The real difficulty is not in finding solutions, but is that the solutions are not unique. That is, there exist eigensolutions. These eigensolutions satisfy homogeneous boundary conditions and exist because the lack of a boundary condition at infinity has rendered the problem ill posed. A simple dimensional analysis can be used to prove that the reduction of the geometry in each of the subject wing regions to an infinite angular sector allows each eigensolution to be expressed in the following form:

$$\phi = r^s \psi(\xi_1, \xi_2) \quad (1)$$

where  $\xi_1$  and  $\xi_2$  are two angular variables. When the preceding form is substituted into Laplace's equation, the result is a differential equation for  $\psi$  which contains a coefficient that is a function of  $s$ . This differential equation and the boundary conditions are both homogeneous and solutions can be found only for certain values of  $s$ . Thus each  $s$  for which a solution can be found is an eigenvalue and the corresponding  $\phi$  or  $\psi$  is an eigenfunction.

In contrast to the analytic solutions that can be used to satisfy the nonhomogeneous boundary conditions, the eigensolutions can be identified as vortex sheets lying in the plane of the wing and the wake. Since these vortex sheets have pressure jumps across them when they lie in the wing and the analytic solutions do not, the eigensolutions are the only ones that can contribute to the loading. Therefore, the lifting pressure distribution in any of the regions indicated in Fig. 1 can be expressed in terms of the eigensolutions only.

A survey of the literature related to this problem (Refs. 1-9) revealed that, in any of the five regions, there are precisely  $n$  independent eigenfunctions when the eigenvalue is in the range  $n - 1$  to  $n$ . In other words, there is always one eigensolution for  $s \leq 1$ , two eigensolutions for  $1 < s \leq 2$ , three eigensolutions for  $2 < s \leq 3$ , etc. The argument to support this result is also given in section 2.3.2. The literature also shows that there is a mistaken belief that eigensolutions valid for region I through III are also valid for region V, provided that the eigenvalue exceeds 1. As is shown later, this is incorrect, because (i) the solutions do not generally satisfy the Kutta condition except right at the apex, and (ii) the solutions do not contain a shed wake. The literature survey also revealed that there were basically two methods of solving problems of this type: separation of variables and finite differences. The first of these is not applicable to regions IV and V. The second would be costly to use in regions IV and V because, as a result of the shed wake, the eigenvalue problem is nonlinear in these regions. The finite-difference method is inconvenient from other viewpoints as well. Therefore, a new method of solving such problems appeared desirable.

## 2. METHOD OF SOLUTION

### 2.1 Basic Equations

The new solution method uses the spherical polar coordinates. A solution of the following form can be assumed:

$$\phi = r^s \psi(\theta, \varphi) \quad (2)$$

Putting Eq. (2) into Laplace's equation results in the following equation for  $\psi$ :

$$\sin^2 \theta \psi_{\theta\theta} + \sin \theta \cos \theta \psi_{\theta} + s(1+s) \sin^2 \theta \psi = 0 \quad (3)$$

In terms of  $\psi$ , the downwash and wake boundary conditions become the following:

$$\psi_{\theta}\left(\frac{\pi}{2}, \varphi\right) = 0 \quad \varphi \text{ on wing} \quad (4)$$

$$\psi\left(\frac{\pi}{2}, -\varphi\right) = f(y)/r^s \quad \varphi \text{ in wake} \quad (5)$$

Equation 5 can be simplified easily because  $y = r \sin \varphi$  in the wake and  $r$  must appear only as  $r^s$ . Therefore, Eq. (5) can be replaced by the more explicit equation

$$\psi\left(\frac{\pi}{2}, -\varphi\right) = \begin{cases} \left(\frac{\sin \varphi}{\sin \varphi_1}\right)^s \psi\left(\frac{\pi}{2}, -\varphi_1\right) & 0 < \varphi \leq \varphi_1 < \pi \\ \left(\frac{\sin \varphi}{\sin \varphi_2}\right)^s \psi\left(\frac{\pi}{2}, -\varphi_2\right) & \pi < \varphi_2 \leq \varphi < 2\pi \end{cases} \quad (6a)$$

$$(6b)$$

Because the lifting case is being considered, the governing differential equation [Eq. (3)] is to be solved only for  $z > 0$  (i.e.,  $0 \leq \theta < \pi/2$ ) and the solution for  $z < 0$  is to be obtained from

$$\psi(\theta, \varphi) = -\psi(\pi - \theta, \varphi) \quad (7)$$

Since the perturbation in  $\phi$  upstream of the wing and in the  $z = 0$  plane is 0, there is the following additional condition:

$$\psi\left(\frac{\pi}{2} - \varphi\right) = 0 \quad \varphi \text{ not in wing or wake} \quad (8)$$

Thus, the problem is to solve Eq. (3) for  $0 \leq \theta \leq \pi/2$  and subject to Eq. (4) and the Kutta condition and, possibly, Eq. (6) and/or Eq. (8). This is an eigenvalue problem that is nonlinear in the eigenvalue if the wake condition [Eq. (6)] is involved.

Once solutions are obtained, it may be necessary to calculate related quantities such as the pressure, jump, and the edge suction force, which is a force caused by the infinite velocities that may occur at leading and side edges and which is in the wing plane and perpendicular to the edge. The pressure jump, which is proportional to the x-derivative of  $\phi(x, y, 0+)$ , can be stated in terms of  $r$  and  $\psi(\pi/2 - \varphi)$  as

$$\Delta P = 2\rho U_\infty r^{s-1} \left[ s \cos \varphi \psi\left(\frac{\pi}{2} - \varphi\right) - \sin \varphi \frac{d\psi(\pi/2 - \varphi)}{d\varphi} \right] \quad (9)$$

The suction force per unit of distance along the edge is given by

$$\frac{ds}{dr} = \frac{\pi}{4} \rho \lim_{\varphi \rightarrow \varphi_1} \frac{\phi^2(x, y, 0+)}{r|\varphi - \varphi_1|} \quad (10)$$

where  $\varphi_1 = \varphi_1$  or  $\varphi_2$ . The streamwise component of the suction is called the leading-edge thrust. The thrust per unit of spanwise distance is also given by Eq. (10). Note that the suction force vanishes (or becomes infinite) as a different power of  $r$  than either the potential or the pressure difference.

## 2.2 Reduction of the Basic Problem

The differential equation for  $\psi$  is now used to obtain a relationship between  $\psi(\pi/2 - \varphi)$  and  $\psi_0(\pi/2, \varphi)$ . This relationship is of the form

$$\psi_0 = F(\psi; s) \quad (11)$$

where  $F$  is a linear operator. The advantage of Eq. (11) is that one of the independent variables (namely  $\varphi$ ) is eliminated. To begin with, the separation of the differential equation for  $\psi$  will be considered (even though the actual solution is not separable). That is, solutions of Eq. (3) in the form

$$\psi(\theta, \varphi) = G(\varphi)P(\theta) \quad (12)$$

are sought. Substituting Eq. (12) into Eq. (3) leads to the following equation for  $G$ :

$$G'' + k^2 G = 0 \quad (13)$$

It is evident that  $k$ , which is the separation constant, must be real and integer because  $G$  must be periodic. Furthermore, it is superfluous to consider negative  $k$ . Thus,

$$G(\varphi) = A(k) \cos(k\varphi) + B(k) \sin(k\varphi) \quad (14)$$

where  $k$  is zero or a positive integer and  $A$  and  $B$  are yet to be determined.

Equation (12) also leads to an equation for  $P(\theta)$  which is a form of the associated Legendre differential equation whose solutions are  $P_s^k(\cos \theta)$  and  $Q_s^k(\cos \theta)$ .  $Q_s^k(\cos \theta)$  is infinite on the  $z$ -axis and can, therefore, be disregarded. Furthermore, as will be evident later, the only need for numerical values is the ratio of the derivative of  $P_s^k$  (with respect to  $\theta$ ) divided by  $P_s^k$  itself and evaluated at  $\theta = \pi/2$ . This ratio is denoted  $T(k, s)$  and is given by

$$T(k, s) = -2 \tan\left[\frac{\pi}{2}(s + k)\right] \frac{\Gamma[1 + (s + k)/2] \Gamma[1 + (s - k)/2]}{\Gamma[(1 + s + k)/2] \Gamma[(1 + s - k)/2]} \quad (15)$$

Values of  $T(k, s)$  for integer  $s$  are shown in Table 1.

Now consider again a  $\psi$  which is not separable. Furthermore, suppose that  $\psi(\pi/2 - \varphi)$  has been Fourier analyzed, i.e., the coefficients  $A(k)$  and  $B(k)$  in the following expansion of  $\psi(\pi/2 - \varphi)$  have been determined:

$$\psi\left(\frac{\pi}{2} - \varphi\right) = \sum_{k=0}^{\infty} [A(k) \cos(k\varphi) + B(k) \sin(k\varphi)] \quad (16)$$

Then, in view of the preceding developments, it is apparent that

$$\psi_0\left(\frac{\pi}{2}, \varphi\right) = \sum_{k=0}^{\infty} T(k, s) [A(k) \cos(k\varphi) + B(k) \sin(k\varphi)] \quad (17)$$

Putting the known expressions for  $A(k)$  and  $B(k)$  into Eq. (17) and interchanging the order of summation and integration results in an equation of the required form [(Eq. (11))].

Thus, the need to solve the differential equation for  $\psi$  has been eliminated in favor of a simpler linear operator, which involves one less independent variable, a Fourier analysis of  $\psi(\pi/2, \varphi)$ , the calculation of the coefficients  $T(k, s)$ , and an inverse Fourier analysis [i.e., summing the right side of Eq. (17)].

### 2.3 Some Analytical Solutions

In general, solutions must be determined numerically, but, in a few cases, exact solutions can be obtained.

2.3.1 The case  $\varphi_2 - \varphi_1 = 2\pi$ . (See also Ref. 7.) Consider first the case in which the angular sector covers the entire  $x-y$  plane. In this case, there is no boundary condition on  $\psi(\pi/2, \varphi)$ , while the downwash boundary condition becomes

$$\psi_0\left(\frac{\pi}{2}, \varphi\right) = 0 \quad 0 \leq \varphi \leq 2\pi \quad (18)$$

With reference to Eq. (16), Eq. (17), and Table 1, it is clear that one eigenvalue is  $s = 0$  and the corresponding eigenfunction is

$$\phi(x, y, z) = P_0^0(\cos \theta) = 1 \quad (19)$$

Another eigenvalue is  $s = 1$  and the corresponding eigenfunctions are

$$\phi(x, y, z) = rP_1^1(\cos \theta) \cos \varphi = x \quad (20)$$

$$\phi(x, y, z) = rP_1^1(\cos \theta) \sin \varphi = y \quad (21)$$

Since  $\phi(x, y, -z) = -\phi(x, y, z)$ , the former of these corresponds to a constant-strength vortex sheet with vorticity in the  $y$ -direction, while the latter can be identified as a constant-strength vortex sheet with vorticity in the  $x$ -direction.

Still another eigenvalue is  $s = 2$ , and the corresponding eigenfunctions are:

$$\phi(x, y, z) = r^2 P_2^0(\cos \theta) = (2z^2 - x^2 - y^2)/2 \quad (22)$$

$$\phi(x, y, z) = r^2 P_2^2(\cos \theta) \cos 2\varphi = -3(x^2 - y^2) \quad (23)$$

$$\phi(x, y, z) = r^2 P_2^2(\cos \theta) \sin 2\varphi = 6xy \quad (24)$$

These can all be identified as types of stagnation point flows.

In general, there are  $n + 1$  independent eigenfunctions for  $s = n$ . If  $n$  is even, then  $n/2$  of the eigenfunctions are even functions of  $y$  and  $n/2$  are odd functions of  $y$ . If  $n$  is odd, then  $(n + 1)/2$  of the eigenfunctions are even and  $(n - 1)/2$  are odd. An important aspect to note about these eigenfunctions is that they are forming a complete basis. This shows that all of the linearly independent eigenfunctions have been identified for this case.

2.3.2 The case  $\varphi_2 - \varphi_1 = 0$ . (See also Ref. 7.) Consider next the case in which the angular sector completely disappears. In this case, there is no downwash boundary condition, while the boundary condition on  $\psi(\pi/2, \varphi)$  becomes

$$\psi\left(\frac{\pi}{2}, \varphi\right) = 0 \quad 0 \leq \varphi \leq 2\pi \quad (25)$$

With reference again to Eq. (16), Eq. (17), and Table 1, it is clear that one eigenvalue is  $s = 1$  and the corresponding eigenfunction is

$$\phi(x, y, z) = rP_1^0(\cos \theta) = z \quad (26)$$

Another eigenvalue is  $s = 2$  and the corresponding eigenfunctions are

$$\phi(x, y, z) = r^2 P_2^1(\cos \theta) \cos \varphi = 3yz \quad (27)$$

$$\phi(x, y, z) = r^2 P_2^1(\cos \theta) \sin \varphi = 3xz \quad (28)$$

In general, there are  $n$  independent eigenfunctions for  $s = n$ . If  $n$  is even, then  $n/2$  of the eigenfunctions are even functions of  $y$  and  $n/2$  are odd functions of  $y$ . If  $n$  is odd, then  $(n + 1)/2$  of the eigenfunctions are even and  $(n - 1)/2$  are odd. An important aspect to note about these eigenfunctions is that they are forming a complete basis for functions satisfying the downwash boundary condition. Thus all of the linearly independent eigenfunctions have been identified for this case.

In view of the preceding section and the fact that the eigenvalues increase monotonically with decreasing  $\varphi_2$  (Ref. 1), it is apparent that, for  $s$  in the range  $(n - 1, n)$ , there are precisely  $n$



independent eigenfunctions. Of these,  $(n+1)/2$  are symmetric if  $n$  is odd and  $n/2$  are symmetric if  $n$  is even, provided that region I, II, or III is being considered. For the other regions, the number of eigen-solutions for  $s$  in the range  $(n-1, n)$  is still  $n$ , although none of them may be symmetric or antisymmetric with respect to the bisector. Thus, the monotonicity property and the exact solutions for the limit cases in which the sector subtends either  $2\pi$  or  $0$  determine precisely how many eigensolutions should be expected for each eigenvalue range.

2.3.3 The case  $-\varphi_1 = \varphi_2 = \pi/2$ . (See also Refs. 1 and 4.) This case consists of the semiplane defined by  $z = 0$  and  $x > 0$ . Solutions can be obtained by rotating this plane 90 degrees about the  $x$  axis so that it becomes the plane  $y = 0$  and  $x > 0$  and then by seeking a separable solution in terms of the spherical polar coordinates. This again leads to Eq. (13) and the associated Legendre differential equation. The solutions are the same as in section 2.2, except (i) the boundary conditions on  $\phi(x, 0+, z)$  require that  $\pm k = \ell + 1/2$ , where  $\ell$  is an integer; (ii)  $B(k) = 0$ ; and (iii) the condition of periodicity in  $\theta$  requires that  $s = m + 1/2$  where  $m$  is an integer. Thus, the eigensolutions for this case (with  $z$ -axis along the leading edge) are

$$\phi = r^{m+1/2} p_{m+1/2}^{-\ell-1/2}(\cos \theta) \cos[(\ell + 1/2)\varphi] \quad (29)$$

The additional condition that  $\phi$  should be finite imposes further restrictions on  $\ell$  and  $m$ . In particular,  $\ell$  and  $m$  must be greater than zero and  $\ell$  must be no larger than  $m$ .

Explicit formulas are now given in terms of the original coordinate system (edge along the  $y$ -axis) and for  $z = 0+$  and  $x > 0$  (and with unnecessary multiplicative constants dropped).

For  $s = 1/2$ , the only eigensolution is

$$\phi(x > 0, y, 0+) = r^{1/2}(\cos \varphi)^{1/2} = x^{1/2} \quad (30)$$

For  $s = 3/2$ , the only eigensolutions are

$$\phi(x > 0, y, 0+) = r^{3/2}(\cos \varphi)^{3/2} = x^{3/2} \quad (31)$$

$$\phi(x > 0, y, 0+) = -r^{3/2}(\cos \varphi)^{1/2} \sin \varphi = yx^{1/2} \quad (32)$$

It should be noted that the second eigensolution for  $s = 3/2$  exhibits an infinite pressure along the leading edge, unless  $y = 0$ .

For  $s = 5/2$ , the only eigensolutions are:

$$\phi(x > 0, y, 0+) = r^{5/2}(\cos \varphi)^{5/2} = x^{5/2} \quad (33)$$

$$\phi(x > 0, y, 0+) = r^{5/2}(\cos \varphi)^{3/2} \sin \varphi = yx^{3/2} \quad (34)$$

$$\phi(x > 0, y, 0+) = r^{5/2}(\cos \varphi)^{1/2}(4 \sin^2 \varphi - 1) = (3y^2 - x^2)x^{1/2} \quad (35)$$

Note that the third eigensolution has an exponent of  $1/2$  on  $x$ . Thus, the corresponding pressure distribution is infinite at the edge. This proves the previous assertion that eigensolutions valid in regions I, II, and III cannot be applied to the trailing edge case even though  $s > 1$ .

2.3.4 The case  $\varphi_1 > 0$  and  $\varphi_2 = \pi$ . This case is the special case of region IV in which the leading edge is a side edge. It is thus typical of the trailing wing tip on a wing with a finite tip chord. Some of the eigensolutions, including the most dominant one as far as span loads are concerned, can be determined for this case. These eigensolutions are

$$\phi(x, y > 0, 0+) = y^{1/2} \quad (36)$$

$$\phi(x, y > 0, 0+) = y^{3/2} \quad (37)$$

$$\phi(x, y > 0, 0+) = y^{5/2} \quad (38)$$

etc.

The corresponding eigenvalues are  $s = 1/2, 3/2, 5/2, \dots$ . It should be noted that these solutions correspond to null lifting-pressure distributions, because the associated vortex lines are all parallel to the  $x$ -axis. However, even though the associated pressure distributions are null, each eigensolution yields a nonzero span-load distribution. Since there is only one eigenvalue less than 1, the principal contributor to the span loading near the wing tip is the  $y^{1/2}$  term, and, near the tip of any finite tip chord wing, the span loading that will be predicted by any correct theory will be proportional to the square root of the distance to the tip. Note that this conclusion can be made regardless of planform details ahead of the tip and regardless of the trailing-edge sweep. Also, note that for  $s$  in the range  $(n-1, n)$  there are still  $n-1$  eigensolutions to be identified for this case. These can be determined by the method described in section 2.4.

2.3.5 Region V. A number of solutions can be identified for this region. They are, in fact, just those particular solutions or linear combinations thereof from section 2.3.1 that are independent of  $x$ . The eigenvalues are 0, 1, 2, ..., and the corresponding eigenfunctions for  $z = 0+$  are 1,  $y$ ,  $y^2$ , ... . The

pressure distributions corresponding to these solutions are all null. The remaining eigensolutions can be determined by the method presented in the next section.

## 2.4 Application of the Collocation Method

The method used to solve the operator equation [Eq. (11)] subject to the various boundary conditions is now explained. The first step is to express  $\psi(\pi/2, \varphi)$  in terms of  $N$  functions or modes and  $N$  unknown, constant coefficients. Specifically,

$$\psi\left(\frac{\pi}{2}, \varphi\right) = \sum_{n=1}^N C_n \psi_n(\varphi) \quad (39)$$

Each of the modes,  $\psi_n(\varphi)$ , is required to satisfy the boundary conditions on  $\psi(\pi/2, \varphi)$ . Namely,  $\psi_n(\varphi)$  must be zero off the wing and wake and, in the wake,  $\psi_n$  must satisfy the wake condition. Also the modes and their first derivatives must be continuous at any trailing edges in order to satisfy the Kutta condition. Substituting the above expansion into the operator equation leads to

$$\psi_0\left(\frac{\pi}{2}, \varphi\right) = \sum_{n=1}^N C_n F_n(\psi_n; s) \quad (40)$$

Recall that  $\psi_0(\pi/2, \varphi)$  must be zero on the wing. This condition cannot be satisfied at all locations on the wing, but it can be enforced at a set of  $N$  locations,  $\varphi_i$ , on the wing. These stations are called collocation or control points. Collocation leads to the following equation:

$$\{0\} = [D]\{C_n\} \quad (41)$$

where  $D_{in}(s)$  is  $F(\psi_n; s)$  evaluated at  $\varphi = \varphi_i$ . This is an algebraic eigenvalue problem that only has a solution when the determinant of the matrix  $D$  is zero. In other words,

$$\det[D] \equiv f(s) = 0 \quad (42)$$

is the characteristic equation that determines  $s$

Thus, the original differential equation and boundary conditions have been reduced to an algebraic eigenvalue problem. All that remains to be considered are certain details concerning the Fourier analysis, an appropriate choice of modes  $\psi_n$ , an appropriate set of control points  $\varphi_i$ , and a method of solving the characteristic equation for the eigenvalues. These details are covered in Ref. 10.

## 3. RESULTS AND APPLICATIONS

This section describes numerical results obtained by the method defined in the previous section. Also some of the results are used to determine the validity of suction and drag distributions near the tips of wings, as calculated by the vortex lattice method and a kernel function method.

### 3.1 Results for Regions I, II, and III

The eigenvalue problem is independent of the freestream direction for these regions. Therefore, without loss of generality, attention may be restricted to region I only. Table 2 compares results calculated by using the present method with results given in Ref. 7. The results compare very favorably with Sack's results.

Figure 3 shows the behavior of  $C_1$  for the second lowest symmetric eigenvalue. When  $C_1$  is nonzero, there is an infinite pressure along the leading edge (Ref. 10). The computed estimates (not shown) of the eigenvalue corresponding to this figure match very closely those calculated by Sack (Ref. 7). Therefore, it is clear that the second eigenvalue cannot be applied to the trailing-edge case, because the Kutta condition is not satisfied (except when the edge is unswept).

### 3.2 Results for Region IV

**3.2.1 The case  $\varphi_1 = \pi/2$ ; tip of delta wing.** Table 3 shows the calculated estimates of the lowest three eigenvalues as functions of  $\varphi_2$  and  $N$  for the case  $\varphi_1 = 90^\circ$ . As discussed in section 2.3.4, two of the eigenvalues are exactly  $1/2$  and  $3/2$  when  $\varphi_2 = 180^\circ$ . The method can be seen to approximate these values closely. The results for  $N = 9$  appear to be accurate to no less than three figures.

**3.2.2 The case  $\varphi_2 = \pi$ ; trailing tip of wing with finite tip chord.** Some of the eigenvalues and eigenfunctions for this case are known exactly (section 2.3.4), but the pressure distributions corresponding to these eigenvalues are null. Therefore, the third eigensolution is the first one for which the pressure distribution is nonzero. Calculated estimates of this eigenvalue are shown in Table 4 as functions of  $\varphi_1$  and  $N$ . For  $N = 9$ , these eigenvalues are accurate to at least about four figures.

### 3.3 Results for Region V

The single eigensolution for  $s$  in the range  $(0,1)$  and one of the two eigensolutions for  $s$  in the range  $(1,2)$  have been identified in section 2.3.5. Therefore, in the range  $(1,2)$  there is one eigenvalue yet to be found. The calculated estimates of this eigenvalue are shown in Table 5 for the case

$2\pi - \varphi_1 = \varphi_2 > 0$  (i.e., corresponding to the trailing edge at the centerline of a symmetric planform). Figure 4 shows the behavior of  $C_{N-1}$  for the eigenvalues corresponding to Table 5. For region V,  $C_{N-1}$  is proportional to the wake strength (Ref. 10). Therefore, there obviously is a wake shed, except when the trailing edge is uncranked. This constitutes further proof that the higher solutions for the leading-edge case cannot be applied to the trailing-edge case.

### 3.4 The 60° Delta Wing

Some of the preceding results are now used to determine the validity of thin-wing analysis methods as applied to a flat, 60° delta wing at an angle of attack of one radian. In particular, the kernel function method reported in Ref. 11 and the vortex lattice method reported in Ref. 12 will be considered. The kernel function method (hereafter denoted KFM) employs continuous mode functions to represent the lifting-pressure distributions on wings, while the vortex lattice method uses discrete vortices. Two variations of the latter are described in Ref. 12. The first of these is the standard vortex lattice method (hereafter denoted as the VLM), in which the vortices extend to the tip of the wing, and the second variation (hereafter denoted as the VLMI) is one for which the vortices do not extend all of the way to the tip. Instead, they are inset from the tip by 1/4 of the spanwise lattice spacing. This inseting has been shown to give the lift-curve slope more accurately than VLM for a given number of vortices.

The span loading can be expressed in terms of the potential at the trailing edge, as follows:

$$\gamma = 2\phi(x_{te}, y, 0+) / (Ub) \quad (43)$$

Therefore, in view of the results in Table 3 for  $\varphi_2 = 150^\circ$ , the span loading near the right wing tip can be expressed as

$$\gamma = a_1(1 - \eta)^{0.64077} + a_2(1 - \eta)^{1.52826} + \dots \quad (44)$$

Thus, if the span loadings predicted by the KFM, VLM, and VLMI are correct, then the span loadings divided by  $1 - \eta$  raised to the 0.64077 power and plotted against  $\eta$  should result in curves that approach a finite value as  $\eta$  approaches 1. Figures 5-7 show such plots. It should be noted that the KFM allows  $\gamma$  to be calculated at any spanwise station and, therefore, the KFM curves were not determined by fairing between the spanwise control points as was necessary in the case of the VLM and VLMI. In all cases, the results at spanwise control points are denoted with symbols. It can be seen that, inboard of the first or second control points, all three methods appear to be giving reasonable results. The KFM loading functions cause the span loading to approach zero as the square root of the distance to the tip. Therefore, the KFM curves in Fig. 5 must approach infinity and can, at best, converge to the correct answer nonuniformly. The VLM and VLMI curves, on the other hand, are not so constrained and, therefore, could converge uniformly, but it appears from Figs. 6 and 7 that the VLM and VLMI results for the control point closest to the tip are incorrect. In other words, the VLM and VLMI also converge nonuniformly, at best.

The best results from each method were each fitted to a curve of the form in Eq. (44). The purpose of this was to allow the leading-edge thrust to be predicted. This prediction is possible because the leading edge, in this case, is in the same region as the trailing edge, and because the eigensolutions determine the local solutions completely, except for overall constants, which can be determined from the span loading. Predictions made in this manner (see Ref. 10 for details) are shown as dashed lines in Figs. 8-10 for  $a_1$  and  $a_2$  determined from the KFM, VLM, and VLMI span loadings, respectively. The actual thrust distributions predicted by these methods are also shown. For the KFM, the agreement is good, except very close to the tip. Furthermore, it appears that the KFM is converging to the correct answer. However, the leading-edge thrust distributions predicted by the VLM and VLMI do not agree well with the predictions determined from the eigensolutions. Although one could not argue convincingly that the VLM and VLMI either would or would not converge to the correct answer as the number of vortices is increased to infinity, it is clear that the convergence is, at best, very slow.

### 3.5 A 45° Swept Wing

The conditions existing near the tip of a wing with a nonzero tip chord are now examined in the light of the current theory. In particular, a flat, constant chord, aspect ratio 2, 45° swept wing at 1 radian angle of attack is considered. A wing of this sweep was considered because it matches the sweep at the tip of the hyperbolic wing considered in Refs. 13 and 14 and because a controversy has arisen over the latter wing. This controversy stems from the fact that Kalman's calculations, which used a vortex lattice method, show that the induced drag at the tip is nonzero, while the kernel function methods used in Ref. 13 show the drag going to zero. Additional communication (Refs. 15 and 16) has failed to resolve the question.

The theory presented herein is now used to determine which results give the correct behavior of the induced drag at the tip. According to section 2.3.4 and 3.2.2 and Table 4, for  $\varphi_1 = 135^\circ$ , the span loading near the right wing tip is of the form

$$\gamma = a_1(1 - \eta)^{1/2} + a_2(1 - \eta)^{3/2} + a_3(1 - \eta)^{1.9564} \quad (45)$$

It has been determined that the lowest three eigenvalues for  $\varphi_1 = 0$  and  $\varphi_2 = 135^\circ$  are 0.64220, 1.51016, and 1.76787. Therefore, according to Eq. (10), the leading-edge thrust near the tip is of the form

$$\tau_t = \frac{[b_1(1 - \eta)^{0.64220} + b_2(1 - \eta)^{1.51016} + b_3(1 - \eta)^{1.76787}]^2}{1 - \eta} \quad (46)$$

The induced drag distribution  $\tau_d$  is given by  $\gamma - t$ . Therefore, it is now clear that the induced drag *does* approach zero at the tip. Furthermore, the thrust becomes the dominant contributor very close to the tip (provided that  $b_1$  is not zero) and, hence, the induced drag will be negative close to the tip. Although the kernel function methods used in Ref. 13 correctly predicted that the drag should approach zero, they showed it approaching from the positive side, although the results did show a region of negative drag close to the tip. The loading functions used in the kernel function methods can be shown to constrain the induced drag so that it will always approach zero from the positive side, provided that the tip chord is nonzero and the lift near the tip is positive.

Numerical results using the KFM (Ref. 11) and the VLM and VLMI (Ref. 12) for the 45° swept wing are now presented. Figures 11-13 show KFM, VLM, and VLMI predictions of the span loading divided by the square root of the distance to the tip. According to Eq. (45) this quantity should be finite at the tip. The KFM loading functions constrain the loading near the tip to be the product of the square root of the distance to the tip times an analytic function of  $\eta$ . Therefore, it is reasonable to assume that the span loading should converge rapidly and uniformly and Fig. 11 shows this to be the case. On the other hand, the VLM results shown in Fig. 12 indicate that the VLM may not be converging to the correct result. At best, the VLM appears to be converging nonuniformly. The VLMI results in Fig. 13 show that the tip inset clearly improves the convergence. However, the VLMI results do not appear to be converging to the same curve as the KFM results.

Figures 14-16 are plots of leading-edge thrust distributions divided by the distance to the tip raised to the 0.28440 power. According to Eq. (46), this quantity should be finite at the tip. The KFM loading functions impose the constraint that the leading-edge suction should vanish linearly. Therefore, all of the KFM curves in Fig. 14 pass through zero at the tip. Nevertheless, if one were to smooth out the oscillations in the KFM curves, the KFM results would be reasonable out to the final control point. The dashed line in Fig. 14 shows such a smooth curve. It was determined by fitting an equation of the form in Eq. (46) to the  $7 \times 11 \times 367$  KFM results at the third, fourth, and fifth control points. It is expected that this dashed curve lies reasonably close to the true answer. The VLM results shown in Fig. 15 do not seem to be converging to a correct result or, at least, do not seem to be converging to the same curve as the KFM results. The same can be said of the VLMI results in Fig. 16.

Figures 17-19 show induced drag distributions calculated by using VLM and VLMI and compare these results against the distribution determined from the  $7 \times 11 \times 367$  KFM results with the leading-edge thrust taken from the dashed curve in Fig. 14. The VLM and VLMI results agree fairly well with each other, but there is a distinct difference between them and the KFM drag distribution.

#### 4. SUMMARY AND CONCLUSIONS

It was shown that, in any of the regions of the thin wing depicted in Fig. 1, the lifting-pressure distribution of the incompressible flow is governed by solutions of the form

$$\phi = r^s \psi(\xi_1, \xi_2)$$

where  $s$  is an eigenvalue,  $\xi_1$  and  $\xi_2$  are angular variables, and  $\psi$  is an eigenfunction satisfying certain homogeneous, mixed, and sometimes nonlinear (in  $s$ ) boundary conditions on the  $z = 0^+$  plane.

A survey of the literature concerned with problems of this type revealed that in the interval  $(n-1, n)$  there are  $n$  linearly independent eigensolutions. The literature contained methods for determining these eigensolutions in regions I through III, but, despite claims to the contrary, not for regions IV and V. The literature also contained a few exact results and numerical results of varying degrees of accuracy and sophistication.

On the basis of the literature survey, it was concluded that a new method of solving such problems was required in order to deal effectively with regions IV and V. Such a method was devised and is basically different than the previous methods. The key feature of the new method is a relationship that allows the determination of the vertical velocity in the  $z = 0$  plane from the potential on the  $z = 0^+$  plane without having to solve any differential equations. This relationship, together with sets of assumed potential modes and a collocation procedure, permitted a nonlinear, algebraic characteristic equation for the eigenvalues to be formed.

The new method was used to calculate eigenvalues and eigenvectors in each of the various regions. Together with some exact results, these calculations provided the lowest three eigenvalues for all of the subject regions. A comparison of some of the results computed for region I with results computed by others showed the current results to be about as accurate as the best previously available. The method was also used to show that previously proposed solutions for region V were generally incorrect because they did not satisfy the Kutta condition except at the origin and because they failed to account for the shed wake.

The calculated results were applied to some practical problems. In particular, the behavior of the span loading and the leading-edge thrust on a delta wing and a swept wing were considered. The correct types of behavior, as predicted by the present theory, were compared against results computed by a kernel-function method lifting-surface theory and two variations of the vortex-lattice method. It is concluded that the kernel-function method always predicts the correct behavior, although the convergence may be nonuniform due to the constraints of the assumed pressure modes. The vortex-lattice methods, however, do not appear to be predicting the correct behavior in all cases.

#### REFERENCES

1. Germain, P., "Sur l'écoulement subsonique au voisinage de la pointe avant d'une aile delta," *La Recherche Aeronautique*, No. 44, Mars-Avril 1955, pp. 3-8.
2. Legendre, Robert, "Écoulement subsonique transversal à un secteur angulaire plan," *Comptes Rendus*, Vol. 243, 1956, pp. 1716-1718.

3. Guiraud, J.-P., "Sur la nature de la singularité d'un écoulement de fluide compressible au voisinage de la pointe avant d'une aile delta en régime subsonique," *Comptes Rendus*, Vol. 243, 1956, pp. 2012-2014.
4. Brown, S. N. and Stewartson, K., "Flow near the Apex of a Plane Delta Wing," *J. Inst. Maths. Applian*, Vol. 5, 1969, pp. 206-216.
5. Rossiter, Patricia J., "The Linearised Subsonic Flow over the Centre Section of a Lifting Swept Wing," Brit. A.R.C. R&M 3630, 1969.
6. Taylor, R. S., "A New Approach to the Delta Wing Problem," *J. Inst. Maths Applian*, Vol. 7, 1971, pp. 337-347.
7. Sack, R. A., "Variational Solutions for Eigenvalues of Single and Coupled Lamé' Equations," *J. Inst. Maths Applian*, Vol. 10, 1972, pp. 279-288.
8. Davies, Patricia J., "The Load near the Apex of a Lifting Swept Wing in Linearised Subsonic Flow," Brit. A.R.C. R&M 3716, 1972.
9. Bazant, Zdenek, P., "Three-Dimensional Harmonic Functions near Termination or Intersection of Gradient Singularity Lines: A General Numerical Method," *Int. J. Engng. Sci.*, Vol. 12, 1974, pp. 221-243.
10. Medan, Richard T., "Aerodynamic Loads near Cranks, Apexes, and Tips of Thin, Lifting Wings in Subcritical Flow," Ph.D. Thesis, Stanford University, May 1976.
11. Medan, Richard T., "Improvements to the Kernel Function Method of Steady, Subsonic Lifting Surface Theory," NASA TM X-62,327, 1974.
12. Hough, Gary R., "Remarks on Vortex Lattice Methods," *J. Aircraft*, Vol. 10, No. 5, 1973, pp. 314-317.
13. Garner, H. C., Hewitt, B. L., and Labrujere, T. E., "Comparison of Three Methods for the Evaluation of Subsonic Lifting Surface Theory," Brit. A.R.C. R&M 3597, 1968.
14. Kalman, T. P., Giesing, J. P., and Rodden, W. P., "Spanwise Distribution of Induced Drag in Subsonic Flow by the Vortex Lattice Method," *J. Aircraft*, Vol. 7, No. 6, Nov.-Dec. 1970, pp. 574-576.
15. Garner, H. C., private communication, 1972.
16. Rodden, William P., private communication, 1972.

TABLE 1 - T(k,s) FOR INTEGER VALUES OF s

k	s						
	0	1	2	3	4	5	6
0	0	$\pm\infty$	0	$\pm\infty$	0	$\pm\infty$	0
1	1	0	$\pm\infty$	0	$\pm\infty$	0	$\pm\infty$
2	2	1.5000	0	$\pm\infty$	0	$\pm\infty$	0
3	3	2.6667	1.8750	0	$\pm\infty$	0	$\pm\infty$
4	4	3.7500	3.2000	2.1875	0	$\pm\infty$	0
5	5	4.8000	4.3750	3.6571	2.4609	0	$\pm\infty$
6	6	5.8333	5.4857	4.9219	4.0635	2.7070	0
7	7	6.8571	6.5625	6.0952	5.4141	4.4329	2.9326

TABLE 3 - CALCULATED ESTIMATES OF THE LOWEST THREE EIGENVALUES FOR THE DELTA WING-TIP CASE (REGION IV WITH  $\varphi_1 = 90^\circ$ ).

$\varphi_2$	N	$s_1$	$s_2$	$s_3$
100°	7	0.95161	1.89868	1.99987
	9	.95161	1.89869	1.99987
110°	7	.89334	1.78114	1.99888
	9	.89336	1.78121	1.99888
120°	7	.82839	1.67867	1.99592
	9	.82845	1.67881	1.99592
130°	7	.76208	1.60535	1.98942
	9	.76220	1.60556	1.98943
140°	7	.69873	1.55758	1.97720
	9	.69890	1.55783	1.97721
150°	7	.64054	1.52798	1.95634
	9	.64077	1.52826	1.95637
160°	7	.58810	1.51069	1.92348
	9	.58838	1.51099	1.92356
170°	7	.54114	1.50187	1.87602
	9	.54147	1.50217	1.87620
180°	7	.49906	1.49923	1.81389
	9	.49943	1.49954	1.81421
	$\infty$	1/2	3/2	

Table 2 - COMPARISON OF CALCULATED ESTIMATES OF THE LOWEST EIGENVALUE FOR REGION I.

$\varphi_2$	Medan N=5	Medan N=6	Medan N=10	Sack (1972)
10°	0.99209	0.99209	0.99209	0.99209
20°	.96615	.96615	.96615	.96615
30°	.91904	.91904	.91904	.91904
40°	.85257	.85257	.85257	.85257
50°	.77543	.77543	.77543	.77543
60°	.69748	.69748	.69748	.69749
70°	.62461	.62461	.62461	.62461
80°	.55880	.55880	.55880	.55880
100°	.44735	.44735	.44735	.44736
110°	.39982	.39982	.39982	.39982
120°	.35636	.35636	.35636	.35636
130°	.31596	.31595	.31595	.31595
140°	.27763	.27755	.27759	.27760
150°	.24019	.24010	.24010	.24010
160°	.20199	.20170	.20166	.20168
170°	.15971	.15845	.15829	.15822

TABLE 4 - THE THIRD LOWEST EIGENVALUES FOR REGION IV AND  $\varphi_2 = 180^\circ$ .

$\varphi_1$	N=5	N=7	N=9
11.25°	1.5551	1.5372	1.5355
22.5°	1.5845	1.5687	1.5681
33.75°	1.6168	1.6038	1.6038
45°	1.6517	1.6418	1.6421
56.25°	1.6893	1.6824	1.6829
67.5°	1.7296	1.7252	1.7257
78.75°	1.7718	1.7695	1.7699
90°	1.8150	1.8139	1.8142
101.25°	1.8571	1.8567	1.8569
112.5°	1.8960	1.8958	1.8959
123.75°	1.9295	1.9294	1.9295
135°	1.9564	1.9564	1.9564
146.25°	1.9764	1.9764	1.9764
157.5°	1.9899	1.9899	1.9899
168.75°	1.9976	1.9976	1.9976

TABLE 5 - THE THIRD EIGENVALUE FOR REGION V.

$\varphi_2$	N=7	N=11	N=15
5.625°	1.187	1.162	1.150
11.25°	1.198	1.178	1.171
22.5°	1.227	1.217	1.214
33.75°	1.261	1.256	
45°	1.298	1.297	
56.25°	1.340	1.340	
67.5°	1.386	1.388	
78.75°	1.439	1.440	
90°	1.500	1.500	
101.25°	1.570	1.568	
112.5°	1.649	1.645	1.643
123.75°	1.737	1.730	1.728
135°	1.827	1.819	1.817
146.25°	1.907	1.900	1.898
157.5°	1.963	1.958	1.957
163.125°	1.980	1.978	1.977

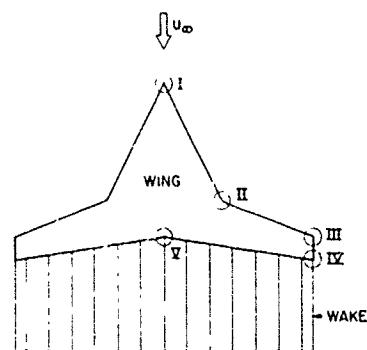


Fig. 1 Regions of interest.

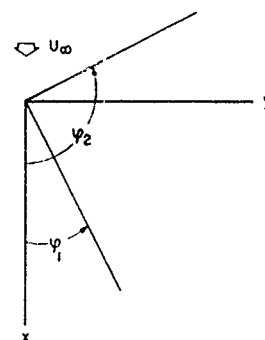


Fig. 2 Notation and coordinate system for the general case.

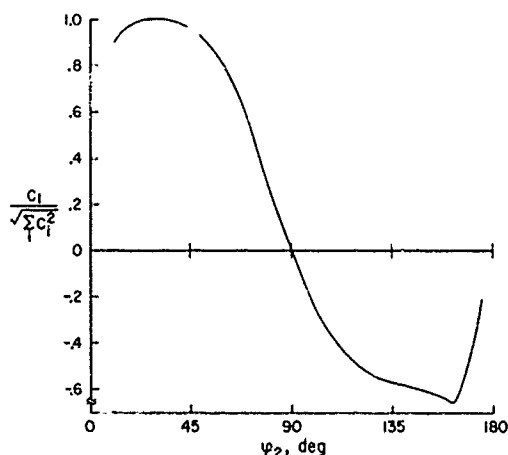


Fig. 3 Relative strength of the suction mode for the second symmetric eigenvalue of region I.

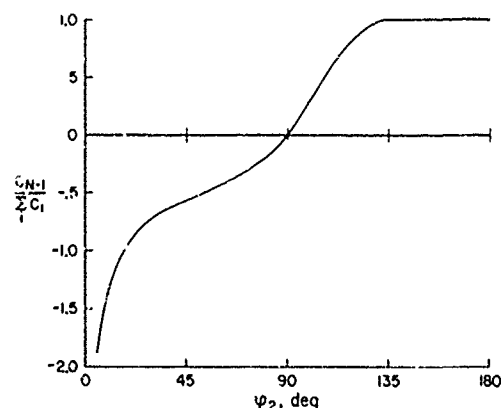


Fig. 4 Relative strength of the wake mode for region V.

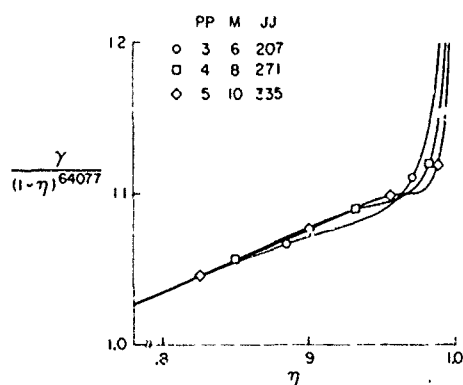


Fig. 5 The span load distribution as predicted by the KFM near the tip of the 60° delta wing.

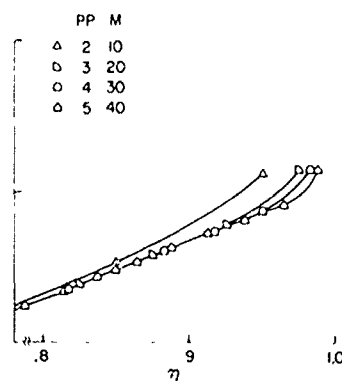


Fig. 6 The span load distribution as predicted by the VLM near the tip of the 60° delta wing.

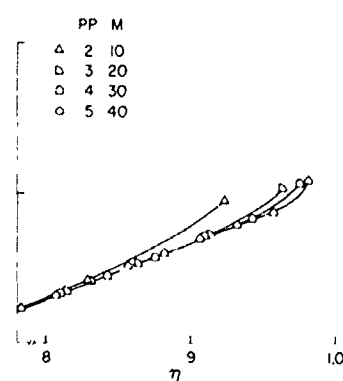


Fig. 7 The span load distribution as predicted by the VLMI near the tip of the 60° delta wing.

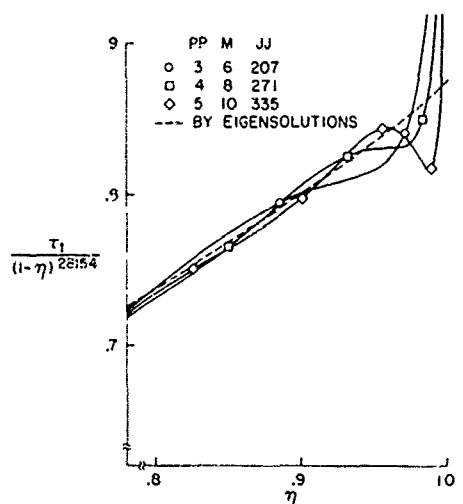


Fig. 8 The leading-edge thrust distribution near the tip of the 60° delta wing as predicted by the KFM and by the present method with constants determined from the KFM span loading.

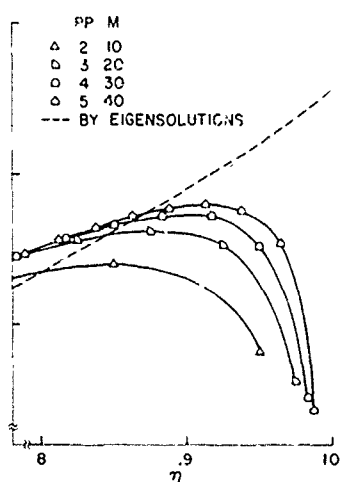


Fig. 9 The leading-edge thrust distribution near the tip of the 60° delta wing as predicted by the VLM and by the present method with constants determined from the VLM span loading.

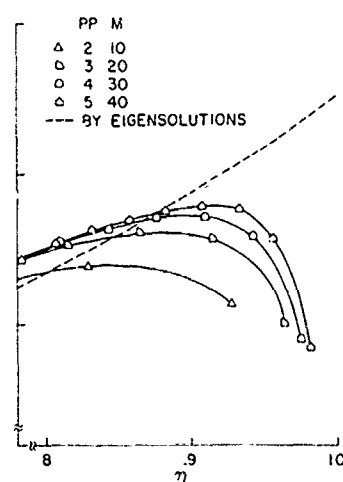


Fig. 10 The leading-edge thrust distribution near the tip of the 60° delta wing as predicted by the VLMI and by the present method with constants determined from the VLMI span loading.

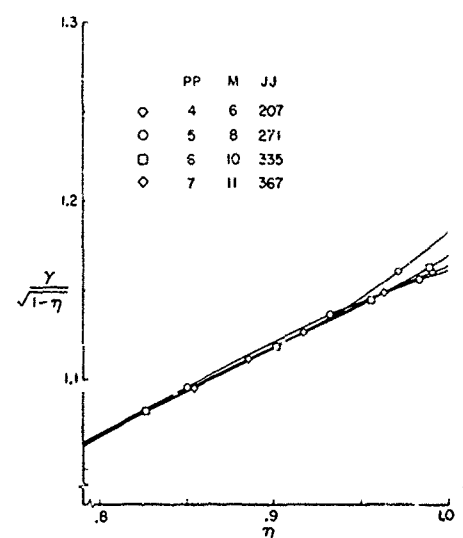


Fig. 11 The span loading predicted by the KFM near the tip of the 45° swept wing.

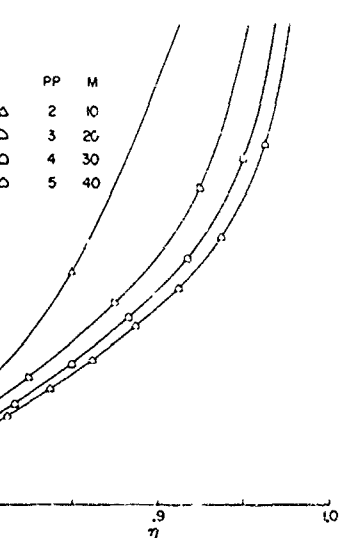


Fig. 12 The span loading predicted by the VLM near the tip of the 45° swept wing.

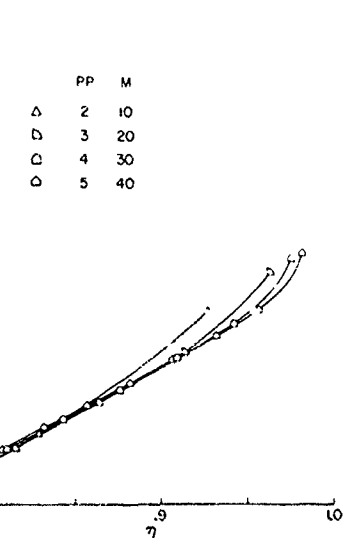


Fig. 13 The span loading predicted by the VLMI near the tip of the 45° swept wing.

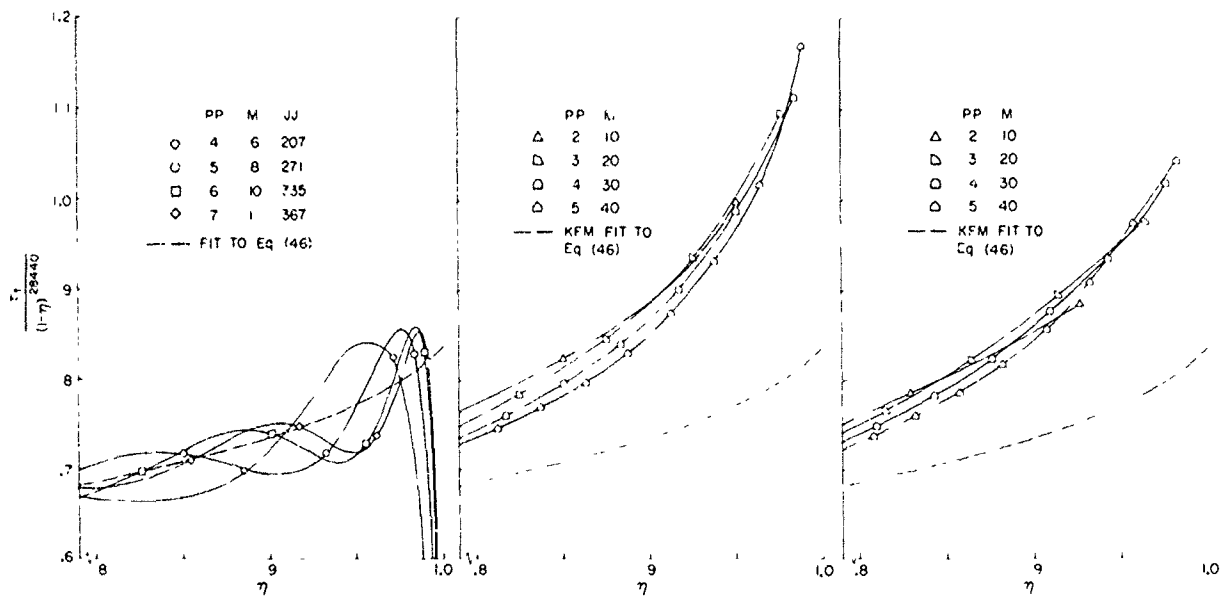


Fig. 14 The leading-edge thrust near the tip of the 45° swept wing as predicted by the KFM and Eq. 46.

Fig. 15 The leading-edge thrust near the tip of the 45° swept wing as predicted by the VLM.

Fig. 16 The leading-edge thrust near the tip of the 45° swept wing as predicted by the VLM.

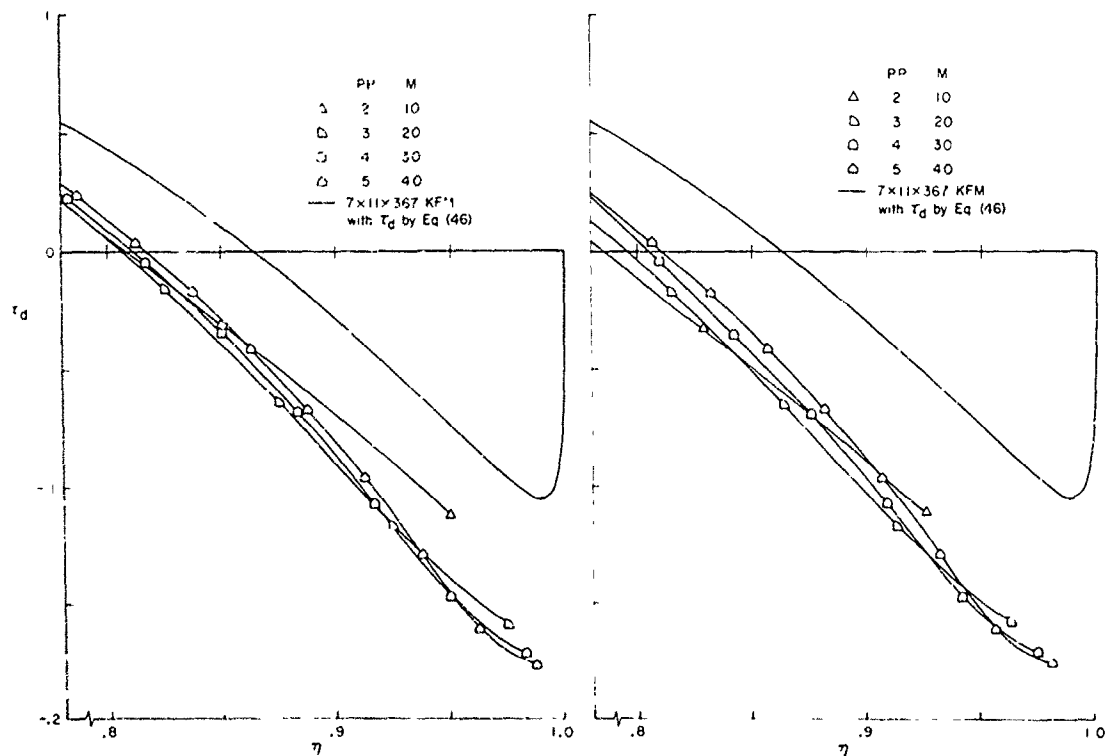


Fig. 17 The induced drag distribution near the tip of the 45° swept wing as predicted by the VLM and the KFM.

Fig. 18 The induced drag distribution near the tip of the 45° swept wing as predicted by the VLM and the KFM.



# VORTEX LATTICE APPROACH FOR COMPUTING OVERALL FORCES ON V/STOL CONFIGURATIONS\*

CIRO W. LUCCHI\*\* AND WOLFGANG SCHMIDT\*\*\*

THEORETICAL AERODYNAMICS GROUP

DORNIER GMBH

7990 FRIEDRICHSHAFEN

West Germany

## SUMMARY

The paper will give a short exposition of the vortex lattice method as it has been developed to handle lifting configurations of arbitrary shapes and will deal in more details on the forces computation when additional lift is induced by a deflected jet as in some VTOL aircrafts.

Since the practical beginning of the vortex lattice method problems which it can treat have increased in complexity, while the accuracy has also improved so that the induced drag and the force distributions are now reliable results. It must be stressed that because of the singular behavior of line vortices, pressures cannot be relied upon and thus are not computed. Complex geometries include wing tip winglets or shrouded propellers with highly deflected jets. A study will be presented centered around the experimental Dornier Aerodyne and discussion will be carried on such problems as mass flow control, jet definition and lattice arrangements on the centerbody, shroud and jet. Results will be presented on a configuration of practical importance.

The paper will also rapidly survey other fields of application of the vortex lattice method such as wing-body interference, ground effect and wind tunnel wall corrections.

## RESUME

Une courte présentation de la méthode "vortex lattice" sera d'abord donnée telle qu'elle a été développée pour étudier des configurations portantes de forme arbitraire et un examen plus détaillé sera ensuite consacré au calcul des forces quand une portance additionnelle est induite par un jet défléchi comme dans le cas de quelques avions VTOL.

Depuis le début pratique de la méthode "vortex lattice", les problèmes qu'elle peut traiter ont augmenté de complexité, tandis que la précision elle aussi s'est améliorée de façon que la traînée induite et les distributions de force sont maintenant des résultats attendibles. Il est à noter que à cause du comportement singulier des vortex linéaires, les pressions ne sont pas attendibles et ne sont donc pas calculées. Formes compliquées sont p.e. des ailettes d'extrémité d'aile ou des hélices carénées avec des jets fortement défléchis. Une étude sera présentée centrée sur l'Aerodyne expérimentelle développée chez Dornier et il sera discuté de problèmes tels que le contrôle de la quantité de masse, la définition du jet et l'arrangement des vortex sur le corps central, l'enveloppe et le jet. Des résultats seront présentés pour une configuration d'importance pratique.

Un coup d'oeil sera jetté sur d'autres champs d'application de la méthode "vortex lattice" tels qu'interférence aile-fuselage, effet de sol et corrections de soufflerie.

\* This work was supported by the Ministry of Defense of the Federal Republic of Germany under ZTL contract T/R 720/R 7600/52001

\*\* Research Scientist

\*\*\* Head of the Theoretical Aerodynamics Group

## INTRODUCTION

Computation of the three-dimensional inviscid subsonic flow requires the solution of the three-dimensional Laplace equation within the whole (infinite) flow field when the linearized Prandtl-Glauert space transformation is used to reduce the problem to the incompressible flow. Solving the Laplace equation in the whole field is equivalent to calculate a two-dimensional integral equation over the surfaces immersed in the fluid. The boundary condition of zero (or imposed) normal flow in the first problem remains unchanged in the second problem. Typically the integral equation is solved by replacing the surfaces with a distribution of singularities; in the vortex lattice method these singularities are closed vortex filaments of constant strength which thus satisfy the Helmholtz laws.

The shape of the vortex filaments is quadrilateral, but triangular rings may be used by specifying the length of one side as zero. The vortices are defined by four nodal points; this allows for geometries of arbitrary shape (fig. 1). The boundary condition is applied at a control point somewhere near the vortex center; since the onset of the vortex lattice method it was recognized the importance of the control point location. Two-dimensional studies [1] precisely located the control point when using equally spaced vortices; three-dimensional studies of wings [2, 3] confirmed these results. It was also shown that an inset is needed at the wing tip [4]. When analysing complex configurations in the three-dimensional space however one never uses equally spaced panels but tries to optimize the sizes. Location of the control point must in this case follow the same law as the vortices both in chordwise and spanwise directions [5]; since that law of distribution is not usually known in analytical form, accurate formulae have been derived using Taylor series [6]. Because of programming difficulties, these formulae have been implemented in chordwise direction only.

The forces are computed by adding the forces acting on each vortex filament immersed in the velocity field induced by the other vortices (Joukowski law): it is assumed that the velocity at each filament middle point is the velocity average over the whole filament. Forces computed in this way provide also the leading edge suction force and thus a realistic induced drag.

Due to the singular flow field induced by vortices, pressure coefficients are not very reliable. If some care is taken, spanwise loading distributions come out to be quite good (they do not have any physical meaning however when a pressure jump is furnished by a propeller due to effects described below). But the main purpose of the vortex lattice method is the computation of total forces.

## SIMULATION OF A JET

As previously done [7, 8], a well established empirical relation has been used to specify the jet axis. In the wind-axes  $\xi, \zeta$  originating at the nozzle center it is written as

$$\frac{\xi}{D} = -\frac{1}{4 \cos \beta} \frac{1}{V_j^2} \frac{\zeta^3}{D^3} - \frac{\zeta}{D} \tan \beta \quad (1)$$

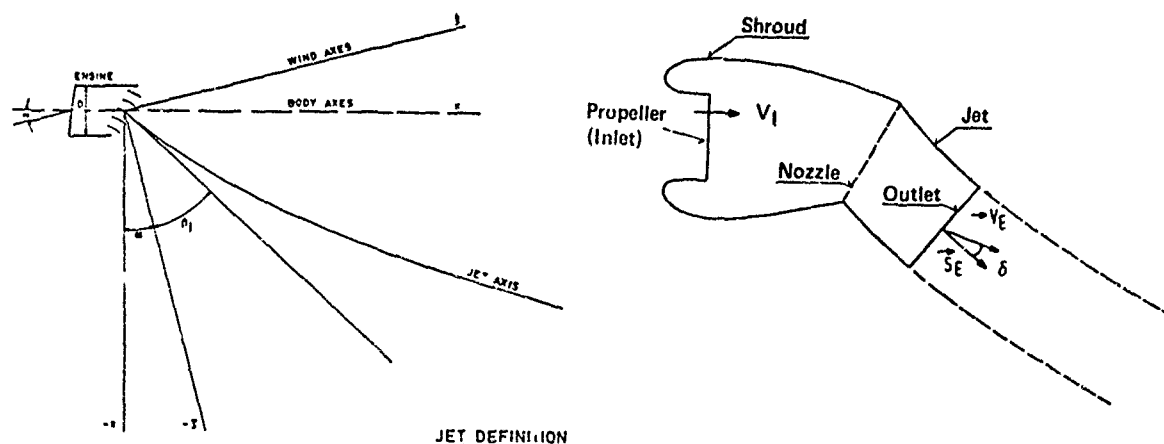
where  $D$  is the fan diameter,  
 $\beta$  is the jet deflection, measured at the jet's origin from the axis  $-\zeta$ ,  
 $V_j$  is the ratio of jet-to-freestream velocity.

The jet surface is defined such that the cross sectional area remains constant along the jet. From a mathematical point of view, the jet is considered a solid surface, thus providing the blockage and distortion associated with a jet. This model does not account for the entrainment effect. It would not a priori be difficult to do that: an empirical relation would have to be used to determine the rate of entrainment. The jet surface would then be considered not as a solid surface anymore, but as a porous surface through which a mass flux (i.e. a normal velocity) would have to be prescribed. Another empirical relation would determine the change of cross sectional area. Since complete and reliable experimental results are not available, it is felt that this approach is the best one. Because of the low jet velocities of the present computation, it is not expected a large error from a lack of entrainment.

## ACCOUNTING FOR THE PROPELLER PRESSURE JUMP

Consider the section by a vertical plane of a shrouded propeller (or for that matter also a jet engine). Closed vortices are placed on the propeller plane and on the outer surface of the shroud; due to the solid body representation, the jet surface also is replaced by vortices.

In the VTOL systems considered for study in the present work, the additional required lift is provided by a cascade deflecting the jet. It can be represented in the vortex lattice method, but for the purpose of forces computation it is equivalent to have the complete deflection produced by the jet acting as the solid surface of a duct: the missing force induced on the cascade is thus computed on a small part of the upper jet. The pitching moment however will not be very accurate since the position of the force acting on the cascade has to be approximated. Therefore the system to be analysed is that represented by a solid line on the right sketch below.



While the potential flow model gives the correct external flow field, since it is assumed that the jet location is almost correctly prescribed, the internal potential flow field does not represent the physical one. First the total pressure jump  $\Delta p$  produced by the propeller is missing. And secondly due to the incompleteness of the internal surface, the internal flow pattern is a fictitious one: notwithstanding this last approximation, the total forces will be correct if the inlet and outlet conditions are properly prescribed, provided the first error is accounted for. The following pressure integration explains this statement.

The total physical force (on the internal and external surfaces) is given by:

$$\vec{F} = \int_{I+S} (p_i - p_e) d\vec{S} \quad (2)$$

where  $I$  is the inlet area,  $S$  is the surface of the shroud and the upper part of the jet,  $p_i$  and  $p_e$  are the internal and external static pressures respectively. Calling  $\Delta p$  the jump in total pressure, the internal static pressure  $p_i'$  as given by the vortex lattice method would be

$$p_i' = p_i - \Delta p \quad (3)$$

and the physical force becomes

$$\vec{F} = \int_{I+S} (p_i' - p_e) d\vec{S} + \Delta p \int_{I+S} d\vec{S} = \vec{F}_{VLM} - \Delta p \vec{S}_E \quad (4)$$

since the Joukowski law gives, as force, the integral of the pressure difference between the outer and inner surfaces.

For the pitching moment computation, the following compensating term has to be added

$$\Delta M = - \Delta p \int_{I+S} \vec{r} \times d\vec{S} \quad (5)$$

$\Delta p$  is not independent of  $V_I$  once this value is prescribed. Assuming  $p_E = p_\infty$ , the stagnation pressure jump furnished by the propeller is

$$\Delta p = \frac{1}{2} \rho (V_E^2 - V_\infty^2) \quad (6)$$

By continuity

$$V_I S_I = V_E S_E \cos \delta \quad (7)$$

Therefore

$$\Delta p = \frac{1}{2} \rho V_I^2 \left[ \left( \frac{S_I}{S_E \cos \delta} \right)^2 - \left( \frac{V_\infty}{V_I} \right)^2 \right] \quad (8)$$

It ought to be mentioned that since the jet is not correctly prescribed, forces will appear on it that will contribute an error to the above additional force. However, since this term is computed near the shroud, one can validly suppose that the jet will be very close to the exact position and that the forces

will be small in that region. For a rightly prescribed jet contour, with a deflection due to a cascade, the following relation must be everywhere verified

$$p_i - p_e = 0 \quad (9)$$

This relation could be used to locate the jet by an iterative procedure; it would however be very time consuming.

## RESULTS

Before concentrating the effort on more specific problems, a variety of problems was surveyed to have an estimate of the difficulties which might occur in each case.

An untapered, swept, cambered wing (fig. 2) was compared with experimental and numerical data [9]: the accuracy is shown to be good. Excellent agreement also was obtained with theory and experiment [10] when analysing a thin circular annular wing (fig. 3).

As an example of extreme use of the vortex lattice method, a wing with tip winglets was studied with the present program [11] (fig. 4). This is a case where triangular vortices were used to optimize the vortex size in regions where high gradients may be expected. The results were quite satisfactory.

A preliminary study of a complete aircraft with ground effect, though without engines, was also performed (fig. 5); the different parts were tested separately to see the problems involved and then assembled together. The figures show that a lack of accuracy occurs at the wing-body connection.

An almost classical test case was provided by the investigation of a wing in a wind tunnel (fig. 6). Here a simple wing at a low angle of attack was examined; the wake was modeled according to the physical geometry it is supposed to take when in a wind tunnel. Naturally it is not planned to use such a method for simple wings at low angles of attack, but for systems producing a large downwash, for which correction formulae are not available; since the wake position would a priori be difficult to determine, an iterative procedure could be used until the forces induced on the wake are brought to zero.

The problem of a flapped wing may also be investigated using the vortex lattice method. Some studies were made to determine the effect of an inset at the flap's and wing's sides; more tests are however needed together with comparison with experimental data.

## AERODYNE

The geometry of the Aerodyne, although relatively simple, is still too complicated to be used in a preliminary investigation project using the vortex lattice method. Therefore a simpler geometry has been defined (fig. 7). Its shape is almost a circular cylinder having an average chord length of 1.066 propeller diameters, the front section being inclined  $6.54^\circ$  and the nozzle section  $30^\circ$  with respect to the vertical. The shroud nose has a thickness down to the vertical propeller plane (placed 0.206 chords downstream of the leading edge) where the thickness-to-chord ratio is 0.042. The jet geometry is as previously described. The centerbody, easily defined, is as in the real model, extending 1.003 chords in front and 0.896 chords behind the leading edge and having a maximum diameter of 0.467 propeller diameters.

The number of vortices on half the configuration is 8x10 on the centerbody, 8x2 on the propeller plane (this representation is described below), 8x2 on the inside of the lip (i.e. from the leading edge to the propeller), 8x9 on the external surface of the shroud and 8x1 on the jet. Two additional line sources have been placed at the nozzle and at the end of the jet (their purpose is described below).

The x and z coordinates of the jet's corner nodes are generated according to the jet description (see above) and such that the average vortex length of a circumferential strip of vortices is equal to 1.3 times the average vortex length of the previous strip, this rule being valid for all the jet including the first strip behind the shroud.

The simplified Aerodyne has been investigated with a ratio of propeller-to-freestream velocity of 2.2, no angle of attack and a jet angle  $\beta$  of  $30^\circ$ , i.e. a jet deflection of  $60^\circ$  with respect to the horizontal.

The results for lift and induced drag (the pitching moment was not computed in this preliminary investigation) are shown on fig. 7. They have been broken down into the contributions from the different parts.

A question may be raised on how to impose the proper velocity in the propeller plane. In an early work [12] the end of the jet surface was flared in such a way that the prescribed velocity was achieved at one point or in the average on the propeller plane; this necessitated a trial-and-error procedure to attain the desired velocity. Later [7] quadrilateral vortices were placed in the propeller plane and the desired normal velocity was imposed at each control point; this method has two advantages: no trial-and-error procedure is needed anymore and an arbitrary velocity distribution (a result of experiment or another theoretical method) may be imposed (in this work a uniform velocity was given). Numerical experiments described in [6] led to the actual number of vortices.

It was noticed that the jet length and the vortices density on it had a considerable influence upon the vortex strengths on the shroud. It is due to leakage effects, i.e. the violation of the mass continuity

equation across a surface simulated by discrete vortices. It was suggested [13] to put a line source at the end of the jet and impose in that region an axial velocity such as the mass continuity would be satisfied. Its effect was to render force computations (on each vortex filament and of course the whole configuration) virtually independent of the jet length so that relatively short jets may be used. It was found too that the line source should be relatively short. An additional source has been placed in the nozzle section.

Almost all of the numerical experiments were made without leading edge thickness, i.e. with the upper and lower surfaces of the lip collapsed into one surface. The effect of leading edge thickness is small but not negligible and should always be incorporated when evaluating a configuration such as the Aerodyne jet engine.

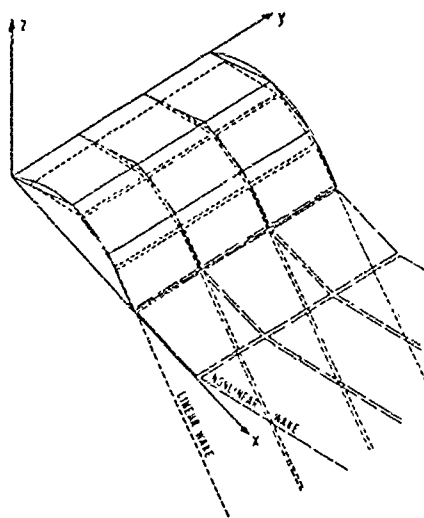
CPU time on the Dornier's IBM 370/158 for one case (i.e. one angle of attack, one ratio of propeller-to-freestream velocity and one jet angle) was 440 secs. It is expected to reduce this cost still more.

## CONCLUSIONS

A wide variety of test cases has shown that the vortex lattice method in general and its present application in particular yield reliable total force coefficients and, when care is taken, also load distributions for quite complex configurations. Further work is of course still required in order to assess the accuracy by comparison with experimental data of an Aerodyne-type of aircraft and later a full VTOL aircraft. One may already say however that because of its low computing cost this method appears as a good tool for preliminary studies.

## REFERENCES

1. R.M. James: On the Remarkable Accuracy of the Vortex-Lattice Discretization in Thin Wing Theory, McDonnell Douglas Aircraft, Rep. DAC-67211, 1969
2. S.G. Hedman: Vortex-Lattice Method for Calculation of Quasi Steady State Loadings on Thin Elastic Wings in Subsonic Flow, Aero. Res. Inst. Sweden, FFA Rep. 105, 1966
3. G.R. Hough: Remarks on Vortex-Lattice Methods, J. Aircraft, V.10, N.5, 314-317, 1973
4. P.E. Rubbert: Theoretical Characteristics of Arbitrary Wings by a Non-Planar Vortex Lattice Method, Boeing Co., Rep. D6-9244, 1962
5. W. Schmidt: Potentialtheoretische Berechnungsverfahren für Unter- und Überschallströmungen - Ein kritischer Überblick, Dornier GmbH, Bericht 74/54 B, 1974
6. C.W. Lucchi: Berechnung der aerodynamischen Beiwerte von Fluggeräten mit Mantelschrauben, Dornier GmbH, Bericht 75/46 B, 1975
7. P.E. Rubbert, G.R. Saaris, M.B. Scholey, N.M. Standen and R.E. Wallace: A General Method for Determining the Aerodynamic Characteristics of Fan-in-Wing Configurations, USAAVLABS, TR 67-61 A, 1967
8. E. Jünke, H. Lükewille, W.R. Schmidt and S. Schultz: Aerodynamische Untersuchungen an Fluggeräten mit Mantelschrauben, Dornier GmbH, Bericht 73/24 B, 1973
9. T.J. Langan and H.T. Wang: Evaluation of Lifting-Surface Programs for Computing the Pressure Distribution on Planar Wings in Steady Motion, Computers and Fluids, V.2, N.1, 53-78, 1974
10. S.M. Belotserkovskii: The Theory of Thin Wings in Subsonic Flow, Plenum Press, New York, 1967
11. H. Zimmer: Widerstandsverminderung an Tragflächen - Teil 2, Dornier GmbH, Bericht 75/15 B, 1975
12. R.E. Moncal: A Method for Representing Fan-Wing Combinations for Three-Dimensional Potential Flow Solutions, J. Aircraft, V.2, N.6, 527-530, 1965
13. P.E. Rubbert: Private Communication, Sept. 1975



VORTEX LATTICE METHOD

Figure 1

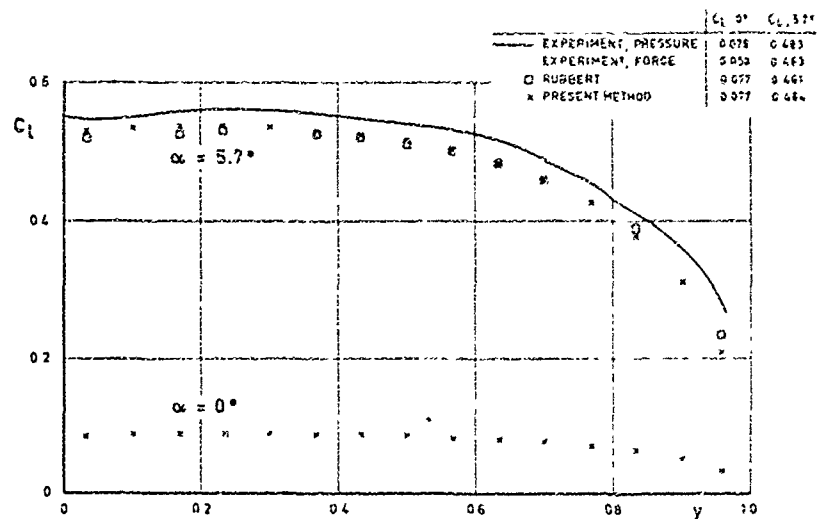
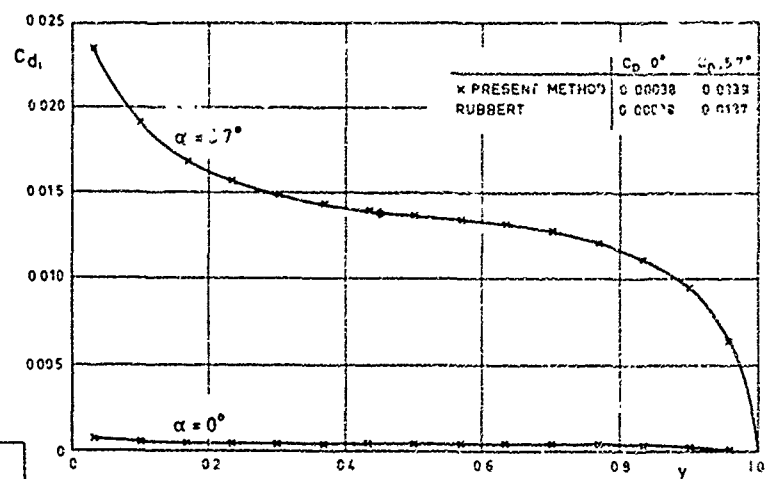
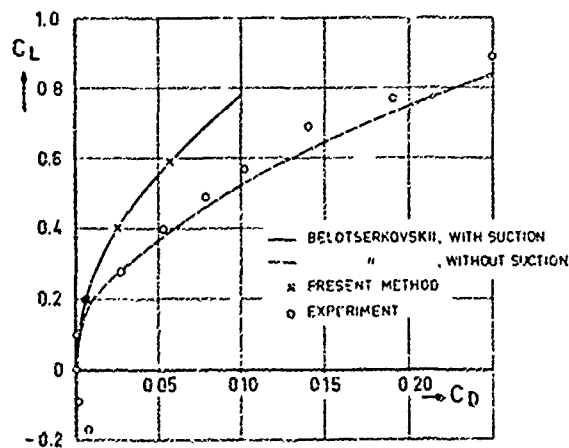
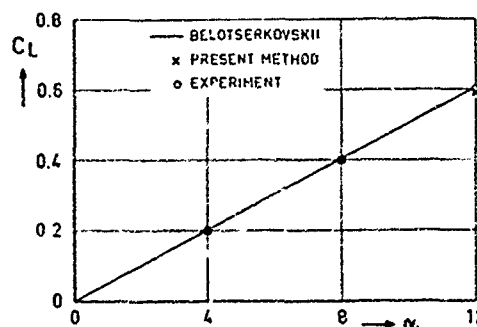
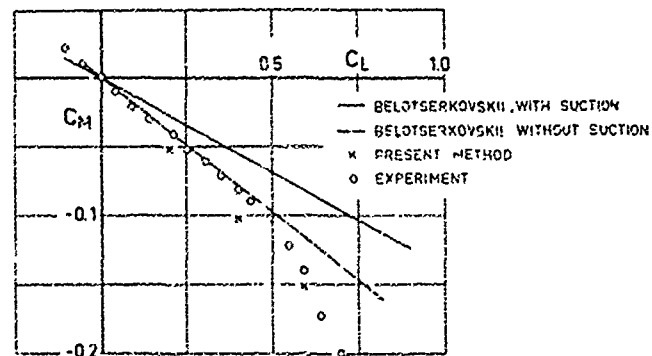
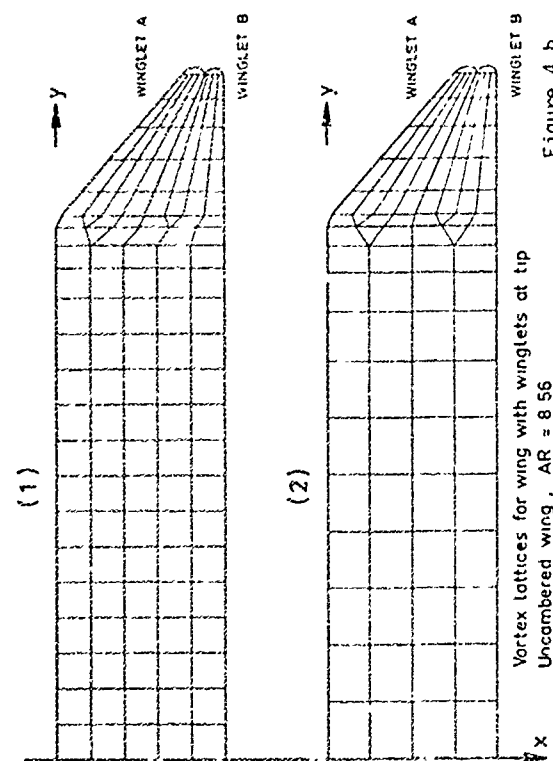
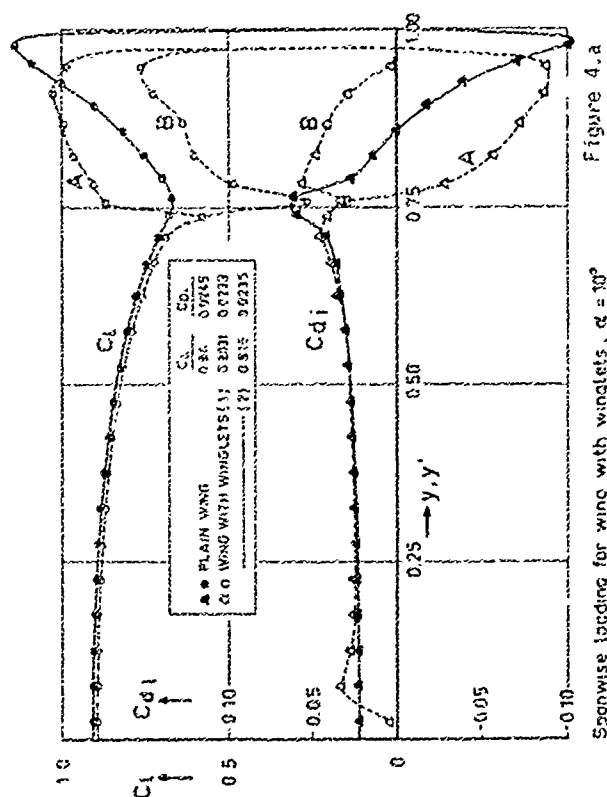
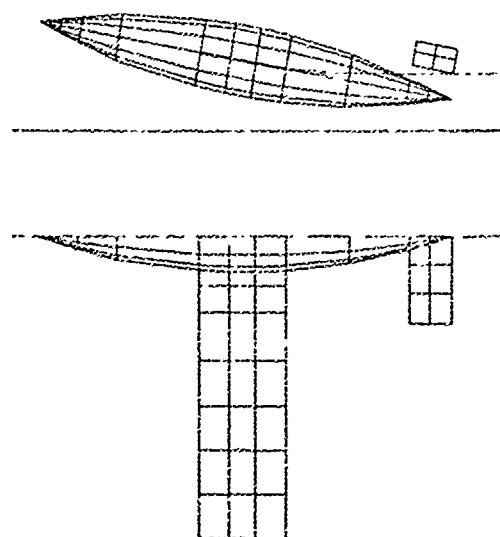
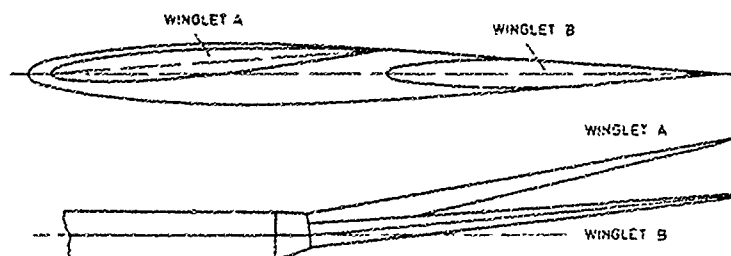
Spanwise loading on an untapered, swept (15°), cambered (NACA 230) wing  
Figure 2.a  
AR=5, M=0,  $\alpha=0^\circ$  and  $5.7^\circ$  - LiftSpanwise loading on an untapered, swept (15°), cambered (NACA 230) wing  
Figure 2.b  
AR=5, M=0,  $\alpha=0^\circ$  and  $5.7^\circ$  - DragCylindrical, annular wing  $\lambda=1, M=0$ 

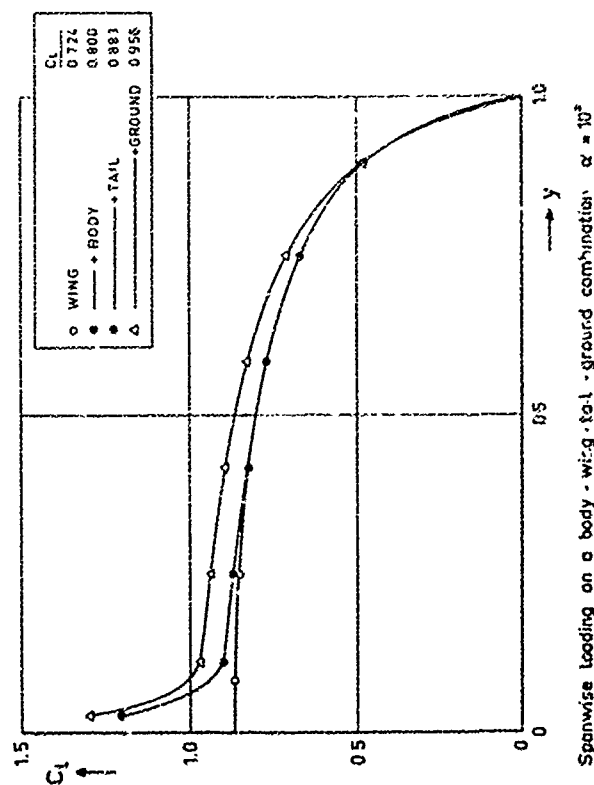
Figure 3

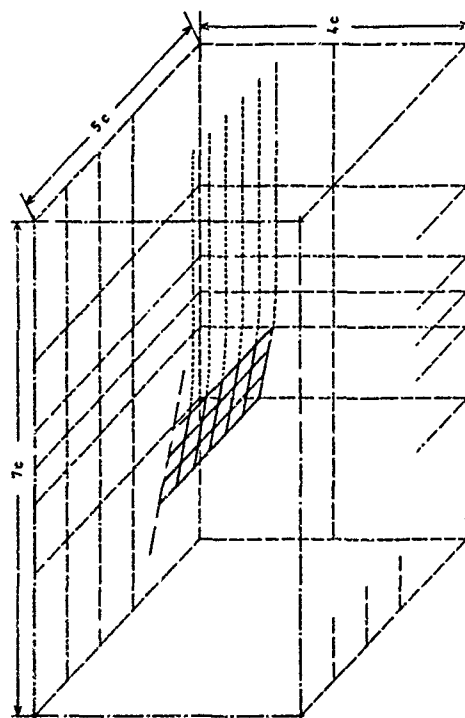


Winglets at wingtip for drag reduction  
Figure 4.c

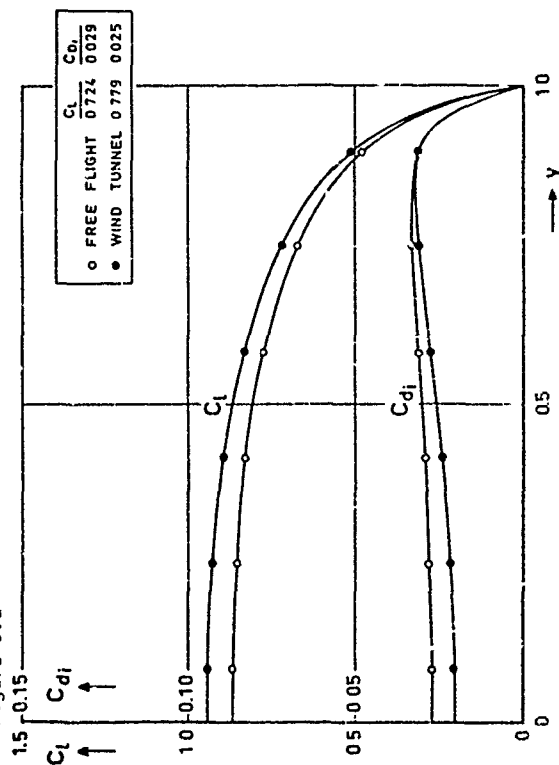


Body-wing-tail-ground combination  
Figure 5.a

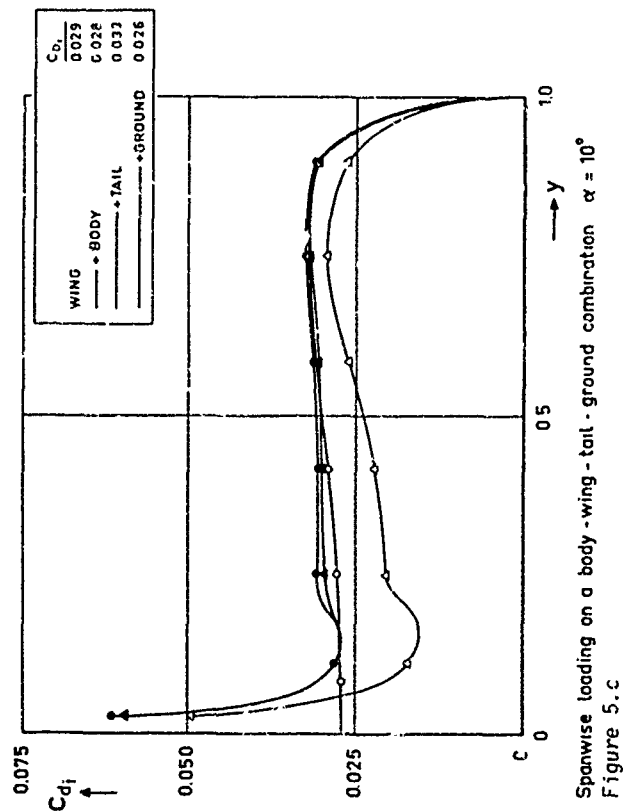




Wing in wind tunnel. Rectangular, planar wing,  $AR = 6$ ,  $M = 0$ ,  $\alpha = 10^\circ$   
Figure 6.a



Spanwise loading on a rectangular planar wing,  $AR = 6$ ,  $M = 0$ ,  $\alpha = 10^\circ$   
Figure 6.b



Spanwise loading on a body-wing-tail-ground combination  $\alpha = 10^\circ$   
Figure 5.c



$$\alpha = 0^\circ, V_p = 2.2, \beta_j = 30^\circ, l_j = 8c$$

SIMPLIFIED AERODYNE  
Centerbody  
Leading edge thickness

	$C_L$	$C_{D_i}$
SHROUD	3.56	0.339
PROPELLER	0	0.163
VLM CENTERBODY	-0.22	0.350
JET	1.06	1.532
PRESSURE JUMP	0.89	-1.819
	5.31	0.566

Figure 7



AIRCRAFT MANEUVERS AND DYNAMIC PHENOMENA RESULTING  
IN RAPID CHANGES OF LOAD DISTRIBUTIONS OR/AND  
FLUCTUATING SEPARATION

BY

DAVID B. BENEPE, SR.  
DESIGN SPECIALIST, AERODYNAMICS  
GENERAL DYNAMICS  
FORT WORTH DIVISION  
P.O. BOX 748  
FORT WORTH, TEXAS  
76101  
U.S.A.

SUMMARY

This paper presents flight data from several maneuvers which produce rapid changes in aircraft component load distribution or/and fluctuating flow separations. The maneuvers include an abrupt pullup, slow and fast windup turns, a slowdown turn at elevated load factor, a rolling pullout at elevated load factor, a sustained rudder roll followed by a spin and recovery and a 1-g deceleration terminating in a slow nose slice and recovery. Where feasible wind tunnel model pressure measurements illustrate the character of the aerodynamic loadings. Comparisons between measured structural loads and predictions are presented and discussed.

LIST OF SYMBOLS

CG, C.G.	Center of Gravity	$T_W$	Wing Torsional Moment
$C_N$	Normal Force Coefficient	$V_W$	Wing Vertical Shear
$C_p$	Pressure Coefficient	$x/c$	Ratio of Chordwise Position to Local Chord
$C_{p_{rms}}$	Root Mean Square Coefficient of Fluctuating Pressure Component	$\alpha$	Angle of Attack
DESIGN	Structural Design Value	$\alpha_{cg}$	Angle of Attack at c.g.
$F_R$	Rudder Pedal Force	$\alpha_s$	Select Angle of Attack (Middle $\alpha$ from 3 Sensors)
$F_X$	Longitudinal Stick Force	$\beta$	Angle of Sideslip
$F_Y$	Lateral Stick Force	$\beta_{cg}$	Angle of Sideslip at c.g.
$GV/q^2L$	Nondimensional Pressure Spectral Density Function	$\gamma$	Coherence Function (Spectral Analysis)
$h$	Altitude	$\delta_{FA}$	Differential Trailing Edge Flap Deflection
$L$	Reference length	$\delta_{HA}$	Differential Horizontal Tail Deflection
$M$	Mach Number	$\delta_{HE}$	Horizontal Tail Deflection
$M_{HT}$	Horizontal Tail Bending Moment	$\delta_{LEF}$	Leading Edge Flap Deflection
$M_{VT}$	Vertical Fin Bending Moment	$\delta_R$	Rudder Deflection
$N_Z$	Normal Load Factor	$\delta_S$	Spoiler Deflection
$P$	Roll Rate	$\eta$	Ratio of Spanwise Location to Semispan
$P_{rms}$	Root Mean Square Value of Fluctuating Pressure Component	$\sigma_{PSV}$	Root Mean Square Value of Buffet Vertical Accelerations at Pilot's Seat
$P_{t0}$	Free Stream Total Pressure	$\phi$	Roll Angle
$q$	Dynamic Pressure		
R/H	Right Hand		

## INTRODUCTION

This paper deals with two areas of interest with respect to transient aerodynamic loadings. Several examples of flight maneuvers are presented in which rapid changes in the aerodynamic loadings occur that are caused by either the rate of change of the aircraft attitude or by the presence of flow separations.

The flight data were obtained during flight test programs of a small highly maneuverable fixed wing fighter (Aircraft A) and a variable-sweep fighter-bomber (Aircraft B).

The examples of flight maneuvers for Aircraft A will be presented first. Where feasible wind tunnel model pressure distributions are also presented to supplement the flight results. Comparisons between measured and predicted structural loads complete the discussion for Aircraft A.

Examples of flight maneuvers of Aircraft B are presented next along with more detailed discussion of wind tunnel measurements of static and fluctuating pressures. Included are comparisons between predicted and measured values of fluctuating wing loads caused by buffet.

## AIRCRAFT A MANEUVERS

The example maneuvers from flight tests of Aircraft A have been selected to illustrate the effects of various dynamic phenomena on the wing or/and tail loads measured during the maneuvers. The maneuvers include an abrupt pullup, slow and fast windup turns, and slowdown turn at elevated load factor, a rolling pullout at elevated load factor, a 1-g deceleration terminating in a slow nose slice and recovery and a rudder roll followed by a departure, spin and recovery.

### Examples Illustrating Effects of Pitch Rate

It is well known that pitch rate can have an effect on the development of the aerodynamic flow field at conditions near and above stall and considerable effort has been expended to develop methodology for predicting dynamic stall effects for two-dimensional airfoils and high aspect ratio wings<sup>(1)</sup>. The effects of dynamic stall phenomenon for fighter-type wings are not well known therefore it is of interest to compare flight data from three maneuvers of Aircraft A: a slow windup turn, a fast windup turn and an abrupt pullup.

Figure 1a presents the variations of normal load factor and normal force coefficient with angle of attack and Figure 1b the variations of wing root bending moment with airplane normal force for the three maneuvers. The time from nominal 1-g flight to an angle of attack of 10 degrees is 20.2, 2.33, and 1.46 seconds, respectively. There is a spread of about 16 percent in the gross weights and about 5 percent in the Mach number for the three maneuvers which accounts for much of the difference in the load factor variations with angle of attack.

There are some differences in the variations of normal force coefficient with angle of attack which might be attributed to differences in the horizontal tail contribution to lift.

The major point to be made however is the fact that there is a progressive increase in the amount of wing bending moment at a given angle of attack with increase in pitch rate even below the apparent stall. It is therefore necessary to account for the dynamic effects of various maneuvers in selecting critical loadings for design purposes. At present this is accomplished using 5-degree-of-freedom aircraft dynamic response simulation to account for inertia effects with the aerodynamic loading inputs based on rigid wind tunnel model pressure distributions corrected by theoretical analysis for static aeroelastic effects. Dynamic effects on the flow field are not included.

This approach correctly identified an abrupt pullup as a critical loading for the wing bending moment. The method uses quasi-steady aerodynamics and is considered satisfactory by the structural loads engineers. It is possible however that improved accuracy could be achieved if the dynamic flow phenomena were better understood and considered in the analysis.

### Example Illustrating the Effects of Wing Rock

One dynamic phenomenon which has caused some concern with respect to the possible impact on design loads is wing rock. While wing rock is not normally encountered to a significant degree for Aircraft A, there was a period during the flight test program when moderate wing rock occurred. Time histories of pertinent flight parameters for a windup turn maneuver presented in Figure 2 illustrate the effects which do not appear to be significant with respect to design loads, but are interesting nevertheless because they contribute to understanding the phenomenon.

The time histories show that the roll rate becomes erratic at about 22 seconds into the maneuver which corresponds to breaks in the variations of angle of attack and wing bending moment with time. It is obvious that wing flow separation has occurred. The rms values of pilot seat dynamic acceleration indicate the occurrence of buffet. Note that the combination of Mach number and angle of attack is such that the leading edge flap has not yet started to deflect.

The roll rate excursions rapidly increase to a maximum value of about 25 degrees per second at 24 seconds into the maneuver, but do not increase further. The wing bending moment exhibits buffeting effects but does not increase significantly. The horizontal tail bending moment does show excursions about equal to the maximum negative quasi-steady value which is about 10 percent of the design values. In addition it changes sign as angle of attack is increased and the tail deflection changes. The buffeting response at the pilot's seat increases slowly except for the data sample taken between 32 and 34 seconds into the maneuver. A spectral analysis (not presented) indicated that a strong input occurred at low frequency (below the natural structural frequencies of the aircraft) which may have been caused by the flight control system as the automatic roll damping feature attempted to compensate for the uncommanded changes in roll rate. Note that the roll angle excursions are not large.

Figure 3 presents wind tunnel model upper surface pressure distributions measured near the wing tip for several combinations of angle of attack and leading edge flap deflection at the nominal Mach number for the maneuver. The point to be made with the pressure data is the fact that if sufficient flap deflection is available at a given angle of attack leading-edge separation does not occur in the tip region. For the particular maneuver shown above the flap deflection was not sufficient. A change to the flap schedule to start the flap motion at a lower angle of attack eliminated wing rock in the moderate angle of attack regime.

### Example of Sudden Transition into Buffet During a Slowdown Turn

Another example of a potential critical design loading occurs during a slowdown turn from supersonic speed at elevated load factor. As the aircraft passes through the transonic Mach number regime there is a sudden transition into buffet.

Figure 4 presents time histories from such a maneuver. As the aircraft slows down to Mach 0.96 the leading edge flap starts to deflect (at about 5 seconds into the maneuver) and the rate of change of angle of attack with time increases. At about 6 seconds wing flow separation starts which is manifested in a rapid increase in the rms value of a normal acceleration at the pilot's seat, a decrease in the wing bending moment and a change in slope of the horizontal tail bending moment. The buffet intensity which occurs during this maneuver is described as light to moderate by the pilot. Note that there is a slight increase in wing bending moment just prior to the decrease caused by flow separation. The ratio of the peak measured wing bending moment to the airplane normal load factor produced at the same point in time is exactly equal to the ratio of design bending moment to design load factor. The unsteady wing bending moment fluctuations produced by buffet do not cause excursions above this peak quasi-steady value and are small. Typically the ratio of rms values of fluctuating wing bending moments to peak quasi-steady values is from .010 to .025 in the transonic range for Aircraft A which is significantly lower than the values obtained on earlier generation fighter aircraft.

Figure 5 presents wind tunnel model wing upper surface pressure distributions which help explain the chain of events which produces the results noted in Figure 4. The flow near the wing tip is initially completely supersonic and the pressure distribution is essentially constant along the chord as illustrated in the lower plot of Figure 5. The center plot shows that a distinct change in the pressure distribution occurs between the two values of attack shown for  $M = 0.95$  and  $\delta_{LEF} = 5^\circ$ . The flight angle of attack is approximately 11.8 degrees when  $\delta_{LEF}$  reaches  $5^\circ$  and wing flexibility reduces the local angle of attack slightly so the appropriate pressure distribution lies somewhere between the two curves presented.

A shock induced separation has occurred which is spreading forward toward the leading-edge and inboard as the angle of attack is increased. The significant increase in buffeting response appears to occur when the flow separation reaches the leading-edge and then progresses inboard along the leading-edge. The upper plot shows that the additional flap deflection which occurs with increasing angle of attack is not effective in reattaching the flow as the Mach number continues to decrease.

#### Example of a Rolling Pullout at Elevated Load Factor

One maneuver which provides a severe test of the ability to predict loads for dynamic conditions is the rolling pullout at elevated load factor. Figure 6 presents time histories of the bending moments produced on the wing horizontal tails and vertical tail of Aircraft A and pertinent flight parameters for a rolling pullout. The maneuver produces a significant amount of sideslip which is reflected in the moment measured for the vertical tail. Despite the fact that the angle of attack increases slightly during the rolling portion of the maneuver, the load factor and the wing bending moments decrease. The peak wing bending moment occurs at initiation of the roll as the flaperons are deflected. The slight difference between right and left horizontal tail bending moments is caused primarily by differential tail deflection. The vertical tail bending moment is higher than predicted. This point will be discussed more fully later in the paper.

#### Example of a Nose Slice

Little information is available for flight loads incurred during very high angle of attack flight. The flight test program for Aircraft A provided data of interest. One case is from a one-g deceleration with the aileron-rudder-interconnect function of the flight control system purposely inoperative. The maneuver produced a slow nose slice. Figure 7 presents time pertinent time histories including the variation of vertical tail bending moment.

The slow nose slice was caused by adverse yaw due to flaperon deflection as the pilot held wings level above angle of attack of 28 degrees. A maximum sideslip angle of 12.7 degrees was developed at 29 degrees angle of attack. An immediate recovery was obtained when the pilot relaxed aft stick force and the angle of attack reduced below 28 degrees.

The maximum vertical fin bending moment measured is small in terms of the design value because the dynamic pressure was low. If one were to project this experience to a high Mach number high dynamic pressure condition one could infer that a nose slice type of departure could produce a critical vertical tail loading. In actual practice it would be nearly impossible to obtain the critical combination of dynamic pressure and angle of attack because the aircraft decelerates rapidly at such high angles of attack.

#### Example of a Rolling Departure and Spin

The previous example was produced under very closely controlled conditions. The next case of interest was produced by an inadvertent rolling departure, oscillatory spin and recovery which occurred as the pilot performed an aggressive high angle of attack rudder roll maneuver. Figure 8 shows pertinent time histories of several flight parameters. A more detailed presentation is given in Reference 2. Figure 9 presents time histories of the vertical fin and wing bending moments.

The rolling departure begins at about 19 seconds into the maneuver and the peak negative vertical fin bending moment occurs about one second later at the first maximum sideslip angle of +15.7 degrees at 34 degrees angle of attack. The peak positive vertical fin bending moment occurs about 2 seconds later as the angle of attack passes through 58 degrees. At this point the wing and tail flow field break down completely into a wakelike flow. The angle of attack continues to increase to about 85 degrees and the oscillatory spin begins. The range of angles of attack during the spin is from 42 to 96 degrees and the range of sideslip angles from +24 to -24 degrees. Wing bending moment peaks occur during spin each time the angle of attack increases through 58 degrees. The negative peaks in vertical fin bending moment slightly precede the peaks in the wing bending moments and appear to be caused by inertia effects because they correspond to the minimums in the roll rate curve.

As with the previous example the magnitude of the wing and fin bending moments are small compared to design values because of the low dynamic pressure. It is apparent however, that the wing bending moments during the departure and subsequent spin decrease from the maximum measured during the rolling maneuver and thus would not produce a critical condition even if the event were to occur at high dynamic pressure. Excursions in sideslip of the magnitude occurring during the departure could produce vertical fin bending moments large enough to be considered in selecting loads design criteria.

#### Comparison Between Predicted and Measured Structural Loads

The limited flight test program completed on Aircraft A produced a significant amount of structural loads data which has been compared with predictions. Example comparisons are presented in Figures 10 and 11.

Balanced pitch maneuver analysis was performed using a digital computer procedure that statically balanced the aircraft at a given load factor. Trim angle of attack and horizontal tail deflection for 1g and total load factor are computed at each point in a large matrix of Mach-altitude conditions. A final balance of each condition is performed after summing all component loads and pitching moments. Shear unbalance is distributed between the wing and fuselage in proportion to their relative lift coefficients. The pitching moment unbalance is corrected by applying a sine wave to the fuselage.

Figure 10 presents comparisons of predicted values of wing bending moment, wing shear, wing torsion and horizontal tail bending moment from balanced pitch maneuver analyses for 1g and 6g with flight data. The predictions are based on a fixed gross weight representative of the test aircraft which is somewhat higher than the flight design gross weight. The flight data represent points obtained at equivalent values of the product of load factor and gross weight and have been normalized by design values. The comparisons for wing bending moment are good although some discrepancies exist at the higher supersonic speeds. The predicted wing shear is generally higher than flight values. The predicted wing torsional moment is lower than flight values at high load factor and supersonic speeds. The predicted horizontal tail bending moment is lower than flight values at high load factor at both subsonic and supersonic speeds. Despite the fact that wing torsion and horizontal tail bending moments are higher than predicted, the flight values are well below the design values which were determined primarily from theoretical analyses early in the design effort.

Analysis of structural design criteria dynamic maneuver response was conducted using a stability and flight control 5 degree of freedom flight simulation. The maneuver response parameters were then used for loads calculation in a separate loads computer procedure. The computer analyses included simulation of structural criteria rolling maneuvers sideslip maneuvers and abrupt pitching maneuvers. Figure 11 presents comparisons of predicted vertical fin bending moment during high load factor rolling pullouts with flight data for two altitudes. The agreement between predicted and flight values is only fair. The flight values are only a small fraction of the design values in this case because they do not represent design conditions.

While the prediction methods have produced "satisfactory" results from the loads engineers viewpoint in the sense that the design loads are generally conservative, it is apparent that improved methods would allow finer tuning of the structural design to reduce conservatism and therefore structural weight.

#### AIRCRAFT B MANEUVERS

Data obtained from two maneuvers performed during structural flight loads testing of Aircraft B are presented in this section. The maneuvers are slow windup turns at low wing sweep and at high wing sweep. These data are of interest because they illustrate the differences in dynamic structural response of the aircraft which occurred due to the differences in the fluctuating flow fields.

Detailed analyses of the structural response were performed during an investigation sponsored by the NASA Ames Research Center (Refs. 3, 4). Wind tunnel studies of the fluctuating flow fields were performed by Dennis Riddle of NASA (Ref. 5) and the wind tunnel fluctuating pressure data were used to predict the aircraft structural response (Ref. 6). Some additional results are presented here.

### Example of Windup Turn at Low Wing Sweep

Flight data from a slow windup turn of Aircraft B performed at 26 degrees sweep, 0.80 Mach number, and 20,000 feet altitude are presented in Figures 12 through 14.

Figure 12 shows time histories of pertinent flight parameters and wing bending and torsional moments measured at  $\eta = .238$  from the pivot along the 26 percent chordline. Buffet onset occurs at about 5.5 degrees angle of attack and above that angle the wing bending and torsional moments exhibit considerable dynamics. Twice during the maneuver a mild wing rock caused the automatic flight control system to input a small spoiler deflection on the right wing.

Stochastic analyses were performed at selected time intervals during this maneuver. Figure 13 presents power spectra for a 2 second data sample which starts at 18.5 seconds into the maneuver. Spectra for the torsional moments at  $\eta = 0.238$  and  $\eta = 0.835$  showed that peak power occurs at 25 hertz which is the frequency for the first torsional vibration mode of the wing. Spectra for wing bending moments at  $\eta = 0.835$  also exhibit a peak at 25 hertz although the frequency for the closest wing bending mode is about 28 hertz (second antisymmetric wing bending). Thus an apparent coupling between wing torsion and wing bending has occurred. This result led to an analysis of narrow band time histories in which the analog inputs were filtered to obtain the response in discrete bands of frequencies.

Figure 14 presents time histories in the band from 25 to 27 hertz for the same three sensors presented in Figure 13. In each case the gains on the playback instrumentation were adjusted to cover the full amplitude range of the strip chart recorder for the maximum value of the signal produced during the maneuver. The dominant frequency evaluated from these time histories and others in adjacent bands was 25 hertz. While the buildup and decay of structural response characteristic of random buffet is present there is also residual response over much of the maneuver which is more aptly described as a wing buzz.

G. F. Moss of the RAE has noted the buzz phenomenon at various combinations of Mach number and angle of attack for which shock induced separation is present in tests of wind tunnel models having flexible wings (Ref. 7). The large half-span model of Aircraft B used a very rigid wing in order to eliminate insofar as possible effects of wing motion on the fluctuating pressure field. Figures 15 through 18 present model data for  $M = 0.80$  and  $\alpha = 10.18$  degrees which is comparable to the flight data sample for which power spectra were shown earlier.

Figure 15 shows the wing upper surface static pressure distributions for five span stations. It is apparent that a significant area of the wing is subjected to shock-induced separation at this test condition. Figure 16 shows the distributions of rms values of fluctuating pressure coefficients. The maximum values occur at the middle spanwise measuring station. These distributions are not as detailed as those appearing in Reference 4. The outputs of three transducers covering a small range of chordwise locations have been combined electrically to produce each measured value because of limitations of readout capacity. This approach was considered satisfactory for use in the buffet response prediction method even though it does limit diagnosis of the detailed flow fields.

Figure 17 presents power spectra of the pressure fluctuations at the middle spanwise measurement station. The pressure spectra are consistent with those presented in Reference 4 both as to magnitude and frequency content. For this particular condition with significant shock-induced flow separation, large peaks in the pressure spectra occur at and aft of the shock wave in the frequency range near the model wing first torsion mode. The model does not have a natural vibration mode corresponding to the aircraft second antisymmetric wing bending mode.

Figure 18 shows the chordwise coherence of the pressure fluctuations for several combinations of chordwise locations. It is obvious that there is a strong correlation between the pressure fluctuations at various chordwise locations in the frequency range corresponding to the model first wing torsion mode.

Figure 19 presents comparisons of predicted wing structural responses and their characteristic frequencies compared to flight results for the windup turn at low wing sweep. The prediction method (Ref. 6) produces upper and lower bounds of possible response. The flight data for wing shear and wing bending moment lie well within the bounds established by the prediction method and the predicted characteristic frequencies are close to the flight values. Wing torsion, however, exceeds the predicted upper bound at the angles of attack where the wing buzz phenomenon is pronounced and the characteristic frequencies are much higher than predictions.

There are two probable reasons why the torsional moment predictions are not more accurate. First the method, at present, uses linear theory values of aerodynamic damping which do not predict the effects of the buzz phenomenon for which the net damping (aerodynamic plus structural) is obviously near zero. Second the possibility exists that the magnitudes and phasing of pressure fluctuations occurring on the flexible responding wing are significantly altered by the wing motion from the measurements obtained on the rigid half-span model wing. Model tests have recently been completed by NASA Ames Research Center (in which both rigid and flexible wings were instrumented to obtain fluctuating pressure measurements) which should provide definitive information for improving the prediction methodology.

#### Example of Windup Turn Maneuver at High Wing Sweep

One would expect the structural response for a high wing sweep configuration for which the aerodynamic flow field is dominated by leading edge vortices to be much different from the previous example for low wing sweep. It is much different. Figure 20 presents time histories from a slow windup turn maneuver of Aircraft B with the wings set at maximum sweep. It is obvious that the fluctuations of wing bending moment and torsional moment are much reduced from the previous example.

Corresponding half-span model wind tunnel data are presented in Figures 21 through 24. The upper surface static pressure distribution shown in Figure 21 illustrate the effects of leading-edge vortex flow. The peak negative pressure coefficients at each span station reflect the chordwise position of the primary vortex core. The dashed line in the figure connects these peaks. The primary vortex originates on the wing glove inboard of the variable sweep wing panel for the condition shown.

Figure 22 shows the distribution of fluctuating pressures. The maximum rms values of fluctuating pressure are small and occur near the chordwise location of the static pressure peaks, i.e., below the vortex core. Power spectra of the pressure fluctuations at the middle measurement station appear in Figure 23 for various chordwise locations and the corresponding plots of coherence between chordwise locations in Figure 24. The power spectra have a distinctive character in the form of a broad peak between frequencies of 50 and 100 hertz. The broad peak is characteristic of a leading edge vortex flow (Ref. 8). Small peaks at frequencies for each natural vibration mode of the model are superimposed on the broad peaks. The origin of the broad peak centered at 50 hertz in the lower surface data is not known. The values of coherence are relatively low except between 75 percent and 90 percent chord where the rms pressure levels are low so it is apparent that the structural responses would be small in magnitude.

Figure 25 presents comparisons between predicted and measured wing structural response for the high sweep windup turn. The measured wing shear and wing torsion lie near the predicted lower bound of possible response and there is good agreement between the predicted and measured characteristic frequencies. Measured wing bending moments lie near the middle of the predicted range of response. The measured characteristic frequencies are higher than prediction. This may be caused by the fact that the model data does not include the effects of a second antisymmetric wing bending mode which are prevalent in the flight data.

#### CONCLUDING REMARKS

Transient maneuvers and dynamic phenomena that result in rapid changes of aerodynamic load distributions can have a significant impact on design loads. The present capability to predict the effects of dynamic maneuvers on aerodynamic loads is reasonably good but there are exceptions where improvement is needed to reduce conservatism.

The ability to predict the effects of buffet on aircraft structural loads is fair to good, but improvements to the method are needed to account for nonlinear aerodynamic damping.

#### REFERENCES

1. W. J. McCroskey, "Recent Developments in Dynamic Stall," Paper included in Unsteady Aerodynamics, Vol 1, University of Arizona, July 1975, pp. 1-33.

2. J. P. Lamers, "YF-16 High Angle of Attack Flight Experience," Paper 25 presented at AGARD Flight Mechanics Panel Symposium, Brussels, Belgium, November 18-21, 1975
3. D. B. Benepe, et al, "A Detailed Investigation of Flight Buffeting Response at Subsonic and Transonic Speeds," AIAA Paper 74-358, presented to AIAA/ASME/SAE 15th Structures, Structural Dynamics and Materials Conference, Las Vegas, Nevada, April 17-19, 1974.
4. D. B. Benepe, et al, "Update on an Investigation of Flight Buffeting Response of a Variable Sweep Aircraft," AIAA Paper 75-68, presented to AIAA 13th Aerospace Sciences Meeting, Pasadena, California, January 20-22, 1975.
5. D. W. Riddle, "Wind Tunnel Investigation of Surface-Pressure Fluctuations Associated with Aircraft Buffet," AIAA Paper 75-67, Presented to AIAA 13th Aerospace Sciences Meeting, Pasadena, California, January 20-22, 1975.
6. A. M. Cunningham, Jr., et al, "Development and Evaluation of a New Method for Predicting Aircraft Buffet Response," AIAA Paper 75-69 presented to AIAA 13th Aerospace Sciences Meeting, Pasadena, California, January 20-22, 1975.
7. Personal Communication
8. D. A. Lovell and T. B. Owen, Low Speed Wind Tunnel Measurements of Surface Pressure Fluctuations on Two Slender-Wing Models, Aeronautical Research Council (Great Britain) Current Paper C.P. No. 1454, 1971.



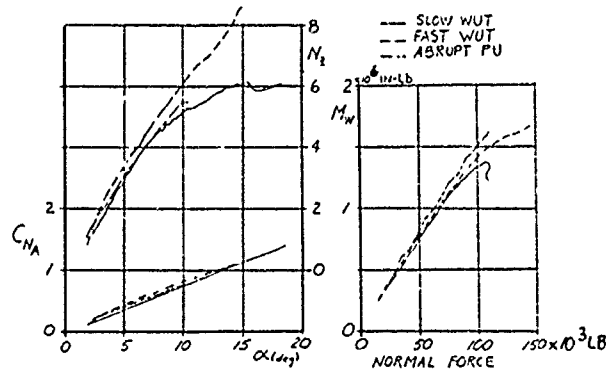


FIG. 1 COMPARISONS OF DATA FROM THREE MANEUVERS AIRCRAFT A SHOWING EFFECT OF PITCH RATE

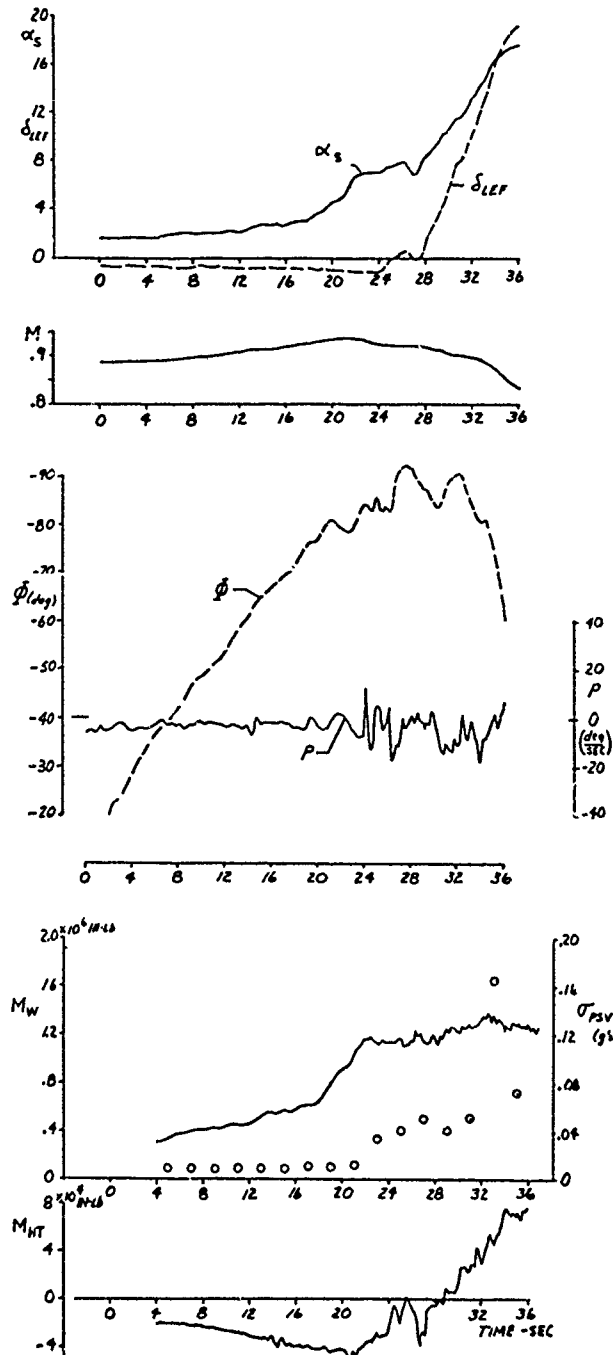


FIG. 2. TIME HISTORIES SHOWING WING ROCK - AIRCRAFT A

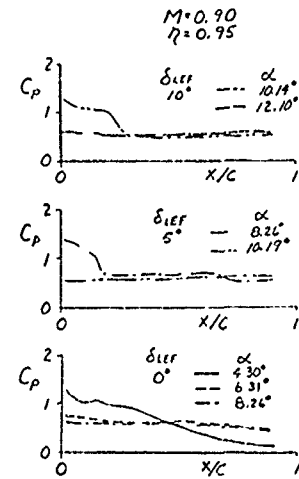


FIG. 3. MODEL UPPER SURFACE PRESSURE DISTRIBUTIONS NEAR WING TIP,  $M = 0.90$  - AIRCRAFT A

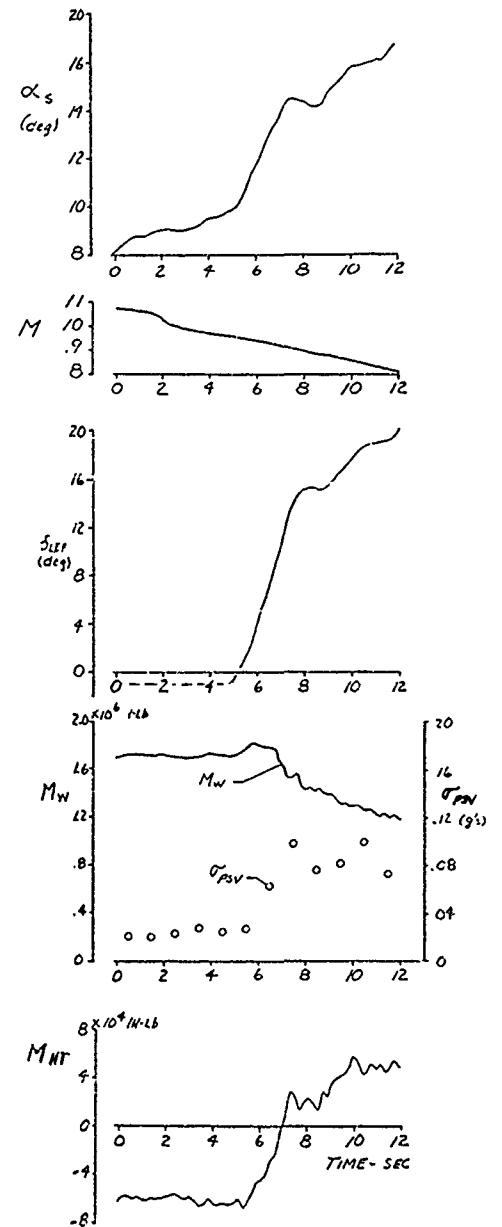


FIG. 4. TIME HISTORIES OF SLOWDOWN TURN - AIRCRAFT A

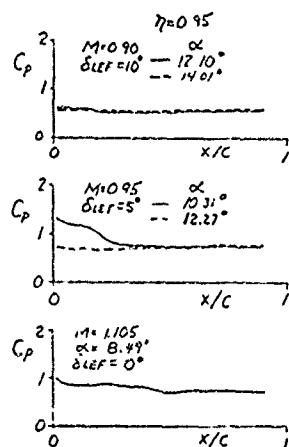


FIG. 5. MODEL UPPER SURFACE PRESSURE DISTRIBUTIONS NEAR WING TIP, VARIOUS MACH NUMBERS - AIRCRAFT A

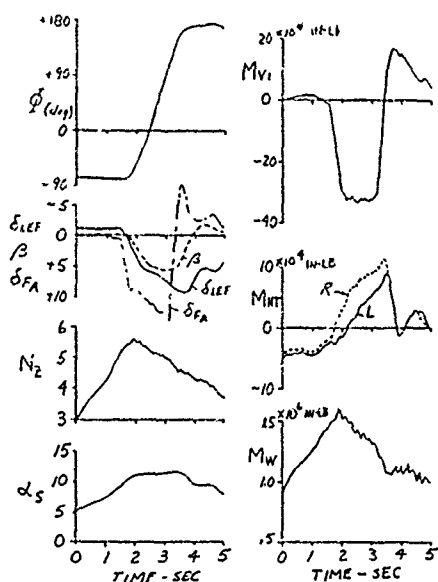


FIG. 6. TIME HISTORIES OF ROLLING PULLOUT - AIRCRAFT A

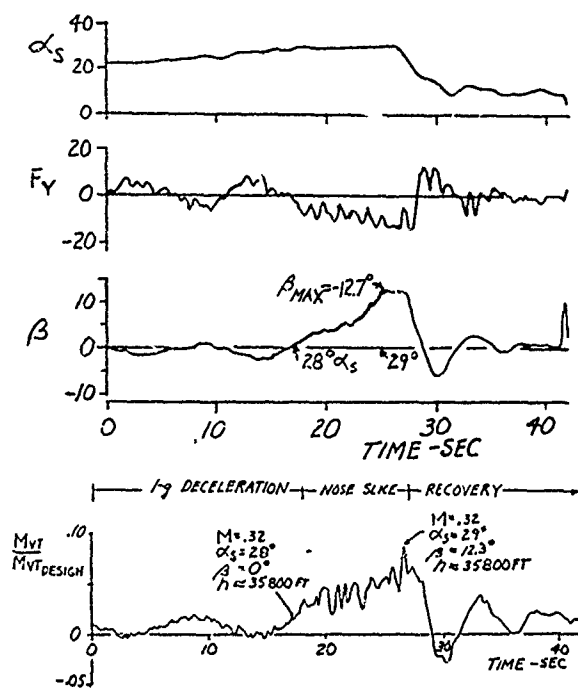


FIG. 7. EXAMPLE OF SLOW NOSE SLICE - AIRCRAFT A

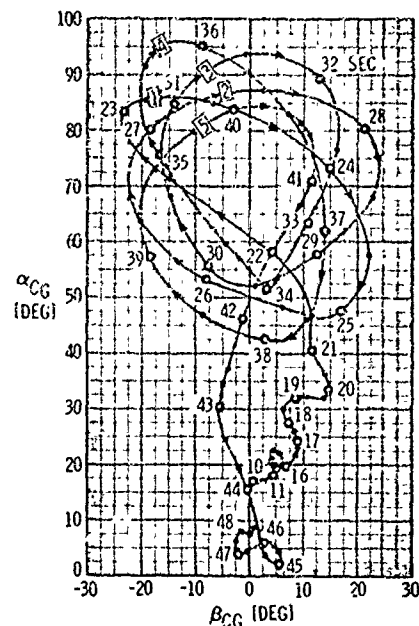


FIG. 8. TIME HISTORIES OF RUDDER ROLL, DEPARTURE AND SPIN - AIRCRAFT A

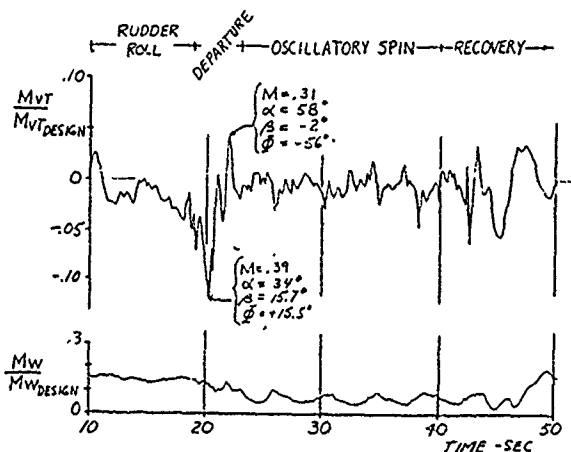


FIG. 9. VERTICAL FIN AND WING BENDING MOMENTS DURING RUDDER ROLL DEPARTURE AND SPIN - AIRCRAFT A

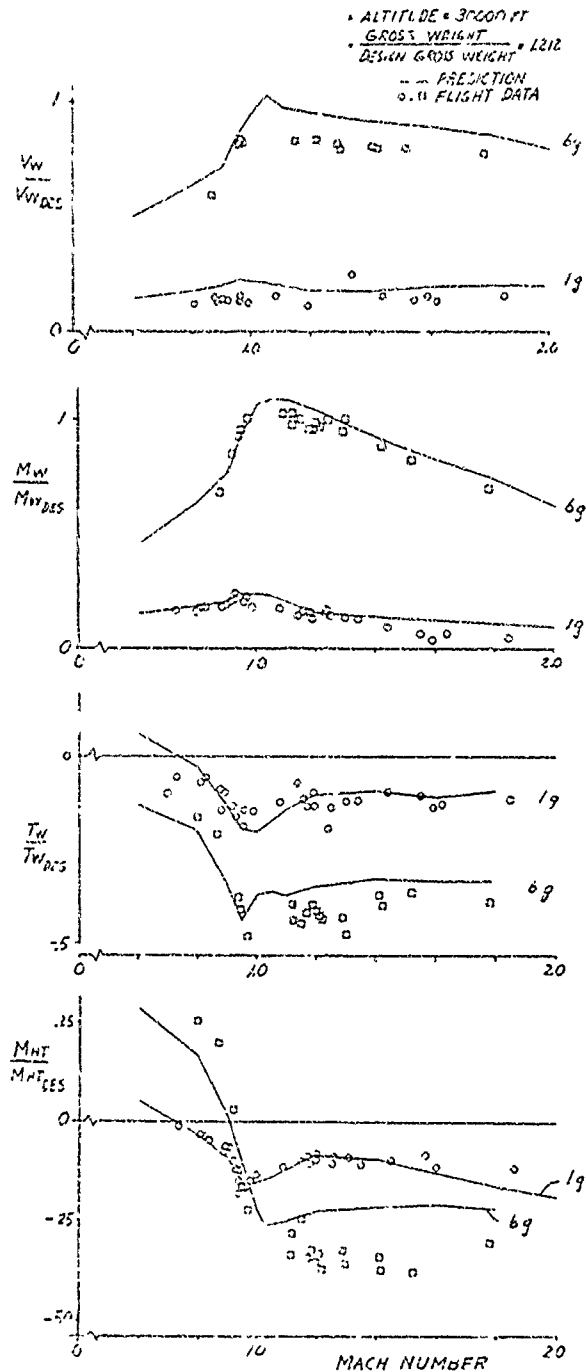


FIG. 10 COMPARISON OF PREDICTED STRUCTURAL LOADS WITH FLIGHT DATA FROM PITCH MANEUVERS - AIRCRAFT A

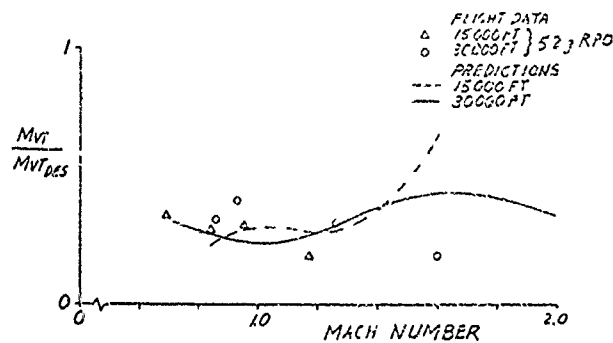


FIG. 11. COMPARISON OF PREDICTED VERTICAL FIN BENDING MOMENT WITH FLIGHT DATA FROM ROLLING PULLOUTS - AIRCRAFT A

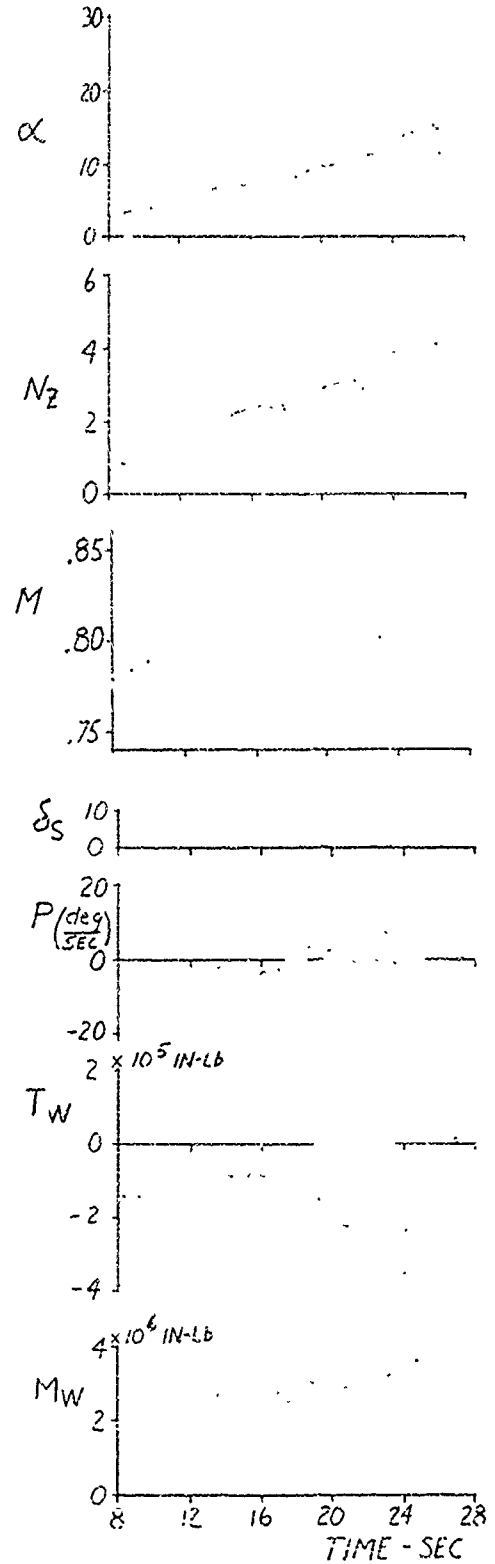


FIG. 12. TIME HISTORIES OF SLOW WINDUP TURN - AIRCRAFT B LOW WING SWEEP

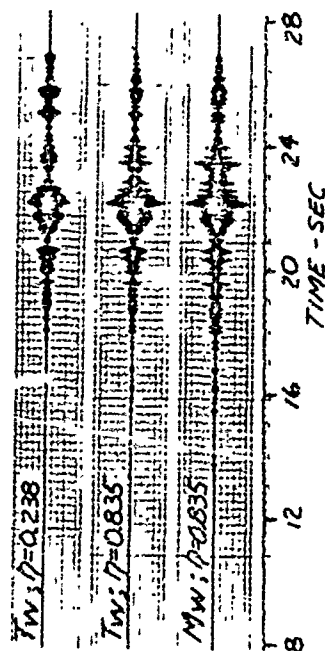


FIG. 14. NARROWBAND TIME HISTORIES OF WING BENDING AND TORSIONAL MOMENTS - AIRCRAFT B - LOW WING SWEEP

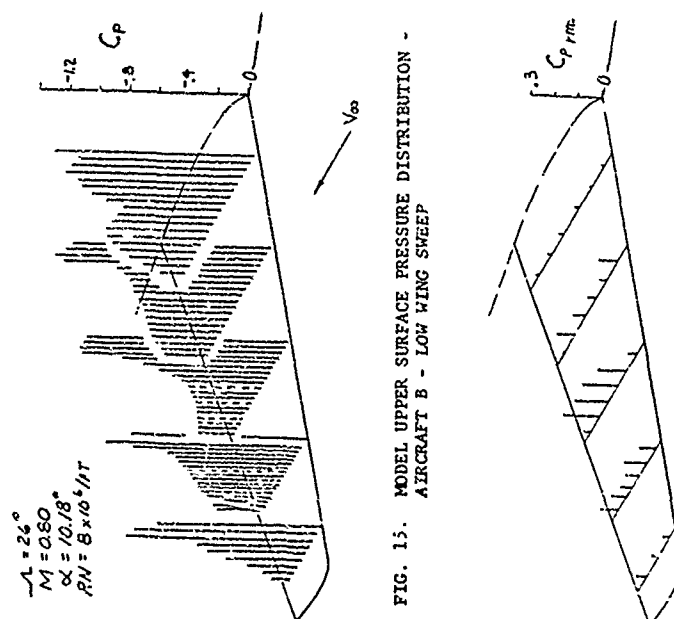


FIG. 15. MODEL UPPER SURFACE PRESSURE DISTRIBUTION - AIRCRAFT B - LOW WING SWEEP

FIG. 16. DISTRIBUTION OF MODEL UPPER SURFACE PRESSURE FLUCTUATIONS - AIRCRAFT B - LOW WING SWEEP

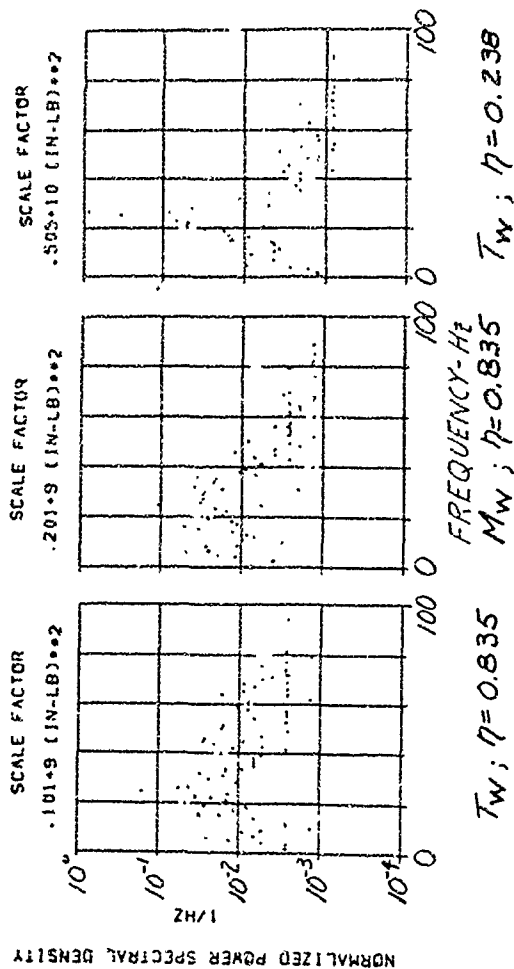


FIG. 17. MODEL PRESSURE SPECTRA AIRCRAFT B - LOW WING SWEEP

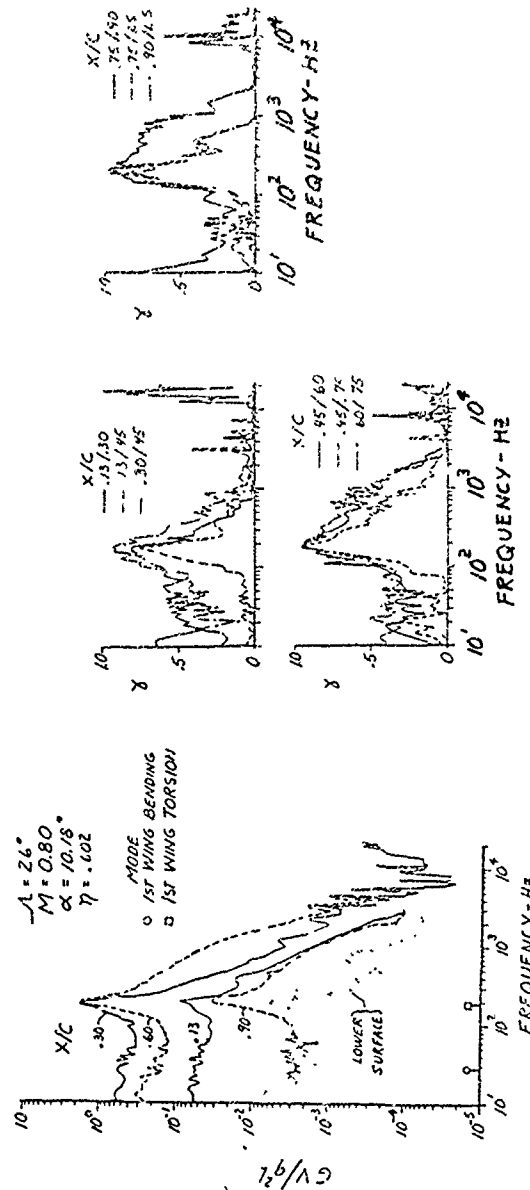


FIG. 18. COHERENCE OF MODEL PRESSURE FLUCTUATIONS - AIRCRAFT B - LOW WING SWEEP

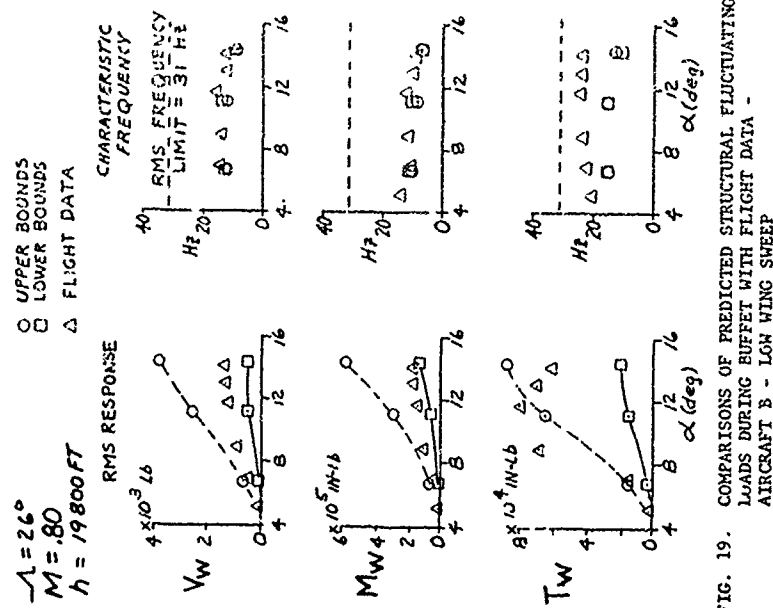


FIG. 19. COMPARISONS OF PREDICTED STRUCTURAL FLUCTUATING LOADS DURING BUFFET WITH FLIGHT DATA - AIRCRAFT B - LOW WING SWEEP

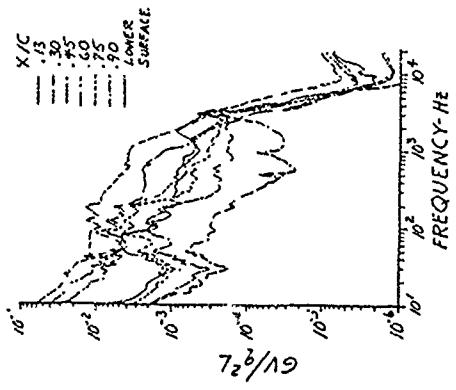


FIG. 23. MODEL PRESSURE SPECTRA - AIRCRAFT B - HIGH WING SWEEP

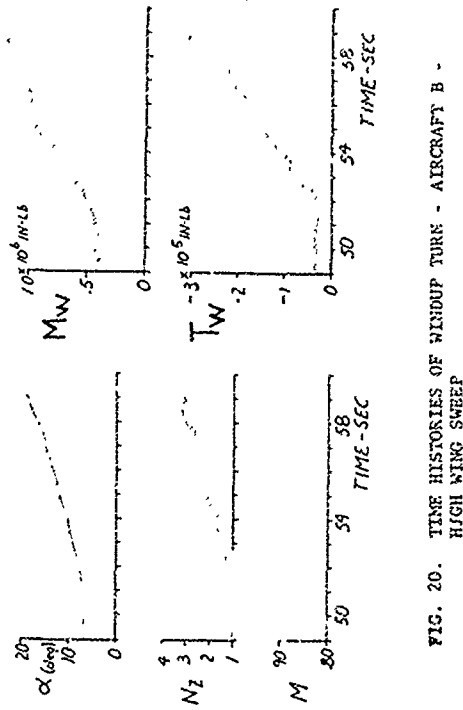


FIG. 20. TIME HISTORIES OF WINDUP TURN - AIRCRAFT B - HIGH WING SWEEP

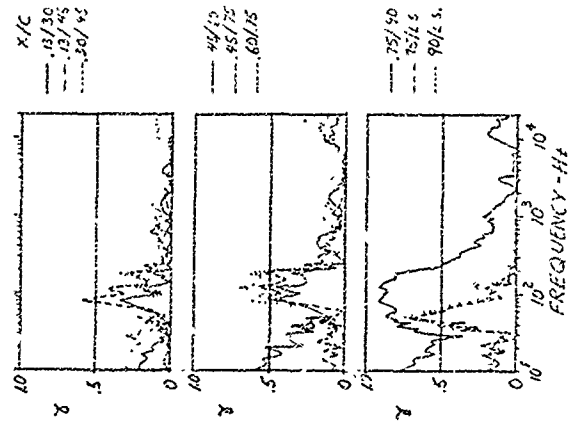


FIG. 24. COHERENCE OF MODEL PRESSURE FLUCTUATIONS - AIRCRAFT B - HIGH WING SWEEP

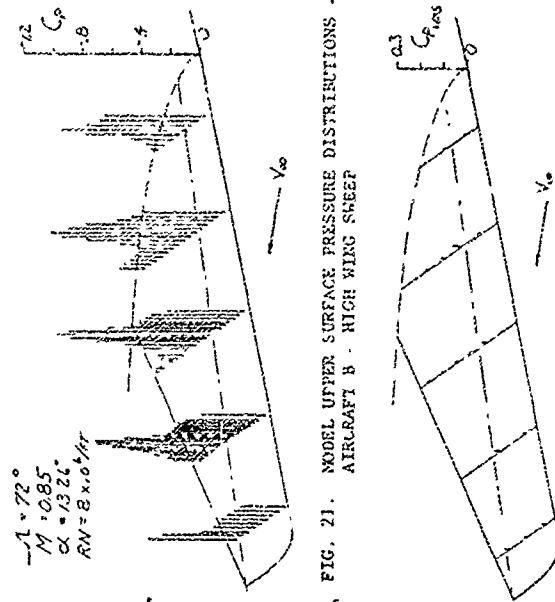


FIG. 21. MODEL UPPER SURFACE PRESSURE DISTRIBUTIONS - AIRCRAFT B - HIGH WING SWEEP

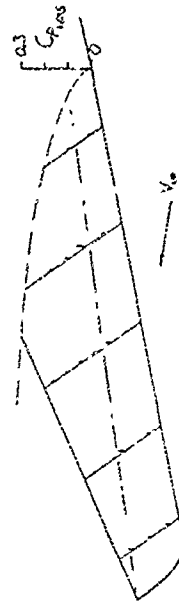


FIG. 22. DISTRIBUTION OF MODEL UPPER SURFACE FLUCTUATIONS - AIRCRAFT B - HIGH WING SWEEP

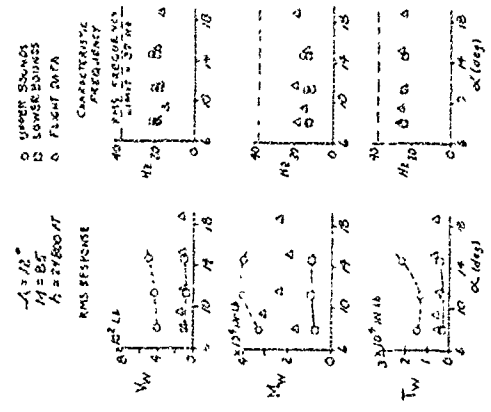


FIG. 25. COMPARISONS OF PREDICTED STRUCTURAL FLUCTUATING LOADS WITH FLIGHT DATA - AIRCRAFT B - HIGH WING SWEEP

THE THEORETICAL PREDICTION OF STEADY AND UNSTEADY AERODYNAMIC LOADING  
ON ARBITRARY BODIES IN SUPERSONIC FLOW

D. L. Woodcock  
Structures Department  
Royal Aircraft Establishment  
Farnborough, Hants  
England

# SUMMARY

A method is developed for the determination of the aerodynamic forces on arbitrary oscillating (and possibly deforming) bodies in linearised irrotational supersonic flow. Use is made of an approximation to the body by a many sided polyhedron. The problem is reformulated as an integral equation of the second kind and its solution is obtained by collocation at the centroids of a large number of regions arranged in bands round the body. The number of regions is much larger than the number of facets of the polyhedron. The steady perturbation potential on the body is obtained as a necessary intermediate result. From the calculated velocity potential the steady and oscillatory components of the loading distribution and the overall forces can be simply evaluated. The method is demonstrated by application to a fighter aircraft fuselage.

# LIST OF SYMBOLS

$C_0$	= $\cos KR$	$g$	mode of oscillation of facet
$C_1$	= $\sin KR/KR$	$l$	reference length defining streamwise spacing of $(\gamma, n)$ lattice
$F_{rs}^{(\tau)}$	see equation (2-9)	$p$	pressure
$G$	integer specifying boundary of $S_1$	$\rho_\infty \frac{v_L^2}{l} (p'_0 + \bar{p} e^{i\omega t})$	perturbation pressure
$K$	= $\omega l M / V \beta$	$t$	time
$L$	body reference length	$x, y, z$	basic coordinates
$M$	Mach number	$x_f, y_f, z_f$	facet coordinates
$P$	parameter in facet equation (equation (2-7))	$\Delta x, \Delta y$	dimensions of uncurtailed facet region
$R$	= $\sqrt{(X_0 - X)^2 + (Y_0 - Y)^2 + (Z_0 - Z)^2}$	$\beta$	= $\sqrt{M^2 - 1}$
$S$	area of body surface or facet inside forward Mach cone from $(X_0, Y_0, Z_0)$	$\gamma$	= $R^2/4$
$S_0$	area of $S$ where $\gamma < 0$	$\gamma_G$	value of $\gamma$ at boundary of $S_1$
$S_1$	area of $S$ where $0 < \gamma < \gamma_G$	$\gamma_{mn}$	see equation (3-13)
$S_2$	area of $S$ where $\gamma_G < \gamma$	$\epsilon$	width of cell of $(\gamma, n)$ lattice
$S_{rs}^{(\tau)}$	see equation (2-10)	$\eta$	= $Y_0 - Y$
$V$	airspeed	$\theta$	facet incidence in OXYZ reference frame
$W_0 + W \exp(i\omega t - iKMX)$	prescribed normal velocity at mean position of facet surface $\times \frac{\sqrt{\beta^2 + \tan^2 \theta} l}{\beta V l}$	$\nu$	distance along co-normal
$W_{mn}^{(s)}$	see equation (3-16)	$\xi$	= $X_0 - X$
$X, Y, Z$	transformed basic coordinates	$\bar{\xi}$	= $-\bar{Z} \tan \theta / (1 - \tan^2 \theta)$
$X_0, Y_0, Z_0$	$X, Y, Z$ coordinates of receiving point	$\rho_\infty$	air density in undisturbed stream
$X_f, Y_f, Z_f$	transformed facet coordinates	$VL\bar{\phi}$	total perturbation velocity potential
$\bar{Z} \cos \theta$	perpendicular distance in transformed coordinates from $(X_0, Y_0, Z_0)$ to facet	$VL\phi'_0$	steady perturbation velocity potential
		$VL\phi' \exp(i\omega t - iKMX)$	oscillatory perturbation velocity potential
		$\omega$	circular frequency

# 1 INTRODUCTION

The fuselages of aeroplanes, particularly those of the fighter type, are often far from being nice smooth cigar like objects. Yet, apart from slender body theory, supersonic theoretical analyses have been almost entirely confined to bodies of revolution in axisymmetric flow or slight perturbations thereto. It does, however, seem feasible to make an attempt to determine the forces (steady and unsteady) on an arbitrarily shaped fuselage on the basis of linearised potential flow theory. It may be argued that the assumptions of irrotational flow and a linear approximation to the field equation are inadequate when one gets away from the slender body of revolution in axisymmetric flow. No doubt, but even then linearised potential flow may give a fair approximation to the truth which could say be used as the basis of semi-empirical solutions. In the absence of anything better, for the general case, such a solution is believed to have some value.

It is common when solving the linearised potential flow equation to use in conjunction linear approximations to the boundary conditions and to the expression for the pressure (Bernoulli's equation). There is no great difficulty in avoiding these approximations and using more exact forms. It is believed there may be some value in adopting such an 'irrational' approach though how far one should go is questionable. The exact oscillatory boundary condition, for example - applied at the mean position of the body surface for small oscillatory displacements - involves second derivatives of the steady perturbation potential, and one has to ask have these been obtained with sufficient accuracy in the steady solution to merit their inclusion here. However, whatever approximation is taken to the boundary condition, once one has taken a linear approximation to the field equation, there is no question of having a nonlinear problem to solve for the exact boundary condition is linear in the velocity potential.

The supersonic field equation, being of hyperbolic type, naturally lends itself to a step-by-step solution moving aft over the body. One can express the velocity potential at a point as an integral of the velocity potential, its derivatives along the surface of the body, and the prescribed normal wash, over that part of the surface of the body which lies in the forward Mach cone from the point. This integral is simpler to evaluate if the body is a polyhedron provided the effect of the discontinuities at the junctions of the body's facets can be neglected. Such an assumption should be acceptable when the discontinuities have only been introduced artificially in the solution procedure. It is suggested therefore that an efficient method of solution for a body of largely arbitrary shape is to represent it by a many sided polyhedron, divide it streamwise into a large number of bands, and then determine by collocation the velocity potential at a set of points on each band starting at the nose.

## 2 THEORY

### 2.1 Basic equations

The perturbation velocity potential  $\tilde{\phi}$  is divided into a steady part and an oscillatory part of circular frequency  $\omega$  :-

$$\tilde{\phi} = \phi_0' + \phi' \exp \left\{ -\frac{i\omega M^2}{V_\infty^2} x + i\omega t \right\} \quad (2-1)$$

It follows, from the linearised field equation, that  $\phi'$  satisfies

$$-\phi_{XX}' + \phi_{YY}' + \phi_{ZZ}' = K^2 \phi' \quad (2-2)$$

where  $K = \omega M/V_\infty$ ; and XYZ are transformed coordinates given by

$$\left. \begin{aligned} x &= \ell \beta X \\ y &= \ell Y \\ z &= \ell Z \end{aligned} \right\} \quad (2-3)$$

The steady perturbation potential  $\phi_0'$  satisfies the same equation with  $K = 0$ .

It can then be shown, by application of the generalised Green's theorem that the perturbation potential at any point  $(X_0, Y_0, Z_0)$  in the field of flow is given by

$$2\pi\phi'(X_0, Y_0, Z_0) = \int_S \left\{ \phi' \frac{\partial}{\partial v} \left( \frac{\cos KR}{R} \right) - \frac{\partial \phi'}{\partial v} \frac{\cos KR}{R} \right\} dS \quad (2-4)$$

where the integration is over that part (S) of the surface of the body which is inside the forward Mach cone from  $(X_0, Y_0, Z_0)$ ,  $\frac{\partial}{\partial v}$  is the derivative with respect to the co-normal\* in the transformed coordinates, and

$$R^2 = (X_0 - X)^2 - (Y_0 - Y)^2 - (Z_0 - Z)^2 \quad (2-5)$$

The values of  $\phi'$  and  $\frac{\partial \phi'}{\partial v}$  in the integral in (2-4) are the values just above the surface of the body. It can in fact be shown that the solution of (2-4) has the form (cf. section 3.1)

$$\phi' = H(v)E(v) \quad (2-6)$$

where H is the Heaviside step function and E is a well behaved function. Thus the values of  $\phi'$  at  $v = +0$  are twice the values at  $v = 0$ . Moreover E(v) will be a solution of the differential equation (2-2) in a volume which extends through the surface of the body.

We want to solve (2-4) subject to given boundary conditions on S. S is taken to be at the mean position of the body surface. From the boundary conditions at the instantaneous position of the body surface equivalent conditions can in general be specified at the mean position using a Taylor expansion. This will be done everywhere though it is not valid in the vicinity of the nose of the body when it is not stationary. For small oscillations the errors thus introduced should only be local.

### 2.2 Facet form of equations

The body surface is considered to be made up of a series of flat facets, and we will now consider the contribution to  $\phi'(X_0, Y_0, Z_0)$  given by one facet. The frames of reference Oxyz, OXYZ are redefined for

\* If  $L', M', N'$  are the direction cosines of the outward drawn normal to the body surface, then  $-L', M', N'$  are the direction cosines of the co-normal.

each particular facet such that OY is parallel to the surface of the facet, OX is in the direction of the free stream, and OZ is outward into the fluid. The equation of the facet then is (see Fig.1)

$$Z + X \tan \theta = P \quad (2-7)$$

where P is a constant, and  $|\theta| < \frac{\pi}{2}$ .

It follows, from (2-4), that the contribution from this facet, to the perturbation potential is

$$2\pi\phi' = -\bar{z} \left\{ K^2 F_{11}^{(1)} + F_{03}^{(1)} \right\} - S_{01}^{(1)} \quad (2-8)$$

where  $\bar{z} \cos \theta$  is the perpendicular distance (in the transformed coordinates) from  $(X_0, Y_0, Z_0)$  to the facet, and\*

$$F_{rs}^{(\tau)} = \int_S \frac{C_r}{R^3} \phi' \tau dXdY \quad (2-9)$$

$$S_{rs}^{(\tau)} = \int_S \frac{C_r}{R^3} \left( \frac{\partial \phi'}{\partial Z} - \frac{\partial \phi'}{\partial X} \tan \theta \right) \tau dXdY \quad (2-10)$$

$$\left. \begin{aligned} C_0 &= \cos KR \\ C_1 &= \frac{\sin KR}{KR} \end{aligned} \right\} \quad (2-11)$$

Differentiating (2-8) we obtain the contributions, from the facet, to  $\frac{\partial \phi'}{\partial X_0}$ ,  $\frac{\partial \phi'}{\partial Y_0}$  and  $\frac{\partial \phi'}{\partial Z_0}$  to be:-

$$\begin{aligned} 2\pi \frac{\partial \phi'}{\partial X_0} &= \bar{z} \left\{ K^2 \left[ 3F_{13}^{(\xi)} - F_{03}^{(\xi)} \right] + 3F_{05}^{(\xi)} \right\} \\ &\quad - \tan \theta \left\{ K^2 F_{11}^{(1)} + F_{03}^{(1)} \right\} + K^2 S_{11}^{(\xi)} + S_{03}^{(\xi)} \end{aligned} \quad (2-12)$$

$$\begin{aligned} 2\pi \frac{\partial \phi'}{\partial Y_0} &= -\bar{z} \left\{ K^2 \left[ 3F_{13}^{(n)} - F_{03}^{(n)} \right] + 3F_{05}^{(n)} \right\} \\ &\quad - \left\{ K^2 S_{11}^{(n)} + S_{03}^{(n)} \right\} \end{aligned} \quad (2-13)$$

$$\begin{aligned} 2\pi \frac{\partial \phi'}{\partial Z_0} &= -\bar{z}^2 \left\{ K^2 \left[ 3F_{13}^{(1)} - F_{03}^{(1)} \right] + 3F_{05}^{(1)} \right\} \\ &\quad + \bar{z} \tan \theta \left\{ K^2 \left[ 3F_{13}^{(\xi)} - F_{03}^{(\xi)} \right] + 3F_{05}^{(\xi)} \right\} \\ &\quad - \bar{z} \left\{ K^2 S_{11}^{(1)} + S_{03}^{(1)} \right\} - \left\{ K^2 F_{11}^{(1)} + F_{03}^{(1)} \right\} \\ &\quad + \tan \theta \left\{ K^2 S_{11}^{(\xi)} + S_{03}^{(\xi)} \right\} \end{aligned} \quad (2-14)$$

When one is summing the contributions from all the facets to the first derivatives of  $\phi'$  one will of course have to resolve them along a common reference frame.

### 2.3 Boundary conditions

The boundary condition to be satisfied at the surface of the body is that the velocity of the fluid normal to the body surface in the physical coordinates shall be equal to the normal velocity of the surface. The surface of a facet is written as

$$z_f = Lg \left( \frac{x_f}{l}, \frac{y_f}{l} \right) e^{i\omega t} + \frac{L\beta P}{\sqrt{\beta^2 + \tan^2 \theta}} \quad (2-15)$$

where  $x_f, y_f, z_f$  are physical coordinates in a frame of reference fixed in the undisturbed position of the facet. It can then be shown that the boundary conditions to be satisfied by the steady and oscillatory perturbation velocity potentials are

\* As noted in section (2.1), the values of  $\phi'$  and its derivatives in the expressions for  $F_{rs}^{(\tau)}, S_{rs}^{(\tau)}$  are the values just above the surface of the facet.



$$\frac{\partial \phi'_0}{\partial Z} + \frac{\tan \theta}{\beta^2} \frac{\partial \phi'_0}{\partial X} = -\frac{\ell \tan \theta}{L\beta} = (\text{say}) W_0 \quad (2-16)$$

$$\text{at } Z = P - X \tan \theta + 0$$

and

$$\begin{aligned} \frac{\partial \phi'}{\partial Z} + \frac{\tan \theta}{\beta^2} \frac{\partial \phi'}{\partial X} - \frac{iKM \tan \theta}{\beta^2} \phi' \\ = e^{iKMx} \left[ \frac{iK}{M} \sqrt{\beta^2 + \tan^2 \theta} g + \left\{ 1 + \frac{L}{\ell \beta \cos \theta} \frac{\partial \phi'_0}{\partial X_f} \right\} \frac{\partial g}{\partial u} + \frac{\sqrt{\beta^2 + \tan^2 \theta}}{\ell \beta} \frac{\partial \phi'_0}{\partial Y_f} \frac{\partial g}{\partial v} \right. \\ \left. + \frac{L}{\ell \beta^3} \frac{(\beta^2 + \tan^2 \theta)^{\frac{3}{2}}}{(1 - \tan^2 \theta)} \left\{ \frac{\partial^2 \phi'_0}{\partial Y_f^2} - \frac{\beta^4 - \tan^2 \theta}{\cos^2 \theta (\beta^2 + \tan^2 \theta)^2} \frac{\partial^2 \phi'_0}{\partial X_f^2} \right\} \right] \\ = (\text{say}) W \end{aligned} \quad (2-17)$$

$$\text{at } Z = P - X \tan \theta + 0$$

where

$$(u, v) = \left( \frac{x_f}{\ell}, \frac{y_f}{\ell} \right) \quad (2-18)$$

and the frame of reference  $OX_f Y_f Z_f$  is obtained by rotating  $OXYZ$  through an angle  $\theta$  about  $OY$  so that the facet is  $Z_f = P \cos \theta$ . The boundary condition for the unsteady perturbation potential thus involves derivatives of the steady perturbation potential along the surface of the facet as well as the mode of oscillatory displacement.

#### 2.4 Determination of the velocity potential

Using the boundary condition (2-17) it is easily shown that, at  $Z_f = P \cos \theta +$ ,

$$\frac{\partial \phi'}{\partial Z} - \frac{\partial \phi'}{\partial X} \tan \theta = \frac{1}{\beta^2 + \tan^2 \theta} \left\{ -\frac{(1 + \beta^2) \tan \theta}{\cos \theta} \frac{\partial \phi'}{\partial X_f} + iKM \tan \theta (1 - \tan^2 \theta) \phi' + (1 - \tan^2 \theta) \beta^2 W \right\} \quad (2-19)$$

If this is substituted in (2-10) and the value of  $\phi'$  obtained by summing the contributions from all the facets as given by (2-8) we have in effect an integral equation of the form

$$\sum_S \int WK_3 dS = 2\pi \phi' - \sum_S \int \left\{ \phi' K_1 + \frac{\partial \phi'}{\partial X_f} K_2 \right\} dS \quad (2-20)$$

where  $K_1, K_2, K_3$  are known kernels and the summation is for all the facets of the body. Similarly, using (2-12), (2-13) and (2-14), we have

$$\sum_S \int WK_6 dS = 2\pi \frac{\partial \phi'}{\partial X_f} - \sum_S \int \left\{ \phi' K_4 + \frac{\partial \phi'}{\partial X_f} K_5 \right\} dS \quad (2-21)$$

where the kernels  $K_4, K_5, K_6$  now involve the orientation of the  $OX_f Y_f Z_f$  frame of reference used at the receiving point  $(X_0, Y_0, Z_0)$  as well as that of the transmitting facet.

The obvious approach is to solve the two integral equations, (2-20) and (2-21), simultaneously for  $\phi'$  and  $\frac{\partial \phi'}{\partial X_f}$  at the body surface. An alternative, which considerably reduces the amount of computation, in a collocation solution for a given number of points, at the expense of some loss in accuracy, is to use equation (2-20), with  $\frac{\partial \phi'}{\partial X_f}$  replaced by a finite difference approximation, and solve it for  $\phi'$  by collocation. The latter approach is the one which we will apply.

The steady perturbation potential  $\phi'_0$  is obtained from a similar equation to (2-20) with  $W$  replaced by  $W_0$  and  $K$  put equal to zero. It is necessary first to determine  $\phi'_0$ , so that  $W$  can be evaluated from (2-17), before proceeding to determine  $\phi'$ . The derivatives of  $\phi'_0$ , that appear in (2-17), can be obtained, from the calculated  $\phi'_0$ , either by finite difference approximations, or else by direct evaluation using equations such as (2-21). Again we will, in our subsequent application, use the finite difference approximations.

Applying (2-20) to determine the potential at a point in the surface of a facet, i.e. where  $Z_0 = P - X_0 \tan \theta$ , and then using the fact that the potential just above the facet is twice that in the facet, we have (see also (2-10))

$$\pi(\phi')_{+0} = -S_{01}^{(1)} - \sum' \left[ \bar{z} \left\{ K^2 F_{11}^{(1)} + F_{03}^{(1)} \right\} + S_{01}^{(1)} \right] \quad (2-22)$$

where the first term is for the current facet (and so  $\bar{z} = 0$ ) and the summation is over all the other facets. The solution procedure uses this equation in the following manner.

The body is first of all divided up into a series of bands by equally spaced planes normal to the free stream direction. Each facet is then further divided by a set of lines parallel to  $OX_f$ . Thus each facet is divided up into a set of mainly rectangular regions. The centroids of these regions are taken as collocation points\*. The integrals  $F_{rs}^{(1)}$ ,  $S_{rs}^{(1)}$  in (2-22) are determined as weighted sums (see section 3.2) of the values of  $\phi'$ ,  $\frac{\partial \phi'}{\partial X_f}$  and  $W$  at these collocation points. The approximation for  $\frac{\partial \phi'}{\partial X_f}$  at a collocation point involves in general just the values of  $\phi'$  at that point and at the collocation point immediately in front of it on the same facet. When there is not such a point a slightly more complicated approximation is used involving  $\phi'$  at several collocation points on a preceding facet. Thus for a particular collocation point as the receiving point  $\phi'$  is expressed as a weighted sum of the values of  $\phi'$  and  $W$  at the collocation points on the same band and on the bands in front of it. We have therefore for each band a set of simultaneous equations which can be solved for  $\phi'$  at the collocation points on that band provided the preceding bands have already been solved. One starts therefore from the nose of body and proceeds backwards band by band.

## 2.5 Determination of the pressure

We write the pressure as

$$p = p_\infty + \rho_\infty \frac{V^2 L}{\ell} \left( p'_0 + \bar{p} e^{i\omega t} \right) \quad (2-23)$$

It follows from Bernoulli's equation that

$$p'_0 \approx -\frac{1}{\beta} \frac{\partial \phi'_0}{\partial X} + \frac{L}{2\ell} \left\{ \left( \frac{\partial \phi'_0}{\partial X} \right)^2 - \left( \frac{\partial \phi'_0}{\partial Y} \right)^2 - \left( \frac{\partial \phi'_0}{\partial Z} \right)^2 \right\} \quad (2-24)$$

which can be alternatively written, for a point at the body surface, in terms of just the derivatives along the surface by making use of the boundary condition (2-16):-

$$\begin{aligned} (p'_0)_{+0} \approx & \frac{1}{(\beta^2 + \tan^2 \theta)^2} \left[ \left\{ \frac{\ell}{2L} \tan^2 \theta - \frac{\beta}{\cos \theta} \frac{\partial \phi'_0}{\partial X_f} \right\} \left\{ \beta^2 + (2 + \beta^2) \tan^2 \theta \right\} \right. \\ & \left. + \frac{L}{2\ell} \left\{ \frac{\beta^4 - \tan^2 \theta}{\cos^2 \theta} \left( \frac{\partial \phi'_0}{\partial X_f} \right)^2 - (\beta^2 + \tan^2 \theta)^2 \left( \frac{\partial \phi'_0}{\partial Y_f} \right)^2 \right\} \right] \quad (2-25) \end{aligned}$$

It is consistent to neglect terms of  $O(\tan^3 \theta)$ , etc., since we are neglecting  $\left( \frac{\partial \phi'_0}{\partial X} \right)^3$ . Consequently the approximation to  $(p'_0)_{+0}$  becomes

$$(p'_0)_{+0} \approx \frac{\ell}{2L} \frac{\tan^2 \theta}{\beta^2} - \frac{1}{\beta} \frac{\partial \phi'_0}{\partial X_f} + \frac{L}{2\ell} \left\{ \left( \frac{\partial \phi'_0}{\partial X_f} \right)^2 - \left( \frac{\partial \phi'_0}{\partial Y_f} \right)^2 \right\} \quad (2-26)$$

The unsteady part,  $\bar{p}$ , of the pressure will be required at the instantaneous position of the body surface. Expressing this in terms of the values of the velocity potential at the mean position gives, neglecting terms of  $O(\phi'^2)$ , it as  $\rho_\infty V^2 (L/2\ell) (p')_{i+} e^{i\omega t}$ , where

$$(p')_{i+} \approx e^{-iKMX} \left\{ -\frac{1}{\beta} \frac{\partial \phi'}{\partial X_f} + \frac{iK}{M\beta} \phi' + \frac{L}{\ell} \left( \frac{\partial \phi'_0}{\partial X_f} \frac{\partial \phi'}{\partial X_f} - \frac{\partial \phi'_0}{\partial Y_f} \frac{\partial \phi'}{\partial Y_f} \right) \right\} \quad (2-27)$$

This expression assumes the only oscillatory displacement of the facet is normal to its surface. If in addition there are displacements of semi-amplitude  $L_e$  and  $L_f$  in the directions  $Ox_f$ ,  $Oy_f$  then, to the same order of approximation we have to add

\* To be exact the collocation points are points almost coincident with the centroids but just outside the body (i.e. just above the facet).

$$- \frac{L}{Z} \left\{ \frac{1}{\beta^2} \frac{\partial \phi_0'}{\partial X_f^2} e + \frac{1}{\beta} \frac{\partial \phi_0'}{\partial X_f \partial Y_f} f \right\}$$

to the right-hand side of (2-27).

### 3 APPLICATION

#### 3.1 The integrals $F_{rs}^{(1)}$

The integrals  $F_{rs}^{(1)}$  (cf. equation (2-9)) are given by

$$F_{rs}^{(1)} = \int_S \frac{C_r}{R^s} \phi' dX dY \quad (3-1)$$

where  $S$  is the region common to the facet and the forward Mach cone from the receiving point  $(X_0, Y_0, Z_0)$  under consideration. For  $s = 3$  or  $5$ , *inter alia*, these are improper integrals which we interpret in the finite part sense (see for example Ref.1, p.31-2). It is convenient to make the coordinate transformation

$$\eta = Y_0 - Y \quad (3-2)$$

$$\gamma = \frac{R^2}{4} = \frac{1}{4} \left\{ (X_0 - X)^2 - (Y_0 - Y)^2 - [\bar{Z} - (X_0 - X) \tan \theta]^2 \right\} \quad (3-3)$$

and so, from (3-1),

$$F_{rs}^{(1)} = \frac{1}{2^{s-1} \sqrt{1 - \tan^2 \theta}} \iint_S \frac{C_r \phi' d\gamma d\eta}{\gamma^{s/2} \sqrt{\eta^2 + 4\gamma + \bar{Z}^2/(1 - \tan^2 \theta)}} \quad (3-4)$$

Note that it is assumed that  $\tan^2 \theta < 1$ , which implies that the direction  $OX_f$  for the particular facet under consideration, is subsonic.

It is shown in Appendix 1 that the following expression holds for the one improper integral  $(F_{03}^{(1)})$  which we require for the use of equation (2-8)

$$F_{03}^{(1)} = \tau \left\{ -\frac{1}{|\bar{Z}|} \phi' - \frac{\tan \theta}{1 - \tan^2 \theta} \operatorname{sgn}(\bar{Z}) \left( \frac{\partial \phi'}{\partial X} - \frac{\partial \phi'}{\partial Z} \tan \theta \right) + O(\bar{Z}) \right\} + F_{03}^{(1)}(0) \quad (3-5)$$

In this equation the value of  $\phi'$  and its derivatives are the values at  $(X, Y, Z) = (X_0, Y_0, P - X_0 \tan \theta + 0)$ . Use of (3-5) in (2-8) enables us to determine the relationship between the values of  $\phi'$  immediately above, in, and immediately below the surface of a facet - the contributions from all the other facets will be the same in each case. One finds, as stated in section 2.2, that

$$\left. \begin{aligned} (\phi')_{+0} &= 2(\phi')_0 \\ (\phi')_{-0} &= 0 \end{aligned} \right\} \quad (3-6)$$

Similar relationships have been obtained for  $\frac{\partial \phi'}{\partial Z}$  and no doubt could be for the higher derivatives. We infer therefore, making use of the Taylor expansion in the region of positive  $\bar{Z}$ , that

$$\phi'(X_0, Y_0, Z_0) = \{1 + \operatorname{sgn}(\bar{Z})\} \left\{ (\phi')_0 + \bar{Z} \left( \frac{\partial \phi'}{\partial Z} \right)_0 + \dots \right\} \quad (3-7)$$

If we are to be able to differentiate this equation and get results consistent with the relationships mentioned above  $\left( \left( \frac{\partial \phi'}{\partial Z} \right)_{+0} = 2 \left( \frac{\partial \phi'}{\partial Z} \right)_0 \right.$ , etc.) it seems that we must understand  $\frac{\partial \phi'}{\partial Z}$ ,  $\frac{\partial^2 \phi'}{\partial Z^2}$  etc. to be generalised functions which are indeterminate in that they contain an arbitrary constant  $\times \delta(\bar{Z})$ . There is a precedent for this in the symbol  $|x|^{-1}$  which is understood (Ref.1, p.39) to represent any generalised function  $f(x)$  which satisfies the equation

$$xf(x) = \operatorname{sgn}(x) \quad (3-8)$$

and so will contain the same sort of arbitrary term.

### 3.2 Approximation to the $F_{rs}^{(1)}$ as weighted sums

For the evaluation of the, sometimes improper, integrals  $F_{rs}^{(1)}$  (equation (3.4)), and the similar integrals  $S_{rs}^{(1)}$ , the facet under consideration is first divided into three parts (cf. Fig.2):-

$$\begin{cases} S_0 & \text{where } \gamma < 0 \\ S_1 & \text{where } 0 < \gamma < \gamma_G \\ S_2 & \text{where } \gamma_G < \gamma \end{cases}$$

$$\text{where } 4\gamma_G = \left( G + \sqrt{n^2 + \bar{z}^2 / (1 - \tan^2 \theta)} \right)^2 - \{ n^2 + \bar{z}^2 / (1 - \tan^2 \theta) \} \quad (3-9)$$

and  $G$  is a chosen positive integer.

There will be no contribution to  $F_{rs}^{(1)}$  from the area  $S_0$  since the region of integration  $S$  is that part of the facet where  $\gamma$  is positive. The parameter  $G$  is chosen to be large enough for a crude method of integration to suffice in the area  $S_2$ . We mentioned above (section 2.4) that each facet was divided up into a set of mainly rectangular regions whose centroids were used as collocation points for  $\phi'$ . In the area common to such a region and  $S_2$  it is assumed that the whole integrand is linear in  $X$  and  $Y$ . Thus the contribution to  $F_{rs}^{(1)}$  from the area  $S_2$  will (cf. equation (3-1)) be

$$\left( F_{rs}^{(1)} \right)_2 = \sum_j \left( \frac{C_{r\phi'}}{R^s} \right)_{\text{at centroid of common area } j} A_j \cos \theta \quad (3-10)$$

where  $A_j$  is the area of the common area which we denote by  $j$  that

$$\sum_j A_j \cos \theta = \int_{S_2} dX dY \quad (3-11)$$

The value of  $\phi'$  at the centroid of  $j$  is obtained by linear interpolation in  $X$  between its values at the centroids, of the region containing the common area  $j$ , and of the region in front of that region.

In the area  $S_1$  a less simple method of integration has to be used.  $S_1$  is divided into a set of cells by a fine  $(\gamma, n)$  lattice chosen such that the  $m$ n cell is bounded by (see Fig.2)

$$\left. \begin{aligned} \gamma &= \gamma_{mn}, \gamma_{m+1, n} \\ \frac{n}{\epsilon} &= n - \frac{1}{2}, n + \frac{1}{2} \end{aligned} \right\} \quad (3-12)$$

$$\text{where } 4\gamma_{mn} = \left( m + \sqrt{n^2 \epsilon^2 + \bar{z}^2 / (1 - \tan^2 \theta)} \right)^2 - \{ n^2 \epsilon^2 + \bar{z}^2 / (1 - \tan^2 \theta) \} \quad (3-13)$$

With this choice of  $\gamma_{mn}$

$$X(\gamma_{m+1, n}, n\epsilon) - X(\gamma_{mn}, n\epsilon) = 1 / \sqrt{1 - \tan^2 \theta} \quad (3-14)$$

This lattice will be different for each different receiving point  $(X_0, Y_0, Z_0)$  as, of course, will be the area  $S_1$ . Since  $\gamma_{Gn} = \gamma_G$  only at the point  $n = n_G$ , the lattice will not fit the upper boundary of  $S_1$  exactly nor will it fit the region and facet boundaries exactly. However, provided the lattice is fine enough any errors so caused should be negligible.

In each of these cells  $C_{r\phi'}$  is assumed constant, having the value appropriate to the point  $(\gamma, n) = (\gamma_{mn}, n\epsilon)$ . At this point  $\phi'$  is obtained by linear interpolation in  $X$  between its values at the collocation points in a similar manner to that used in  $S_2$ . Thus the contribution to  $F_{rs}^{(1)}$  from the area  $S_1$  can be written as

$$\left( F_{rs}^{(1)} \right)_1 = \frac{1}{2^{s-1} \sqrt{1 - \tan^2 \theta}} \sum_m \sum_n (C_{r\phi'})_{mn} W_{mn}^{(s)} \quad (3-15)$$

where

$$w_{mn}^{(s)} = \frac{(n+1)\epsilon}{(n-1)\epsilon} \int_{Y_{mn}}^{Y_{m+1,n}} d\eta \int \frac{dy}{Y^{s/2} \sqrt{\eta^2 + 4\epsilon^2} \sqrt{1 - \tan^2 \theta}} \quad (3-16)$$

Formulas for the determination of these integrals are given in Appendix 2.

Thus by the use of (2-10) and (3-15) we have expressed  $F_{rs}^{(1)}$  as a weighted sum of the values of  $\phi'$  at the collocation points (centroids of the facet regions) which lie inside or just outside the forward Mach cone from the receiving point  $(X_0, Y_0, Z_0)$ .

### 3.3 Choice of parameters

For a given polyhedron body the accuracy of the solution that is obtained will depend on the choice of a number of parameters that have been introduced. In the first place there is the specification of the size of the regions, of the facets, whose centroids are taken as the collocation points. The bandwidth  $\Delta x$  is taken to be constant and so the length of each region in the free stream direction will in general be also  $\Delta x$  except in so far as facet boundaries may introduce some curtailment. The standard region width  $\Delta y$  could be specified independently but, in the absence of any good reason to the contrary, it is suggested that one should make  $\Delta y = \beta \Delta x$  (thus making  $\Delta Y = \Delta X$ ). The facet boundaries will of course reduce the width of some regions. Alternatively one could also insist that any intersection of a band and facet is divided into at least, say, three regions, and reduce  $\Delta y$  locally to achieve this. Such an additional condition may enable one to manage with a larger value of  $\Delta x$  than would otherwise be the case.

In the second place there are the parameters which determine the accuracy with which the integrals  $F_{rs}^{(1)}$ ,  $S_{rs}^{(1)}$  are evaluated. These are:-

- (i)  $G$  which defines the boundary between the areas where the different methods of integration are used (cf. section 3.2).
- (ii)  $\ell$  and  $\epsilon$  which specify the cell size of the lattice used in the integration procedure for the area  $S_1$ , i.e. for the area adjacent to the surface of the forward Mach cone from the receiving point (cf. section 3.2 and equation (2-3)). The mean  $(X, Y)$  dimensions of each cell are  $(1/\sqrt{1 - \tan^2 \theta}, \epsilon)$ ; which in the  $(x, y)$  coordinates are  $(\ell \beta / \sqrt{1 - \tan^2 \theta}, \ell \epsilon)$  (see equations (3-14) and (2-3)).

Errors in the integrals can be ascribed to three possible causes - the finiteness of the lattice, the dislocation between the boundaries of the area  $S_1$  and the lattice boundaries (cf. Fig.2), and the use of the cruder method of integration for the area  $S_2$ . These can be reduced respectively by the reduction of  $\ell$  and/or  $\ell \epsilon$ , the reduction of  $\ell \epsilon$  and/or  $\ell$  and/or  $\frac{\ell \epsilon}{G}$ , and the increase of  $\ell G$ , where the most effective parameter is believed to be that mentioned first in each case.

## 4 RESULTS

### 4.1 Configuration

Once one departs from the body of revolution one finds an extreme paucity of theoretical estimates of the forces on bodies in supersonic flow. There is therefore virtually no opportunity of assessing the value of this method by comparison with others. The first application was not unexpectedly to the simplest body of revolution the right circular cone. Representing it as an eight sided (excluding base) regular pyramid in the present method gave satisfactory agreement<sup>2</sup> with the analytical results at zero and small incidences.

For the present meeting it is however, no doubt more interesting to consider more practical shapes and so the results to be described are for the fuselage of a fighter aircraft and in particular for the front part of the fuselage. Its representation as a many sided polyhedron is shown in Fig.3. The results described are for it at an incidence of 0.1 radian, that is the line joining the vertices 1 and 27 on Fig.3 is at that incidence.

### 4.2 Steady calculations

Calculations were made for various values of the parameters mentioned in section 3.3 above. Initial studies for the nose of the fuselage, i.e. the first five facets on port and starboard sides, were used to establish values which would ensure adequate accuracy in the evaluation of the integrals  $F_{rs}^{(1)}$ ,  $S_{rs}^{(1)}$ .

As a result the following values were taken for calculations on the complete fuselage

$$\begin{aligned} \ell &= 825/L \\ \epsilon &= 0.066 \\ G &\geq 15 \end{aligned}$$

where the reference length  $L = 700$ , this being of the order of the length of the fuselage in the units used\*.

\* The distance from vertex 1 to vertex 27 is actually 600 units.

The steady perturbation potential  $\phi_0$  was calculated for the fuselage at an incidence of 0.1 radian at a Mach number = 1.22475 (which gave  $\beta z = 0.6$ ). These calculations were made with  $\Delta x = 5$  and consequently over 1000 collocation points on each half of the fuselage. Of the whole mass of results the calculated potential on two adjacent facets is illustrated, as a typical example, in Figs. 4 and 5. Also shown on these figures are some values obtained when using a much larger value of  $\Delta x$  ( $\approx 30$ ). The facets chosen are facet 9, the back side of the canopy, and facet 8, the adjacent part of the fuselage (cf. Fig. 3). In each case the values plotted are the potential at points on the median line from the sharp end of the facet, obtained by interpolation where necessary. It will be noted that there is some scatter in the calculated values, and this was found to be particularly noticeable at points where there was a change in the number of collocation points per facet per band. On each of the two facets in question there were either one or two collocation points on each band.

#### 4.3 Oscillatory calculations

Calculations of the oscillatory perturbation velocity potential were made for small oscillations in the rigid body modes of heave, pitch, yaw and roll. The computer program caters for much more complicated modes, which can be specified either as overall polynomial modes or as polynomial modes of the individual facets, but for the purpose of demonstrating the method the rigid body modes are just as instructive.

The unsteady calculation, as programmed, uses a considerable amount of output from the steady calculation (in the boundary condition (2.17) for example, and in particular the calculated values of the coefficients  $W(s)$  (3.16)). Computing efficiency has been gained at the expense of considerable storage problems with the result that for the fuselage being considered it was not practicable to do the unsteady calculation with anything like the same number of collocation points as had been used in the steady case. Results were obtained using a value of  $\Delta x = 30$ . As shown on Figs. 4 and 5 the steady potential then obtained agreed reasonably well with that determined with  $\Delta x = 5$ . For the roll mode the oscillatory potential was, as one would expect, extremely small. With the heave mode it was also small for the frequencies investigated ( $\omega L/V = 0.1, 0.2$ ). A selection of the results for the other two modes is shown in Figs. 6 and 7. These show the modulus of the oscillatory potential on the same two facets. The difference between the calculated values for the two different frequencies was too small to show. Slightly more variation with frequency was found in the phase of the oscillatory potential, but this is not illustrated because in each case - for each of these two facets and each mode - it was practically the same linear variation with frequency; going from  $-\pi$ , at  $\omega L/V = 0$ , to  $-2.90$  radians, at  $\omega L/V = 0.2$ , at the rear of the facet. At the front of these facets the phase variation was rather less.

#### 5 Conclusions

A step-by-step collocation method has been developed for the determination of the forces on a stationary or oscillating body of arbitrary shape (with certain limitations) in linearised supersonic potential flow. Apart from providing a means of solution for the isolated body, it also has potential for combination, with methods of a similar type for lifting surfaces, to provide a method that can be applied to the complete aircraft. For many purposes however one can treat a non-isolated body as if it were isolated. For example in wing-store flutter problems it is usually sufficiently accurate to neglect aerodynamic interference effects between the wing and the store.

## Appendix 1

BEHAVIOUR OF THE INTEGRAL  $F_{rs}^{(\tau)}$  AS  $\bar{Z} \rightarrow 0$ We can write (cf. equation (3-4)), assuming the surface  $\gamma = 0$  cuts the facet\*

$$F_{rs}^{(1)} = \frac{1}{2^{s-1} \sqrt{1 - \tan^2 \theta}} \int_0^{\gamma_0(\bar{Z})} \frac{C_r d\gamma}{\gamma^{s/2}} \int_{-\infty}^{\infty} \frac{\phi' d\eta}{\sqrt{\eta^2 + 4\gamma + \bar{Z}^2/(1 - \tan^2 \theta)}} \quad (A-1)$$

where  $\phi'$  is taken to be zero off the facet and

$$\left. \begin{aligned} C_0 &= \cos \{2K\sqrt{\gamma}\} \\ C_1 &= \frac{\sin \{2K\sqrt{\gamma}\}}{2K\sqrt{\gamma}} \end{aligned} \right\} \quad (A-2)$$

Denote the inner integral by  $F(\gamma)$ , i.e.

$$F(\gamma) = \int_{-\infty}^{\infty} \frac{\phi' d\eta}{\sqrt{\eta^2 + 4\gamma + \bar{Z}^2/(1 - \tan^2 \theta)}} \quad (A-3)$$

Then this function can be considered to be well behaved throughout the range of integration. Kinks in the boundary of the facet will invalidate this but they will be of no consequence for our purpose and will therefore be ignored. The functions  $C_r$  (equation (A-2)) can be expanded as power series in  $(K^2\gamma)$ . Consequently we can write

$$F_{rs}^{(1)} = \frac{1}{2^{s-1} \sqrt{1 - \tan^2 \theta}} \sum_{j=0}^{\infty} b_j^{(r)} K^{2j} \int_0^{\gamma_0} \frac{F(\gamma) d\gamma}{\gamma^{\frac{s}{2}-j}} \quad (A-4)$$

and, since  $s$  is odd, the only terms in this expression which may possibly not be well behaved at  $\bar{Z} = 0$  are those for which  $\left(\frac{s}{2} - j\right) \geq \frac{3}{2}$ , i.e. those involving finite part integrals. For these (cf. Ref.1, p.31-2)

$$\int_0^{\gamma_0} \frac{F(\gamma) d\gamma}{\gamma^{\frac{s}{2}-j}} = \frac{\frac{s-2j-1}{2}}{(s-2j-2)(s-2j-4) \dots 1} \int_0^{\gamma_0} \frac{F\left(\frac{s-2j-1}{2}\right)(\gamma) d\gamma}{\gamma^{\frac{1}{2}}} + \text{terms well behaved at } \bar{Z} = 0. \quad (A-5)$$

The terms not stated explicitly involve powers of  $\gamma_0$  and the derivatives of  $F(\gamma)$  at  $\gamma = \gamma_0$  and, as stated, will be well behaved at  $\bar{Z} = 0$ . We can expand  $\phi'$  on the facet as a Taylor series about its value at  $\left(X_0 + \frac{\bar{Z} \tan \theta}{1 - \tan^2 \theta}, Y_0, P - X_0 \tan \theta - \frac{\bar{Z} \tan^2 \theta}{1 - \tan^2 \theta} + 0\right)$ , i.e. at the point (cf. Fig.1) on the facet from which the co-normal goes through  $(X_0, Y_0, Z_0)$ . Writing

$$\xi = X_0 - X \quad (A-6)$$

$$\bar{\xi} = -\frac{\bar{Z} \tan \theta}{1 - \tan^2 \theta} \quad (A-7)$$

$$a_{mn} = \left( \frac{\partial^{m+n} \phi' \left( \left\{ X_f + P \sin \theta \right\} \cos \theta, Y_f, P \cos^2 \theta - X_f \sin \theta + 0 \right)}{\partial X_f^m \partial Y_f^n} \right) (-\sec^m \theta) \quad (A-8)$$

$$\begin{aligned} X_f &= (X_0 - \bar{\xi}) \sec \theta - P \sin \theta \\ Y_f &= Y_0 \end{aligned}$$

\* If not there are no problems with  $F_{rs}^{(\tau)}$  when  $\bar{Z} \rightarrow 0$ .

this expansion is

$$\phi'(X, Y, P - X \tan \theta + 0) = \sum_{m=0}^{\infty} \sum_{n=0}^{\infty} \frac{a_{mn} (\xi - \bar{\xi})^m \eta^n}{m! n!} \quad (A-9)$$

Now

$$\frac{\partial \xi}{\partial \gamma} = \frac{2}{(\xi - \bar{\xi})(1 - \tan^2 \theta)} \quad (A-10)$$

and

$$\eta^2 + 4\gamma + \bar{Z}^2/(1 - \tan^2 \theta) = (\xi - \bar{\xi})^2(1 - \tan^2 \theta) \quad (A-11)$$

Hence from (A-3)

$$F^{(1)}(\gamma) = \frac{2}{(1 - \tan^2 \theta)^{\frac{1}{2}}} \sum_{n=0}^{\infty} \frac{1}{n!} \int_{-\infty}^{\infty} \left\{ -\frac{a_{0n}}{(\xi - \bar{\xi})^3} + \frac{a_{2n}}{2(\xi - \bar{\xi})} + \dots \right\} \eta^n d\eta + \dots \quad (A-12)$$

$$F^{(2)}(\gamma) = \frac{2^2}{(1 - \tan^2 \theta)^{\frac{3}{2}}} \sum_{n=0}^{\infty} \frac{1}{n!} \int_{-\infty}^{\infty} \left\{ \frac{3a_{0n}}{(\xi - \bar{\xi})^5} - \frac{a_{2n}}{2(\xi - \bar{\xi})^3} + \frac{a_{4n}}{8(\xi - \bar{\xi})} + \dots \right\} \eta^n d\eta + \dots, \quad (A-13)$$

etc.

The terms omitted outside the integrals, arise from our assumed discontinuity, for the purposes of equation (A-1), in  $\phi'$  at the facet boundary. They will involve positive and negative powers of the value of  $(X - X_0 - \frac{\bar{Z} \tan \theta}{1 - \tan^2 \theta})$  (i.e.  $\bar{\xi} - \xi$ ) at the facet boundary, and hence they will be well behaved when  $\bar{Z} \rightarrow 0$  provided the receiving point  $(X_0, Y_0, Z_0)$  does not become, in the limit, a point on the facet boundary. Assuming this is not so, we find, on substituting the above expressions for the derivatives of  $F(\gamma)$  in equation (A-5) and changing one of the integration variables, that

$$\int_0^{\gamma_0} \frac{F(\gamma) d\gamma}{\gamma^{\frac{3}{2}}} = \frac{4}{\sqrt{1 - \tan^2 \theta}} \sum_{n=0}^{\infty} \frac{1}{n!} \int_{\bar{\xi} + |\bar{\xi}| \cot \theta}^{\infty} \left\{ -\frac{a_{0n}}{(\xi - \bar{\xi})^2} + \frac{a_{2n}}{2} + \dots \right\} d\xi \int_{-\eta_0}^{\eta_0} \frac{\eta^n d\eta}{\sqrt{\eta_0^2 - \eta^2}} + \text{terms well behaved at } \bar{Z} = 0 \quad (A-14)$$

$$\int_0^{\gamma_0} \frac{F(\gamma) d\gamma}{\gamma^{\frac{5}{2}}} = \frac{16}{3(1 - \tan^2 \theta)^{\frac{3}{2}}} \sum_{n=0}^{\infty} \frac{1}{n!} \int_{\bar{\xi} + |\bar{\xi}| \cot \theta}^{\infty} \left\{ \frac{3a_{0n}}{(\xi - \bar{\xi})^4} - \frac{a_{2n}}{2(\xi - \bar{\xi})^2} + \frac{a_{4n}}{8} + \dots \right\} d\xi \int_{-\eta_0}^{\eta_0} \frac{\eta^n d\eta}{\sqrt{\eta_0^2 - \eta^2}} + \text{terms well behaved at } \bar{Z} = 0 \quad (A-15)$$

where

$$\eta_0 = \sqrt{1 - \tan^2 \theta} \sqrt{(\xi - \bar{\xi})^2 - \bar{Z}^2 \cot^2 \theta} \quad (A-16)$$

and so

$$\gamma = \frac{\eta_0^2 - \eta^2}{4} \quad (A-17)$$

It is easily seen that

$$\int_{-\eta_0}^{\eta_0} \frac{\eta^n d\eta}{\sqrt{\eta_0^2 - \eta^2}} = \begin{cases} (n \text{ even}) \frac{1.3.5 \dots (n+1)}{(n+1)2^{n/2} \left(\frac{n}{2}\right)!} \eta_0^n \\ (n \text{ odd}) 0 \end{cases} \quad (A-18)$$

and so the only discontinuous terms that appear come from:-



$$\int_{\bar{\xi} + |\bar{\xi}| \cot \theta}^{\xi} \frac{d\xi}{(\xi - \bar{\xi})^4} = \frac{1}{3|\bar{\xi}| \cot \theta|^3} + \text{terms well behaved at } \bar{Z} = 0 \quad (\text{A-19})$$

$$\int_{\bar{\xi} + |\bar{\xi}| \cot \theta}^{\xi} \frac{\eta_0^2 d\xi}{(\xi - \bar{\xi})^4} = \frac{2(1 - \tan^2 \theta)}{3|\bar{\xi}| \cot \theta|^3} + \text{terms well behaved at } \bar{Z} = 0 \quad (\text{A-20})$$

$$\int_{\bar{\xi} + |\bar{\xi}| \cot \theta}^{\xi} \frac{d\xi}{(\xi - \bar{\xi})^2} = \frac{1}{|\bar{\xi}| \cot \theta} + \text{terms well behaved at } \bar{Z} = 0 \quad (\text{A-21})$$

Consequently

$$\int_0^{Y_0} \frac{F(\gamma) d\gamma}{\gamma^{\frac{3}{2}}} = - \frac{4a_{00} |\tan \theta|}{\sqrt{1 - \tan^2 \theta}} \frac{\pi}{|\bar{\xi}|} + O(\bar{\xi}) + \text{terms well behaved at } \bar{Z} = 0 \quad (\text{A-22})$$

$$\int_0^{Y_0} \frac{F(\gamma) d\gamma}{\gamma^{\frac{5}{2}}} = \frac{16\pi}{3(1 - \tan^2 \theta)^{\frac{3}{2}}} \left[ \frac{a_{00} |\tan^3 \theta|}{|\bar{\xi}|^3} + \frac{|\tan \theta|}{2|\bar{\xi}|} \{2(1 - \tan^2 \theta)a_{02} - a_{20}\} \right] + O(\bar{\xi}) + \text{terms well behaved at } \bar{Z} = 0 \quad (\text{A-23})$$

The phrase " $O(\bar{\xi}) + \text{terms well behaved} \dots$ " is used to indicate the fact that these remaining terms do not include any term which is discontinuous at  $\bar{\xi} = 0$ . The terms represented by  $O(\bar{\xi})$  may include for example  $|\bar{\xi}|$ .

Putting these expressions in equation (A-4) and substituting for the values of the coefficients\*  $a_{mn}$  finally gives

$$F_{r3}^{(1)} = \pi \left\{ - \frac{1}{|\bar{Z}|} \phi' - \frac{\tan \theta}{1 - \tan^2 \theta} \operatorname{sgn}(\bar{Z}) \left( \frac{\partial \phi'}{\partial X} - \frac{\partial \phi'}{\partial Z} \tan \theta \right) + O(\bar{Z}) \right\} + F_{r3}^{(1)}(0) \quad (\text{A-24})$$

$$\bar{Z}^2 F_{r5}^{(1)} = \frac{\pi}{3} \left\{ \frac{1 - \tan^2 \theta}{|\bar{Z}|} \phi' + \tan \theta \operatorname{sgn}(\bar{Z}) \left( \frac{\partial \phi'}{\partial X} - \frac{\partial \phi'}{\partial Z} \tan \theta \right) + O(\bar{Z}) \right\} \quad (\text{A-25})$$

Similarly one can show that

$$F_{r5}^{(\xi)} = \frac{\pi \tan \theta}{1 - \tan^2 \theta} \operatorname{sgn}(\bar{Z}) \phi' + O(\bar{Z}) + F_{r3}^{(\xi)}(0) \quad (\text{A-26})$$

$$\bar{Z} F_{r5}^{(\xi)} = \frac{\pi}{3} \left\{ - \frac{\tan \theta}{|\bar{Z}|} \phi' + \operatorname{sgn}(\bar{Z}) \left( \frac{\partial \phi'}{\partial X} - \frac{\partial \phi'}{\partial Z} \tan \theta \right) + O(\bar{Z}) \right\} \quad (\text{A-27})$$

$$F_{r3}^{(n)} = F_{r3}^{(n)}(0) + O(\bar{Z}) \quad (\text{A-28})$$

and

$$\bar{Z} F_{r5}^{(n)} = \frac{\pi}{3} \left\{ - \operatorname{sgn}(\bar{Z}) \frac{\partial \phi'}{\partial Y} + O(\bar{Z}) \right\} \quad (\text{A-29})$$

---

\*  $a_{00} = \phi' \left( x_0 - \bar{\xi}, y_0, p - \{x_0 - \bar{\xi}\} \tan \theta + 0 \right)$   
 $= \phi' (x_0, y_0, p - x_0 \tan \theta + 0) - \bar{\xi} \left( \frac{\partial \phi'}{\partial X} - \frac{\partial \phi'}{\partial Z} \tan \theta \right) + O(\bar{\xi}^2)$

## Appendix 2

THE INTEGRALS  $W_{mn}^{(s)}$ 

The integrals  $W_{mn}^{(s)}$ , defined as:-

$$W_{mn}^{(s)} = \int_{(n-\frac{1}{2})\epsilon}^{(n+\frac{1}{2})\epsilon} d\eta \int_{Y_{mn}}^{Y_{m+1,n}} \frac{dY}{Y^{\frac{s}{2}} \sqrt{\eta^2 + 4\eta + \bar{Z}^2/(1 - \tan^2 \theta)}} \quad (A-30)$$

$$\text{where } 4Y_{mn} = \left( m + \sqrt{n^2 \epsilon^2 + \bar{Z}^2/(1 - \tan^2 \theta)} \right)^2 - \left\{ n^2 \epsilon^2 + \bar{Z}^2/(1 - \tan^2 \theta) \right\} \quad (A-31)$$

can be expressed in terms of the integrals

$$T_s(x, \beta) = \frac{1}{4} \int_{-x}^x du \int_0^1 \frac{dv}{v^{\frac{s}{2}} \sqrt{u^2 + v + \beta^2}} \quad (A-32)$$

Thus

$$W_{mn}^{(s)} = \left[ R_{n+1}^{(s)}(Y) - R_n^{(s)}(Y) \right]_{Y=Y_{mn}}^{Y=Y_{m+1,n}} \quad (A-33)$$

$$\text{where } \left. \begin{aligned} R_n^{(s)}(Y) &= \frac{2}{Y^{\frac{s}{2}-1}} T_s \left( \frac{(n-\frac{1}{2})\epsilon}{2Y^{\frac{1}{2}}}, \frac{|\bar{Z}|}{2Y^{\frac{1}{2}} \sqrt{1 - \tan^2 \theta}} \right) & (Y \neq 0) \\ &= 0 & (Y = 0) \end{aligned} \right\} \quad (A-34)$$

For  $\beta \neq 0$  the required  $T_s(x, \beta)$  are given by the following expressions:-

$$T_1(x, \beta) = \log \left\{ \frac{x + \sqrt{x^2 + \beta^2 + 1}}{\sqrt{\beta^2 + 1}} \right\} + x \log \left\{ \frac{1 + \sqrt{x^2 + \beta^2 + 1}}{\sqrt{x^2 + \beta^2}} \right\} - \beta \tan^{-1} \left\{ \frac{x}{\beta \sqrt{x^2 + \beta^2 + 1}} \right\} \quad (A-35)$$

$$T_3(x, \beta) = -\log \left\{ \frac{x + \sqrt{x^2 + \beta^2 + 1}}{\sqrt{\beta^2 + 1}} \right\} - \frac{1}{\beta} \tan^{-1} \left\{ \frac{x}{\beta \sqrt{x^2 + \beta^2 + 1}} \right\} \quad (A-36)$$

$$T_5(x, \beta) = \frac{1}{3} \left[ -\log \left\{ \frac{x + \sqrt{x^2 + \beta^2 + 1}}{\beta^2 + 1} \right\} + \frac{1}{\beta^3} \tan^{-1} \left\{ \frac{x}{\beta \sqrt{x^2 + \beta^2 + 1}} \right\} + \frac{1}{\beta^2} \frac{x \sqrt{x^2 + \beta^2 + 1}}{x^2 + \beta^2 + 1} \right] \quad (A-37)$$

For  $\beta = 0$ , we have

$$T_1(x, 0) = \log \left\{ x + \sqrt{x^2 + 1} \right\} + x \log \left\{ \frac{1 + \sqrt{x^2 + 1}}{|x|} \right\} \quad (A-38)$$

$$T_3(x, 0) = -\log \left\{ x + \sqrt{x^2 + 1} \right\} + \frac{\sqrt{x^2 + 1}}{x} \quad (A-39)$$

$$T_5(x, 0) = \frac{1}{3} \left[ -\log \left\{ x + \sqrt{x^2 + 1} \right\} + \frac{(x^2 - 2)\sqrt{x^2 + 1}}{3x^3} \right] \quad (A-40)$$

There is no point in substituting these expressions (A-35) to (A-40) in (A-33) and (A-34) to get general expressions for the  $W_{mn}^{(s)}$ . It is however, of interest to look at the  $W_{00}^{(s)}$  since these illustrate the analysis of Appendix 1. For this purpose we might as well take  $\epsilon = 1$ . We then have:-

(a) For  $\bar{Z} = 0$

$$\left. \begin{aligned} W_{00}^{(1)} &= \log \left\{ \frac{11 + 5\sqrt{5}}{2} \right\} \\ W_{00}^{(3)} &= 8 \left[ \sqrt{5} - \log \left( \frac{1 + \sqrt{5}}{2} \right) \right] \\ W_{00}^{(5)} &= -8 \left[ \frac{28}{9} \sqrt{5} + \frac{4}{3} \log \left( \frac{1 + \sqrt{5}}{2} \right) \right] \end{aligned} \right\} \quad (A-41)$$

(b) For  $\bar{z} \neq 0$ 

$$w_{00}^{(1)} = \log \left\{ \frac{2\theta_1 + \theta_2}{\theta_3} \right\} + 2\theta_1 \log \left( \frac{1 + \theta_2}{\theta_4} \right) - 2|b| \tan^{-1} \left\{ \frac{\theta_1}{\theta_2|b|} \right\} \quad (A-42)$$

$$w_{00}^{(3)} = -\frac{8}{|b|} \tan^{-1} \left\{ \frac{\theta_1}{\theta_2|b|} \right\} - \frac{8}{\theta_1} \log \left\{ \frac{1 + \theta_2}{\theta_4} \right\} \quad (A-43)$$

$$w_{00}^{(5)} = \frac{32}{3b^2|b|} \tan^{-1} \left\{ \frac{\theta_1}{\theta_2|b|} \right\} + \frac{32}{3b^2} \frac{\theta_2}{\theta_1\theta_3} - \frac{32}{3\theta_1^3} \log \left\{ \frac{1 + \theta_2}{\theta_4} \right\} \quad (A-44)$$

where

$$\left. \begin{aligned} \theta_1 &= \sqrt{1 + 2|b|} \\ \theta_2 &= \sqrt{5 + 8|b| + 4b^2} \\ \theta_3 &= \sqrt{1 + 4b^2} \\ \theta_4 &= 2(1 + |b|) \end{aligned} \right\} \quad (A-45)$$

$$b = \bar{z} / \sqrt{1 - \tan^2 \theta} \quad (A-46)$$

Expanding the expressions, for  $\bar{z} \neq 0$ , in terms of  $b$  one then finds

$$w_{00}^{(1)} = w_{00}^{(1)}(0) + O(\bar{z}) \quad (A-47)$$

$$w_{00}^{(3)} = -\frac{4\pi\sqrt{1 - \tan^2 \theta}}{|\bar{z}|} + w_{00}^{(3)}(0) + O(\bar{z}) \quad (A-48)$$

$$w_{00}^{(5)} = \frac{16\pi(1 - \tan^2 \theta)^{\frac{3}{2}}}{3\bar{z}^2|\bar{z}|} + w_{00}^{(5)}(0) + O(\bar{z}) \quad (A-49)$$

It follows then, using equation (3-15), that the above expressions ((A-48) and (A-49)) confirm the first terms in the expansions for  $F_{r3}^{(1)}$  and  $F_{r5}^{(1)}$  which were obtained in Appendix 1 (equations (A-24) and (A-25)). The second terms in these latter expressions are not given by the  $w_{00}^{(s)}$  because of the assumption that  $(C_r \phi')$  is constant in a cell  $\left( \frac{\partial \phi'}{\partial X} - \frac{\partial \phi'}{\partial Z} \tan \theta \equiv \frac{\partial \phi'}{\partial X_f} \sec \theta \right)$ .

## REFERENCES

- 1 M.J. Lighthill An introduction to Fourier analysis and generalised functions. Cambridge University Press (1958)
- 2 D.L. Woodcock, A.J. Lawrence Flutter research in the United Kingdom 1969-71. Unpublished RAE Technical Memorandum Structures 813 (1971)

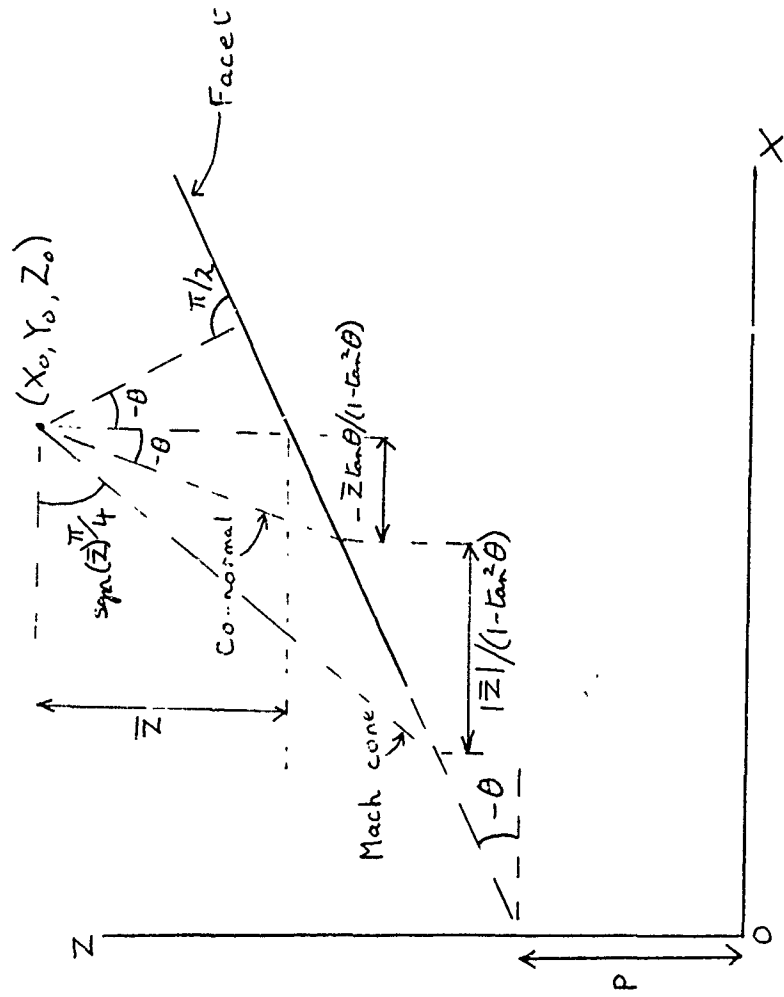
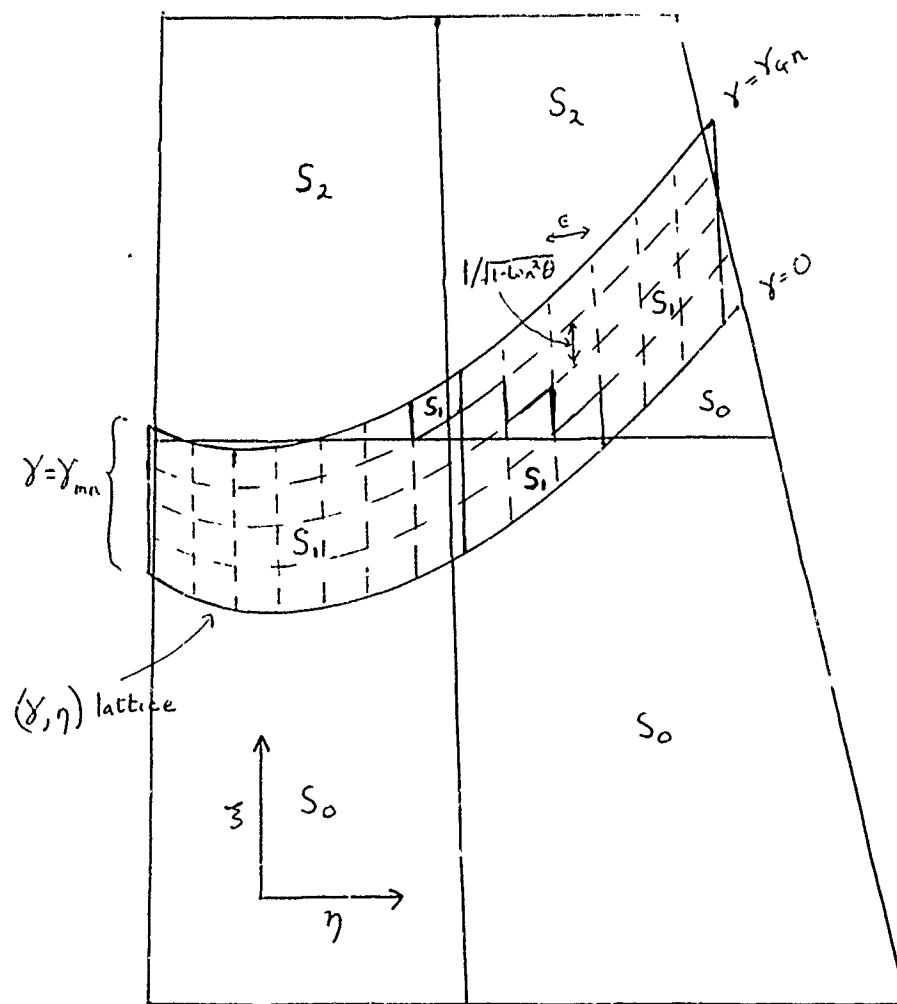


FIG 1 Facet / Receiving - point parameters



N.B. The discontinuities in the lines  $\gamma = \gamma_{mn}$  ( $m \neq 0$ ) are too small to show on this diagram which is for a non-small value of  $b (= \frac{Z}{\sqrt{1-\tan^2\theta}})$

FIG 2 Integration lattice on a facet

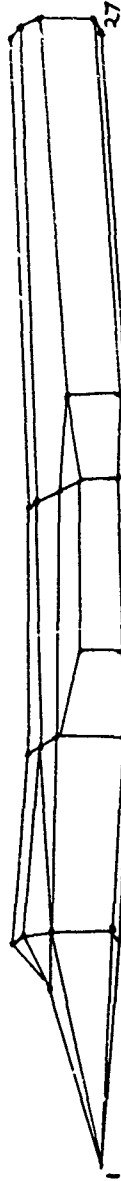


FIG 3 Sketch of polyhedron representation of fighter fuselage.

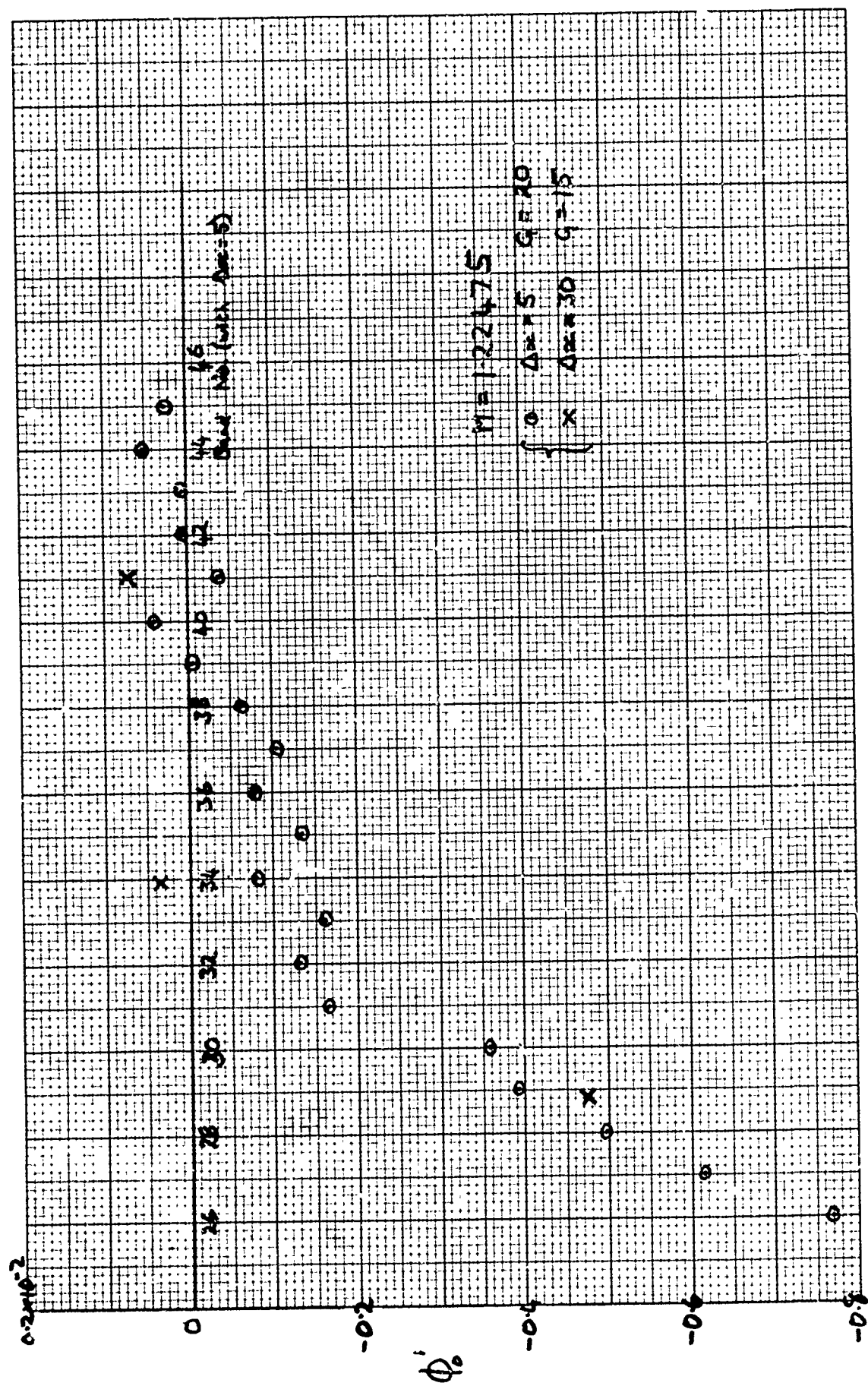


FIG 4 Steady potential on sacet 8 - foliage adjacent to backside of canopy

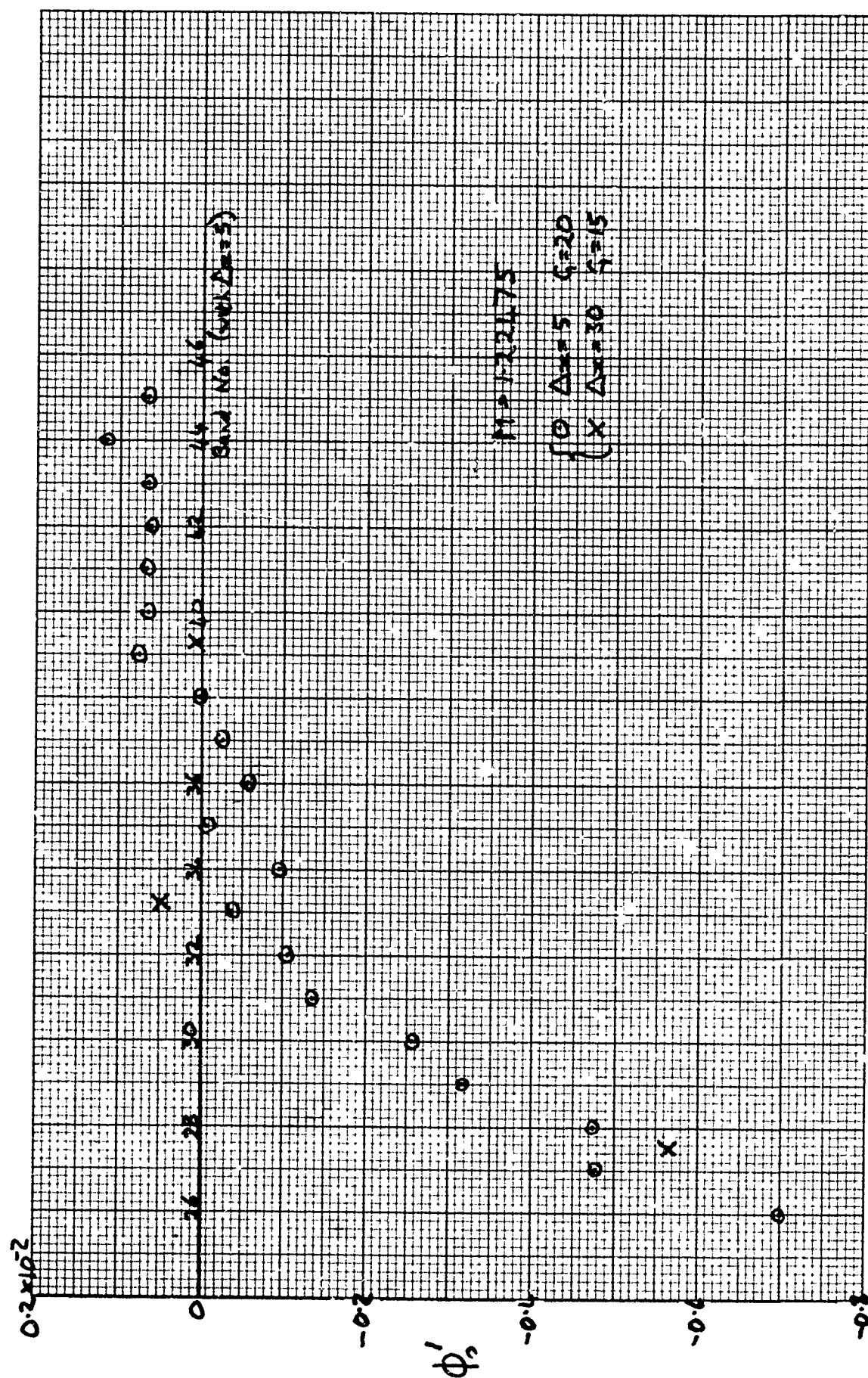


FIG. 5 Steady potential on facet 9; - backside of canopy



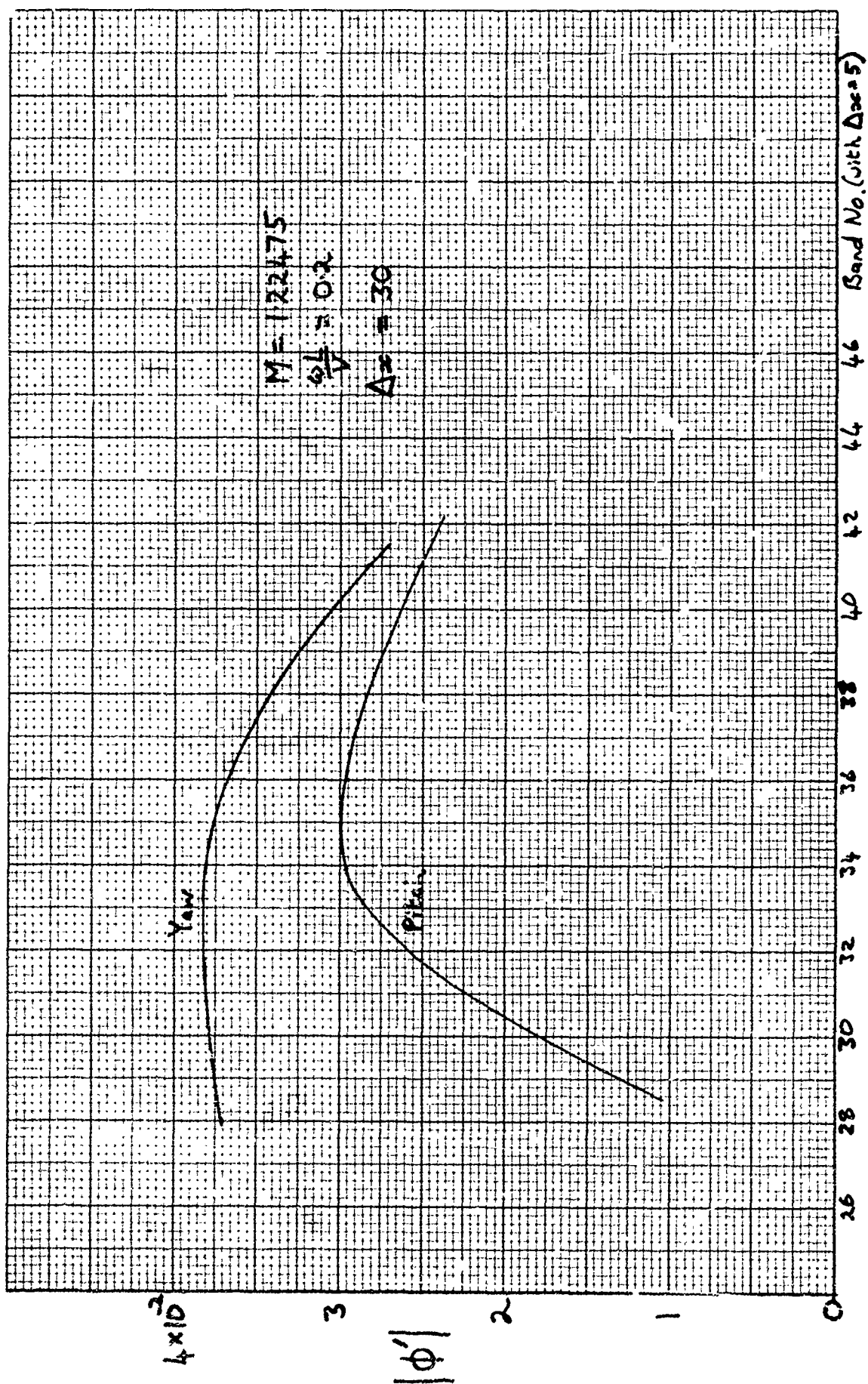


FIG 6 Modulus of oscillatory potential on facet 8 (fuselage adjacent to backside of canopy)

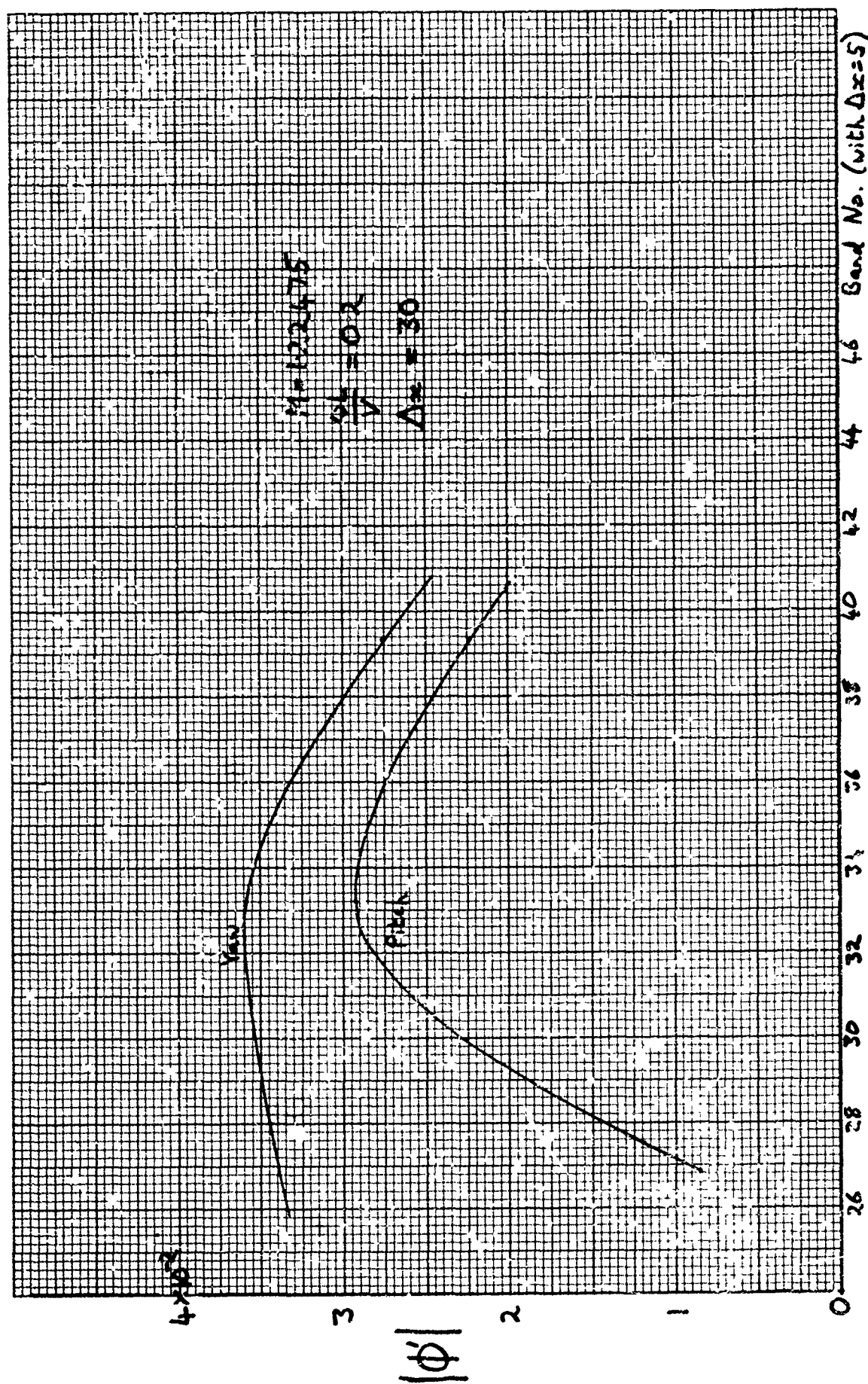


FIG 7 Modulus of oscillatory potential on facet 9 - backside of canopy

## THE PREDICTION OF BUFFET ONSET AND LIGHT BUFFET BY MEANS OF COMPUTATIONAL METHODS

G. Redeker

Deutsche Forschungs- und Versuchsanstalt  
für Luft- und Raumfahrt e.V. (DFVLR)  
Flughafen, 3300 Braunschweig, FRG

V.-J. Proksch

Dornier GmbH  
7990 Friedrichshafen, FRG

## SUMMARY

The design of aircraft penetrating the transonic flight regime is strongly influenced by the occurrence of buffeting which can reduce the flight performance considerably. In order to reduce the amount of expensive model testing computational methods, which are able to provide the project engineer with buffeting boundaries are a useful tool in the first design step of an aircraft.

The present paper gives a review of methods which have been developed for prediction purposes for the buffeting problem. The methods discussed are

- the method of Thomas for predicting buffet onset for wing sections including supercritical airfoils at higher angles of attack,
- the method of Redeker for predicting buffet onset for infinite yawed wings,
- and the method of Proksch for predicting light buffeting for finite wings.

The basic ideas of these methods are outlined and the application is shown in comparison with experimental results.

## NOTATION

M	Mach number	$c_s$	length of separated region equ.(1)
$\alpha$	angle of attack	$c_L$	lift coefficient
Re	Reynolds number based on airfoil chord or wing reference chord	$c_{Bi}$	buffeting coefficient equ.(1)
x	coordinate along airfoil chord	p(x)	pressure distribution
$n = y/s$	dimensionless coordinate in spanwise direction of the wing	$c_p$	pressure coefficient
s	half span of the wing	$\delta$	boundary layer thickness
S	wing area	H	form parameter of boundary layer
$A = 4s^2/S$	aspect ratio	$\sqrt{\sigma_H^2}$	root mean square value of wing root bending moment
$\Lambda$	wing sweep	Subscripts	
$\lambda$	wing taper	sep	separation
t	airfoil thickness	B	buffet onset
c	airfoil chord	D	design point
$\bar{c}$	wing reference chord	S	shock location
		R	wing root

## 1. INTRODUCTION

An important feature of transonic flow over wings is the occurrence of buffeting which is usually more severe than at low speeds due to the larger aerodynamic forces involved. Buffeting is the aircraft response to random aerodynamic load fluctuations associated with unsteady flow separation. For the transonic flow regime buffet is closely connected with the shock boundary layer interaction, which can either cause boundary layer separation beneath the shock leading to a separation bubble or result in an early rear separation due to the increased susceptibility of the post shock boundary layer in an adverse pressure gradient. Both types of flow separation lead to fluctuations of the aerodynamic forces stimulating the aircraft structure. The aircraft structure itself acts as a selective filter for the excitation so that spectra of vibrations always contain pronounced peaks at structural frequencies. The performance of an aircraft thus might be limited by vibrations of the airframe, which can be strong enough to cause a rapid failure of the structure.

Rigid body modes may also be excited such as "wing rocking", "wing dropping" or "nose slicing" which are highly undesirable and lead to a degradation of the handling qualities. These effects belong to the flight mechanical problem area and do have a direct effect on controllability and the ability to hold an accurate flight path. These problems are of great importance but they are outside the scope of this paper.

As wing buffeting leads to severe limitations in the flight envelope of an aircraft great efforts for understanding the physical phenomenon and controlling its undesirable effects have been undertaken in the past.

The publications of AGARD on "Fluid Dynamics of Aircraft Stalling" in 1972 [1], on "Aircraft Stalling and Buffeting" in 1975 [2] and the advisory report on "The Effects of Buffeting and other Transonic Phenomena on Maneuvering Combat Aircraft" in 1975 [3] show the great importance which is attributed to this problem by all people working in aircraft industry and research.

Because of the complexity of this problem considerable emphasis is placed on buffet investigations, experimentally as well as by computational means. The target is to provide buffet boundaries for designers to establish the performance of an aircraft and to produce informations about buffet loads for stressing purposes.

Typical results of buffeting boundaries for a fighter and a transport aircraft in a  $C_L$ -M-diagramme are shown in Fig. 1. For the fighter aircraft boundaries are defined by buffet onset, corresponding to the beginning of boundary layer separation. Light buffeting is defined by the first appearance of sizable vibrations being noticed by the pilot. Moderate buffeting can be said to represent a boundary for the aircraft acting as a stable weapon platform, that means this boundary is the limit for the pilot fulfilling his tracking task. The boundary denoted by heavy buffeting is given by structural limits.

For the fighter aircraft the margin to moderate buffeting represents the manoeuvrability in terms of "n.g." instantaneous pullup or in turn rates. The factor  $n$  will be in the magnitude of  $n = 5 \dots 6$ , depending on the combat aircraft.

For the transport aircraft other requirements have to be applied. Buffet onset is defined in the same way mentioned above. The cruise point of the aircraft has to be kept away from the buffet onset by a  $1.3 \cdot g$  margin in order to allow the aircraft to cover light manoeuvres. During a normal cruise, the aircraft may encounter a strong gust, which carries the aircraft beyond the buffet onset boundary. Therefore, a  $1.6 \cdot g$  margin from maximum penetration, or a definite gust velocity, must be applied to provide a safety margin for the aircraft structure.

From this figure the requirements for predictions methods for the buffeting problem are clear. For the fighter aircraft the moderate buffeting boundary is the main interesting feature giving information about the manoeuvrability of the aircraft. The intensity of the vibrations of the airframe has to be known. For the transport aircraft the buffet onset boundary is the interesting parameter which influences the performance of the aircraft considerably.

Several methods have been developed to solve these problems. Wind tunnel test methods on rigid models have proved to give together with correlation functions for the large scale aircraft reasonable results about buffeting. More expensive are model tests on dynamically scaled elastic models which can be used to predict vibration levels and buffet loads. Response calculations for the aircraft structure are performed using the statistical analysis proposed by Liepmann with the aerodynamic input from unsteady pressure measurements on semi-rigid models. Flight tests are performed to check these methods and to gain more insight in the physical phenomenon.

All these methods give valuable informations about the buffeting problem, but they are not suitable for the first step in the design of an aircraft, e.g. for selecting wing sweep angle or the shape of the airfoil.

Therefore, a computational method which is able to provide the project engineer with buffet boundaries is a useful tool in the design process. Considering the complexity of the buffeting problem a complete solution seems to be a hopeless venture.

Therefore, the problem has to be simplified resulting in models which can be handled by computational methods. Such methods have been built up by Thomas/Redeker [4] for predicting buffet onset for airfoils and infinite yawed wings and by Proksch [5] for estimating light buffeting for finite wings.

The present paper gives a short description of these methods and the application is shown.

## 2. THE METHOD OF THOMAS FOR PREDICTING BUFFET ONSET FOR AIRFOILS

As buffeting is closely connected with unsteady flow conditions as flow separation and shock oscillations, a treatment of this phenomenon with an unsteady method seems to be adequate. This is true for flow conditions beyond buffet onset, where unsteady pressures act on the airfoil. Considering buffet onset only a steady approach can be justified looking at the physical background and the model which will be used. Such a flow model has been postulated by Thomas [6] and has been successfully used for predicting buffet onset for airfoils [4] and infinite yawed wings [7].

After Thomas shock boundary layer interaction takes place in such a way that the shock itself causes no boundary-layer separation at the foot of the shock. The boundary layer remains still attached but is already near separation in consequence of the strong adverse pressure gradient. The following adverse pressure gradient between the shock and the trailing edge will lead to a rear separation. With increasing Mach number or increasing angle of attack the rear separation will move from the trailing edge further upstream. This model of the shock boundary layer interaction is one of the various possibilities shown by Pearcy [8]. The formation of a separation bubble beneath the shock which will often occur is neglected and it is assumed that the rear separation is of major influence. With this flow model a numerical treatment under certain assumptions is possible.

If we assume that the pressure jumps across the shock is spread due to boundary layer effects to a

strong adverse pressure gradient over three to five boundary layer thicknesses as shown by Gadd [9], conventional boundary layer methods can be applied to calculate the development of boundary layer on transonic pressure distributions with shocks.

As buffet onset is defined by the beginning of flow separation this boundary can be established from boundary layer calculations on transonic pressure distributions. After Thomas buffet onset starts if the point of rear separation coming from the trailing edge has reached 90 % of the airfoil chord in his calculations.

The criterion of 90 % location of rear separation has been established by comparing the calculations with experimental results.

The process of estimating buffet onset is schematically shown in Fig. 2. For a set of angles of attack and Mach numbers in the range where buffet onset is expected transonic pressure distributions have to be calculated. This has been done in the original paper by the empirical Sinnott method [10], which now has been replaced by the method of Bauer/Garabedian/Korn [11]. To these pressure distributions the mentioned assumptions on shock boundary layer interaction are applied and boundary layer calculations are performed using the integral method of Walz [12]. With the criterion of buffet onset - rear separation at 90 % of airfoil chord - buffet onset can be established. With this method reasonable results have been achieved in the past [4].

The process described above has been improved in the last years [13]. The progress in the treatment of transonic flows has lead to new airfoil shapes, known as supercritical airfoils. These airfoils characterized by a large supersonic region on the upper surface with a shockfree isentropic recompression to the trailing edge near the design point give better aerodynamic characteristics in the transonic flow regime. Compared with conventional airfoils the drag rise and buffet onset occur if we consider a constant lift coefficient at higher Mach numbers or for a constant Mach number at higher lift coefficients. These good points will be used to design transport aircraft which operate more economically or combat aircraft with improved manoeuvrability. Various experimental investigations on supercritical airfoils have shown that a shockfree pressure distribution only could be obtained in a small region near the design point. In off-design conditions shock waves will occur. Fig. 3 shows schematically experimental results for a supercritical airfoil in the neighbourhood of the design point, the pressure distribution of which is presented in the middle of the figure denoted by  $\alpha_D$  and  $M_D$ . If we decrease the Mach number  $M < M_D$  at  $\alpha_D$  two shock waves will occur due to the collapse of the supersonic region. Increasing the Mach number  $M > M_D$  will result in one strong shock. The same effects will happen if we keep the Mach number constant  $M = M_D$  and change the angle of attack. At  $\alpha < \alpha_D$  the supersonic region breaks down, two shock waves appear and at  $\alpha > \alpha_D$  one strong shock occurs.

These effects may have undesirable consequences on the aerodynamic behaviour, especially on buffet onset. Therefore, a method has to be used for the calculation of transonic pressure distributions which is able to model this behaviour. The Sinnott method used in the original paper of Thomas is not able to represent these pressure distributions. Thus the method of Bauer/Garabedian/Korn is applied which provides reasonable results for transonic flows. Another advantage is that also higher angles of attack can be treated.

To check this improved method the supercritical airfoil Korn No. 1 has been investigated. This airfoil designed by Garabedian/Korn [14] has a shockfree distribution at design condition  $M_D = 0.75$  and  $\alpha_D = 0^\circ$  with a lift coefficient of  $c_{L,D} = 0.63$ . Experimental investigations were done by Kacprzynski [15] from NAE Canada including buffet experiments. Buffet onset was detected by the beginning of strong unsteady fluctuations of the normal force  $c_N$ .

Fig. 4 shows a comparison between calculated buffet onset and experimental results in a  $c_{L,B}$ - $M$ -diagramme, where  $c_{L,B}$  denotes the lift-coefficient at buffet onset. The Reynolds number based on airfoil chord is  $Re = 2.1 \times 10^7$ . The experiments marked by the full points are well represented by the calculated curve up to high values of lift coefficient.

Fig. 5 shows the influence of modern airfoil shapes on buffet onset compared with conventional airfoils. This figure contains buffet onset boundaries for three airfoils all having nearly the same thickness of nearly 12 % of airfoil chord. The Reynolds number is  $Re = 2.1 \times 10^7$ . Buffet onset for the NACA 0012 profile lies at very low Mach numbers and lift coefficients. The second airfoil is of Airbus Standard, that means airfoil like this has been used in the wing design of the European Airbus A300. The buffet onset boundary for this airfoil shows the large progress in design research of high speed airfoils. The third airfoil represents the Korn airfoil No. 1 from Fig. 4 which still has a better buffet onset boundary.

These figures indicate that with the improvement in predicting buffet onset reasonable results for supercritical airfoils up to high values of lift coefficients could be obtained.

### 3. THE PREDICTION OF BUFFET ONSET FOR INFINITE YAWED WINGS

An extension of the method of Thomas to the case of infinite yawed wings has been described in [7]. The basic idea is the same as outlined in section 2 of this paper. This extension became necessary when swept wings were treated with the Thomas method using instead of the free stream conditions of the swept wing those normal to the leading edge. The Mach number and the lift coefficient for calculated buffet onset  $c_{L,B}$  converted to streamwise values by the cosine law of the sweep angle gave too optimistic results, especially for higher angles of sweep.

In order to achieve better results for swept wings the correct representation of the three-dimensional boundary layer had to be taken into account. For this purpose the boundary layer method of Cumpsty/Head [16] extended to compressible flows [7] has been used.

The process of predicting buffet onset is as follows:

The inviscid transonic pressure distribution for infinite yawed wings can easily be derived from the pressure distribution for the wing section normal to the leading edge by applying the cosine law. With this pressure distribution, corrected for viscous effects in the shock region, boundary-layer calculations have to be performed with the three-dimensional boundary-layer method.

The Mach number and the lift coefficient for buffet onset is then derived from the location of the separation line on the infinite yawed wing. Buffet onset is said to occur - as in the two-dimensional case - if separation has reached the 90° line of the wing.

Fig. 6 shows two examples of calculated results taken from [7] for swept wing aircraft, which were obtained from calculations for the infinite yawed wing having the same sweep angle at the quarter chord line of the finite wing.

The prediction method briefly outlined in this section is restricted to wings with moderate to large aspect ratios, e.g. wings for transport aircraft, for which the flow on the main parts of the wing behaves like the flow on an infinite yawed wing.

The occurrence of a complicated shock pattern on the wing surface in off-design flow conditions limits this methods to low angles of attack or low lift coefficients.

#### 4. THE PREDICTION OF LIGHT BUFFETING FOR FINITE WINGS

A new approach to calculate light buffeting has been published by Jünke et al. [17] and Proksch [5]. The method, applicable for finite wings, is based on the idea of Thomas to conclude from boundary layer separation on the buffeting behaviour. As finite wings are being considered the criterion for the buffeting boundary as given in section 2 and 3 has to be replaced by a new one taking into account the different spanwise loading of the wing. For this reason a buffeting coefficient  $c_{Bi}$  which can be calculated as shown later is defined which is directly related to the root mean square (rms) value of the wing root bending moment  $\sqrt{\sigma_M^2}$  which has been proofed in experiments on rigid models to be a good indicator for buffeting [18]

$$(1) \quad c_{Bi} = \int_{\eta_R}^1 \frac{c_S(\eta)}{c} (\eta - \eta_R) d\eta \sim \sqrt{\sigma_M^2}$$

This equation is established by assuming that the fluctuations of the wing root bending moment are proportional to the integral evaluated along the wing span of the product of local lift fluctuations and the distance from the wing root  $(\eta - \eta_R)$ . A further assumption is that the local lift oscillations caused by flow separation are proportional to length  $c_S(\eta)$  of the separated flow at a spanwise station of the wing.

The linear relationship from equ.(1) between  $\sqrt{\sigma_M^2}$  and  $c_{Bi}$  is proofed by experiments which are shown in Fig. 7, which is depicted from [5]. For a 12% thick wing of aspect ratio  $A = 4.8$ , sweep angle of  $\Lambda = 35^\circ$  measured values of  $\sqrt{\sigma_M^2}$  [19] were taken at  $c_L = \text{const.}$  for several Mach numbers and plotted against calculated  $c_{Bi}$ -values. It can be seen that up to a value of  $c_{Bi} = 0.1$  a linear dependence of  $c_{Bi}$  from  $\sqrt{\sigma_M^2}$  is established.

The most important fact for prediction purposes is that the  $c_{Bi}$ -value can be evaluated by applying proper numerical methods. The calculation procedure for the buffeting coefficient  $c_{Bi}$  has to start with the calculation of the transonic pressure distribution on a finite wing for a set of angles of attack and Mach numbers. This was done in [5] by using the RAF-Standard method with the local lift curve slopes from the two-dimensional method of Murman/Krupp [20]. This provides the effective angle of attack along the wing span, with which the actual pressure distributions at several spanwise stations are calculated by the Murman/Krupp method.

As methods for calculating transonic pressure distributions on finite wings have become available [21], this calculation step can be improved now.

To evaluate equ.(1) the area of separated flow on the wing has to be determined by boundary layer calculations. In [5] the quasi-three-dimensional method already mentioned in section 3 has been used at several spanwise stations. This step also can be improved by applying a full three-dimensional boundary layer calculation method. The result of the described procedure are lines of constant value  $c_{Bi}$  plotted in a  $c_L$ -M-diagramme, as shown in Fig. 8 for the Bell XS-1 aircraft. These lines are compared with flight test results [22]. The buffet boundary of the flight test was determined by time-history recordings of load fluctuations, as indicated by strain gages mounted on the wing root and in addition by measurements of the acceleration oscillations at the center of gravity. The minimum acceleration detectable on the accelerometer records was approximately  $\pm 0.03$  g.

This value can be interpreted as light buffeting. The lines of  $c_{Bi} = \text{const.}$  show the same trend as indicated by the flight tests and it can be said that a value of  $c_{Bi} = 0.08$  to  $0.1$  will coincide with the measured light buffeting boundary.

Another calculation is shown in Fig. 9 for a wind-tunnel model of a 12% thick  $35^\circ$  sweptback wing, for which buffeting intensity measurements have been carried out [23]. The calculated lines  $c_{Bi} = \text{const.}$

represent reasonably well the measured curves of  $\sqrt{\sigma^2} = \text{const.}$  The line  $c_{Bi} = 0.1$  coincides with the boundary of light buffeting. The comparison in these two figures show that a value of  $c_{Bi} = 0.1$  seems to be a reasonable criterion for the boundary of light buffeting.

The limitation of this method is reached if the linear relationship from equ.(1) between the  $c_{Bi}$ -value and  $\sqrt{\sigma^2}$  is no longer valid. Fig. 7 shows that with increasing Mach numbers the deviation from the straight line occur at decreasing values of  $c_{Bi}$ . The reason for this behaviour is the fact that the flow separation has reached the shock and cannot move further upstream. For this case the length of the separated region is no longer proportional to the strength of the force oscillations. This occurs especially at higher Mach numbers where the shock position is located in the rear part of the wing.

Another limitation results from the numerical method used for the calculation of the  $c_{Bi}$ -value. The relaxation method for calculating the transonic pressure distribution is based on the transonic small perturbation equation, which is restricted to low angles of attack.

To overcome these difficulties a semi-empirical method has been developed combining calculated results with experimental data derived from a lot of published buffeting experiments. In [5] working plots for the estimation of light buffeting have been established. This treatment is well documented in [5] and should not be reported in this paper.

## 5. CONCLUSIONS

In this paper computational methods have been outlined which are able to provide the project engineer with data on buffeting boundaries for buffet onset and light buffeting. The methods described are valuable in the first design stage of an aircraft and can reduce the amount of expensive model testing.

By incorporating an advanced method for the inviscid transonic flow computation the method of Thomas for predicting buffet onset for airfoils has proved to be valid for modern airfoil shapes and higher angles of attack. The extension of the Thomas method to infinite yawed wings has become less important due to the new approach of Proksch for predicting light buffeting for wings of finite aspect ratio. This method has been checked up till now only by few calculations and more comparisons with wind tunnel and flight test results are necessary to determine the range of applicability. It should be improved by the incorporation of the advanced inviscid and viscous aerodynamic prediction programs which are available now.

All methods are based on boundary layer calculations with inviscid transonic pressure distributions. The further development of the buffeting prediction methods should be concerned with prediction methods for viscous transonic pressure distributions with better models of the shock boundary layer interaction.

## 6. REFERENCES

- [1] Fluid Dynamics of Aircraft Stalling.  
AGARD-CP-102, 1972.
- [2] Aircraft Stalling and Buffeting.  
AGARD-LS-74, 1975.
- [3] The Effects of Buffeting and other Transonic Phenomena on Maneuvering Combat Aircraft.  
AGARD-AR-82, 1975.
- [4] Thomas, F.  
Redeker, G. A Method for Calculating the Transonic Buffet Boundary including the Influence of Reynolds Number.  
AGARD-CP-83, 1971.
- [5] Proksch, H.-J. Ermittlung der Buffeting-Grenzen von Kampfflugzeugen.  
Dornier GmbH, Rep. EA 101/2916, 1973.
- [6] Thomas, F. Die Ermittlung der Schüttelgrenzen von Tragflügeln im transsonischen Geschwindigkeitsbereich.  
WGLR-Jahrbuch, 1967, 126-144.
- [7] Redeker, G. Die Berechnung der Schüttelgrenzen von Pfeilflügeln.  
Z. Flugwiss. 21, 1973, 345-359.
- [8] Pearcey, H.H.  
Haines, A.B.  
Osborne, J. The Interaction between Local Effects at the Shock and Rear Separation.  
AGARD-CP-35, 1968.
- [9] Gadd, G.E. Interactions between Shock Waves and Turbulent Boundary Layers.  
ARC R&M 3262, 1962.

- [10] Sinnott, C.S.                      On the Prediction of mixed Subsonic/Supersonic Pressure Distributions.  
J. Aero/Space Sci. 27, 1960, 767-778.
- [11] Bauer, F.  
Garabedian, P.  
Korn, D.                              Supercritical Wing Sections.  
Lecture Notes in Economics and Mathematical Systems.  
Berlin/Heidelberg/New York, Springer, 1972.
- [12] Walz, A.                              Strömungs- und Temperaturgrenzschichten.  
Karlsruhe, G. Braun, 1966.
- [13] Redeker, G.                              Calculation of Buffet Onset for Supercritical Airfoils.  
Symposium Transsonicum II.  
Ed.: K. Oswatitsch, D. Rues  
Berlin/Heidelberg/New York, Springer, 1976, 66-74.
- [14] Garabedian, P.  
Korn, D.                              Analysis of Transonic Airfoils.  
Comm. Pure Appl. Math. 24, 1971, 841-851.
- [15] Kacprzynski, J.J.                      An Experimental Analysis and Buffet Investigation of the Shockless  
Lifting Airfoil No. 1.  
NRCC AR LR-569, 1973
- [16] Cumpsty, N.A.  
Head, M.R.                              The Calculation of Three-dimensional Turbulent Boundary Layers.  
Part I and II.  
Aeron. Quart. 18, 1967, 55-84, 150-164.
- [17] Jünke, E.  
Moeken, B.  
Proksch, H.-J.                              Estimation of Buffet Intensity.  
Dornier Rep., presented at Euromech 40, Stockholm, 1973.
- [18] Mabey, D.G.                              An Hypothesis for the Prediction of Flight Penetration of Wing Buffeting  
from Dynamic Tests on Wind Tunnel Models.  
ARC CP 1171, 1971.
- [19] Vanino, R.  
Welte, D.                              Tragflügelentwurf für transsonische Strömungen.  
Dornier Rep. ZTL FAG4 DO 4.05, 1970.
- [20] Krupp, J.A.  
Murman, E.M.                              The Numerical Calculation of Steady Transonic Flow past Thin Lifting  
Airfoils and Slender Bodies.
- [21] Bailey, F.R.  
Steger, J.L.                              Relaxation Techniques for Three-dimensional Transonic Flow about Wings.  
AIAA Paper, 72-189, 1972.
- [22] Gadeberg, B.L.  
Ziff, H.L.                              Flight determined Buffet Boundaries of ten Airplanes and Comparison  
with five Buffet Criteria.  
NACA RM A50I27, 1951.
- [23] Vanino, R.  
Wedemeyer, E.                              Wind Tunnel Investigation of Buffet Loads on four Airplane Models.  
AGARD-CP-83, 1971.



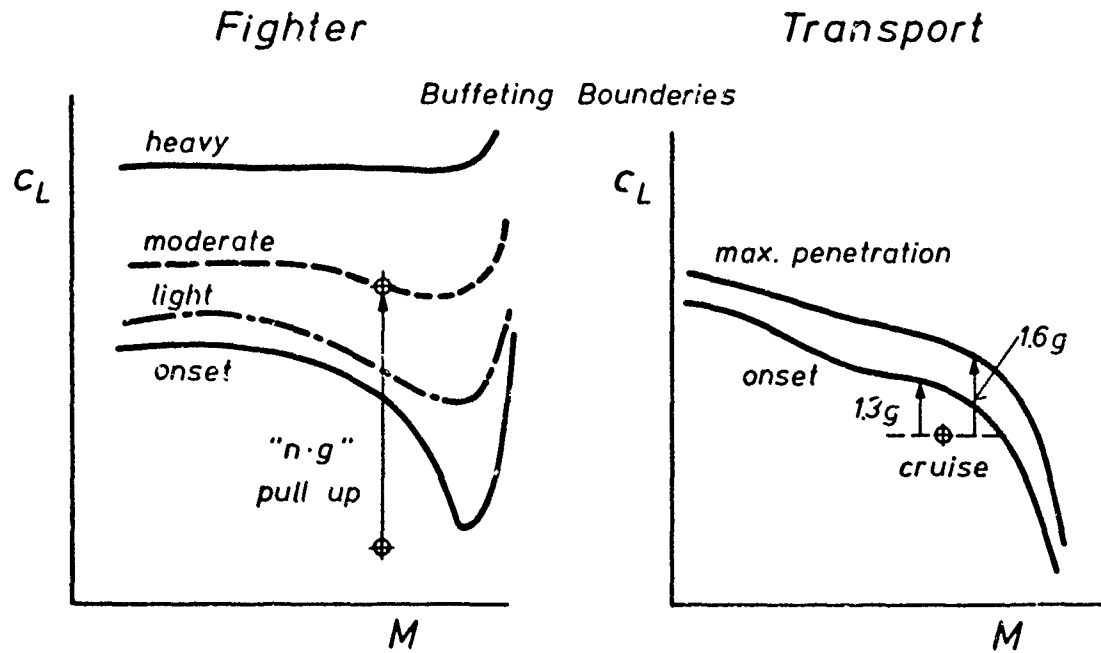


Fig. 1 Buffeting criteria for fighter and transport aircraft

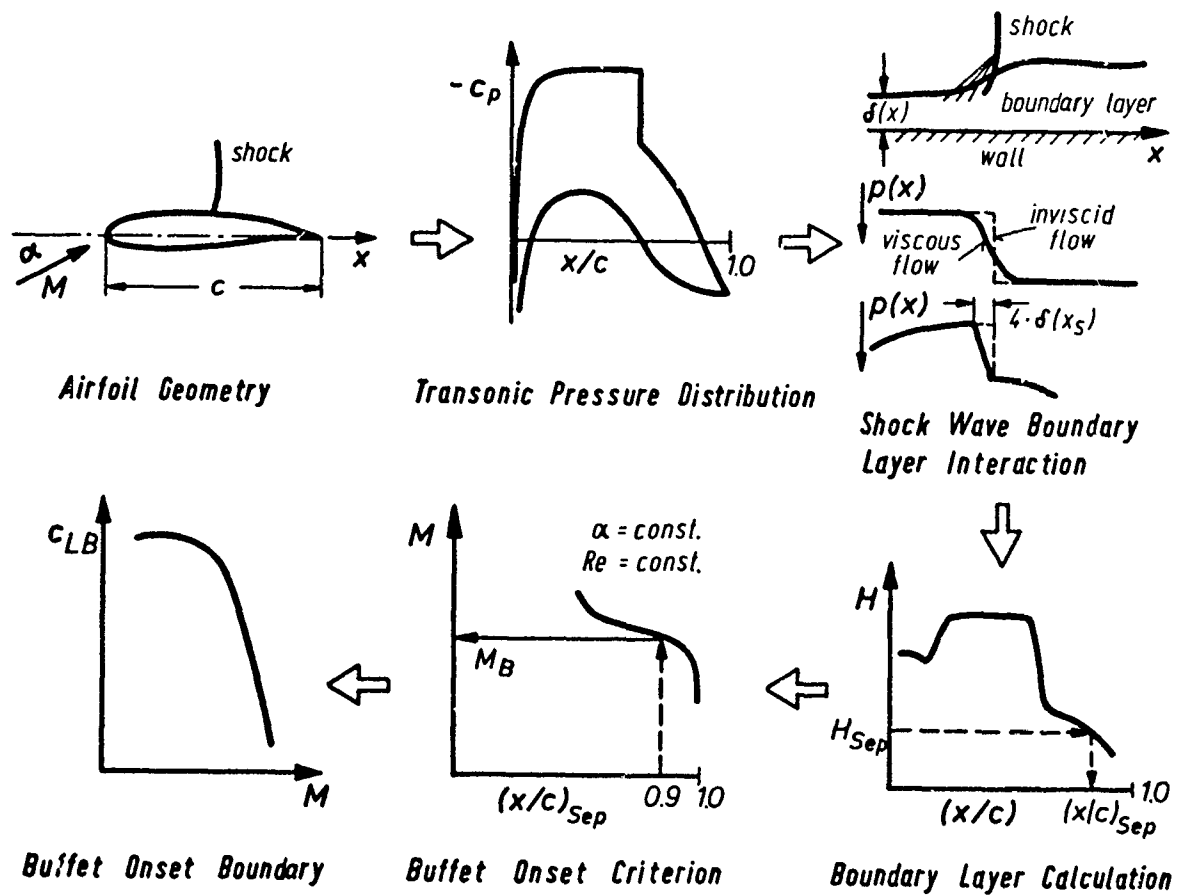


Fig. 2 Calculation procedure for buffet onset

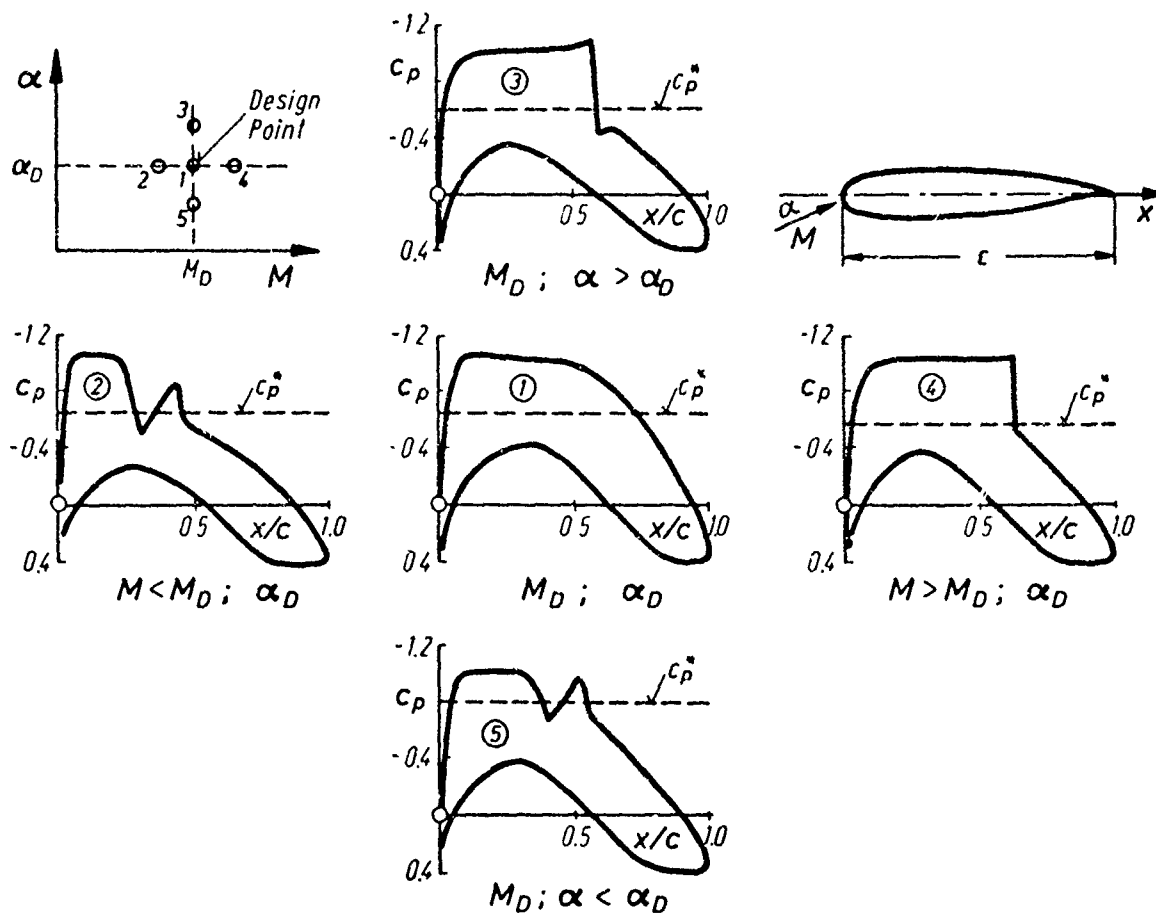


Fig. 3 Pressure distributions for a supercritical airfoil in off-design conditions

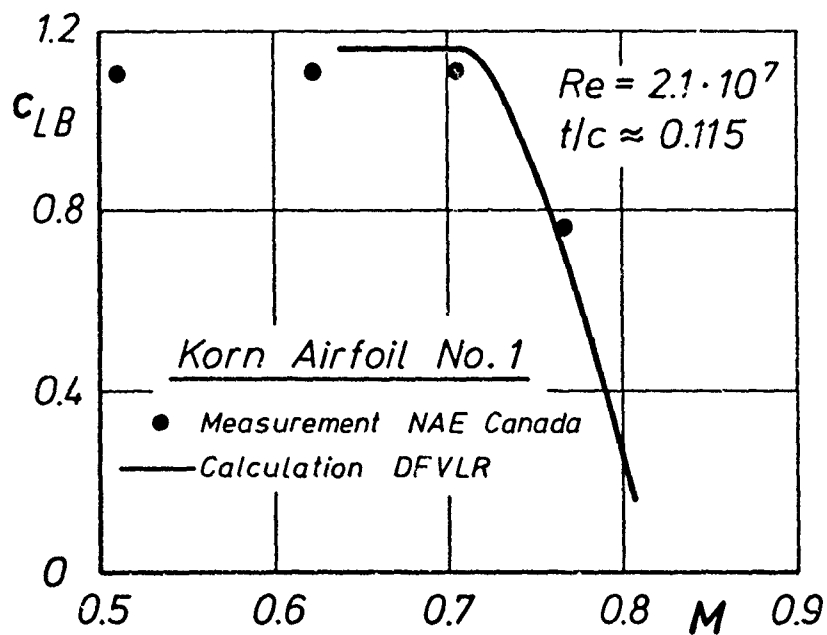


Fig. 4 Comparison of calculated buffet onset with wind tunnel results for Korn airfoil No. 1

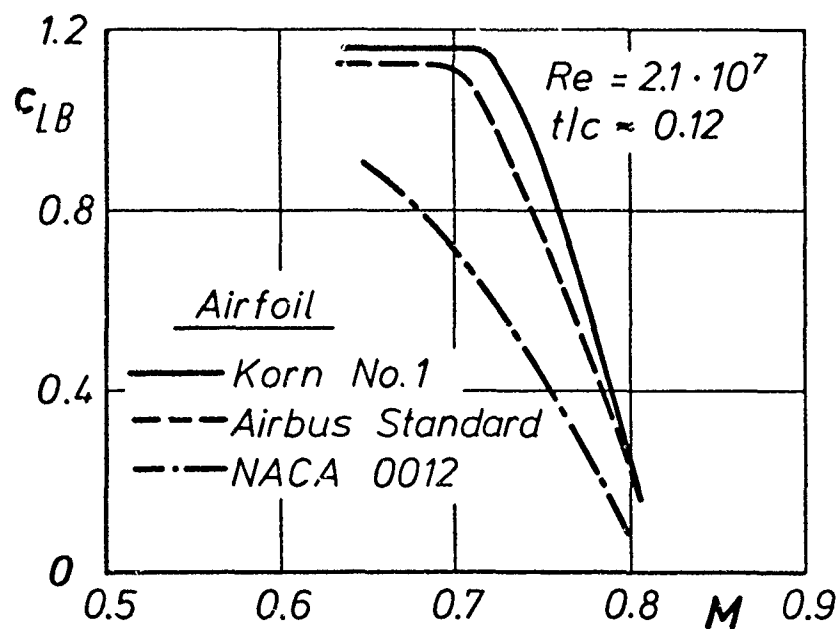


Fig. 5 Comparison of calculated buffet onset for a supercritical airfoil with conventional airfoils

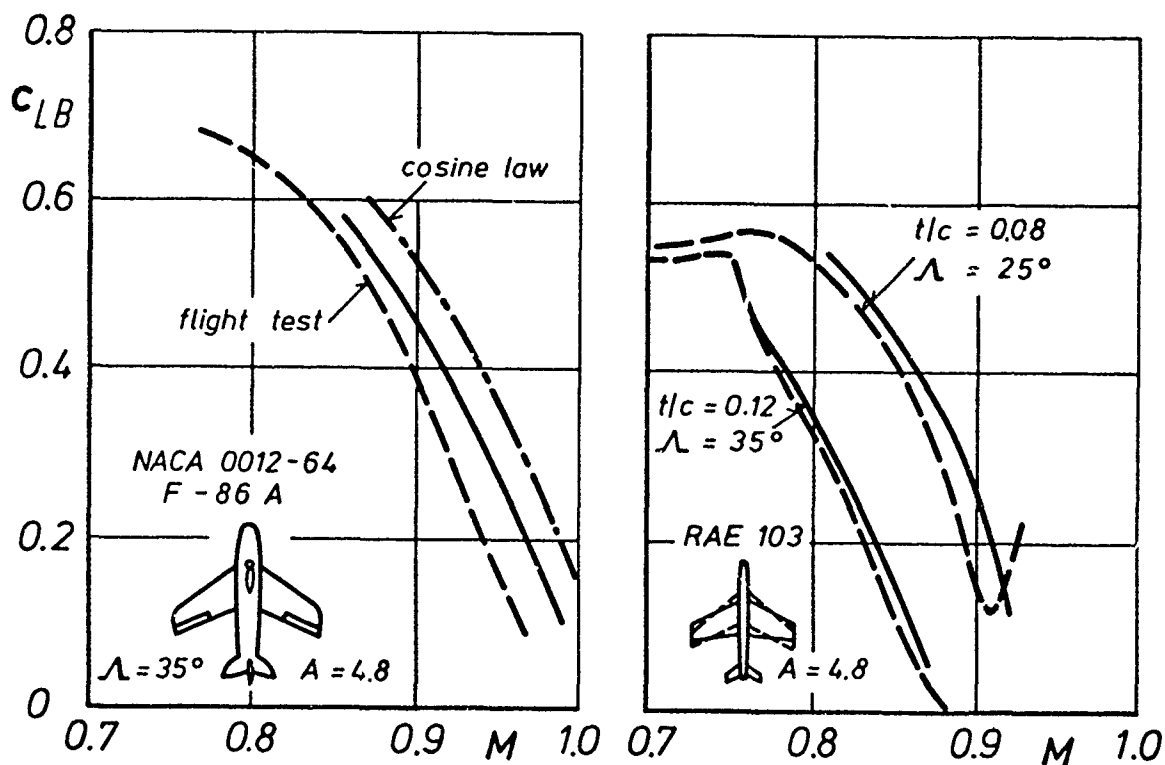


Fig. 6 Comparison of calculated buffet onset for swept wings after Redeker with wind tunnel and flight tests

--- flight test [22]  $Re \approx 10^7$       --- wind tunnel [23]  $Re \approx 1.3 \cdot 10^6$   
 --- calculation  
 --- 2D-calculation and cosine law

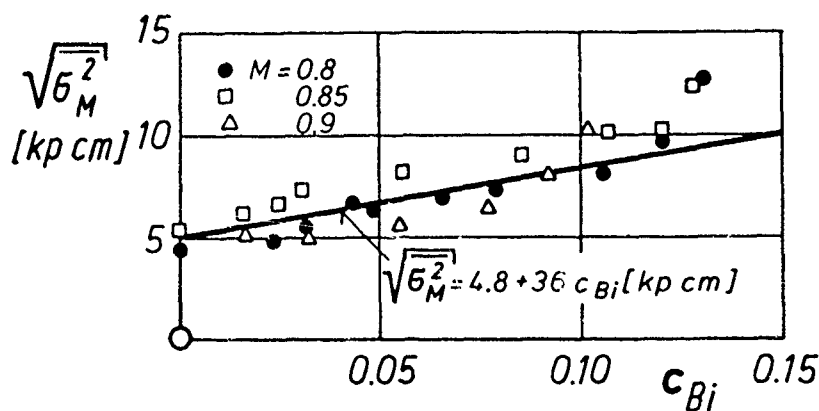


Fig. 7 Relation between buffeting intensity  $\sqrt{\sigma_M^2}$  and buffeting coefficient  $c_{Bi}$  on a wing model ( $A = 4.8$ ,  $t/c = 0.12$ ,  $\Lambda = 35^\circ$ ) after [5]

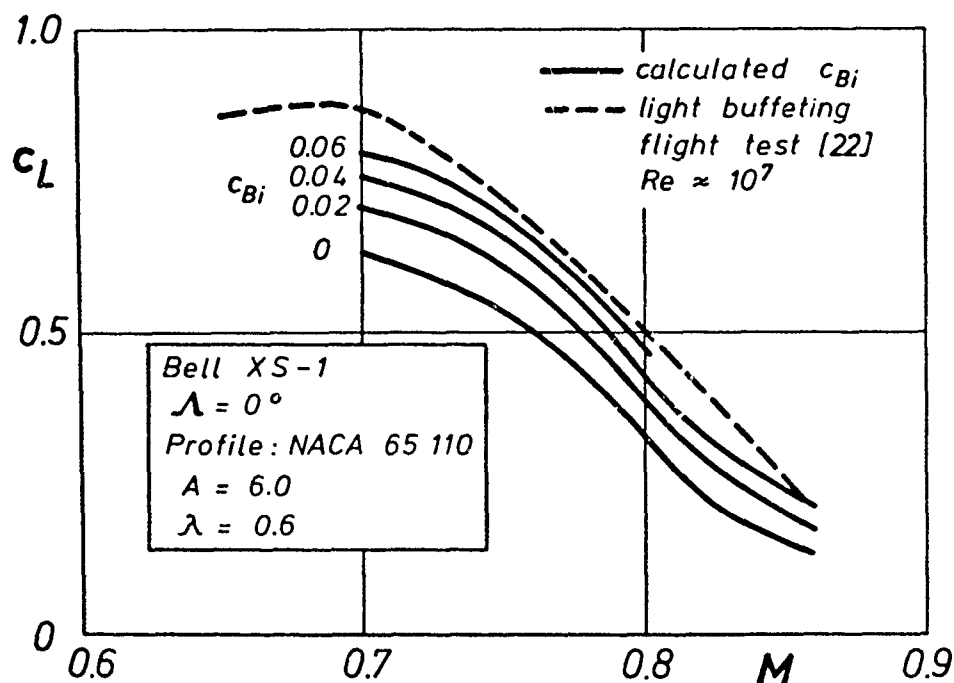


Fig. 8 Comparison of calculated buffeting coefficients  $c_{Bi}$  with light buffeting from flight test [22]

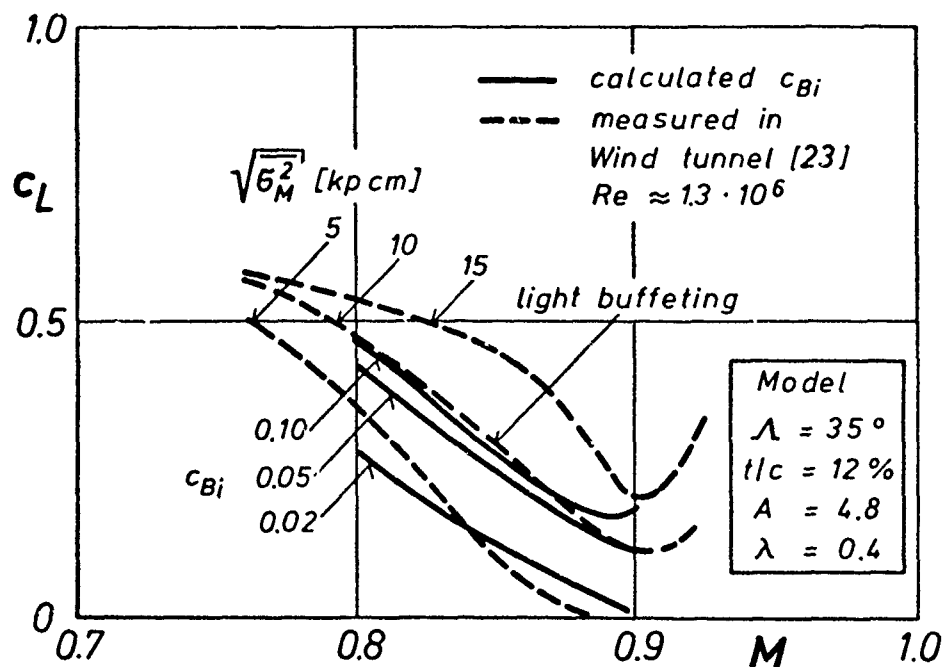


Fig. 9 Comparison of calculated buffeting coefficients  $c_{Bi}$  with wind tunnel results of  $\sqrt{\sigma_M^2}$  [23]

PRELIMINARY EVALUATION OF A TECHNIQUE FOR PREDICTING  
BUFFET LOADS IN FLIGHT FROM WIND-TUNNEL MEASURE-  
MENTS ON MODELS OF CONVENTIONAL CONSTRUCTION.

G F Butler and G R Spavins

Aerodynamics Department, Royal Aircraft Establishment, Bedford, United Kingdom

SUMMARY

A technique is described for predicting buffet loads in flight from wind-tunnel measurements of the response of models of conventional construction. The rms response and damping ratio in each mode are used to calculate non-dimensional buffet excitation and aerodynamic damping parameters, which can be used in combination with the aircraft structural damping to predict the buffeting response under flight conditions. Results are presented from wind-tunnel tests on a model of a small combat trainer aircraft and predictions made using these results are compared with flight measurements. In addition, some remarks are made on methods for determining rms response and damping ratio from accelerometer or strain gauge signals recorded under buffeting conditions.

NOTATION

$\bar{c}$	mean chord	$R(\tau)$	autocorrelation function
$f$	frequency	$S$	wing area
$f_0$	undamped natural frequency	$V$	flow velocity
$h$	mode shape function	$X(t)$	generalised aerodynamic excitation
$m$	generalised mass	$\alpha$	angle of incidence
$n_0$	non-dimensional natural frequency	$\delta(\tau)$	randomdec function
$q$	dynamic pressure	$\zeta$	total damping ratio
$t$	time	$\zeta_a$	aerodynamic damping ratio
$z(t)$	generalised coordinate	$\zeta_s$	structural damping ratio
$z_s$	randomdec selection level	$\rho$	air density
$C_N$	normal force coefficient	$\sigma$	rms acceleration
$E$	non-dimensional buffet excitation parameter	$\tau$	time delay
$G(f)$	power spectral density function	$\omega$	angular frequency
$H(\omega)$	transfer function	$\omega_0$	undamped angular natural frequency
$K$	non-dimensional aerodynamic damping parameter		

1 INTRODUCTION

The behaviour of aircraft under buffeting conditions has become increasingly important as a factor in the process of aircraft design and there is a continuing need for improved techniques for predicting buffet loads from wind-tunnel experiments, particularly early on in project development.<sup>1,2</sup> Two fundamentally different methods of predicting buffeting intensity in flight are often used. In the first, measurements are made of the pressure fluctuations on a nominally rigid model. These are then used to calculate the dynamic response when these pressures act on the flexible aircraft structure. Major disadvantages of this approach for general use lie (a) in the sophisticated data handling and analysis techniques required to correlate the unsteady pressure data before the buffet excitation can be extracted and (b) in the need to estimate aerodynamic damping. A more direct method of predicting buffeting response in flight is to use aeroelastic models with scaled structural and inertial properties.<sup>3</sup> Besides being expensive in model manufacture, this method has the disadvantage that the models are not usually strong enough to be tested at high enough Reynolds numbers to ensure similarity of model and full-scale flows. In addition, the model cannot be designed until the structural and inertial properties of the aircraft have been defined in detail. In other words, not until a late stage in the development programme.

Recently, Jones<sup>4</sup> has suggested an alternative technique which is intended to give an indication of the buffeting behaviour of an aircraft early on in a project. It involves the measurement of unsteady accelerations or bending moments on a wing of solid construction of the type normally produced for conventional "force" tests. An outline of the approach is given below and illustrated in Fig. 1. The method is described in more detail in Section 2. If each mode of the model is assumed to behave as a single-degree-of-freedom mechanical system, the response of the model under buffeting conditions can be analysed to give a measure of the aerodynamic excitation and the total damping ratio. The latter comprises both structural and aerodynamic components, and since the structural damping of the model can be measured in a wind-off resonance test, the aerodynamic damping can be extracted. The buffeting response of the aircraft can then be predicted using values of aerodynamic excitation and aerodynamic damping scaled from model tests, and either estimated or measured values of aircraft structural damping. In general, a conventional wind-tunnel model has modes of vibration which, for the lower and more important modes, are similar to those of the aircraft and, in principle, the technique can be applied

to all aircraft modes which can be reproduced on the model.

An important requirement is that the structural damping of the model should be low, thus allowing the aerodynamic damping to be estimated from the measurements of total damping with reasonable accuracy. In general, for wind-tunnel tests of conventional steel models, the structural damping is predominant, in contrast to the corresponding flight conditions, where the major damping component is usually of aerodynamic origin. Recent measurements of buffeting on steel and magnesium delta wing models, however, have shown that significant levels of aerodynamic damping can be measured under tunnel conditions, provided the model and mounting are constructed with as few joints as possible, so as to minimise structural damping. In addition, since the level of aerodynamic damping is inversely proportional to the density of the model, a magnesium or light-alloy model will give, in general, a greater aerodynamic damping component than one made of steel. In order to evaluate the prediction method proposed by Jones, experiments have been carried out on a model of a small combat trainer aircraft, so that buffeting response and damping predictions can be compared with measurements made in flight. These tests are discussed in Section 4. Before this, the prediction method is described in more detail in Section 2, while in Section 3 some remarks are made on techniques for estimating the damping ratio from random response records.

## 2 THE BUFFETING PREDICTION METHOD OF JONES

In this Section the method of buffet prediction proposed by Jones in Reference 4 is described. The aim of the analysis is to find a nondimensional representation of the important aerodynamic parameters, so that measurements of these parameters in the wind-tunnel can be used to predict buffeting response in flight. Jones assumes a linear forced-vibration model and considers the equations governing the response of a flexible wing to the unsteady excitation associated with flow separations. The response in any flexible mode may be expressed as a function of time  $t$  in terms of a generalised coordinate  $z(t)$ , representing the displacement in that mode and a generalised aerodynamic excitation  $X(t)$  assumed to have no feedback from the wing motion. (to obtain the displacement at an arbitrary point on the wing,  $z(t)$  can be multiplied by the mode shape function  $h$ ). The response in the single degree of freedom mode is then defined by the differential equation,

$$m \frac{d^2 z}{dt^2} + 2m \zeta \omega_0 \frac{dz}{dt} + m \omega_0^2 z = X(t) \quad (1)$$

In this equation,  $m$  is a generalised mass (which depends upon the wing geometry, mode shape and mass distribution) and the term  $m \omega_0^2$  represents the structural stiffness. The undamped natural frequency  $\omega_0$  (in radians  $s^{-1}$ ) is assumed to be independent of aerodynamic forces (stiffness and inertia). This approximation, together with the neglect of aerodynamic coupling between modes, appears on the basis of experimental data to be acceptable in many practical buffeting situations, as long as we are well away from regions of conventional flutter. The total damping ratio  $\zeta$  is given by,

$$\zeta = \zeta_a + \zeta_s \quad (2)$$

where  $\zeta_a$  is the aerodynamic damping ratio and  $\zeta_s$  is the structural damping ratio. (Here a viscous type of structural damping is assumed, although this is not essential to the analysis). We now consider the aerodynamic excitation term on the right-hand side of equation (1). We assume that the appropriate length and velocity parameters for scaling frequency are mean wing chord  $\bar{c}$ , and flow velocity  $V$  and that Reynolds number effects are negligible so that the mean square fluctuating pressure scales with  $(qS)^2$ , where  $q$  is the dynamic pressure and  $S$  is the wing area. If the power spectral density  $G_X(f)$  is assumed to be approximately constant in the neighbourhood of the mode natural frequency,  $f_0 = \omega_0/2\pi$  then we may write<sup>5</sup>,

$$G_X = \frac{E^2 \bar{c}}{V} (qS)^2 \quad (3)$$

where  $E$  is a nondimensional aerodynamic parameter, a function of wing incidence, Mach number and Reynolds number. A power-spectral density analysis of equation (1) then gives the rms acceleration  $\sigma_z$  associated with the mode as,

$$\sigma_z = \frac{1}{2\sqrt{2}} \left( \frac{\bar{c} \omega_0}{V \zeta} \right)^2 \frac{qES}{m} \quad (4)$$

This can be rearranged to give the aerodynamic excitation parameter  $E$  as,

$$E = 2\sqrt{2} n_0^{-1/2} \left( \frac{m}{S} \right)^{1/2} \left( \frac{\zeta^2 \sigma_z}{q} \right) \quad (5)$$

where  $n_0 = (\bar{c} \omega_0)/V$  is the nondimensional modal frequency. On the assumption that wing-root bending moment is proportional to wing displacement, an analogous parameter to  $E$  may be based on a strain-gauge signal. Equation (4) illustrates the quantities required in a buffeting prediction method based on wind-tunnel measurements. For an aircraft flying at given wing loading, speed and altitude, the aerodynamic-dependent quantities are  $E$  and  $\zeta$ . One method for the evaluation of  $E$  involves the measurement of fluctuating pressures on relatively rigid wind-tunnel models and the derivation of the generalised force by means of cross-correlation techniques. Alternatively, Jones suggests that  $E$  may be derived from wind-tunnel tests on the basis of equation (5) using models for which the relevant mode shape is approximately correct, but not necessarily aeroelastic models. To obtain  $E$  from equation (5)

wind-tunnel measurements of the rms acceleration and total damping ratio are required, together with a knowledge of the modal frequency and generalised mass. We now assume that the parameter  $E$  characterises the aerodynamic excitation in the mode considered for a given Mach number and incidence, and can be used to determine the buffeting loads and response for the full-scale aircraft from equation (4). Again a knowledge of the aircraft modal frequency and generalised mass is required as well as the total damping ratio.

The total damping ratio under flight conditions can be estimated from the total damping ratio measured in wind-tunnel tests as follows. If the structural damping ratio  $\zeta_s$  for the model is determined in a wind-off resonance test, the aerodynamic damping ratio  $\zeta_a$  can be determined from the measured total damping using equation (2). It should be noted that this step may be difficult to perform with accuracy since the structural damping may be a function of both mean and fluctuating load (see Section 4.1). For attached flow, the aerodynamic damping force arises from the effective incidence of the wing due to its vibration, and the corresponding term in equation (1) can be expressed in the form<sup>6,9</sup>:

$$2m \zeta_a \omega_o \dot{z} = 2qSK \frac{\dot{z}}{V}, \quad (6)$$

where  $K$  is a nondimensional parameter which depends on the mode shape, the planform of the wing and the (frequency-dependent) lift curve slope distribution over the wing. Although equation (6) has been formulated for attached flow conditions, we will assume that it also applies to the aerodynamic damping forces associated with separated flows. Hence from (6),

$$\zeta_a = \frac{qSK}{m\omega_o V} \quad (7)$$

$$\text{and} \quad K = \frac{m \omega_o V \zeta_a}{qS} \quad (8)$$

It is now assumed that the parameter  $K$  characterises the aerodynamic damping in the mode considered for a given Mach number and incidence, and that once determined from model tests can be used to calculate the aerodynamic damping under full-scale flight conditions from equation (7). By combining this with the aircraft structural damping measured in a ground resonance test, an estimate of the total damping ratio in flight can be derived.

The complete prediction method is summarised below.

- (i) Determine wing area  $S$  and mean chord  $\bar{c}$  for model and aircraft.
- (ii) Determine modal frequency  $\omega_o$ , generalised mass  $m$ , structural damping  $\zeta_s$ , and mode-shape function  $h$ , from resonance tests on model and aircraft.
- (iii) Measure rms acceleration or bending moment  $\sigma$  at a point on the wing, total damping  $\zeta$ , flow velocity  $V$ , and dynamic pressure  $q$ , at a given Mach number and incidence in wind-tunnel tests.
- (iv) Relate  $\sigma$  to  $\sigma_z$  in generalised coordinates using the mode-shape function  $h$ .
- (v) Derive  $E$  from equation (5).
- (vi) Derive  $K$  from equation (8).
- (vii) Predict total damping in flight from equations (7) and (2).
- (viii) Predict rms acceleration or bending moment at a point on the aircraft wing from equation (4) and the mode-shape function  $h$ .

### 3 REMARKS ON THE DETERMINATION OF DAMPING FROM RANDOM RESPONSE SIGNALS

In order to carry out the analysis described in Section 2, the rms response and damping ratio in each mode need to be extracted from the unsteady accelerometer or strain gauge signals recorded in a wind-tunnel experiment. Although the excitation parameter  $E$  is dependent only on the square root of the damping ratio  $\zeta$ , gross errors can still be introduced unless care is taken over its determination. In addition, the estimation of the small aerodynamic damping component for a steel model, where the ratio of model density to air density is high, demands that the total damping be determined as accurately as possible. In this section, various methods for the estimation of damping ratio and rms response from random signals are discussed. The emphasis is on the practical application of the methods, although reference is made to theoretical aspects when required. While some of the simpler processes can be carried out by analogue means, it is assumed throughout that the random signals are digitised and that the analyses are performed on a digital computer. A random response signal, typical of buffeting, is shown in Fig.2. The curve itself is so variable that it is difficult to extract modal information (ie frequency, rms response and damping) directly, although all the information is, in fact, contained within this time history. For further information on the problem of identifying modal parameters directly from random response records, the reader is referred to References 10 and 11. In general, however, some technique of condensing the information into a more orderly format is used, and the three procedures which are applied most commonly (see Fig.2) are (i) power spectral density (ii) auto-correlation and (iii) random decrement (randomdec)<sup>12</sup>.

### 3.1 Power Spectral Density

The power spectral density method is equivalent to the response amplitude method for discrete frequency excitation of the structure. The power spectrum of the response will exhibit a number of peaks associated with the natural frequencies of the structure. The rms response in each mode can be evaluated from the area beneath the response peak and the damping, as with discrete frequency excitation, can be calculated from the bandwidth of the peak (ie the width of the peak at half its maximum value). For well-separated peaks this is possible in principle, but in practice it is difficult to estimate the peak value particularly for modes where the damping is small. The example shown in Fig. 3 is taken from Reference 12 and the difficulty of estimating the damping from the bandwidth of the half-power point can be readily appreciated. Various smoothing techniques<sup>13</sup> can be applied to reduce the spikiness of the spectral points, but experience has shown that even then it is difficult to obtain consistent estimates of damping. Hence, although the power spectral density function is useful in giving a broad picture of the modal frequencies and responses, the method cannot be recommended for obtaining reliable estimates of damping ratio.

### 3.2 Autocorrelation

An alternative is to form the one-sided autocorrelation function  $R(\tau)$  of the random response. (One-sided in this context means that the ordinates of the function are zero for negative values of  $\tau$ ). For isolated modes, it may be shown that the autocorrelation function of the random response has the same form as the free-vibration decay curve of the system with an initial displacement. The damping ratio can be determined from the rate of decay and the mean square response is given by the initial value  $R(0)$ . Provided the modes are well separated in frequency, each mode can be isolated by filtering the original time history. The modal parameters can then be determined by forming the autocorrelation function and treating this as a single-degree-of-freedom decay. The advantage of this method of analysis is that the damping ratio can be determined by a linear least-squares fit to the logarithmic peak values (see Fig. 4a) and any distortions will show up as a departure from linearity in the decay. Two difficulties can occur with this basically simple approach, which may mean that the rms response  $\sigma$  and damping ratio  $\zeta$  are estimated incorrectly. Firstly, if there is noise at the measurement end of the system, the autocorrelation function will be increased for small values of  $\tau$ <sup>14</sup>. This will give artificially high values for both damping and rms response. The effect can be minimised, by ignoring the first few peaks when measuring the decay. Secondly, if two modes lie close together and if the mode of interest has not been isolated completely by filtering, the autocorrelation function can exhibit beating between the two modal contributions. An example of this is shown in Fig. 4b. If there is sufficient time-delay  $\tau$  in the function, experimental data in this form would simply indicate the presence of more than one mode. If data is only available over a shorter time-delay, however, the function would indicate erroneously a single heavily damped mode. A combination of the two effects outlined above can lead to a gross over-estimation of the damping ratio. In spite of these difficulties, the determination of damping from the decay of the single-degree-of-freedom autocorrelation function is one of the most reliable methods. Its main advantage is that it presents the damping information in a linear form and consequently the user can see immediately whether the decay is uniform. Finally, a word about the convergence properties of the autocorrelation process. This is dealt with in statistical terms in Reference 13, where it is shown that the number of cycles of random response in the mode concerned, which are needed for a specified level of confidence in the signature is inversely proportional to the damping ratio. In general, the theoretical approach tends to over-estimate the length of record needed for convergence in practical terms. In practice it is usually found that a record length of 1000 cycles is sufficient to ensure that for values of damping ratio between 1% and 5% critical,  $\zeta$  can be determined to within 10%.

### 3.3 Randomdec

The third method of reducing the random response data is to form the "random decrement" or randomdec function<sup>12</sup> defined in Fig. 2. This may be regarded as a simplification of the autocorrelation process described above. The randomdec procedure consists of averaging segments of the random time-history, the initial point of each segment being taken to be the point at which the curve crosses a pre-defined selection level  $z$ . Each segment of the random time-history is assumed to be formed by the superposition of a step response, an impulse response and a random response. Cole<sup>12</sup> argues that for the given selection level, all of the step responses are the same, whereas the impulse responses have initial slopes with alternate signs. Consequently, when a large number of segments are averaged, only the step response remains, since the impulse and random response will average to zero. Cole shows, in fact, that for a linear single-degree-of-freedom system, to a 9.6% confidence level, the randomdec function has the same form as the free vibration decay curve with an initial displacement. In an earlier paper, Cole<sup>15</sup> applied similar heuristic arguments to describe the autocorrelation process, which can be shown analytically to produce a function which is related to the free decay of the system<sup>7</sup>. The random decrement analysis then follows as a simplification of the averaging procedure inherent in autocorrelation. For a linear single-degree-of-freedom system, the randomdec and autocorrelation signatures are effectively identical and either can be used to determine the damping ratio. When randomdec is used, the rms response is determined in a separate calculation and it is usual to set the selection level  $z$  to this value. With autocorrelation, the mean square response is given by the initial value  $R(0)$ . For a multi-degree-of-freedom system, the situation is not so clear cut. Heron et al<sup>16</sup> show that as long as the exciting forces for each mode are uncorrelated, the autocorrelation function of the random response will yield the correct modal parameters. On the other hand, Cole<sup>12</sup> claims that for two degrees of freedom (and by implication for more than two), the randomdec and autocorrelation functions are distinct, and that randomdec gives a better representation of the free vibration decay of the system. Practical experience of applying both methods indicates that there is very little difference between the functions for multi-degree-of-freedom buffeting data. The main advantages of randomdec over autocorrelation are the speed of computation and convergence. The computation speed increase is a direct result of the fact that randomdec involves a summation of the time-series points whereas autocorrelation involves a summation of products by pairs of points. Even when the autocorrelation function is computed by Fast Fourier Transform (FFT) techniques<sup>13</sup>, rather than the direct lag-product method, the randomdec process is again usually faster. By computing practical examples, Cole<sup>12</sup> shows that the convergence of randomdec is directly



related to the damping ratio, and hence randomdec converges very rapidly for lowly-damped systems. For systems with a damping ratio of greater than 1% critical, practical experience indicates that both randomdec and autocorrelation converge at comparable rates.

### 3.4 Multi-degree-of-freedom systems

In Section 3.2, the behaviour of the autocorrelation function when more than one mode is present was discussed. Often the unwanted mode can be eliminated by adjusting the filters on the signal, but sometimes two modes occur with frequencies so close together that they cannot be separated by filtering. Alternatively it may be desired to obtain the response and damping in several modes from a single random record without running through the data several times with different filter settings. In both of these instances, the autocorrelation or randomdec functions (hereafter referred to as response functions) will no longer exhibit a straightforward exponential decay and a further analysis step will be needed to extract the modal information. In this section, we consider a number of methods which can be applied to this problem. These fall under two general headings (1) time-domain processes and (2) frequency-domain processes. In the time-domain processes, the response function data is curve fit to a sum of exponentially-decaying sine waves, whereas in the frequency domain processes, the response function data are Fourier-transformed and the resultant complex function, which has many properties in common with a multi-degree-of-freedom transfer function is curve fit to a sum of single-degree-of-freedom transfer functions. Of the time-domain procedures, that of Wilcox and Crawford applies only to dual-mode systems and comprises an iterative least squares fit of two damped sine waves to the response function data. The user has to provide initial estimates of the modal parameters and if these are not accurate enough or the response function data are distorted, the convergence of the process is not guaranteed. The method of Spitznogle and Quazi<sup>18</sup> is more comprehensive, in that several modes can be dealt with and no initial estimates are necessary. The main problem is that the number of modes actually identified is dependent on the length of the response function, rather than on the number of modes actually present. In general, frequency domain methods for identifying parameters of multi-mode systems have found more favour. The main reason is that for multi-mode systems the transfer function data are easier to interpret physically than the corresponding response function (see Fig. 5a). This enables some engineering judgement to be used in guiding the curve-fitting routines. The analysis method developed by Skingle et al.<sup>19</sup> is based on the Vector plot (a plot of real v. imaginary parts) of the transfer function in which each modal resonance appears as a circle (see Fig. 5b). The user inspects the data, decides which modes are present and provides initial estimates of frequency and damping. The modal parameters are then estimated by an iterative routine which finds the "circles" which can be summed to give a close approximation to the original vector plot. Once again, if the initial estimates are poor or the response function data is distorted, the convergence of the process is not guaranteed. It should be noted that one advantage of the vector plot representation is that the measurement noise referred to in Section 3.2 appears as a shift of the circles relative to the origin<sup>14</sup>. An alternative approach is to fit a function of the form,

$$H(\omega) = -\frac{1}{2} \sum_{k=1}^m \frac{r_k}{\omega + ip_k} - \frac{r_k^*}{\omega + ip_k^*},$$

to the complex transfer function data<sup>20</sup>, where \* denotes the complex conjugate. The poles  $p_k$  are given by,

$$p_k = -\frac{\omega_k \zeta_k}{(1 - \zeta_k^2)^{1/2}} + i\omega_k,$$

where  $\omega_k$ ,  $\zeta_k$  are the natural frequency and damping ratio respectively in the kth mode. The mean square error between  $H(\omega)$  and the transfer function data is minimised using an iterative optimisation algorithm<sup>21</sup>. Again the user provides initial estimates of the number of modes and the modal parameters by inspection of the transfer function, but in this case the optimisation procedure always reduces the mean square error so that convergence is guaranteed, albeit very slowly at times. A good idea of how well the optimised function fits can be obtained by superimposing plots of the optimised transfer function and the original data. This approach is currently being implemented at RAE to facilitate the analysis of buffeting response records containing contributions from several modes.

## 4 FLIGHT/TUNNEL COMPARISON OF BUFFETING FOR SMALL COMBAT TRAINER AIRCRAFT

In order to evaluate the prediction method described in Section 2, tests have been carried out in the 8' x 8' Wind Tunnel at RAE on a half-model of a small two-seat combat trainer aircraft. The wing, which was machined out of a solid block of aluminium alloy, was attached to a steel root-block and thence to the balance by an arrangement of pre-stressed bolts, known to have low structural damping. The wooden fuselage was mounted independently on an earth-ring surrounding the balance. The fin and tail-plane were not represented and the intakes were faired over. The model was instrumented with eight accelerometers, six in the wing for determining mode shape and two in the fuselage, one at the nose and one at the tail. A wing-root-bending-moment bridge was also fitted, and four static pressure tappings were used to indicate flow separations at the trailing edge. The tests were performed at three Mach numbers: 0.7, 0.8 and 0.85 over a Reynolds number range which was typical of the full-scale flight tests. At each angle of incidence, a one-minute sample of the transducer signals was recorded on magnetic tape, giving about 2000 cycles at the wing fundamental bending frequency of 33 Hz. The measurements were analysed on two Honeywell 316 computers (one with 4K words of storage and one with 16K words) which form part of the data handling system of the 8' x 8' Tunnel. The randomdec process described in Section 3.3 was used. The analogue signal from magnetic tape was filtered to isolate the mode of interest, converted to digital form and sampled by the 4K computer. The sample rate was chosen to give approximately 10 samples per cycle at the modal frequency. After approximately 100 cycles of the

mode, the data block of 1000 cycles was transferred to the 16K computer for processing, while sampling was continued by the 4K machine. In this way the average randomdec signature for a large number of cycles was built up from the individual signatures of blocks of data representing about 100 cycles. In addition, by a suitable choice of tape replay speed and sample rate, it could be arranged that the analysis time for a block of data was less than the sampling time for the next block, thus ensuring that all of the original analogue signal was processed. The damping ratio was estimated by linear regression on the logarithmic decay of the peak amplitudes of the randomdec signature, as described in Section 3.2. So far, the analysis of the data for buffeting response in the first wing bending mode has been completed. Results for rms wingtip acceleration and damping ratio vs. angle of incidence are shown in Fig. 7, for  $M = 0.7$  and dynamic pressures of 55.2 and 27.6 kN/m<sup>2</sup>, corresponding to Reynolds numbers of  $18.5 \times 10^6$  and  $9.5 \times 10^6$ .

It can be seen that, in general, for a given angle of incidence both the response  $\sigma$  and damping  $\zeta$  are higher for the higher dynamic pressure. This is to be expected if the aerodynamic damping is predominant, in which case  $\sigma \sim p^{1/2}$  and  $\zeta \sim p$ , where  $p$  is the air density<sup>5,9</sup>. At high incidence the rms response is virtually independent of dynamic pressure. The results for  $M = 0.8$  and  $C.85$  exhibit similar characteristics.

#### 4.1 Determination of nondimensional parameters E and K

In order to make use of the wind-tunnel data for the prediction of flight buffeting response, the buffet excitation parameter E and the aerodynamic damping parameter K must be calculated (see Section 2). To determine E from equation (5), besides the model geometrical parameters,  $\bar{c}$  and S, the flow parameters, V and q, and the response parameters  $\sigma$  and  $\zeta$ , we need to know  $\omega_0$ , the natural

frequency and m, the generalised mass of the mode. These structural parameters were measured in a wind-off resonance test, in which the model was excited with an electromagnetic shaker. The natural frequency of the mode was taken to be the point of maximum phase-shift between the response and excitation for equal frequency increments, and the generalised mass m was determined directly by considering the change in natural frequency due to the addition of a small mass to the wing<sup>22</sup>. The mode shape function h was also estimated by measuring the response at a grid of points on the wing.

To determine k from equation (8), besides the structural, flow and geometrical parameters, we need to separate the total damping, measured from the decay of the randomdec signature, into structural and aerodynamic components. As noted in Section 2, the estimation of the aerodynamic damping ratio  $\zeta_a$  from equation (2) may be difficult to perform with accuracy, since the structural damping is not necessarily constant and equal to the wind-off value. Previously observed variations in structural damping during buffeting tests<sup>9,23</sup> suggest that the structural damping term  $\zeta_s$

can be expressed as a function of normal force and rms response. Some indication of the behaviour of  $\zeta_s$  with response can be obtained from a wind-off resonance test, by varying the excitation amplitude and observing directly the structural damping for various levels of response. Such a test will not be conclusive, in general, because (i) the wing will not be subject to a representative aerodynamic loading and (ii) the exciter itself may contribute a damping component which varies with response. For the data shown in Fig. 7 the resonance test indicated an increase in structural damping from 0.2% to 0.6% critical as the rms response was increased from 0.1 g to 0.4 g. Further information on the variation of  $\zeta_s$  with response and normal force can often be inferred from

the buffeting response and damping measurements. To illustrate this we consider the data of Fig. 7. The wind-tunnel measurements were carried out at two different Reynolds numbers for which the density ratio and hence the dynamic pressure ratio was two. We would therefore expect that the aerodynamic damping components would differ by a factor two also. In Fig. 7, at low angles of incidence, total damping values of approximately 3% and 1.6% critical are consistent with the tunnel density ratio and a structural damping of 0.2%. At high angles of incidence, total damping values of approximately 3.8% and 2.2% are consistent with a structural damping ratio of about 0.6%.

The similarity of the response curves for both dynamic pressures in Fig. 7 indicates that the inferred variation in  $\zeta_s$  is probably a function of rms response rather than normal force and the results of the resonance test tend to confirm this. For the data of Fig. 7 we therefore assume that the structural damping remains constant at 0.2% up to buffet onset and then increases to 0.6% at heavy buffet. The example above shows how results from resonance tests, and tunnel results at different densities can be combined to separate the damping components. Similar arguments are involved in Reference 6, where measurements at low incidences in the attached flow regime and at high incidences with the wing stalled, are used to infer that the structural damping component is constant.

In general the separation of structural and aerodynamic damping components is a heuristic process, involving the resolution of information from a number of aspects of the measurements into a consistent framework. In the example given above the aerodynamic damping is much larger than the structural component and the separation is relatively straightforward. It should be emphasised that with a wing made of steel, the aerodynamic component would be reduced by a factor of 3, whereas the structural damping would be approximately the same. The separation problem would therefore be subject to much greater uncertainty.

The values of E and K corresponding to the data of Fig. 7 have been calculated and are shown in Fig. 8. In this case E is plotted on a logarithmic scale to show that the reduction of the measurements to nondimensional form has collapsed the rms response data successfully over most of the incidence range. The difference in the two curves at high incidence may be anticipated from Fig. 7, where the response is virtually independent of dynamic pressure at high incidence. This may be due to scale effects on the wing flows over the 2:1 range in dynamic pressure and hence in Reynolds number. It should be noted, however, that this occurs at angles of incidence beyond those obtainable in flight and will, therefore, not affect the flight/tunnel comparison. The curves for K against  $\alpha$  show no significant variation of

aerodynamic damping with incidence or dynamic pressure.

#### 4.2 Prediction of flight buffeting response and comparison with measurements

The curves for E and K (Fig. 8) have been used to predict the buffeting response in the first wing bending mode for full-scale flight conditions. The aircraft structural parameters  $\omega_0$  and  $m$  were

measured in a ground resonance test. The mode shape function  $h$  was also measured for the aircraft and found to be very similar to that of the model. Measurements of the variation of structural damping with response were also made, but no significant variation was found over the range 0.1 to 0.3 g rms at the wingtip accelerometer. The aircraft structural damping was therefore assumed to be constant at the measured value of 1.1% critical. Using equations (2), (7) and (4), the total damping in the mode and the rms response at the aircraft accelerometer position were predicted. In order to facilitate comparison with flight results, the predicted variation of these parameters with normal force coefficients,  $C_N$ , has been calculated and is plotted in Fig. 9.

Also shown in Fig. 9 are values obtained from flight measurements. The aircraft was instrumented with an accelerometer at each wing tip (see Fig. 6) and buffeting response data was obtained at Mach numbers of 0.7, 0.8 and 0.9. In flight it was not possible to hold Mach number, altitude and angle of incidence constant for a large number of cycles of the wing bending mode (12 Hz) and so measurements were made at constant incidence and Mach number with the aircraft losing height. Data was taken over three distinct altitude ranges as shown in Fig. 9. It was found that the Mach number and incidence could be held virtually constant for period of between 10 and 50 seconds, the higher the Mach number and incidence, the shorter the time. As with the wind-tunnel measurements described earlier, the flight data were analysed using the randomdec technique. The flight damping values given in Fig. 9 were determined from the average randomdec signature for a number of runs, at the same conditions, chosen so that at least 500 cycles of the mode were covered. Fig. 9 indicates that the predicted damping ratios agree very well with measured flight data, ranging from 3% critical at the higher altitudes to 6% critical at lower altitudes. In addition, it can be seen that the predicted variation of response with normal force coefficient  $C_N$  is in good agreement with flight measurements over the entire range of incidence for which a comparison is possible.

#### 5 CONCLUDING REMARKS

A preliminary evaluation of a technique for predicting buffet loads or response in flight from wind-tunnel measurements has been carried out, using a light-alloy half-model of a small combat trainer aircraft. Comparison of predicted response values with flight measurements of buffeting in the first wing bending mode indicate that both the rms response and the damping ratio can be predicted with good accuracy. It is planned to extend the analysis initially to include response in the second bending mode and possibly other modes which are common to both model and aircraft. The ability to deal with a number of modes will depend to some extent on the successful implementation of the model analysis methods referred to in Section 3.

In addition tests will be carried out on a geometrically similar model with a wing made of steel rather than light alloy. It is hoped that these will indicate whether the smaller response and aerodynamic damping component associated with the heavier model can still lead to flight predictions of acceptable accuracy.

Plans are also in hand for the generalisation of the approach to cover situations in which the mode shapes on the model and the full-scale aircraft are not necessarily similar. One possibility which is currently being explored is to use information about the extent and position of the separated flow regions, to eliminate the mode-shape from the excitation function E and thus produce a measure of the generalised unsteady pressure field over the wing.

It is felt that the initial results from the evaluation are sufficiently encouraging to justify continued development of the method. In particular, the relative simplicity of the model construction and analysis procedures make this approach particularly attractive for predicting buffeting characteristics at an early stage of project development.

#### REFERENCES

1. C G B Mitchell Calculation of buffeting of slender wing aircraft at low speeds. RAE Tech Report TR 58169. 1968.
2. R E Mullans Buffet dynamic loads during transonic manoeuvres. C E Lemley AFFDL Tech Report TR-72-46. 1972.
3. P A Hanson Evaluation of an aeroelastic technique for predicting airplane buffet loads. NASA TN D-7066. 1973.
4. J G Jones Modelling of systems with a high level of internal fluctuations. Paper presented at AGARD Specialists meeting on Methods for Aircraft State and Parameter Identification, NASA Langley, November 1974.
5. J G Jones A Survey of the dynamic analysis of buffeting and related phenomena. RAE Tech Report TR 72197. 1973.
6. D G Mobey Measurement of buffeting on two 65° delta wings of different materials. G F Butler RAE Tech Report 76009. 1976.

7. E J Richards  
D J Mead      Noise and Accoustic Fatigue in Aeronautics.  
Wiley, London.      1968.
8. D Williams      An introduction to the theory of aircraft structures.  
Arnold, London.      1960.
9. D D Davis      Buffet tests of an attack airplane model with emphasis on data from wind-tunnel tests.  
NACA RM L47H13.      1958.
10. W Gersch      Estimation of the autoregressive parameters of a mixed autoregressive-moving average time series.  
IEEE Trans Auto Control AC-15, 583,      1970.
11. W Gersch  
S Luo      Discrete time series synthesis of randomly excited structural system response.  
J. Acoust.Soc. Amer. 51, 102,      1972.
12. H A Cole Jr.      On-line failure detection and damping measurement of aerospace structures by random decrement signatures.  
NASA CR 2205-      1973.
13. J S Bendat  
A G Piersol      Random data : Analysis and measurement procedures.  
Wiley, New York.      1971.
14. F Kandianis      Correlation techniques in the analysis of transient processes.  
J. Sound. Vib,26, 161,      1973.
15. H A Cole, Jr      On-the-line analysis of random vibrations.  
AIAA Paper 68-288.      1968.
16. K H Heron  
D R Gaukroge-  
C W Skingle      The processing of response data to obtain modal frequencies and damping ratios.  
RAE Tech Report 74027.      1974.
17. P R Wilcox  
W L Crawford      A least squares method for the reduction of free-oscillation data.  
NASA TN D-4503.      1968.
18. F R Spitznogle  
A H Quazi      Representation and analysis of time limited signals using a complex exponential algorithm.  
J. Acoust Soc.Amer.47, 1150.      1970.
19. C W Skingle  
K H Heron  
D R Gaukroger      Numerical analysis of plots of vector response loci.  
RAE Tech Report TR 73001.      1973.
20. M Richardson      Modal anlysis using digital test systems.  
Paper presented at a seminar on digital control and analysis in vibration test systems, Shock and Vibration Information Center, Naval Research Laboratory, Washington.      1975.
21. R Fletcher      A new approach to variable metric algorithms  
Computer Journal 13, 317,      1970
22. P W Hanscn      Structural and aerodynamic quantities of the dynamic system, similarity laws. and model testing.  
From AGARD-AR-82.      1975.
23. A G Rainey  
T A Byrdsong      An examination of methods of buffeting analysis based on experiments with wings of varying stiffness.  
NASA TN D-3.      1959.

## ACKNOWLEDGEMENTS

The authors wish to acknowledge the assistance of Mr T Turvey and M. A Haynes in the analysis and preparation of flight data presented here.

Copyright © Controller HMSO, London, 1976.

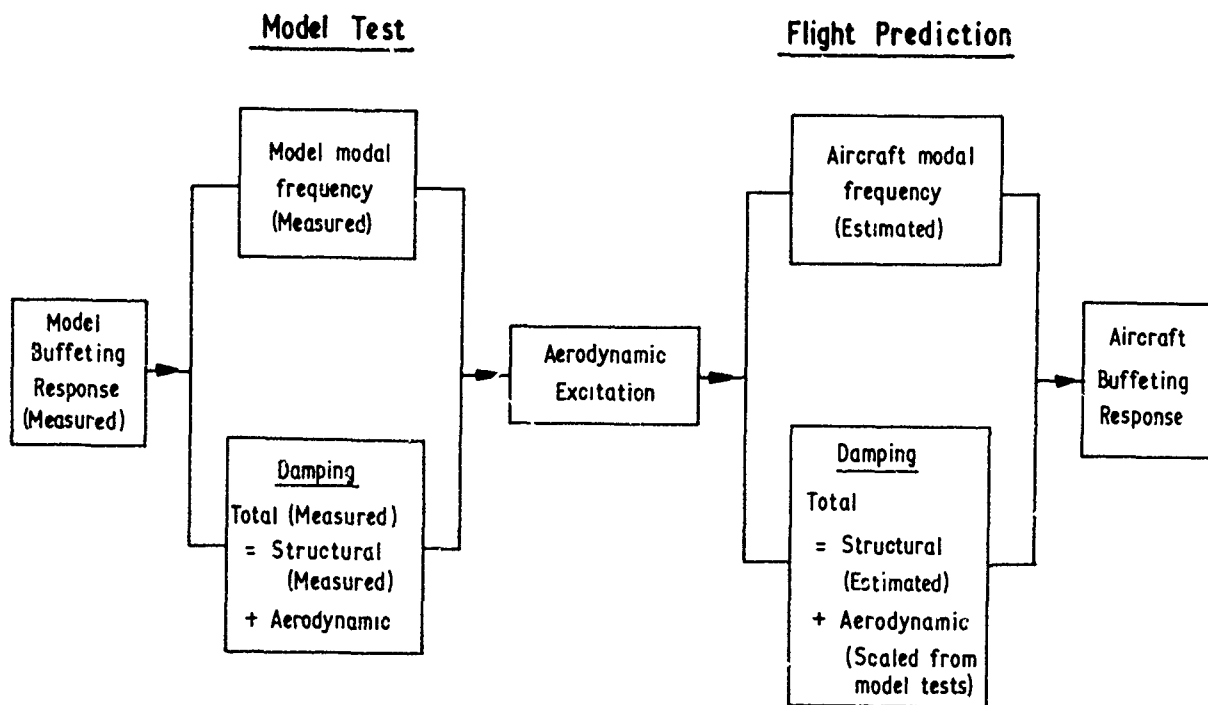
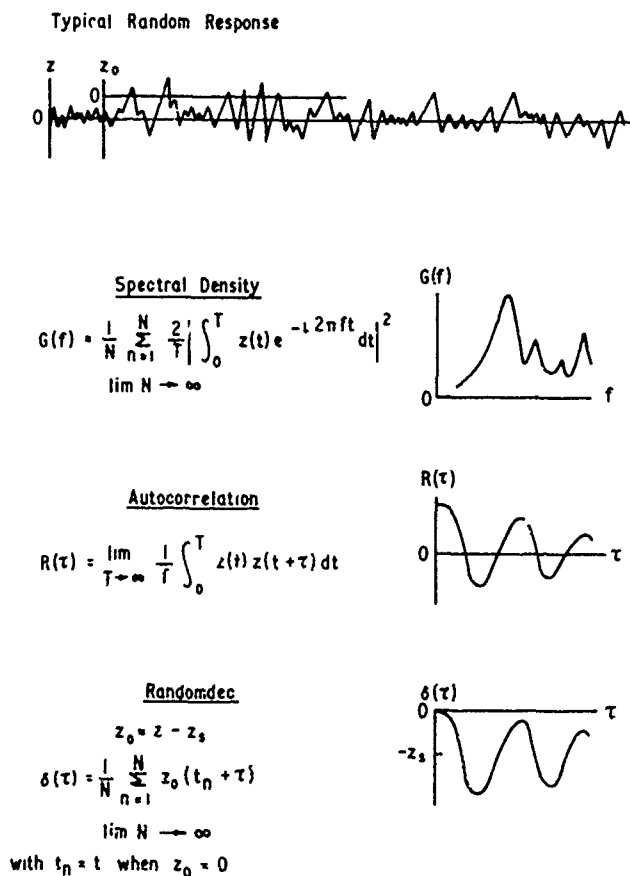
Fig.1 The buffeting prediction method suggested by Jones<sup>4</sup>

Fig.2 Characteristic functions obtained from a random response

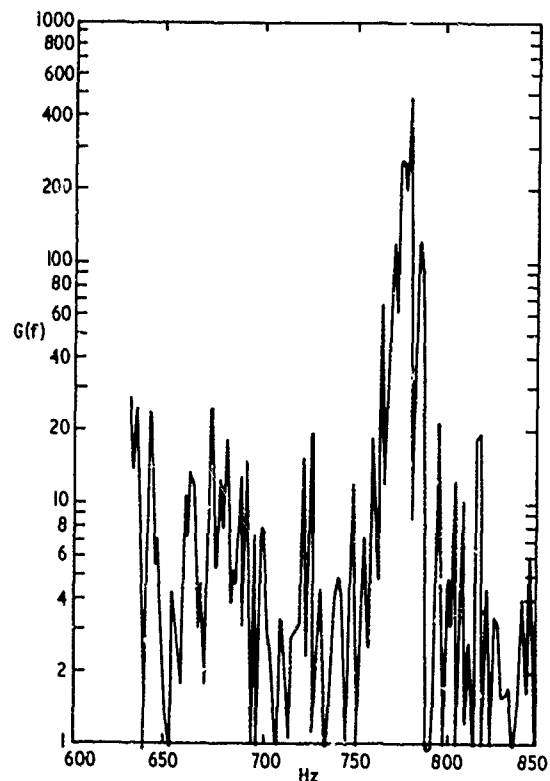


Fig.3 Power Spectral density of an isolated mode (from Cole, Reference 12)

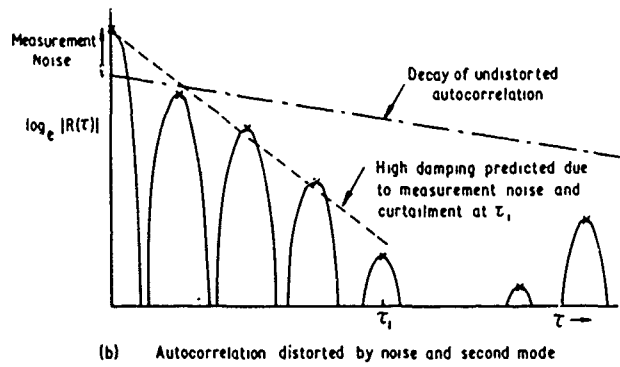
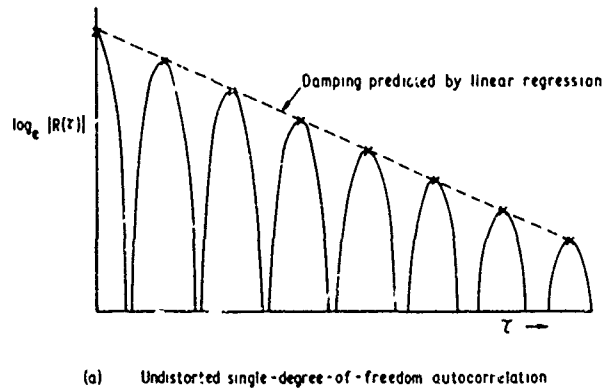


Fig.4 Distortion of autocorrelation function

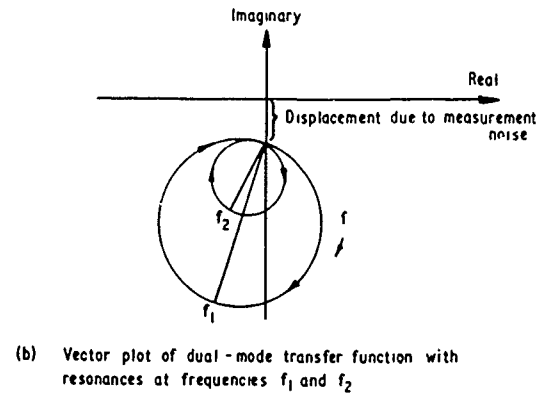
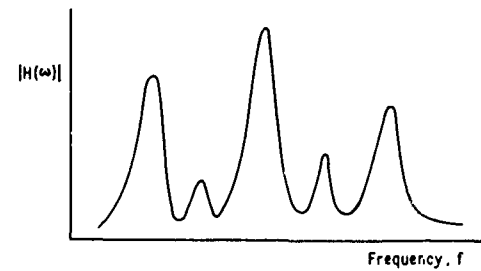


Fig.5 Transfer function representations

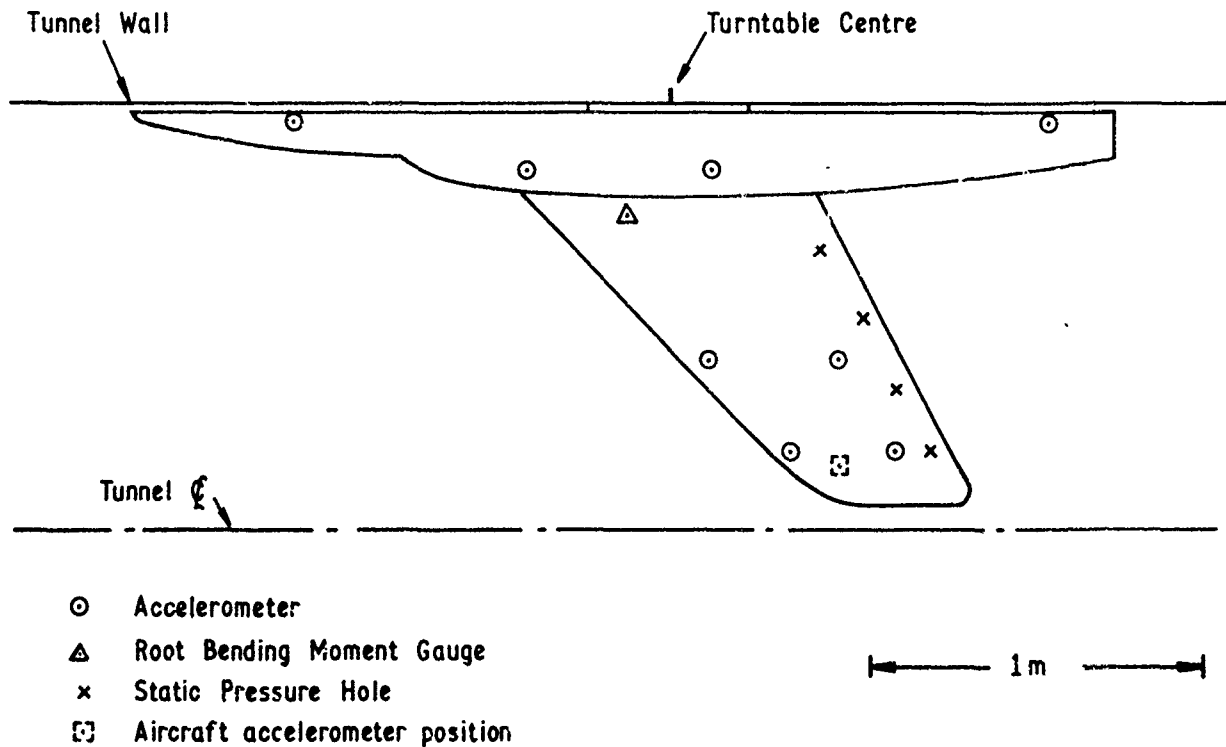


Fig.6 Model of small combat trainer aircraft in RAE 8' x 8' wind tunnel

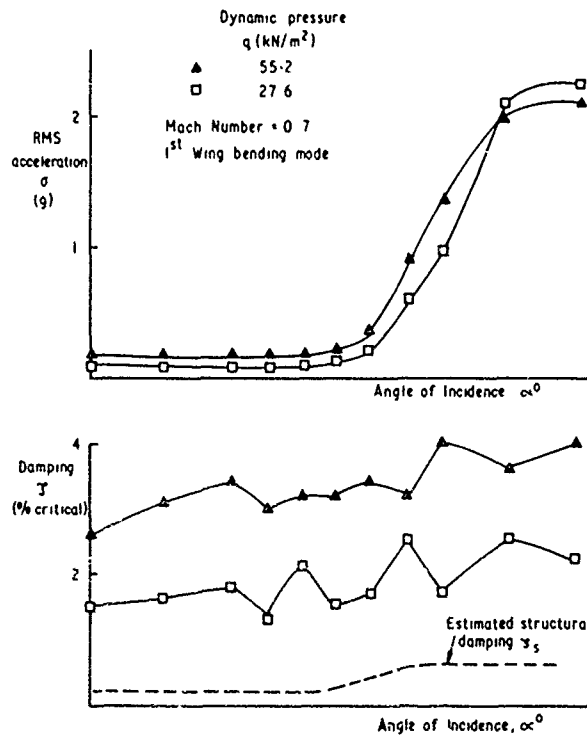


Fig.7 Tunnel measurements of rms wing tip acceleration,  $\sigma$  and damping  $\gamma$  v angle of incidence,  $\alpha^\circ$ .  $M = 0.7$

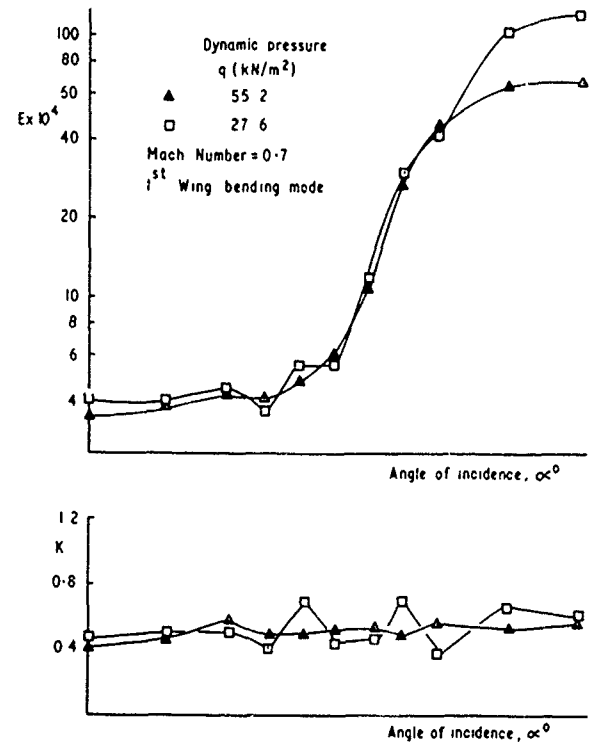


Fig.8 Non-dimensional buffet excitation parameter,  $Ex$  and aerodynamic damping parameter,  $K$  v angle of incidence,  $\alpha^\circ$ .  $M = 0.7$

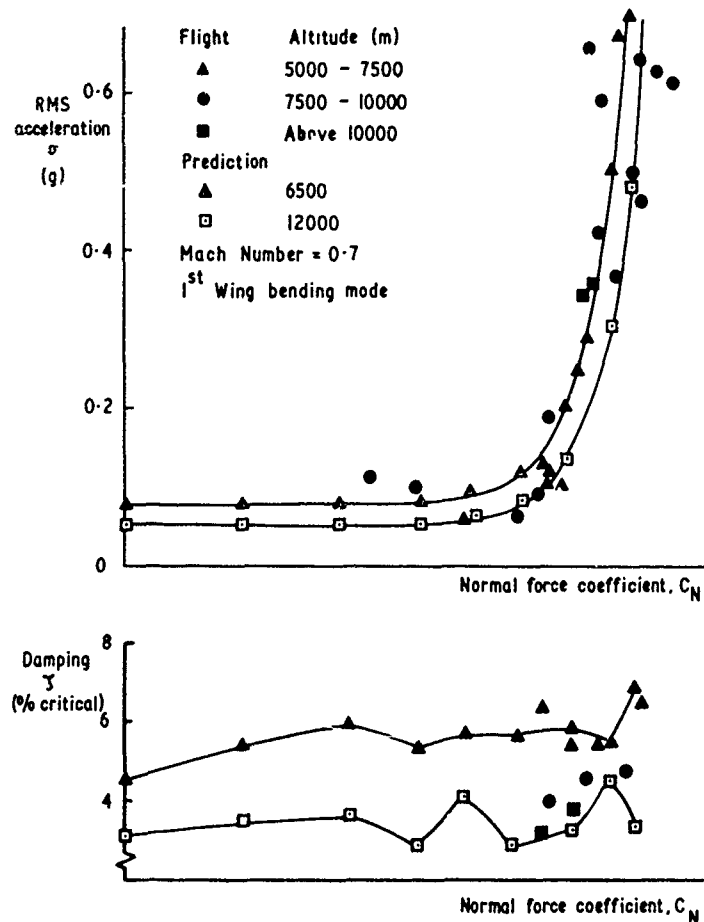


Fig.9 Predicted and measured rms wing tip acceleration,  $\sigma$  and damping  $\gamma$  v normal force coefficient,  $C_N$ :  $M = 0.7$

## QUASI-STEADY AND TRANSIENT DYNAMIC STALL CHARACTERISTICS

by

Lars E. Ericsson and J. Peter Reding  
 LOCKHEED MISSILES & SPACE COMPANY, INC.  
 Sunnyvale, California, 94088, U.S.A.

## SUMMARY

Dynamic airfoil stall is characterized by two separate events: 1) There is a substantial overshoot of the static stall angle and static lift maximum before bona fide separation occurs, 2) After separation has occurred, a "spilled" leading edge vortex travels downstream over the chord causing large changes in the aerodynamic force distribution. With some license the first event can be characterized as quasi-steady, whereas the second event is truly a transient phenomenon. An analysis is presented which extends the earlier developed quasi-steady theory to include the transient effect of the "spilled" leading edge vortex. The large effects of compressibility on the dynamic stall characteristics are also accounted for in the analysis. The analytic results are in good agreement with available dynamic experimental data.

## LIST OF SYMBOLS

AR	aspect ratio, $AR = b^2/S$	$\xi$	dimensionless x-coordinate, $\xi = x/c$
b	wing span	$\rho$	air density
c, $\bar{c}$	reference length: $c = 2\text{-D chord}$ ; $\bar{c} = S/b$	$\rho_N$	nondimensional nose radius, $\rho_N = r_N/c$
$K_a$	dynamic overshoot coefficient, Eq. (1)	$\phi$	wake lag, Eq. (1)
k	reduced frequency, $2k = \bar{\omega}$	$\phi_s$	stall-induced additional phase lag, Eq. (1)
L	lift: coefficient $C_L = L/[(\rho_\infty U_\infty^2)/2] S$	$\omega, \bar{\omega}$	oscillation frequency, $\bar{\omega} = \omega c/U_\infty$
$\ell$	section lift: coefficient $c_\ell = \ell/[(\rho_\infty U_\infty^2)/2] c$	<u>Subscripts</u>	
M	Mach number	AC	aerodynamic center
$M_p$	pitching moment: coefficient $C_m$ $= M_p/[(\rho_\infty U_\infty^2)/2] S \bar{c}$	CG	center of gravity, oscillation axis
$m_p$	section pitching moment: coefficient $c_m$ $= m_p/(\rho_\infty U_\infty^2/2) c^2$	c	convection
n	section normal force, coefficient $c_n$ $= n/(\rho_\infty U_\infty^2/2) c$	crit	critical
p	static pressure: coefficient $C_p$ $= (p - p_\infty)/(\rho_\infty U_\infty^2/2)$	DYN	dynamic
Re	Reynolds number based on chord length	e	boundary layer edge conditions
$r_N$	nose radius	LE	leading edge
S	reference area	MAX	maximum
t	time	N	nose
U	velocity	s	stall
v	velocity ratio, $v = U_e/U_\infty$	SLE	shock-augmented leading-edge separation
X	axial distance from apex of delta wing	STE	shock-augmented trailing-edge separation
x	length coordinate along the chord	sp	separation point
y	airfoil surface height	vs	vortex shedding
$\alpha$	angle of attack	w	wake
$\Delta$	increment	1, 2	numbering subscript
$\eta$	dimensionless y-coordinate, $\eta = y/c$	$\infty$	undisturbed flow
$\theta$	angle-of-attack perturbation	<u>Differential Symbols</u>	
		$\dot{\alpha}$	$= \frac{\partial \alpha}{\partial t}$ ; $\ddot{\theta} = \frac{\partial^2 \theta}{\partial t^2}$
		$c_{\ell \alpha}$	$= \frac{\partial c_\ell}{\partial \alpha}$



## 1. INTRODUCTION

In a recent review of the state of the art in predicting the aerodynamic loading on an airfoil during dynamic stall McCroskey (Ref. 1) points out two main deficiencies; we can predict neither the large effects of the "spilled" leading edge vortex nor the equally large effects of compressibility on the dynamic stall characteristics. The "spilled" vortex effect has been documented by McCroskey et al (Refs. 2 and 3) and by Ham and Garellick (Ref. 4). The large effect of compressibility on the damping in stall has been demonstrated by experiments performed by Lliva et al (Ref. 5) and by Moore et al (Ref. 6). In the present paper, analytic methods developed earlier (Refs. 7 and 8) are extended to include the "spilled" vortex effect and the effect of compressibility thereon.

## 2. DISCUSSION

Dynamic airfoil stall is characterized by two separate events: 1) There is a substantial overshoot of static stall angle and static lift maximum before bona fide separation occurs, 2) After separation has occurred, a "spilled" leading edge vortex travels downstream over the chord causing large changes in the aerodynamic load distribution. The first event can be characterized as quasi-steady, whereas the second event is truly a transient phenomenon. In earlier work (Refs. 7 and 8), only the quasi-steady phase of dynamic stall was considered. It was shown that neglecting the transient phase was permissible when considering the airfoil damping in pitch, provided that the reduced frequency of the pitch oscillation was small. The soundness of this analytic approach has been verified by later results obtained in numerical and experimental investigations (Ref. 9). However, McCroskey et al (Refs. 1 and 2) recently have demonstrated that the occasions when the transient effect can be neglected are probably rare and of little practical consequence to the helicopter designer.

## 3. ANALYSIS

Comparing the large-amplitude oscillatory data of McCroskey et al (Ref. 2), shown in Fig. 1, with the  $\alpha$ -ramp data of Ham et al (Ref. 4), shown in Fig. 3, one finds great similarities in the "upstroke" characteristics. It appears that the first half cycle of the post-stall oscillation in Fig. 2 is captured by the large-amplitude oscillation in Fig. 1. It is discussed in Ref. 10 how the ramp data by Ham et al (Ref. 4) are similar to those obtained by Lambourne (Ref. 11) at high subsonic speed where shock-induced flow separation is the prevailing stall type. In both cases the separation point is describing a pseudo-harmonic oscillation around a quasi-steady mean position. In the low speed stall case the separation point overshoots all the way to the leading edge in the first half cycle before a leading edge vortex is "spilled". In subsequent oscillatory cycles the separation point does not reach as far forward and the "spilled" vortices become more diminutive (Ref. 3). Fig. 1 shows that it can be very important to include the transient "spilled" vortex effect.

## 3.1 Quasi-Steady Effects

McCroskey et al (Ref. 2) measured the phase angle  $(\omega t)$  at which three dynamic events take place, viz., Begin Moment Stall,  $c_n \text{ MAX}$  and  $-c_m \text{ MAX}$  (Fig. 3). The first event should coincide with the phase angle  $(\omega t)_{vs}$  at which the leading edge vortex is first "spilled" downstream. The analysis method of Refs. 8 and 9 can be applied to give this phase angle  $(\omega t)_{vs}$ . Eq. (9) of Ref. 9 gives:

$$\left. \begin{aligned} \alpha_s + K_a \Delta \theta \bar{\omega} \cos(\omega t)_s &= \alpha_0 + \Delta \theta \sin(\omega t - \phi - \phi_s) \\ \phi &= \begin{cases} \xi_w \bar{\omega} : \bar{\omega} \leq 0.16 \\ 0.245 : \bar{\omega} > 0.16 \end{cases} \\ \phi_s &= \xi_{sp} \bar{\omega} \\ K_a &= 2(1 + 2 \xi_{CG}) \end{aligned} \right\} \quad (1)$$

For the special case  $\alpha_0 = \alpha_s$ , Eq. (1) gives

$$(\omega t) = \tan^{-1} \frac{K_a \bar{\omega} + \sin(\phi + \phi_s)}{\cos(\phi + \phi_s)} \quad (2)$$

The test data in Figs. 1 and 3 are for  $\alpha = 15^\circ$ . According to the available static data (Ref. 12) the stall angle for NACA-0012 is  $\alpha_s = 15.5^\circ$  for an effective Reynolds number of 3.5 million. The test data in Figs. 1 and 3 are for  $Re = 2.5 \times 10^6$ , and Eq. (2) should be valid within the expected data accuracy.

McCroskey et al (Ref. 2) showed that the dynamic stall for the data shown in Fig. 3 is for a turbulent boundary layer. Thus,  $\xi_{sp} = 0.75$  according to our quasi-steady analysis (Refs. 8 and 9). For  $\xi_{CG} = 0.25$ , Eqs (1) and (2) give the  $(\omega t)_{vs}$  values shown by the solid line in Fig. 3. The agreement with the corresponding measured event, Begin Moment Stall, is very satisfactory.

## 3.2 Transient Effects

According to measurements (Refs. 13 and 14), the "spilled" leading edge vortex travels down the chord with a velocity  $\bar{U}_v \approx 0.55 U_\infty$ . The phase lag,  $(\Delta \omega t)_{vTE}$ , corresponding to the time needed for the vortex to travel from the leading edge to the trailing edge is simply

$$(\Delta \omega t)_{vTE} = (U_\infty / \bar{U}_v) \bar{\omega} \approx 1.8 \bar{\omega} \quad (3)$$

Adding this lag to  $(\omega t)_{VS}$  gives the phase angle for vortex passage over the trailing edge, which is shown by the dash-dotted line in Fig. 3. It agrees very well with the measured phase lag for the occurrence of  $-c_m \text{ MAX}$ . The moment should, of course, peak just before the vortex leaves the airfoil; and  $c_n \text{ MAX}$  should occur somewhat earlier (Ref. 15). The test data in Fig. 3 indicate that the phase lag that should be added to  $(\omega t)_{VS}$  to predict the occurrence of  $c_n \text{ MAX}$  is approximately 70 percent of  $(\Delta \omega t)_{VTE}$ . This estimate is shown by the dashed line in Fig. 3.

With the phase characteristics of the "spilled" vortex phenomenon known, it remains to determine the magnitude of the vortex-induced load before the full effects on dynamic stall characteristics can be predicted. The leading edge vortex of the delta wing is very similar to the "spilled" vortex on the airfoil. Both cause a nonlinear lift increase (Fig. 4). The shed vortex causes the dynamic overshoot of the infinite Reynolds number lift ceiling discussed earlier, and the leading edge vortex on the delta wing causes an excess lift relative to conventional "attached flow" theories (Ref. 16). The effect of both vortices on the section pressure distribution is illustrated in Fig. 5. For the pitching airfoil, the results by Ham et al. (Ref. 4) show the usual attached flow pressure distribution to persist well beyond static  $\alpha_{MAX}$ . This is due to the "spilled" vortex and its suction effect. The leeside pressure distribution on the delta wing shows a similar suction peak under the leading edge vortex (Ref. 17). Furthermore, both effects are associated with a flow field time lag (Fig. 6). Thus, the transient "spilled" leading edge vortex is the two-dimensional time-dependent equivalent to the three-dimensional steady-state leading edge vortex shedding off a highly swept leading edge.

For a delta wing with apex half angle  $\theta_{LE}$  and center chord  $c_o$ , Polhamus' leading edge suction analogy (Ref. 16) gives the following vortex-induced normal force:

$$N_v = q_\infty c_o \bar{c} \pi \sin^2 \alpha \quad (4)$$

where

$$\bar{c} = (c_o/2) \tan \theta_{LE} \quad (5)$$

The angle of attack normal to the leading edge is

$$\alpha_1 = \tan^{-1} \left( \frac{\tan \alpha}{\sin \theta_{LE}} \right) \quad (6)$$

The corresponding dynamic pressure  $q_1$  as a fraction of free stream dynamic pressure,  $q_\infty$ , is

$$q_1/q_\infty = \sin^2 \alpha + \cos^2 \alpha \sin^2 \theta_{LE} \quad (7)$$

Combining Eqs. (4) through (7) gives the following average strip load:

$$c_{n1} = N_v/q_1 c_o \bar{c} = \pi \sin^2 \alpha_1 \quad (8)$$

Eq. (8) should give an estimate of the normal force associated with the "spilled" leading edge vortex if  $\alpha_1$  is substituted by the vortex shedding angle  $\alpha_{VS}$ .

$$\alpha_{VS} = \alpha_s + K_a \Delta \theta \bar{\omega} \cos (\omega t)_{VS} \quad (9)$$

Static data show the lift  $\Delta c_{LV}$  lost with the "spilled" leading edge vortex (See inset in Fig. 7). Fig. 7 shows that with  $\Delta c_{LV} = c_{n1} \cos \alpha_s$ , Eq. (8) gives a rather good prediction of the measured vortex lift loss (Refs. 12 and 18).

Application of Eqs. (8) and (9) to the data in Fig. 1 gives a substantial underprediction of the experimentally observed "spilled" vortex effects. The reason for the underprediction could be the following. The static data (Ref. 12) show a pre-stall loss of lift (Fig. 8). It is caused by trailing edge separation, which does not have time to develop in the case of dynamic stall, due to the additional convective time lag (Ref. 9). Thus,  $\Delta c_{LV}^*$  rather than  $\Delta c_{LV}$  should be used (see inset in Fig. 9). The variation of the ratio  $\Delta c_{LV}^*/\Delta c_{LV}$  with Reynolds number, obtained from Fig. 8 for NACA-0012, is shown in Fig. 9. The infinite Reynolds number asymptote applicable to the dynamic stall case (Refs. 8 and 9) gives  $\Delta c_{LV}^*/\Delta c_{LV} = 1.5$ . Thus, for the NACA-0012 airfoil at least, the value given by Eq. (8) should be increased by 50 percent.

$$\Delta c_{nv} = 1.5 \pi \sin^2 \alpha_{VS} \quad (10)$$

Combining Eq. (9) with the analysis in Ref. 7 gives  $(c_{nMAX})_{DYN}$  and  $(c_{mMAX})_{DYN}$  in the following form:

$$\left. \begin{aligned} (c_{nMAX})_{DYN} &= (c_{nMAX})_{Q.S.} + \Delta c_{nv} \\ (c_{nMAX})_{Q.S.} &= c_{n\alpha} \alpha_{VS} + \Delta c_{ns} \end{aligned} \right\} \quad (11)$$

$$\left. \begin{aligned} - \left( c_{m_{MAX}} \right)_{DYN} &= \left( c_{m_{MAX}} \right)_{Q.S.} + \Delta c_{n_v} \\ - \left( c_{m_{MAX}} \right)_{Q.S.} &= c_{n_{\alpha}} \alpha_{vs} \left( \xi_{AC} - \xi_{CG} \right) - \Delta c_{m_s} \end{aligned} \right\} \quad (12)$$

$\Delta c_{n_s}$  and  $\Delta c_{m_s}$  are the effects of pitch rate induced camber and apparent mass terms. It was shown in Refs. 8 and 9 that  $\Delta c_{n_s}$  usually can be neglected, whereas  $\Delta c_{m_s}$  can be significant.

For the case usually considered,  $\xi_{AC} = \xi_{CG} = 0.25$ , Eq. (12) simplifies to

$$- \left( c_{m_{MAX}} \right)_{DYN} = - \Delta c_{m_s} + \Delta c_{n_v} \quad (13)$$

where  $-\Delta c_{m_s}$  is a function of  $(c\dot{\theta}/U_{\infty})_{vs} = -\Delta\theta\omega \cos(\omega t)_{vs}$  and  $(c^2\ddot{\theta}/U_{\infty}^2)_{vs} = -\Delta\theta\omega^2 \sin(\omega t)_{vs}$  (see Ref. 7).

Fig. 10 is Fig. 19 of Ref. 1 in which the old Lockheed prediction has been substituted with the present one that includes the effect of the "spilled" vortex. The figure shows good agreement between experimental results and present prediction.

### 3.3 Rampwise $\alpha$ - Change

In the case of rampwise  $\alpha$  - change, Eq. (1) is substituted by the following equation (Refs. 8 and 9)

$$\left. \begin{aligned} \alpha_{vs} &= \alpha_s + \Delta\alpha_w + \Delta\alpha_s + \Delta\alpha_{sp} \\ \Delta\alpha_w &= \xi_w c\dot{\alpha}/U_{\infty} \\ \Delta\alpha_s &= K_a c\dot{\alpha}/U_{\infty} \\ \Delta\alpha_{sp} &= \xi_{sp} (c\dot{\alpha}/U_{\infty}) \end{aligned} \right\} \quad (14)$$

and the equation corresponding to Eq. (3) is<sup>#</sup>

$$\Delta\alpha_{vTE} = 1.8 c\dot{\alpha}/U_{\infty} \quad (15)$$

For the turbulent type leading edge stall occurring on most airfoils (Refs. 1 and 2), the following parameter values apply (Ref. 9)

$$\left. \begin{aligned} \xi_w &= 1.5 \\ K_a &= 2 \left( 1 + 2 \xi_{CG} \right) \\ \xi_{sp} &= 0.75 \end{aligned} \right\} \quad (16)$$

The experimental results obtained by Ham et al (Ref. 4) are replotted in Fig. 11 together with the angle of attack variation with time. The angular rate can be approximated by two constant values, a slow rate of  $c\dot{\alpha}_1/U_{\infty} = 0.012$  below  $\alpha_1 = 5^\circ$  and a much higher rate,  $c\dot{\alpha}_2/U_{\infty} = 0.043$ , for  $\alpha_2 > 5^\circ$ . At  $\alpha = 5^\circ$  the flow is attached, and the total time lag before the new rate is influencing the lift is simply the Karman - Sears lag (Ref. 19). That is,  $\Delta\alpha_{w2} = 1.5 c\dot{\alpha}/U_{\infty} = 3.7^\circ$ . Adding this time lag effect to  $\alpha_1 = 5^\circ$  gives the angle of attack,  $\alpha_2 = 8.7^\circ$ , at which the higher angular rate starts affecting the aerodynamic characteristics. Due to pitch-rate-induced camber and apparent mass effects, the attached flow lift curve will lag the static lift by only half the Karman - Sears wake lag (Ref. 9). Thus, the lag is  $\Delta\alpha_{w1}/2 = 0.5^\circ$  for  $\alpha < \alpha_2$  and  $\alpha_{w2}/2 = 1.9^\circ$  for  $\alpha > \alpha_2$ . To this attached flow lift is added the "spilled" vortex effect as described earlier. The resulting predicted lift is shown by the solid line in Fig. 11. It appears that aside from an  $\alpha$  - zero shift of  $2.5^\circ$  (in the apparent static reference data) the attached flow lift characteristics are in good agreement with experimental results. Applying this  $\alpha$  - zero shift gives the

<sup>#</sup> Note that dynamic  $c_{l_{max}}$  occurs after 70 percent of the phase lag  $\Delta\alpha_{vTE}$  as was discussed earlier.

prediction shown in Fig. 12. The agreement between present prediction and experimental results (Ref. 4) is rather good. In regard to the differences, the following can be said.

Three-dimensional flow phenomena can distort the "two-dimensional" measurements made in one chord-wise strip using fast response pressure transducers, as in the present case (Ref. 20). The  $\alpha$ -zero shift could have been caused by such interference effects, although it, as well as the deviation between static and dynamic stall moment characteristics, could also have been introduced electronically during the data recording and processing. Moss and Mordin (Ref. 21), who performed almost the same experiment as Ham and Garellick (Ref. 4) conclude that their anomalous dynamic results were in large part due to the three-dimensional flow effects illustrated in Fig. 13. McCroskey et al (Ref. 2) observed in their test "large three-dimensional interactions between the model and the tunnel-wall boundary layers", but found the effects to be decreasing with increasing  $k$  until they were effectively filtered out and "could hardly be detected for  $k \geq 0.15$ ." Thus, the results in Fig. 1 and the high frequency results ( $\bar{\omega} \geq 0.3$ ) in Figs. 3 and 10 are free from 3-D flow interaction effects. However, the lower frequency results in Figs. 3 and 10 as well as the  $\alpha$ -ramp data in Figs. 2, 11, and 12 presumably all would have been influenced by the airfoil-wall flow interaction. Of course, it may accidentally happen that the end plate vortex in a two-dimensional test supplies venting of the separated flow region similar to that of the tip vortex on a rotating helicopter blade (Fig. 14). Twaites (Ref. 22) has discussed how the wall-boundary-layer separation caused by a cylindrical protuberance rolls up into a horseshoe vortex (see left part of Fig. 14). Gregory et al (Ref. 23) show how at stall the end plate boundary-layer separates to form a similar wing-end plate vortex (see right half of Eq. 14), which is of the same direction as the tip vortex for a loaded wing tip (see bottom part of Fig. 14).

#### 4. COMPRESSIBILITY EFFECTS

The large effect of subsonic Mach number on dynamic stall observed by Liiva et al (Ref. 5) in their experiments is shown in Fig. 15. Goetz (Ref. 24) measured similar large M-effects on the stall flutter boundary of a straight wing (Fig. 16). It was shown in Ref. 25 how this flutter boundary could be predicted analytically. The analytic methods of Ref. 25 will be applied here to predict the Mach number trend of the data in Fig. 15.

##### 4.1 Effect of Compressibility on $c_{LMAX}$

Using the simple analysis by Vile (Ref. 26) one can determine the compressibility effect as follows. Near the leading edge, all NACA airfoil shapes are well approximated by a parabola, with the nose radius as the characteristic length

$$\eta^2 = 2\rho_N \xi \quad (17)$$

The velocity determined by potential flow theory is as follows for moderate  $\alpha$  (Refs. 26 and 27)

$$U_e/U_\infty = \left\{ \xi^{0.5} + \left[ 1 + (\rho_N/2)^{0.5} \right] \alpha \right\} / (\xi + \rho_N/2)^{0.5} \quad (18)$$

$$\partial v / \partial \xi = \left\{ (\rho_N/2) \xi^{-3.5} - \left[ 1 + (\rho_N/2)^{0.5} \right] \alpha \right\} / 2 (\xi + \rho_N/2)^{1.5} \quad (19)$$

From Eqs. (18) and (19) one obtains

$$(U_e/U_\infty)_{MAX} = \left\{ 1 + \left[ 1 + (\rho_N/2)^{0.5} \right]^2 \alpha^2 / (\rho_N/2) \right\}^{0.5} \quad (20)$$

For a typical nose radius (e.g.,  $\rho_N = 1\%$ ), the tunnel Mach number at  $\alpha = 10^\circ$  would have to be  $M_\infty \leq 0.1$  in order to correspond to the low angle-of-attack assumption for incompressibility; i.e.,  $M_\infty \leq 0.4$ . Thus, for all practical purposes there is no such thing as incompressible airfoil stall. Unfortunately, there is no information available about the test Mach number for most of the available static stall data. The range usually given is 150 mph  $\leq U_\infty$  300 mph, which corresponds to  $0.2 \leq M_\infty \leq 0.4$ . This Mach number range can cause quite a change in  $C_{LMAX}$ , as is shown in Ref. 25.

The effect of surface slope or thickness is scaled by the Prandtl-Glauert Analogy (Ref. 28)

$$\eta' = \frac{\partial \eta}{\partial \xi} \sim (1 - M_\infty^2)^{0.5} \quad (21)$$

This applies for a sharp leading-edge airfoil at low  $\alpha$ , when maximum velocity is determined by airfoil thickness. However, on a "round-nosed" airfoil at stall, the maximum velocity occurs at the nose, and surface curvature rather than slope determines the peak velocity. Following the usual procedure of neglecting the effect of  $\eta'$  compared to  $\eta''$  when determining the curvature, the peak velocity near stall is scaled by  $\eta''$ . Equations (17) and (21) give

$$\eta'' = -\eta'^3/\rho_N \sim (1 - M_\infty^2)^{1.5} \quad (22)$$

That is,

$$\left[ (C_{LMAX})_2 / (C_{LMAX})_1 \right] R_c \rightarrow \infty = \left[ (1 - M_2^2) / (1 - M_1^2) \right]^{1.5} \quad (23)$$

At higher Mach numbers, the M-dependence given by Eq. (23) is obviously not valid. When the leading edge stall is shock induced, the effect of Mach number on  $c_{l\max}$  becomes much less. Tests indicate that the M-dependence is the same for rounded leading edge airfoils as for double circular arc airfoils (Ref. 30). This insensitivity to geometry has also been demonstrated for other airfoils. Thus, the maximum lift is determined by the airfoil thickness and one would expect that the sharp-leading-edge/thickness-dominated case, Eq. (21), is the appropriate scaling model for  $M_{SLE} < M_\infty < M_{STE}$ . That is

$$\left[ (c_{l\max})_2 / (c_{l\max})_1 \right] = \left[ 1 - M_1^2 / 1 - M_2^2 \right]^{0.5} \quad (24)$$

The critical Mach number  $M_{SLE}$  is that giving shock-augmented leading-edge separation. For Mach numbers above  $M_{STE}$ , the shock is moving back towards the trailing edge, and the separation is of the shock-augmented trailing edge-type. It is obviously important to determine  $M_{SLE}$  for the particular airfoil of interest. Percy (Ref. 31) shows that incipient separation occurs when the shock strength is  $p_2/p_1 \approx 1.4$ , and that full, shock-augmented, leading-edge separation occurs when the local Mach number approaches  $M_e = 1.4$  (slightly lower  $M_e$  for thinner airfoils than 12 percent). The corresponding  $M_\infty$  is determined as follows: Determine  $U_{e\max}(\alpha_0)/U_\infty$ , where  $\alpha_0$  is the angle-of-attack, giving "flat-top" velocity distribution over the airfoil (Ref. 27). Determine  $U_{e\max}(0)/U_{e\max}(\alpha_0)$  and  $U_{e\max}(0)/U_{e\max}(\alpha_s)$  from Eq. (20). Then

$$\frac{U_{e\max}(\alpha_s)}{U_\infty} = \left[ \frac{U_{e\max}(0)}{U_{e\max}(\alpha_0)} / \frac{U_{e\max}(0)}{U_{e\max}(\alpha_s)} \right] \frac{U_{e\max}(\alpha_0)}{U_\infty} \quad (25)$$

For  $M_e = 1.4$ , the Mach number ratio corresponding to Eq. (25) is simply

$$M_{e\max}(\alpha_s) / M_\infty = \left[ U_{e\max}(\alpha_s) / U_\infty \right]^{0.85} \quad (26)$$

For the airfoil used in the stall flutter test (Ref. 24), NACA 64-012, the value is  $M_{SLE} = 0.35$ .

In summary, the compressibility effects on the maximum lift are given by Eq. (23) when  $M_\infty < M_{SLE}$ , and by Eq. (24) when  $M_\infty \geq M_{SLE}$ .

#### 4.2 Dynamic Stall and Reattachment Angles of Attack

For the Mach number range  $M_\infty \leq 0.6$ , the lift curve slope variation with Mach number is predicted by the Prandtl-Glauert compressibility factor. (See Fig. 17 and Ref. 28.)

$$(c_{l\alpha})_2 / (c_{l\alpha})_1 = \left[ (1 - M_1^2) / (1 - M_2^2) \right]^{0.5} \quad (27)$$

Fig. 17 shows that there is a dramatic decrease in  $c_{l\alpha}$  for higher Mach numbers, e.g., at  $M_\infty > 0.7$  for NACA 0012-63 (Ref. 32). It is likely that this critical Mach number is simply  $M_\infty = M_{STE}$ , as previously discussed. The finite aspect ratio (AR) lift curve slope is simply:

$$C_{L\alpha} = c_{l\alpha} / \left( 1 + c_{l\alpha} / \pi AR \right). \quad (28)$$

With the linear relationship:  $c_{l\max} = c_{l\alpha} \alpha_s$ , one obtains the following definition of the stall angle of attack

$$\left. \begin{aligned} \left( \alpha_{s2} / \alpha_{s1} \right)_{R_c \rightarrow \infty} &= \left[ (1 - M_2^2) / (1 - M_1^2) \right]^2 \\ M_\infty &< M_{SLE} \\ \left( \alpha_{s2} / \alpha_{s1} \right)_{R_c \rightarrow \infty} &= \left( \alpha_{s2} / \alpha_{s1} \right)_{R_c \rightarrow 0} = (1 - M_2^2) / (1 - M_1^2) \\ M_{SLE} &< M_\infty < M_{STE} \quad M_\infty < M_{STE} \end{aligned} \right\} \quad (29)$$

The stall flutter boundary in Fig. 16 was obtained with continually decreasing angle-of-attack to simulate the space shuttle transition maneuver (Ref. 33). Thus, the  $\alpha$ -boundaries are as follows (Ref. 25). The high  $\alpha$ -boundary is the highest  $\alpha$  for which flow reattachment can be established on the "upstroke" and the low  $\alpha$ -boundary is the lowest  $\alpha$  at which separated flow can be reestablished on the "downstroke" of the pitching airfoil section. Due to the large reduced frequencies (Ref. 25) the high and low  $\alpha$ -limits for stall flutter are given by the static stall angles for "infinite" and "zero" Reynolds number. The stall flutter boundaries determined in this manner for the NACA 64-0012 airfoil tested by Goetz (Ref. 24) agree rather well with experimental results (Fig. 18). At  $M_\infty = 0.7$ , the  $c_{l\alpha}$ -slope changes drastically for a 12-percent thick airfoil (Fig. 17), thus indicating that  $M_{STE} = 0.7$ ; i.e., the shock starts moving aft over the airfoil for  $M_\infty > 0.7$ . The  $\alpha = \text{constant}$  line for  $M_\infty > M_{STE}$  agrees with the combined effect of  $c_{l\alpha}$ -loss and  $c_{l\max}$ -increase for increasing Mach number. At some Mach number between  $M_\infty = 0.8$  and  $M_\infty = 0.9$ , the shock has moved aft of the elastic axis, or nearly so (the flutter model had 5 percent structural damping), and flutter is not observed. In other words, this high-Mach-number/low frequency cutoff of the flutter boundary is a pure

Mach number effect, independent of reduced frequency but somewhat dependent upon elastic axis location and structural damping.

The results in Fig. 15 are all for nearly the same frequency and oscillation amplitude, and the effective (lift-generating) overshoot  $\Delta\alpha_s$  of the static stall angle  $\alpha_s$  will be the same. Furthermore, due to the rather high frequency,  $\Delta\alpha_s$  will be small,  $1.78^\circ \leq \Delta\alpha_s \leq 2.05^\circ$ . (see Eq. (8)). That is, the variation of  $\alpha_{vs}$ , (and consequently of  $\Delta c_{ny}$ ) with Mach number is mainly generated by the variation with  $M_\infty$  of static stall angle  $\alpha_s$ , similarly to what was the case for the stall flutter boundary discussed earlier. Figure 19 shows that the predicted vortex effect on the pitching moment,  $-\Delta c_{my} = \Delta c_{ny}$ , is in fair agreement with experiment. (The inset in Fig. 19 shows how  $-\Delta c_{my}$  was determined from the experimental results.)

Figure 1 illustrates that the spilled vortex has a much larger effect on the area enclosed by the lift loop than on that enclosed by the  $c_m(\alpha)$  - loop. This implies that although the vortex effect on the pitch damping is small, the effect on wing bending can be large if structural coupling is supplied by mass unbalance (Refs. 34 and 35) or by leading edge deformation (Ref. 36), as was discussed in Ref. 10. As the first half cycle (at least) of the transient will be caught each time the effective angle of attack exceeds  $\alpha_{vs}$ , the transient starts having a strong influence on the damping in bending (especially) and in pitch long before the structural frequencies approach the resonance value prescribed by the oscillating transient (see Fig. 2). In the case of the buffet problem discussed in Ref. 10, the "first half cycle" could possibly explain the extremely high apparent damping ratios measured by Jones (Ref. 37).

## 5. CONCLUSIONS

A previously developed quasi-steady theory for dynamic stall has been extended to include the transient effects of the "spilled" leading edge vortex. The more important results are:

- o Adding the moving separation point effect to the quasi-steady separation value correctly predicts the "spilling" of the leading edge vortex.
- o The travel of the "spilled" leading edge vortex over the chord occurs at 55 percent of free stream speed. Peak pitching moment values occur shortly before the "spilled" vortex leaves the trailing edge, and peak normal force occurs 30 percent earlier.
- o Using Polhamus' leading edge suction analogy, a simple means is provided for prediction of the vortex induced loads.

The present analytic method correctly predicts the large vortex effect measured in high amplitude oscillations in pitch, including the large effects of subsonic Mach number. Furthermore, with the developed analytic means the very nonlinear behaviour observed by Ham et al of the airfoil aerodynamics during a rampwise change of angle of attack can be predicted (within the expected data accuracy of the experiment). This indicates that the present analytic method could be applied to predict the nonlinear, nonharmonic unsteady characteristics of a helicopter blade passing through the stall region.

Undoubtedly much theoretical and experimental work is still needed before the dynamic stall phenomenon will be fully understood. It appears, however, that the presented engineering method, which uses static experimental data as an input, could after some further development provide a much needed design tool in the helicopter and compressor industries.

## REFERENCES

1. McCroskey, W. J., "Recent Developments in Dynamic Stall," Symposium on Unsteady Aerodynamics, University of Arizona, Tucson, Arizona, March 18-20, 1975.
2. McCroskey, W. J., Carr, L. W., and McAllister, K. W., "Dynamic Stall Experiments on Oscillating Airfoils," AIAA Journal, Vol. 14, No. 1, Jan. 1976, pp. 57-63.
3. Martin, J. M., Empey, R. W., McCroskey, W. J., and Caradonna, F. X., "An Experimental Analysis of Dynamic Stall on an Oscillating Airfoil," Journal of the American Helicopter Society, Vol. 19, No. 1, Jan. 1974, pp. 26-32.
4. Ham, N. D., and Garelick, M. S., "Dynamic Stall Considerations in Helicopter Rotors," American Helicopter Society Journal, Vol. 13, April 1968, pp. 44-55.
5. Liiva, J., Davenport, F. J., Gray, L., and Walton, I. C., "Two-Dimensional Tests of Airfoils Oscillating Near Stall," TR 68-13A & B, April 1968, U. S. Army Aviation Material Labs., Fort Eustis, Va.
6. Moor, A. W., Lambourne, N. C., and Woodgate, L., "Comparison Between Dynamic Stability Boundaries for NACA 9615 and NACA 0012 Airfoils Pitching about the Quarter-Chord," C. P. No. 1279, Aug. 1971, Aer. Res. Council, London, Great Britain.
7. Ericsson, L. E., and Reding, J. P., "Unsteady Airfoil Stall, Review and Extension," Journal of Aircraft, Vol. 8, No. 8, August 1971, pp. 609-616.
8. Ericsson, L. E., and Reding, J. P., "Analytic Prediction of Dynamic Stall Characteristics," AIAA Paper No. 72-682, June 1972.
9. Ericsson, L. E., and Reding, J. P., "Dynamic Stall Analysis in Light of Recent Numerical and Experimental Results," Journal of Aircraft, Vol. 13, No. 4, April 1976, pp. 248-255. See Also AIAA Paper No. 75-76.
10. Ericsson, L. E., "Dynamic Effects of Shock-Induced Flow Separation," Journal of Aircraft, Vol. 12, No. 2, Feb. 1975, pp. 86-92.
11. Lambourne, N. C., "Some Instabilities Arising from the Interaction Between Shock Waves and Boundary Layers," C. P. No. 473, Feb. 1968.
12. Jacobs, E. N. and Sherman, A., "Airfoil Section Characteristics as Affected by Variations in the Reynolds Number," Tech. Report 586, 1937, NACA.
13. Philippe, J. J., "LeDecrochage Instationnaire d'un Profil," TP No. 936, 1938, ONERA.

14. Werlé, H. et Armand, C., "Mesures et Visualisations Instantanées sur les Rotors," T. P. No. 777, 1969 ONERA.
15. Ericsson, L. E. and Reding, J. P., "Dynamic Stall of Helicopter Blades," *Journal of the American Helicopter Society*, Vol. 17, No. 1, Jan. 1972, pp. 10-19.
16. Polhamus, E. C., "Predictions of Vortex-Lift Characteristics by Leading Edge Suction Analogy," *Journal of Aircraft*, Vol. 8, No. 4, April 1971.
17. Hummel, D., "Zur Umströmung Scharfkantiger Schlanke Deltaflügel bei grossen Anstellwinkeln," *Z. Flugwiss.*, Vol. 15, No. 10, 1967, pp. 376-385.
18. Critzos, C. C., Heyson, H. H., and Boswinkle, R. W. Jr., "Aerodynamic Characteristics of NACA-0012 Airfoil Section at Angles of Attack from  $0^\circ$  to  $180^\circ$ ," TN 3361, 1955, NACA.
19. von Karman, Th and Sears, W. R., "Airfoil Theory for Non-Uniform Motion," *J. Aer. Sci.*, Vol. 5, No. 10, August 1938, pp. 379-390.
20. Ericsson, L. E. and Reding, J. P., "Dynamic Stall Simulation Problems," *J. Aircraft*, Vol. 8, No. 7, July 1971, pp. 579-583.
21. Moss, G. F. and Murdin, P. M., "Two-Dimensional Low-Speed Tunnel Tests on the NACA 0012 Section Including Measurements Made During Pitch Oscillation at the Stall," CP No. 1145, 1971, Aeronautical Research Council, Great Britain.
22. Twaites, B., "Incompressible Aerodynamics," *Fluid Motion Memoirs*, Oxford at the Clarendon Press, 1960, pp. 211, 223.
23. Gregory, N., Quincey, V. G., O'Reilly, C. L. and Hall, D. J., "Progress Report on Observations of Three-Dimensional Flow Patterns Obtained During Stall Development on Airfoils, and the Problem of Measuring Two-Dimensional Characteristics," CP No. 1146, 1971 (Also NPL Aero Report 1309, 1969), Aeronautical Research Council, Great Britain.
24. Goetz, R. C., "Exploratory Study of Buffet and Stall Flutter of Space Shuttle Vehicle Wing Concepts," NASA LWP-872, 22 May 1970.
25. Ericsson, L. E. and Reding, J. P., "Stall Flutter Analysis," *J. Aircraft*, Vol. 10, No. 1, January 1973, pp. 5-13.
26. Abbot, I. H., Von Doenhoff, A. E., and Stivers, L. S., "Summary of Airfoil Data," TR 824, 1945, NACA.
27. Ville, G., "Influence des Decallements au Bord d'Attaque sur les Caracteristiques Aerodynamiques des Voilures," *Association Francaise des Ingenieurs et Techniciens de l'Aeronautique et de l'Espace*, Colloque d'Aerodynamique Appliquée, 4th, Lille, France, 8-10 Nov. 1967.
28. Glauert, H., "The Effect of Compressibility on the Lift of Airfoils," *Proc. Royal Soc., Series A*, CXVIII (1927), pp. 113-119.
29. Harper, P. W. and Flanigan, R. E., "The Effect of Rate of Change of Angle of Attack on the Maximum Lift of a Small Model," TN 2061, 1949, NACA.
30. Daley, B. N. and Lord, D. R., "Aerodynamic Characteristics of Several 6-Percent-Thick Airfoils at Angles of Attack from  $0$  to  $20^\circ$  at High Subsonic Speeds," TN 3424, 1955, NACA.
31. Pearcey, H. H., "Some Effects of Shock-Induced Separation of Turbulent Boundary-Layers in Transonic Flow Past Airfoils," Paper 9, *Proceedings of Symposium on Boundary Layer Effects in Aerodynamics*, National Physics Laboratory, Great Britain, 31 Mar. - 1 Apr. 1955.
32. Abbot, I. H. and von Doenhoff, A. E. *Theory of Wing Sections*, McGraw Hill Book Co., New York (1949).
33. Stengel, R. F., "Optimal Transition From Entry to Cruising Flight," AIAA Paper No. 70-1018, Aug. 1970.
34. Erickson, L. L., Gambucci, B. J., and Wilcox, P. R., "Effects of Space Shuttle Configurations on Wing Buffet and Flutter, Part II, Thick High-Aspect Ratio Wing," NASA Space Shuttle Technology Conference, Vol. III: Dynamics and Aeroelasticity, TM X-2274, 1971, pp. 201-229, NASA.
35. Erickson, L. L., "Transonic Single-Mode Flutter and Buffet of a Low Aspect Ratio Wing Having a Subsonic Airfoil Shape," TN D-7346, Jan. 1974, NASA.
36. Moss, G. F., "Some Notes on the Aerodynamic Problems Associated with the Phenomenon of Buffeting," *Tech. Memo. Aero 1293*, Feb. 1971, Royal Aeronautical Establishment, London.
37. Jones, J. G., "The Dynamic Analysis of Buffeting and Related Phenomena," Paper 23, AGARD-CP-120, 1972.

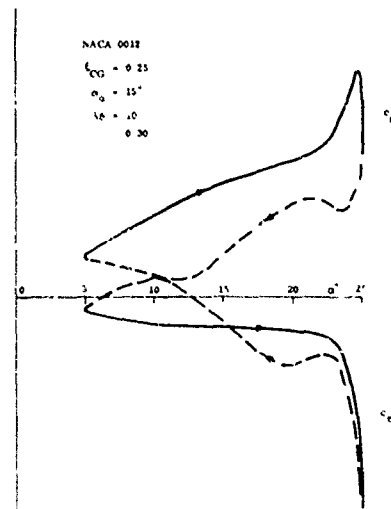


Fig. 1 Large-amplitude oscillation data (Ref. 4).

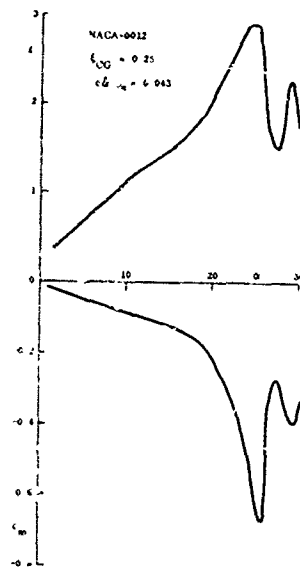
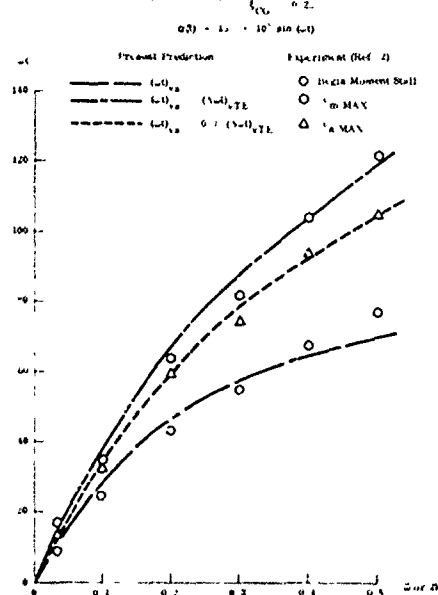
Fig. 2 Data for  $\alpha$ -ramp overshoot of static stall (Ref. 4).

Fig. 3 Predicted and measured dynamic stall phase angles.

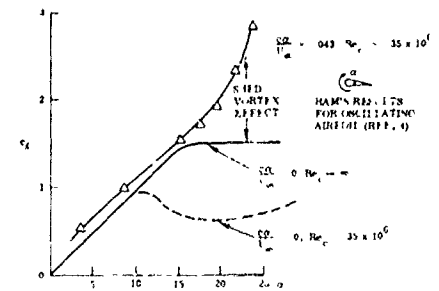


Fig. 4 Nonlinear vortex-induced lift.

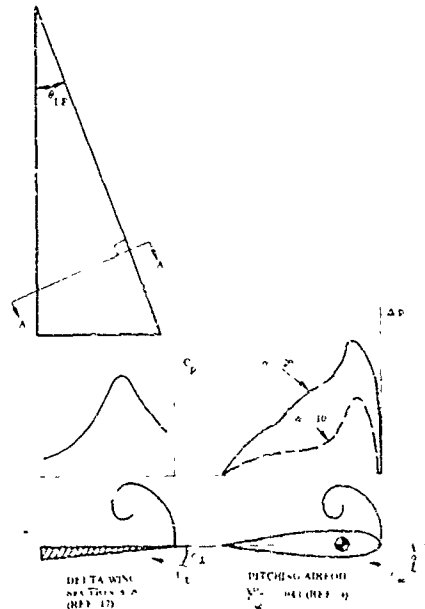


Fig. 5 Vortex-induced suction loads.

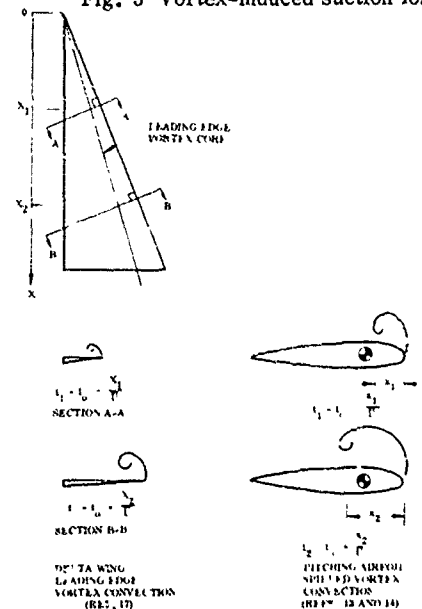


Fig. 6 Space-time equivalent vortex effects.



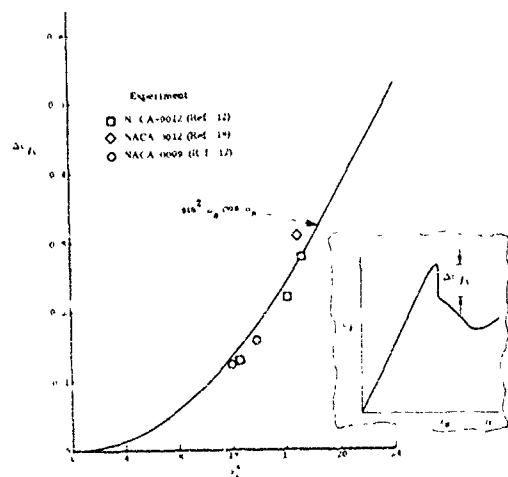


Fig. 7 Lift loss due to "spilled" leading edge vortex.

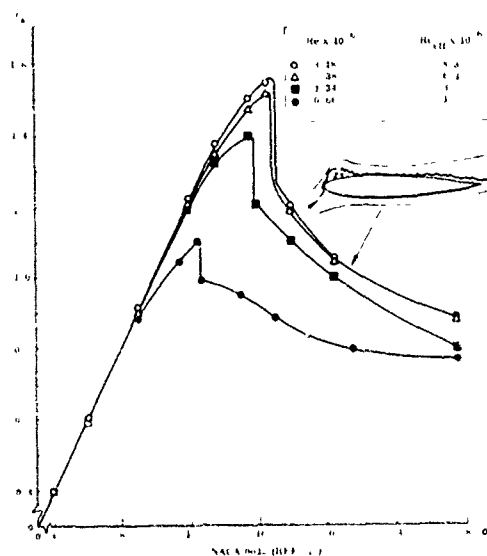


Fig. 8 Section lift of NACA 0012 (Ref. 12).

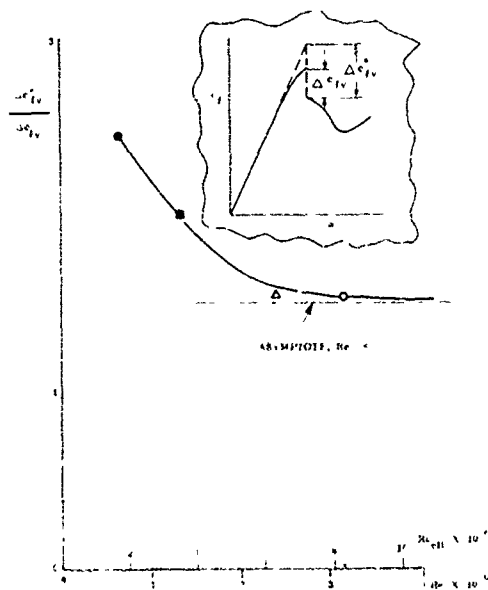


Fig. 9 Linear overshoot of stall.

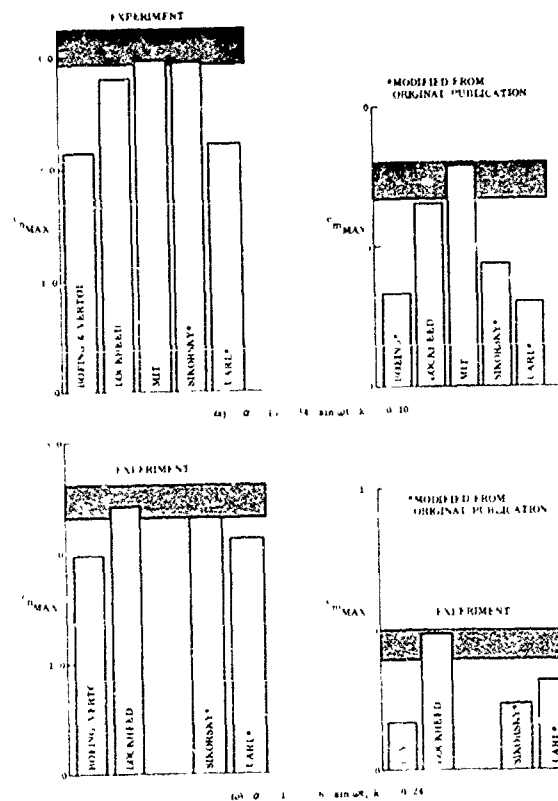
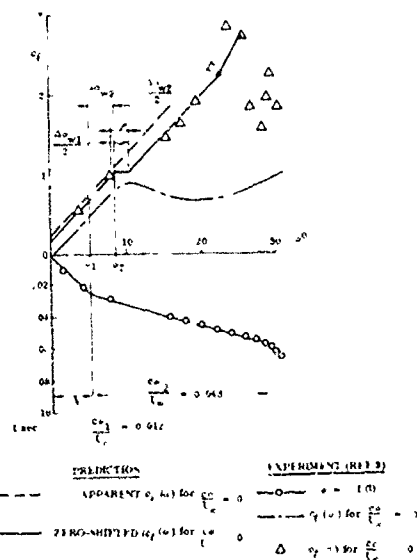


Fig. 10 Predictions and measurements of maximum normal force and pitching moment coefficients for an oscillating NACA 0012 airfoil.

Fig. 11 Nonlinear  $\alpha$ -ramp characteristics.

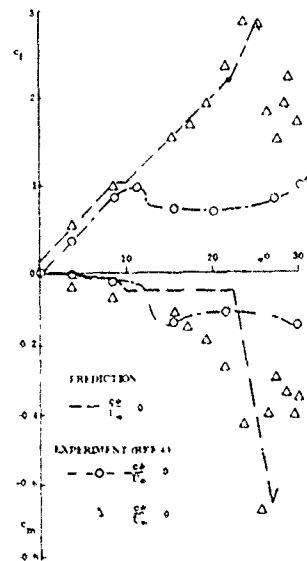


Fig. 12 Comparison of experimental  $\alpha$ -ramp results with refined predictions.

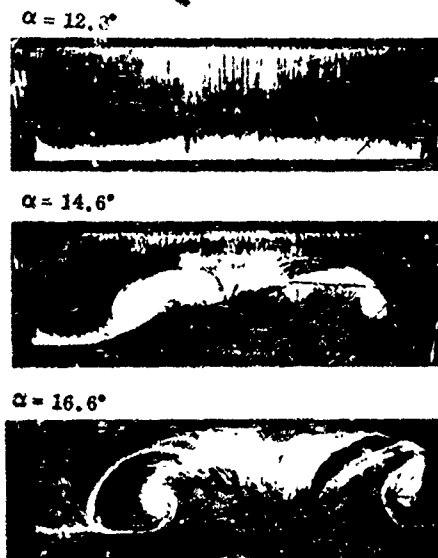
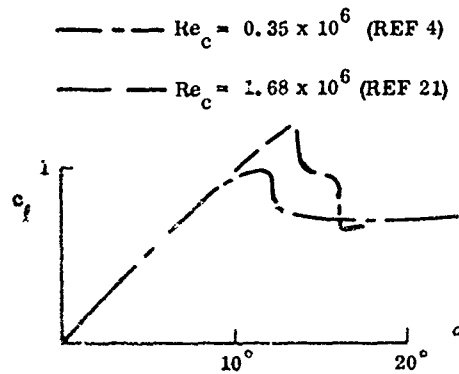


Fig. 13 Wall interference effects on "2-D" stall.

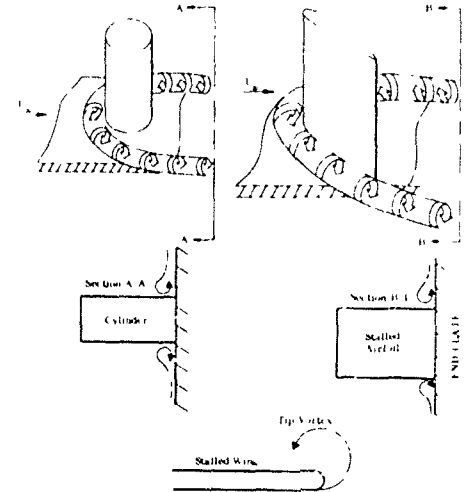


Fig. 14 Endplate vortex.

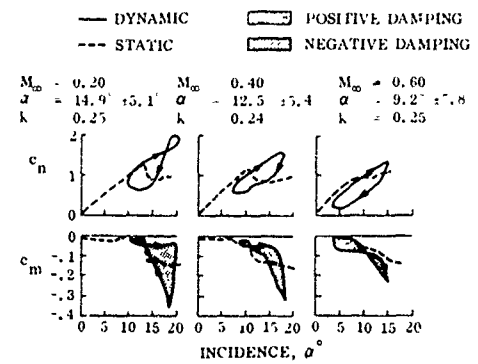


Fig. 15 Effect of Mach number on dynamic stall on an oscillating NACA 0012 airfoil.

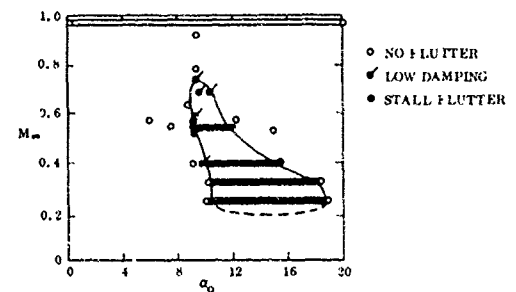


Fig. 16 Effect of Mach number on the  $\alpha$ -boundary for stall flutter of a NACA 64-012 airfoil in air.

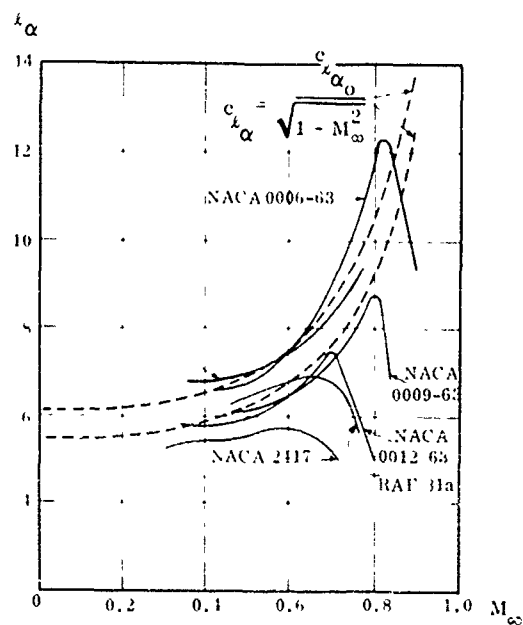


Fig. 17 Effect of Mach number on lift-curve slope.

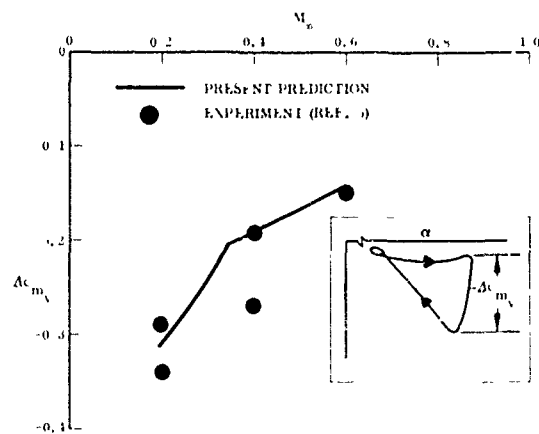


Fig. 19 Mach number influence on the "spilled" vortex effect.

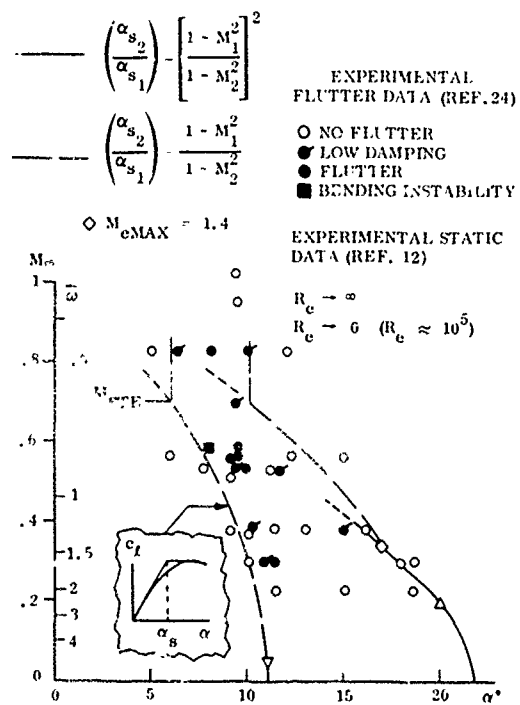


Fig. 18 Predicted and measured boundaries for stall flutter.

## THEORY OF WING SPAN LOADING INSTABILITIES NEAR STALL

by

E. S. Levinsky

General Dynamics, Convair Division, San Diego, CA., USA

## SUMMARY

A nonlinear, lifting line procedure with unsteady wake effects has been developed for predicting wing-body aerodynamic characteristics up to and beyond stall. The procedure may prove useful for simulating and alleviating such adverse wing stalling characteristics as wing rock, wing drop, loss of roll control or roll control reversal.

A discrete vortex lattice representation is used for the time dependent wake, whereas the wing load distribution is assumed concentrated along the 25% chord line. Each chordwise section is assumed to act aerodynamically (including stall) like a 2D airfoil in steady flow at an effective angle of attack, which may be time dependent. Other assumptions are incompressible flow, moderate sweep, large aspect ratio and conditions for stall progression across the span.

Comparisons are made with existing theory and test data. Effects of planform geometry and of airfoil section characteristics on stall are presented. For airfoils with a large post-stall negative lift curve slope, the solutions sometimes exhibit lift hysteresis and "zero-beta" rolling and yawing moments. These results are due to the existence of multiple solutions of the lifting line equations (first shown by R. S. Schairer, 1939). Increasing aspect ratio and decreasing negative lift curve slope ameliorates the severity of these adverse stalling characteristics.

## 1. INTRODUCTION

As is well known, there are a large number of aerodynamic effects which may limit aircraft maneuverability. These include shock induced buffet, wing rock and wing drop (probably due to asymmetrical separation with a subsequent rolling-yawing motion), nose slice, pitch-up, loss of lateral stability, loss of roll control and roll control reversal, and large drag increases. It is generally believed that some type of flow separation is responsible for each of these phenomena. The present paper deals with the development of a modified lifting line approach for estimating the aerodynamic characteristics of wing-body configurations undergoing transient pitching motion with flow separation and may prove useful for the prediction, simulation and possible inhibition of those adverse stalling phenomena included within the framework of the theory. A more detailed exposition of the method, along with extensive calculations, is presented in Ref. 1.

The present formulation is for wings of moderate to high aspect ratio to which lifting line theory may be applied. In this regard there has appeared some interesting analytical work (2-4), based on Prandtl lifting line theory, which indicates that multiple solutions of the lifting line equations are possible under certain conditions. The multiple solutions are predicted only if the two-dimensional lift curves have either discontinuities or regions of high negative slope, beyond stall, as illustrated in Figure 1. One interesting feature of the multiple solutions is that they can yield span load distributions which are either symmetrical or asymmetrical about the wing centerline even at zero sideslip angle. According to Sears<sup>(2)</sup>, the asymmetrical solutions suggested to von Karman that large rolling moments could be produced near the stall without postulating any initial rolling velocity or other lateral asymmetries. Sears states that the usual "textbook" explanation for the large rolling moments near stall, which is based on an initial rolling velocity which stalls one panel and destalls the other, fails to account for the violence of the rolling moments experienced in a wind tunnel with a model held fixed to the sting. The establishment of any one particular load distribution (either symmetrical or asymmetrical) probably depends on the relative stability of the corresponding circulation distribution to small disturbances.

An attempt is made herein to apply nonlinear lifting line theory to the modeling and prediction of aerodynamic effects during stall penetration at high angles of attack. Previous discussions of stall aerodynamics have noted the occurrence of asymmetrical flow separation at zero yaw angle as a possible forcing mechanism for wing rock and other types of pre and post-stall motions (e.g. References 5-8). It is postulated herein that the time dependent zero beta yawing and rolling moments predicted by the non-linear lifting line theory are contributory to the limit cycle type of motions apt to occur during stall. This, of course, will require careful experimental verification.

The nonlinear lifting line formulation utilized herein is a finite element, unsteady wake, incompressible flow theory and may be applied at either zero or non zero yaw angle (yaw is handled by skewing the wing panels). Both symmetrical and asymmetrical load distributions may be obtained, even at zero yaw angle. Three dimensional unsteady aerodynamic effects are included by allowing shed vortices in the wake to vary in strength with distance and time. The strengths of the shed vortices are related to those of the corresponding bound elements at an earlier time, based on the convective time delay at free stream velocity between the bound vortex and the particular wake station. Although the theory is unsteady from the point of view of wake induced effects, it is assumed that the two-dimensional airfoil chordwise loadings and sectional characteristics in stall are steady state. Thus, the assumption is implicit that unsteady two dimensional phenomena such as associated with the dynamic stall of helicopter blades are of a shorter time scale than the unsteady wake effects, (see also section 2.2).

Lifting line theory assumes that each chordwise section acts like a two-dimensional airfoil at an effective angle of attack equal to the local geometric angle of attack less the induced angle of attack. In order for this assumption to remain valid, (i.e. for the chordwise load distribution to remain two-dimensional) the aspect ratio must be sufficiently large to limit spanwise flow effects, and vortex effects associated with high leading edge sweep angles must not be dominant in the stall. The method also requires the selection of (or switching between) the various multiple span load solutions which may exist at a given angle of attack. Some of these solutions may be indicative of unstalled load distributions, some of partly stalled distributions and some of nearly fully stalled distributions. The criterion used for selecting among the various mathematically possible solutions is empirical, and it is recognized that this aspect of the formulation requires further analysis. Because of this empiricism, and as a result of the assumptions noted previously, the need for wind tunnel tests involving dynamic measurements of aerodynamic forces, moments and span load distribution can not be over-emphasized.

Another application of non linear lifting line theory to departure and spin entry aerodynamics, but presumably based on somewhat different assumptions, has been presented by Kroeger and Felstel<sup>(9)</sup>. Included in Ref. 9 are also corroborating wind tunnel test data.

The mathematical basis for the present theory is reviewed in Section II. The method of solution is presented in Section III. Numerical results involving comparisons with existing test data and with linear theory, and limited parametric studies, are found in Section IV. More extensive parametric calculations are given in Ref. 1.

## 2. THEORY AND ASSUMPTIONS

The present section presents the mathematical basis and assumptions for the nonlinear lifting line theory with a time dependent wake as utilized herein. The theory may be used to obtain the time dependent span load distribution and corresponding time dependent force and moment coefficients for wings and wing-bodies experiencing a predetermined schedule of pitching motion and/or of lateral control deflections.

### 2.1 VORTEX SYSTEM

The vortex system used in the analysis is pictured in Figures 2 and 3 and is assumed planar except for the vertical displacement of the image vortices in the fuselage. The exposed wing, is depicted in Figure 2 as segmented into N equal-span elements of width  $h$  in the spanwise  $y$  direction. Each element is a parallelogram in shape and consists of a bound vortex segment along the  $1/4$  chord line, two streamwise trailing segments and a closing shed vortex element at a downstream distance  $\Delta x = V_\infty \Delta t$ , where  $V_\infty$  is the free stream velocity and  $\Delta t$  is the time step. In the time dependent solution the strength  $\Gamma_{j,1}(t)$  of this vortex element represents the circulation carried by the wing at the  $j$ 'th spanwise element ( $j = 1, 2 \dots N$ ) at the current time  $t$ . The downstream trailing vortex elements are of identical shape, but are of varying strength as

$$\Gamma_{j,k}(t) = \Gamma_{j,k-1}(t - \Delta t) \quad (1)$$

where  $k$  is an index describing the vortex element number in the wake (see Figure 3). If the maximum number of downstream parallelogram elements to be included is  $M-1$ , then

$$1 \leq k \leq M$$

where  $k=1$  corresponds to the wing element at the current time  $t$ , and  $k=M$  refers to the final wake element, which is assumed unclosed. If  $M=1$ , the solution reduces to that for a steady state wake.

The method of representing the fuselage (assumed an infinite circular cylinder) by trailing image vortices as depicted in Figures 3 has found extensive use in the literature, e.g. Ref. 10, and will not be discussed further.

### 2.2 LIFTING LINE EQUATIONS

The lifting line assumption states that each spanwise station  $i$  of a wing acts like a two-dimensional airfoil at an effective angle of attack  $\alpha_{EFF_i}(t)$  equal to the local geometric pitch angle of attack  $\alpha_{p_i}(t)$  (includes effects of wing incidence, twist, control deflection, and body cross flow) less the downwash angle of attack  $\alpha_{D_i}(t)$  induced by the trailing vortex systems, viz.

$$\alpha_{EFF_i}(t) = \alpha_{p_i}(t) - \alpha_{D_i}(t) \quad (2)$$

Thus, for an airfoil with two-dimensional, steady state, lift, pitching moment, and profile drag curves of functional form

$$C_L = C_L(\alpha_p), C_M = C_M(\alpha_p), \text{ and } C_{D_P} = C_{D_P}(\alpha_p), \quad (3)$$

The present lifting line theory assumes that

$$C_{L_i}(t) = C_{L_i} \left[ \alpha_{EFF_i}(t) \right], C_{M_i}(t) = C_{M_i} \left[ \alpha_{EFF_i}(t) \right], C_{D_{F_i}}(t) = C_{D_{F_i}} \left[ \alpha_{EFF_i}(t) \right] \quad (4)$$

Equations (2) and (4) indicate that the unsteady effects to be included in the theory enter only through the time dependence of  $\alpha_{EFF_i}$ , viz. through changes with time in  $\alpha_{p_i}$  and/or  $\alpha_{D_i}$ . As noted in the Introduction, the basic section characteristics as defined functionally by Equations (3) are assumed independent of time. This requires that various linear and nonlinear two-dimensional unsteady flow effects, such as dynamic stall (e.g. Reference 11), be of an appreciably shorter time scale than the wake and geometric effects included herein. This assumption is equivalent to assuming that the chordwise pressure distribution, which affects the nature of flow separation on the airfoil, rapidly approaches the steady state distribution for the current angle of attack, and is consistent with the single lifting line representation of the wing. Combining unsteady two-dimensional effects with the nonlinear lifting line theory, or going to multiple lifting lines, was assumed beyond the scope of the present effort.

The control point for evaluating  $\alpha_{EFF_i}$  is taken at an axial distance  $x_{cp_i}$  from the leading edge. In the usual Prandtl lifting line formulation  $x_{cp_i} = c_i/4$ . Hence, there would be no induced velocity contribution from the wing bound vortex segments. In order to generalize the formulation for arbitrary  $x_{cp_i}$ , the downwash angle  $\alpha_{D_i}$  has been defined as the difference between the total three-dimensional downwash angle  $\alpha_{3D_i}$  at the control point and an equivalent two-dimensional downwash angle  $\alpha_{2D_i}$  from an infinite span bound vortex along the  $c/4$  line and equal in strength to  $\Gamma_{i,1}(t)$ . Thus

$$\alpha_{D_i}(t) = \alpha_{3D_i}(t) - \alpha_{2D_i}(t) \quad (5)$$

In terms of downwash velocity components  $\Delta w$  induced by the parallelogram lattice elements of unit circulation strength

$$\alpha_{3D_i}(t) = \frac{w_i(t)}{V_\infty} = \frac{1}{V_\infty} \sum_{j=1, k=1}^{j=N, k=M} \Delta w_{i,j,k} \Gamma_{j,k}(t) \quad (6)$$

where for each  $j, k$  lattice element and at each control point  $i$ ,  $\Delta w_{i,j,k}$  consists of contributions from forward and aft bound or shed elements, the two trailing elements and the body image elements, all of unit strength. Mathematical expressions for the  $\Delta w_{i,j,k}$  are readily found from the law of Biot and Savart.

The equivalent two-dimensional downwash angle is simply

$$\alpha_{2D_i}(t) = \left( \frac{1}{V_\infty} \right) \Delta w_{2D_i} \Gamma_{i,1}(t) = \frac{1}{V_\infty} \frac{\Gamma_{i,1}(t)}{2\pi (x_{cp} - x_{c/4}) \cos(\Lambda_i - \beta)} \quad (7)$$

where  $\Lambda_i$  is the quarter chord sweep angle (assumed negative for the left wing panel,  $1 \leq i \leq N/2$ , and positive for the right wing panel,  $N/2 + 1 \leq i \leq N$ ), and  $\beta$  is the side slip angle. The usual sign convention taking the downwash as positive has been employed in the above expressions.

The pitch angle of attack is composed of the elements

$$\alpha_{P_i}(t) = \alpha(t) + \alpha_{T_i} + \Delta\alpha_{R_i}(t) + \Delta\alpha_{B_i}(t) \quad (8)$$

where  $\alpha(t)$  is the angle of attack of the root section,  $\alpha_{T_i}$  is the built in geometric twist,  $\Delta\alpha_{R_i}(t)$  is the effective roll asymmetry angle of attack due to deflection of ailerons and  $\Delta\alpha_{B_i}(t)$  is the additional angle of attack due to the body upwash (see Ref. 1).

The unknowns are the current time values of the circulation on the wing  $\Gamma_{i,1}(t)$ , and may be found by first inserting Equations (5), (6), (7) and (8) into Equation (2) giving

$$\alpha_{EFF_i}(t) = \alpha(t) + \alpha_{T_i} + \Delta\alpha_{R_i}(t) + \Delta\alpha_{B_i}(t) - \frac{1}{V_\infty} \sum_{j=1, k=1}^{j=N, k=M} \Delta w_{i,j,k} \Gamma_{j,k}(t) + \frac{1}{V_\infty} \Delta w_{2D_i} \Gamma_{i,1}(t) \quad (9)$$

Expressing  $C_{L_i}(t)$  in Equation (4) in terms of the bound circulation gives

$$\frac{2\Gamma_{i,1}(t)}{V_\infty c_i} = C_{L_i} \left[ \alpha_{EFF_i}(t) \right] \quad (10)$$

Equation (10) implies that the Kutta-Joukowski law  $L_i(t) = \rho V_\infty \Gamma_i(t)$  holds in the unsteady as well as in the steady state case. This assumption is discussed further in Section 2.5.

Equations (9) and (10) constitute the set of lifting line equations to be solved for  $\alpha_{EFF_i}(t)$  and  $\Gamma_{i,1}(t)$ . The  $\Gamma_{j,k}(t)$ ,  $k > 1$ , are known from solutions at previous times through Equation (1).

### 2.3 SIMPLIFICATIONS FOR A LINEAR LIFT CURVE

In general, Equations (10) and (11) must be solved by an iterative method, because the lift curve is nonlinear. It is precisely this nonlinearity which lead to the occurrence of multiple span loadings, lift hysteresis, and zero beta rolling and yawing moments. However, it is beneficial to examine several simplifications which occur when the lift curve is linear, in order to compare the theory with existing methods and to better understand the nature of the nonlinear effects.

#### 2.3.1 Linear Lift Curve

In the case of a linear lift curve Equation (10) becomes

$$\frac{\Gamma_{i,1}(t)}{V_\infty c_i} = a_i \alpha_{EFF_i}(t) \quad (11)$$

where  $a_i$  is the section lift curve slope. Combining Equation (11) with Equation (9) then gives a single set of linear equations which may be solved directly for  $\Gamma_{i,1}(t)$ . The result is

$$\left[ \frac{\Delta w_{i,i,1}}{V_\infty} + \delta_{ij} \left( \frac{2}{V_\infty a_i c_i} - \frac{\Delta w_{2Di}}{V_\infty} \right) \right] \Gamma_{j,1}(t) = \alpha_{p_i}(t) - \frac{\Delta w_{i,i,k}}{V_\infty} \Gamma_{j,k}(t) \quad (12)$$

$2 \leq k \leq M$

where the repeated indices indicate a summation, and  $\delta_{ij}$  is the Kronecker delta symbol.

Equation (12) represents a linear set of algebraic equations which may be solved directly for each step in time. If the problem is initiated from a steady state condition, then  $M = 1$  for  $t = 0$  and the summation over  $k$  vanishes. In matrix notation Equation (12) now becomes

$$[\Delta W] \{ \Gamma_1(0) \} = \{ \alpha_p(0) \} \quad (13)$$

where elements of the  $[\Delta W]$  square matrix are given by the term in square brackets in Equation (12), whereas  $\{ \Gamma_1(0) \}$  and  $\{ \alpha_p(0) \}$  are column matrices made up of the elements  $\Gamma_{j,1}(0)$  and  $\alpha_{p_i}(0)$  respectively. Inverting Equation (13) gives

$$\{ \Gamma_1(0) \} = [\Delta W]^{-1} \{ \alpha_p(0) \} \quad (14)$$

At subsequent time steps the  $k$  summation plays a role in the solution. Thus, according to Equation (1), with  $t = \Delta t$ ,  $k = 2$  now corresponds to the solution  $\Gamma_{j,1}(0)$ . Hence, we require  $M \geq 2$  in order to account for unsteady wake effects.

#### 2.3.2 Equivalence with Weissinger Theory

##### 2.3.2.1 Steady State

The present lifting line formulation reduces to the Weissinger L-method (Ref. 12) for a linear lift curve in the steady state case, provided the control point  $x_{cp}$  is placed at distance equal to 50% of the local chord from the lifting line. This may be shown by considering a single horseshoe vortex element ( $k = 1$  only), with a bound segment and two trailing segments. Using the steady state form of Equations (5) and (7) with  $(x_{cp} - x_{c/4})_i \cos(\Lambda_i - \Theta) = (1/2) c_i$ , Equation (2) becomes

$$\alpha_{EFF_i} = \alpha_{p_i} - \alpha_{3D_i} + \frac{\Gamma_{i,1}}{\pi V_\infty c_i} \quad (15)$$

For thin airfoil aerodynamics,  $a_i = 2\pi$ , therefore by the steady state form of Equation (11)

$$\frac{\Gamma_{i,1}}{\pi V_\infty c_i} = \alpha_{EFF_i}$$

and substitution in Equation (15) yields

$$\alpha_{3D_i} = \alpha_{p_i} \quad (16)$$

which is the flow tangency boundary condition at the 75% chord control point used in the Weissinger approach.

##### 2.3.2.2 Unsteady Theory (Two-Dimensional)

It should be noted that the theory also reduces to an unsteady form of the Weissinger theory, both for two-dimensional and three-dimensional flows. Thus, for a two-dimensional unsteady flow, Equation (2) becomes

$$\alpha_{EFF}(t) = \alpha_p(t) - \frac{1}{V_\infty} \Delta w_k \Gamma_k(t) + \frac{\Gamma_1(t)}{2\pi V_\infty (x_{cp} - x_{c/4})}$$

where  $\Delta w_k$  is the downwash at  $x_{cp}$  due only to forward and aft spanwise segments of the  $k$ 'th element and the double index implies a summation.

Using the linearized form of the unsteady Kutta-Joukowski law, Equation (11), assuming the lift curve slope  $a = 2\pi$ , and taking  $x_{cp} = x_c/4 = c/2$  then gives

$$\frac{1}{V_\infty} \Delta w_k \Gamma_k(i) = \alpha_p(t) \quad k = 1, 2, \dots \quad (17)$$

Equation (17) states that the instantaneous downwash angle at the 75% chord position from all bound and shed spanwise vortex segments is equal to the instantaneous angle of attack, or equivalently that the unsteady theory reduces to satisfying a flow tangency condition in the two-dimensional case when the control station is taken at the 75% chord position.

The equivalence of the present unsteady wake lifting line formulation with the classical solution of Wagner (Ref 13) for a two dimension airfoil in unsteady flow is readily shown. Thus, Figure 4 compares the calculated value of the change in lift coefficient  $\Delta C_L(t)$  due to a step change in angle of attack  $\Delta \alpha_i$ , as calculated from the above method, with the Wagner function. Lift coefficient was calculated from the bound circulation strength  $\Gamma_1(t)$  through the unsteady Kutta-Joukowski law, Equation (11).

The step size used in the computation for the shedding of discrete vortices was one chord length. The close correspondence between the discrete vortex formulation and the continuous vortex sheet theory of Wagner shows that very little accuracy is lost in the present discrete vortex model. It is also clear that unsteady wake effects, due to the variation of shed as well as of trailing vorticity, are accounted for in the formulation. Effects of wake vorticity on chordwise load distribution are not included, as was mentioned previously. Incorporation of these effects would require addition bound vortex elements and additional control point locations on the wing.

#### 2.3.2.3 Unsteady Theory (Three-Dimensional)

The unsteady finite element representation may also be readily shown to lead to a flow tangency condition at the 75% chord position in the three dimensional case.

The demonstration is similar to that for the steady state case, except that the unsteady form of the Kutta-Joukowski law is used and the summation is carried out over  $k = 1, 2, \dots, M$  rows of vortex elements in the wake. The result is

$$\alpha_{3D,i}(t) = \frac{1}{V_\infty} \Delta w_{i,j,k} \Gamma_{j,k}(t) = \alpha_{p,i}(t) \quad (18)$$

provided the control point is located a distance  $c/2$  behind the lifting line, and provided the steady state thin airfoil theory, lift curve slope is used.

#### 2.4 GENERALIZED FORM OF THE KUTTA-JOUKOWSKI LAW FOR UNSTEADY FLOW

A generalized form of the two-dimensional Kutta-Joukowski, law, viz.

$$L(t) = \rho V_\infty \Gamma_1(t) \quad (19)$$

has been used throughout the formulation in Sections 2.2 and 2.3 and is the basis for Equations (10) and (11). In the present section we derive Equation (19) from the condition that the negative rate of change of total momentum associated with the spanwise vortex segments gives the magnitude of the lift. For a two-dimensional vortex system composed of discrete elements  $\Delta \Gamma_k(t)$  spaced along the  $x$  axis at distances  $x_k$  from the leading edge, as shown in Figure 5, the unsteady two-dimensional lift becomes

$$L(t) = -\rho \frac{d}{dt} \left[ \Delta \Gamma_k(t) x_k \right] \quad (20)$$

where the subscript  $i$  has dropped for simplicity of notation (see also Eq. (1) of reference (14)).

The conditions that the shed vortex elements,  $k \geq 2$ , are convected downstream at velocity  $V_\infty$ , and that the total vorticity  $\sum_{k=1}^{M-1} \Delta \Gamma_k(t)$  remain zero for all time are  $\Delta \Gamma_k(t + \Delta t) = \Delta \Gamma_{k-1}(t)$  and  $\Delta \Gamma_2(t + \Delta t) = -[\Gamma_1 + \Delta t] - \Gamma_1(t)$ , respectively. The instantaneous bound vortex strength is  $\Delta \Gamma_1(t) = \Gamma_1(t)$ .

Referring to Figure 5b, taking time steps with  $n = 1$  (one chord length between elements), placing the bound vortex at the 25% chord position, the total momentum  $\rho \Delta \Gamma_k(t) x_k$  at time  $t = (M-1)c/V_\infty$  is

$$\rho \Delta \Gamma_k \left[ (M-1)c/V_\infty \right] x_k = -c \sum_{k=1}^{M-1} \Gamma_1(kc/V_\infty) \quad (21)$$

where use has been made of the above convection and conservation conditions.



Taking  $t = (M-2)c/V_\infty$  and subtracting the result from Equation (21) gives

$$\rho \{ \Delta \Gamma_k [(M-1)c/V_\infty] x_k - \Delta \Gamma [(M-2)c/V_\infty] x_k \} = -c \Gamma_1 [(M-1)c/V_\infty]$$

Dividing by  $\Delta t = c/V_\infty$ , we obtain

$$\frac{\rho \Delta \{ \Delta \Gamma_k [(M-1)c/V_\infty] x_k \}}{\Delta t} = -V_\infty \Gamma_1 [(M-1)c/V_\infty]$$

and comparing with Eq. (2) in difference form gives

$$L [(M-1)c/V_\infty] = \rho V_\infty \Gamma_1 [(M-1)c/V_\infty] \quad (22)$$

The same result may be obtained for arbitrary step sizes  $n$ , and in the limit  $n \rightarrow 0$  Equation (22) reduces to the generalized Kutta Joukowski law, as stated by Equation (19).

### 3. METHOD OF SOLUTION AND ITERATION PROCEDURE

The set of nonlinear lifting line expressions as given by Equations (9) and (10) constitute a system of  $2N$  algebraic equations in the  $2N$  unknowns  $\Gamma_i(t)$  and  $\alpha_{EFF_i}(t)$ ,  $i = 1, 2, \dots, N$ , which must be solved for each step in time. The equations are nonlinear, because the functional relation between  $\Gamma_i(t)$  and  $\alpha_{EFF_i}(t)$ , expressing the two-dimensional lift curve at station  $i$ , is generally nonlinear in the stall region and beyond. Hence an iteration procedure is required for their solution.

The nonlinear lifting line equations were programmed for solution on the CDC Cyber 70 computer. The method of solution will be reviewed below, because several of the assumptions in the iteration procedure require further clarification.

#### 3.1 ITERATION PROCEDURE

The iteration procedure assumes the aircraft wing and fuselage geometry, sideslip angle, etc. are given, and that the schedule of pitch angle  $\alpha_p(t)$  and lateral control deflection  $\Delta \alpha_R(t)$  have been specified. Two iteration loops will be described, one for  $t = 0$  and the second for  $t > 0$ .

##### 3.1.1 Initial Solution

The method is started by determining the steady state solution for  $t = 0$ . The root solving procedure consists of a simple iteration loop on the induced angle of attack  $\alpha_{D_i}(0)$ . A guess is first made for the spanwise variation of induced angle of attack  $\alpha_{D_i}^{(1)}(0)$ . This, together with the known  $\alpha_{p_i}(0)$ , establishes  $\alpha_{EFF_i}^{(1)}(0)$  through Equation (2). The wing bound vortex strengths  $\Gamma_{i,1}^{(1)}(0)$  are then found by table look-up from the input aerodynamic lift curves expressed by Equation (10). For  $t = 0$  we may take  $M = 1$ , or equivalently take  $\Gamma_{i,k}(0) = \Gamma_{i,1}(0)$ , hence no wake vortices need be considered. The induced angles are then recalculated, based on the downwash velocity components  $\Delta w_{i,k}$  and  $\Delta w_{2D_i}$ , and on the initial iterate for the vortex strengths  $\Gamma_{i,1}^{(1)}(0)$ , and compared with the assumed values of  $\alpha_{D_i}^{(1)}(0)$ . The difference may be designated  $\Delta \alpha_{D_i}^{(1)}(0)$ . The values to be used in the next iteration are

$$\alpha_{D_i}^{(2)}(0) = \alpha_{D_i}^{(1)}(0) + C \Delta \alpha_{D_i}^{(1)}(0) \quad (23)$$

where  $C$  is a weighting factor. The value of  $C$  affects the stability and convergence of the iteration procedure. Increasing  $C$  speeds up convergence (reduces the number of required iterations), but may destabilize the iteration procedure. In general, the maximum values for  $C$  depends on wing aspect ratio, the number  $N$  of spanwise elements, and on lift curve slope. Some further discussion of effects of  $C$  on stability are contained in Reference 1.

With  $\alpha_{D_i}^{(2)}(0)$  given by Equation (23) the procedure is repeated, viz.

$$\alpha_{D_i}^{(2)}(0) \rightarrow \alpha_{EFF_i}^{(2)}(0) \rightarrow \Gamma_{i,1}^{(2)}(0) \rightarrow \Delta \alpha_{D_i}^{(2)}(0), \text{ etc.}$$

until either convergence is obtained, or until a maximum number of iterations has occurred. Convergence is assumed when  $\Delta \alpha_{D_i}^{(m)}(0) \leq 0.1^\circ$  for all  $i$ .

##### 3.1.2 Solution at Subsequent Time Steps

The iteration procedure at succeeding time steps  $t > 0$  is similar to that at  $t = 0$  with the following exceptions:

- (i) The vortex strengths  $\Gamma_{i,k}(t)$  in the wake are no longer identical to those on the wing ( $k = 1$ ), but are found by indexing from the previous time step according to Equation (1).
- (ii) A special logic is used to specify the initial guess  $\alpha_{D_i}^{(1)}(t)$ .

The later requirement was found necessary, especially near stall, because of the possibility of multiple solutions, and because the iteration procedure apparently tends to disallow roots on the steep negative slope regions of the section lift curves (see also Ref. 9 in this regard). Therefore, the wing elements appear in the solutions as either unstalled or fully stalled (region where the post stall lift curve is near zero). A dominant form for the solution in the stall region appears to be a spanwise alternating pattern of unstalled and fully stalled elements. The significance of this saw-tooth type of solution was not entirely clear. For example, if for a high density of spanwise elements the stall pattern could be shown to become independent of the number  $N$  of vortex elements as  $N \rightarrow \infty$ , then such a pattern over a given spanwise portion of the wing might well represent partial stall or heavy buffeting in that region. However, since the computer program was limited to 10 elements per wing panel ( $N_{\max} = 20$ ), this type of saw-tooth stall pattern did not appear to be physically realistic. It was found that the saw-tooth stall pattern could be avoided in most cases by choosing the initial guess for  $\alpha_{D_i}(t)$  according to the following special logic.

- a) When no wing sections are stalled at the prior time step (i.e. all converged values of  $\alpha_{EFF_i}(t - \Delta t)$  are less than  $\alpha_{\max_i}$ , corresponding to the section angle of attack for maximum  $C_L$ ), then the  $\alpha_{D_i}^{(0)}(t)$  are taken equal to the converged values from the previous time step  $\alpha_{D_i}(t - \Delta t)$ . This will produce solutions with all spanwise elements unstalled, if such solutions exist.
- b) When the iteration procedure at the end of the previous time step, or during the current iteration, gives a solution with one or more stalled sections on a wing panel (e.g.  $\alpha_{EFF_i}(t - \Delta t)$  exceeds  $\alpha_{\max_i}$ ), then the iteration procedure is started (or restarted) with the assumption that the induced angles are zero on that particular wing panel. This procedure tends to force solutions with as many stalled elements on that panel as the lifting line equations will allow.

The special logic represented by a) forces the spanwise wing elements to remain unstalled until such time that one or more elements must be stalled to satisfy the governing equation. Partially stalled solutions with either saw-tooth stall patterns or uniform stall patterns, are avoided during this time, even though they may satisfy the lifting line equations. The special logic given by b) assumes that once any spanwise element has stalled, it tends to induce all adjacent elements of the same panel to stall within the limits of the lifting line equations. Shielding of stall progression from one side of the airplane to the other is assumed provided by the presence of the fuselage (at least for low and mid-wing configurations). Unstalled solutions, or solutions with saw-tooth stall patterns, are avoided during this time even though they may be mathematically acceptable.

It should be noted that the above logic will tend to maximize the extent of any stall hysteresis loop (and the  $\alpha_p$  range for the occurrence of zero beta rolling and yawing moments) for a wing undergoing a pitching motion through the stall. Clearly, the physical validity of the assumptions implicit in the iteration procedure have yet to be established. In fact dynamic test data by Gregory, et al (Ref. 15), which has recently come to the attention of the author, indicates that multiple "stall cells" of limited spanwise extent sometimes occur over straight wings undergoing pitching motion through the stall region. The connection, if any, between these stall cells and the saw-tooth stall pattern is not clear. An alternative type of mathematical formulation, wherein the selection between the various multiple solutions is based on their physical stability, rather than on a special logic for the initial iterate, would clearly be desirable.

### 3.2 COMPUTATION OF FORCE AND MOMENT COEFFICIENTS

Once the converged vortex strength distribution has been determined at a particular time step, total force and moment coefficients for the wing body combination may be found by integrating the section force and moment coefficients over the  $N$  wing elements. The integration is carried out in Ref. 1 and includes contributions from the bound image elements in the fuselage in order to account for fuselage lift. These fuselage terms are, however, omitted from the computation of drag, side force, and rolling moment coefficient, since the fuselage is believed to make only a negligibly small contribution to these coefficients.

Expressions for the overall lift coefficient  $C_L$  and rolling moment coefficient  $C_\ell$ , as used in the following section, are

$$C_L = \sum_{i=1}^N \left( \frac{hc_i}{s} \right) C_{L_i} \cos \alpha_{D_i} \left[ 1 + \left( y_{IL_i} - y_{IR_i} \right) / h \right] \quad (23)$$

$$C_\ell = \sum_{i=1}^N \left( \frac{hc_i y_i}{Sb} \right) C_{L_i} \cos \alpha_{D_i} \quad (24)$$

Here  $y_{IL_i}$  and  $y_{IR_i}$  refer to the spanwise locations of the fuselage image vortices of the left and right hand trailing vortices of the  $i$ 'th wing element,  $S$  is the reference area and  $b$  is the span.

#### 4. SAMPLE CALCULATIONS

A series of computations were made with the nonlinear lifting line computer program described in Sections 2 and 3 to compare with test data, with previous theories and to assess effects of wing planform geometry and section lift curve shape on stalling characteristics.

##### 4.1 COMPARISON WITH AVAILABLE THEORY

Several computations were made to evaluate the accuracy and generality of the procedure. A comparison of the accuracy of the finite element representation with the essentially exact potential theory results of Wagner (Reference 13) has been given previously in Figure 4 for the case of a two-dimensional airfoil with a linear lift curve subject to a step change in angle of attack. Because of the simplifications introduced by two-dimensional flow, results by the present method in Figure 4 were hand computed instead of being run on the digital computer. The similarity of the present finite element method with the exact results is apparent in Figure 4. Both methods give an initial lift increment equal to  $1/2$  of the steady state value.

The present method is compared with calculations by W. P. Jones (Ref. 16) and Djojodihardjo and Widnall (Ref. 17) in Figure 6, for the response to a step change in angle of attack for a rectangular wing of aspect ratio 6. The lift curve was again linear, and as can be seen from the figure good correlation with the more exact theories was found. Both the present and more exact methods show an initial lift increment greater than  $1/2$  of the steady state value when the aspect ratio is finite.

The present method was also used to determine the development of lift following a step change in angle of attack for rectangular wings of various aspect ratios, again with linear lift curves. The results are plotted in Figure 7 and compare well with similar variations obtained by Jones (Ref. 16) for wings of elliptic planform. Once again we note that the starting circulatory lift increment exceeds one-half the steady state value for the finite aspect ratio cases, with the excess increasing for the lower aspect ratios. The computations in Figures 6 and 7 are with  $M = 20$  and  $N = 14$ .

##### 4.2 COMPARISON WITH TEST DATA

The wing planform of the T-2C Navy trainer aircraft served as the basic geometry for the remaining computations (with various modifications and adjustments). Lift and rolling moment data from Reference 18 and from recent unpublished test results (1976) obtained at NASA (ARL) and supplied by Mr. A. Piranian of the Navy (NADC) will be compared with the T-2C computations using a steady state wake ( $M = 1$ ), since the testing was done with the model held fixed at a given angle of attack (pitch and pause).

The basic T-2C configuration has a wing of aspect ratio  $AR = 5.07$ , taper ratio  $\tau = 0.495$ , a quarter chord sweep angle  $\Lambda = 2.27^\circ$ , a wing root incidence angle  $i = 1.7^\circ$  with  $2.5^\circ$  of washout at the tips, and a dihedral angle  $\gamma = 3^\circ$ . The airfoil is a NACA 64<sub>1</sub>A212 section with an  $a = 0.8$  (mod) camber line (flaps and ailerons rigged 3 degrees up), and is constant across the span. The wing was mounted at mid-height to a fuselage whose shape was approximated in the computations by a circular cylinder of a radius  $R_B = 0.119$  ( $b/2$ ). The wing paneling is shown in Figure 8 in the case of  $N = 14$ . Nonlinear aerodynamic section data used for the T-2C and parametric computations are plotted in Figures 9 and 10, respectively. Curves labeled #1, #2 and #3 in Figure 9 are for a NACA 64<sub>1</sub>A212 section at Reynolds number  $3 \times 10^6$ ,  $6 \times 10^6$  and  $> 6 \times 10^6$ . Curves labeled #11, #12 and #13 in Figure 9 were adjusted for the  $-3^\circ$  trailing edge rigging of the T-2C model, and are to be used in comparing with the T-2C wind tunnel data. Curves labeled #4 and #5 in Figure 10 are for a NACA 64-209 section at Reynolds numbers  $3 \times 10^6$  and  $6 \times 10^6$ , respectively, and were used in the parametric calculations together with curves #6 - #8 to examine effects of the steepness of the negative lift curve slope  $-b$  in the post stall region. The airfoil section characteristics in Figures 9 and 10 were extrapolated from published NACA data (e.g. Ref. 19).

A comparison between the calculated and measured lift values for the T-2C at zero and ten degrees yaw angle is shown in Figure 11. The tests were conducted tail on, and corrections were made for the estimated tail lift contribution as shown in Figure 11b. The test data are static measurements and average out any fluctuating values of  $C_L$ . The model was not pitched in a manner to produce lift hysteresis in Ref. 18. However, the 1976 test results were taken with  $\alpha_p$  increasing and then decreasing with time, and exhibit lift hysteresis for  $\alpha_p > 12^\circ$  (Figure 11a). The calculations appear to indicate a hysteresis loop which extends over a somewhat broader  $\alpha_p$  band ( $11^\circ \leq \alpha_p \leq 18^\circ$ ) than the data. This is in accordance with the special computational logic employed in the method, which as discussed previously may lead to the maximum allowable hysteresis.

On the other hand, the test data from Ref. 18 do show a sudden rolling moment asymmetry at zero yaw angle for  $\alpha_p \geq 12^\circ$  (Figure 12). This may be an indication of the stall (or partial stall) of one wing panel, and occurs at the lower limit of the zone of lift hysteresis shown in Figure 11. The T-2C zero beta rolling moment data have been plotted in Figure 12. Also shown are computations made with the current method, wherein a roll asymmetry is introduced for a very short period and then removed, in order to perturb the asymmetrical loadings. As seen from Figure 12, the resulting rolling moment coefficients (with the roll asymmetry removed) correlate well with the test data.

### 4.3 PARAMETRIC STUDIES

Parametric calculations were made with the current method, to determine effects of wing planform (aspect ratio, taper ratio, sweep back angle, and twist) and of airfoil section characteristics (steepness of negative lift slope beyond stall) on the occurrence of lift hysteresis and zero-beta rolling moment. The purpose of the calculations was to obtain trends and guidelines which might lead to the design of safer aircraft which are less subject to adverse departure and spin entry characteristics during high performance maneuvers. More extensive parametric variations may be found in Reference 1.

#### 4.3.1 Effect of Negative Lift Curve Slope and Aspect Ratio

Effects of the abruptness of the negative lift curve slope beyond stall and of aspect ratio for zero yaw angle are shown in Figures 13 and 14. Each plot represents a pitch hysteresis computation through the stall with the angle of attack first increasing (denoted by circles) and then decreasing (denoted by triangles). Where no triangles appear, the points are coincident with the increasing  $\alpha_p$  points. This notation has been used throughout the present section. Figure 13 is for  $AR = 8$ , and shows that the extent of lift hysteresis gradually decreases as the steepness of the negative lift curve slope diminishes. Figure 14 shows that increasing aspect ratio reduces the zone of hysteresis for a given negative lift curve slope. A similar set of pitch sweeps were made for a yaw angle  $\beta = 10^\circ$ . Lift hysteresis characteristics similar to those for  $\beta = 0^\circ$  were obtained. The corresponding variation of rolling moment coefficient versus angle of attack has been plotted in Figure 15 for the  $AR = 8$  case. A hysteresis loop for rolling moment coefficient, which behaves with respect to lift curve slope (and aspect ratio) in a manner very similar to lift coefficient, is indicated.

#### 4.3.2 Effects of Taper Ratio and Twist

Effects of taper ratio  $\tau$  and twist  $\alpha_T$  on lift hysteresis were obtained for the  $AR = 8$  case with section lift curves #4, 6 and 7. Figure 16 shows effects of varying  $\tau$  from 0.2 to 1.0 on lift hysteresis for curve #6. The calculations for the intermediate value  $\tau = 0.495$  exhibit a slightly greater tendency for lift hysteresis (for all negative lift curve slopes) than do either of the other two  $\tau$  cases. This may be true, because the  $\tau = 0.495$  taper ratio provides a more uniform spanwise distribution of section  $C_L$ , and hence causes the initial stall to be delayed to higher values of overall lift coefficient when the pitch rate is positive.

Figure 17 shows results for a wing with  $-3^\circ$  linear wash out at the tips ( $0 \leq \alpha_T \leq -3^\circ$ ), an untwisted wing ( $\alpha_T = 0$ ), and a wing with positive linear twist ( $0 \leq \alpha_T \leq +3^\circ$ ). As is apparent from Figure 17 twist has only a minor influence on the extent of lift hysteresis. It is recognized that the effects of twist, taper ratio, aspect ratio, and sweep back on stall hysteresis are interrelated. The particular combination of wing geometric parameters which provides the most uniform spanwise distribution of section  $C_L$  may also exhibit increased stall hysteresis. Because of the correspondence between the occurrence of stall hysteresis and zero beta rolling and yawing moments (see Section 4.3.3), it is expected that similar conclusions may be made with regard to the effects of wing planform parameters on the zero-beta moments.

#### 4.3.3 Zero Beta Rolling (and Yawing) Moments

Computations were made to illustrate the occurrence of zero-beta rolling and yawing moments during the pitch sequence. Sample results are shown in Figures 18 and 19 for the  $AR = 8$  case. The pitching motion was initiated at  $\alpha_p = 10^\circ$  with the wing symmetrical. The pitching motion was halted at  $\alpha_p = 12.4^\circ$ , and an asymmetry  $\Delta\alpha_R = \pm 1^\circ$  was applied to each wing panel and then subsequently removed, to simulate an aileron perturbation. The pitching motion was then resumed, either positive or negative, with the wing again symmetrical. Figure 18 shows the lift variation during this process for various lift curves. The corresponding rolling moment variations are shown in Figure 19. The theory predicts the occurrence of zero-beta rolling and yawing moments (not plotted) over nearly the same  $\alpha_p$  zone as that for which lift hysteresis occurs. Reducing the abruptness of the stall (steepness of the negative lift curve slope) is seen to ameliorate the effect. Reducing the aspect ratio from 8 to 5 increased the  $\alpha_p$  zone over which the zero-beta lateral moments occurred (see Ref. 1).

#### 4.3.4 Effects of Number of Elements

The parametric calculations presented so far were made with 14 vortex elements across the span ( $N=14$ ) and with only four rows of vortex elements in the wake ( $M=4$ ), the fourth being horseshoe in shape, to conserve computer time. Although effects of varying  $N$  between 10 and 20, and of  $M$  between 1 and 40 were obtained in specific cases (see Ref. 1), further studies are still required to establish the optimum values of  $N$  and  $M$  for wings of arbitrary planform. In addition, effects of  $N$  (and possibly of  $M$ ) on the nature of the saw-tooth stalling pattern mentioned in Section 3.1.2 should be considered.

### 4.4 HYSTERESIS CORRELATION

An attempt was made to correlate the computations of lift hysteresis. One such correlation is shown in Figure 20. Here the product  $\Delta C_{LH} \cdot \Delta\alpha_H$  has been plotted versus  $57.3b/\pi AR$ , where  $\Delta C_{LH}$  is the maximum  $C_L$  difference in the hysteresis zone, and  $\Delta\alpha_H$  is the width of the zone. The product  $\Delta C_{LH} \cdot \Delta\alpha_H$  is a measure of the area of the lift hysteresis loop. The value  $b$  is the maximum negative lift curve slope (per degree), and the ratio  $57.3b/\pi AR$  represents the ratio of this slope to the slope  $dC_L/d\alpha_D$  for a wing with constant downwash angle  $\alpha_D$  across the span. Thus, the correlation includes 2D and 3D parameters.

It is readily seen from Figure 1 that multiple solutions (symmetric case) will not occur unless  $b/(dC_L/d\alpha_D) \geq 1$ , corresponding to  $57.3 b/\pi AR \geq 1$  in the constant downwash angle case. Thus, the parameter  $57.3 b/\pi AR$  appears reasonable for predicting the occurrence of multiple asymmetric as well as of symmetric solutions.

The correlations predict the occurrence of lift hysteresis whenever  $57.3 b/\pi AR > 0.18$ , although the area of the hysteresis loop is seen to be dependent on other planform characteristics. Thus, the method predicts the occurrence of lift hysteresis for wings with negative lift curve slopes only approximately 1/5 as abrupt as thought necessary based on the idealized constant downwash angle criterion. This may be due to increased local downwash angle over regions of the wing with stalled or partially stalled flow.

## 5. CONCLUSIONS AND RECOMMENDATIONS

A nonlinear lifting line theory, with an unsteady wake, has been developed and applied to the prediction of forces and moments on aircraft undergoing a pitching motion through the stall region. The procedure is an outgrowth of the steady state, nonlinear lifting line approaches in Ref. 2-4, which predicted the occurrence of multiple solutions to the lifting line equations under certain conditions. The present theory predicts lift hysteresis and rolling and yawing moments, even at zero yaw angle, for wings with a negative lift curve slope of sufficient steepness subsequent to stall. It is anticipated that the theory and computations may serve as a guide in predicting the susceptibility of various aircraft of moderate to high aspect ratio and low sweep to adverse stall and departure characteristics.

Specific conclusions relating to the computations and assumptions are summarized below.

- (i) The method has been programmed for solution on the CDC Cyber 70 computer. Computer solutions are simple to execute and reasonably economical.
- (ii) The method compares well with steady state T-2C test data (aspect ratio 5.07), both for lift and rolling moment. No lift hysteresis appeared in the data but both test data and theory showed the occurrence of zero-beta rolling and yawing moments.
- (iii) The theory predicts lift hysteresis and zero beta rolling and yawing moments when the parameter  $57.3 b/\pi AR > 0.18$  ( $-b$  is the maximum negative lift curve slope of the two-dimensional airfoil sections comprising the wing). The severity of these effects is found to increase with increasing  $b$  and with decreasing aspect ratio. Other planform parameters, such as sweepback angle, twist and taper ratio have a lesser influence on these adverse stalling characteristics.
- (iv) The converged solutions obtained at angles of attack for which multiple roots exist are non unique and depend upon the starting solutions used in the iteration procedure.
- (v) The iteration procedure employed a special logic, which used either the converged solution from the previous time step as the initial iterate (unstalled) case, or set the initial iterate for downwash angle equal to zero over a wing panel (stalled case). This empiricism eliminates solutions with saw-tooth stalling patterns, delays stall during pitch-up, and postpones destall during pitch down, thereby maximizing the hysteresis zone. Consideration should be given to alternative methods, possibly based on stability theory, for selecting among the various possible solutions.
- (vi) The formulation does not include geometric effects of sweep and dihedral angle on the effective section angle of attack. These effects should be included to produce satisfactory correlation with test data, particularly for the sideslip case.
- (vii) Test data, which include dynamic effects relating to unsteady wing forces, moments, load distributions and stall patterns, are required to substantiate the method and provide a data base for building an improved formulation.
- (viii) An unsteady, nonlinear lifting surface theory, with two or more spanwise lifting lines, may be required for low aspect ratio fighter applications. The expanded theory might also include unsteady effects on chordwise load distribution and section stall.

## 6. REFERENCES

1. Piszkin, S. T. and Levinsky, E. S., "Nonlinear Lifting Line Theory for Predicting Stalling Instabilities on Wings of Moderate Aspect Ratio," General Dynamics Convair Report, CASD-NSC-76-001, June 1976.
2. Sears, W. R., "Some Recent Developments in Airfoil Theory," Journ. Aerospace Sciences, Vol. 23, No. 5, May 1956, pp 490-493.
3. Schairer, R. S., "Unsymmetrical Lift Distributions on a Stalled Monoplane Wing," California Institute of Technology, Thesis, 1939.

4. Sears, W.R., "A New Treatment of Lifting Line Theory with Applications to Rigid and Elastic Wings," *Quat. Appl. Math.*, Vol. VI, No. 3, Oct. 1948, pp. 239-255.
5. Cord, T.J., "Hysteresis Induced Wing Rock," Air Force Flight Dynamics Lab. Rept., AFFDL-TM-75-76-FGC, June 1975.
6. Anderson, C.A., "Stall/Post-Stall Characteristics of the F-111 Aircraft," AGARD Proceedings #102, Fluid Dynamics of Aircraft Stalling, 1972, pp. 18-1 to 18-9.
7. Jones, J.G., "The Dynamic Analysis of Buffeting and Related Phenomena," AGARD Proceedings #102, Fluid Dynamics of Aircraft Stalling, 1972, pp. 23-1 to 23-10.
8. Shaw, D.E., "Pre-Stall Behavior of Combat Aircraft," AGARD Lecture Series #74, Aircraft Stalling and Buffeting, 1975, pp. 6-1 to 6-18.
9. Kroeger, R.A., and Feistel, T.W., "Reduction of Stall-Spin Entry Tendencies Through Wing Aerodynamic Design," SAE Preprint 760481, April 1976.
10. Zlotnick M. and Robinson, S.W., Jr., "A Simplified Mathematical Model for Calculating Aerodynamic Loading and Downwash for Midwing Wing-Fuselage Combinations with Wings of Arbitrary Planform," NACA RM L52J27a, 16 January 1953.
11. Ham, N.D. and Johnson, W., "On the Mechanism of Dynamic Stall," *Journal of the American Helicopter Society*, Vol. 17, No. 4, Oct. 1972.
12. Weissinger, J., "The Lift Distributions of Swept-Back Wings," TM 1120 National Advisory Committee for Aeronautics. March 1947.
13. Wagner, H., "Dynamischer Auftreib von Tragflügeln," *Zeitschrift für Angew. Math. u. Mech.*, Bd. 5, 1925, 11. 17-35.
14. Von Karman, T.H., and Sears, W.R., "Airfoil Theory for Non-Uniform Motion," *Journ. of Aeronautical Sciences*, Vol. 5, No. 10, Aug., 1938.
15. Gregory, N., Quincey, V.G., O'Reilly, C.L., and Hall, D.J., Progress Report on Observations of Three-Dimensional Flow Patterns Obtained During Stall Development on Airfoils, and on the Problem of Measuring Two Dimensional Characteristics, Nat. Physics. Lab. Aero Report 1309, A.R.C. 31,702, Jan. 1970.
16. Jones, W.P., "Aerodynamic Forces on Wings in Non-Uniform Motion," British, A.R.C., R&M 2117, 1945.
17. Djojodihardjo, R.H., and Widnall, S.E., "A Numerical Method for the Calculation of Nonlinear Unsteady Lifting Potential Flow Problems," *AIAA Journal*, Vol. 7, No. 10, Oct. 1969, pp. 2001-2009.
18. Schuetz, A.J., and Bailey, D.B., "Low Speed Wind Tunnel Investigation of a 0.09 Scale, Navy Model T-2C Subsonic Jet Trainer Aircraft from -8 to +83 Degrees Angle of Attack," Naval Air Dev. Center Report NADC 73259-30, Dec. '73.
19. Abbott, I.H. and Von Doenhoff, A.E., Theory of Wing Sections, Dover Publications, N.Y., N.Y., 1959.

#### ACKNOWLEDGEMENT AND DEDICATION

This research was sponsored by the U.S. Navy, Naval Air and Development Center under Contract N62269-75-C-0356. Thanks are due to the NADC Scientific Officer, Mr. A. Piranian, and to Professor L. Schmidt, U.S. Navy Postgraduate School, who was acting as Navy Technology Administrator for Aerodynamics, for their many helpful suggestions and directions.

The research was begun by Mr. Stanley T. Piszkin, who passed away suddenly and without warning shortly after completing the formulation and computer check-out phases of the work. Mr. Piszkin also performed the majority of the computer calculations and was able to demonstrate the occurrence of zero beta rolling and yawing moments. The present author was privileged to have worked closely with Mr. Piszkin during the formulative stages of the program, and hopes that he has been able to convey the ideas and results of Mr. Piszkin in a clear and precise manner.

Mr. Piszkin, as an aerodynamicist and as a private pilot with experience in aerobatics, not only dealt with the theory of stalling instabilities from a theoretical standpoint, but also from a very practical flight safety point of view. It was his hope that these efforts would someday lead to a better understanding of the nature and cause of the adverse departure and spin entry characteristics of high performance aircraft and thereby result in improved flight safety. It is to this goal and to Mr. Piszkin's memory that the present report has been dedicated.

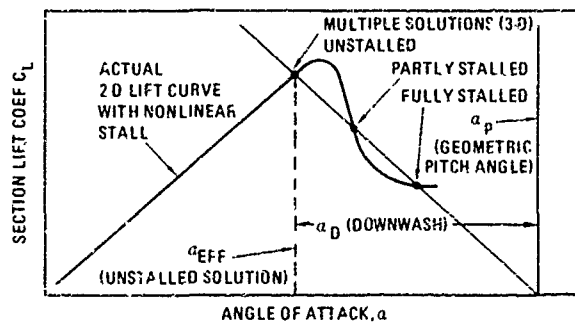


Figure 1 Nonlinear Two-Dimensional Section Lift Curve Which Yields Multiple Solutions of the Lifting Line Equations.

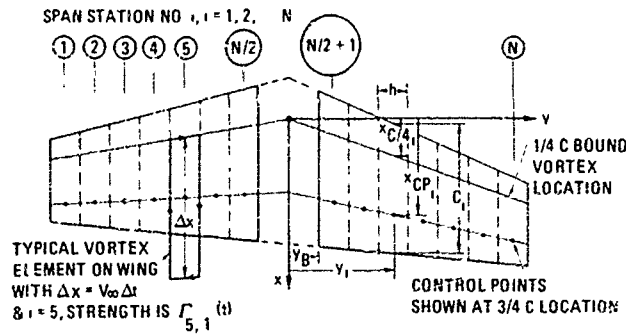


Figure 2. Wing Planform Geometry and Vortex Element Placement

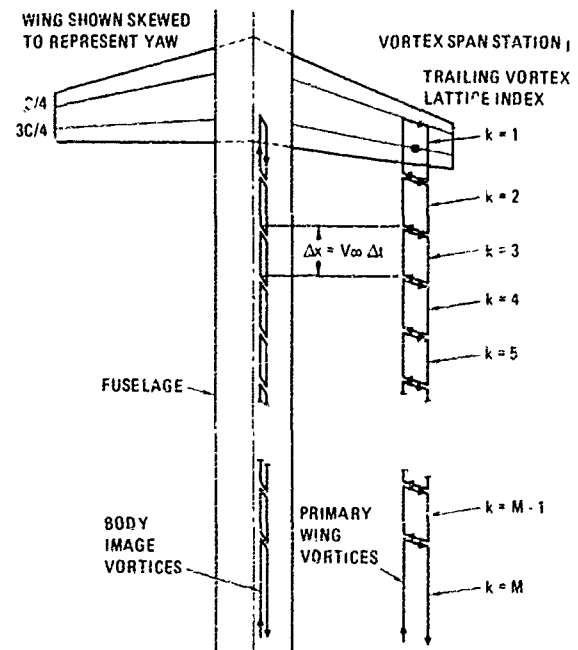


Figure 3. Vortex Elements for Unsteady Wake Formulation.

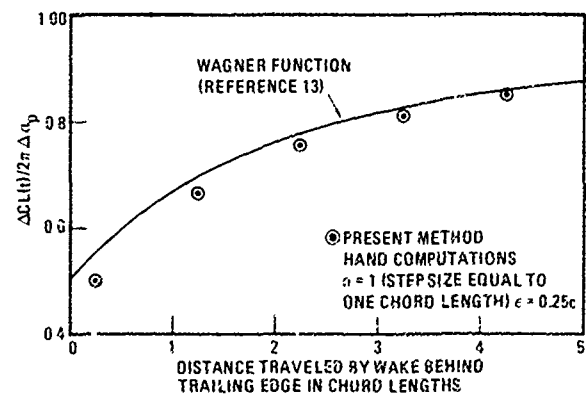


Figure 4. Comparison of Discrete Vortex Wake Model with Wagner Function (Continuous Vortex Wake) for Two-Dimensional Flow.

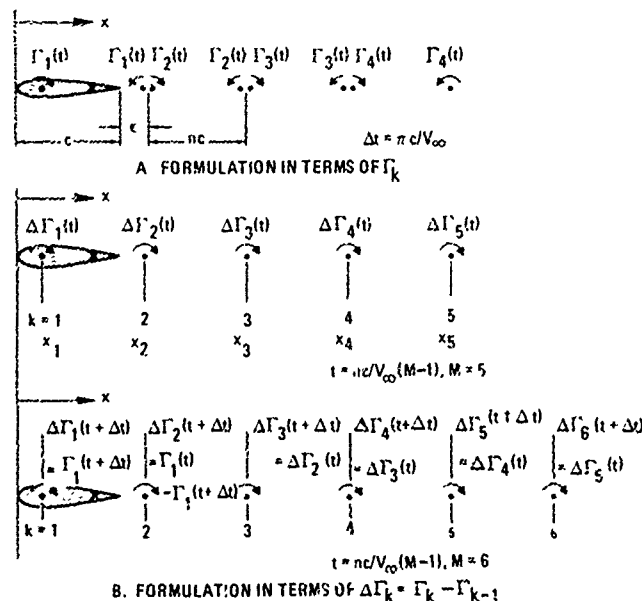


Figure 5. Two-Dimensional Representations of Unsteady Wake.

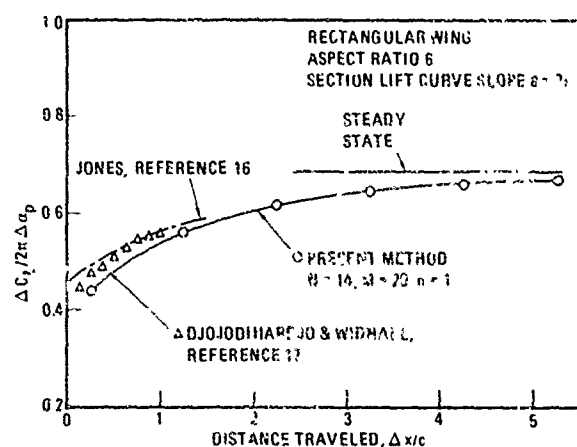


Figure 6. Effect of a Step Change in Angle of Attack on Lift, AR=6

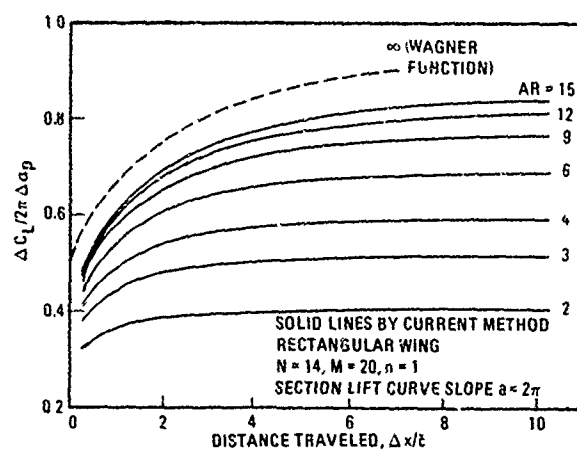


Figure 7. Effect of Aspect Ratio on Lift Following a Step Change in Angle of Attack.

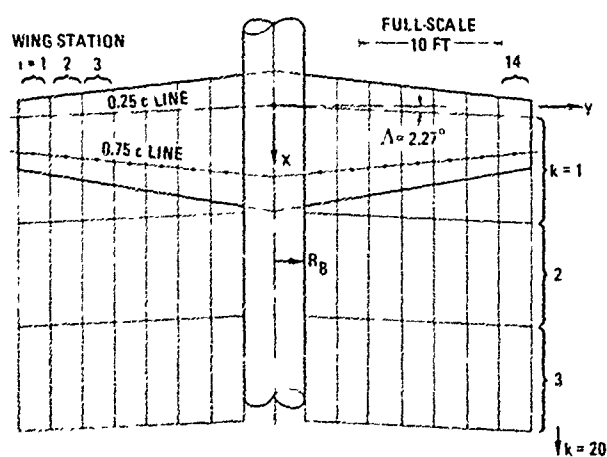


Figure 8. Planform Geometry and Paneling Used for T-2C Computations (N=14).

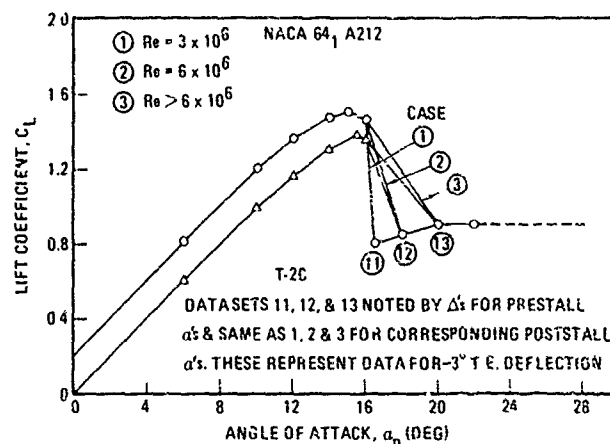


Figure 9. Section Lift Characteristics of NACA 64<sub>1</sub> A212 and T-2C Airfoils.

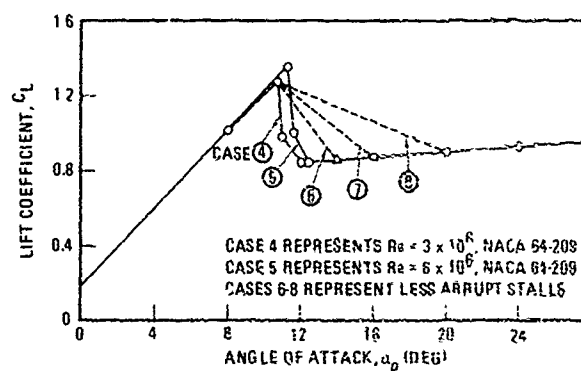


Figure 10. Nonlinear Airfoil Section Lift Characteristics Used for Parametric Calculations.

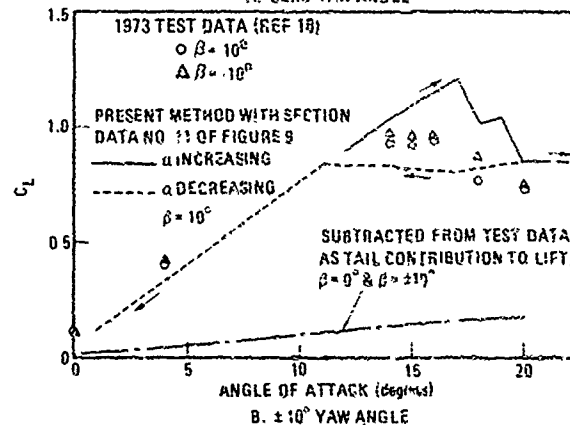
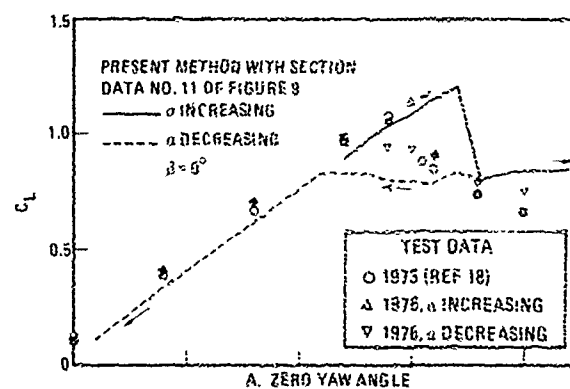
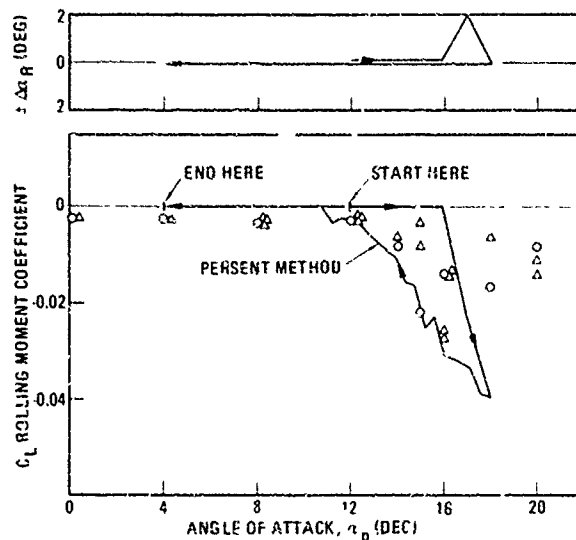


Figure 11. Comparison of Present Method with T-2C Wind Tunnel Data for Lift.





TEST DATA FROM REF 18  
 $Re \approx 4 \times 10^6$  BASED ON  $c$   
 GRIT OFF,  $\Delta GRIT$  ON  
 CALCULATED BY PRESENT METHOD  
 SHOWN BY LINE WITH ARROWS  
 $N = 20, M = 1$ , SECTION DATA  
 FROM CURVE NO. 11 OF FIGURE 9

Figure 12. Comparison of Present Method with T-2C Wind Tunnel Data for Rolling Moment at Zero Yaw Angle.

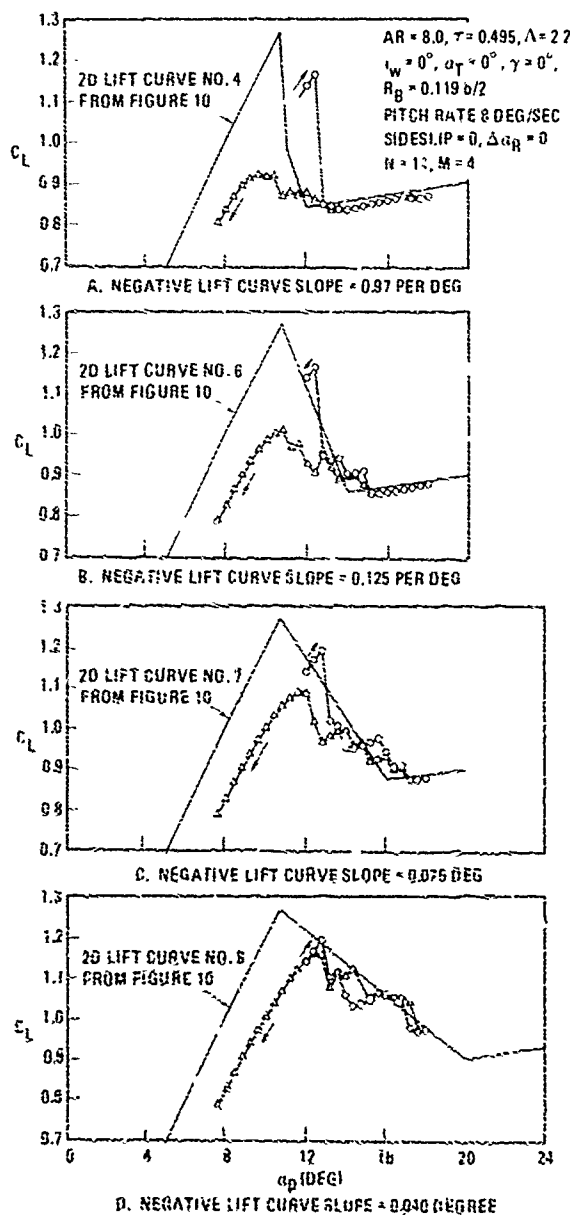


Figure 13. Effect of Negative Lift Curve Slope on Lift Hysteresis, Aspect Ratio 8.0.

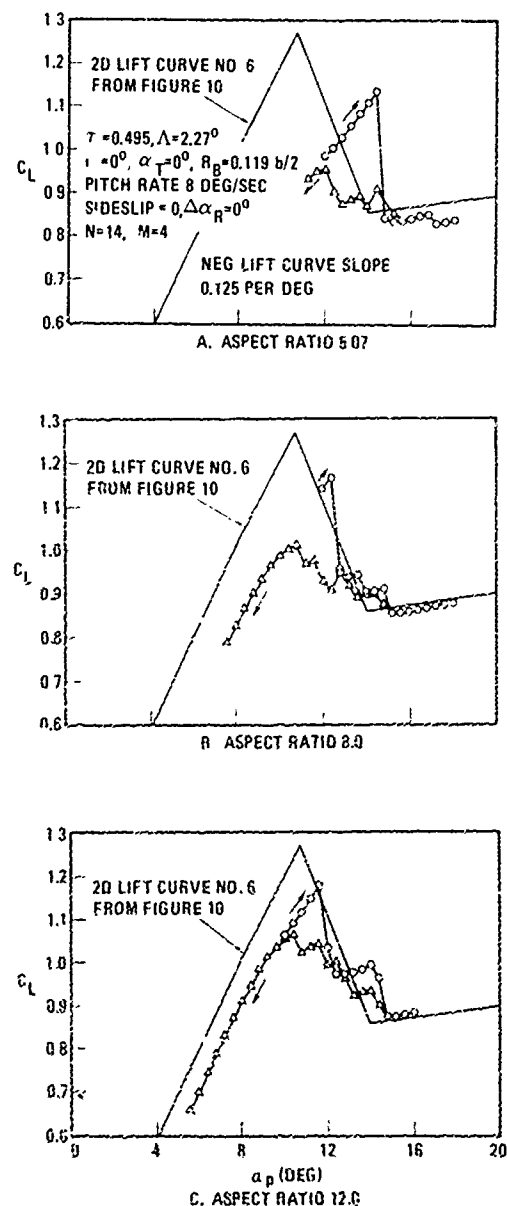


Figure 14. Effect of Aspect Ratio on Lift Hysteresis.

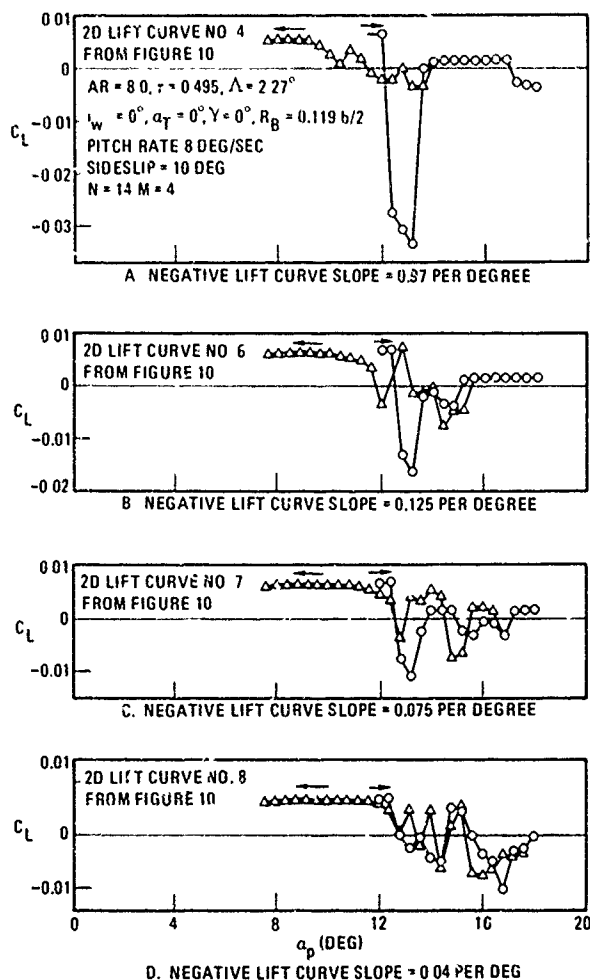


Figure 15. Effect of Negative Lift Curve Slope on Rolling Moment Hysteresis at  $10^\circ$  Sideslip Angle, Aspect Ratio 8.0.

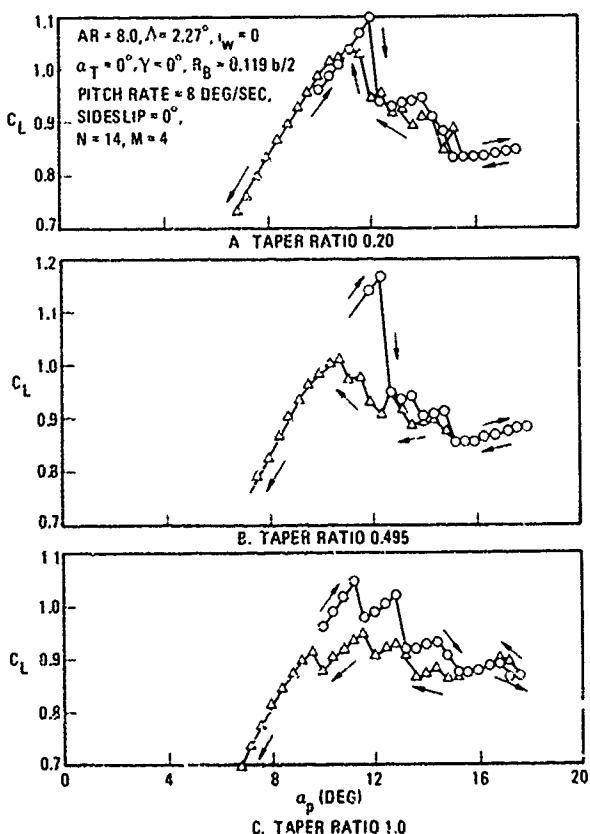


Figure 16. Effect of Taper Ratio on Lift Hysteresis, Aspect Ratio 8.0, Lift Curve Number 5 from Figure 10.

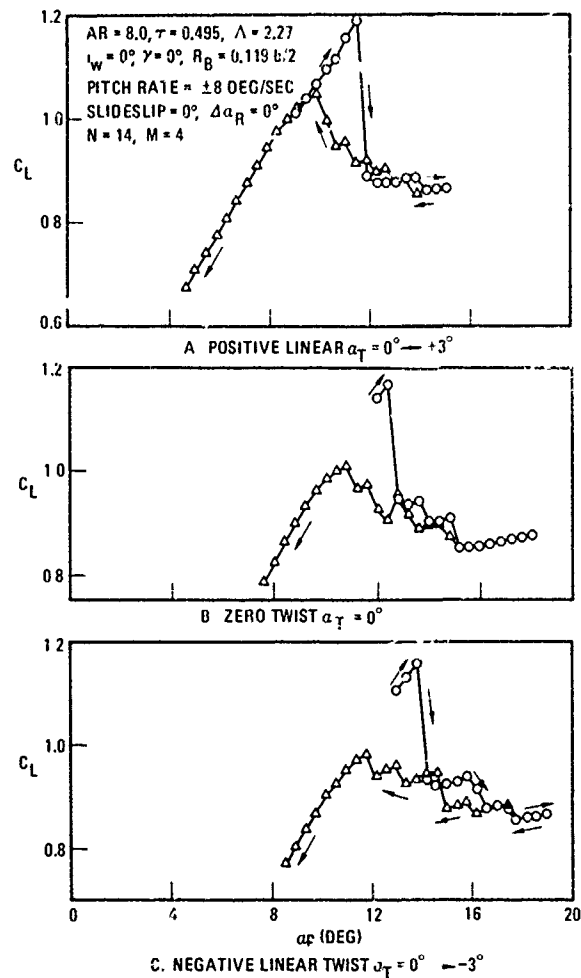


Figure 17. Effect of Twist on Lift Hysteresis, Aspect Ratio 8.0, 2D Lift Curve Number 6 from Figure 10.

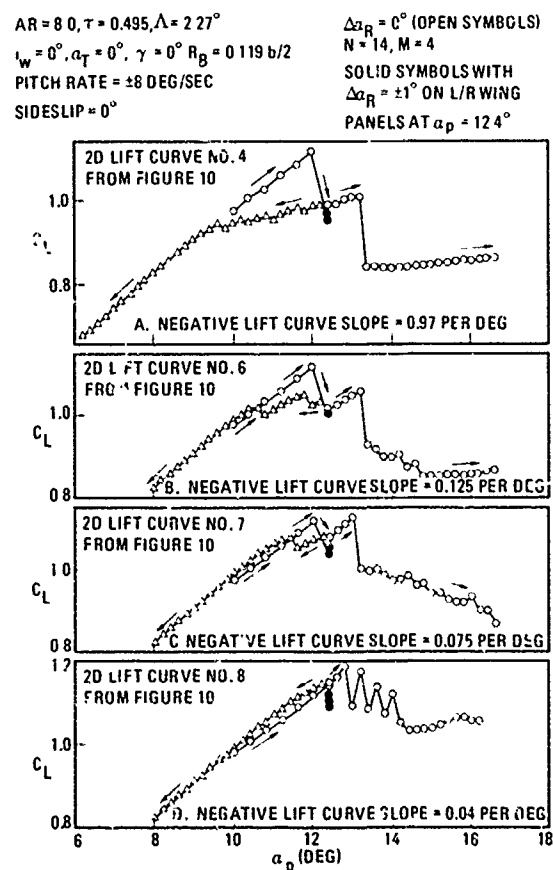


Figure 18. Effect of Roll Perturbation at  $\alpha_p = 12.4$  Degrees on Lift Hysteresis Aspect Ratio 8.0.

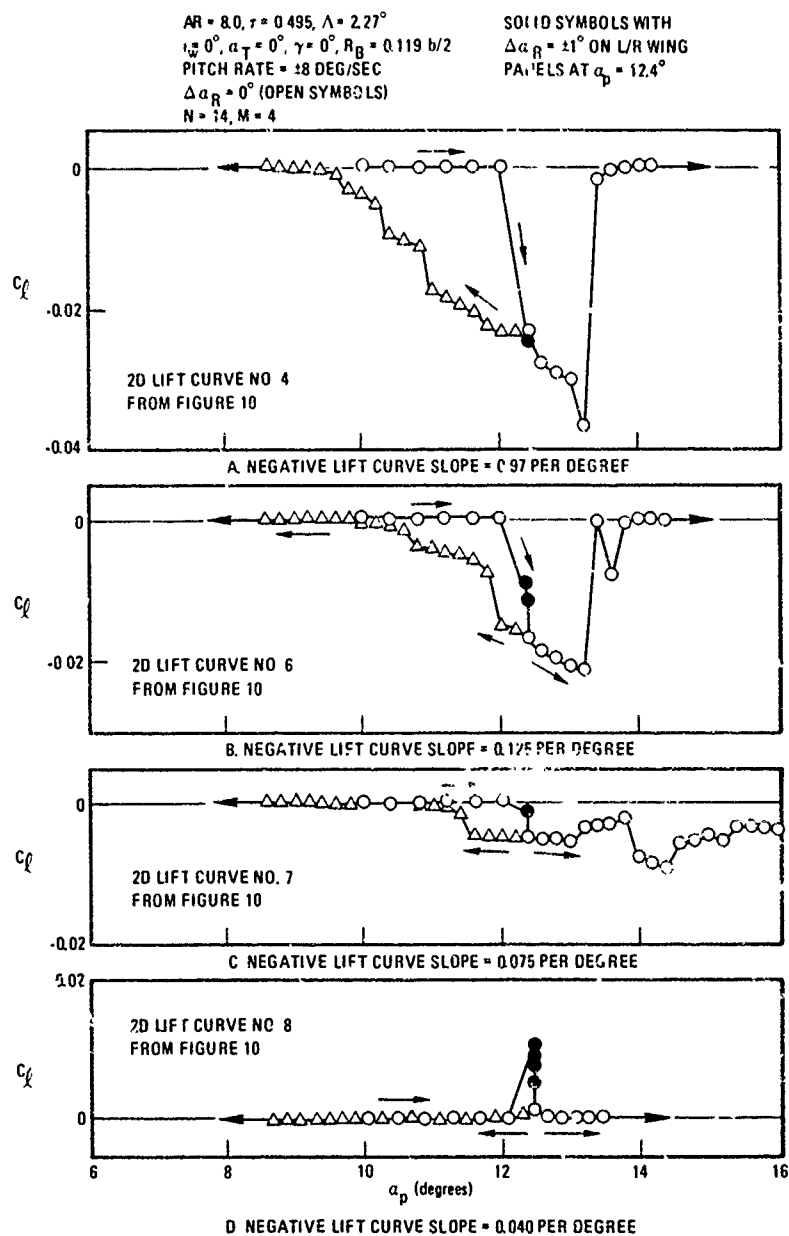


Figure 19. Effect of Roll Perturbation at  $\alpha_p = 12.4$  Degrees on Zero Beta Rolling Moment, Aspect Ratio 8.0.

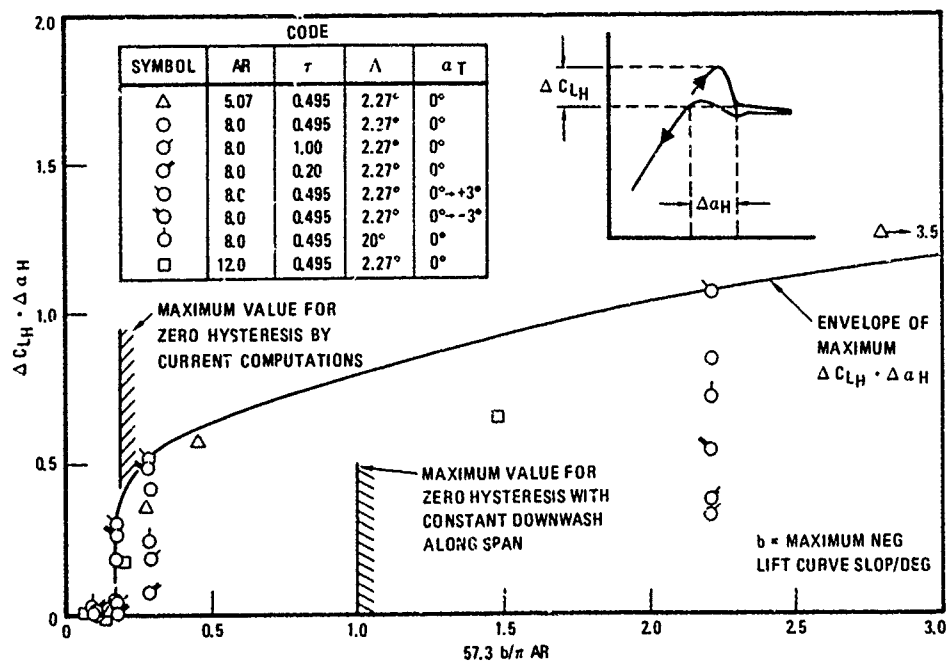


Figure 20. Lift Hysteresis Correlation.

## DYNAMIC LOADING ON AN AIRFOIL DUE TO A GROWING SEPARATED REGION

by

James D. Lang, Associate Professor  
Department of Aeronautics

and

Michael S. Francis, Chief, Mechanics Division  
Frank J. Seiler Research Laboratory

U.S. Air Force Academy, Colorado U.S.A. 80840

## SUMMARY

Experiments examining the unsteady growth of a separated region on an airfoil in incompressible flow are employed to verify aspects of a semi-empirical model which attempts to predict the loading and unsteady flow effects associated with the region. Measurements of surface pressures downstream of an oscillating fence-type spoiler confirm the existence of the two essential features of the model, namely, (1) a lag in the growth of the separation zone due to the unsteady nature of the flowfield, and (2) modification of the approximate "roof-top" pressure distribution associated with a separating and reattaching shear layer which occurs on a surface in steady flow. Also examined briefly are the effects of Reynolds number variation and the observation of secondary flow phenomena. Limitations of the model, including its inability to predict detailed spatial and temporal distributions of pressure behavior, are discussed along with recommendations for improvements. One recommended improvement to the model is the inclusion of the flow field mean vorticity distribution.

## SYMBOLS

a	shear layer parameter	$l_o, \Delta l$	non-dimensional mean length and amplitude
b	flap/spoiler mechanical coupling parameter	p	surface static pressure
c	airfoil chord	t	time
$\Delta C_H$	hinge-moment coefficient due to spoiler-induced loading	U	velocity
$C_p$	pressure coefficient, non-dimensionalized by free-stream dynamic pressure	x	non-dimensional chordwise distance measured aft from mid-chord based on half chord length
$C_{pb}$	pressure difference coefficient associated with a roof-top distribution	$x_t$	non-dimensional pressure transducer location
$\tilde{C}_{pb}$	unsteady perturbation to $C_{pb}$	$\beta$	flap deflection angle
E	ratio of separated region length to spoiler height	$\beta_o, \Delta \beta$	center and amplitude of flap oscillation
$h_s, n$	actual and non-dimensional spoiler height, $h \equiv h_s/(c/2)$	$\delta$	shear-layer thickness
$h_o, \Delta h$	non-dimensional mean spoiler height and amplitude	$\theta$	instantaneous phase angle, $\theta = \omega t/2\pi$ which relates to spoiler height through the formula $h(t) = h_o - \Delta h \cos 2\pi \theta(t)$
$h_{o1}$	non-dimensional mean spoiler height for zero flap deflection in the coupled configuration	$\omega$	angular frequency of oscillation
k	reduced frequency parameter, $k = \frac{\omega c}{2U_\infty}$	Subscripts	
$l_s, \bar{l}$	actual and non-dimensional length of separated region, $\bar{l} \equiv l_s/(c/2)$	a	pressure elbow value on spoiler upstroke
		b	pressure elbow value on spoiler downstroke
		c	convective velocity value
		o	constant, average value
		r	value near the reattachment point
		$\infty$	free-stream value

## 1. INTRODUCTION

During maneuvers at high angles of attack, dynamic stall or other similar flow phenomena related to a growing unsteady separated region may result in aerodynamic loading which differs significantly from that in steady flow. This often causes departure from controlled flight or in the very least alters the predicted behavior of the flight vehicle.

The problem of dynamic stall has been recognized for some time,<sup>1</sup> with various aspects having been investigated either experimentally,<sup>2</sup> analytically,<sup>3</sup> or numerically.<sup>4</sup> An excellent survey of past progress in the general area of separated flow may be found in reference 5. The extension of some of the ideas for steady flow to the problem of unsteady flow has only recently been attempted<sup>6</sup> but these efforts are still in their infancy.

A useful approach to achieving an understanding of the flow physics in such problems is to conceive of a flow situation in which the region parameters (for example, separated region geometry) can be somewhat "controlled" but which exhibits the main features common to all such flows. For that reason, a separated region produced downstream of an oscillating fence-type spoiler located at the midchord of a symmetric airfoil was examined. In addition to providing the characteristics discussed above, this flow field is thought to be somewhat of a subsonic analog of shock induced separation<sup>7</sup> which, in the unsteady case, involves approximately normal shocks that traverse the surface of an airfoil and result in a growing separation zone.

Previous work by the first author with a similar configuration led to an experiment which was performed at the Cranfield Institute of Technology (C.I.T.), England. It involved an oscillating spoiler and flap combination with which limit cycle behavior was observed when the spoiler and flap were mechanically coupled.<sup>8</sup> The resultant flow model espoused in a subsequent report<sup>9</sup> and in a recent paper<sup>10</sup> contains two essential features consistent with observed characteristics. The first, involving a lag in the growth of the separation zone, is attributed solely to the unsteady nature of the flow field. The second involved a modification to the approximate "roof-top" type pressure distribution (Figure 1) which is associated with a shear layer that separates and reattaches on a surface in steady flow.

The current effort seeks to further examine these two features in a more direct fashion and their effect on the surface loading in the region immediately adjacent to the separation "bubble." The experiments described below were conducted to provide a more complete description of the details of the flow field behavior for comparison with elements of the model of reference 10.

## 2. MODEL OF THE SEPARATED REGION

The following is a summary of important aspects of the analytical model used to predict unsteady loading due to spoiler-induced separation. The model is based, in part, on earlier experimental results which have been reported in detail in reference 8, and in summary in reference 11. Detailed steps in its development may be found in references 9 and 10. The model considers small perturbations to a separated region of the so-called "long bubble" type, due to a spoiler oscillation of the form  $h = h_0 - \Delta h \cos \omega t$  where  $|\frac{\Delta h}{h_0}| \ll 1$ .

### 2.1 The Lag in Bubble Growth

The basic premise upon which the model is founded is that the separated region in unsteady flow at any instant retains the characteristic geometric shape of a "bubble" found in steady flow. Of course, the quantitative aspects of the region (size, induced loading, etc.) are not assumed a priori.

Mass flow into the separated region is related to spoiler motion by the assumption that the outer shear-layer (i.e., portion of the shear-layer external to the steady-flow dividing streamline) reacts in a quasi-steady manner to transfer fluid into the bubble. A significant additional assumption, which was used by Trilling<sup>12</sup>, is that mass flux perturbations are propagated in a reversed flow direction at a characteristic convective speed,  $U_c$ . A relationship for instantaneous nondimensional length of the separated region was then shown to be:

$$l(t) \approx l_0 - \Delta l \cos(\omega t - \phi)$$

where the phase angle,  $\phi$ , could be related to the mean length,  $l_0$ , and  $U_c$ .<sup>9,10</sup> A more general expression, which is applicable to the larger amplitude cases of interest here involves a phase angle which depends on instantaneous length. The equation for the length then becomes:

$$l(t) = l_0 - \Delta l \cos \omega \left[ t - \frac{l_s(t)}{U_c} \right]$$

or

$$l(t) = l_0 - \Delta l \cos \left[ 2\pi \theta(t) - \frac{U_\infty}{U_c} l(t) \right] \quad (1)$$

Mean bubble length and amplitude may also be related to mean spoiler height and amplitude. A linear relation is given by the approximation of reference 10,  $l_0 = Eh_0$  and  $\Delta l = E\Delta h$ . Equation (1) shows that the bubble lags its quasi-steady length by a time varying phase angle which depends on reduced frequency and the velocity ratio  $\frac{U_\infty}{U_c}$ . In the present model, this velocity ratio is assumed constant. It may be thought of as relating a characteristic bubble length (defined, say, as the distance between the reattachment point and the spoiler) and the average time it takes for an element of fluid to travel this distance within the bubble interior.

### 2.2 Unsteady Pressure Distribution

The characteristic shape of the surface pressure distribution adjacent to a separated shear-layer which reattaches onto a solid surface may be approximated by the "roof-top" distribution shown below in Figure 1. In this figure (and in the model), a pressure difference coefficient is employed as the ordinate. Its distribution, which reflects the difference between separated and attached flow values of pressure, also represents the difference in chordwise loading on the aft portion of the airfoil. The region of pressure rise between the roof-top value and that near reattachment may involve an "overshoot" in pressure downstream of reattachment which is associated with the effects of turbulent mixing and reattachment.

In steady flow, the roof-top value of pressure coefficient,  $C_{p_b}$ , may be thought of as a base pressure. It does not change significantly with spoiler height for moderate to large values of height.<sup>5</sup> As spoiler height increases, the separated region length increases in the downstream direction. A long region may involve recompression on the surface with a point of confluence (not properly called reattachment) in the wake. This type of bubble has been discussed previously.<sup>8,9</sup> The present model is valid for reattachment on the surface only.

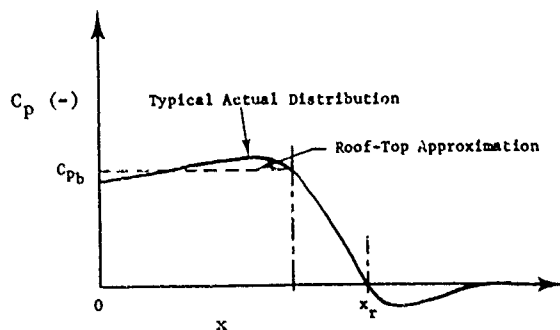


Fig. 1 Actual and Approximate Surface Pressure Distributions in Steady Flow

Under the assumption of quasi-steady behavior of the outer shear layer and following the development of Norbury and Crabtree,<sup>13</sup> a relationship between spoiler motion and an assumed perturbation to the roof-top pressure can be written as:

$$\tilde{C}_{pb} = -a k \Delta h \sin \omega t$$

where

$$a \approx 4E \frac{h_{s0}}{0.70}$$

for an average roof-top pressure coefficient of  $C_{pb0} \approx -0.4$  (see references 5 and 10).

With an approximate value for the ratio of mean spoiler height to shear-layer thickness at reattachment taken from reference 8 and the empirically derived value of  $E \approx 23$ , we have the final result:

$$\tilde{C}_{pb} \approx -30 k \Delta h \sin \omega t \quad (2)$$

That is, pressure perturbations are directly related to the spoiler rate of motion. Note that the value of  $E$  was evaluated from results of the present experiment where, for long bubbles,  $E = d\ell/dh$  in steady flow.

### 2.3 Use of the Model to Predict Loading

Earlier experiments<sup>8,9</sup> involved the spoiler mechanically coupled to a plain flap-type control surface so that spoiler height and flap angle,  $\beta$ , were related by the coupling equation:

$$h(t) = h_{01} + b\beta(t)$$

The complete system equation of motion included mechanical and aerodynamic hinge-moment terms in addition to the added effect of an incremental hinge-moment coefficient,  $\Delta C_H(t)$ , which is due solely to spoiler induced unsteady loads. The incremental quantity,  $\Delta C_H$ , was shown in reference 9 to depend on separated region length and roof-top pressure in the following functional form:

$$\Delta C_H(t) = f_1 \{C_{pb}(t)\} f_2 \{\ell(t)\} \quad (3)$$

where

$$f_1 \approx C_{pb0} + \tilde{C}_{pb}$$

and  $f_2$  was expressed as a polynomial in  $\ell$ .

Stability of the coupled, autonomous spoiler and flap system was studied upon its release from a flap angle which corresponds to an equilibrium condition in steady flow. Results are reported in detail in references 9 and 10. It was shown that a range of values of mean spoiler height,  $h_{01}$ , and coupling parameter,  $b$ , resulted in self-excitation. Stable limit cycle behavior was predicted and observed.

The model was shown to be useful in predicting not only frequency, but amplitude and center of oscillation of the limit-cycle with good accuracy. Figure 2 contains a typical map of theoretical predictions for these parameters.<sup>9,10</sup>

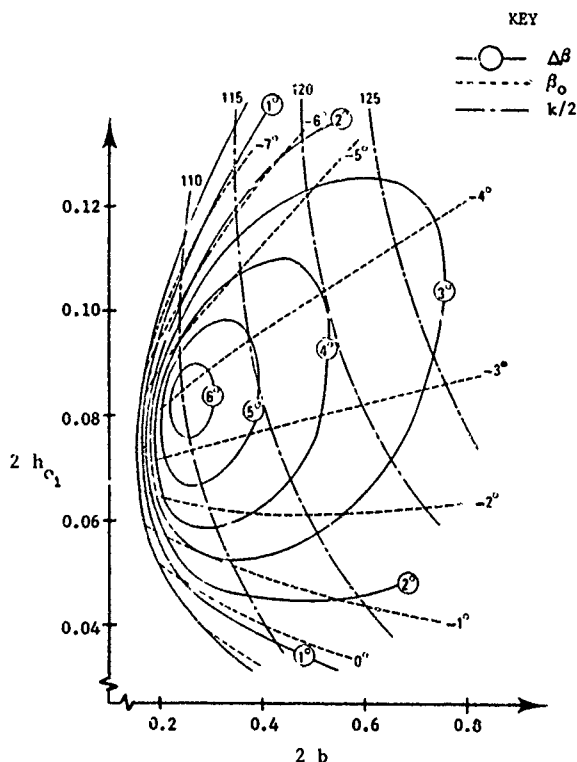
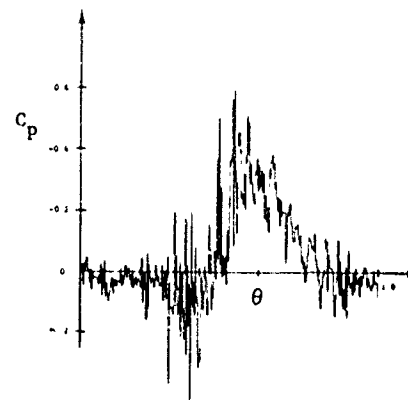
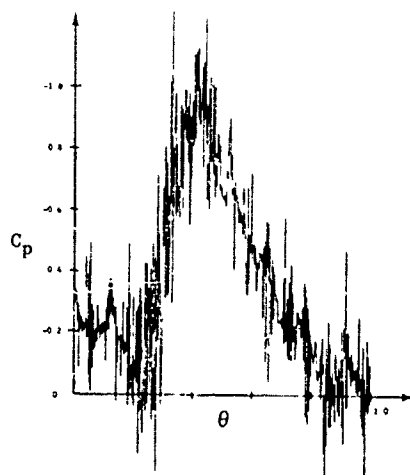


Fig. 2 Predicted Limit-Cycle Behavior

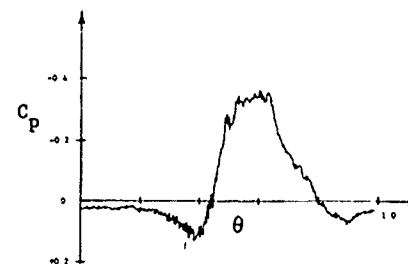
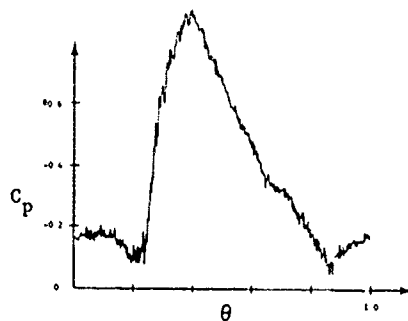
$$h = 0.03 - 0.03 \cos 2\pi\theta(t)$$

$$k = 0.20$$

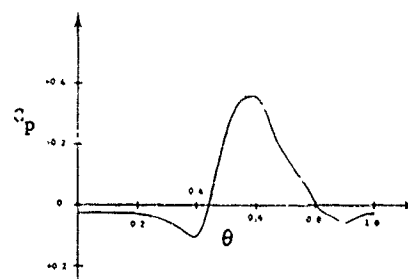
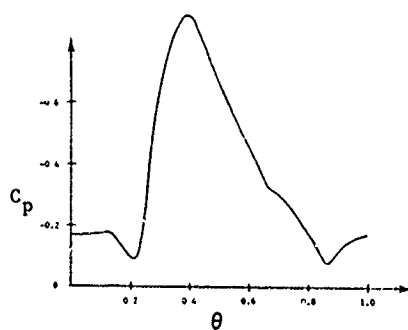
Single Cycle  
Raw Data



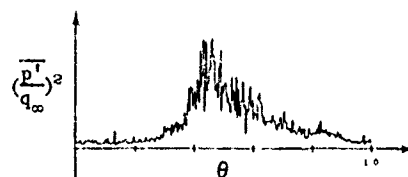
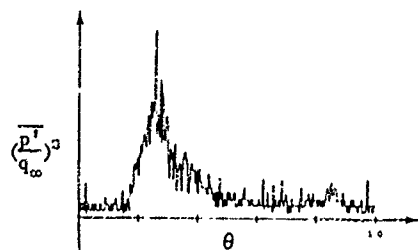
80 Cycle  
Ensemble  
Average



Interpolated  
Ensemble  
Average  
for Infinite  
Cycles



Mean Square  
Pressure Coefficient  
Fluctuations



60% Chord Data

87.5% Chord Data

Fig. 3 Pressure Histories Before and After Ensemble Averaging

### 3. DESCRIPTION OF THE EXPERIMENTAL EFFORT

A NACA 0012 airfoil model having a ten inch (25.4 cm) chord with an oscillating fence-type spoiler protruding from one surface at midchord was constructed and mounted in the 2 foot by 3 foot subsonic wind tunnel at the U.S. Air Force Academy. The model spanned the tunnel across the shorter dimension. It was instrumented with precision miniature pressure transducers located at nine chordwise locations along the centerline. Six of these were located on the same surface as the spoiler and downstream of it (at 52, 60, 70, 80, 87.5, and 93.5 per cent chord). One was located on the airfoil lower (opposite to spoiler) surface at 92 per cent chord. The remainder were located on the upper surface ahead of the spoiler (at 25 and 45 per cent chord). Data from these two transducers is not presented here. All transducers were installed so that their natural frequency of operation (upper limit), including duct-work, was never lower than 400 Hz.

The oscillator apparatus was constructed so that spoiler motion was sinusoidal. Both mean height and amplitude could be adjusted prior to the commencement of a run. Oscillation frequencies could be varied between zero and 20 Hz to within 0.01 Hz resolution. This corresponds to a reduced frequency range extending from  $0.0 \leq k < 1.0$  depending on the flow velocity.

All measurements were made with the airfoil angle-of-attack at zero degrees. The velocity was varied from 50 feet per second to 135 feet per second providing a Reynolds number variation of  $207,000 < Re < 560,000$  where Reynolds number is based on airfoil chord length.

Transducer data were recorded on FM tape using a 7-channel Philips Recorder/Reproducer with a 10 kHz bandwidth. Reduction and analysis was accomplished using a Hewlett-Packard 5452B Fourier Analyzer/Computer System.

Time varying mean pressures were obtained over a cycle of spoiler oscillation by using an ensemble averaging technique. Synchronizing the pressure signal data with a spoiler position "trigger," data were inputted, digitized and stored in the analyzer. Subsequent block addition (point-by-point) and normalization of the correlated data provided the desired result. A sample of the original input data adjacent to the "average" is displayed in Figure 3 for two transducer signals.

Mean square values of the pressure coefficient fluctuations were obtained with an ensemble averaging scheme similar to that used for mean flow data. Noting that, in unsteady flow,

$$\overline{p'^2} = \overline{p^2} - \overline{p}^2$$

where

$$p = \overline{p} + p'$$

and  $\overline{p}$  is a time-varying mean quantity, the square of the pressure was computed and averaged along with the square of the mean pressure. The desired mean square value was obtained after block subtraction. This data is also displayed in Figure 3.

Spectral information was also obtained using standard Hewlett-Packard FFT software.

### 4. EXPERIMENTAL RESULTS

#### 4.1 General

Experimental verification of the essential features of the analytical model described above was attained through examination of available mean surface pressure data. A typical variation of this quantity with spoiler height for surface locations downstream of the spoiler and for steady flow is displayed in Figure 4. Attached flow values (spoiler fully retracted,  $h = 0$ ) of pressure coefficient were computed using the NACA method. These data were obtained at a Reynolds number of 414,000 ( $U_\infty = 100$  ft/sec) as was most of the experimental data which follows.

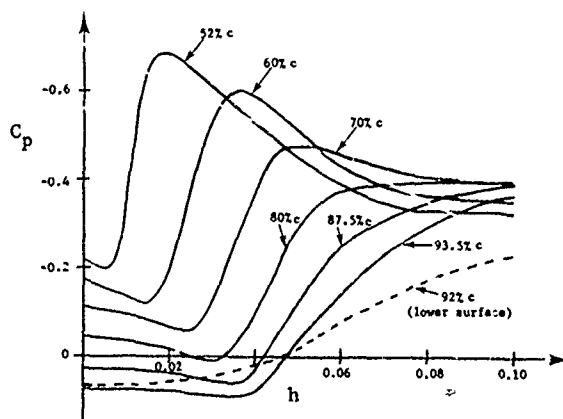


Fig. 4 Steady Flow Pressure Variations at Locations Aft of the Spoiler

It is observed that a region of markedly lower pressure appears downstream of the spoiler as its height is increased. This low pressure region then grows in the downstream direction as the spoiler height continues to increase. No significant pressure changes are observed in the vicinity of the trailing edge for spoiler heights less than 0.2 inches ( $h \leq 0.04$ ).

The above results can be displayed in a slightly different manner when cross-plotted against the variable " $\theta$ ," a quantity directly related to spoiler height. Figures 5a, 6a and 7a depict this variation for cases where the mean spoiler height and amplitude are the same and equal to 0.15 inches, 0.10 inches and 0.25 inches, respectively. (That is,  $h_0 = \Delta h = 0.03, 0.02$  and  $0.05$ , respectively.) These cases all correspond to situations where the spoiler is flush with the wing surface at its minimum height and may be taken as limiting cases of "quasi-steady" motion; i.e., the reduced frequency ( $k$ ) may be regarded as approaching zero. The symmetry of these waveforms with respect to the spoiler position characteristic is quite evident.



$$h = 0.03 - 0.03 \cos 2\pi\theta(t)$$

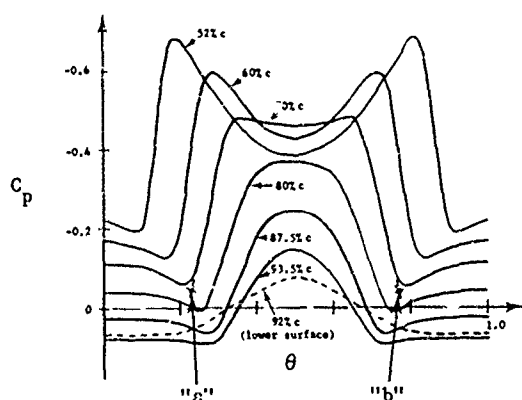
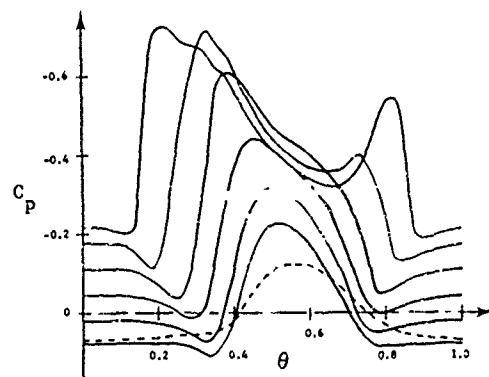
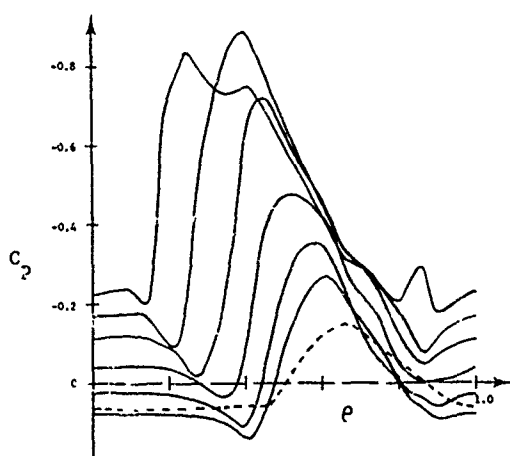
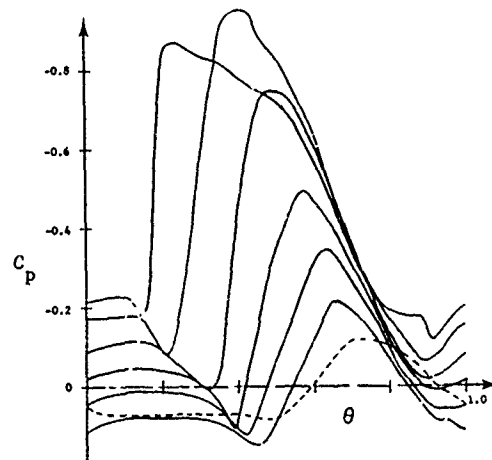
(a)  $k = 0.00$ (b)  $k = 0.10$ (c)  $k = 0.20$ (d)  $k = 0.30$ 

Fig. 5 Pressure Coefficient Time Histories  
for  $h = 0.03 - 0.03 \cos 2\pi\theta$

Figures 5b-d, corresponding to the first mean height and amplitude case above, show pressure coefficients for the situation where the spoiler was oscillated sinusoidally at reduced frequencies of 0.1, 0.2, and 0.3, respectively. Similar results for other spoiler characteristics appear in Figures 6b and 7b but only for values of  $k = 0.2$ . The deviations and relative asymmetries of these unsteady flow data from their steady flow counterparts are evident upon inspection. In particular, the effect of frequency is evident in Figures 5b-d where it can be seen that suction values are increased over the quasi-steady values on the spoiler upstroke (i.e., for  $0 < \theta < .5$ ) and decreased on the downstroke (for  $.5 < \theta < 1.0$ ).

$$h = 0.02 - 0.02 \cos 2\pi\theta(t)$$

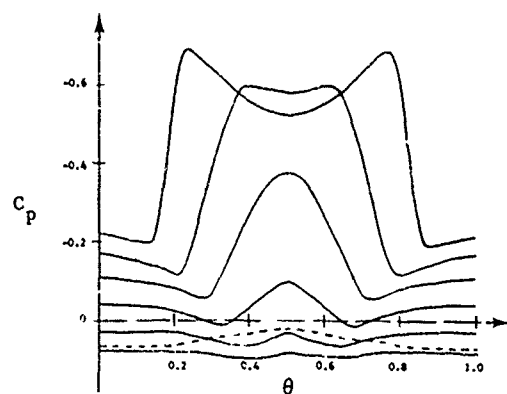
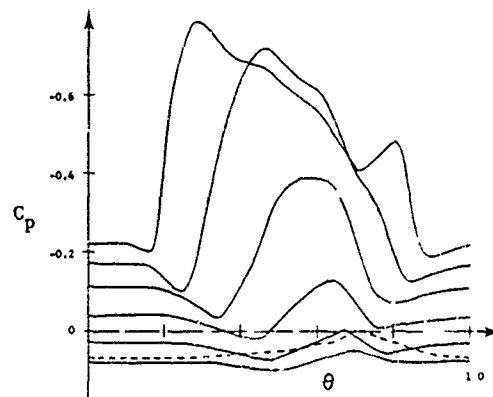
(a)  $k = 0.00$ (b)  $k = 0.20$ 

Fig. 6 Pressure Coefficient Time Histories  
for  $h = 0.02 - 0.02 \cos 2\pi\theta$

$$h = 0.05 - 0.05 \cos 2\pi\theta(t)$$

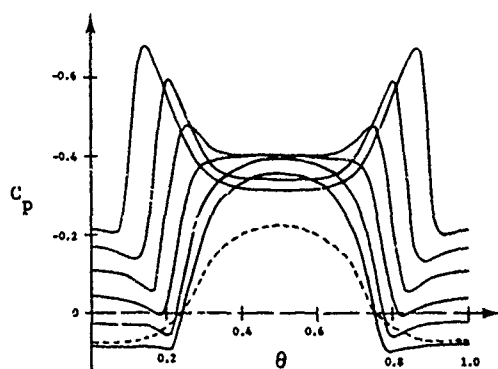
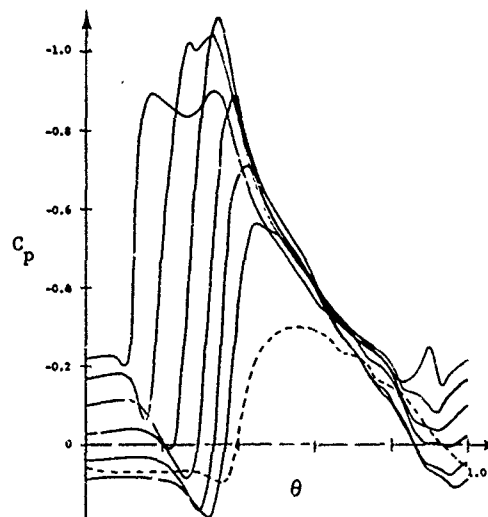
(a)  $k = 0.00$ (b)  $k = 0.20$ 

Fig. 7 Pressure Coefficient Time Histories  
for  $h = 0.05 - 0.05 \cos 2\pi\theta$

$$h = 0.03 - 0.03 \cos 2\pi\theta(t)$$

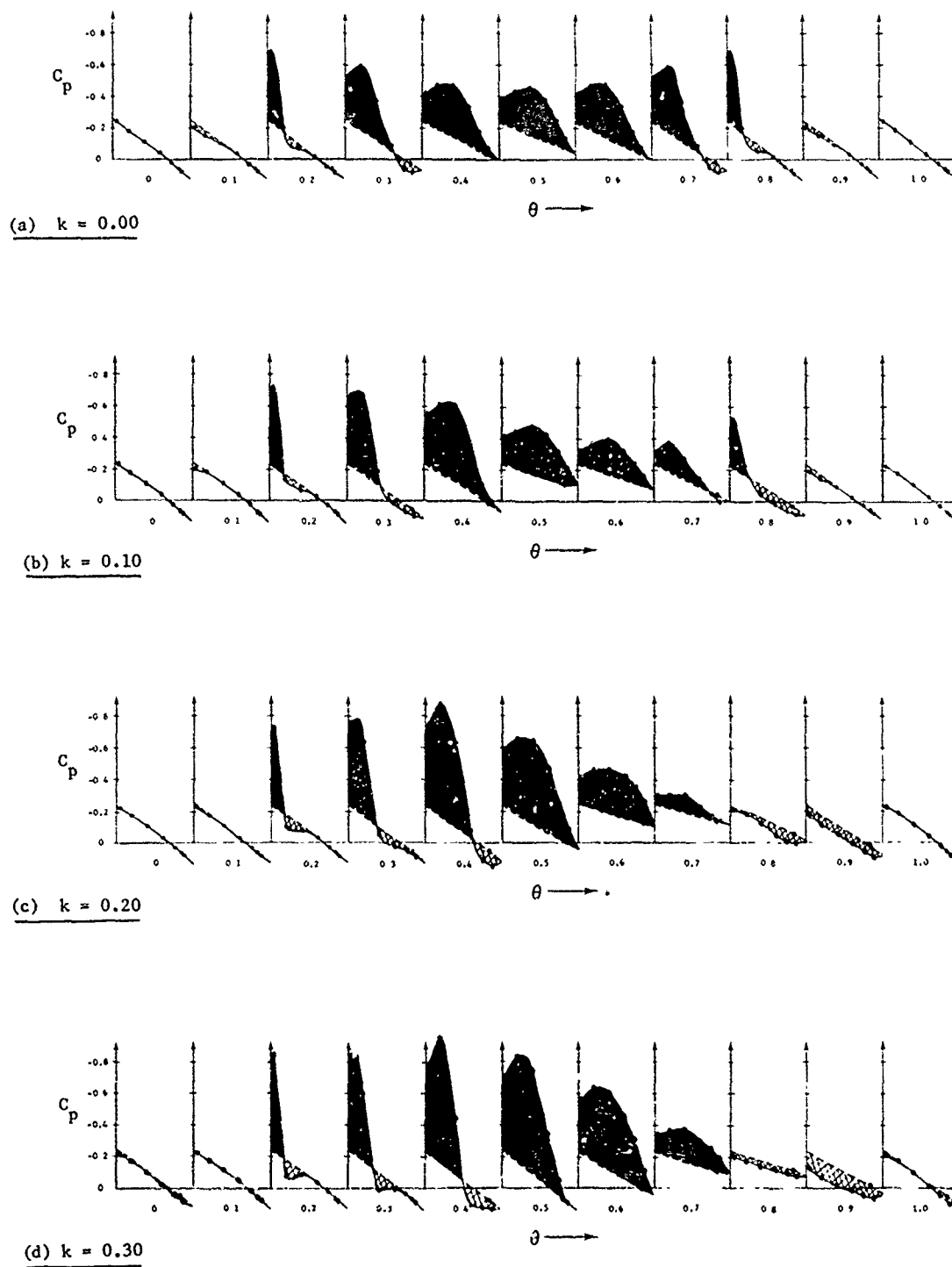


Fig. 8 Chordwise Pressure Distributions During a Cycle for  $h = 0.03 - 0.03 \cos 2\pi\theta$

$$h = 0.05 - 0.05 \cos 2\pi \theta(t)$$

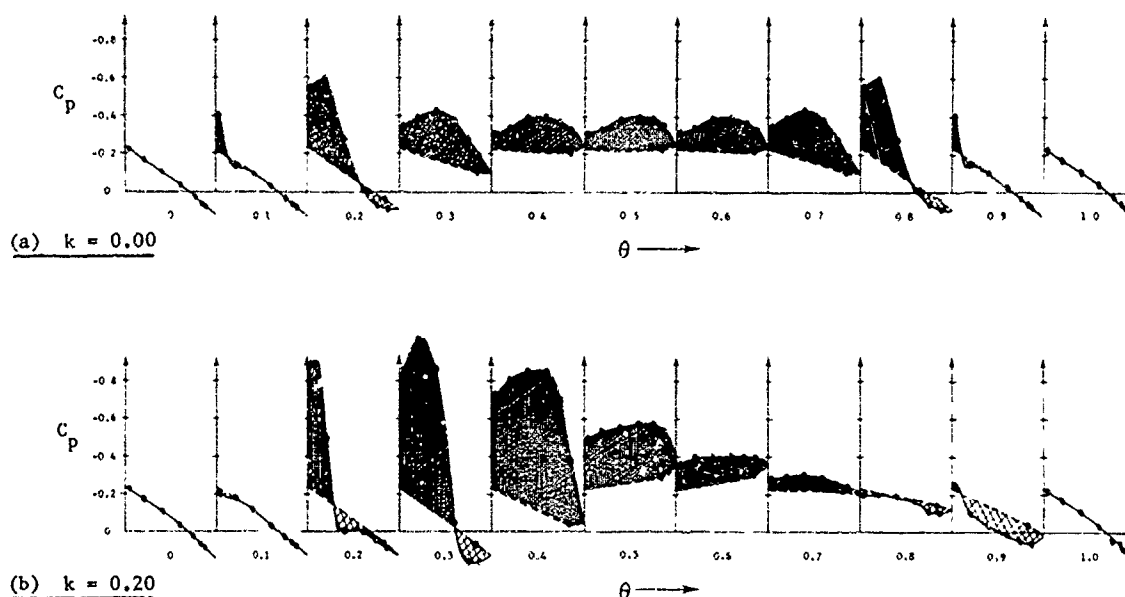


Fig. 9 Chordwise Pressure Distributions During a Cycle for  $h = 0.05 - 0.05 \cos 2\pi \theta$

Chordwise pressure coefficient distributions of the region downstream of the spoiler were constructed from the above data by employing the variable  $\theta$  as a reference quantity. (See Figures 8 and 9.) These distributions are depicted at ten equally spaced instants during a cycle of spoiler motion. The completed curves were generated with the aid of earlier experimental observations<sup>8</sup> since data from only seven transducers (including one on the lower surface) were employed in the present case. It is reasonable and convenient to show lower surface pressures as recovering nearly linearly from the single measured value (at 92 per cent chord) to the zero spoiler height value at midchord. The shaded areas represent regions of upward loading on the surface, while the cross-hatched segments depict downloading.

Careful observation of the above data confirms the existence of the two effects inherent in the unsteady flow model: (1) The lag in growth of the low pressure region is evident on both the spoiler upstroke and downstroke for all spoiler mean height and amplitude characteristics. The effects of frequency will be discussed below. (2) The predicted increase in suction values within the low pressure region on the upstroke (and corresponding decrease on the downstroke) are observed to be both frequency and amplitude dependent.

#### 4.2 Characteristic Growth Lag

A quantitative investigation of the lag effect is best accomplished by selecting a significant "event" on the time-pressure graphs which corresponds to a change in surface loading due to separation. A readily identifiable "signature" is available in the bend or "elbow" as shown in Figure 5a. At any given transducer location, event "a" corresponding to the elbow on the upstroke can be further identified with the variable  $\theta_a$ . On the spoiler downstroke, the elbow "b" is similarly associated with the parameter,  $\theta_b$ . For the case of  $k = 0.0$ , and a surface location of 70 per cent chord, these values are  $\theta_a = 0.230$  and  $\theta_b = 0.770$ , as shown. The same identification technique is employed in the unsteady flow case.

Figure 10 shows the elbow locations as discussed above corresponding to Figures 5 and 8. In these cases, the lag is apparent. Although this information is not depicted with spoiler height directly, a cross-plot of this nature would reveal a non-linear behavior near the origin. This change in character may relate to the existence of a so-called "short separation bubble" discussed in reference 8. Once the "bubble" length has increased so that  $h/l \ll 1$ , the relationship between pressure elbow location and spoiler height is approximately linear. The distance between the spoiler and a given transducer (given by  $x_c \frac{c}{2}$ ) can be combined with the difference between the unsteady flow value of  $\theta$  and the corresponding steady flow value for events a and b (i.e.,  $\theta'_a - \theta_a$  and  $\theta'_b - \theta_b$ ) and related to the assumed convective lag velocities,  $U_a$  and  $U_b$ .

$$\frac{U_\infty}{U_a} = \frac{2\pi(\theta'_a - \theta_a)}{x_c k} \quad \text{and} \quad \frac{U_\infty}{U_b} = \frac{2\pi(\theta'_b - \theta_b)}{x_c k}$$

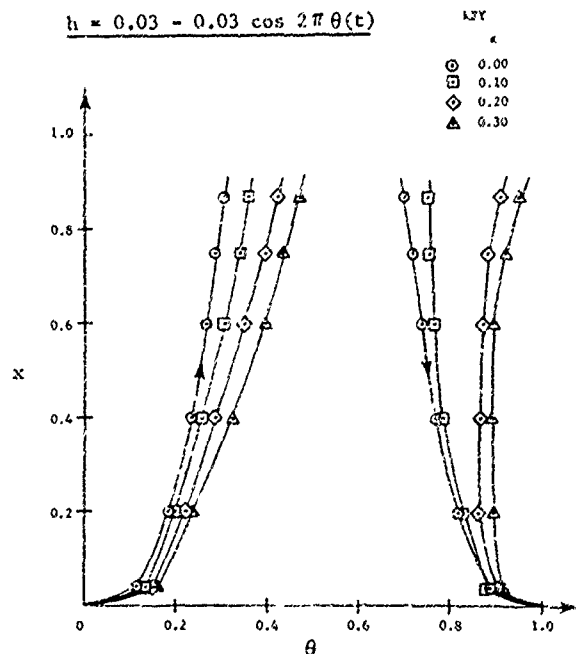
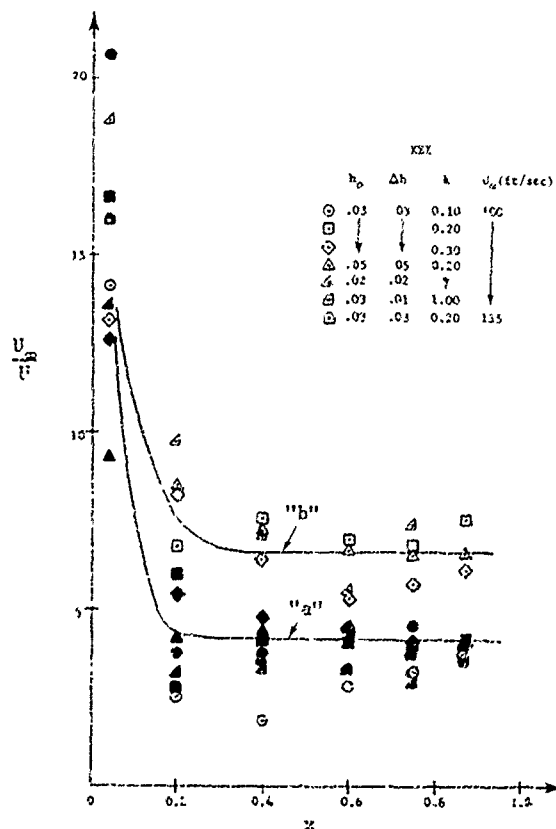


Fig. 10 Pressure Elbow Location During a Cycle of Spoiler Motion



The pressure field data of Figures 8 and 9 reveal that the "roof-top" concept is, at best, an approximation to the actual distribution in the unsteady situation. Significant suction peaks are observed to exist on the spoiler upstroke. Therefore, a comparison of the data with the model required that the actual measured distributions be replaced with an equivalent average value for the pressure coefficient.

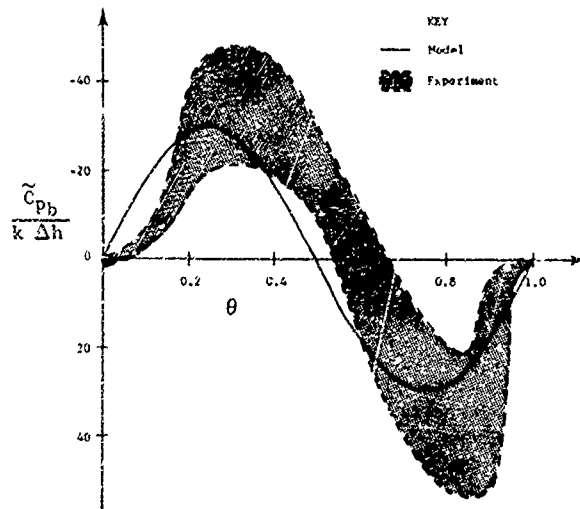


Fig. 12 Predicted and Measured Values of Pressure Perturbation

An additional factor in the criteria for experimental data comparison involved the compensation for the time lag discussed above. Since bubbles of the same lengths were required for direct comparison (the length of the region is accounted for in the model), they did not coincide with identical values of spoiler height. For example, the equivalent "roof-top" pressure at  $\theta = 0.40$  (Figure 8c) was compared to the pressure at  $\theta = 0.285$  in the quasi-steady case (Figure 8a).

Comparison between the five unsteady cases and their quasi-steady counterparts yield results which fall inside the shaded region of Figure 12. The model postulates that these results should fall on a single sinusoidal curve when compensation has been made for reduced frequency and amplitude (note the vertical scale). No significant departures from this scaling law were observed for the amplitudes and frequencies investigated. The amplitude of the "theoretical" curve shown in Figure 12 was found by substitution of empirical values of the shear layer parameters into equation (2).

#### 4.4 Other Observations

Though limited in scope, measurements depicting Reynolds number variation reveal this to be a significant parameter over the range of investigation. Both the bubble geometry and the magnitude of the unsteady pressure variations were found to be dependent on Reynolds number, at least for the lowest value observed ( $Re = 207,000$ ).

The earlier experiments reported in reference 8 were all accomplished at a relatively high range of Reynolds number,  $0.9 \times 10^5 < Re < 2 \times 10^6$ , and no significant Reynolds number variation was observed. Although the mid-range data ( $Re = 414,000$ ) and highest value data ( $Re = 560,000$ ) seem to be in good agreement, the data obtained at the low end of the Reynolds number range indicate a marked deviation. The significance of these effects and their relation to the physical mechanisms which drive bubble growth will be the subject of future experiments.

A final comment concerns the possible presence of a secondary flow phenomenon which is observed in the data of Figures 5b-d, 6b and 7b. The transient "ripple" in the pressure histories at 52 and 60 per cent chord has been related to a reduced frequency of about 7.15 k for all cases examined. This effect, which has been determined to be independent of transducer and ducting properties, represents a real flow phenomenon possibly relating to values of the vorticity of the "shed structure" at the spoiler tip. It, too, will be a subject of further investigation.

#### 5. CONCLUSIONS AND RECOMMENDATIONS

The experimental results discussed above confirm the existence of both a lag in separated region length and an overshoot in steady flow pressure thereby confirming the model's essential features. Despite its necessary restriction to small perturbations, the model can be extended to cases involving large variations in separated region geometry as examined in this paper. This discussion would not, however, be complete without a more thorough examination of the model's limitations and possible areas of improvement.

It should be recalled that the model is inherently linear--a result achieved at the expense of a significant number of "limiting" assumptions. The application and determination of the "shear layer parameters" is, at best, an empirical procedure thus limiting the flexibility and broad generalization of the model to other configurations and flow regimes. At the same time, it must, in all fairness, be noted that the application of these concepts was successful when applied to the coupled spoiler/flap system in the prediction of system stability and limit cycle motion.<sup>8</sup>

The most questionable aspect involved in the extension of the model beyond its assumed limits, i.e., small perturbations in region geometry, is the accuracy of the flow field description itself. While the concept of a growing and shrinking bubble-like structure is consistent with the assumed limitations, there is little evidence to support this picture in the large perturbation situation. Indeed, if the rms pressure measurements have been correctly interpreted, the shear layer at reattachment makes contact with and moves downstream on the airfoil surface on the spoiler upstroke (growing bubble) but exhibits no converse behavior on the downstroke. The assumption of a shrinking bubble on the downstroke is, therefore, not properly warranted. The fact that the inferred characteristic convective velocities on the upstroke and downstroke differ by a significant amount is further confirmation of the observation.

Although the flow description may not be accurate on the downstroke, the measured pressure histories confirm (both qualitatively and quantitatively) the lag associated with the mean flow pressure elbow which may be expressed in the form

$$c(t) = c_0 - \Delta c \cos \left( \omega t - \frac{\omega l}{U_c} \right)$$

where  $U_c \approx U_a, U_b$  for the spoiler upstroke and downstroke, respectively. The length,  $l$ , must be divorced from the "bubble length" concept, at least on the downstroke, if the above flow field description is employed.

The obvious oversimplification of a "roof-top"-shaped distribution is evident from an examination of experimental pressure peaks and distributions. The non-linear and non-sinusoidal behavior associated with the equivalent values of  $C_{pb}$  is shown in Figure 12 but the primary difference between analysis and experiment occurs in the phase. The probable reason for this discrepancy relates to the quasi-steady arguments which led to the relation for  $C_{pb}$  (equation 2).

It must then be conceded that the model provides only an "average" description insofar as the spatial variables are concerned. Improvement on the approach must be centered on methods which are more capable of assessing the local details of the flow characteristics. A technique which entails a more representative description of the flow field is appealing. Instead of merely examining the mass transfer characteristics, a more significant parameter related directly to the flow dynamics such as vorticity (including production, transfer and diffusion) should be incorporated. An approach which involves the shear layer characteristics as a consequence rather than an assumption may prove a more effective vehicle in extending the loading predictions to a wider variety of configurations and flow regimes.

A model which employs the above concepts is currently being formulated. It does not restrict itself to the "bubble" description but is more flexible in its treatment of the flow field geometry. Future experiments directed at verification of the nature and extent of the vorticity field are already in the construction phase.

It should be mentioned that the three-dimensional behavior which is observed to exist in this seemingly two-dimensional problem must be further investigated. These effects and those of aspect ratio and wing sweep must be more completely understood before any attempt to extend the model to complex configurations can be entertained.

As a final note, it should be emphasized that while numerical solution to the equations of motion may seem a more straightforward method to the solution of this problem, the primary advantage in analytically modeling the flow field lies in the resulting capability to readily extract the nature and extent of the dominant physical mechanisms. This is the primary objective of the current research effort.

## 6. ACKNOWLEDGEMENTS

The authors gratefully acknowledge the assistance of Mr. Carl Geddes, instrument maker, whose exceptional craftsmanship and tireless efforts made these experiments possible. The Department of Aeronautics greatly assisted by allowing use of their wind tunnel facility. Our thanks are also extended to Mrs. Donna Weiss for her painstaking efforts in the preparation of this manuscript. The research effort described in this report is supported by the Frank J. Seiler Research Laboratory (AFSC).

## 7. REFERENCES

1. Lambourne, N.C. "Flutter in One Degree of Freedom," AGARD Manual on Aeroelasticity, Part V, Ch. 5, 1968.
2. McCroskey, W.J., Carr, L.W. and McAlister, K.W. "Dynamic Stall Experiments on Oscillating Airfoils," AIAA Journal, Vol. 14, No. 1, January 1976, pp. 57-63.
3. McCroskey, W.J. "Inviscid Flowfield of an Unsteady Airfoil," AIAA Journal, Vol. 11, No. 8, August 1973, pp. 1130-1137.
4. Crimi, F. and Reeves, B.L. "A Method for Analyzing Dynamic Stall of Helicopter Rotor Blades," NASA CR-2009, May 1972.
5. Chang, P.K. Separation of Flow, 1st Ed., London, Pergamon Press, 1970.
6. Sears, W.R. "Unsteady Motion of Airfoils with Boundary-Layer Separation," AIAA Journal, Vol. 14, No. 2, February 1976, pp. 216-220.
7. Newman, B.G. "The Re-Attachment of a Turbulent Boundary-Layer Behind a Spoiler," Aeronautical Research Labs, Report A64, Melbourne, Australia, 1949.
8. Lang, J.D. "Experiments on an Airfoil with Oscillating Spoiler and Flap," F.J. Seiler Research Laboratory TR-74-0011, June 1974 (AD-783251).
9. Lang, J.D. "The Dynamics of a Growing Separated Region on an Airfoil," F.J. Seiler Research Laboratory TR-75-0005, February 1975 (AD-A068773).
10. Lang, J.D. and Francis, M.S. "The Interaction of an Oscillating Control Surface with an Unsteady Separated Region," (to be published in the Journal of Aircraft, Vol. 13, No. 9, September 1976).
11. Lang, J.D. "Experimental Results for an Airfoil with Oscillating Spoiler and Flap," Unsteady Aerodynamics, Vol. 1, University of Arizona Press, July 1975.
12. Trilling, L. "Oscillating Shock Boundary-Layer Interaction," Journal of the Aeronautical Sciences, Vol. 25, No. 5, May 1958, pp. 301-304.
13. Norbury, J.F. and Crabtree, L.F. "A Simplified Model of the Incompressible Flow Past Two-Dimensional Aerofoils with a Long Bubble Type of Flow Separation," RAE Tech Note Aero 2352, June 1955.

## PRESSIONS SUR UNE CARÈNE DE PRISE D'AIR A LÈVRE MINCE FONCTIONNANT EN SUBSONIQUE A DÉBIT RÉDUIT

par Gérard LARUELLE et Paul LEVART

*Office National d'Études et de Recherches Aéronautiques (ONERA)  
92320 CHATILLON - France*

### RÉSUMÉ

Un montage d'essais en soufflerie a été réalisé pour étudier l'écoulement autour du bord d'attaque aigu d'une prise d'air fonctionnant en subsonique à débit réduit.

Une comparaison des répartitions de pression sur la carène, calculées, sur une configuration donnée, pour le vol et pour le montage en soufflerie, montre que l'écoulement local est correctement simulé dans le cas d'une réduction de débit.

A débit réduit, les forces agissant sur la prise d'air sont fonction du bulbe de décollement qui se forme sur la paroi externe de la carène.

La méthode utilisée pour calculer l'écoulement potentiel a été adaptée pour prendre en compte ce bulbe, selon les paramètres qui le caractérisent.

Cette méthode est actuellement limitée aux écoulements subsoniques, mais doit être développée pour des cas transsoniques.

La détermination des paramètres caractérisant le bulbe est recherchée à partir des règles empiriques établies expérimentalement ; le résultat ne peut donc être étendu sans vérification à des cas assez éloignés des conditions de l'essai.

Les sondages effectués sur la paroi supérieure de la carène permettent par ailleurs de caractériser le profil et l'épaisseur de la couche limite qui dépendent du sillage du bulbe, lesquels sont également déterminés par le calcul.

Enfin, des mesures instantanées et un film stroboscopique révèlent le caractère instationnaire du décollement de bord d'attaque.

## PRESSURES OVER A SHARP-EDGED AIR INTAKE FUNCTIONING IN SUBSONIC FLOW AT REDUCED FLOWRATE

### ABSTRACT

A wind tunnel test set-up has been designed for studying the flow around the cowl with sharp leading edge of an air intake functioning at subsonic velocity and with a reduced flowrate.

A comparison of the pressure fields around the intake lip, calculated in an approximate configuration for the free flight and for that particular set-up, shows that local flows are correctly simulated in the case of moderately reduced flowrates.

The forces acting on the air intake casing are dependent upon a separation bubble that forms on the external lip of the intake when the flowrate is sufficiently reduced.

The method used for calculating the potential flow has been adapted to take account of this bubble, through parameters characterizing it. This method is presently limited to subsonic flows, but will be developed for transonic flows.

The determination of these bubble parameters is sought from empirical rules based on test results ; thence these rules should not be extended too far beyond the actual test conditions.

Moreover, probings performed along the external surface of the cowl make it possible to characterize the profile and thickness of the boundary layer, which is dependent on the bubble wake, and which is predicted by the calculation method.

Lastly, fast response pressure measurements and a film of schlieren pictures reveal the unsteady character of the leading edge separation.



## NOTATIONS.

## SYMBOLS

- $A$  : section d'un tube de courant  
 $A_c$  : section critique  
 $a_e, b_e$  : facteurs de contraction  
 $C_f$  : coefficient de frottement  
 $H$  : hauteur  
 $H$  : paramètre de forme  $H = \delta_2 / \delta_1$   
 $\bar{H}$  : paramètre de forme  $\bar{H} = \delta_2 / \delta_1$   
 $K_p$  : coefficient de pression  $K_p = \frac{P - P_\infty}{q}$   
 $M$  : nombre de Mach  
 $\vec{n}$  : vecteur unitaire normal  
 $p$  : pression  
 $q$  : pression dynamique  $q = \frac{1}{2} \rho V^2$   
 $u$  : composante de la vitesse selon  $Ox$   
 $v$  : composante de la vitesse selon  $Oy$   
 $V$  : module de la vitesse  
 $X_d$  : longueur de décollement  
 $\delta$  : rapport des chaleurs spécifiques  
 $\delta$  : épaisseur de la couche limite  
 $\delta_1$  : épaisseur de déplacement  
 $\delta_2$  : épaisseur de quantité de mouvement  
 $\delta_3$  : épaisseur d'énergie  
 $\mathcal{E}, \mathcal{E}'$  : coefficients de débit  
 $\phi$  : fonction de dissipation  
 $\psi, \chi$  : fonctions de courant  
 $\rho$  : masse volumique  
 $(x, y)$  : systèmes de coordonnées  
 $(\xi, \eta)$   
 $\Sigma(M) = A / A_c$   
 $\theta$  : direction de l'écoulement potentiel  
 $\tau$  : force de frottement par unité de surface

## INDICES.

- $\infty$  : infini amont (ou plan d'entrée dans le montage en soufflerie)  
 $a$  : plan de l'entrée d'air  
 $d$  : décollement  
 $e$  : limite extérieure de la couche limite  
 $r$  : recollement

## 1 - INTRODUCTION.

Les prises d'air d'un avion de transport supersonique sont optimisées pour la croisière ; elles présentent une carène à l'avant mince qui permet de minimiser la traînée.

Pendant certaines phases subsoniques du vol, avec débit d'air réduit, les lignes de courant abordent la carène avec une forte incidence : il en résulte un décollement de bord d'attaque, sur la paroi externe de la carène, qui modifie la répartition des pressions locales. En particulier l'effet de succion est réduit, ce qui accroît la traînée. Une méthode de calcul des efforts sur la carène, et de l'écoulement d'entrée obtenu dans ces conditions est proposée ; elle est basée sur des lois assez empiriques établies à partir de résultats expérimentaux. A cet effet, un montage d'essai qui permet de créer des décollements de bord d'attaque très proches de ceux qui apparaissent sur les prises d'air a été réalisé dans la soufflerie S5 de Chalais-Meudon.

## 2 - PRESENTATION DU PROBLEME.

Le débit d'air capté par le moteur sera caractérisé par  $\mathcal{E}$  : "coefficient de débit" qui représente le rapport de la section du tube de courant capté, à l'infini amont ( $A_0$ ) à la section de l'entrée d'air ( $A_1$ ) (fig.1). Le domaine qui nous intéresse, dans cette étude, est celui des faibles valeurs des  $\mathcal{E}$ , pour lequel le point d'arrêt est situé sur la carène interne.



Fig. 1 - Définition du coefficient de débit.

En fluide parfait, le contournement de la lèvre mince induit des vitesses infiniment grandes (fig.2), avec création d'un effet de succion local très prononcé.

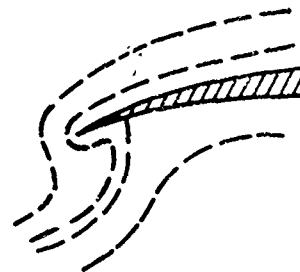


Fig. 2 - Schéma théorique

Au-delà du bord d'attaque, se produit une très rapide recompression externe qui ramène la pression à une valeur voisine de  $p_\infty$  à une certaine distance à l'aval du bord d'attaque.

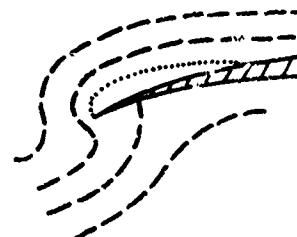


Fig. 3 - Schéma réel.

En fluide réel, un tel schéma ne peut exister ; un bulbe de décollement se forme au bord d'attaque (fig.3), qui atténue l'effet de succion et modifie la répartition des pressions sur la carène.

Actuellement la théorie ne peut traiter ce cas de décollement, qui, à notre connaissance, n'a encore fait l'objet que de recherches expérimentales partielles [1] ; les recherches ont surtout précédemment porté sur des cas voisins de bords d'attaque d'ailes arrondis, où la couche limite laminaire se développe avant de décoller, pour former un bulbe court dans lequel la transition se produit ; elles ont donné naissance à des méthodes de prévision semi-théoriques des caractéristiques du bulbe, telles que celle qui est présentée en [2] .

La méthode proposée, consiste à modéliser les répartitions de pression au niveau du bulbe de décollement obtenues expérimentalement, et à introduire cette modélisation dans un programme de calcul de fluide parfait. La référence [3] présente un travail comparable.

Les lois expérimentales ont été obtenues sur une forme de carène particulière ; elles ne peuvent être généralisées sans des essais complémentaires.

### 3 - MONTAGE EXPERIMENTAL.

#### 3.1 - Description du montage -

Le montage expérimental a été réalisé pour la soufflerie S5 de Chalais-Meudon.

La carène utilisée reproduit, à l'échelle 1/7, la forme réelle d'une carène d'avion supersonique, et les parois de la veine ont été définies de façon que, sur cette carène, les répartitions de pression soient très voisines de celles qui existent en vol : les parois épousent la forme de lignes de courant proches de la carène dans les conditions du vol subsonique.

La pression génératrice est un peu inférieure à celle du vol (0,50 bar au lieu d'environ 0,7 bar), mais le nombre de Reynolds demeure significatif, et le montage doit par conséquent donner une reproduction assez fidèle des décollements réels de bords d'attaque.

Le montage est présenté figures 4 et 5.

La hauteur  $H_1$  d'entrée de la prise d'air du montage est de 44,7 mm ; celle de la prise d'air réelle,  $H_2$  serait de 90 cm environ. La largeur de la veine est de 300 mm.

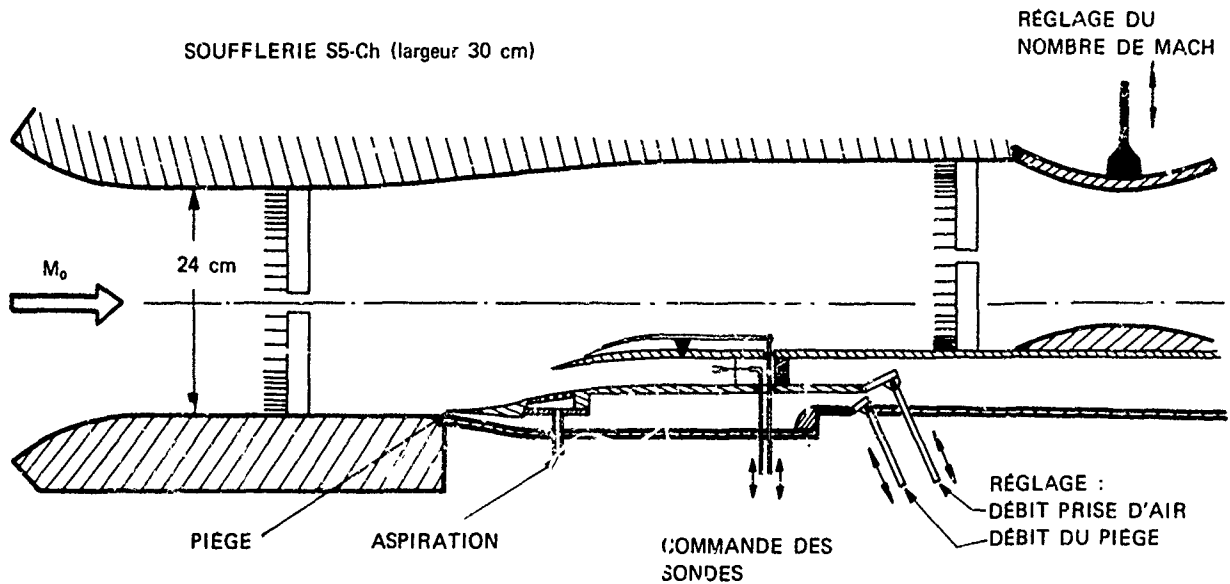


Fig. 4 - Schéma du montage.

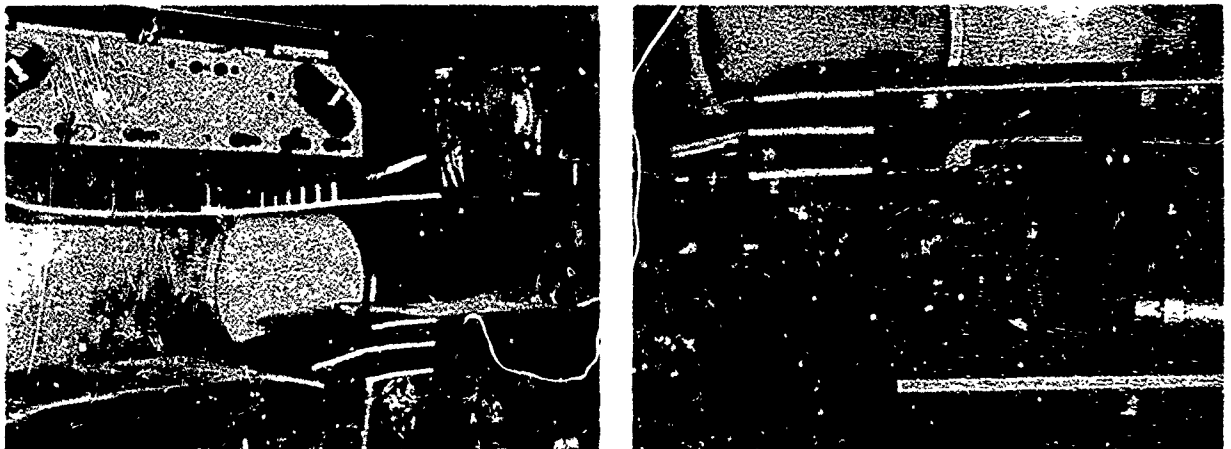


Fig. 5 - Montage en veine.

La faible valeur du rapport de la hauteur d'entrée  $H_1$  à la largeur de la veine permet d'assurer une bonne bidimensionnalité de l'écoulement, ce qui a été vérifié par des visualisations de l'écoulement pariétal. La longueur des bulbes étudiés, dont la dimension peut atteindre 45 mm, reste en particulier constante sur toute la largeur de la veine, hors des couches limites latérales de la soufflerie.

La couche limite de la paroi inférieure de la veine est éliminée par un piège en "Pitot" placé juste en amont de la partie évolutive du profil.

La couche limite qui se forme sur cette partie évolutive est elle-même contrôlée par aspiration, dans la région d'entrée de la prise d'air où les forts gradients que l'on obtient à débit réduit provoqueraient un décollement.

Cette aspiration représente environ 2% du débit de la prise ; elle est assurée par 25 rangs décalés de trous de 0,8 mm au pas de 2,5 mm. L'absence de décollement a été vérifiée par visualisation pariétale. Un essai préliminaire, avec une perméabilité moindre, n'avait pas permis d'éviter ce décollement.

L'uniformité de l'écoulement amont, dans la veine d'entrée, a été vérifiée par un sondage en pressions statique et totale.

Le montage ainsi défini permet des comparaisons précises des résultats expérimentaux aux résultats de calcul : un écoulement régulier est assuré sur les parois de la veine qui serviront de frontières au domaine de calcul en écoulement potentiel.

Divers réglages sont possibles :

- débit du piège à couche limite
- débit d'aspiration
- débit de la prise d'air (coefficient de débit :  $C_d = H_0/H_1^2$ )
- nombre de Mach  $M_0$

### 3.2 - Equipement en mesures de pression.

75 prises de pression pariétales sont réparties : sur la paroi supérieure de la soufflerie (1.), sur la paroi inférieure (34), et sur la carène (25 sur la paroi externe et 3 à l'intérieur de la prise) ; une prise supplémentaire sert à la mesure du débit piégé contrôlé par un col sonique.

Toutes ces prises sont placées dans le plan médian de la veine.

Deux peignes amovibles, l'un en amont de la carène (10 prises) l'autre entre la paroi supérieure de la veine et la carène (24 prises) permettent de vérifier l'uniformité de l'écoulement et l'état des couches limites se développant sur les parois.

Une sonde mobile à deux branches permet d'explorer l'écoulement pénétrant dans la prise d'air et de mesurer le débit capté.

Sur la carène, une sonde mobile dont la longueur peut être modifiée, permet de relever les profils de pressions d'arrêt dans le bulbe et dans la couche limite aval.

Un capteur instationnaire a été installé à 5 mm du bord d'attaque, sur la paroi supérieure de la carène.

### 3.3 - Ecoulement sur la carène.

Les figures 6 et 7 présentent deux exemples de

répartitions de nombres de Mach relevées sur les parois de la carène et de la soufflerie. Les conditions correspondent à la figure 6,  $M_0 = 0,5$  et coefficient de débit  $C_d = 0,6$ , sont telles qu'il

n'y a pas formation de bulbe de décollement sur la paroi externe de la carène, (la valeur de  $C_d$  à l'adaptation à  $M_0 = 0,5$  est d'environ 0,59). La figure 7 ( $M_0 = 0,5$  et  $C_d = 0,34$ ) met par contre en évidence la formation d'un bulbe de décollement sur la carène, avec un plateau de pression suivi d'une recompression ; la longueur du bulbe est d'environ 3 cm.

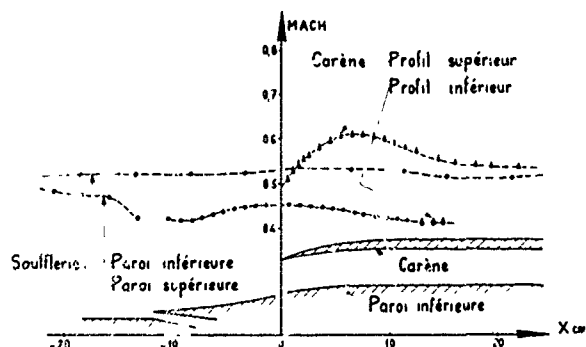


Fig. 6 - Répartitions expérimentales  $M_0 = 0,5$ ,  $C_d = 0,6$ .

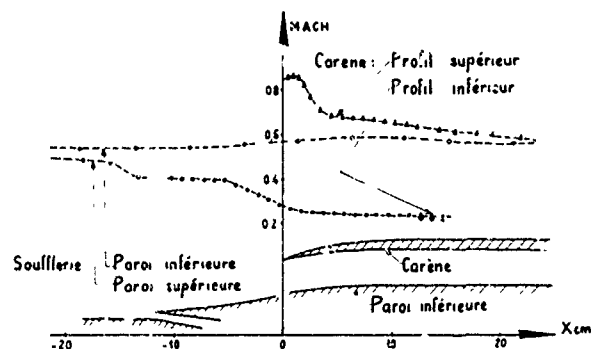


Fig. 7 - Répartitions expérimentales  $M_0 = 0,5$ ,  $C_d = 0,34$ .

### 3.4 - Étude expérimentale du bulbe de décollement.

#### 3.4.1 - Analyse des pressions pariétales.

La figure 8 fournit quelques exemples de répartitions de pressions obtenues sur la paroi externe de la carène pour diverses configurations d'essai ( $M_0$ ,  $C_d$ ).

La variation importante du niveau de pression sur la partie aval de la carène, à  $M_0$  fixé, lorsque le débit aspiré par la prise d'air varie, résulte évidemment de la limitation de la veine.

Une visualisation par enduit gras, a permis de préciser en première approximation les points de recollement. Ces points sont indiqués sur la figure 8.

Les répartitions obtenues avec décollement ( $C_d \leq 0,42$ ) présentent, entre le bord d'attaque de la carène (point de décollement) et le point de recollement une similitude d'évolution, avec une zone quasi isobare, suivie d'une zone de recompression rapide jusqu'au point de recollement.

La référence [3] qui présente une étude sur le recollement turbulent incompressible indique, que pour une couche limite initiale nulle au

point de décollement, le rapport  $(p_r - p_d)/q_d$  est voisin de 0,3.

L'application de cette relation au cas des présents essais (pour lesquels la pression de décollement  $p_d$  est la pression de la zone quasi isotare dans le bulbe) permet de calculer la pression de recollement  $p_r$  et donc de localiser le point de recollement sur les courbes de pression relevées expérimentalement.

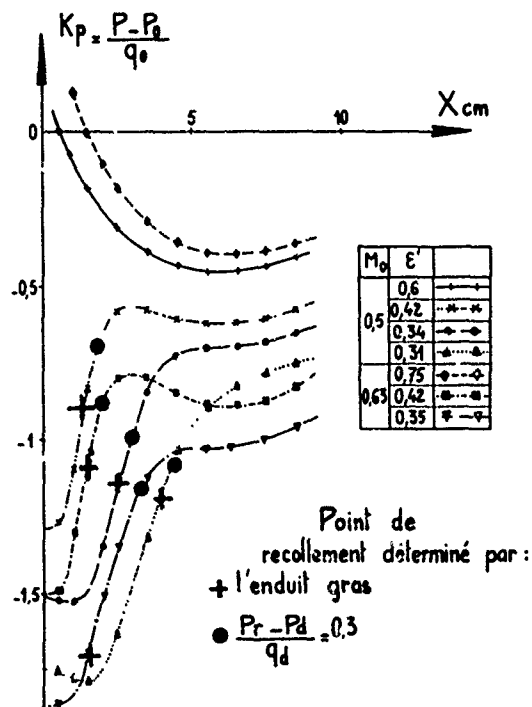


Fig. 8 - Pressions relevées sur la carène.

On constate, figure 8 un accord relativement bon entre les positions ainsi déterminées et les positions fournies par les essais de visualisation par enduit visqueux, l'écart étant d'environ 5 mm, sauf pour la configuration  $M = 0,63$  et  $\epsilon' = 0,35$  où il atteint 15 mm. Dans ce dernier cas apparaissent des chocs instables, en lambda, se déplaçant de façon aléatoire et l'emploi, aussi bien de la relation précédente que de la technique de visualisation, n'est plus justifié.

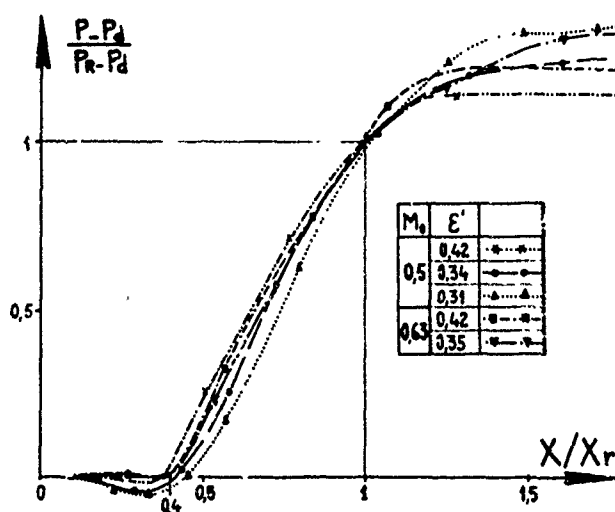


Fig. 9 - Normalisation des pressions pariétales.

La figure 9 présente une normalisation des pressions dans la zone décollée sous la forme

$$\frac{p - p_d}{p_r - p_d} = f\left(\frac{X}{X_r}\right)$$

La zone quasi isobare représente environ 40% de la zone décollée pour la carène considérée.

### 3.4.2 - Analyse des couches dissipatives

Des profils de vitesse à l'intérieur du bulbe déduits de mesures de pression d'arrêt sont présentés, figures 10 et 11 pour deux réglages ( $M_0, \epsilon'$ ).

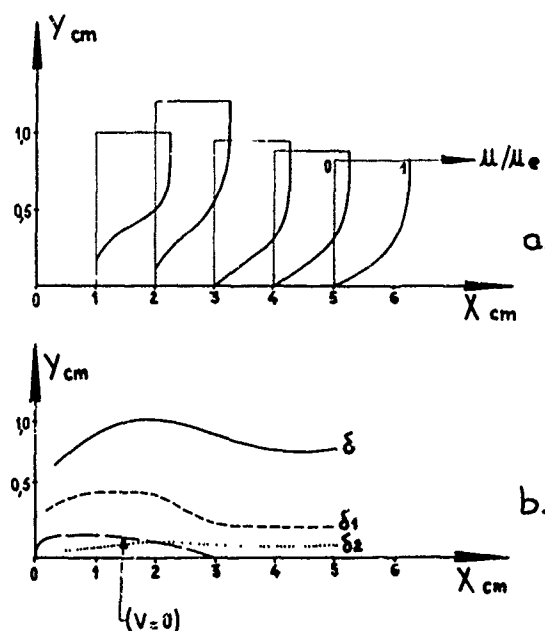


Fig. 10 - a) Profils de vitesse  
 b) Epaisseurs caractéristiques  $M_0 = 0,5, \epsilon' = 0,34$

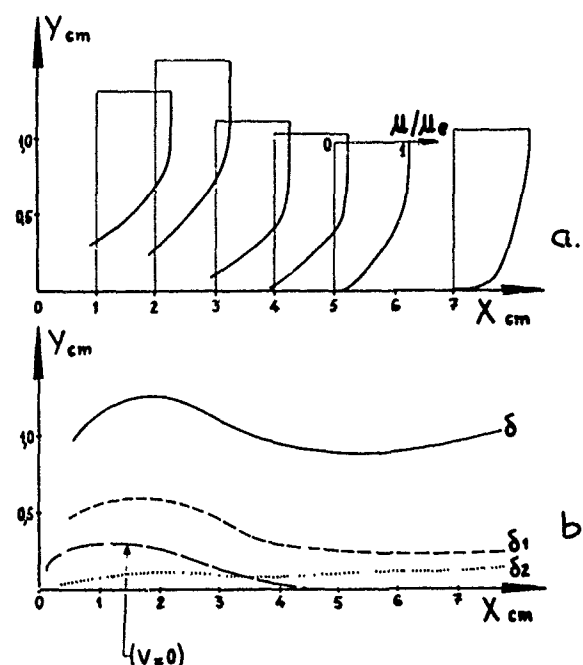


Fig. 11 - a) Profils de vitesse  
 b) Epaisseurs caractéristiques  $M_0 = 0,5, \epsilon' = 0,31$

La partie inférieure des profils de vitesse, dans la zone de courant de retour, n'est pas définie : l'exploration en pression d'arrêt n'a été effectuée que selon la direction de l'écoulement externe.

Sur ces mêmes planches sont présentées les évolutions des grandeurs caractéristiques :  $\delta_1$  épaisseur de déplacement,  $\delta_2$  épaisseur de quantité de mouvement et  $\delta$  épaisseur de la couche dissipative.

La figure 12 présente l'évolution en fonction de l'abscisse  $X$  sur la carène du paramètre de forme  $H = \delta_1 / \delta_2$  au voisinage du recollement pour quelques cas étudiés en soufflerie. Sur cette même planche sont rappelées les positions des points de recollement. On y constate que le recollement s'effectue pour un paramètre de forme voisin de 3.

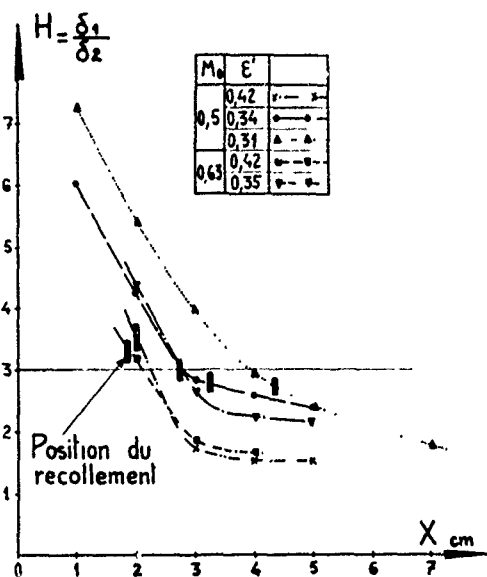


Fig. 12 - Evolution du paramètre de forme.

On constate, figure 13, que les diverses courbes d'évolution de  $H$  se regroupent en amont du point de recollement, si l'on porte  $H$  en fonction de  $X/X_r$  ; en fait, pour l'établissement de cette planche 13, les valeurs de  $X_r$  ont été assimilées aux valeurs de  $X$  pour lesquelles  $H$  est égal à 3 (figure 12).

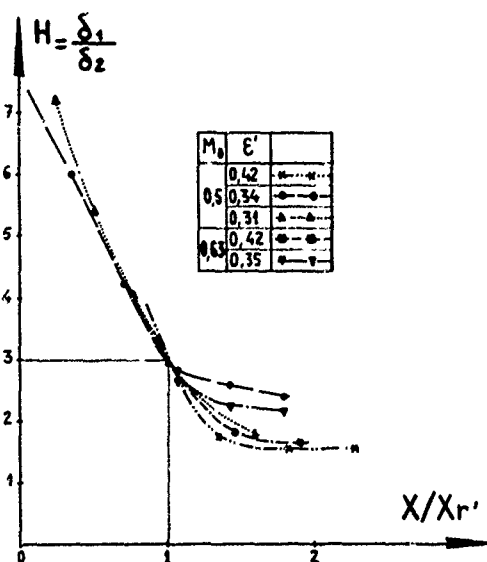


Fig. 13 - Evolution du paramètre de forme.

### 3.5 - Instationnarité du phénomène.

Une mesure de pression instationnaire a été effectuée sur la paroi supérieure de la carène, au voisinage du bord d'attaque. La planche 14 présente le spectre de pression relevé pour une configuration d'essai où se produit un décollement important ( $M_0 = 0,5$  ;  $E' = 0,31$ ).

Le pic qui apparaît à une fréquence de 380 Hz environ correspond à la fréquence propre du montage et non à un phénomène aérodynamique, comme le montre l'enregistrement de la réponse du capteur dont l'orifice a été obturé, qui présente lui aussi ce pic de 380 Hz. Des fluctuations sont détectées entre 100 Hz et 300 Hz. Au-delà et jusqu'à 20000 Hz (limite de la gamme de fréquences étudiée) aucune fréquence privilégiée n'est mise en évidence.

Le phénomène est donc pulsatoire, mais aucune fréquence n'est prépondérante et le niveau reste très faible.

Un film de visualisation stroboscopique à grande vitesse (1000 images/seconde) de ces décollements a également été réalisé.

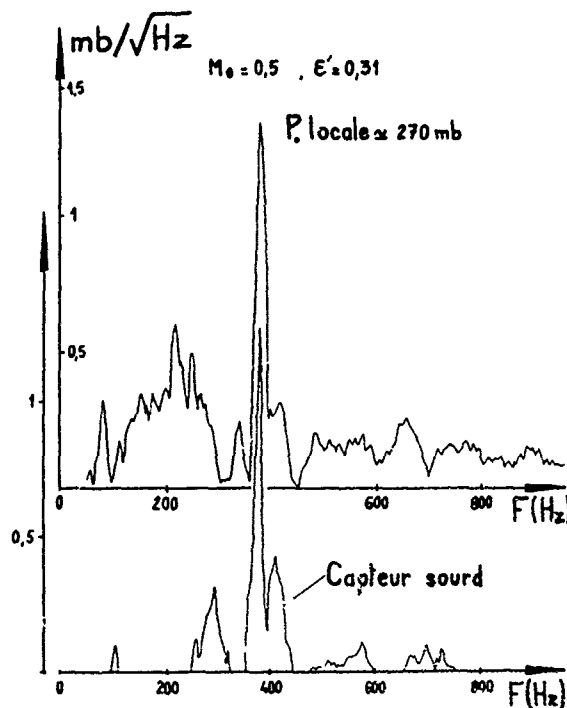


Fig. 14 - Spectres des fluctuations de pression.

### 4 - METHODE DE CALCUL.

#### 4.1 - Ecoulement sans décollement.

##### 4.1.1 - Hypothèses et pose des équations.

On considère un fluide parfait, en écoulement bidimensionnel plan compressible et isoénergétique, permanent, uniforme à l'infini amont et sans discontinuités. L'écoulement est donc isentropique et irrotationnel.

On introduit la fonction de courant  $\Psi$  définie par,  $\rho u = \partial \Psi / \partial y$ ,  $\rho v = -\partial \Psi / \partial x$  qui, compte tenu de l'équation de conservation

de la masse  $\text{div } \rho V = 0$ , vérifie

$$\Delta \Psi = \frac{1}{\rho} \text{grad } \Psi \cdot \text{grad } \rho \quad (A)$$

$V$  s'exprime à partir de  $\rho$  et des dérivées de  $\Psi$  par

$$V^2 = u^2 + v^2 = \frac{1}{\rho^2} \left[ \left( \frac{\partial \Psi}{\partial x} \right)^2 + \left( \frac{\partial \Psi}{\partial y} \right)^2 \right] \quad (B)$$

et  $\rho$  par l'expression

$$\frac{\rho}{\rho_0} = \left[ 1 + \frac{\gamma-1}{2} M_0^2 \left( 1 - \frac{V^2}{V_0^2} \right) \right] \quad (C)$$

obtenue à partir de l'équation d'Euler

$$\frac{d\rho}{\rho} + \frac{dV}{V} \text{ est de } \frac{d\rho}{\rho} + \frac{dV}{V} = \text{constante.}$$

Le problème se ramène donc au calcul de la fonction  $\Psi$

#### 4.1.2 - Conditions aux limites.

##### Ecoulement en atmosphère infinie.

Le domaine de calcul (fig.15) est simplement limité à la partie inférieure, par la rampe de compression. A l'infini, l'écoulement est uniforme, de vitesse  $V_0$ , sauf à l'aval, à l'intérieur de la prise d'air, supposée prolongée indéfiniment, où la vitesse  $V_0$  s'obtient facilement à partir du coefficient de débit  $\epsilon$  par la relation

$$\epsilon = \frac{H_b - H_a}{H_0} \times \frac{\epsilon(M_0)}{\epsilon(M_2)}$$

Pour le calcul numérique, il faut préciser les valeurs de la fonction  $\Psi$  sur les contours du domaine ; la référence  $\Psi = 0$  étant imposée sur la rampe de compression,  $\Psi$  s'écrit, à l'infini amont,  $\Psi = \rho_0 V_0 y$  ; sur la ligne de courant limitant le tube de courant capté  $\Psi$  a la

valeur  $\Psi_0 = \rho_0 V_0 H_0$  qu'elle garde sur toute la carène. A l'infini aval,  $\Psi$  s'écrit :

$$\Psi = \Psi_0 \times \frac{y - H_a}{H_b - H_a} \quad \text{à l'intérieur de la prise d'air}$$

et  $\Psi = \rho_0 V_0 [y - (H_c - H_0)]$  à l'extérieur.

Pour la frontière  $y = +\infty$ , il est nécessaire d'assurer la continuité de la fonction  $\Psi(x, y)$

lorsque  $x$  varie de  $-\infty$  à  $+\infty$ .

La fonction  $\Psi = \rho_0 V_0 y + (H_c - H_0) / \pi \cdot \text{Arctg}(\rho_0 y / x)$  répond bien à cette condition.

Pour simplifier le calcul numérique, on remplace, pour  $y = \infty$ , cette condition de Dirichlet par la condition de Neumann équivalente  $\partial \Psi / \partial y = \rho_0 V_0$  qui exprime l'uniformité de la vitesse à l'infini. (fig.16).

##### Ecoulement en soufflerie.

Le domaine de calcul est présenté sur la figure 17. On fait l'hypothèse que dans les plans d'entrée et de sortie, les écoulements sont uniformes, ce qui permet d'y exprimer les fonctions  $\Psi$  sous forme linéaire.

On choisit comme référence  $\Psi = 0$  sur la paroi inférieure de la soufflerie,  $\Psi$  prend alors la valeur  $\Psi_c = \rho_0 V_0 H_c$  sur la paroi supérieure, et la valeur  $\Psi_0 = \rho_0 V_0 H_0 = \Psi_0$  sur la carène,  $H_0$  représentant la hauteur du tube de courant pénétrant dans l'entrée d'air. (fig.18)

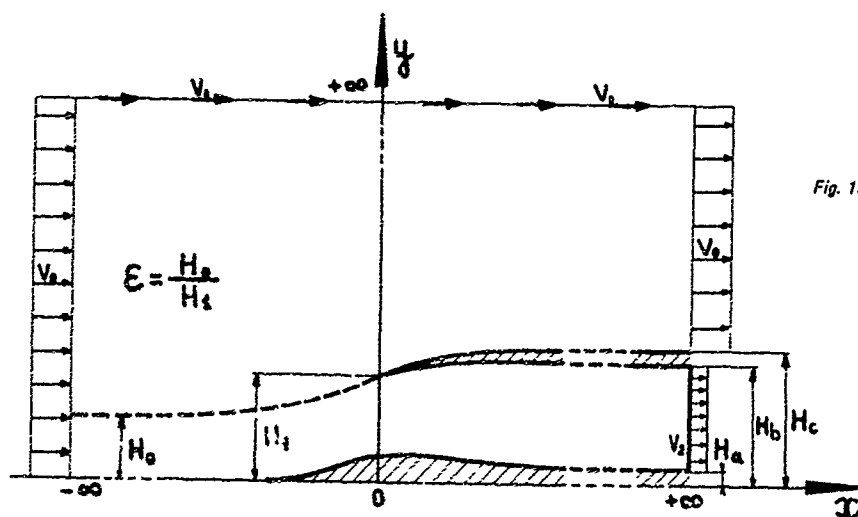


Fig. 15 - Domaine de calcul (atmosphère illimitée)

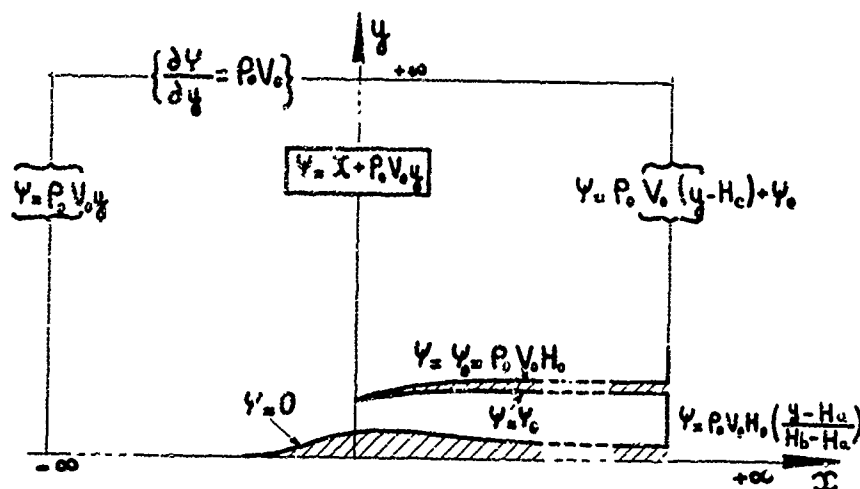


Fig. 16 - Conditions aux limites (atmosphère illimitée).

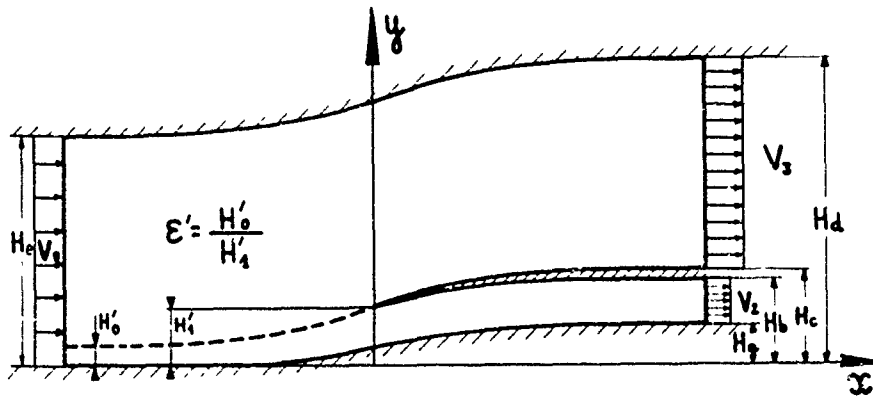
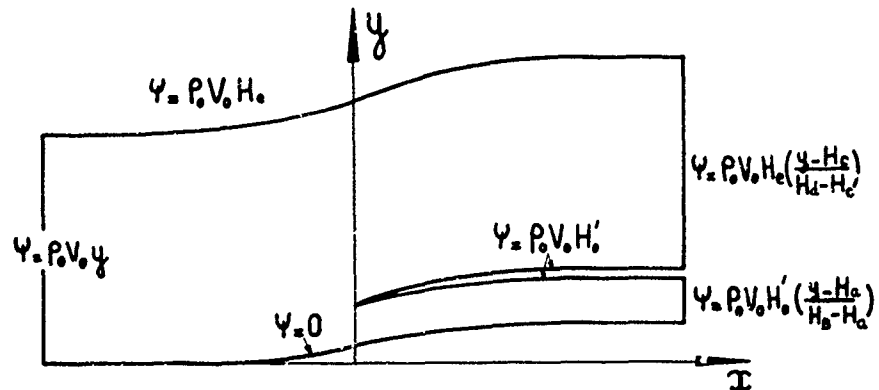


Fig. 17 - Domaine de calcul (essais en soufflerie).

Fig. 18 - Conditions aux limites (essais en soufflerie).



#### 4.1.3 - Méthode de résolution.

Le principe du calcul consiste à résoudre l'équation  $\Delta\psi = \frac{p}{\rho}$  par itérations successives, en considérant  $p$  comme une donnée dont la valeur est calculée, à chaque pas d'itération, à partir des résultats de l'itération précédente.

Après discrétisation, l'équation A est résolue par la méthode de Gauss-Seidel, avec introduction d'un paramètre de surrelaxation assurant la convergence.

Lors de la première itération, on suppose  $p = p_0$  et on est ramené à l'équation de Laplace  $\Delta\psi = 0$ .  $\psi$  étant alors définie en chaque noeud du maillage, on en déduit les dérivées  $\partial\psi/\partial x$  et  $\partial\psi/\partial y$  en chacun de ces points.

L'équation (B) permet alors d'obtenir la vitesse  $V$ , puis l'équation (C) donne la masse volumique  $\rho$ . Le deuxième membre de l'équation (A),  $(1/\rho) \cdot \text{grad } \psi \cdot \text{grad } p$  est ensuite calculé en chaque noeud du maillage, et on procède à une seconde itération.

En pratique, de 5 à 10 itérations sont nécessaires.

On trouvera, en annexe, des détails complémentaires sur la mise en oeuvre de cette méthode.

#### 4.2 - Calcul de l'écoulement, en présence d'un bulbe de décollement.

La méthode de calcul approché utilisée s'inspire de celle qui est présentée [3].

- on utilise une modélisation du bulbe de décollement dépendant de 2 paramètres : la longueur du décollement  $X_d$  et la pression de la zone isobare  $p_d$  ; à un couple de valeurs ( $X_d, p_d$ ) correspond donc une distribution de pression connue sur la carène, dans le décollement ;

- A partir de cette distribution donnée de pression sur la carène, on calcule par une méthode

inverse, la forme correspondante de la frontière de déplacement de la carène.

- Les valeurs correctes de  $X_d$  et  $p_d$  sont finalement déterminées par la prise en compte de conditions de compatibilité au point de recollement.

Ces trois points vont maintenant être successivement précisés :

##### 4.2.1 - Modélisation du bulbe de décollement.

Les courbes ci-dessous (Fig. 19) d'évolution de la pression et du paramètre de forme  $H$  dans le bulbe ont été déduits des figures 9 et 13.

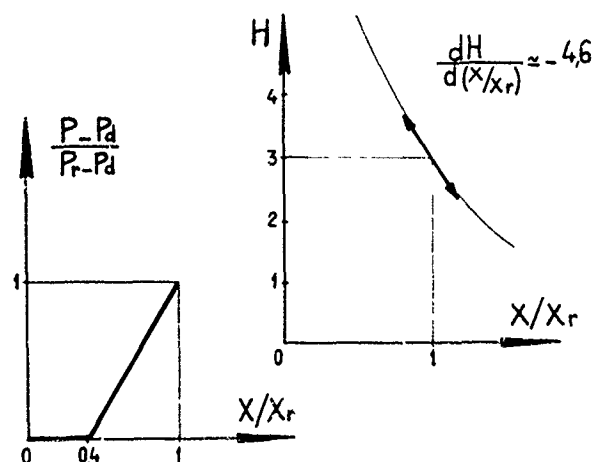


Fig. 19 - Modélisation du bulbe de décollement.

##### 4.2.2 - Méthode de calcul inverse.

Supposons donc que la distribution de pression  $p$  est donnée sur la paroi de la carène, dans le cas d'un bulbe de décollement. Nous ferons l'hypothèse que le gradient de pression  $\partial p / \partial x$

normal à la paroi est suffisamment faible, dans la zone décollée pour que la distribution de pression donnée soit aussi celle qui existe à la frontière du bulbe.

Il est possible, en utilisant ces données, de représenter le bulbe par une injection et une aspiration de fluide, à travers la carène :

$\partial\psi/\partial n = \rho V \cos \alpha = \beta(\mu) \cos \alpha$   
Les lignes de courant de l'écoulement potentiel fictif à l'intérieur du bulbe étant peu inclinées sur la carène,  $\cos \alpha$  est voisin de 1 et  $\partial\psi/\partial n \approx \rho V$ . La donnée de  $\beta$  fournit donc  $\partial\psi/\partial n$  en première approximation (fig.20).

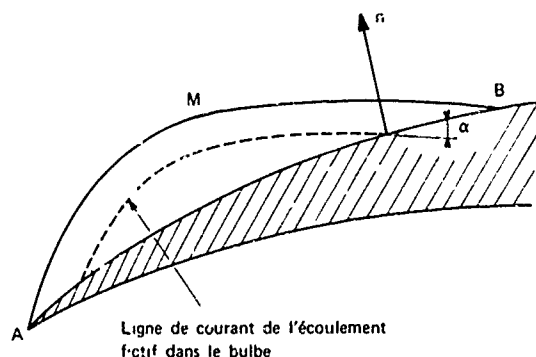


Fig. 20 - Schématisation du bulbe

L'intégration de l'équation A (§ 4.1) est effectuée, en modifiant les conditions aux limites, pour tenir compte de cette donnée de  $\partial\psi/\partial n$  sur la carène AB, (et de  $\psi = \psi_A = \psi_B$  au-delà de B). Ce calcul fournit une première approximation de la forme du bulbe, AMB, sur laquelle en général, la distribution de pression est différente de celle qui a été donnée. [4]

Des itérations successives peuvent alors être faites, en remplaçant la carène réelle AB, par la frontière AMB déterminée à l'itération précédente. Le calcul aura convergé et donné la forme correcte du bulbe lorsque la distribution de pression imposée sera bien retrouvée.

La figure 21 présente les divers lignes de courant obtenues au cours de 4 calculs itératifs.

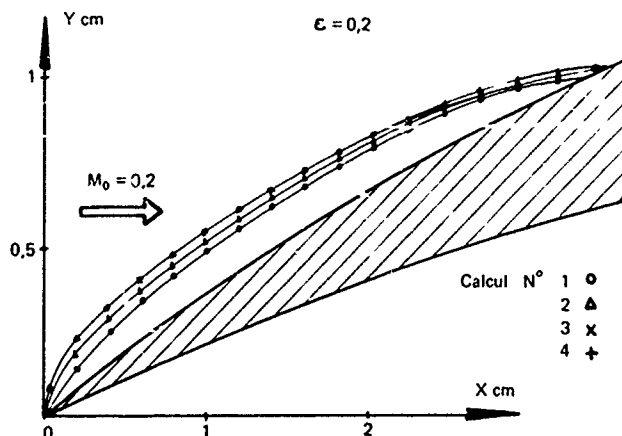


Fig. 21 -

#### 4.2.3 - Conditions au point de recollement.

On dispose pour le calcul de la couche dissipative de trois équations différentielles globales de continuité, de quantité de mouvement et d'énergie cinétique :

$$\begin{cases} \frac{d\delta_1}{dx} = \lg \theta & (a) \\ \frac{1}{\delta_1} \frac{d\delta_1}{dx} + (H+2) \frac{d \lg V}{dx} - \frac{1}{H} \frac{dH}{dx} = \frac{H}{\delta_1} \frac{C_f}{2} & (b) \\ \bar{H}(\bar{H}-1) \frac{d \lg V}{dx} - \frac{d\bar{H}}{dH} \frac{dH}{dx} = \frac{H}{\delta_1} (\bar{H} \frac{C_f}{2} - 2\bar{\Phi}) & (c) \end{cases}$$

ou  $\bar{H}$  est le paramètre de forme  $\delta_1/\delta_2$  et  $\bar{\Phi}$  la fonction de dissipation ( $\bar{\Phi} = \frac{1}{\rho V^3} \int_0^{\delta_2} \tau dv$ )

Au point de recollement où  $H$  est voisin de 3, la référence [3] indique que  $\bar{\Phi} \approx 0,01$ ,  $\bar{H} \approx 1,64$  et  $d\bar{H}/dH = 0$ . Par ailleurs en ce point le frottement est nul, le système écrit ci-dessus conduit à

$$\left( \frac{dV/V}{dx/\delta_1} \right)_e = - \left( \frac{2\bar{\Phi}H}{\bar{H}(\bar{H}-1)} \right)_{H=3} \approx -0,018 \quad (d)$$

(condition 1)

Cette relation définit inversement l'épaisseur de déplacement  $\delta_1$ , au recollement, si l'on connaît le gradient de vitesse locale.

En associant les équations (b) et (d) on définit la pente locale de la frontière de déplacement, au recollement.

$$(\lg \theta)_e = \left( \frac{d\delta_1}{dx} \right)_e = \left( \frac{\delta_1}{H} \frac{dH}{dx} + (H+2) \frac{d \lg V}{dx} \right)_e$$

L'expérience nous fournit le rapport  $\frac{dH}{d(X/\lambda_x)} = -4,6$  ce qui conduit à :

$$(\lg \theta)_e = - \left( \frac{\delta_{1e}}{\lambda_x} 1,55 - 0,09 \right) \quad (e)$$

(condition 2)

#### 4.2.4 - Méthode pratique de calcul.

La distribution de pression sur la carène, nécessaire pour le calcul inverse, est déterminée de la façon suivante :

- on se donne un couple de valeurs ( $X_r$ ,  $p_d$ ), ce qui définit complètement l'évolution de la pression dans le bulbe (courbe 1, fig.22).

- on raccorde cette courbe, à celle des pressions calculées en problème direct, sans tenir compte de la présence du bulbe de décollement (courbe 2); comme on le vérifiera par la suite la partie aval de cette courbe est en effet très voisine de la distribution expérimentale.

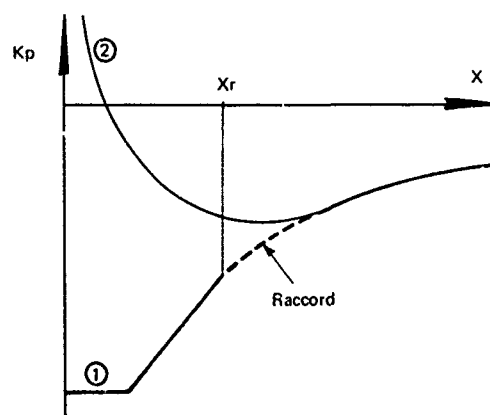


Fig. 22 - Calcul inverse : conditions aux limites.



Le calcul inverse donne la frontière de déplacement, et la distribution des vitesses sur cette frontière, et en particulier, en  $x = X_2$ ,  $\delta_1$ ,  $\theta$ ,  $V$  et  $dV/dx$ . Le problème est résolu, et la distribution de pression considérée ci-dessus est bien la distribution des pressions s'exerçant sur la carène si  $\delta_1$ ,  $\theta$ ,  $V$  et  $dV/dx$  vérifient les conditions (1) et (2) au point de recollement.

On procède de la façon suivante : pour diverses valeurs de  $X_2$  on recherche la valeur à donner à la pression  $p_d$  pour que la condition n° 1 soit satisfaite; la solution recherchée est constituée par celui des couples  $(X_2, p_d)$  précédents qui vérifie la condition n° 2.

On peut ensuite, connaissant les caractéristiques de la couche limite au point de recollement, calculer son évolution ultérieure sur la carène et reprendre le calcul général sur la carène modifiée, pour tenir compte de l'effet de déplacement de la couche limite.

## 5 - COMPARAISONS CALCUL-EXPERIENCE.

### 5.1 - Calcul sans prise en compte du bulbe de décollement.

Trois comparaisons calcul-expérience vont être présentées ; elles illustrent les possibilités et les limites du programme utilisé, dans la version où le bulbe de décollement n'est pas pris en compte.

$$M_0 = 0,5 \quad \epsilon' = 0,6 \quad (\text{Fig 23})$$

Ce cas correspond à l'adaptation de la carène pour  $M_0 = 0,5$ . La ligne de courant aborde la carène avec une direction voisine de la pente moyenne du bord d'attaque ; les déviations de part et d'autre du bord d'attaque sont minimes.

Dans ce cas il n'y a pas de décollement, et les résultats obtenus par le calcul sont très proches des relevés acquis en soufflerie.

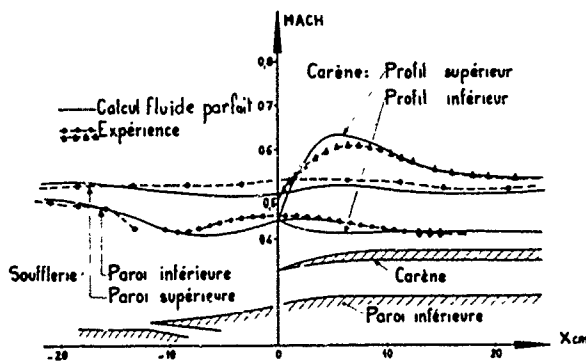


Fig. 23 - Evolution du nombre de Mach ( $M_0 = 0,5$ ,  $\epsilon' = 0,6$ )

$$M_0 = 0,5 \quad \epsilon' = 0,31 \quad (\text{Fig 24})$$

Le débit capté par la prise d'air est réduit par rapport au premier cas ; il y a contournement du bord d'attaque et décollement sur la partie externe de la carène.

Le calcul est en bon accord avec les résultats expérimentaux, sauf naturellement sur la paroi supérieure de la carène, au niveau du bord d'attaque ; la suritesse réelle, induite par le décollement, n'est pas indiquée par le calcul en fluide parfait, qui donne seulement un pic de suritesse très localisé. Comme on l'a indiqué précédemment, l'accord est encore acceptable entre calcul et expérience, sur la partie aval de la carène externe.

Une légère discontinuité du nombre de Mach est relevée sur la paroi inférieure de la veine au niveau du piège à couche limite. ( $x \approx -12$  cm) ; mais cette perturbation reste très locale et limitée.

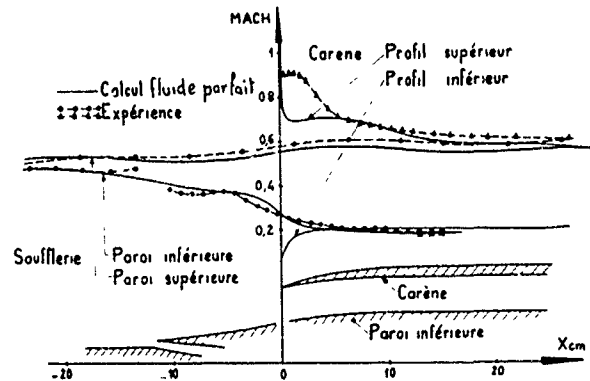


Fig. 24 - Evolution du nombre de Mach ( $M_0 = 0,5$ ,  $\epsilon' = 0,31$ )

$$M_0 = 0,63 \quad \epsilon' = 0,35 \quad (\text{Fig 25})$$

Cette figure présente les résultats expérimentaux qui mettent en évidence une suritesse largement supersonique sur la carène. Ce cas n'est donc pas justiciable, a priori, de la méthode de calcul utilisée ; cependant, le calcul a convergé car, en fluide parfait (et sans prise en compte du bulbe de décollement et de l'épaisseur de déplacement des couches limites), l'écoulement reste subcritique. Ces résultats de calcul ont été reportés sur la figure 25 qui met bien en évidence l'écart avec les valeurs expérimentales.

On peut noter que le maillage trop lâche, utilisé pour le calcul en fluide parfait ne permet pas de mettre en évidence la suritesse de bord d'attaque. Dans ce cas particulier, le calcul avec un maillage plus serré s'arrête dès l'apparition d'une vitesse supersonique dans la région du bord d'attaque.

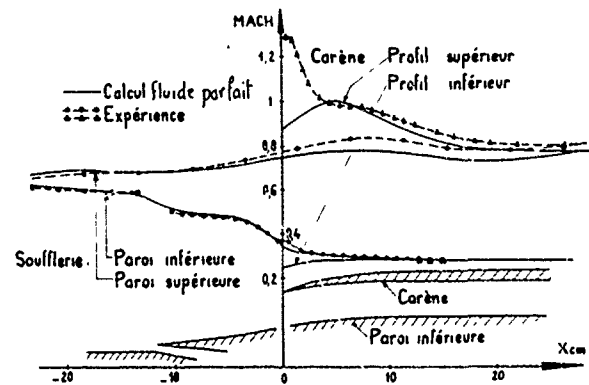


Fig. 25 - Evolution du nombre de Mach ( $M_0 = 0,63$ ,  $\epsilon' = 0,35$ )

### 5.2 - Calcul complet avec bulbe de décollement

Un exemple de comparaison calcul-expérience a été effectué pour la configuration ( $M_0 = 0,5$ ,  $\epsilon' = 0,31$ ).

Pour le calcul, plusieurs valeurs du paramètre  $X_2$  ont été essayées, comprises entre 22 et 66 mm. Pour les deux valeurs extrêmes, aucune valeur de la pression de la zone quasi-isobare  $p_d$  ne permet de vérifier la première condition.

Pour  $X_2 = 38, 44$  et  $50$  mm, la condition (2) est vérifiée pour deux valeurs de  $p_d$ ;

l'ensemble des deux conditions (1) et (2) n'est vérifié que pour  $X_c = 44$  mm et une seule valeur de  $P_d$ .

La figure 26 montre un assez bon accord entre les répartitions de vitesse obtenues expérimentalement et par le calcul.

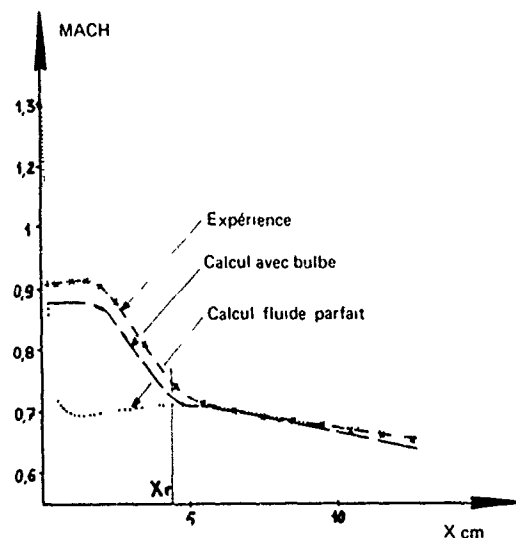


Fig. 26 - Prise en compte du bulbe ( $M_0 = 0,63$ ,  $\varepsilon' = 0,35$ )

Dans la zone quasi-isobare, au voisinage du bord d'attaque, le niveau de pression est retrouvé à environ 3 % près.

#### 6 - CONCLUSION.

L'étude du contournement d'un bord d'attaque aigu d'une carène a été abordée et les résultats actuellement disponibles viennent d'être présentés.

Sur le plan expérimental, un montage d'essai en courant plan a été mis au point dans la soufflerie S5 de Chalais-Meudon. Il permet de reproduire de façon assez réaliste les phénomènes qui prennent naissance, en subsonique, sur une carène à lèvre mince, d'un avion supersonique, lorsque le moteur ne demande qu'un débit réduit.

Les dispositions prises assurent une bidimensionnalité satisfaisante de l'écoulement et un bon contrôle des couches-limites de la veine d'essai.

Un programme de calcul, en écoulement subcritique, a été adapté au cas étudié expérimentalement ; la comparaison des résultats de calcul aux valeurs expérimentales est très satisfaisante lorsqu'il n'y a pas de décollement.

La détermination de lois semi-empiriques pour caractériser le développement d'un bulbe de bord d'attaque aigu a été réalisée pour une définition de carène particulière.

L'introduction de ces lois dans un programme de calcul d'écoulement de fluide parfait permet de restituer le profil de vitesse sur la carène ; ce qui fournit les pressions sur le bord d'attaque à moins de 5% près.

L'étude des limites d'application des lois retenues et l'utilisation des méthodes de calculs supercritiques restent à entreprendre pour généraliser les résultats obtenus.

Le caractère instationnaire du décollement de bord d'attaque a enfin été précisé, dans un cas particulier.

#### ANNEXE

##### Calcul en atmosphère illimitée

Pour le calcul en atmosphère illimitée, on opère une contraction du domaine d'intégration infini sur un domaine fini, par exemple  $-1 \leq \xi \leq +1$  et  $0 \leq \eta \leq 1$ , en faisant les changements de variables

$$x = g(\xi), \quad y = f(\eta)$$

Pour conserver une bonne précision de définition dans la région des lèvres de la carène ( $x$  et  $y$  voisins de zéro), on recherchera des fonctions  $x = g(\xi)$  et  $y = f(\eta)$  telles que

$$\left(\frac{\partial \psi}{\partial \eta}\right)_{\eta=0} \approx 1, \quad \left(\frac{\partial x}{\partial \xi}\right)_{\xi=0} \approx 1$$

[on a évidemment,  $\left(\frac{\partial \psi}{\partial \eta}\right)_{\eta=1} = \infty$  et  $\left(\frac{\partial x}{\partial \xi}\right)_{\xi=1} = \infty$ ]

Pour travailler numériquement sur des grandeurs finies, on remplacera la fonction  $\psi$  par la

fonction  $\chi$  définie par  $\psi = \chi + \rho_0 V_0 y$  ;

La condition aux limites  $(\partial \psi / \partial y)_{y=\infty} = \rho_0 V_0$

écrite précédemment entraîne  $(\partial \chi / \partial y)_{y=\infty} = 0$  ; la condition aux limites à afficher sur le contour

du domaine contracté  $\eta = 1$  est  $(\partial \chi / \partial \eta)_{\eta=1}$ .

$$\text{Or } \left(\frac{\partial \chi}{\partial \eta}\right)_{\eta=1} = \left(\frac{\partial \chi}{\partial y}\right)_{y=\infty} \times \left(\frac{dy}{d\eta}\right)_{\eta=1}$$

apparaît sous la forme indéterminée  $0 \times \infty$ . Il faut donc veiller à choisir un changement de variable  $y = f(\eta)$ , tel que  $\partial \chi / \partial \eta$  reste fini pour  $\eta = 1$ .

Cela a été obtenu, en prenant la fonction  $y = \frac{b_c \eta}{(1-\eta)^2}$  où  $b_c$  est un facteur de contraction voisin de l'unité, qui permet de dilater plus ou moins la région de la carène.

Avec cette fonction,  $\partial \chi / \partial \eta$  est nul pour  $\eta = 1$ , quel que soit  $\xi$ .

Pour le changement de variable  $x = g(\xi)$  nous avons choisi une fonction voisine  $x = \frac{a_c \xi}{(1-\xi^2)}$  (où  $a_c$  est également un facteur de contraction).

Dans le cas de la configuration essayée en soufflerie, le programme de calcul permet aussi des changements d'échelle dans la région du bord d'attaque de la carène de façon à améliorer la précision.

##### Écoulement à la paroi

Les noeuds du maillage utilisé pour le calcul numérique ne permettent pas la description exacte des parois de la carène ou de la soufflerie. Les grandeurs  $\mu$ ,  $\rho$ ,  $\mu$ ,  $\nu$  sur les parois doivent être obtenues par extrapolation à partir des valeurs calculées aux trois noeuds voisins du maillage. Ceci explique que, si les vitesses calculées dans le champ extérieur doivent toujours être subsoniques, il arrive que des vitesses supersoniques soient trouvées sur la carène, par exemple.

## REFERENCES.

- [1] WERLE H. - Sur l'écoulement du bord d'attaque d'un profil portant ; Rech. Aérosp. N° 1973-4, p.147-216.
- [2] VINCENT DE PAUL M. - Prévision du décrochage d'un profil d'aile en écoulement incompressible, dans "Fluid Dynamics of Aircraft Stalling" - AGARD Conf.Proc. n°102 (1972), mémoire n° 5.
- [3] DE BALLEUR J.C. et MIRANDE J. - Etude expérimentale et théorique du recollement bidimensionnel turbulent incompressible, dans "Flow Separation" - AGARD Conf. Proc. n°168 1975 mémoire n° 17.
- [4] LEYNAERT J. - Etude par analogie rhéoelectrique de prises d'air auxiliaires pour le décollage des avions supersoniques. La Rech. Aérosp. N° 119, (Juillet, Août 1967), p.47-49.

## ROUND TABLE DISCUSSION

**Mr Bore:** Good afternoon ladies and gentlemen. We reassemble for the final session of the symposium. First, I will remark that keener-eyed members of the audience might have noticed that this table is not very round so you will discern then, that the idea of a round table discussion is not to sit at a geometrically described table, but in fact to involve the members of the audience. That is the whole idea. We are not up here as a brains trust, we are here only to try to direct your thoughts and your contributions from the audience to the aim of the symposium. The whole idea of this symposium was to help aircraft designers to get a bit further advanced in their methods of load predictions. So we have on this occasion had a very much engineering- and aircraft-oriented program. Let us be reminded then, that all the way through our discussions, what we have to do is to underline the conclusions that have been presented by the authors and to formulate in our minds in what direction any further work should go.

As far as the procedure is concerned, I have four of the five session chairmen here. The session chairmen will be asked to present some brief thoughts about what they saw of their sessions. They will do this in turn. As soon as one session chairman has presented his thoughts, we will then immediately go to the audience and ask for their contributions. What we are hoping for here is that the authors and the people who haven't spoken yet will be the main contributors to this discussion.

First, I will call on Mr Coursimault, who was chairman of the first session, to say what he thought that session brought out.

**Mr Coursimault:** Thank you, Mr Chairman. From the first session, I would like to make two brief comments about two points I noticed. Obviously, one of the main problems which arose from this meeting was about our lack of understanding, our lack of capability to compute separated flows. From one of the papers, namely the paper about aerodynamics of wings with spoilers, I noticed that, although the flow around the profile in the two-dimensional case cannot be computed because we do not have any theory about separated flows, we can use empirical measurements of the two-dimensional case in a three-dimensional theory, provided that the characteristics of the airfoils with angle of attack, for instance, are still linear. We can successfully use linear theory to predict the behavior of the profile in the three-dimensional case. That is one of the points which arose from this paper. A second point I would like to bring up is about two other papers; one about the load prediction on the slats of the F28 airliner, and the paper about the sectional loads technique. These two papers dealt with trying to avoid the use of very complex pressure models. They tried to avoid also the expenses and difficulties connected with high Reynolds numbers. The paper about the sectional loads technique seems to me very promising and successful in avoiding the use of very complex pressure models with a great number of pressure measurements, but it seems to me that this kind of technique must be used with great care. That was pointed out by the authors, particularly the effects of the gaps between the different parts of the models, the effects of possible internal flows. I think that this kind of technique must be used with great care in order to lead to correct results. Probably with some cross-checks between this kind of technique and more conventional techniques, it is possible to achieve good results. The paper about prediction of loads on slats on the F28 airliner seems to me a very good example of how we can avoid the use of expensive models to make tests at high Reynolds numbers. The use of the two-dimensional model made possible tests at relatively high Reynolds numbers, and of course, higher than what could be done on the three-dimensional model. It proved to be successful in that case, but probably in other cases, the three-dimensional effects would be very important if, for instance, the sweep angle of the aircraft had been higher. This technique is probably limited in that respect. Also, I noticed the importance of the transonic conditions to predict the loads on the leading edge. The authors show that when the shock sweeps the slot between the leading edge and the main part of the profile, this significantly affects the loads and the slats. That is an important point to mention.

**Mr Parkinson:** I would like to thank Mr Coursimault for his remarks about our work on spoilers. I would like also to point out that even for the two-dimensional case, we can predict the loading within one unknown parameter, the base pressure coefficient, provided that it is a low speed problem and that the flow is completely separated, that the flow doesn't reattach, as in the example Mr Lang was talking about this morning.

**Mr Staudacher:** I should like to make some comments on the paper presented by Ewald and Franz. Part of this work is done in a working group which is instituted by the German Ministry of Defense and is called wings with controlled separation. I am a member of this party, and to your first comment, there are different types of models used, especially concerning the strake development. There is a force model, only taking 6 component force data; there is a partial load or sectional load model (VFW); and there are pressure distribution models. I can confirm for VFW that the method works. Perhaps another comment is that there was a question of Dr Hummel concerning Figure 15. Figure 15 is correct in the paper and is correct here. It was an error because the load is only taken in this case on the body, not on the wing, too, which was not clearly defined by Mr Ewald. It is true with the strake on that the load on the body behind the strake is lower.

**Mr Coursimault:** I would like to make additional comment about this technique. If you want to test configurations at extremely high angle of attack, heavily loaded models, the difficulties of this technique are still greater. You have extreme differences in pressure between different parts of the fuselage. In this case you have to be extremely careful to fill the gaps.

**Mr Staudacher:** Those tests were done up to angle of attack of  $30^\circ$ . I think the loads are high enough to say that one can do it in this way.

**Mr Coursimault:** Do you think that eventually, if the gaps are not correctly filled, you don't measure the loads exactly? Could you imagine that you have an influence of the air leakage on the external flow, the influence of internal flow on external flows? For example, a change of conditions in which separation occurs.

**Mr Staudacher:** You are speaking of leakage?

**Mr Coursimault:** Yes, leakage . . . If the gaps between the different parts of the model are not correctly filled, you could have some kind of blowing of the external flow by the internal parasitic flow.

**Mr Benepe:** I would like to comment on that same paper, the sectional load technique. It could be a very valuable diagnostic tool, not just for air loads, but for discerning what kind of flow field you actually have. I would like to see the work extended, as was mentioned, to the case of significant combinations of angles of attack and sideslip. That is where real problems occur. One can predict what the pressure distribution due to the vortex flow is. One can predict the lift, but cannot predict what occurs in sideslip. The sectional loads model may have a lot of benefits in that respect.

**Dr Schmidt:** I would like to make a comment on this technique also. I think we should be a little bit careful. Actually, from experiments we would like to get an insight in the physics. I would say it is very hard to get physics from total forces. So to really understand problems, I think we need pressure distributions and pressure measurements. All those techniques can only be for basic first test, on different configurations, to get an idea about the range of configurations which seem to be good or not. Finally, nothing can really give the physics except the pressure measurements.

**Dr Hensch:** In that light I would like to add another set of measurements. Very recently, we conducted some tests at NASA Langley, in connection with spin entry, for the Office of Naval Research. We were considering a configuration with a main wing on a fuselage with and without strakes. We obtained flow field information as well as loads. We found some startling things as a result of taking flow field data over the main wing with the strake and without the strake. The strake organized the flow, created large axial velocities that were just not there at all when the main wing was stalled, and so on. Therefore, I agree with the previous speakers. I like the sectional load technique for initial insight as to where difficulties are, because it is fast, and one doesn't have enormous amounts of data to sort out. Then one can go to pressure distribution measurements. I also think that the flow field data are exceptional in that respect. The near field with vortices present is very complex. In fact the speaker who was dealing with the close-coupled canard configurations demonstrated that, without flow field information, he would not have been able to come up with an analytical model. So please get flow field data, too.

**Mr Staudacher:** I would like to make a comment on what Dr Schmidt has said. I think the question is not partial load (or sectional loads) or pressure distributions, but sectional loads and pressure distributions.

**Mr Bore:** We will now move on to the second session which was really concerned with two separate topics. We will discuss these separately. The first of these topics was concerned with external stores, on which there were really about two and one-half papers. One was the account by Rudnicki and Waggoner of their semi-empirical correlation technique for predicting external stores, an account of a massive program of testing and correlation, which has to be an important way of approaching the topic because in many ways, maximum loads on things as complicated as stores, are not very amenable to theoretical calculation, for the reason that there are boundary layer separations and extremely complicated shapes and a lot of excrescences often in the store region. But, for all that, the paper by Ahmed on the prediction of external store and tip-tank loads showed a very brave attempt at computing these things by theoretical methods. So far, naturally, such a technique won't be adaptable to all the complexities of store load predictions, but nevertheless, going hand-in-hand with experimental measurements, it has to be regarded as an important contribution to methods of understanding how these loads vary. I'll turn it over to the audience now for further discussion on store loads.

**Dr Hensch:** I would like to mention a computer program that was developed by Nielsen Engineering for the Air Force Flight Dynamics Laboratory for prediction of store loads at subsonic speeds below the critical speed. An analytical

program was developed in conjunction with a massive test program, and we found after applying the program to a number of configurations, that we can do very well for a variety of stores, and we have no problems with changing the configuration, changing Mach numbers, or changing the parent aircraft. I would like to add also that we are in the middle of continuing the program into the supersonic speed range in conjunction again with an experimental program. I don't have the references here, and I can't give them to the audience, but if anybody wants to contact me, I can give them the references.

**Mr Bore:** It is also appropriate to mention that there is, as many of us know, an AGARD working group compiling a report on aerodynamic effects of external stores, in which the Nielsen method and the Rudnicki method, and now I have no doubt, the Ahmed method as well, will all be discussed. This report is due to go to the printers by next March and should be available to those people who have the right security classifications. It will be an AGARD Advisory Report.

**Mr Bobbitt:** The theoretical work related to the prediction of store loads started in the early 1950's. During the next decade, several methods were formulated for the prediction of store loads at subsonic speeds. The work has continued over the years though probably at a reduced pace. These methods, similar to the second paper shown today, do have a capability of giving fair-to-good predictions of the forces and moments, as well as the loads on a variety of store configurations. I think that if one is going to do an empirical job, such as represented by the first paper yesterday, that would be the place to start. The incorporation of empirical factors into one of the theoretical techniques is what's required to come up with a good overall engineering design method.

**Mr Slooff:** We did some work on store interference about three or four years ago which followed a line somewhere in between the completely empirical approach and the fully theoretical approach as presented by Dr Ahmed. We split up in a rather formal way, the total forces on the store into forces on the store in isolation and interference forces. The forces on the store alone were obtained from wind tunnel tests and thus included viscous effects. The interference forces were determined by means of a method very similar to the one used by Dr Ahmed. We calculated the average induced flow angularity at the position of the store and also the forces on the store due to the non-uniformity of the flow field. Combining those forces we got good results as far as, e.g., store trajectory predictions, were concerned. I think it is really a must for any store load prediction method to have the viscous effects on the store loads in, and I do not very well understand the extremely good correlation that Dr Ahmed obtained by using potential flow theory only, but maybe he can comment on that.

**Dr Ahmed:** My comments to the remarks of Mr Slooff are that the ARA results which I have shown depict forces and moments of the store assembly. No details were available about pressure distribution measurements on these models, and I do not think this has been done at ARA in England.

If one looks at the theoretical and experimental pressure distributions which we have obtained at DFVLR/Germany (Figures 4 and 5), the discrepancy due to viscous effects is noticeable in the corners, at the store aft end, and at all critical places where the body curvature changes rapidly.

I do not think it is a chance that our theoretical results for ARA model agree well with experiment. The ARA store is a slender body of revolution so that the viscous effects remain fairly small. It is not that the viscous effects are absent, but their effect on total forces remains for most configurations and attached flow, small. The results may not be as good if store configurations with a number of excrescences, winglets and fins are considered.

In the printed version of my paper a comparison of theoretical and ARA experimental results for moments acting on store assembly components is presented (Fig. 15). The effects of viscosity come out clearly in this illustration, their magnitude depending upon whether the component is a smooth body such as the store or provided with sharp leading edge such as the fins. The agreement, especially in the case of the fins is not so good, because by the slightest incidence one can expect flow separation at the fin leading edge.

**Mr Bore:** What this may mean is that perhaps the near future should see a good deal more comparison and interlacing of theoretical and empirical methods, so that both methods might be reinforced.

We will move on now to the second group of topics in the second session. These were concerned with vortex interactions, largely, although Mr Kloos gave us a comparison of various aerodynamic loads compared with flight test results, which is useful information. The three remaining papers were quite closely related; all concerned with the effects of vortices from canards, from leading edge extensions or strakes, and the very brave work on calculating the vortex jet wing interaction by viscous numerical analysis. One thing that came out in the earlier discussion, was that the canard vortex that was talked about by Mr Hale, burst early, and this appeared to be a different phenomenon from what I understood to be the case on the Viggen. It occurred to me that maybe the vortex from the canard helps to organize the vortex on the main wing, whether or not it is burst. Let's hear from the audience on that.

**Dr Scruggs:** I think in regard to the question of bursting, it was clear at the time of that paper, although we couldn't continue discussion, that one has to consider what one's definition of bursting is. It may simply be a confusion in terms here. Many of us regard bursting as the situation when the axial flow component of velocity in the vortex in fact goes to zero or reverses at any point in the vortex. What is observed by Mr Hale with his bubble machine, if you will, is a very sudden and large increase in apparent diameter of this vortical flow field. I am not sure whether we can see with the bubbles, that there is in fact axially reversed flow. Certainly, with the bubbles you can see large-scale turbulence but what this means in terms of the mean flow in the vortex is quite another matter. One's eyes can in fact get one in trouble in situations like this with flow visualization.

**Mr Dixon:** I would like to add a comment to that. Within the last year we have conducted tests at Lockheed Georgia Company with a canard configuration with spanwise blowing on the canard. We know very well that the canard does not have the vortex bursting, and we have gotten very favorable interaction results. This is a very large-scale test that we conducted. They are there and I wanted to make that comment.

**Prof. Young:** It struck me, as has been mentioned earlier, that in the use of the word bursting there may be a degree of confusion between what different people mean. When we talk of bursting of a wing-tip vortex, we generally have a picture of a vortex which initially for quite a distance is apparently very stable and does not diffuse very rapidly. Then at some stage, it begins to go wavy, usually under the influence of the other vortex, and in the process, a marked instability of the vortex as a whole develops and then it blows up fairly suddenly. However, it seems to me that what happens with regard to vortices from canards and slender wings is probably somewhat different. I think that there is evidence to show that the typical wing-tip vortex is basically not turbulent, even though it may spring from a flow which is initially turbulent. The turbulence is very rapidly damped out in the strongly swirling flow inside the vortex. The diffusion of the vortex as a whole is more nearly that of a laminar flow than a turbulent flow. If you calculate the rate of diffusion as Squire did many years ago, you find that it is in practice an order of magnitude less than anything you might predict if you assume that turbulent diffusion is taking place. So evidence suggests that the final instability process is then essentially of the vortex distorting and interacting with itself or with the other vortex. On the other hand, the kind of vortex flow from a canard, strake or junction passing over a wing that we were talking about yesterday, could well be one where the vortex is being continuously fed with turbulent flow from the wing surface, because it is passing over the wing surface, and it is fed with flow from the edge where it originated. This continual injection of turbulent flow into the vortex causes it to diffuse much more rapidly than it would otherwise do. It does not really burst, it just spreads a lot more rapidly than in the case of the wing tip vortex. I would guess that it can then preserve some kind of identity for quite a long way behind the wing, once it survives in a clear fashion back to the trailing edge.

**Mr White:** In answer to the direct question that you raised, Mr Bore, even if the vortex is burst, it does in fact still organize the flow over the surface of the wing. Leaving aside for the moment the aspect of whether the vortex bursts or does not burst, the primary effect of the canard vortex on the flow field on the main wing is that of its induced effect. If one considers the relative locations of the canard vortex to the main wing, it is probably at a distance greater than the core diameter of the vortex, regardless of core size. In that type of a condition, the induced effect of the canard vortex on the main wing is controlled by the Biot-Savart law. If we assume that the canard vortex itself conserves vorticity for the time period we are talking about, then whether or not the vortex is "burst" or not "burst", it will have the same induced effect on the flow field of the main wing, which would tend to organize it the same way whether it was a small core diameter or a large core diameter.

**Prof. Hummel:** I would like to point out that there exist a lot of experimental investigations on the physics of vortex bursting. I agree with Prof. Young that the vortex sheet rolling up from the leading-edge is not significantly disturbed by vortex bursting. The vortex sheet exists also downstream of the vortex bursting position. The abrupt changes of the flow field take place at the center of the vortex core which is the region within the rolled up vortex sheet. The retardation of the flow starts at the vortex axis and spreads downstream over the whole vortex core within the conical vortex sheet.

**Mr Benepe:** Several years ago there was published in Great Britain, a series of visual flow studies on some waverider wings which had slightly rounded planforms. I have forgotten the particular name that was given to the planforms, but one of them had a very peculiar characteristic with regard to the formation of the vortex. It was a turbulent vortex almost immediately from the apex, which turned out to be very stable and provided very large components of vortex lift. Apparently the phenomenon was similar to what is being seen on the canard of the particular configuration we are talking about. Whether or not a burst vortex exists in the sense of the mathematics of the problem, or whether or not a burst turbulent vortex exists in the sense of the physics as to what happens downstream, this turbulent vortex may be as useful or perhaps more useful and more stable than is the usual leading edge vortex.

**Mr Kloos:** I would like to confirm a few points of view expressed here. We at Saab-Scania have observed, that, before a real vortex burst occurs, there is a thickening of the core. We have, in instances where the canard was some distance

from the main wing, observed the fact that a thickening of the core over or behind the canard can occur. When the vortex enters the low pressure field over the main wing, the core thins out again and the vortex remains stable. We consider therefore at Saab-Scania the term "vortex burst" somewhat misleading because it isn't something that happens all of a sudden on a well organized vortex, but things are happening in the core as Prof. Hummel also says, i.e., it thickens and you can in certain cases halt this process.

**Prof. Hummel.** Some early experiments have shown that a pressure rise along the vortex core creates vortex bursting whereas a pressure drop avoids vortex bursting. The same result has been found by Mr Kloos on canard configurations.

Finally, I would like to express, that the bursting phenomenon occurring in the center of a vortex seems to me to be the link between a three-dimensional type flow separation with a certain preferred flow direction in the separated region and a two-dimensional type flow separation in which no flow direction is preferred. In the vortex flow over a slender delta wing a regular three-dimensional separation takes place upstream of the burst position and downstream of it the character of the flow turns over to a two-dimensional type flow separation.

**Mr Bore.** What we have concluded is that we have now got the makings of a strong attack on calculating and measuring the important flow field effects of vortices. We will move on now to Session 3, which will be introduced by Dr Zonars.

**Dr Zonars.** Session 3 was very informative and timely in that it enabled us to link the fluid dynamicist's work with aircraft flying today. The theories appear to be advancing with deliberate speed and commensurate with man's abilities to properly assume the correct parameters and solve the associated equations of motion. We have seen this trend in the well established theories of Drs Pandolph, Thiede, Headman and Gregorio. It is evident that the development of vortical theories is dominating the scene because of the very powerful lifting mechanism involved. In the excellent paper given by Mrs Manro, I detected a vortex bursting or instability at the trailing edge at  $12^\circ$  angle-of-attack. This problem needs to be addressed in terms of the stability parameters that provide a continuation of the lift. Our experiences with the vortex development and its instabilities, both from wind tunnel tests and confirming flight tests, have indicated that airplanes, particularly the highly maneuvering types, do have sideslip. Nevertheless, if an aircraft with a swept wing is flying at a sideslip angle, we find that the vortex from the forward wing will break down first, whereas the highly swept trailing wing will have a longer lived vortex stability. We have seen these vortices burst when the wing was into the stream (a lower sweep characteristic) and cause a traumatic maneuver. The air literally engulfed and went over the top of the vertical tail, destroying the directional stability. There have been endless problems, confirmed by both ground and flight tests, in trying to direct the aircraft as the pilot intends. I also want to commend Miss Landrum for her outstanding paper. It was an honest assessment of our abilities to calculate the flow fields and the loadings. If structural designers were present, they would feel a bit apprehensive about our ability to compute the compressive side of the flow field. These techniques can be improved, however, and Miss Landrum indicated logical ways in which the improvements could be undertaken. The experimental data and the theories we have seen during this session (from a user standpoint and from our involvement with the flight article itself) indicate a great disparity between what we have to work with and what we are experiencing in flight. We see a lot of high angle-of-attack data both from a purposely deflected control surface standpoint where the pilot is maneuvering and from other unknown sources. We have seen asymmetrical forces, both in the rolling and the yawing motions, which have a tendency under certain conditions to transfer the moments to the pitch axis. It merely indicates that today we have a serious lack of theory regarding the dynamics of motion with regard to the aircraft. We have seen cases, such as described in Mr Benepe's paper, where a dynamic increase in lift can result from the motion involved. We have also seen cases where the pilot has pulled up directly, wings level, at a very slight rate of increase (approximately  $3^\circ$  per second), and reached a high angle-of-attack. Because the asymmetrical forces were such that the yawing moment was to the left and the rolling moment to the right (even though in a wings level maneuver), the aircraft would lose energy, fall through straight, and recover. When the rate was increased to 8 or  $9^\circ$  per second, the story changed drastically to a very strong departure (nose slice). The aircraft subsequently went into a spin, and then had to be recovered. There are cases where this dynamic condition occurred at an angle-of-attack less than the one which we have observed in slow motion. We must not lull ourselves into a false sense of security, feeling that, because we do the maneuver faster, we are going to be safer. There are dynamics (time dependencies associated with the development of the flow field) that differ from side-to-side on an aircraft. These dynamics are presently unknown and are causing difficulties. What we currently need are parametric studies between the theoreticians and the experimentalists to help describe the sensitivities of the influencing factors, such as the configuration, the strakes proposed on highly maneuvering aircraft, sweep, aspect ratio, leading edge bluntness, sharpness, and the moments of inertia of the aircraft. Besides needing this type of data to assess the flight characteristics, we must have an active means (such as over-the-wing blowing) by which we can recover the aircraft from such awkward positions. The canard system also appears to be attractive once we can power it to play an active role in recovery. We have seen engines continue to run at  $90^\circ$  angle-of-attack. Perhaps we can harness that type of system to help us recover when the dynamic pressure has gone to zero. One particular area that we need to develop (as referred to by Dr Levinsky) is dynamic methods by which we can assess the high angle-of-attack dynamic flight mode. We have a good background from the standpoint of the high pitch rates obtained in our hypersonic shock tunnels. This method of assessing model angle-of-attack at a very rapid rate needs to be developed so that we can, in turn, assess the parameters involved. We must discover what these limiting maneuvering attitudes are as a function of configuration and of course, develop the methodology that accompanies it. The problem



is so complex at this time that probably the experimental techniques will dominate and suggest guidelines as to how we develop the theories.

**Dr Hemsch:** You really outlined a lot of work. I want to make a comment about one of the first things that you said, i.e., that you noticed that vortex bursting was accelerated on the windward fin when it was sideslipping and delayed on the leeward fin. I think that can be explained in terms of a wing that is not sideslipping, if you think about the leading edge sweep. The windward fin has now got a lower leading edge sweep, and therefore, a lower strength vortex.

**Dr Zonars:** That is absolutely correct.

**Dr Hemsch:** I noticed this very recently, when I was writing up a final report on missile aerodynamics. I found that if I took two opposing fins at a particular angle of attack with roll, so that one was a windward fin and one was a leeward fin, that I would have exactly the same situation that you are discussing. I also found something that was very interesting with respect to the external vortex coming back over the wing and organizing the flow in a situation for which the fins should have been stalled (the Mach number was subsonic). I found that the fuselage vortices, or body vortices, appeared to be organizing the flow, even though the body vortices on a missile are very large, and I was getting 25 to 35 percent greater lift on the fins than I could have gotten from a wing-alone curve. I thought that was very interesting and closely coupled, no pun intended, with the strake-wing type of configuration.

**Dr Zonars:** This type of flow is a very complex phenomenon, particularly when body characteristics dominate the departure characteristics. We have found from model tests in the Langley Research Facility that a large variety of wings could be installed without changing the departure characteristics. The flow is a function of body parameters and how they are integrated with the strake system. For that reason, I would encourage Mr. Atraghj to investigate simple geometries of a body of revolution to determine the interrelation between time dependent effects and pitch rates. We note that the same type of asymmetries are applicable to missiles.

**Dr Hemsch:** I mentioned an ONR contract. As part of the work for ONR we are now looking into vortex shedding from noncircular slender bodies under conditions of sideslip and angle of attack. I think that this work is going to shed a great deal of light on the phenomena you are talking about.

**Prof. Hummel:** I am wondering about Dr. Zonars' comment on wings with angle of sideslip and with vortex bursting. Dr. Redeker and I have published a paper in 1967 in which we have investigated the unsymmetrical vortex bursting and the corresponding effects on the rolling moment of wings having different aspect ratios. In this paper you will find diagrams in which the same combinations of incidence and sideslip are indicated and in which the sudden changes of aerodynamic characteristics due to an unsymmetrical burst condition are shown. I will give you the reference.\*

**Dr Zonars:** I appreciate your comments. I would also like to mention that we have taken much wind tunnel test data and the associated dynamic derivatives that are needed for assessing them on simulators. We were unable to duplicate the departure characteristics in our simulator, however, even though we used input data from both ground and flight tests and had pilots in the loop. We were only able to repeat these characteristics in flight in a few isolated cases.

**Dr Ericsson:** I would like to amplify what Dr. Zonars said in the introduction, i.e., the dynamic effect on the vortex and the vortex burst. In work that was done in Britain, it was shown that on the gothic wing where the leading edge sweep increases towards the trailing edge, vortex burst is delayed. There is also more vortex-induced load on the rear half of the wing than for a delta wing. This is because changes in the "tightness" of the vortex shedding are delayed also. The quasi-steady equivalent to this increase of L.E. sweep towards the T.F. is the "downwind" side of a yawing delta wing. The yaw rate will increase the effective sweep of the backward moving wing-half and decrease it on the forward moving half. This affects the location of burst (and also the vortex induced loads on the two wing halves) with associated large effects on the lateral stability. In regard to the stability in pitch it has been shown by Lambourne that if one cambers the delta wing, i.e., increases the local angle of attack towards the trailing edge, the vortex burst is delayed. On the other hand, if one bends the apex up, i.e., gives the delta wing negative camber, the vortex burst is promoted and occurs very early, near the apex. This is the quasi-steady equivalent to a pitching wing. One can, of course, expect especially dramatic effects when considering the dynamic cross-coupling between yaw, pitch, and roll degrees of freedom, as has been pointed out by Orlik-Rückemann.

\* D. Hummel, G. Redeker. "Über den Einfluss des Aufplatzens der Wirbel auf die aerodynamischen Beiwerte von Deltaflügeln mit kleinem Seitenverhältnis beim Schiebeflug. Jahrbuch 1967 der WG<sup>1</sup> R, 232-240.

**Mr Bobbitt:** Because of the limited time available for the paper of M.E. Manro dealing with the arrow wings, she didn't go into the loads data for control surfaces, particularly trailing edge control surfaces. There were several phenomena observed that are worth bringing to your attention, because they have been largely ignored here in the other presentations. One was the lack of effectiveness of the outboard control surface underneath the leading edge vortex. The other was the inboard control surface, which was generally effective, but did have the type of separation in the vicinity of the hinge line that one sees on control surfaces for wings of moderate sweep. We tried in the course of the study to make a prediction of the separated-flow effect but it was not very successful. There was a paper given earlier by Mr Thiede who mentioned in presenting his technique for calculating separated flows the possible application of his method to separation at control surface hinges. I think both of these problem areas are in really shabby shape in terms of being able to predict the control effectiveness. We really need to do a lot of work to obtain reliable predictive technique.

**Dr Zonars:** In the case discussed by M.E. Manro, I detected the burst or at least the beginning of an instability at the trailing edge. We have seen surface pressure distributions very similar to what she outlined. I would strongly recommend to her that a trail of smoke be put into the vortex, if resources permit. This approach provides a very dramatic means by which one may observe what is happening. At low angle-of-attack, the vortex looks just like a thread. As the angle-of-attack increases, it opens up and becomes very large. It would also be very appropriate to observe the instability further downstream or in the trailing edge region using the smoke trace method.

**Major Lang:** I was especially intrigued by some remarks by Mr Atraghji on the high angle of attack, asymmetrical vortex shedding, and his mention of the fact that very small protruberances play an important part. I would like to generalize and talk about the leading edge vortex phenomenon on airplane wings. We all know the importance of spanwise blowing and the shape of the leading edge. It seems to me we are on a threshold, with the potential, that by use of very small control surfaces (perhaps canard type) or spanwise blowing, that could be automated, we are maybe capable of controlling a lot of these phenomena that induce high loads and cause things like nose slice, wing rock, departure, etc. This also appears related to dynamic stall. I think the threshold is a very important one. I speak in terms of the possibility that, in the future, we can have airplanes that manoeuvre readily in what we now consider that dark, forbidding area of stall. This has great payoff and potential, and I think we have scratched the surface recently and should continue to dig for the answers.

**Mr Atraghji:** I would like to add briefly to the last remark by Major Lang. I have often read, in various newspaper articles on captured Soviet aircraft, that your adversaries planes are "dirty". Dirty in the sense that the surface finish is rough, rivet heads are left showing, skin panels are overlapping, etc. . . . a practice which, on this side, would be considered as a sloppy design.

However, in watching the Soviets play hockey I get a different impression. Far from being sloppy, one realizes very early on in the game, from the moves made by their various players, that they are invariably deliberate. Because I have a tendency to judge a nation's characteristics by the manner in which its sportsmen and sportswomen conduct themselves, and the Russians are no exception, I suspect that their deliberate approach in hockey is being applied in other walks of life also, like engineering, design and manufacture. I am wondering, therefore, if those dirty protruberances are in fact intentional.

Those who are sports minded among you would know that Team Canada is beginning to win more often in matches against the Russians not because we are playing better hockey now than they used to, but because the Canadians have learned to prevent the Soviets from organizing into a strategy before it becomes too powerful to overcome.

Have the Russians already discovered that such seemingly parasitic protruberances do in fact have their usefulness? Namely, in disrupting the organized vortex pattern I talked about earlier in my paper, when the effects on other parts of the structure of the aircraft from such a pattern become detrimental.

Of course, I cannot speak with certainty on this matter, since the available information is rather limited. I merely wish to make the plea that this alternative explanation to a 'dirty' aircraft be given some consideration instead of simply dismissing the product as yet another example of poor design by the other side.

**Mr Bore:** I think that we must move on from that topic, although I am afraid the discussion centered very largely on the first three-quarters of that session. Has anyone got comments on the interesting mathematical paper from Dr Medan on aerodynamic loads near cranks and apexes? We had a compliment on that from Mr Slooff. Is there any more to add on that? That stands as one complimented paper. There was one more, a brave vortex lattice approach for computing overall forces; this time, getting around to including jet efflux effects from Lucchi and Schmidt. Any comments on that? As there are none we will move on to Session 4. Dr McCroskey chaired part of that.

**Dr McCroskey:** I can't make many comments on the ones of yesterday afternoon, as I was occupied elsewhere. But this morning, we have seen a presentation on some semi-empirical modelling of dynamic stall, a paper addressing the hysteresis

of the lift and moment curves on airfoils and wings going into stall and back out again, the oscillating spoiler, and finally the leading edge bubble on a cowl. There is a certain commonality in these problems. In a more general sense there is also a commonality with the problems discussed yesterday, since the fluctuating loads very often involve separated flows. Most of the papers this morning dealt in some sense with separated regions that can be considered bubbles, that is, with free-shear layers which may or may not reattach. The reattachment characteristics of this separating zone are as important, if not more so, than the initial separation, and certainly the reattachment is very difficult to predict.

For the leading edge bubble, whether it is on an oscillating airfoil or wing, whether it is the mechanism for the abrupt leading edge stall that gives the large amount of hysteresis that was shown in Dr Levinski's paper, or whether it occurs on a cowl, it is not very difficult to predict where the bubble starts. Usually the flow is laminar at that point. Then the flow undergoes some sort of transition, and the real trick is to model semi-empirically or make any sensible calculations of how this turbulent free-shear layer will reattach. This remains virtually an unsolved problem, even in incompressible flow. I do not believe that compressibility effects are very important in the viscous flow, but the potential flow field outside, which is strongly coupled with these viscous shear layers, is highly susceptible to compressibility effects. Therefore, one has to include in any rational analysis some mechanism for allowing either high subsonic, transonic, or supersonic potential flow. There are Reynolds number effects as well.

To analyze these kinds of problems, one is going to have to develop some sort of viscous-inviscid interaction models that take into account turbulent shear layers, and that is a formidable challenge. In the meantime, we expect further refinements along the lines of the semi-empirical modelling, which makes very generous use of wind tunnel data. Of course, this has been a good technique for many years. We will continue that way, but we will need better fundamental understanding. I would like to offer the suggestion that there may be a role to be played by carefully conducted and carefully scrutinized Navier-Stokes solutions obtained with modern computational capabilities, even though you could not expect to get brilliant engineering solutions or something that is truly representative of the actual Reynolds numbers you want to study. These would probably be only for laminar flows at this point, or maybe with some simple turbulence modelling. One might use such solutions as a guide toward developing more simplified approximate analyses or to better correlate the data in the semi-empirical methods.

It will be important in the future to make systematic studies of the influence of compressibility on some of these separated regions, such as the leading edge bubbles. When the flow is incompressible, we are beginning to get a pretty good understanding of how it develops, such as the oscillating airfoil to which Dr Eriksen was referring. But when you examine this leading edge vortex shedding phenomenon at compressible Mach numbers, as the Mach number increases, there is some tendency for the shock-induced separation to interfere with the vortex development. But we do not know much about that, what really happens, so there is a need for more detailed experiments along these lines.

**Mr Dixon:** I hadn't noticed many comments about the rate of vorticity being shed from the leading edge which forms this bubble. I think it is rather obvious that the leading edge vortex from a dynamically stalled wing, or a steady-state vortex that is being controlled by some means, that the strength of the vortex is a function of the rate of vorticity being shed from the leading edge, which is in turn a function of the potential flow where the angle of attack of a wing or airfoil at that station and the vortex strength is also a function of the position it has assumed, so that in any dynamic flow it appears this should be taken into account. The vorticity shed is a function of time and also its position is a function of time.

**Prof. Young:** In your remarks, Dr McCroskey, you said that we had practically no information about the reattachment process. I think that it is true that we haven't got the whole story yet, but there is some work that has been done on this. There was a paper by Horton (ARC CP 1073) some years ago, where he developed his theory of the reattachment process, which seemed to line up pretty well with experiment. Inevitably, as we are dealing with turbulent entrainment, any theory must be semi-empirical. We have yet to arrive at the stage where we understand enough about turbulence to be able to have complete theories of it. But, the point that might be of interest here is that as long as the bubble is short the effect of sweep on bubbles we find is relatively small as far as the flow normal to the bubble is concerned. You can predict its characteristics from two-dimensional data just considering the flow normal to the bubble, including the condition under which the bubble will suddenly become long or burst. The main difference due to sweep, however, is that there is a very strong spanwise flow along the bubble, because a bubble in three-dimensions is no longer a closed volume. It is entraining flow from the main stream, and that flow must eventually go along the bubble. You can get velocities of flow in a bubble in the spanwise direction of the same order as the main stream velocity. These velocities can therefore be high and no doubt they account for the considerable effect on the pressure distribution underneath the bubble. There is therefore work going on, but I agree that there is a lot more work to be done.

**Dr McCroskey:** My choice of words was probably not correct, as it appears that I indicated that not much work had been done. I realize that there has been Horton's work on the bubbles, there are a number of other investigations that have been done, and still other work is in progress. On this question of the bubbles, I recently tried to take all the analyses that are available in the literature and apply them systematically to the same problem. I got quite a wide range of results, even though each method had originally compared favorably with some limited set of experimental data. I think the

methods are better in agreement for the relatively uninteresting case of when the reattachment occurs, than in the more significant case of when it fails to occur, that is to say, bubble bursting. When I considered several two-dimensional airfoils that are supposed to stall by the mechanism of leading edge bubble bursting, I found little correlation between the predictions of bubble-bursting incidence as a function of Reynolds number and the experimentally-observed stalling angles. Also, there was a very wide discrepancy among the different predictions. A lot of work has been done and we understand many of the general features of the leading edge bubbles. But quantitatively, it really remains an unsolved problem, even in two-dimensions for incompressible flow.

**Mr Benepe:** With regard to the effect of compressibility on the leading edge spilled vortex phenomenon, I recently had occasion to go back and look at data on blast wave effects, and it is interesting to observe, from the limited amount of data that does exist that there is an apparent compressibility effect in which the spilling of the leading edge vortex is indeed very much disturbed by the presence of a shock wave on an airfoil. The very high pressure rise obtained at sub-critical speeds disappears. I suspect that we will find that to be true for the cases that you people have been looking at.

**Mr McKeeney:** We have particular interest in the assessment of the unsteady flow on aircraft motion, particularly the wing rock. I have a question for the audience here, and that is, could anyone identify areas in the unsteady dynamic flow areas where full-scale flight tests might be of benefit, something we can look at?

**Mr Bore:** In the UK some work is being considered on both wind tunnel model and flight work in the wing rock, i.e., the low incidence wing rock, and also into the high incidence almost fully stalled wing rock situation which arises as a sort of dutch-roll coupling phenomenon. I would doubt that the UK will cover the whole field, and some American contributions in that same field would be welcome.

**Mr Coe:** In connection with the wing rock phenomenon at Ames Research Center, we have recently completed wind tunnel tests of a fighter-type configuration that was mounted on a sting with bearings so it could roll freely with only the restraint of a torsion bar spring which passed through the center of the sting. A variable damper was also installed in the system to guard against a diverging oscillation. There were pressure transducers installed on the model that will allow us to make some deduction of the motion dependence of the local pressures associated with the problem of wing rock. The configuration was selected because some flight data are available which will allow correlations to be made between the wind tunnel and flight data in the future. It is premature to say anything of the results of the investigation, other than that the model did oscillate freely, both at intermediate and at very high angles of attack. These tests were just recently completed and the data are now being analyzed. Hopefully, in the near future, the results will yield useful information on the problem of wing rock.

**Mr Bore:** Now we will move on to the remaining half of Session 4. The session chairman is not with us. That contained one paper by Mr Benepe on a whole range of aircraft manoeuvres and dynamic phenomena, which really we have been discussing in relation to the other topics to a good extent. Also, there were three papers on different approaches to buffet prediction. One of these used conventional wind tunnel models in order to correct the wind tunnel behaviour to flight behavior, and it looked quite promising. Another one was a computational method and the third even more mathematical. One might remark, that as far as fighters are concerned, it isn't buffet onset that is usually the worry, it is usually the prediction of moderate or even severe buffet, which is much more to the point as an aircraft limitation. From this point of view then, essentially any computational method has to include some account of the separated flow regime. This was attempted in the Redeker and Proksch method. It is a welcome attempt. Any comments from the audience on those?

**Mr Benepe:** I would like to remark on buffet predictions. I have been involved with many approaches, from very simple-minded ones which were similar to Mr Bore's first attempts 12 or 14 years ago, to very complicated ones where we are trying to predict what will occur over the entire structure. As far as a project is concerned, it is not a matter of predicting how much buffet intensity is going to occur, but whether or not you can get rid of it. The real aim that we have is to determine what the physics of the phenomena are, not necessarily to compute a solution, but to minimize the problem. We have accomplished that goal for a specific configuration. I would not generalize and say that the approach is going to work for all configurations, because I am sure that won't happen. The approach that Mr Butler is taking looks very fruitful. Computationally you can estimate what the model is going to do ahead of time in terms of its vibration modes. If you know enough about the airplane structural arrangement at that point in time, then you ought to be able to estimate what the airplane vibration modes are. If the model doesn't vibrate in modes similar to those of the airplane, then there is no point in taking the measurements, because you are not going to get anything significant. You have to have dynamic modelling in that sense. I do not say that you have to have a completely dynamically similar aeroelastic model in order to get useful project information. We used a technique very similar to that which Mr Butler is using, to arrive at a configuration which was significantly better with regard to buffet than all the others we had looked at. While we do have a need to get at the entire problem from the standpoint of aerodynamic loadings, the fatigue life of the airplane, etc., we also have another need, and that is to arrive at configurations during development which are worthwhile

**Dr Zonars:** I certainly want to commend the authors of that particular session on transient and fluctuating loads. In Mr Benepé's example, I am sure that there was a lot of configuration iteration before the buffet characteristics were suppressed. I think his paper was outstanding in telling us what the flight problems are. We must improve the correlation of our ground test and analysis methods in order to be able to predict what will happen to an aircraft in maneuvering flight. What we desperately need is configuration sensitive iterations, similar to Dr Median's cranks and configuration inputs. In a sense, it is like doing configuration studies in the same vein as described in the old NACA airfoil series that would define sensitivity for high angle-of-attack, etc.

**Mr Bore:** We have come to the end of our allotted time for this round table discussion. It has been filled with a great deal of constructive comments from the audience, which was exactly what it was meant to do. Looking back, it seems to me that we have had a session that has been very much directed to the problems of real aircraft with all their complexities, all their separated flows. From the point of view of aircraft designers, this must be regarded as a very relevant and practical symposium.

It is now my lot to thank all the people who are concerned in bringing about this symposium and making it work. As far as the organization at this end of the chain of communications is concerned, the administrative tasks were shared between Mr Lloyd Jones and Dr McCroskey. As far as I can see, the whole affair has run on rails and not quite the early days of BART-type rails. Everything has moved extremely slickly, and there have been no slip-ups whatsoever. They can rest happy. Of course, there have been the efforts of Mike Fischer, the Fluid Dynamics Panel Executive and the Secretary, Ann Marie, who has been looking after all manner of aspects of organization behind the scenes. Of course, we must never forget the other behind-the-scenes workers here, the projectionists and the sound technicians. Not too much seen here, although I suppose a bit heard, I have to thank very much the Program Committee, who assisted me in trying to find authors for papers and choosing which ones to have. They have done a fine job, but of course that fine job would be utterly impossible without the essential contributors, the authors. As far as I can see, they have done some really strong work. Finally, not least, the participants from the floor without whom the whole exercise would have been quite pointless. Thank you all very much for your attendance and your very constructive participation. For the final remarks, I would now like to ask the Chairman of the Fluid Dynamics Panel, Mr J.P. Hartsuiker, to wind up the final proceedings.

**Mr Hartsuiker:** I would like to say just a few words. Mr Bore, in thanking everybody who cooperated in the success of this meeting, more or less deliberately left out one person, i.e., the Chairman of the Program Committee, Mr Bore himself. From my own experience, I know that, in preparing a meeting which is to be successful, you have to put in a lot of time in preparing the call for papers, in reviewing the abstracts, in selecting the authors and guiding the whole meeting through a successful two and one-half days. I would like to thank Mr Bore for everything he did to make this meeting so successful. With that I would like to call this symposium closed.

REPORT DOCUMENTATION PAGE												
1. Recipient's Reference	2. Originator's Reference AGARD-CP-204	3. Further Reference ISBN 92-835-1238-4	4. Security Classification of Document UNCLASSIFIED									
5. Originator	Advisory Group for Aerospace Research and Development North Atlantic Treaty Organization 7 rue Ancelle, 92200 Neuilly sur Seine, France											
6. Title	PREDICTION OF AERODYNAMIC LOADING											
7. Presented at	The NASA Ames Research Center, Moffett Field, California, USA, 27-29 September, 1976.											
8. Author(s) Various			9. Date February 1977									
10. Author's Address Various			11. Pages 342 333									
12. Distribution Statement	This document is distributed in accordance with AGARD policies and regulations, which are outlined on the Outside Back Covers of all AGARD publications.											
12 Keywords/Descriptors												
<table border="0"> <tr> <td>Aerodynamic loads</td> <td>External stores</td> <td>Loads (forces)</td> </tr> <tr> <td>Predictions</td> <td>Flight tests</td> <td>Variations</td> </tr> <tr> <td>Aerodynamic forces</td> <td>Wind tunnel tests</td> <td>Design criteria</td> </tr> </table>				Aerodynamic loads	External stores	Loads (forces)	Predictions	Flight tests	Variations	Aerodynamic forces	Wind tunnel tests	Design criteria
Aerodynamic loads	External stores	Loads (forces)										
Predictions	Flight tests	Variations										
Aerodynamic forces	Wind tunnel tests	Design criteria										
14. Abstract												
<p>This FDP Symposium, held at NASA Ames Research Center, Moffett Field, California in September 1976, was primarily concerned with the fluid dynamic aspects of predicting aerodynamic loads on aircraft and their external stores, and in particular those loads that represent difficult design and operating problems. Emphasis was on theoretical and semi-empirical methods for determining the level and distribution of the expected loading, and on assessing and evaluating the accuracy of the predicted values through comparison with available experimental data from windtunnels or from flight tests.</p> <p>Four sessions were conducted: Experimental and Semi-Empirical; External Stores and Vortex Interactions; Calculation, Quasi-Steady Loads; and Transient or Fluctuating Loads. Following the last session, a Round Table Discussion was conducted, led by session Chairmen, in which all participants were invited to comment.</p>												

<p>AGARD Conference Proceedings No.204 Advisory Group for Aerospace Research and Development, NATO PREDICTION OF AERODYNAMIC LOADING Published February 1977 342 pages</p> <p>This FDP Symposium, held at NASA Ames Research Center, Moffett Field, California in September 1976, was primarily concerned with the fluid dynamic aspects of predicting aerodynamic loads on aircraft and their external stores, and in particular those loads that represent difficult design and operating problems. Emphasis was on theoretical and semi-empirical methods for determining the level and distribution of the expected loading, and on assessing and evaluating the</p> <p>P.T.O.</p>	<p>AGARD-CP-204</p> <p>Aerodynamic loads Predictions Aerodynamic forces External stores Flight tests Wind tunnel tests Loads (forces) Variations Design criteria</p>	<p>AGARD Conference Proceedings No.204 Advisory Group for Aerospace Research and Development, NATO PREDICTION OF AERODYNAMIC LOADING Published February 1977 342 pages</p> <p>This FDP Symposium, held at NASA Ames Research Center, Moffett Field, California in September 1976, was primarily concerned with the fluid dynamic aspects of predicting aerodynamic loads on aircraft and their external stores, and in particular those loads that represent difficult design and operating problems. Emphasis was on theoretical and semi-empirical methods for determining the level and distribution of the expected loading, and on assessing and evaluating the</p> <p>F.T.O.</p>	<p>AGARD-CP-204</p> <p>Aerodynamic loads Predictions Aerodynamic forces External stores Flight tests Wind tunnel tests Loads (forces) Variations Design criteria</p>
<p>AGARD Conference Proceedings No.204 Advisory Group for Aerospace Research and Development, NATO PREDICTION OF AERODYNAMIC LOADING Published February 1977 342 pages</p> <p>This FDP Symposium, held at NASA Ames Research Center, Moffett Field, California in September 1976, was primarily concerned with the fluid dynamic aspects of predicting aerodynamic loads on aircraft and their external stores, and in particular those loads that represent difficult design and operating problems. Emphasis was on theoretical and semi-empirical methods for determining the level and distribution of the expected loading, and on assessing and evaluating the</p> <p>P.T.O.</p>	<p>AGARD-CP-204</p> <p>Aerodynamic loads Predictions Aerodynamic forces External stores Flight tests Wind tunnel tests Loads (forces) Variations Design criteria</p>	<p>AGARD Conference Proceedings No.204 Advisory Group for Aerospace Research and Development, NATO PREDICTION OF AERODYNAMIC LOADING Published February 1977 342 pages</p> <p>This FDP Symposium, held at NASA Ames Research Center, Moffett Field, California in September 1976, was primarily concerned with the fluid dynamic aspects of predicting aerodynamic loads on aircraft and their external stores, and in particular those loads that represent difficult design and operating problems. Emphasis was on theoretical and semi-empirical methods for determining the level and distribution of the expected loading, and on assessing and evaluating the</p> <p>P.T.O.</p>	<p>AGARD-CP-204</p> <p>Aerodynamic loads Predictions Aerodynamic forces External stores Flight tests Wind tunnel tests Loads (forces) Variations Design criteria</p>

<p>accuracy of the predicted values through comparison with available experimental data from windtunnels or from flight tests.</p> <p>Four sessions were conducted: Experimental and Semi-Empirical, External Stores and Vortex Interactions; Calculation; Quasi-Steady Loads; and Transient or Fluctuating Loads. Following the last session, a Round Table Discussion was conducted, led by session Chairmen, in which all participants were invited to comment.</p> <p>ISBN 92-835-1238-4</p>	<p>accuracy of the predicted values through comparison with available experimental data from windtunnels or from flight tests.</p> <p>Four sessions were conducted: Experimental and Semi-Empirical, External Stores and Vortex Interactions; Calculation, Quasi-Steady Loads; and Transient or Fluctuating Loads. Following the last session, a Round Table Discussion was conducted, led by session Chairmen, in which all participants were invited to comment.</p> <p>ISBN 92-835-1238-4</p>
<p>accuracy of the predicted values through comparison with available experimental data from windtunnels or from flight tests.</p> <p>Four sessions were conducted: Experimental and Semi-Empirical, External Stores and Vortex Interactions; Calculation; Quasi-Steady Loads; and Transient or Fluctuating Loads. Following the last session, a Round Table Discussion was conducted, led by session Chairmen, in which all participants were invited to comment.</p> <p>ISBN 92-835-1238-4</p>	<p>accuracy of the predicted values through comparison with available experimental data from windtunnels or from flight tests.</p> <p>Four sessions were conducted: Experimental and Semi-Empirical, External Stores and Vortex Interactions; Calculation; Quasi-Steady Loads, and Transient or Fluctuating Loads. Following the last session, a Round Table Discussion was conducted, led by session Chairmen, in which all participants were invited to comment.</p> <p>ISBN 92-835-1238-4</p>



AGARD

NATO  OTAN

7 RUE ANCELLE · 92200 NEUILLY-SUR-SEINE  
FRANCE

Telephone 745.08.10 · Telex 610176

DISTRIBUTION OF UNCLASSIFIED  
AGARD PUBLICATIONS

AGARD does NOT hold stocks of AGARD publications at the above address for general distribution. Initial distribution of AGARD publications is made to AGARD Member Nations through the following National Distribution Centres. Further copies are sometimes available from these Centres, but if not may be purchased in Microfiche or Photocopy form from the Purchase Agencies listed below.

NATIONAL DISTRIBUTION CENTRES

**BELGIUM**

Coordonnateur AGARD VSL  
Etat-Major de la Force Aérienne  
Caserne Prince Baudouin  
Place Dailly, 1020 Bruxelles

**CANADA**

Defence Scientific Information Service  
Department of National Defence  
Ottawa, Ontario K1A 0Z2

**DENMARK**

Danish Defence Research Board  
Østerbrogades Kaserne  
Copenhagen Ø

**FRANCE**

O.N.E.R.A. (Direction)  
29 Avenue de la Division Leclerc  
92 Châtillon sous Bagneux

**GERMANY**

Zentralstelle für Luft- und Raumfahrt-  
dokumentation und -information  
Postfach 860880  
D-8 München 86

**GREECE**

Hellenic Armed Forces Command  
D Branch, Athens

**ICELAND**

Director of Aviation  
c/o Flugrad  
Reykjavik

**ITALY**

Aeronautica Militare  
Ufficio del Delegato Nazionale all'AGARD  
3, Piazza Adenauer  
Roma/EUR

**LUXEMBOURG**

See Belgium

**NETHERLANDS**

Netherlands Delegation to AGARD  
National Aerospace Laboratory, NLR  
P.O. Box 126  
Delft

**NORWAY**

Norwegian Defence Research Establishment  
Main Library  
P.O. Box 25  
N-2007 Kjeller

**PORTUGAL**

Direccao do Servico de Material  
da Forca Aerea  
Rua de Escola Politecnica 42  
Lisboa  
Attn: AGARD National Delegate

**TURKEY**

Department of Research and Development (ARGE)  
Ministry of National Defence, Ankara

**UNITED KINGDOM**

Defence Research Information Centre  
Station Square House  
St. Mary Cray  
Orpington, Kent BR5 3RE

**UNITED STATES**

National Aeronautics and Space Administration (NASA),  
Langley Field, Virginia 23365  
Attn: Report Distribution and Storage Unit

THE UNITED STATES NATIONAL DISTRIBUTION CENTRE (NASA) DOES NOT HOLD  
STOCKS OF AGARD PUBLICATIONS, AND APPLICATIONS FOR COPIES SHOULD BE MADE  
DIRECT TO THE NATIONAL TECHNICAL INFORMATION SERVICE (NTIS) AT THE ADDRESS BELOW

PURCHASE AGENCIES

*Microfiche or Photocopy*

National Technical  
Information Service (NTIS)  
5285 Port Royal Road  
Springfield  
Virginia 22151, USA

*Microfiche*

Space Documentation Service  
European Space Agency  
10, rue Mario Nikis  
75015 Paris, France

*Microfiche*

Technology Reports  
Centre (DTI)  
Station Square House  
St. Mary Cray  
Orpington, Kent BR5 3RF  
England

Requests for microfiche or photocopies of AGARD documents should include the AGARD serial number, title, author or editor, and publication date. Requests to NTIS should include the NASA accession report number. Full bibliographical references and abstracts of AGARD publications are given in the following journals:

Scientific and Technical Aerospace Reports (STAR),  
published by NASA Scientific and Technical  
Information Facility  
Post Office Box 8757  
Baltimore/Washington International Airport  
Maryland 21240, USA

Government Reports Announcements (GRA),  
published by the National Technical  
Information Services, Springfield  
Virginia 22151, USA

RECEIVED

APR 11 1970



NTIS - Input Branch

Printed by Technical Editing and Reproduction Ltd  
Harford House, 7-9 Charlotte St, London: W1P 1HD